

Lawrence Berkeley National Laboratory

Lawrence Berkeley National Laboratory

Title

Project X

Permalink

<https://escholarship.org/uc/item/9wx8b6zp>

Author

Holmes, Steve

Publication Date

2013-07-02

Project X

Edited by Steve Holmes¹, FERMILAB

Russ Alber¹, David Asner⁴, Pushpa Bhat¹, Mark Champion¹, Brian E. Chase¹, Paul Derwent¹, Keith Gollwitzer¹, Stuart D. Henderson¹, David E. Johnson¹, Marc Kaducak¹, Robert D. Kephart¹, Jim Kerby¹, Arkadiy Klebaner¹, Ioanis Kourbanis¹, Andreas Kronfeld¹, Valeri A. Lebedev¹, Anthony F. Leveling¹, Derun Li², Shekar Mishra¹, Sergei Nagaitsev¹, Peter N. Ostroumov³, Ralph J. Pasquinelli¹, Jim Patrick¹, Robert K. Plunkett¹, Lionel R. Prost¹, John S. Reid¹, Vic E. Scarpine¹, Alexander Shemyakin¹, Nikolay A. Solyak¹, Jim Steimel¹, Bob Tschirhart¹, Bob Webber¹, Manfred Wendt¹, and Vyacheslav P. Yakovlev¹

¹ Fermi National Accelerator Laboratory, ² Lawrence Berkeley National Laboratory, and
³ Argonne National Laboratory, ⁴ Pacific Northwest National Laboratory

Part 1, Accelerator Reference Design, Physics Opportunities, Broader Impacts

Part 2, Physics Opportunities

Part 3, Broader Impacts

Date June 23, 2012

This work was supported by the Director, Office of Science, Office of Fusion Energy Sciences, of the U.S. Department of Energy under Contract No. DE-AC02-05CH11231.

Project X

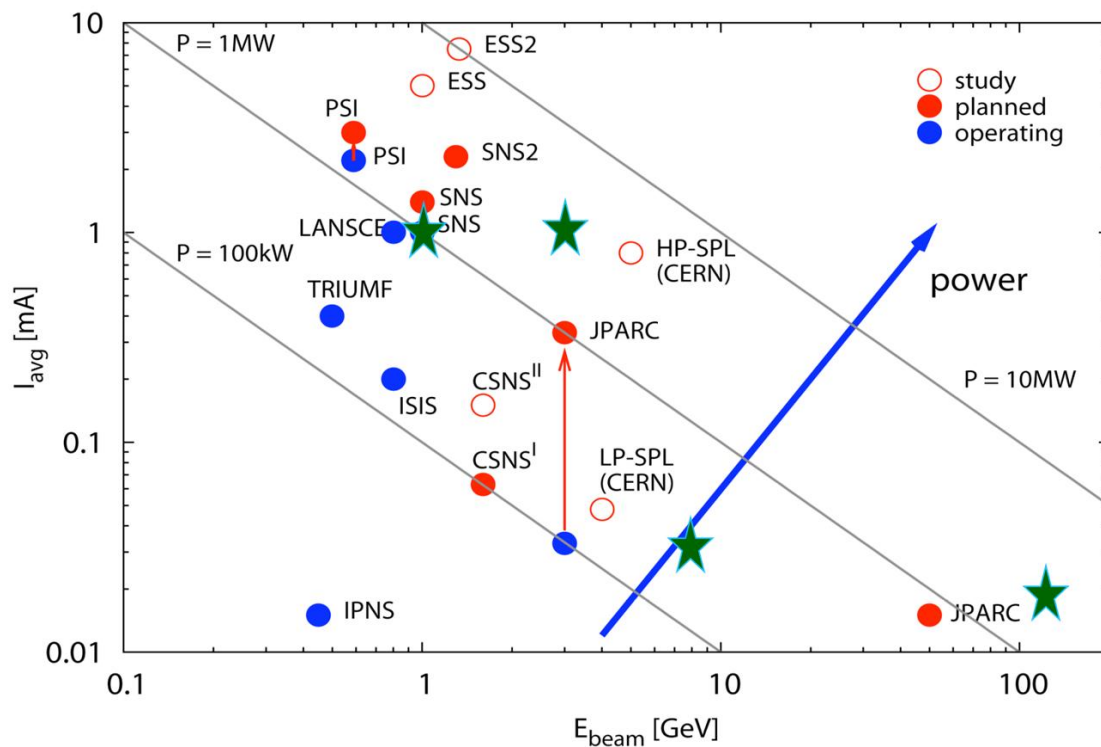
**Accelerator Reference Design, Physics Opportunities,
Broader Impacts**

June 2013

Preface

Particle physics has made enormous progress in understanding the nature of matter and forces at a fundamental level and has unlocked many mysteries of our world. The development of the Standard Model of particle physics has been a magnificent achievement of the field. Many deep and important questions have been answered and yet many mysteries remain. The discovery of neutrino oscillations, discrepancies in some precision measurements of Standard-Model processes, observation of matter-antimatter asymmetry, the evidence for the existence of dark matter and dark energy, all point to new physics beyond the Standard Model. The pivotal developments of our field, including the latest discovery of the Higgs Boson, have progressed within three interlocking frontiers of research—the Energy, Intensity and Cosmic frontiers—where discoveries and insights in one frontier powerfully advance the other frontiers as well.

Project X is an opportunity to continue this legacy through developing a world-leading Intensity Frontier facility at Fermilab that can support a very diverse and rich physics program in this quest. The Project X proton accelerator is ready to construct, and will leverage the substantial investment the U.S. research enterprise has made broadly in developing superconducting radio frequency (SCRF) accelerator technology. This accelerator technology is the most efficient mechanism to prepare and accelerate beams of charged particles and has excellent scaling properties for delivering very high power beams. Laboratories worldwide have now embraced SCRF as core technology for leading facilities in material science, energy research, nuclear physics and particle physics. In the domain of particle physics, SCRF is the enabling technology for both the highest energy beams that drive the Energy Frontier and the highest intensity beams that drive the Intensity Frontier. A key metric for the Intensity Frontier, including a variety of existing and planned proton-beam future facilities, is beam power, and the worldwide power landscape is illustrated in the figure opposite. It is clear from this figure that megawatt-class beam facilities are the emerging standard, and that Project X (green stars) establishes a world leading facility enabled by SCRF accelerator technology.



Currently operating, planned, and under-study proton-beam facilities. Beam energy and average current are on the horizontal and vertical axes; the diagonal lines are contours of constant beam power. The Project X footprint is indicated by the green stars. Figure courtesy M. Seidel, PSI.

The Intensity Frontier research program enabled by Project X can address some of the most compelling and fundamental questions in particle physics today including:

Are there new forces in nature? Experiments have established flavor-changing processes in quarks and neutrinos, so it seems conceivable that charged leptons change flavor too. With Project X, one can search for these phenomena via muon-to-electron conversion and related processes. Many of the theoretical ideas unifying forces and flavor violation anticipate baryon-number violation, and Project X can extend the limits on neutron-antineutron oscillations by orders of magnitude. These same ideas posit measurable flavor-changing neutral currents that may amplify rare decays such as (charged and neutral) $K \rightarrow \pi \nu \bar{\nu}$.

Are there new properties of matter? According to the Sakharov conditions, the baryon asymmetry of the universe requires CP-violating interactions, but their strength in the Standard Model is insufficient to account for the observed excess. It is not known whether the missing CP violation takes place in the neutrino sector or the quark sector. Project X will aid both searches, by increasing the reach of neutrino oscillation experiments and by enabling a new suite of searches for nonzero electric dipole moments (EDMs). The latter program is broad, looking for an EDM of the neutron, proton, muon directly, and the electron through isotopes produced by Project X.

Are there new dimensions? Many popular extensions of the Standard Model introduce extra dimensions: in the case of supersymmetry, the dimensions are fermionic. The space of non-standard interactions opens up possibilities for the interactions mentioned above: quark and neutrino CP violation and quark-flavor-changing neutral currents with supersymmetry, and flavor-changing neutral currents from a warped fifth spatial dimension. Rare kaon decays, EDMs, and neutron-antineutron oscillations are closely tied to these possibilities.

In addition to probing these fundamental questions the Project X research program includes experiments that can test and enrich our understanding of quantum chromodynamics and the electroweak theory.

The Project X accelerator architecture presents opportunities to stage construction of the complete facility if necessary, with a robust research program at the first stage and each successive stage growing both the versatility of beams available and the intensity of those beams. A key and unique characteristic of the Project X complex is that the multiplicity of beams required by the research program can largely be provided *simultaneously*, enabling multiple experiments to proceed in parallel. Inspired by the research opportunities of Project X and the maturity of SCRF technology, the High Energy Physics Advisory Panel (HEPAP) in a recent review of facilities¹ characterized Project X as being “absolutely central” to the future of particle physics and “ready to initiate construction” in terms of technical maturity.

Project X also provides opportunities for research beyond the domain of particle physics. These potential Broader Impacts include an opportunity to provide irradiation resources for the study of materials important to energy applications and provision of low energy muons for muon spin rotation experiments which can incisively probe the magnetic properties of materials.

The three parts of this book form a comprehensive discussion of Project X. Part 1 is the Reference Design Report (RDR) for the Project X accelerator complex. Part 2 describes the Project X Particle Physics Research Program opportunities. Part 3 describes the Broader Impacts opportunities realized in irradiation resources from a spallation target and low energy muons to support muon-spin-rotation experiments (as the only such facility in the US) for materials science research.

¹HEPAP Facilities Subpanel, “Major High Energy Physics Facilities, 2014-2024, Input to the prioritization of proposed scientific user facilities for the Office of Science”, March 2013
http://science.energy.gov/~media/hep/hepap/pdf/Reports/HEPAP_facilities_letter_report.pdf

Project X Reference Design Report

V1.02
June 2013

The Project X Collaboration:

Argonne National Laboratory
Brookhaven National Laboratory
Cornell University
Fermi National Accelerator Laboratory
Lawrence Berkeley National Laboratory
Michigan State University
North Carolina State University

Oak Ridge National Laboratory/SNS
Pacific Northwest National Laboratory
SLAC National Accelerator Laboratory
University of Tennessee
Thomas Jefferson National Accelerator Facility
ILC/America's Regional Team

Bhabha Atomic Research Center, Mumbai

Raja Ramanna Center for Advanced Technology,
Indore

Inter-University Accelerator Center, Delhi

Variable Energy Cyclotron Center, Kolkata

Edited by:

Stephen D. Holmes/Fermi National Accelerator Laboratory

Table of Contents

I	INTRODUCTION	5
I.1	Evolution of the Reference Design	6
I.2	Assumptions.....	7
I.3	Facility Scope and Staging	8
II	PERFORMANCE GOALS	11
II.1	Technical Goals.....	11
II.2	Operational Scenarios and Beam Formatting	12
III	ACCELERATOR FACILITY DESIGN	17
III.1	CW Linac	18
III.1.1	Warm Front End.....	18
III.1.2	CW Linac Physics Design	26
III.1.3	CW Linac – Cryomodule Requirements	34
III.1.4	CW Linac – Beam Dynamics	36
III.2	1 GeV Beam Handling	40
III.2.1	Transport Line Requirements and Physics Design	40
III.2.2	H ⁻ Transport to 3 GeV Linac	43
III.2.3	H ⁻ Transport to Experimental Areas and Booster.....	45
III.2.4	Beam Loss	46
III.2.5	Provisions for sub-GeV proton based research	47
III.3	3 GeV Beam Handling	48
III.3.1	Transport Line Requirements and Physics Design	48
III.3.2	Beam Loss	49
III.3.3	H ⁻ Dump	52
III.3.4	H ⁻ Transport to Pulsed Linac.....	53
III.3.5	H ⁻ Transport to Experimental Area.....	54
III.3.6	Splitter/Lambertson Optics.....	55
III.4	3-8 GeV Pulsed Linac.....	56
III.4.1	Linac Parameters.....	56
III.4.2	Accelerating Cavities and Cryomodules.....	57
III.4.3	Pulsed Linac – Beam dynamics	58
III.4.4	RF Requirements and LLRF	61
III.5	8 GeV Transport Line	62
III.5.1	Transport Line Requirements and Physics Design	62
III.5.2	Beam Loss	63

III.5.3	H ⁻ Linac Dump	64
III.5.4	H ⁻ Transport to Recycler.....	65
III.6	Recycler/Main Injector.....	66
III.6.1	Recycler Modifications.....	67
III.6.2	Main Injector Modifications	67
III.6.3	Electron Cloud Mitigation	67
III.6.4	RF System Modifications.....	67
IV	DESIGN CONCEPTS OF MAJOR SUBSYSTEMS.....	69
IV.1	CW Linac.....	69
IV.1.1	Ion source, LEBT, RFQ and MEBT	69
IV.1.2	CW Accelerating Structures Requirements	78
IV.1.3	Low-beta section (2.1-10 MeV, 162.5 MHz)	78
IV.1.4	Low-beta section (10-160 MeV, 325 MHz)	84
IV.1.5	Medium-beta section (160 – 3000 MeV, 650 MHz)	98
IV.1.6	RF power	106
IV.1.7	RF Splitter.....	107
IV.2	Collimators and Beam Dump.....	109
IV.2.1	8 GeV Collimators	109
IV.2.2	Recycler Injection Beam Absorber.....	113
IV.3	3-8 GeV Pulsed Linac	119
IV.3.1	Accelerating Structures.....	119
IV.3.2	RF Power	123
IV.4	MI/RR.....	126
IV.4.1	H ⁻ Injection.....	127
IV.4.2	Main Injector γ_t jump.....	132
IV.4.3	Electron Cloud Mitigation	133
IV.4.4	RF Systems	134
IV.5	Cryogenics	136
IV.6	Instrumentation.....	139
IV.7	Controls	142
IV.8	LLRF	143
IV.8.1	LLRF for the CW 3 GeV SRF LINAC.....	144
IV.8.2	LLRF for the Pulsed Linac	144
IV.9	Safety and radiation shielding	145
IV.9.1	Radiation Limits.....	146
IV.9.2	Radiological Design Requirements and Consequences of Project X Radiation Limits	148
IV.10	Machine Protection System.....	155
IV.10.1	MPS Configuration	156
IV.10.2	Protection System R&D.....	157

V	SITING AND CONVENTIONAL FACILITIES	159
V.1	Siting Options	159
V.2	Conventional Facilities	163
V.3	Site Power Requirements	165
APPENDIX I:	STAGING SCENARIOS	167
I.1	Staging Scenario.....	167
I.2	Booster Upgrades for Stage 1	175
	Booster Intensity Limitations	175
	Existing Booster Injection Straight section	176
	Injection at 1 GeV.....	180
	Harmonic RF Systems.....	190
APPENDIX II:	POSSIBLE PERFORMANCE/SCOPE ENHANCEMENTS	200
II.1	High power at 8 GeV	200
II.2	Accumulator rings	202
REFERENCES.....		205

I Introduction

Project X is a high-intensity proton facility being developed to support a world-leading program of Intensity Frontier physics over the next two decades at Fermilab. Project X is an integral part of the U.S. Intensity Frontier Roadmap as described in the P5 report of May 2008 [1] and within the Fermilab Strategic Plan of November 2011 [2].

This document represents Part I of the “Project X Book” describing the Project X accelerator facility and the broad range of physics research opportunities enabled by Project X. Parts II and III provide in-depth descriptions of the physics research program, both within and beyond particle physics [3]. The primary elements of the U.S. program to be supported by Project X include:

Neutrino Experiments: Experimental studies of neutrino oscillations and neutrino interaction physics with ultra-intense neutrino beams provided by a high-power proton source with energies up to 120 GeV, utilizing near detectors at the Fermilab site and massive detectors at distant underground laboratories.

Goal: At least 2 MW of proton beam power at any energy between 60 to 120 GeV; several hundred kW of proton beam power on target at 8 GeV.

Kaon, Muon, Nucleon, and Neutron Precision Experiments: World-leading experiments studying ultra-rare kaon decays, searching for muon-to-electron conversion and nuclear electron dipole moments (EDMs), and exploring neutron properties at very high precision.

Goal: MW-class proton beams supporting multiple experiments at 1 and 3 GeV, with flexible capability for providing distinct beam formats to concurrent users while allowing simultaneous operations with the neutrino program.

Material Science and Nuclear Energy Applications: High-intensity accelerator, spallation, target and transmutation technology demonstrations will provide critical input into the design of future energy systems, including next generation fission reactors, nuclear waste transmutation systems and future thorium fuel-cycle power systems. Possible applications of muon spin rotation techniques provide sensitive probes of the magnetic structure of materials.

Goal: Provide MW-class proton beams at 1 GeV, coupled with novel targets required to support a broad range of materials science and energy applications.

Platform for Evolution to Future Frontier Facilities: A high-intensity proton source will strengthen and modernize the Fermilab injector complex, providing a robust platform upon which to build future frontier facilities. The Neutrino Factory and Muon Collider are examples that would provide world-leading capabilities at the Intensity and Energy Frontiers for many decades to come.

Goal: Provide a straightforward upgrade path for a 4 MW, low-duty-factor source of protons at energies between 5 and 15 GeV.

These four elements are expected to form the basis of the Mission Need statement required for the Department of Energy (DOE) Critical Decision 0 (CD-0), and represent the fundamental design criteria for Project X.

The following chapters present the Reference Design for the Project X accelerator facility. The Reference Design is based on a continuous wave (CW) superconducting (SC) linac providing up to 1 and 3 MW of beam power at 1 and 3 GeV respectively. A pulsed linac provides acceleration of roughly 4% of the beam delivered from the CW linac to the 8 GeV injection energy of the existing Recycler/Main Injector complex. Upgrades to the Recycler and Main Injector support a factor of three increase, beyond current capabilities, in proton beam power at 60 to 120 GeV.

The Reference Design represents a facility that will be unique in the world with unmatched capabilities for the delivery of very high beam power, with flexible beam formats, to multiple users at multiple energies. The utilization of linacs within the Project X facility enables capabilities beyond what is achievable with circular accelerators. It is anticipated that the final configuration and operating parameters of the complex will be further refined through the R&D program in advance of CD-2.

1.1 Evolution of the Reference Design

The Reference Design represents an evolution of the Project X design concept over a number of years, incorporating continuous input on physics research goals and advances in the underlying technology development programs. The initial Project X goals and associated design concept [4] were primarily driven by technology synergies with the International Linear Collider (ILC) and the 2-MW operational goal for the Main Injector in support of the long baseline neutrino program. This concept was based on an 8-GeV superconducting pulsed linac, paired with the existing Recycler and Main Injector rings. Operations in support

of programs beyond long-baseline neutrinos were not considered in this first concept. While some enhancements were introduced in the Project X Initial Configuration Document-1 (ICD-1 [5]) it followed the same path as the initial Project X concept but with an increased beam current. The accelerator complex defined in ICD-1 could drive the long-baseline neutrino program, and provided enhanced capabilities in the muon-to-electron conversion experiment (Mu2e); It did not, however, provide a flexible platform for pursuit of a broader research program in rare muon, kaon, nucleon, and neutron processes based on high duty-factor beams.

ICD-2 [6] addressed the lack of flexibility in ICD-1 by introducing a 2-GeV CW linac and a 2-8 GeV rapid cycling synchrotron (RCS), still paired with the existing Recycler and Main Injector. The intent of ICD-2 was to strengthen the broader physics research program while preserving the 2-MW neutrino beam program from the Main Injector. However, it was soon recognized that the 2-GeV CW linac energy was inadequate for supporting a compelling set of kaon experiments, and that utilization of a rapid-cycling synchrotron would ultimately limit the ability to support future facilities of interest to the U.S. particle physics community, such as the Neutrino Factory and Muon Collider.

These considerations have led to the development of the Reference Design. The Reference Design continues to be based on a superconducting CW linac; however, the energy has been raised to 3 GeV to provide a more robust kaon program, and the selection of RF frequencies has been changed to provide more efficient acceleration. As opportunities for research in materials science and energy applications were identified, the capability for delivering high power beams at 1 GeV was incorporated. In order to retain greater flexibility for future programs the RCS was replaced by a pulsed linac. The configurations of the Main Injector and Recycler remain as developed in the ICD-1 and ICD-2.

1.2 Assumptions

The following assumptions are made in determining the Project X facility configuration that meets the mission elements defined above:

- Project X will be constructed on the Fermilab site and will utilize the upgraded Main Injector and Recycler for the generation of a long-baseline neutrino beam.
- The long-baseline neutrino program will require a capability of greater than 2 MW proton beam power on a neutrino production target at any energy within the range 60-120 GeV, and will eventually require additional beam power upgrades.

- The precision experiments program requires MW-class proton beams, high duty factors, and flexible bunch patterns. This is best accomplished with a CW linac based on superconducting radio frequency (SRF) technologies.
- The production yield curve of kaons vs. incident proton energy sets the minimum CW linac energy at ~ 3 GeV
- Precision experiments based on nuclei and neutrons, as well as materials science and energy applications programs require MW-class proton beams at 1 GeV.
- A proton electric dipole moment program would require a very low duty factor beam at 236 MeV.
- All experimental programs must operate simultaneously.
- The Recycler operates at a fixed energy of 8 GeV; the upgraded Main Injector nominally accepts beam at 8 GeV, but potentially can be capable of operating at injection energies as low as 6 GeV.
- The NOvA Project will have upgraded the Main Injector (MI) to support a 1.333-second cycle time at 120 GeV, and will have converted the Recycler Ring (RR) to serve as a proton accumulator ring, resulting in 700 kW beam power. Additional upgrades to the MI/RR will be needed for 2-MW operations.
- A neutrino beamline directed towards Lead, South Dakota as part of the Long Baseline Neutrino Experiment (LBNE) will be operating with beam power on target of 700 kW, with shielding and infrastructure designed to accommodate at least 2.3 MW.
- Secondary beam requirements and facilities associated with the experimental program will be established prior to CD-1;
- Project X construction is likely to be staged; however, the reference design represents the capabilities required to meet the fundamental design criteria at the end of the final stage.

1.3 Facility Scope and Staging

The scope of Project X has been developed to support the mission needs and assumptions outlined above. The primary elements of the accelerator facility are:

- An H^- source consisting of a 30-keV DC ion source, Low Energy Beam Transport (LEBT), 2.1 MeV RFQ, and Medium Energy Beam Transport (MEBT) augmented with a wideband bunch-by-bunch chopper capable of generating bunch trains of arbitrary patterns at to 162.5 MHz;

- A 3-GeV superconducting linac operating in CW mode, and capable of accelerating an average (averaged over $>1 \mu\text{sec}$) beam current of 2 mA to 1 GeV and 1 mA to 3 GeV, with a peak beam current (averaged over $<1 \mu\text{sec}$) of 5mA;
- A 3 to 8 GeV pulsed superconducting linac capable of accelerating an average current of 43 μA with a 4.3% duty cycle;
- A pulsed dipole that can switch the 3-GeV beam between injection into the pulsed linac and the rare processes program;
- An RF beam splitter that can extract 1 mA of beam at 1 GeV;
- An RF beam splitter that can deliver the 3 GeV beam to multiple (three or more) experimental areas;
- Upgrades to the 8-GeV Booster to support injection at 1 GeV (Stages 1 and 2);
- Upgrades to the Main Injector/Recycler complex to support a factor of three increase in beam intensity (Stage 3);
- Target facilities required to produce secondary particle beams needed by the experimental program.

Anticipated financial constraints have led to consideration of a staged approach to Project X, based on application of the following principles:

- Each stage must present compelling physics opportunities;
- Each stage should utilize existing elements of the Fermilab complex to the extent possible;
- At the completion of the final stage the full vision of a world leading intensity frontier program at Fermilab should be realized.

A three stage approach to the Reference Design consistent with the above principles has been developed and discussed with the Department of Energy. The stages are envisaged as follows:

Stage 1: Construction of a 1-GeV CW linac operating with an average current of 1 mA, providing beams to the existing 8-GeV Booster, to the muon campus currently under construction, and to a new 1-GeV experimental facility.

Stage 2: Addition of a 1-3-GeV linac operating with an average current of 1 mA providing beam to a new 3 GeV experimental facility, and accompanied by upgrades of the 1-GeV linac to 2 mA average current and the Booster to 20 Hz capability.

Stage 3: Addition of the 3-8-GeV pulsed linac, accompanied by upgrades to the Recycler and Main Injector.

This report describes the Reference Design for all three stages of Project X. The staging strategy, including associated performance goals, is discussed in greater detail in Appendix 1. However, the siting and configuration associated with the Reference Design is strongly influenced by the staging plan, and a particular siting has been selected for this report consistent with the three stage plan. The siting is shown in Figure I-1. As displayed in the figure the 1-GeV, 1-3-GeV, and 3-8-GeV linacs are physically distinct, and are connected by two isochronous arcs, each with bending angle of 180 deg. Further details on the siting and associated conventional construction requirements are discussed in Chapter V.

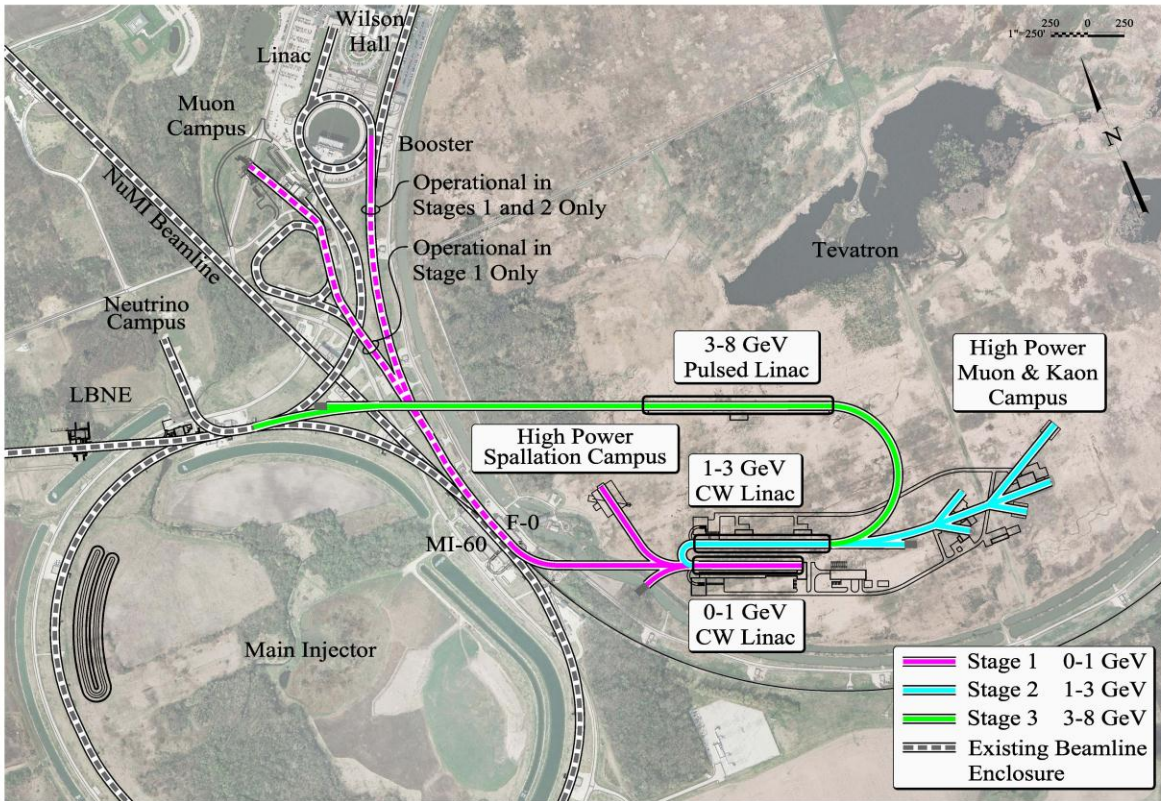


Figure I-1: Layout of Project X on the Fermilab Site

II Performance Goals

The overall goals of the Reference Design are to provide a context for the Project X R&D program and to define a scope that will provide a basis for supporting the mission needs identified in Section I and for the cost estimate necessary as part of the Critical Decision 0 (CD-0) evaluation – the first step in the critical decision process mandated by DOE order 413.3b. The cost range required for CD-0 will be established via variations of a number of assumptions inherent in the Reference Design, including:

- Options for acceleration from 3 to 8 GeV;
- Options for direct injection from the pulsed linac into the Main Injector accompanied by elimination of the Recycler from the scope of Project X;
- Alternative siting options;
- Alternative staging scenarios.

Beyond CD-0 the Reference Design will provide the starting point for development of the Conceptual Design Report required for CD-1.

II.1 Technical Goals

The performance goals for Project X are defined through a Functional Requirements Specification (FRS [7]). It is anticipated that the FRS will be approved by the Director of the DOE Office of High Energy Physics (OHEP) and the Fermilab Director as part of the CD-0 process. High level performance goals associated with the Project X Reference Design are listed in Table II-1.

Performance Parameter	Requirement	Unit
Linac Beam Power @ 1 GeV	1	MW
Linac Beam Power @ 3 GeV	3	MW
Main Injector Beam Power @60-120 GeV	>2	MW
1 GeV Linac Average Beam Current	2	mA
3 GeV Linac Average Beam Current	1	mA
Bunch Patterns at 1 and 3 GeV	Programmable	
Linac Beam Power at 8 GeV	350	kW
Upgrade Potential at 8 GeV	4	MW
Availability at 1 and 3 GeV	90	%
Availability at 60-120 GeV	85	%

Table II-1: Performance Goals for the Project X Accelerator Facility

The proposed experimental program determines the CW linac energies: 1 GeV has been chosen as the optimum for the materials and energy programs, and 3 GeV has been determined to be sufficient to meet the requirements of both the muon and kaon programs. The 8 GeV pulsed linac energy is aligned with the injection energy of the Main Injector/Recycler complex.

Project X will provide beams to the 1 and 3 GeV programs, with variable bunch patterns, concurrently. Table II-2 presents the experimental research requirements associated with the CW linac. Sophisticated beam chopping and RF separation techniques, capable of supporting simultaneous beam delivery four different target halls¹, are being developed to support for these operations.

	Beam Energy (GeV)	Train Frequency (MHz)	Pulse Width (nanoseconds)	Inter-Pulse Extinction
Materials/Energy	1	10-20	0.1-0.2	
Kaon Decays	3	20-30	0.1-0.2	$<10^{-3}$
Muon Conversion	1-3	1-2	<100	$<10^{-9}$
Nuclei/Neutrons	1-3	10-20	0.1-0.2	

Table II-2: Bunch train requirements for the CW linac-based programs

II.2 Operational Scenarios and Beam Formatting

Project X will have unique capabilities for delivering high power proton beams simultaneously to a variety of experimental programs with different bunch structure and intensity requirements. The CW linac will provide, simultaneously, high duty factor proton beams to the 1 GeV and 3 GeV experimental programs, with 4.3 % of the 3 GeV beam delivered to the pulsed linac for acceleration to 8 GeV and injection into the Recycler/Main Injector complex. The Main Injector will be capable of delivering 2 MW of beam power at any energy between 60 and 120 GeV for neutrino programs. We briefly outline the sub-systems and techniques to be used in implementing these capabilities through the staged construction and development of the Project X program.

¹ In this document we consider one end user at 1 GeV and three at 3 GeV. However the number of users can be increased, as required, by the serial installation of additional RF splitters.

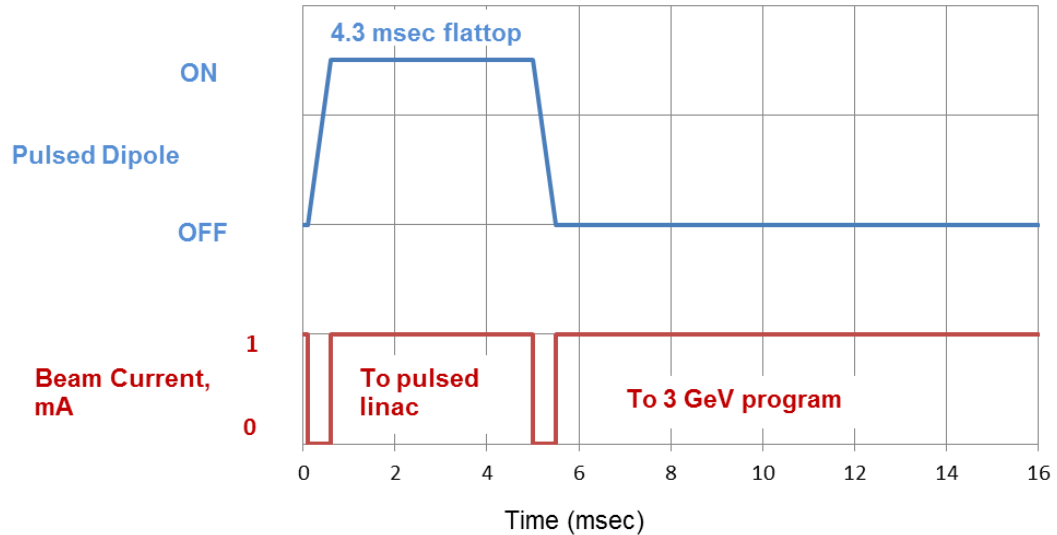


Figure II-1: A schematic timeline for linac beam current (first 16 ms of the 100 ms cycle). The pulsed magnet’s rise and fall time is 0.5 ms.

Figure II-1 shows the CW linac timeline schematically. There are two timeline intervals: (1) the 4.3 ms long time interval associated with a 10 Hz injection rate into the pulsed linac, and (2) the ~95 ms long time interval associated with the 3 GeV rare-processes experiments (discussed below). Six 4.3 ms pulses, spaced by 100 ms, are provided for acceleration in the pulsed linac and transfer to the Recycler/Main Injector in support of the long baseline neutrino program. This beam is directed into the pulsed linac by a pulsed dipole with a rise time of 0.5 ms. In order to create these gaps for the pulsed dipole, the beam is interrupted by the chopper located within the Low Energy Beam Transport line. The linac average current during this pulse is 1 mA. For the duration of the ~95 ms between pulsed linac pulses the beam is directed toward the rare processes program, again with an average current of 1 mA. In Stages 1, and 2 the timeline for the 1 GeV linac current will be similar to that in Figure II-1 with beam directed towards the Booster rather than the pulsed linac. The flattop for the Booster injection will be 1 ms at a rate of 15 Hz.

Several front end subsystems are employed to provide beam users with variable bunch patterns concurrently. These subsystems are described in detail in the following sections; here we briefly describe the main considerations. For optimal linac operation the power of the RF system should be matched to the required beam power. If the average beam intensity stays constant but the peak intensity varies with time so that the beam power (temporarily) exceeds the power available from the RF system, the beam energy begins to droop. Fortunately, superconducting cavities have a comparatively large stored energy that strongly suppresses the energy variations if the beam intensity variations are sufficiently fast. For the

accelerating gradients chosen within the CW linac the stored energy is sufficient to limit the energy gain variation to less than 0.1% over a 1 μ s period at 5 mA beam current. This means that currents of up to 5 mA can be sustained for less than 1 μ s as long as the average current is maintained at 2 mA (1 mA beyond 1 GeV) over timescales of 1 μ s and greater. All presently suggested experiments require significantly faster beam intensity variations (or bunching patterns) than 1 μ s, leading to these variations being “invisible” to the accelerating structures.

The Reference Design utilizes a DC ion source capable of delivering 0-5 mA of H⁻ ions. After acceleration and bunching in a 162.5 MHz RFQ the beam is chopped by a wideband chopper (at 2.1 MeV) that allows populating the linac rf buckets in arbitrary patterns at 162.5 MHz. Utilization of RF separation at the exit of the linac allows each experiment to receive a desired bunch pattern. The only limitations are that: (1) the beam current, when averaged over time spans in excess of \sim 1 μ s, should not exceed 2 mA (1 mA beyond 1 GeV), (2) all bunches should have the same intensity,² and (3) the peak current should not exceed 5 mA.

Figure II-2 presents a possible beam structure to support simultaneous operations of a muon conversion experiment and a nucleon based experiment at 1 GeV as part of Stage 1 of Project X (see Appendix I for discussion of Stages). The bunch pattern shown repeats itself every 1 μ s, with the bunch train generated by the front end (black, red) shown at the top of the figure. An RF splitter operating at $(n + 1/2) \times 162.5$ MHz is deployed at the end of the 1 GeV linac, applying kicks in opposite directions to the black bunches (arriving at a splitter RF phase of 270°) and the red bunches (arriving at 90°). The result after the splitter is a stream of (black) bunches at a frequency of 40 MHz and a pulse of (red) bunches with a width of \sim 40 ns repeating at 1 MHz. The latter pattern would be appropriate for an upgrade of the Mu2e experiment. For a peak current of 3.64 mA (1.4×10^8 protons per bunch) the average current accelerated to 1 GeV is 1 mA, with 910 kW of beam power contained in the black beam and 90 kW in the red beam.

² A possibility of partial bunch scraping and, consequently, bunch current regulation will be experimentally studied at Project X Injector Experiment (PXIE) and outside the scope of this RDR.

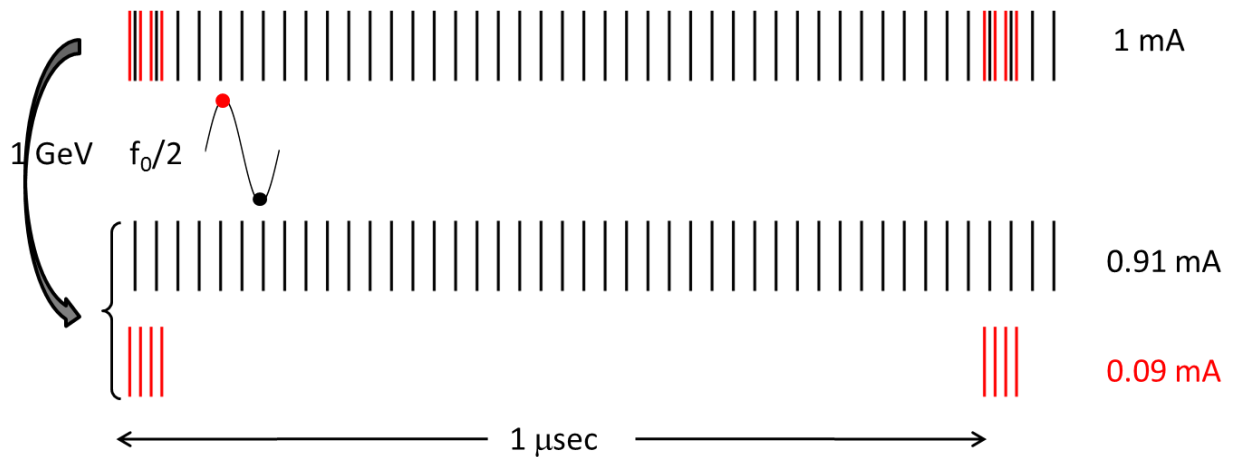


Figure II-2: Bunch structure of the 1 GeV CW linac beam at Stage 1. The pattern shown repeats with a 1 μ s period. The linac bunch structure (top) is deconvolved into a beam supporting the materials/energy/nuclei program (black bunches) and a beam supporting a next generation muon-to-electron conversion experiment (red). The individual bunch intensity is 14×10^7 with a 50 ps (FW) bunch length. The total beam power delivered is 910 kW (black) and 90 kW (red).

Operations become somewhat more complex following completion of the 3 GeV linac at Stage 2. It is envisioned to support three experiments at 3 GeV: a muon conversion experiment, a rare kaon experiment, and a nuclear physics experiment(s). In parallel the 1 GeV program established in Stage 1 is continued. Two RF splitters are employed to support joint 1 and 3 GeV operations – the splitter at 1 GeV operating at $(n+1/2) \times 162.5$ MHz, and at 3 GeV a splitter operating at $(n \pm 1/8) \times 162.5$ MHz. Figure II-3 shows a possible arrangement – the bunch patterns are reproduced every 0.5 μ s, with the bunch train generated by the front end (black, red, blue, and green bunches) shown at the top of the figure. This bunch train is separated at 1 GeV into two trains with the black bunches receiving a kick from the splitter corresponding to arrival at 90° phase and serving as the beam for the 1 GeV program while the red, blue, and green bunches arrive at 270° phase and are sent to the 1-3 GeV linac. At 3 GeV this train is separated into three trains, again depending upon the arrival phase at the splitter. For a peak current of 5 mA (1.9×10^8 protons per bunch) the average current is 2 mA to 1 GeV and 1 mA from 1 to 3 GeV, with 1 MW delivered to the 1 GeV program, and 3 MW delivered to the 3 GeV program and allocated between the red, blue, and green programs as 750/1500/750 kW. The red bunch train is appropriate to a muon to electron conversion experiment – a burst of four bunches (~ 75 ns) separated by 0.5 μ s. The blue and green trains provide continuous beam at approximately 20 MHz and 10 MHz respectively, structures appropriate for rare kaon decays and a variety of nuclear physics measurements.

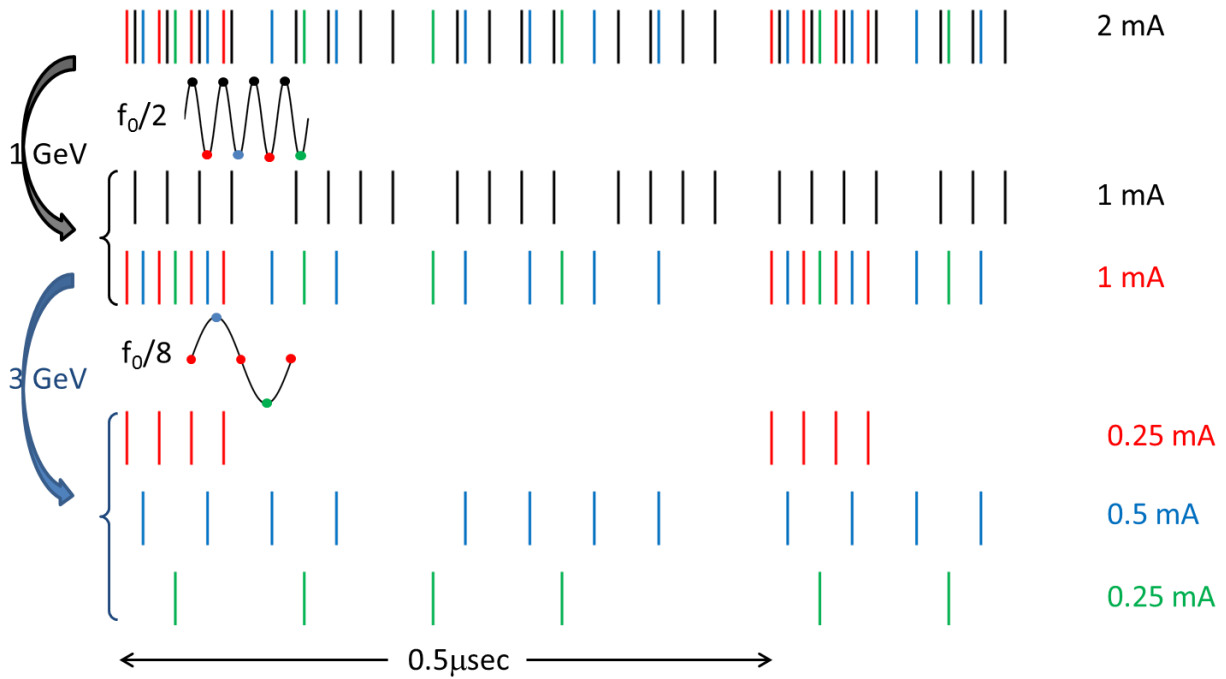


Figure II-3: Bunch structure of the 1 GeV CW linac beam at Stage 2. The pattern shown repeats with a 1 μ s period. The top diagram shows the bunch pattern in the linac up to 1 GeV; this pattern is initially deconvolved into a beam supporting the materials/energy program at 1 GeV (black bunches) and a beam continuing on to the 1-3 GeV linac (red, blue, green). At 3 GeV the beam is further deconvolved to provide different bunch patterns to the three experiments with red pulses delivered to a muon conversion experiment, blue to a rare kaon decay experiment, and green to a third (presently unspecified) experiment. The individual bunch intensity is 19×10^7 with a 40 ps (FW) bunch length.

The patterns shown in Figure II-2 and Figure II-3 are created in the MEBT by a wideband chopper that disposes up to 80% of the beam delivered from the RFQ in a pre-determined, repetitive pattern, creating a continuous load of up to 8 kW on the MEBT absorber. The functioning of the front-end system, including the wideband chopper that provide great flexibility in developing variable bunch patterns, is described in Chapters III and IV.

III Accelerator Facility Design

Figure III-1 shows the configuration of all linear acceleration elements within Project X. A room temperature (RT) section accelerates beam to 2.1 MeV and creates the desired bunch structure for injection into the superconducting linac. The CW linac accelerates 2 mA (1 mA in Stage 1) of beam current to 1 GeV and 1 mA to 3 GeV. The pulsed linac accepts beam at 3 GeV and accelerates it to 8 GeV with a 4.3% duty factor. The pulsed linac provides beam for injection into the Recycler via an 8 GeV transport line. After accumulation in the Recycler beam is transferred to the Main Injector and accelerated to anywhere between 60-120 GeV. Beam is available for experiments at any of the following energies simultaneously: 1, 3, 8 and 60-120 GeV. The operational parameters for the CW linac are given in Table III-1.

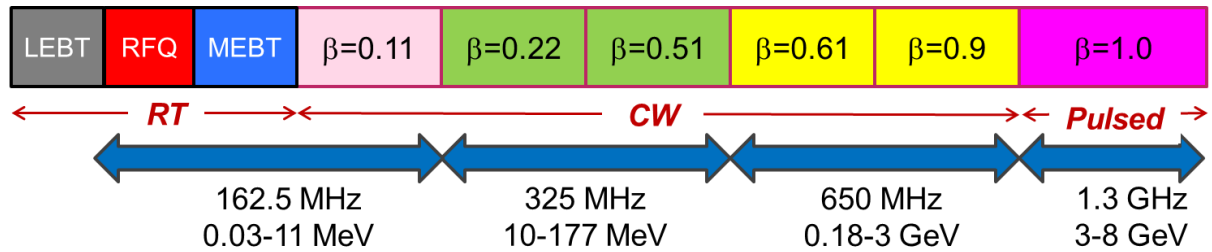


Figure III-1: The Project X Linacs

CW Linac	Requirement	
Particle species	H ⁻	
Input beam energy (Kinetic)	2.1	MeV
Output beam energy (Kinetic)	3.0	GeV
Pulse repetition rate	162.5	MHz
RF pulse length	CW	
Beam pulse length	Programmable	
Average beam current to 1 GeV	2	mA
Average beam current to 3 GeV	1	mA
3 GeV rms norm. transverse emittance, ϵ_x/ϵ_y	0.6/0.4	mm-mrad
3 GeV rms norm. longitudinal emittance	0.65/1.9	mm-mrad /keV-ns
3 GeV rms bunch length	3	ps

Table III-1: CW Linac Parameters

III.1 CW Linac

The CW linac comprises the sections labeled “RT” and “CW” as shown in Figure III-1. The CW linac accelerates H^- ions from an ion source to 3 GeV, at which point they are directed either towards the 3 GeV experimental areas or towards the 3-8 GeV pulsed linac. The average beam current is 2 mA to 1 GeV and 1 mA to 3 GeV, with peak currents up to 5 mA for periods of less than 1 μ s. The entire CW linac includes the following major elements:

- 1) The warm front-end;
- 2) One accelerating SC cryomodule based 162.5 MHz Half-Wave Resonators (HWR);
- 3) Two accelerating SC sections based on 325 MHz Single-Spoke Resonators (SSR1 & SSR2);
- 4) Two accelerating SC sections of 650 MHz elliptical cavities with $\beta = 0.61$ and 0.9 (LB650 and HB650)

III.1.1 Warm Front End

The front-end of the Project X linac provides H^- beam to the first superconducting module within the CW linac. The front-end must provide beam formatted correctly for utilization in the 1 and 3 GeV experimental programs, and for injection into the Recycler.

The front end consists of an ion source, Low Energy Beam Transport (LEBT), Radio Frequency Quadrupole accelerator (RFQ), and Medium Energy Beam Transport (MEBT). The nominal beam current from the ion source through the RFQ is 5 mA. The ion source delivers 5 mA of H^- at 30 keV. The 162.5 MHz RFQ accepts and accelerates this beam to 2.1 MeV. A wideband chopper situated within the MEBT removes $\sim 80\%$ of the bunches emanating from the RFQ in order to form appropriate bunch patterns for acceleration in the CW linac as described in Chapter II.2.

The RFQ energy of 2.1 MeV is chosen because it is below the neutron production threshold for most materials. At the same time this energy is sufficiently large to mitigate the space charge effects in the MEBT at currents as high as 10 mA (the maximum capability of the source). The choice of a comparatively low energy for the LEBT (30 keV) allows reducing the length of RFQ adiabatic buncher, and, consequently, achieving sufficiently small longitudinal emittance so that at the exit of the RFQ the beam phase space will be close to emittance equipartitioning. To mitigate the space charge effects in the LEBT compensation of beam space charge by residual gas ions can be applied either for the full LEBT length or over its initial part only.

Low Energy Beam Transport (LEBT)

The layout of the ion source and LEBT is shown in Figure III-2. Two ion sources are installed to improve the beam availability. Each source can be removed for repairs, reinstalled, and conditioned without interrupting the operation of the other source. The LEBT transports the beam from the ion source to the RFQ entrance. It also matches the beam optical functions to the RFQ. In addition, the LEBT forms a low-duty factor beam as required for commissioning and tuning of the downstream beam line and interrupts the beam as part of the machine protection system (MPS).

The LEBT functional requirement specifications are listed in [8]. The LEBT includes 3 solenoids (for each leg), a slow switching dipole magnet, a chopper assembly (a kicker followed by a beam absorber), and diagnostics to characterize and to tune the beam. The length of the beam line, ~ 3 m, insures that the gas migration from the ion source to the RFQ is tolerable. Fast machine protection and pulsed beam operation are achieved via the chopper assembly, which is comprised of a kicker followed by an absorber. In some scenarios, it can be used also as a pre-chopper to assist the MEFT chopping system. Note that the primary machine protection mechanism is to disable the beam from the ion source by turning off its extraction and bias voltages, with the LEBT chopper serving as a fast beam switch during the ion source turn off time.

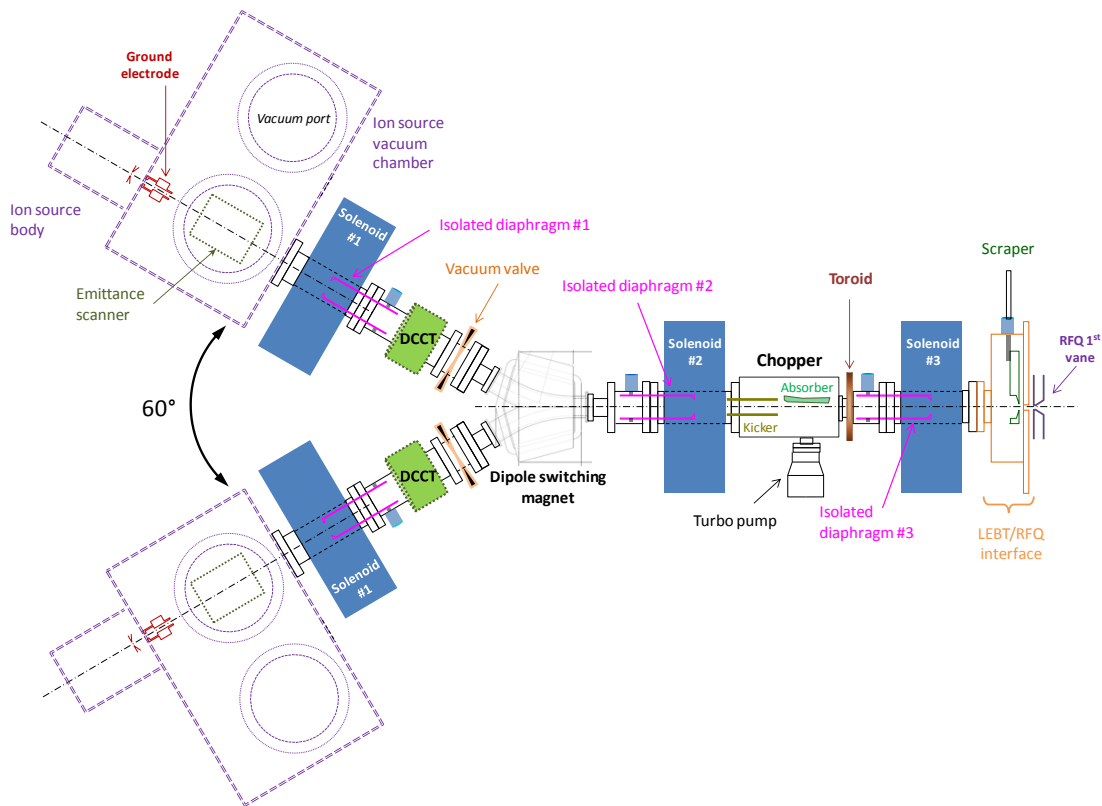


Figure III-2: Schematic of the LEBT with two ion sources.

The LEBT optics design (Figure III-3) incorporates two regions. The beam is nearly fully neutralized from the exit of the ion source to immediately upstream of the (chopper) kicker. Depending on the operational mode the beam can be either neutralized or un-neutralized downstream of the kicker to the RFQ entrance. The edge focusing of the switching dipole is adjusted to minimize asymmetry between horizontal and vertical focusing. In the un-neutralized mode, the secondary ions created in the downstream region are removed by a constant electric field on the kicker plates, and the upstream ions are trapped by a positive voltage on the insulated diaphragm #2. In the neutralized mode, the kicker plates as well as the insulated diaphragm #2 have normally ground potential, while the insulated diaphragm #3 or the scraper is biased positively to prevent the ion escape longitudinally.

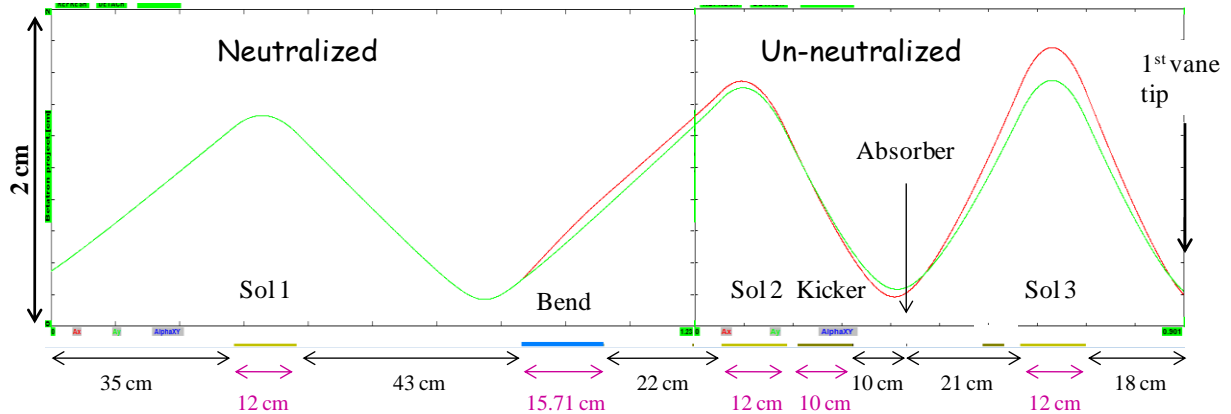


Figure III-3: Beam horizontal (red) and vertical (green) envelopes (rms) of the partially un-neutralized LEBT (with OptiM [9])

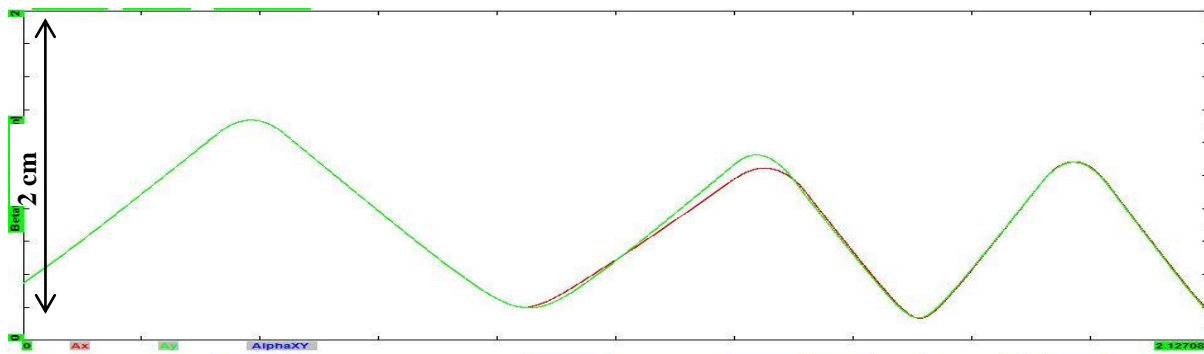


Figure III-4: Beam horizontal (red) and vertical (green) envelopes (rms) in the LEBT with neutralized transport only. All optical elements are identical to those in Figure III-3; only the solenoid currents were adjusted.

The LEBT scheme is flexible enough to accommodate both versions by adjusting potentials and solenoid currents (see Figure III-4 for simulations of a fully neutralized transport case). The transport with the un-neutralized downstream section is beneficial for minimizing the difference between short pulse and CW operations, as well as for minimizing transient effects during beam switching on; but un-neutralized beam transport does result in emittance growth as can be seen in Figure III-5 and Figure III-6 . The relative benefits of each scenario will be clarified via experiments undertaken at PXIE (Project X Injector Experiment [10]).

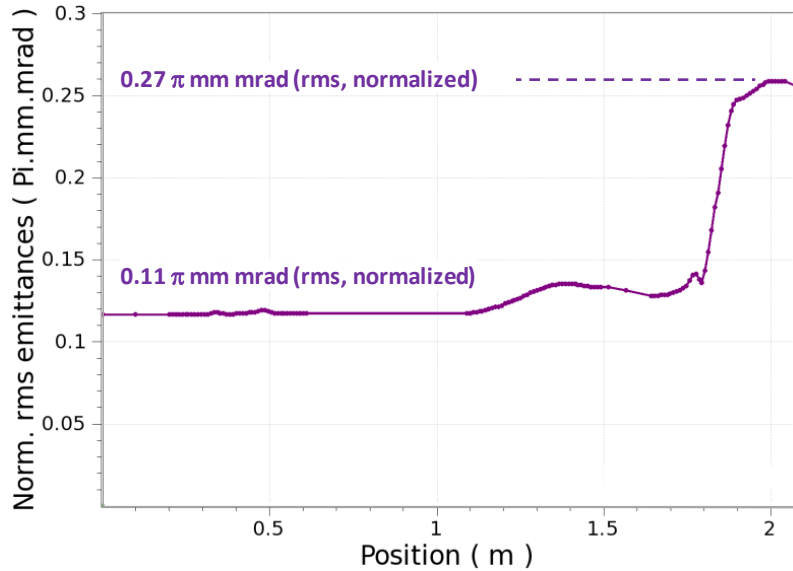


Figure III-5: Emittance evolution along the LEBT for a 5 mA, 30 keV (with TraceWin) for partially neutralized transport. The start of the emittance growth shows where the transition between the neutralized and un-neutralized beam transport occurs.

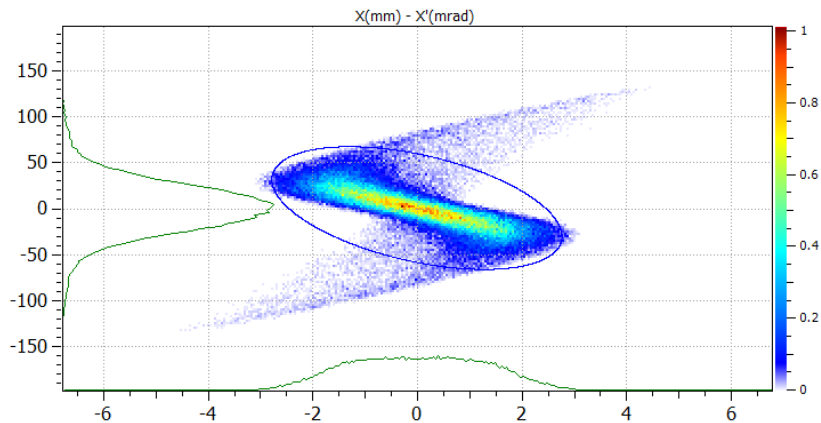


Figure III-6: Phase space distribution ($x-x'$) at the entrance of the RFQ (with Tracewin) for partially neutralized transport. The initial distribution was Gaussian.

Radio Frequency Quadrupole

The 162.5 MHz RFQ accelerates H⁻ ions with beam currents up to 10 mA from 30 keV to 2.1 MeV. The beam dynamics design of the RFQ is optimized using the measured beam distribution from the D-Pace H⁻ ion source [11]. The design has over 96% transmission for beam current from 1 to 15 mA. At 5 mA (nominal current) 99.8% beam capture is achieved with transverse and longitudinal emittances (rms, norm) of 0.15 mm-mrad and 0.64 keV-ns (0.204 mm-mrad), respectively. The beam dynamics design was conducted using PARMTEQM and TraceWin; Figure III-7 shows the simulated 3 σ beam envelopes at 5 mA, from the ion source through the exit of the RFQ. Error analyses indicate that the RFQ design has adequate tolerance for mechanical and field errors, as well as errors in TWISS parameters.

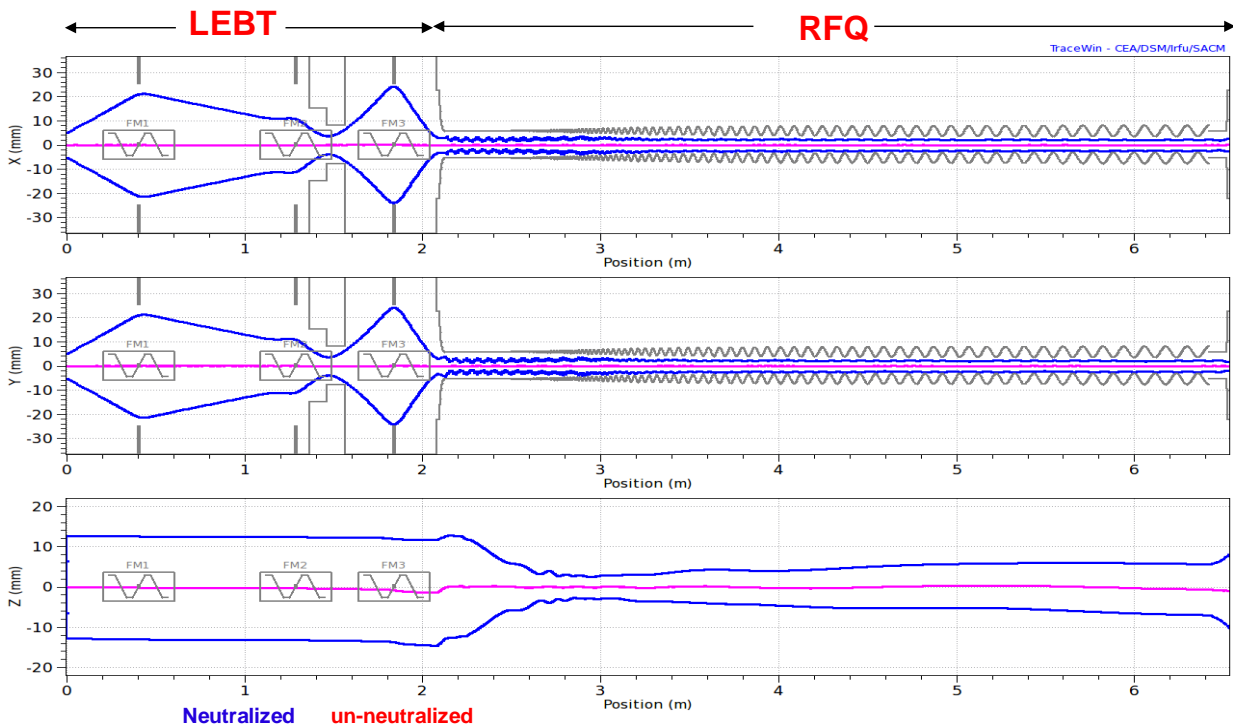


Figure III-7: TraceWin simulations of 3 σ beam envelopes (horizontal, vertical, and longitudinal) through the LEBT and RFQ for a 5-mA beam current.

Medium Energy Beam Transport (MEBT)

The required bunch structure for Project X operations will be formed in the MEBT, the ~10m section between RFQ and HWR cryomodule. The heart of the MEBT is a wideband chopping system that directs unwanted bunches to an absorber according to a pre-selected

pattern and passes the bunches chosen to be accelerated into the SRF linac with minimum distortions. Beam chopping in the MEBT is used in other facilities (e.g. SNS [12]), but the concept of a bunch-by-bunch selection results in significantly more demanding requirements to the chopping system. In addition, the MEBT provides proper optical matching between the RFQ and the SRF section, includes instrumentation to measure the properties of the beam coming out of the RFQ and transported to the SRF cavities, and has means of protecting the SRF section from excessive beam loss.

The nominal H^- beam current in the MEBT input is 5 mA. However the design of MEBT absorber supports damping up to 10 mA. Consequently, the operation with beam current twice larger than nominal is expected to be possible. Such an operational regime is also supported by beam transport simulations with 10 mA current. Experimental studies to be carried out in PXIE should demonstrate a possibility of 10 mA operation. To minimize emittance growth ($\Delta\varepsilon/\varepsilon < 10\%$) the MEBT transverse focusing is made sufficiently smooth. It is provided by equidistantly placed quadrupole triplets with the only exception of two doublets located immediately after RFQ (Figure III-8) which match the RFQ beam envelopes to the MEBT periodic focusing structure. Each triplet or doublet is followed by a pair of dipole correctors. The complete list of functional requirements is in Ref. [13]. The specifications for the quadrupoles and correctors are listed in Ref. [14]. The spaces between neighboring triplets or doublets are referred to as MEBT sections. The period in the regular part is 1140 mm. This leaves a 650-mm long (flange-to-flange) space for various equipment (350 mm in the section between doublets labeled #0 in Figure III-8).

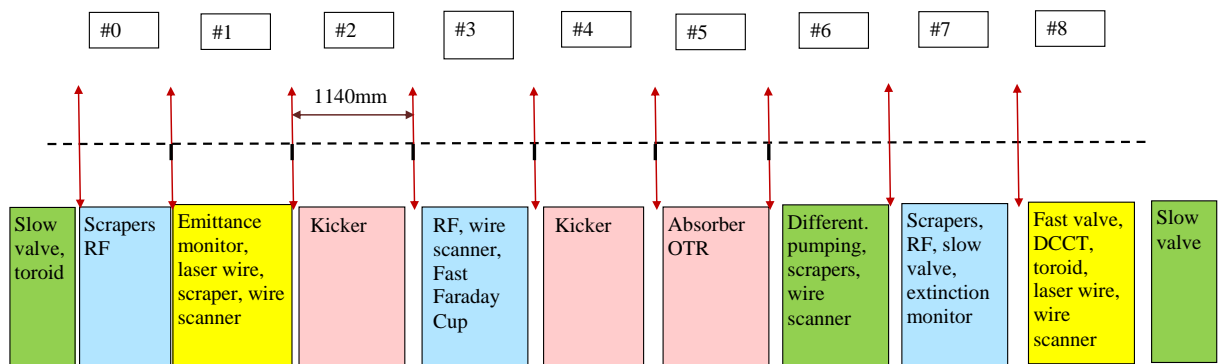


Figure III-8: The MEBT structure. Sections are colored according to their main functions. The red vertical arrows schematically show the transverse focusing (doublets or triplets) elements.

The undesired beam bunches will be removed in the MEBT by a chopping system, represented in Figure III-8 by the red boxes. The chopper consists of two identical 50 cm

long kickers separated by a 180° transverse phase advance and an absorber (90° from the last kicker). In the broadband, travelling-wave kicker, the transverse electric field propagates with the phase velocity equal to the speed of H^- ions (~ 20 mm/ns, $\beta = 0.0668$). Such a two-kicker scheme allows creating a vertical kick sufficiently large for separation of passed and removed bunches with moderate voltage on the kicker plates. Detailed specifications for the kicker can be found in Ref. [15].

Figure III-9 presents the simulated transverse beam envelopes in the MEBT for both passing and chopped bunches. The chopped bunches are directed to the absorber which is displaced vertically from the beam trajectory. Presently two versions of the kicker, which differ by the structure's impedance, are being investigated [16]. To keep the beam properly bunched and matched to the first SC section, the MEBT includes 3 identical bunching cavities [17].

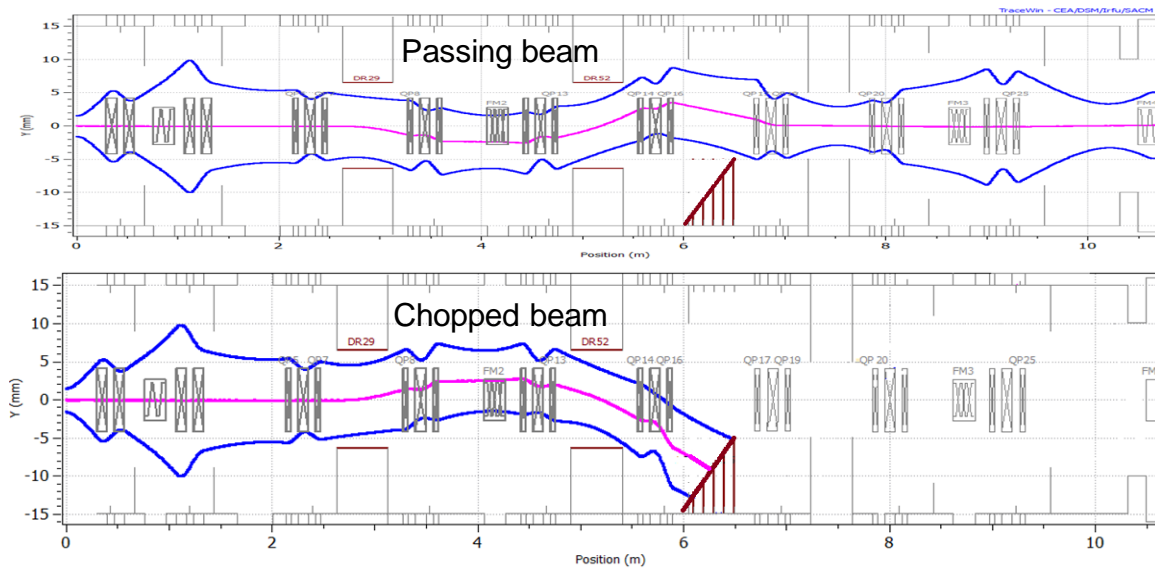


Figure III-9: The simulated transverse 3σ beam envelopes in the MEBT.

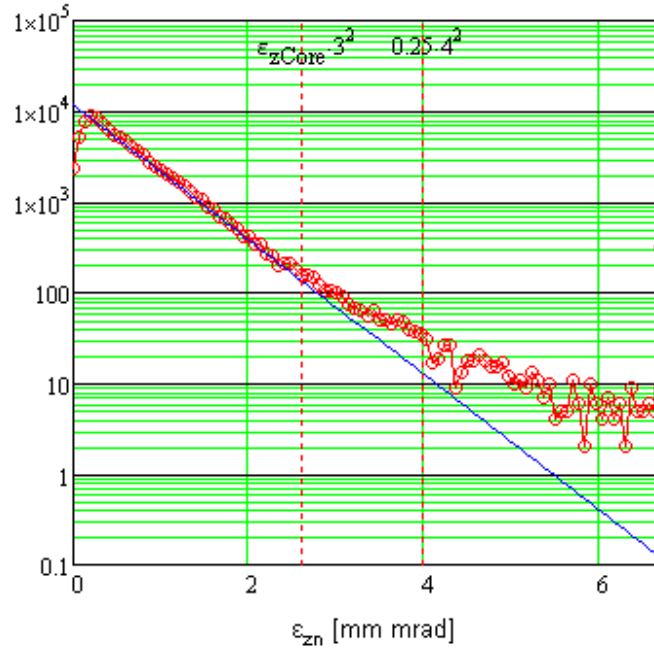


Figure III-10: Beam longitudinal distribution at the end of RFQ simulated for 5 mA beam current. Vertical lines mark the 1σ and 4σ boundaries for 0.25 mm-mrad (rms) normalized emittance.

Some of the Project X experiments are expected to require extremely good extinction for removed bunches. The target value is smaller than 10^{-9} , i.e. less than one particle per bunch. A finite population in the longitudinal RFQ tails (see Figure III-10) can be the main limitation to achieve the required beam extinction. Although there is very good rejection of the tails in the first SC cryomodule the weak longitudinal focusing in the MEBT and its long length allow momentum tails of allowed bunches to move to the nearby rejected bunches and be accepted in their RF bucket. Figure III-11 presents the phase space at the location of bunch chopper for particles that are accepted for further acceleration. Particles in the lanes above and below the main bunch will be accepted in the nearby buckets. As one can see to be accepted to these buckets the tails have to extend beyond $\sim 10\sigma$. None of the 10^6 particles used in the simulation approached this limit. The final result for the extinction of removed bunches has to be determined by experiment. The suppression of longitudinal RFQ tails is expected to be the key in achieving the extinction goal.

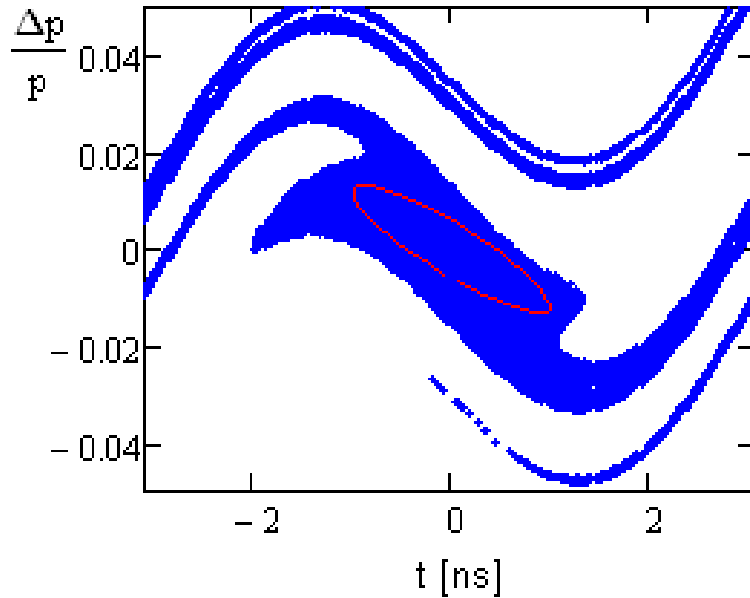


Figure III-11: Longitudinal phase space at the beam chopper location for particles accepted for further acceleration (blue dots). The red line designates the 4σ bunch boundary.

III.1.2 CW Linac Physics Design

The CW linac starts immediately downstream of the MEBT. It accelerates the beam from 2.1 MeV to 3 GeV and consists of two SC linacs connected by an arc bending the beam by 180 deg. The first linac belongs to the Project X Stage I. It accelerates the beam to 1 GeV. In Stage I the beam can be RF separated between a few 1 GeV experiments or sent to one of them. The beam can be also delivered to the Fermilab Booster and muon campus. Later, when Stage II is implemented, the beam will be RF separated between the 1 GeV experimental area and the second linac accelerating the beam to 3 GeV. Two linacs are connected by the isochronous bending arc. This arc belongs to Stage II. The arc introduction addresses two problems. First, it minimizes civil construction in Stage I and, consequently, results in a cost reduction. Second, it allows one to proceed with the construction of Stage II without an interruption of Stage I operation.

Accelerating cavities

Five types of superconducting cavities are used in the CW part of Project X to cover the entire velocity range required for acceleration of H^- (or protons) from 2.1 MeV to 3 GeV. The selection of cavity frequencies and cell configuration are chosen to maximize acceleration efficiency for each accelerating structure, minimize cost of the accelerator and its operation, and to address other factors helping to minimize the beam loss.

The primary efficiency factor is the transit time factor, which has a dependence on the beam velocity, β , as shown in Figure III-12 for different number of cells in a cavity. One can see that the range of betas over which the beam can be efficiently accelerated increases with decreasing number of cells. On the other hand, too small number of cells reduces effective gradient and increases costs due to end effects. As one can see from Figure III-12 the maximum of acceleration is achieved for the velocities slightly larger than β_G , which is called the geometric-beta. The velocity where the maximum is achieved, β_{opt} , is called the optimal beta. For a periodic structure with harmonic distribution of electric field along the axis, $E \propto \sin(\omega z / \beta c) \exp(i\omega t)$, the transit time factor can be expressed by the following formula:

$$T(\beta) = \frac{2\beta}{\pi n} \left(\frac{\sin(\pi n(\beta - \beta_G)/(2\beta))}{\beta - \beta_G} - (-1)^n \frac{\sin(\pi n(\beta + \beta_G)/(2\beta))}{\beta + \beta_G} \right), \quad (1)$$

where n is the number of cells in the cavity operating at π -mode. The transit time factor is normalized such that $T(\beta_G) = 1$. The above expression approximates very well the transient factors obtained by numerical integration of actual time dependent electric field for the Project X cavities. The β_G presented below were obtained by fitting Eq. (1) to the numerical integration results. For multi-cell elliptic resonators this definition yields slightly larger values of β_G than the more commonly used definition of β_G as the ratio of cavity period to half-wavelength.

Recent developments of the 1.3-GHz ILC cavity technology at Fermilab [18] and elsewhere make it a preferred choice for the acceleration of ultra-relativistic beams and, in particular, the preferred choice for the Project X pulsed linac, accelerating protons from 3 to 8 GeV. This selection determined the base frequency of the project to be 1300 MHz. The choice of other frequencies was set by a requirement that all other frequencies have to be harmonically related to the base, which yielded 162.5, 325 and 650 MHz. Such a choice results in a comparatively smooth frequency increase during beam acceleration, accommodating bunch shortening due to adiabatic damping.

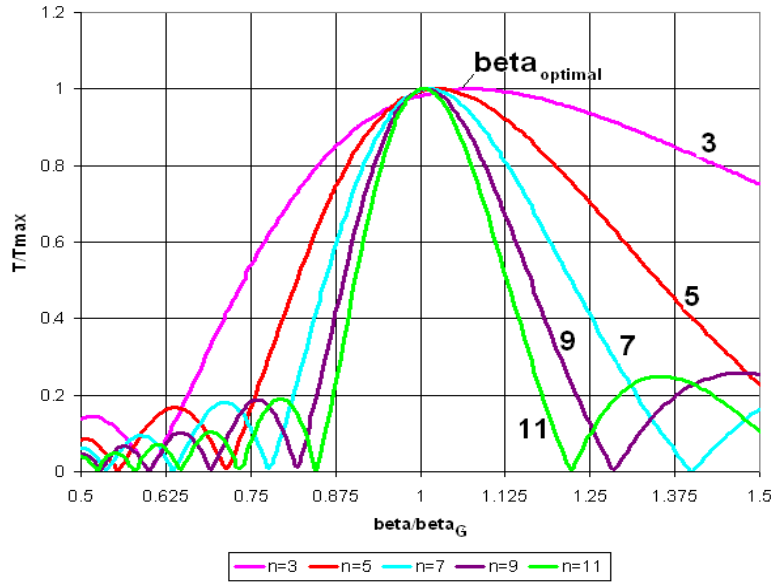


Figure III-12: Transit time factor versus the ratio of the beta to the geometric beta, β/β_G , for different number of cells in a cavity, n .

Name	β_G	β_{opt}	Freq (MHz)	Type of cavity	Energy range (MeV)
HWR	0.094	0.112	162.5	Half wave resonator	2.1-11
SSR1	0.186	0.222	325	Single-spoke resonator	11-38
SSR2	0.431	0.515	325	Single-spoke resonator	38-177
LB650	0.61*	0.647	650	Elliptic 5-cell	177 - 480
HB650	0.9*	0.95	650	Elliptic 5-cell	480 - 3000

* To be consistent with previously written documents β_G for the elliptic cavities is defined as the ratio of regular cell length to half-wavelength.

Table III-2: Accelerating cavity types for the CW linac.

Table III-2 and Figure III-13 presents the cavity types utilized, and their deployment, through the CW linac. Acceleration starts with the half-wave resonators (HWR) operating at 162.5 MHz. It is followed by two types of single spoke resonators (SSR1 and SSR2) operating at 325 MHz, and finally by two types of elliptical 5-cell cavities, low beta (LB650) and high beta (HB650), at the 650 MHz. Figure III-14 presents the transient factors for the CW linac. The voltage gain in each next cavity type is significantly larger than in the previous one. That

determines that the transition happens earlier than the transit time factors for two types are equal.

The choice of the RFQ frequency was determined by a possibility of bunch-by-bunch chopping which would be beyond the present “state-of-the art” implementation for 325 MHz but is feasible for 162.5 MHz. The use of the same frequency for the first superconducting cryomodule results in reduced transverse defocusing from cavity fields and reduced longitudinal focusing. This yields the possibility of increasing the cavity voltage for the first SC cavities, otherwise limited by beam dynamics. As a consequence the number of cavities, and linac length, required to get the beam accelerated to 11 MeV is reduced by more than a factor of 2. Note that even this frequency choice does not allow using all available voltage for first few cavities. In particular, the first cavity uses about half of nominal voltage.

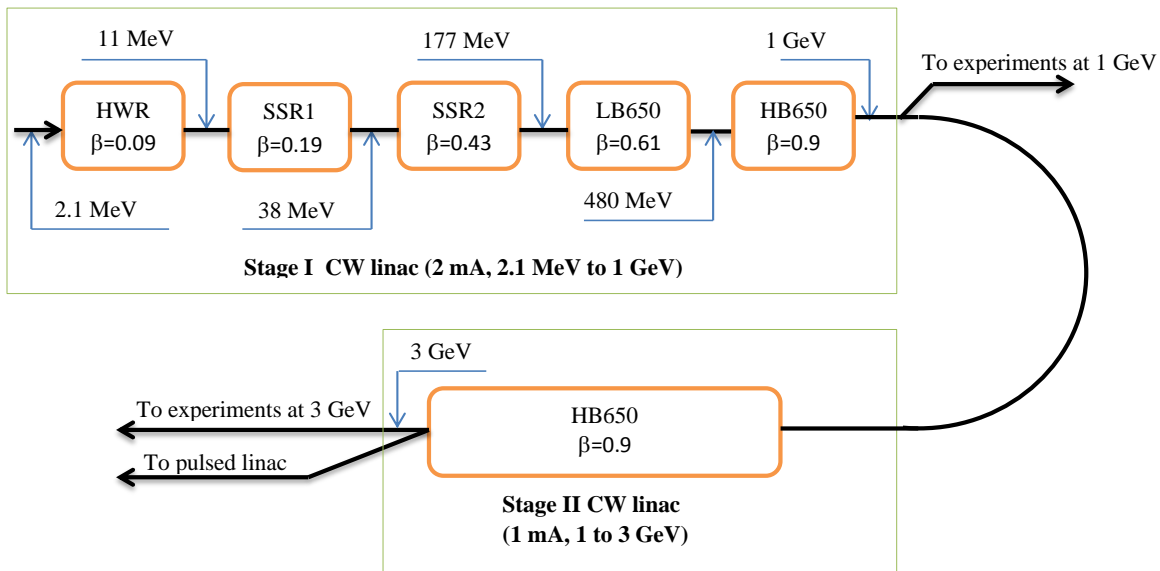


Figure III-13: SRF technology map for CW portion of Project X. β refers to the cavity optimum beta for HWR, SSR1, and SSR2, and the cavity geometrical beta for LB650 and HB650.

In summary, the primary benefits of the cavity arrangement described above are:

- The longitudinal beam dynamics at each transition is simplified by limiting the frequency jump to no more than a factor of two from one cavity type to another.
- The lower frequency sections provide sufficient aperture for minimizing uncontrolled beam loss to tolerable levels (0.1 - 0.2 W/m). In particular, it allows

for operation at reduced focusing strength which minimizes the intra-beam stripping.

- The choice of cavities with a low frequency at the beginning of the linac reduces effects of the acceleration cavities' focusing/defocusing to an acceptable level, thus, allowing for operation at maximum possible accelerating gradients.

However, there are also some disadvantages related to the preference of 650 MHz to 1300 MHz frequency for the major part of CW linac:

- Microphonics presents a more serious issue at lower frequencies.
- Cavities for 650 MHz are more expensive (more niobium) than at 1300 MHz, but the cost increase is compensated (with the accuracy we can presently account) by a smaller number of the cavities and RF sources.

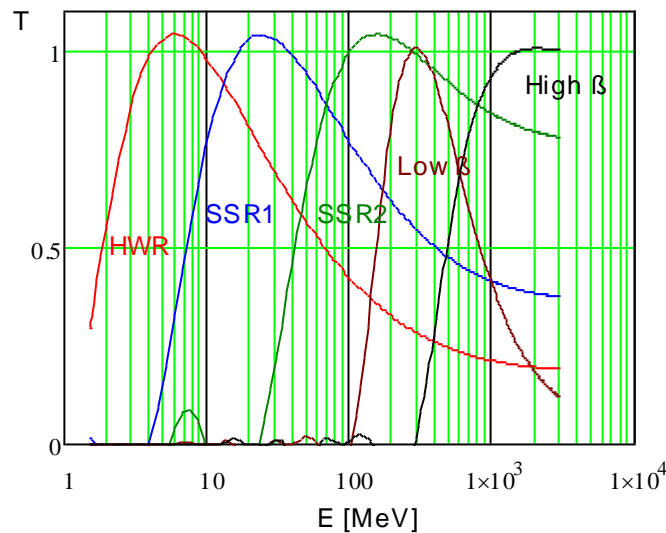


Figure III-14: Transient factors for CW SC Project X cavities.

The operating gradient is chosen to provide a peak surface magnetic field that allows operation below high-field Q-slope; see Figure III-15 taken from [19]. For the frequency of 162.5 MHz we adopted the maximum magnetic field of about 40 mT; while for the frequencies of 325 and 625 MHz the peak magnetic field was chosen below about 70 mT. For all frequencies the peak surface electric field is lower than 40 MV/m [20] in order to avoid the risk of strong field emission (see details in Section IV).

The transition from the 325 MHz single-spoke cavities to the 650 MHz section based on elliptical cavities is chosen at the energy of about 170 MeV, because for lower energies

elliptical cavities lose efficiency. It is inefficient to accelerate H^- ions from 170 MeV to 3 GeV using only one cavity type and, thus, two families of 650 MHz cavities have been chosen.

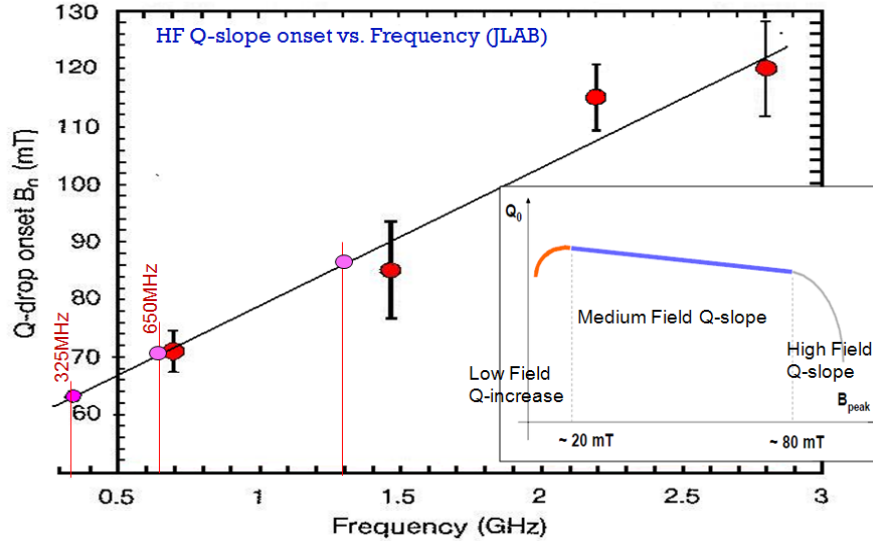
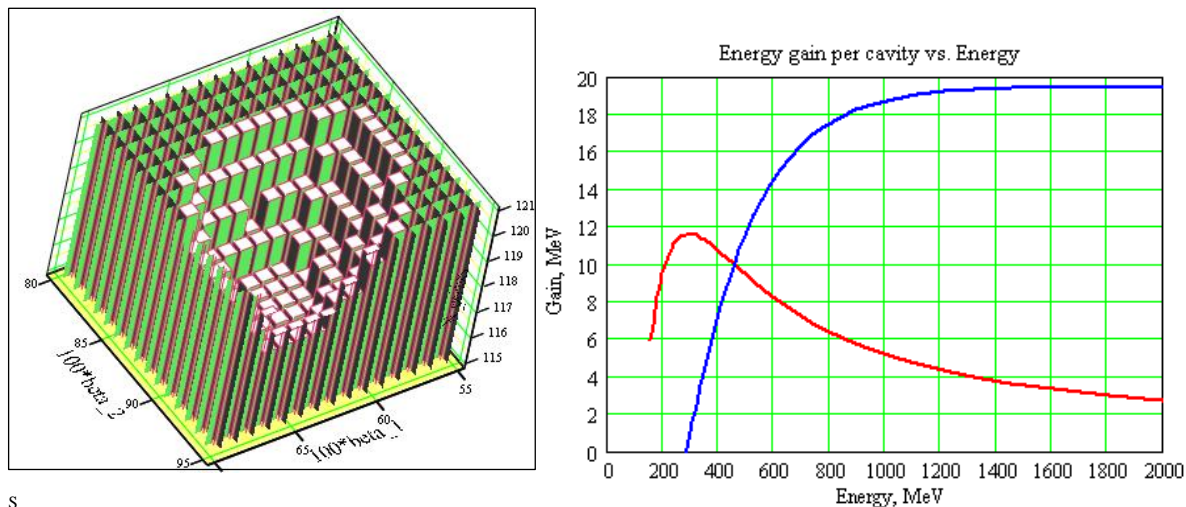


Figure III-15: High field Q-slope versus frequency.

Figure III-16 demonstrates the optimization of the transition energy between the two families of 650 MHz cavities and their geometric betas assuming a linear dependence of the field enhancement factors versus beta [21]. The upper figure shows the number of cavities required as a function of the betas of the two sections. The lower figure shows the energy gain per cavity vs. beam energy for $\beta_G=0.61$ cavities (red curve) and $\beta_G=0.9$ cavities (blue curve). The fully optimized geometric betas for the two 650 MHz sections are 0.64 and 0.9 respectively (upper figure), and the optimal transition energy is 466 MeV (lower figure). The initial synchronous phase is -30° , and it increases as the square root of the energy. More exact simulations taking into account realistic enhancement factors show optimal choice of geometric betas of 0.61 and 0.9.



s

Figure III-16: Left: Number of cavities required versus cavity beta in the two 650 MHz sections. Right: Energy gain per cavity versus particle energy for beta=0.61 (red curve) and beta=0.9 (blue curve) cavities.

The resultant characteristics of the six cryomodule types identified for the Project X CW linac are summarized in Table III-3. The cavity Q_0 's are based on an assumed operating temperature of 2K and a residual surface resistance of 10 n Ω . The energy gain per cavity throughout the CW linac is shown in Figure III-17. The gap in the energy gain for HB cavities is related to the longitudinal matching around 1 GeV energy.

Section	Freq. (MHz)	Energy (MeV)	Cav/mag/CM	Gradient (MV/m)	Energy Gain (MeV)	$Q_0@2K$ (10^{10})	CM Config.	CM length (m)
HWR	162.5	2.1-11	8 / 8 / 1	8.2	1.7	0.5	8 x (sc)	5.8
SSR1	325	11-38	16 / 8 / 2	10	2.05	0.2	4 x (csc)	5.2
SSR2	325	38-177	35 / 21 / 7	11.2	5.32	1.2	sccscsc	6.5
LB650	650	177-480	30 / 20* / 5	16.5	11.6	1.5	ccc-fd-ccc	7.1
HB650	650	480-1000	42 / 16† / 7	17	17.6	2.0	cccccc	9.5
HB650	650	1000-3000	120 / 30† / 15	17	17.6	2.0	cccccccc	11.2

*5 superconducting and 5 warm (external to the cryomodule) doublets

†All doublets are warm, i.e. external to the cryomodule

Table III-3: Accelerating cryomodule requirements for the CW linac. Within the CM configuration column “c” refers to an individual accelerating cavity, “s” refers to a solenoid magnet, “f” refers to a single quadrupole magnet, and “fd” refers to a quadrupole doublet.

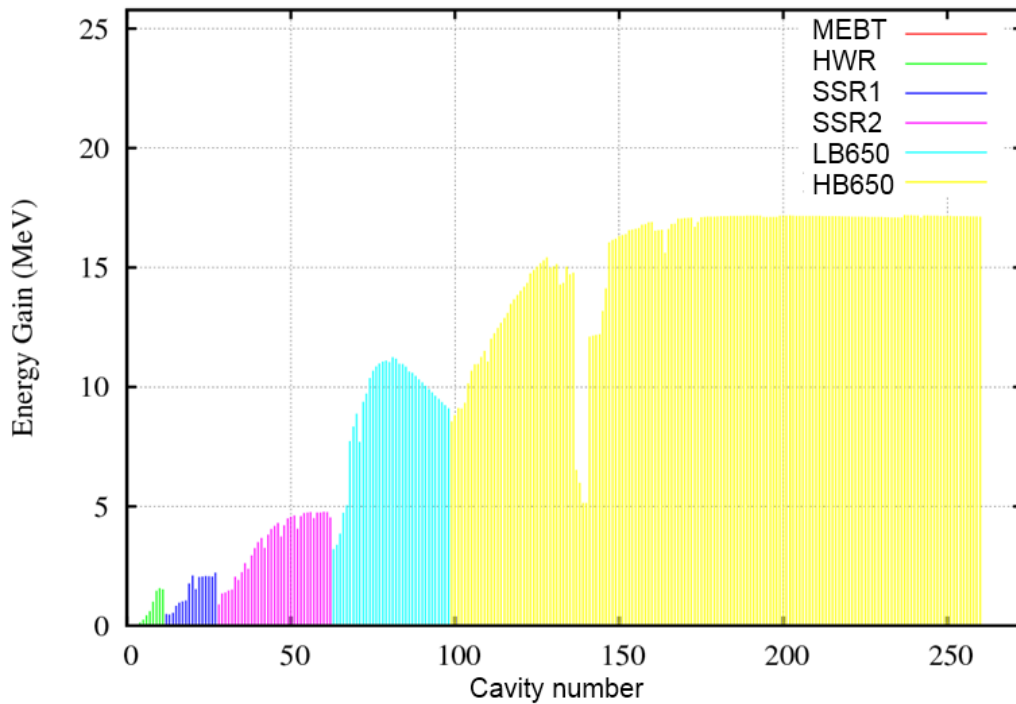


Figure III-17: The energy gain per cavity in the CW linac.

III.1.3 CW Linac – Cryomodule Requirements

Cavities and focusing elements, as necessary, are grouped within cryomodules. In the 162.5 and 325 MHz sections the transverse focusing is provided by superconducting solenoids. In the 650 MHz sections quadrupole doublets (FD lattice) are used. Normal conducting doublets are located between cryomodules for both low-beta (LB650) and high-beta (HB650) cryomodules. Additional superconducting doublets are located in the center of low-beta cryomodules. The arrangement of focusing periods by cryomodule type is shown in Table III-3.

For beam diagnostics purposes, and for beam steering, each magnet package includes vertical and horizontal built-in correctors and a 3-coordinates beam position monitor (BPM). All cryomodules are separated by warm sections. These warm sections are used for additional diagnostics (bunch transverse and longitudinal profile monitors, beam loss monitors, *etc.*) and for collimation required to avoid uncontrolled beam loss in SC cryomodules. The makeup for each of the warm insertions will be determined by requirements of safe and reliable operations, diagnostics, collimation, and cryogenic segmentation constraints.

Integrated estimates of RF power consumption and cryogenic losses for the CW linac are shown in Table III-4, and plotted by cavity in Figure III-18 and Figure III-19.

Section	R/Q (Ω)	$Q_0@2K$ (10^{10})	E_{peak} (MV/m)	B_{peak} (mT)	Max. RF power per cavity* (kW)	Max. RF power per CM (kW)	Cryo-losses per CM (W)
HWR	272	0.5	38	41	4.9	39	24
SSR1	242	0.5	38	58	5.5	44	27
SSR2	275	1.2	40	70	17	85	43**
LB 650	378	1.5	37.5	70	34	204	145**
HB 650	638	2.0	35.2	64	50	300	147**
HB 650	638	2.0	35.2	64	31	248	196**

* Power is computed for 2 mA to 1 GeV linac and 1 mA from 1-3 GeV. Allowances for transmission loss and microphonics suppression are included.

** To be updated at the technical design stage. Only dynamic losses are taken into account.

Table III-4: Integrated RF power consumption and cryogenic losses in the CW linac.

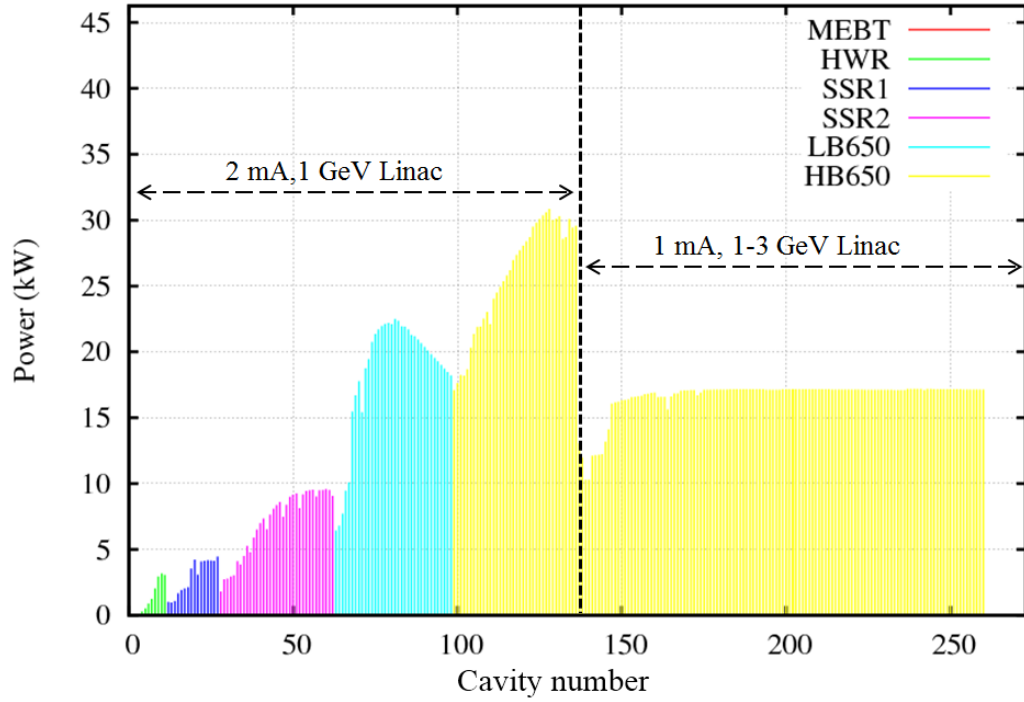


Figure III-18: Distribution of the RF power (per cavity) transferred to the beam; the beam current is 2 mA in 1 GeV linac and 1 mA in 1-3 GeV linac.

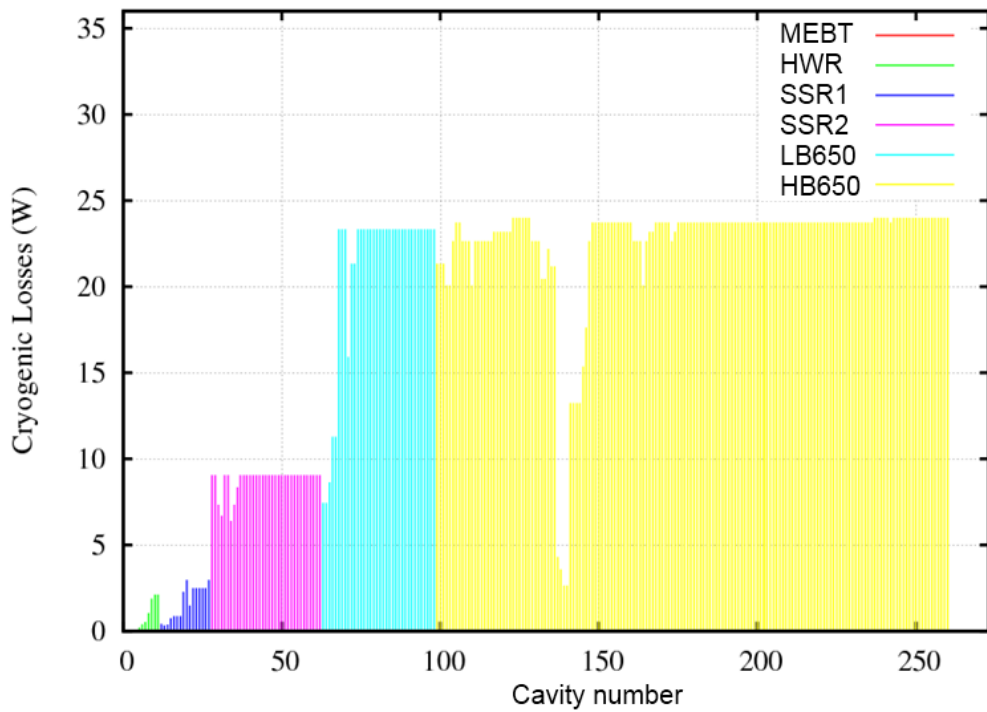


Figure III-19: Distribution of the cryogenic losses (dominated by cavity wall losses) per cavity in the linac.

III.1.4 CW Linac – Beam Dynamics

The rms normalized beam emittance budget for the CW linac is established as 0.15 mm-mrad at the ion source and 0.4 mm-mrad at the exit of 3 GeV linac. The lattice design and the beam dynamics optimization are made utilizing the TRACK, TraceWin and GenLinWin codes. The results of the beam dynamics simulations are shown as an evolution of 1σ beam envelopes through the entire CW linac in Figure III-20. The top figure shows the two transverse dimensions and the bottom figure the bunch length. Figure III-21 shows the transverse and longitudinal rms envelopes through HWR and SSR1 sections which are not clearly seen in Figure III-20. Figure III-22 displays the evolution of rms longitudinal and transverse normalized emittances through the Stage I linac. There is only modest transverse and longitudinal emittance growth. Due to diminishing space charge effects there is no significant emittance growth in the 1-3 GeV linac. However long transport through the 1 GeV arc results in a considerable emittance growth excited by beam space charge. Details are discussed in Section III.2.2. Figure III-23 displays the actual particle density distribution and Figure III-24 the evolution of beam energy through the linac. Figure III-25 shows a calculation of beam power loss (W/m) due to intra-beam stripping of H^- thru through the linac. As one can see the losses due to this mechanism are below 0.1 W/m everywhere.

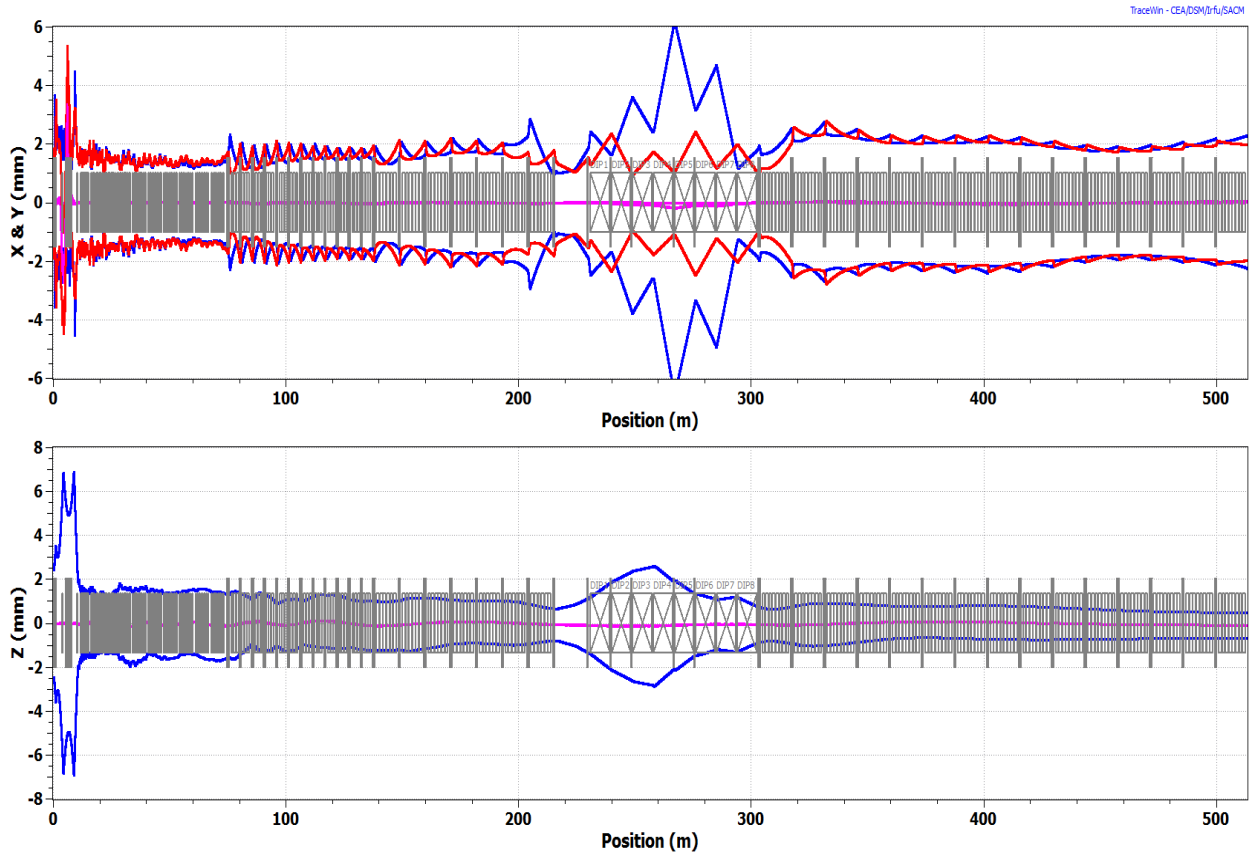


Figure III-20: Transverse (x (blue) and y (red)) rms envelopes (upper) and rms bunch length (lower) along entire CW linac (from MEBT to the end of 1-3 GeV linac) including the 180 degree bend.

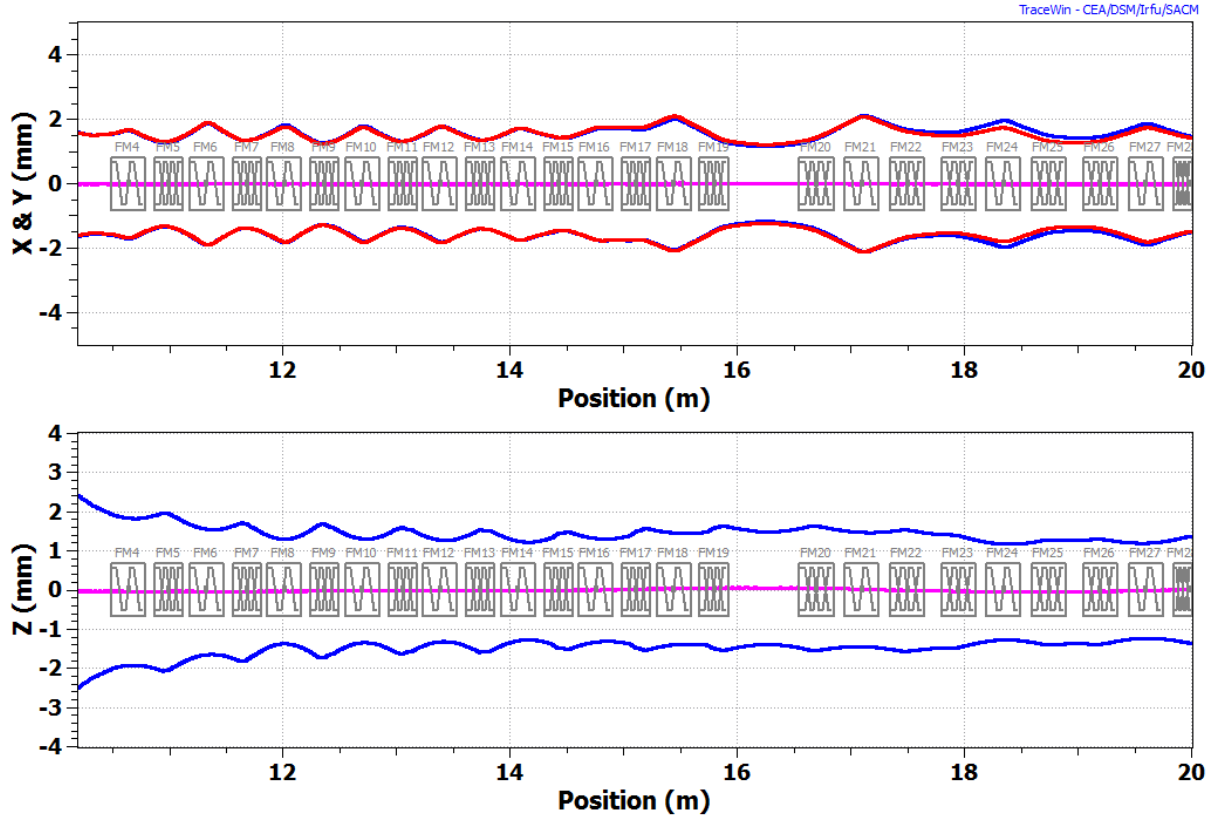


Figure III-21: Transverse (upper) and longitudinal (lower) rms envelopes through HWR and SSR1 sections.

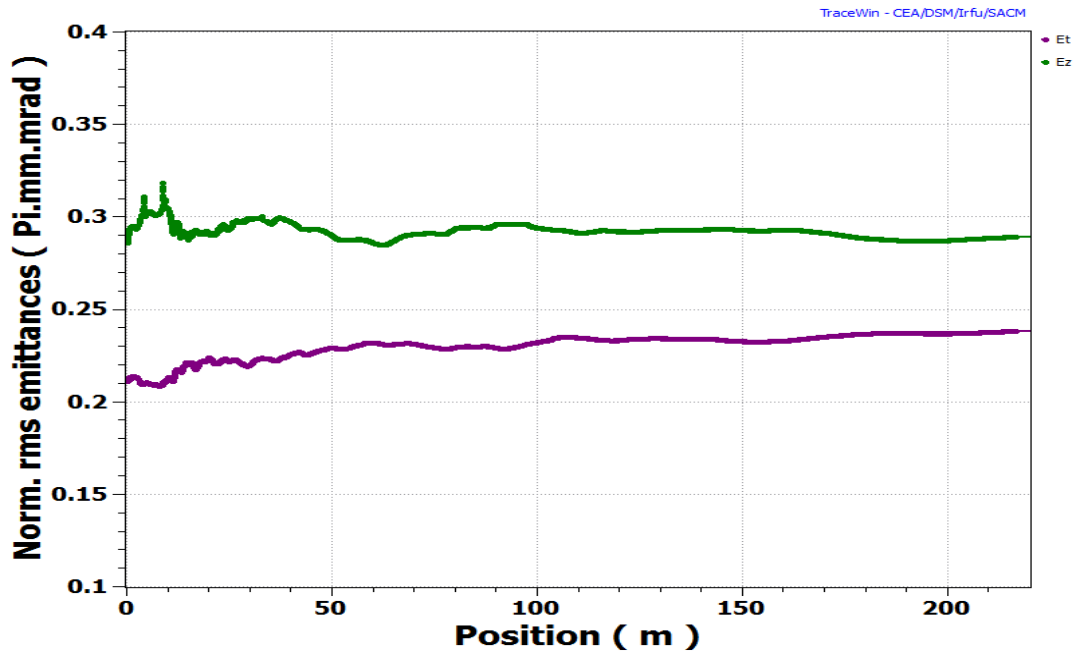


Figure III-22: Normalized transverse (magenta) and longitudinal (green) emittances along the linac (from MEBT entrance to the end of 1 GeV linac).

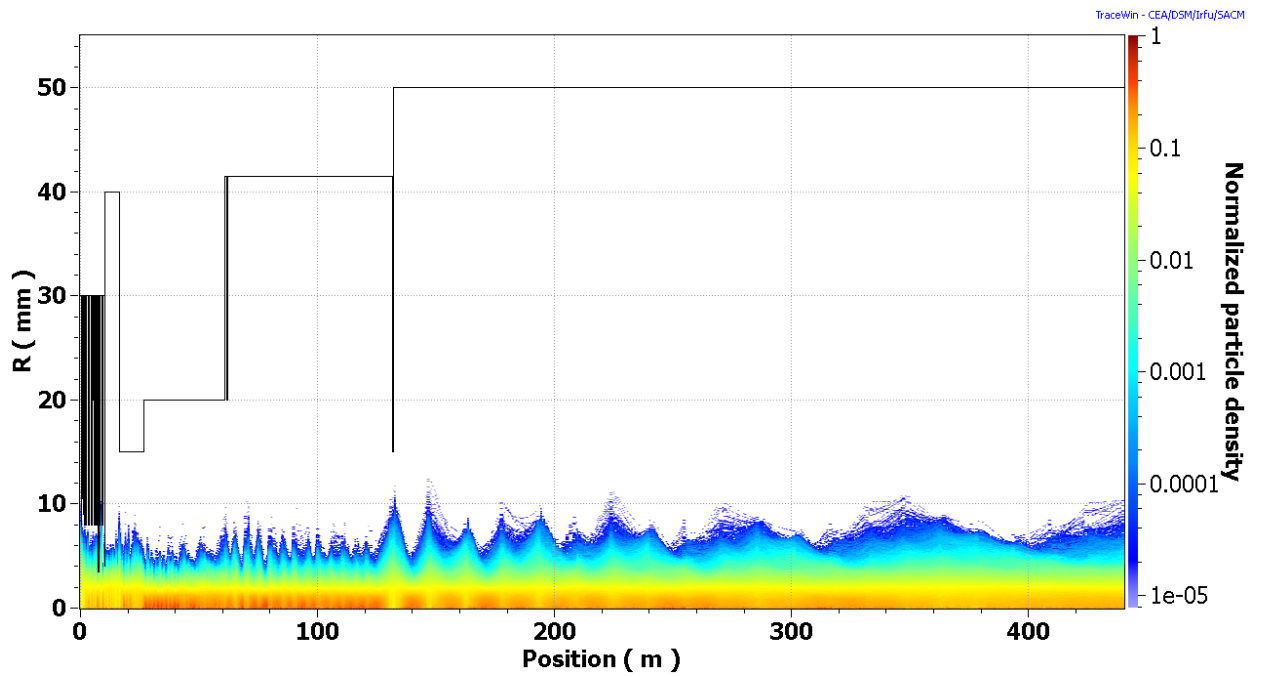


Figure III-23: Aperture and Particle density distribution along the linac. 100,000 particles tracked by PARTRAN. Simulations are performed without 1 GeV arc.

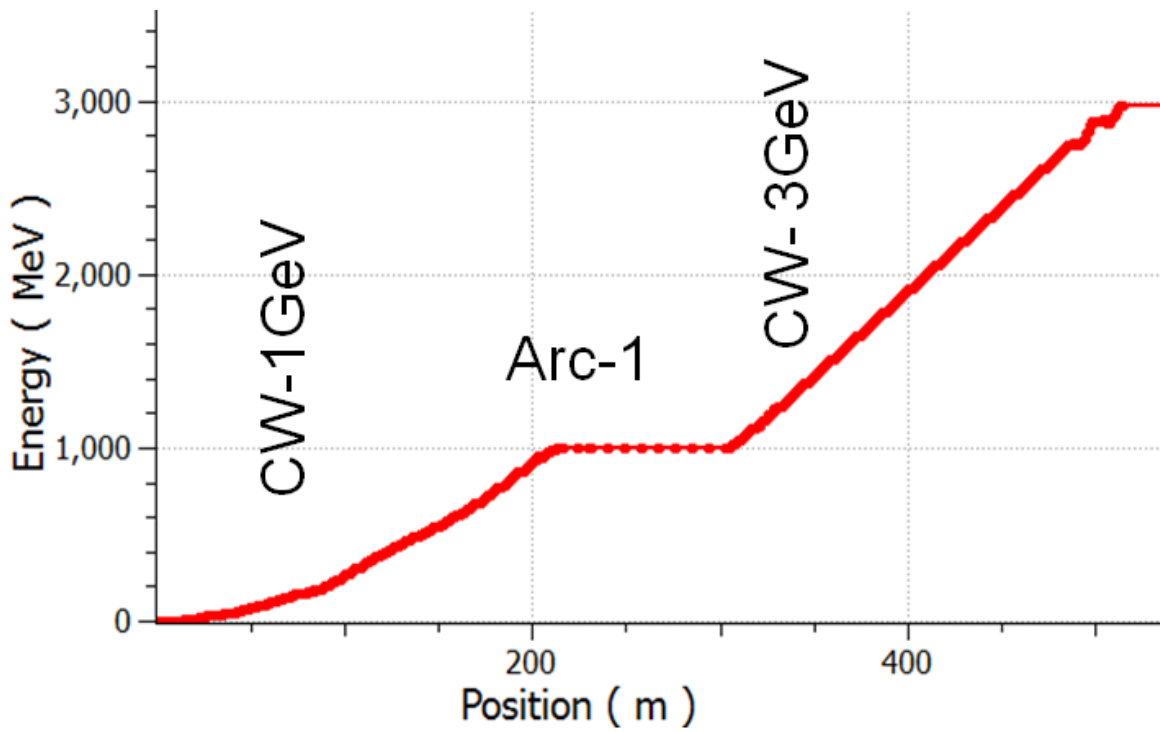


Figure III-24: Energy versus longitudinal coordinate.

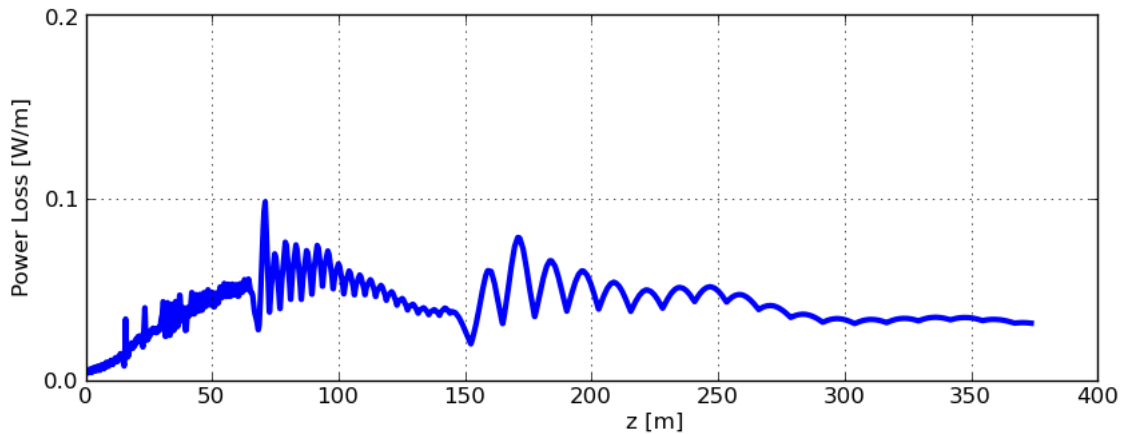


Figure III-25: The beam power losses per unit length caused by intra-beam stripping. Simulations are performed without 1 GeV arc which has significantly reduced intrabeam stripping due to bunch lengthening (see details in the next section).

III.2 1 GeV Beam Handling

III.2.1 Transport Line Requirements and Physics Design

Stage 1 of Project X will provide up to 1 MW beam power split between the 1 GeV Experimental Area (EA) and the Muon Campus (MC), while providing 15 kW beam power to the Booster at a 15 Hz rate. The simultaneous beam delivery to the EA and MC is supported by an RF deflecting cavity that splits the EA and MC beams onto different trajectories. The final separation is produced by a three-way Lambertson magnet. Figure III-26 shows the concept for beam separation for the first two stages of Project X. As the Project matures and Stage 2 is added, it is assumed that the muon conversion experiment is relocated to the 3 GeV Experimental Area. Stage 2 provides 1 MW beam power to the 1 GeV EA and 3 MW to the 3 GeV EA. This is accomplished by increasing the 1 GeV CW linac current to 2 mA so that 1mA each can be sent to the 1 GeV and 3 GeV programs.

An RF deflecting cavity/Lambertson combination will be installed to provide the bunch structures to both the EA and MC as presented in Figure III-26. The Lambertson will provide a three-way split similar to the magnet used in the 3 GeV Experimental Area. A vertical trim dipole located near RF deflecting cavity will be used to allow for beam re-steering from the two upper to the two bottom apertures of the Lambertson. A horizontal dipole will be installed downstream of the Lambertson in the Booster/MC line to send beam to the linac dump.

The deflecting cavity deflects the EA and MC bunches in different directions. The bunches destined for the MC are given a positive deflection such that they end up going through the field region of the Lambertson while the bunches intended for the EA are given a negative deflection and end up going through the field-free region of the Lambertson. Adding a positive DC deflection equal to the deflection by the deflection cavity will offset the beam trajectory at the Lambertson such that the EA beam will once again be on the linac centerline. When Stage 2 is implemented, the trim dipole will change its polarity to offset the positive and negative kicks in the opposite direction thus splitting beam between the EA and the 1-GeV arc for the 3-GeV linac. Table III-5 summarizes the operation of the deflecting cavity/dipole for sending beam to the different destinations for both Stages.

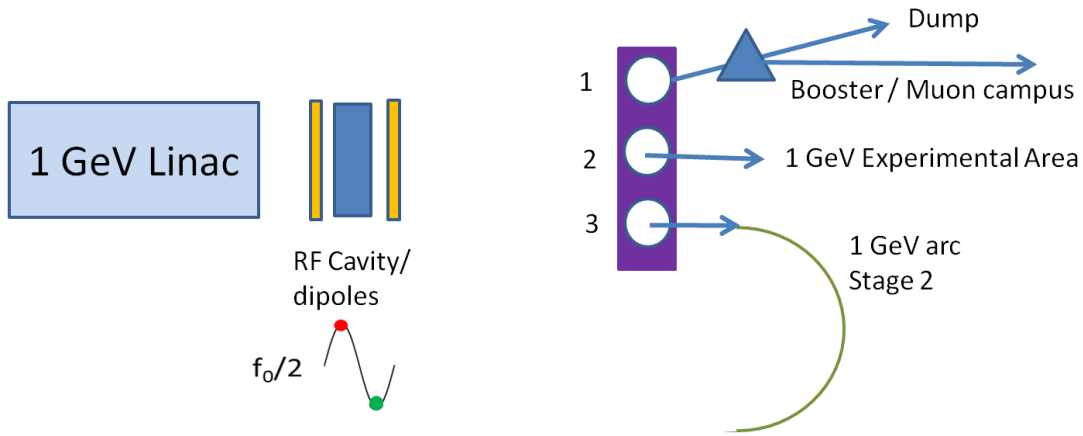


Figure III-26: Concepts for the 1 GeV beam separation for Stages 1 and 2.

Stage	Destination	deflecting cavity	Dipole	DSW
1	Muon Campus	$+\theta$	$+\theta$	
	1 GeV EA	$-\theta$	$+\theta$	
	Booster	off	$+2\theta$	
	Dump	off	$+2\theta$	on
2	1 GeV EA	$+\theta$	$-\theta$	
	Booster	off	$+2\theta$	
	Dump	off	$+2\theta$	on
	1 GeV arc	$-\theta$	$-\theta$	

Table III-5: Required powering for the Deflecting cavity and dipole to send beam to the various destinations in Stages 1 and 2

Booster injection requires a 162.5-MHz beam structure which is incompatible with simultaneous operation of the 1 GeV EA and MC. This means both programs will be interrupted during Booster injections. The MEBT chopper will prepare the required bunch pattern to fill the Booster's 47 MHz buckets during the 1-ms injection period. The chopper will remove bunches that would land at the RF bucket boundaries and create a 50 to 60 ns "notch" at the revolution period to provide a gap for beam extraction. The RF deflecting cavity is turned off during Booster injections and the vertical trim dipole near splitting cavity is energized creating twice the deflection of the RF deflecting cavity. Allowing 0.5 ms for turning the cavity off and on and ramping the dipoles would create a total interruption of approximately ~2 ms out of 67 ms, or a 3% effect. The beam line (immediately downstream of the Lambertson) for Booster injections is identical to that for sending beam to the MC. A dipole switch located in F0 sector of the Tevatron tunnel will be energized (or not) to steer beam to the MC (or Booster).

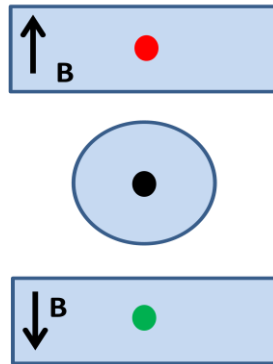


Figure III-27: Concept of the 1 GeV switchyard three-way Lambertson showing the beam centroids for the beam directed to the EA (black) and the MC/Booster (red) and the 1 GeV arc to the 3 GeV linac (Stage 2).

The required frequency of the deflection cavity is $f_{RFS} = (n + 1/2) \cdot 162.5$ MHz, where n is an integer. The frequency of 406.25 MHz ($n = 2$) is chosen. This choice of frequency is determined by a compromise between the overall sizes of SC cavity, required voltage and a variation of the kick value due to the finite bunch length.

Both field and field-free apertures of the Lambertson should be a factor of two or three larger than the 6σ beam envelope to assure loss-free transfer. From the TraceWin output we see that both the horizontal and vertical rms sizes are approximately 1.5 mm, giving a 99% beam envelope of roughly 10 mm. A 2 kG dipole field for a meter long Lambertson will give a 35-mrad horizontal deflection, sufficient to clear the downstream magnets. This will be a symmetric Lambertson with a septum thickness of approximately 10 mm, consistent with existing designs. The septum aperture is selected to be approximately $\pm 9\sigma$ so that minimize

possible beam scraping in the septum. Figure III-27 shows a conceptual design of the Lambertson aperture.

Taking into account aperture considerations, a ± 20 -mm displacement is required at the entrance to the Lambertson. To meet this separation, the RF deflection cavity should provide approximately ± 3 -mrad vertical kick. Based on the required angle, the transverse deflection voltage should be ≈ 5 MV. The deflection cavities in both the 1 and 3 GeV areas are close in frequency and maximum deflection voltage (7 MV); therefore they will have similar designs (see details in Section IV.1.7.)

III.2.2 H⁻ Transport to 3 GeV Linac

The transport line between the 1 and 3 GeV linacs is achromatic and isochronous to suppress horizontal beam emittance growth and bunch lengthening in the course of beam transport through the arc. The arc has the total bending angle of 180 deg. Its optics is based on FODO focusing. Figure III-28 presents the beta-functions, the horizontal dispersion and beam envelopes through the line. The beamline is tuned to be isochronous at 1 GeV beam energy. If required, the isochronous energy can be varied within about $\pm 5\%$, achieved by adjustments of strength of a few quadrupoles located in the large dispersion areas. In the case of small beam intensity when beam space charge can be neglected the transport through the line does not create any bunch lengthening and therefore does not produce any complications for the longitudinal beam dynamics. However for nominal intensity the space charge will result in an emittance growth as presented in Figure III-29. Although the emittance growth is not negligible it is within Project X specifications up to bunch population corresponding to 10 mA RFQ current.

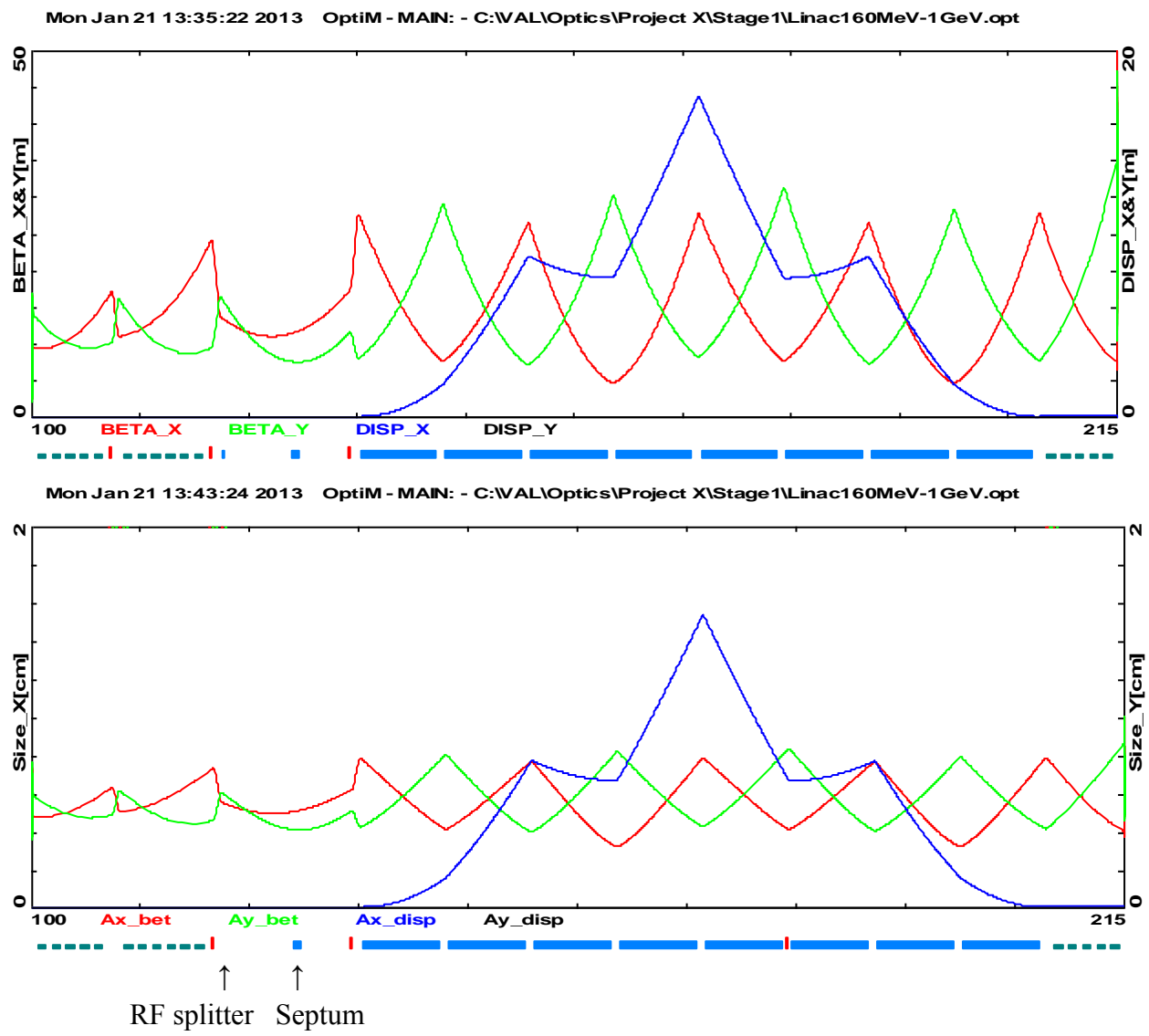


Figure III-28: Beta-functions and dispersion (top) and 4σ transverse beam sizes due to betatron motion and the energy spread (bottom) for the beam transport through 1 GeV arc connecting 1 GeV and 3 GeV linacs.

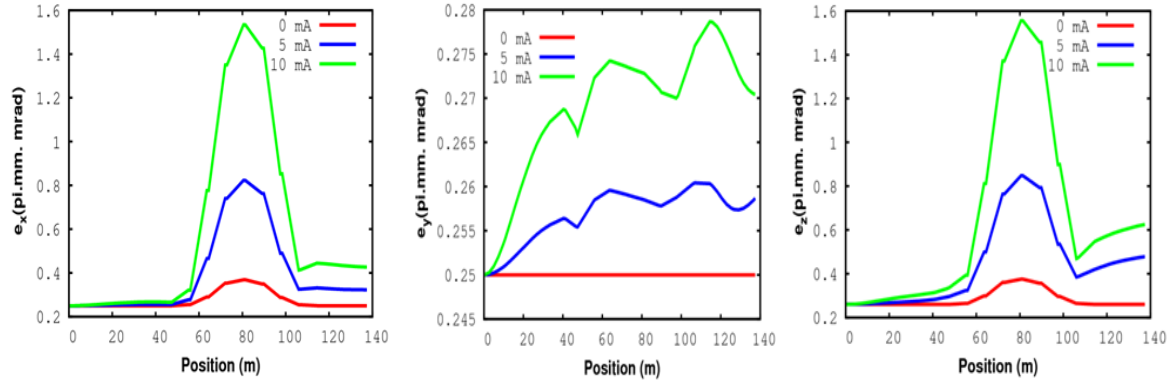


Figure III-29: Transverse and longitudinal emittance growths for the beam transport through transfer line between 1 and 3 GeV linacs for bunch populations corresponding to the RFQ currents of 0, 5 and 10 mA. The peaks in the horizontal and longitudinal emittances are an artifact of emittance computation related to non-zero dispersion in the arc and should be neglected. Note also that the scale for the vertical emittance is greatly expanded.

III.2.3 H- Transport to Experimental Areas and Booster

Transport to the Booster will utilize the decommissioned Tevatron enclosure. The transport line will be at the elevation of the Tevatron (*i.e.* installed under the existing Main Ring remnant used to transport MI beam to the Muon Source and Switchyard), which will require a compact magnet design. The new beam line will enter the Tevatron enclosure upstream of F0 where a switch dipole will be installed to divert the 1 GeV beam into the Main Ring remnant, called the P2 line, for transport to F17 and the Muon campus. The transport line to Booster will follow the footprint of the decommissioned Tevatron ring till about F35 (a length of about 750 meters) where the transport line will leave the Tevatron enclosure. This will be at a point almost tangent to both the Tevatron and Booster. A new tunnel will be created for the last several hundred meters between the two enclosures. The location and length of this tunnel section will be designed to minimize interference with existing facilities and to optimize transport optics design to match into Booster injection.

A preliminary lattice for transport between the 1 GeV Linac and Booster has been designed. It matches the curvature of the Tevatron and provides an existence proof of a solution. While the design is compatible with permanent magnets, this line will use electromagnets to provide flexibility for accommodating possible energy variations in the Booster and polarity change for the proton EDM experiment (see Section III.2.5). There are four distinct sections to this transport line: 1) straight section from the Linac to the Tevatron enclosure, 2) bend to match into Tevatron F0 straight section, 3) follow the Tevatron trajectory around to F35, and 4) a straight section that transports the beam from the Tevatron tunnel to the Booster enclosure around Long 13 H Linac Dump.

The 1 GeV linac dump will be predominately utilized for low intensity tune up. It is not expected to be used as a full intensity dump. Therefore, it will be designed for no more than 10% of full beam power, *i.e.* 100 kW. The capacity of this beam dump will need further discussion and will be optimized for price/performance and expected operational scenarios. The beam power will be controlled by duration and rep rate of the Linac. The beam will be directed toward the dump when the RF deflecting cavity is off and the dump selection dipole is powered, as shown in Figure III-25. The location of the dump on the facility site needs to be addressed. The determination of whether this will be an isolated enclosure or accessible from the transport enclosure needs to be determined by shielding considerations. The beam parameters and power range are well within the SNS operating envelope. Therefore we do not anticipate any outstanding problems for the beam dump design.

III.2.4 Beam Loss

Low loss beam transport is critical in the operation of MW class facility. The primary loss mechanisms for 1 GeV transport are H^- intra-beam stripping, Lorentz stripping, inelastic beam-gas scattering, and scraping of beam halo on the apertures. Stripping due to black-body radiation inside the room temperature beam pipe is negligible at this energy. The overall requirement is to keep the beam loss below 100 mW/m; assuring residual radiation at below 15 mrem/hour at 1 foot – the level where the radiation does not represent a problem for machine servicing. For 1 GeV beam 100 mW/m corresponds to the fractional beam loss of less than $10^{-7}/m$.

Intrabeam stripping is the main mechanism for the beam loss. It requires, if possible, avoiding tight beam focusing. As one can see from Figure III-25 it generates a beam loss rate of about 50 mW/m at 1 GeV. This loss rate is reduced due to beam debunching in the course of beam transport through the 1 GeV transport line.

Lorentz stripping (see Section III.3.2) limits magnetic field to less than 2.9 kG, corresponding to the loss rate of about below $5 \times 10^{-8}/m$ for 1 GeV beam. Leaving room for a possible 5% energy increase implies a maximum field of 2.7 kG in the dipoles of the 1 GeV bending arc. This generates the loss rate of about $5 \times 10^{-9}/m$ for 1 GeV beam.

The cross section of H^- stripping for 1 GeV beam on residual gas is about 10^{-19} cm^2 for molecular hydrogen and grows approximately proportional to Z for heavier atoms. The requirement of 2×10^{-8} for partial loss rate yields a vacuum requirement of 10^{-8} Torr or better for H_2 and about an order of magnitude better for heavy molecules (hydrocarbons, water, etc.). The beam intensity transported to the Muon Campus is approximately 100 kW.

Consequently an application of vacuum practices developed in Fermilab for not-baked vacuum systems, which routinely achieve low 10^{-8} Torr, has to be sufficient.

The aperture, optics, and vacuum level of the transport lines will be designed with the goal of a loss free transport. This is most critical for the sections of transport line which will transport high beam power. This means that the aperture should be greater than 12σ and preferably closer to 18σ to minimize any losses to steering errors or scraping of any halo that is formed during acceleration or transport. Due to the concern of generating transverse halo by the beam space charge in a strong focusing transport line, the transverse focusing properties of the 1 GeV Linac should be continued into the beam line to the point just past the Experimental Area switch dipole to keep a more or less uniform beam size through the high intensity part of the line. At that point, we have the option to match into a FODO lattice for transport to the Booster. Due to bunch lengthening the problem of the space charge is fast diminishing with further beam transport and becomes much less significant after about first 100 m of beam transport.

III.2.5 Provisions for sub-GeV proton based research

A proton electric dipole moment (EDM) experiment is planned as a part of the Project X physics program. This experiment will require infrequent injections (once in about 20 min.) of polarized proton beam into a newly constructed ring with electrostatic bending at beam energy of 235 MeV. A one-turn injection of 1 mA beam will take $\sim 2 \mu\text{s}$ and deliver about 10^{10} protons with normalized emittance equal or below $\sim 0.25 \text{ mm mrad}$. If larger intensity is required a few turn injection is possible too as well as larger current from the ion source which can be supported for a few μs time by energy stored in the SC cavities.

A few actions will be required to support sub-GeV proton operations. First, a polarized proton source is required. This source can be installed in place of the spare H^- ion source. This implementation minimizes changes in the LEBT while leaving room for alternative implementations. In spite of the fact that protons are positively charged further beam acceleration can be achieved with the Project X accelerator without any significant changes from H^- operations. Neither the solenoidal focusing in the HWR, SSR1 and SSR2 nor the quadrupole focusing in the LB650 requires any changes. The only change from the beam dynamics point of view will be interchanging x and y -coordinates. However, there are three actions that are required. First, some beam re-steering will be required due to imperfections of machine alignment. Normally this should not require more than 1 sec. Second, to obtain the required beam energy the phases of cavities located downstream of 235 MeV point have to be shifted to “no acceleration” and their voltage reduced to prevent longitudinal over-focusing and to reduce transverse defocusing. The low level RF controlling the cavity voltage

and phases should be able to do this within 10 ms without additional modifications of the hardware. Third, the quadrupole focusing in the HB650 part of the linac has to be reduced. This action should not take much longer than 1 s for laminated quadrupoles which will be a requirement for their design if a short switching time is required. The necessity to reduce focusing in the HB650 section is related to the following: the design optics for 1 GeV linac implies gradual reduction of quadrupole focusing with energy to minimize intrabeam stripping. Therefore the quadrupole strength in the LB650 section normally accelerating beam from 177 to 480 MeV is reduced with energy and an absence of energy growth downstream of 235 MeV point does not cause over focusing. The period of quadrupole focusing is approximately doubled in the HB650 section and its focusing is set to obtain close to 90° betatron phase advance per period at the section beginning, with beta-functions matched to the growing beta-functions of LB650 section. Therefore the reduction of energy at the HB650 entrance will result in over focusing and loss of particle motion stability. To avoid it a reduction of focusing in HB650 section is required.

If the EDM ring is located in the (former) antiproton source tunnel it can use the 1 GeV transport line directed to Muon campus. In this case the polarity of all dipoles has to be changed. If required, running the EDM experiment in normal operating conditions should not take more than 0.2% from the Project X duty cycle.

III.3 3 GeV Beam Handling

III.3.1 Transport Line Requirements and Physics Design

At Stage 2, the current in the 1 GeV Linac will be increased to 2 mA. The RF splitter at the end of the 1 GeV Linac will send half of the bunches to the 1 GeV Experimental Area and the other half to the 3 GeV Linac, each with a bunch structure of 81.25 MHz. After acceleration in the 3 GeV Linac, the beam will be transported to either the 3 GeV Experimental Area, where it will be further distributed to experiments by a 3-way RF splitter/Lambertson magnet combination, or the 3 GeV beam dump. The selection between the Experimental Area and the dump will be controlled by a DC dipole, DS3. If it will be required in the future, additional RF splitters can be installed downstream of the primary splitter allowing an increase in number of experiments.

At Stage 3, a 3-8 GeV pulsed Linac will be added to accelerate the beam for injection into the existing Recycler. The MEBT chopper will prepare a 162.5 MHz bunch structure for acceleration in the 1 and 1-3 GeV linacs. A pulsed dipole switch, DS4, will be energized for approximately 4.4 ms to direct the 3 GeV beam into a 180 degree arc. The arc is isochronous and achromatic. Figure III-30 shows a concept of the 3 GeV Switchyard for both Stages 2

(blue components) and Stage 3 (green components). The location of all the components for Stage 2 and upgrade to Stage 3 will be further optimized according to optical design, site conditions, and cost minimization.

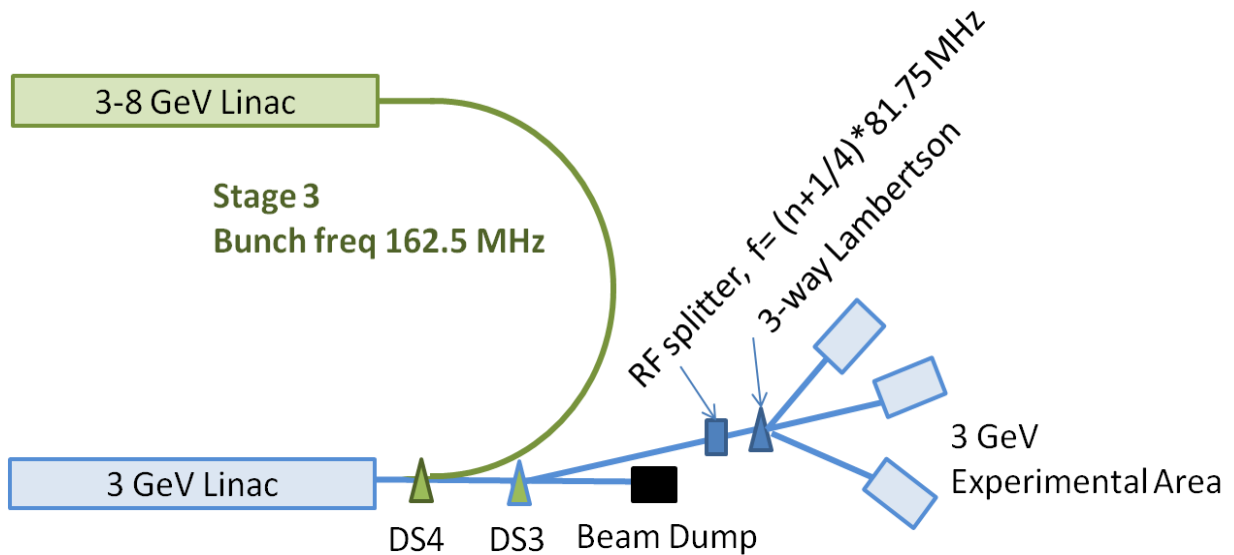


Figure III-30: Preliminary layout of the 3 GeV Switchyard showing the splitting to the Experimental Area (Stage 2 in blue) and the HE Linac (Stage 3 in green).

III.3.2 Beam Loss

The configuration of transport lines supports H⁻ beam transport both to the Pulsed Linac (135 kW) and to the Experimental Area (3 MW). The requirements to the fractional beam loss are dominated by the higher intensity beam transport to the Experimental Area.

The H⁻ transport should have sufficiently small loss to minimize residual radiation in the tunnel. It is highly desirable to keep residual radiation level below 15 mRem/hr. Many facilities use the metric of 1 W/m as a limit for “hands on” maintenance, however, at 3 GeV, a 1W/m loss rate corresponds to a loss of 2.1×10^9 p/m/s and produces a peak contact residual dose rate of ~ 150 mrem/hr [22] on a bare beam pipe. This loss rate produces significantly lower residual activation on external surfaces of magnets due to shielding by the magnet core steel. However, a main concern is the residual level at magnet interfaces and instrumentation locations. These levels are based upon MARS calculations and used for order of magnitude estimations. A more accurate estimation will be required once a detailed model of the transport line is available. Setting a desirable activation level to 15 mrem/hr results in a loss goal of ~ 0.1 W/m, and, consequently, a fractional loss rate of 7.8×10^{-7} /m and 3.4×10^{-8} /m for 135 kW beam to the pulsed linac and 3 MW beam to the experiments, respectively. The single particle mechanisms contributing to the beam loss are the Lorentz stripping in dipoles,

the beam stripping in the residual gas, the photo detachment by blackbody radiation in the beam pipe, and loss due to intra-beam stripping, which in a normal operational state will be a dominant contribution.

Beam motion in a magnetic field excites an electric field in the beam frame. If this electric field is sufficiently strong, it can detach the weakly bound outer electron (Lorentz stripping). Figure III-31 shows the loss rate per meter of dipole field for a 3 GeV kinetic energy H^- as a function of magnetic field. One can see that a dipole field of 1.3 kG produces a fractional loss of 3.7×10^{-8} /m. As the dipoles occupy a significant fraction of the beam line, in particular in the 180° arc, one would like to select a field which produces negligible loss. A dipole field of 1.2 kG is chosen as the maximum field to be used in the 3 GeV transport lines. This produces a fractional loss of $\sim 3.4 \times 10^{-9}$ /m.

The loss rate due to H^- scattering on the residual gas molecules is proportional to their density and the ionization cross section of the molecules present. The cross section decreases proportionally to β^{-2} and therefore is only marginally smaller than for 1 GeV. Taking into account the three times larger beam power, one needs three times better vacuum to achieve the same radiation levels. Thus vacuum of 3×10^{-9} Torr or better is required.

The contribution from the blackbody photons at 3 GeV at room temperature is 1.3×10^{-7} /m as seen in Figure III-32. It is well within specifications for transport to the pulsed linac, where the beam power is limited to 130 kW at 3 GeV, however for transport of 3 MW beam power it is only slightly below the specification. Lowering the beam pipe temperature to 150 degrees K reduces the fractional loss to 5×10^{-10} /m. At room temperature, one can see that the black body radiation is expected to make a major contribution.

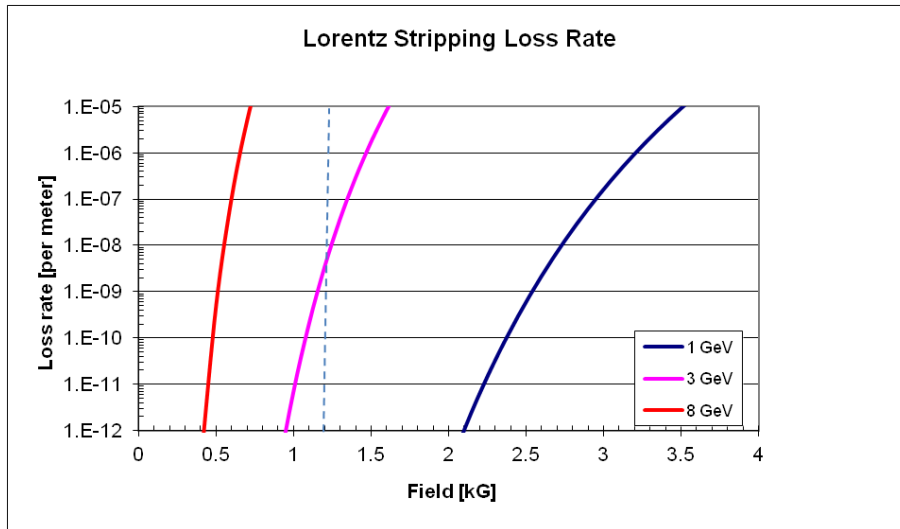


Figure III-31: Fractional loss for a 3 GeV H^- ion traveling in a dipole field. The dashed line marks a magnetic field of 1.2 kG.

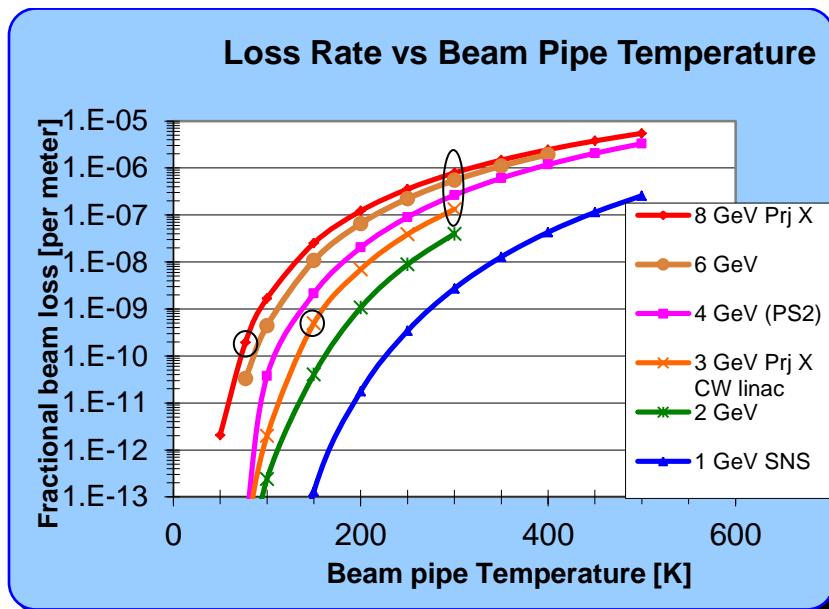


Figure III-32: Loss rate [m^{-1}] due to the interaction of blackbody photons as a function of internal beam pipe surface temperature for several values of H^- kinetic energy.

Estimation of loss due to intra-beam stripping has been carried out for the entire CW linac. The loss depends on the local transverse velocity of the ions and proportional to the lattice functions. The transport line utilizes the same FODO structure as the 1.3 GHz linac so the contribution due to intra-beam stripping should be comparable to that calculated for the end

of the CW linac, namely ~ 30 mW/m. This will be smaller in the arc due to bunch lengthening.

Table III-6 summarizes the contributions of the four single particle loss mechanisms discussed above. Note that the value for the intra-beam stripping contains only an estimated beam loss power where the value was taken from the CW Linac estimates. For the HE linac transport line, the loss rate due to Lorentz stripping with the selection of the dipole field of 1.4 kG is the dominant loss but acceptable at only 37 mW/m. Losses within the transport line to the Experimental Areas is dominated by blackbody radiation and is 0.4 W/m – on the edge of acceptability. Lowering the beam tube internal surface temperature with a beam screen to gaseous nitrogen temperature, 150°K, and improving the vacuum to 5×10^{-9} Torr lowers the total beam loss to ~ 60 mW/m and expected residual activation on a bare beam pipe to ~ 10 mrem/hr.

Loss Mechanism	CW to Pulsed Linac			CW to Experiments wo/ shield			CW to Experiments w/shield		
	Value	Loss/m	W/m	Value	Loss/m	W/m	Value	Loss/m	W/m
Vacuum	1E-08 Torr	1.3E-08	0.002	1E-08 Torr	1.3E-08	0.04	5E-09 Torr	6.9E-9	0.021
Lorentz	1.4 kG	2.9E-07	0.037	1.2 kG	3.4E-09	0.01	1.2 kG	3.4E-09	0.01
Blackbody	300 K	1.3E-07	0.017	300 K	1.3E-07	0.39	150 K	5.0E-10	0.001
Intra-beam			0.001			0.03			0.03
Total		4.3E-07	0.057		1.5E-07	0.47		1.1E-08	0.062
Residual Activation, bare beampipe, mrem/hr	8.5			69.5			9.2		

Table III-6: Summary of beam losses in the 3 GeV transfer lines between the CW linac and the pulsed linac and experimental areas. The beam power within the pulsed linac transfer line is ~ 130 kW, while the beam power within the Experimental Areas transfer line is ~ 3 MW.

III.3.3 H- Dump

A straight-ahead beam dump is provided for beam tune up. The transport line to the dump has optics similar to FODO lattice used in the linac-to-Experimental Area transport line. The beam dump is located in a separate enclosure at a distance of about 150 m from the end of the linac. Beam sweeping on the dump face reduces the power density to an acceptable level. A buried beam pipe connects the beam-line enclosure to the beam dump enclosure. For a rms emittance of 0.25π mm-mrad, the spot size on the face of the dump with a beta of 250 m is about 25 mm.

III.3.4 H- Transport to Pulsed Linac

Similar to the 1 GeV area, the beam delivery to the next stage proceeds through 180 deg. arc. The arc is isochronous and achromatic. Its optics is built similar to the 1 GeV arc but higher beam energy requires the following changes to be taken into account. Mitigation of Lorentz stripping results in smaller field in dipoles and much larger length of the arc. An energy increase reduces the dependence of particle velocity on its momentum. It requires stronger focusing to make the linac-to-linac beam transport isochronous. The beam line Twiss functions are presented in Figure III-33. Similar to the 1 GeV transport the beam space charge results in an emittance growth. The results of simulations are presented in Figure III-34. In spite of higher energy the emittance growth is larger than for 1 GeV beam due to much larger length of the beam transport.

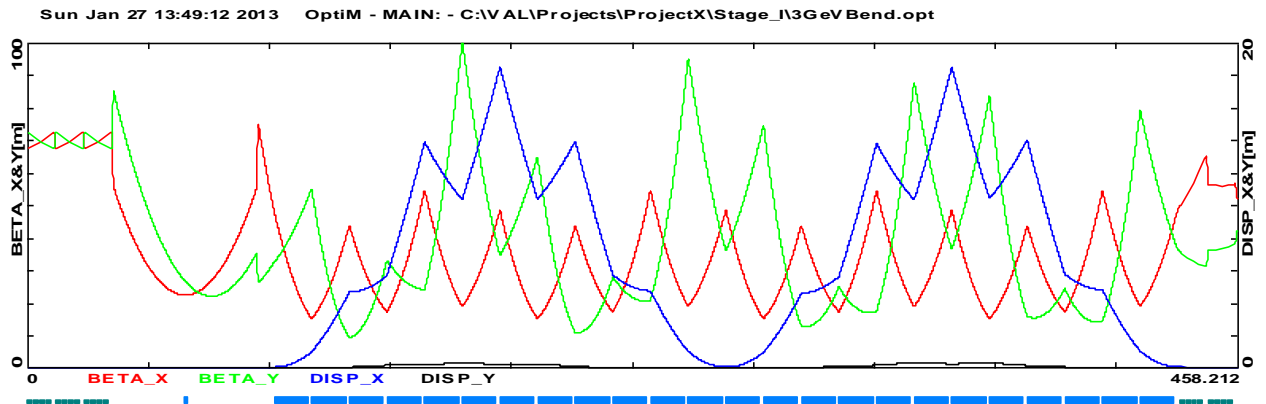


Figure III-33: Beta-functions and horizontal dispersion for the beam transport from 3 GeV CW linac to Pulsed linac.

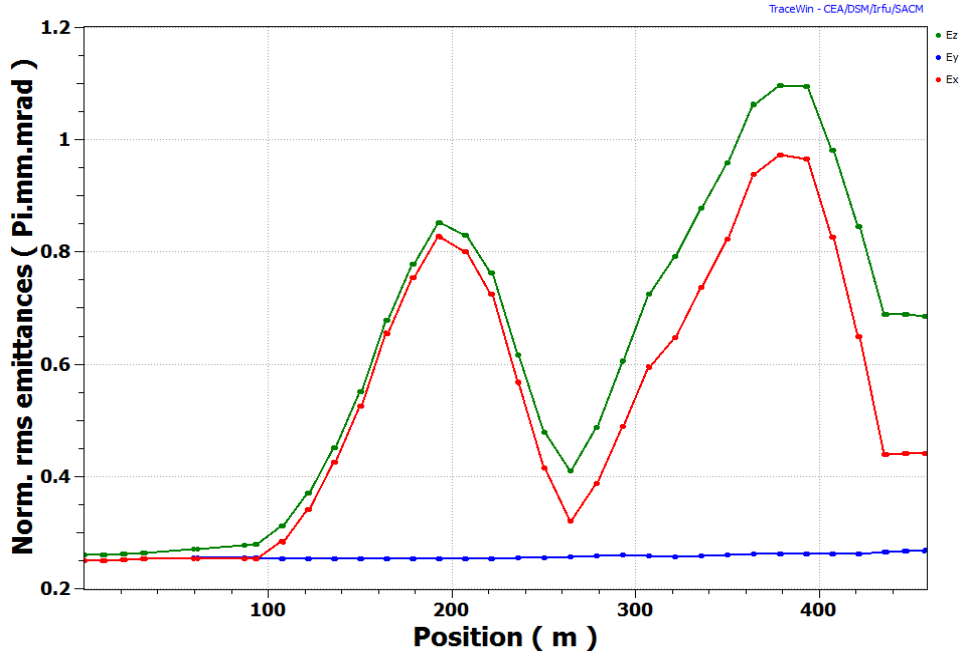


Figure III-34: Dependence of beam emittances on distance from the CW linac for the beam transport from 3 GeV CW linac to Pulsed linac.

III.3.5 H- Transport to Experimental Area

If the pulsed HE linac switch, DS4, magnet is off (in Stage 3) and the DC Experimental Area switch magnet, DS3, is on, the 3 GeV H⁻ beam will be directed toward the Experimental Area. The beam power in this transport line is up to 3 MW. It is critical to minimize single particle losses, provide sufficient aperture, and provide collimation to remove large amplitude particles that could become lost in unprotected areas.

Immediately after splitting off the dump line via a horizontal 2 dipole achromat, a section of the FODO lattice is reserved for a potential collimation system. It can increase the power handling capability of the transport line but a cooled beam screen and good vacuum are required to keep losses at acceptable level for the rest of transport line.

The beam may be directed toward any one of three experimental areas utilizing and RF splitter giving bunches (separated in time, see Figure II-3) either a positive, negative, zero vertical kick (depending on their arrival phase). A downstream three way Lambertson magnet finally separates the beams horizontally.

III.3.6 Splitter/Lambertson Optics

Figure III-35 shows the beam positions at the face of the Lambertson magnet. The RF splitter will impart a small vertical angle based upon the phase of the beam with respect to the RF splitter phase. As this Lambertson is expected to distribute up to 3 MW beam power to the experimental facility, its apertures should not be limiting. A conservative estimate of the required aperture dictates an aperture that is at least a factor of two to three greater than the 99% beam envelope. This gives rise to a separation of 12σ to $18\sigma + \Delta s$, where Δs is the septum thickness of the Lambertson. To avoid septum saturation at the expected field of 0.64T the septum thickness of 5 mm is required.

For a normalized rms transverse emittance of 0.37 mm-mrad at the entrance to the Lambertson, the rms vertical size varies from 1.25 mm, at the entrance, to 1.02 mm at the exit of the 2 m Lambertson. Using the 18σ figure the separation at the entrance to the Lambertson should be ± 27.5 mm. The required deflection angle, $\Delta\theta$, is given by $\Delta y / (\beta_c \beta_L) \sin\phi$, where β_c and β_L are the beta functions at the cavity and Lambertson, respectively, and ϕ is the vertical phase advance between the two locations, is ± 1.3 mrad. It requires the RF splitter voltage of 5 MV which value is well within specified 7 MV voltage for the RF splitter cavities. The kick variation during bunch passage through the splitting cavity results in an emittance growth. This effect is much stronger for the central (not deflected) bunch which sees the largest derivative of voltage change, dV/dt . An estimate of transverse emittance growth for this bunches shows that this is not an issue if distance between the linac and RF splitting cavity does not exceed ~ 100 m.

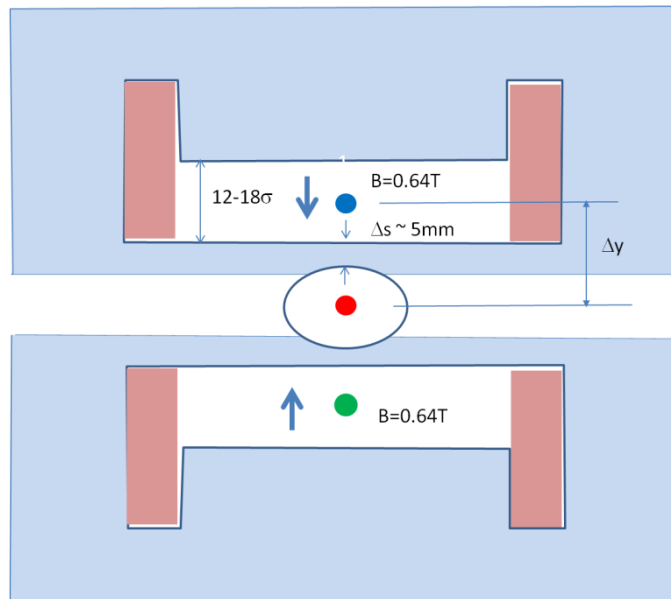


Figure III-35: Beam positions at the entrance of the 3 way horizontal Lambertson for μ -to- e (blue), Kaon (red), and the other experiment (green). Arrows indicate field direction.

III.4 3-8 GeV Pulsed Linac

III.4.1 Linac Parameters

The 3-8 GeV linac is a pulsed superconducting linac accelerating beam from 3 to 8 GeV. It can support a beam current of 1 mA with a pulse length of 4.3 ms and a repetition rate of 10 Hz. Figure II-1 shows the linac timeline. The bunch micro-structure (at the microsecond level) in the pulsed linac is determined by the Recycler RF bucket frequency (52.8 MHz) and the Recycler revolution frequency (90.3 kHz). The former requires bunches at the RF buckets boundaries to be removed. The latter requires removal of bunches to form a 200 ns extraction gap. The beam from the 3 GeV CW linac is directed to the pulsed linac by a pulsed dipole with a rise time of 0.5 ms. After acceleration in the pulsed linac the beam is transported to the Recycler and injected with a multi-turn strip-injection utilizing stripping foils or laser assisted stripping. Six 4.3 ms pulses are required to fill the Recycler to its maximum intensity ($1.6E14$) required for the neutrino program. Then, the beam is transferred to Main Injector (MI). The complete injection cycle requires 0.5 s. This time fits well within MI cycle which is of duration 1.2 s for 120 GeV operation and 0.7 s for 60 GeV operation. Additional linac pulses are available for an 8 GeV research program. The pulsed dipole and the beam line transporting the beam from the 3 GeV CW linac to the 3-8 GeV pulsed linac have been described in Section III.3.4. Table III-7 presents the basic parameters of the pulsed linac.

Parameter	Quantity	Unit
Particle Species	H-	
Input Beam Energy	3.0	GeV (kinetic)
Output Beam Energy	8.0	GeV (kinetic)
Pulse Repetition Rate	10	Hz
RF pulse length	8.4	ms
Beam Pulse Length	4.3	ms
Average Pulse Beam Current	1	mA
8-GeV Transverse Emittance	0.4	mm-mrad (rms norm)
8-GeV Longitudinal Emittance	1.6	keV-nsec
8-GeV Bunch Length	1.0	ps (rms)
Quad aperture (diameter)	75	mm
Quad strength	1.7- 2.4	T/m

Table III-7: Pulsed Linac Parameters

III.4.2 Accelerating Cavities and Cryomodules

The pulsed linac is based on XFEL/ILC technology: 1.3-GHz 9-cell cavities (Figure III-36) optimized for $\beta = 1$ and ILC-type cryomodules, providing a FODO focusing structure (Figure III-37). All quadrupoles are superconducting and located at the center of each cryomodule. Each quadrupole has built-in vertical and horizontal correctors and an attached Beam Position Monitor (BPM) for beam based alignment and orbit control. Basic parameters of the cavity and cryomodule are presented in Section IV.

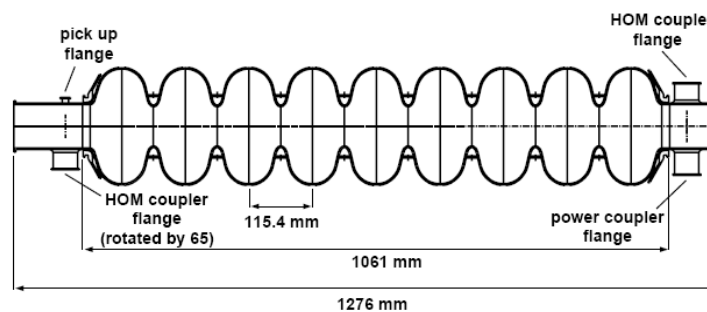


Figure III-36: Schematic of a 9-cell 1.3-GHz cavity

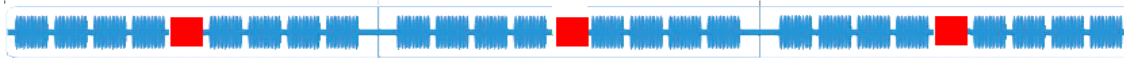


Figure III-37: Schematic of the linac focusing structure (red – quadrupoles, blue – SCRF cavities)

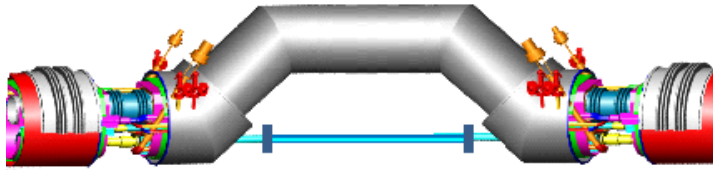


Figure III-38: Schematic of the warm section in between two cryogenic strings.

Each cryomodule contains 8 cavities and one quadrupole in the middle. For the average cavity gradient of 25 MV/m with acceptable gradient spread $\pm 10\%$ the linac require 28 cryomodules with 224 cavities. The total length of the linac is ~ 390 m. The pulsed linac has a cryogenic segmentation consisting of three cryo-strings with 10, 9 and 9 cryomodules in each string. Cryogenic strings are separated by warm sections required for beam instrumentation and collimation. In the current configuration the distance between cryo-strings is equal to the length of a cryomodule, providing ~ 5 m of empty space for collimation and beam diagnostics. The possible solution with bypass transfer lines, designed for XFEL linac is shown in Figure III-38.

III.4.3 Pulsed Linac – Beam dynamics

The lattice design and the beam dynamics optimization are made utilizing the TRACK and TraceWin codes. In the current lattice the gradient is set to 23.5 MV/m and synchronous phase to 8 degrees for all cavities in the linac. Over the linac energy range space-charge effects are not severe. The total number of oscillations in longitudinal phase-space is less than one over the whole linac and the longitudinal envelope is relatively smooth even without proper matching. Figure III-39 shows the simulated beam envelopes along the linac and Figure III-40 displays the actual particle density distribution through the linac. Emittance growth and structural phase advance along the Linac are shown in Figure III-41. Figure III-42 contains several plots characterizing the linac: energy gain per cavity; average cryogenic losses per cavity with $Q_0=1.10^{10}$; focusing quadrupole strengths; and beam energy.

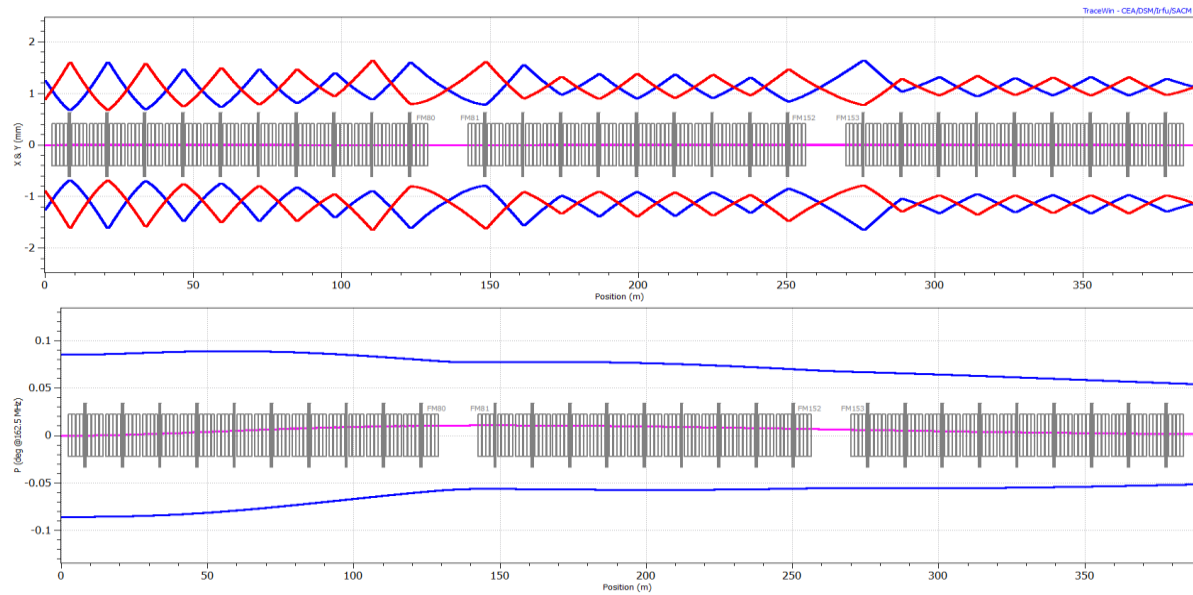


Figure III-39: Simulated rms beam envelopes in the pulsed linac: transverse (top) and longitudinal (bottom).

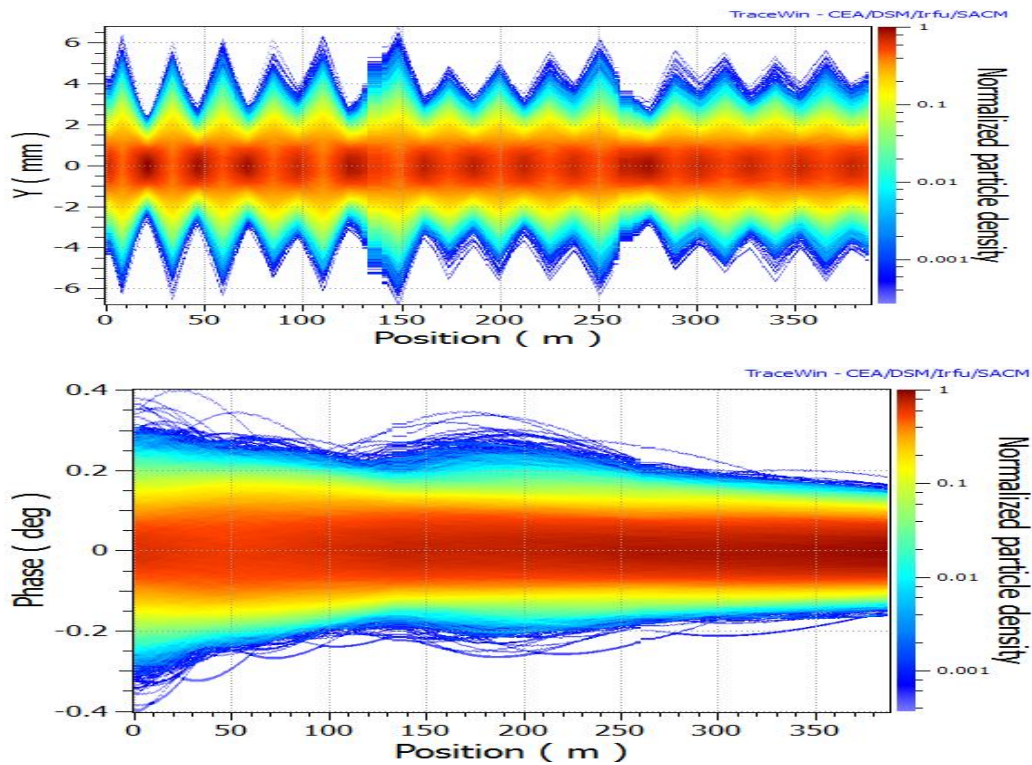


Figure III-40: Particle density distribution along the pulsed linac. 100k tracked by PARTRAN.

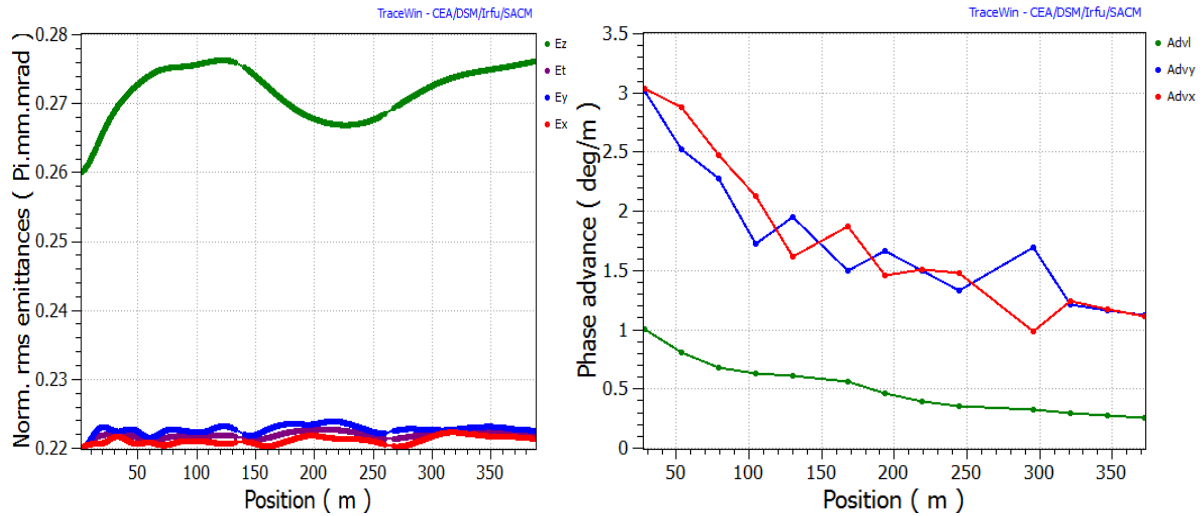


Figure III-41: (Left): Longitudinal (green) and transverse emittance growth along the linac. (Right): Structural phase advance along the linac: longitudinal (green), X&Y – (red/blue).

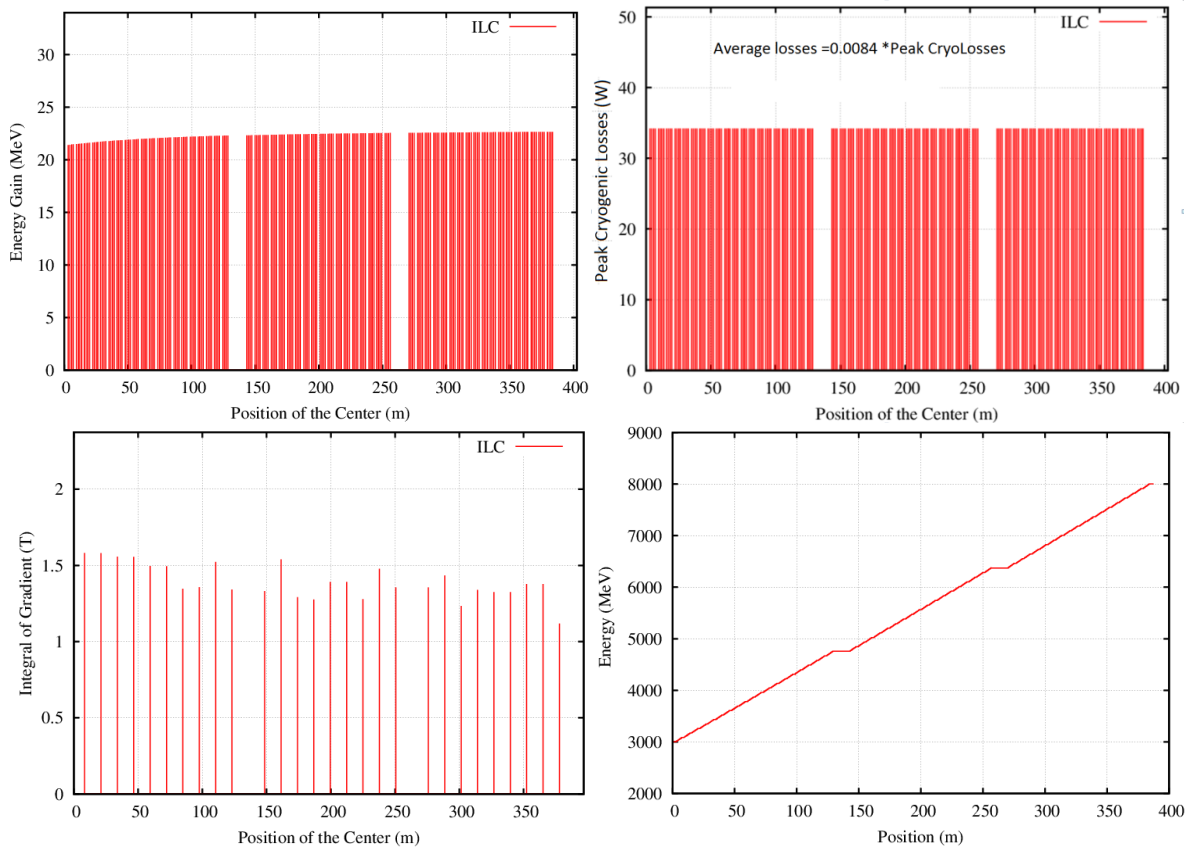


Figure III-42: Energy gain per cavity (top-left); Peak cryogenic losses (top-right); integrated strength of the quadrupoles (bottom-left); and Energy along the linac.

III.4.4 RF Requirements and LLRF

Each cavity requires 50 kW RF power taking into account the overhead needed for LLRF control and compensation of losses in the distribution system. One RF station (klystron with modulator) will feed one (or two) cryomodules. Thus, klystron power is 400 (or 800) kW and total number of klystrons in the linac is 28 (14). The vector sum (VS) signal from cavities fed by one klystron is controlled by LLRF system with required stability of $\sim 0.5\%$ and ~ 0.5 degrees in amplitude and phase. The final choice between 1 or 2 cryomodules per klystron system will be based on R&D on Lorentz force detuning compensation and errors studies.

The half-bandwidth of the cavity is 65 Hz for the designed value of $Q_L=1\times 10^7$, while Lorentz forces from electromagnetic fields will detune cavity up to ~ 1 kHz at the nominal gradient of 25 MV/m. A fast piezo-tuner and dedicated Lorentz Force Detuning Compensation (LFDC) algorithm are thus necessary to achieve the required < 30 Hz frequency stability of the cavity during the RF pulse. Preliminary results from LFDC studies in long pulse operation for 2 cavities in the cryomodule tested in NML are presented in Figure III-43. These studies clearly demonstrate that the adaptive compensation algorithm is able to achieve cavity frequency detuning of ~ 3 Hz rms (20 Hz peak-to-peak). Note that the measured level of detuning from microphonics, 2-3 Hz rms, is comparable with total frequency detuning.

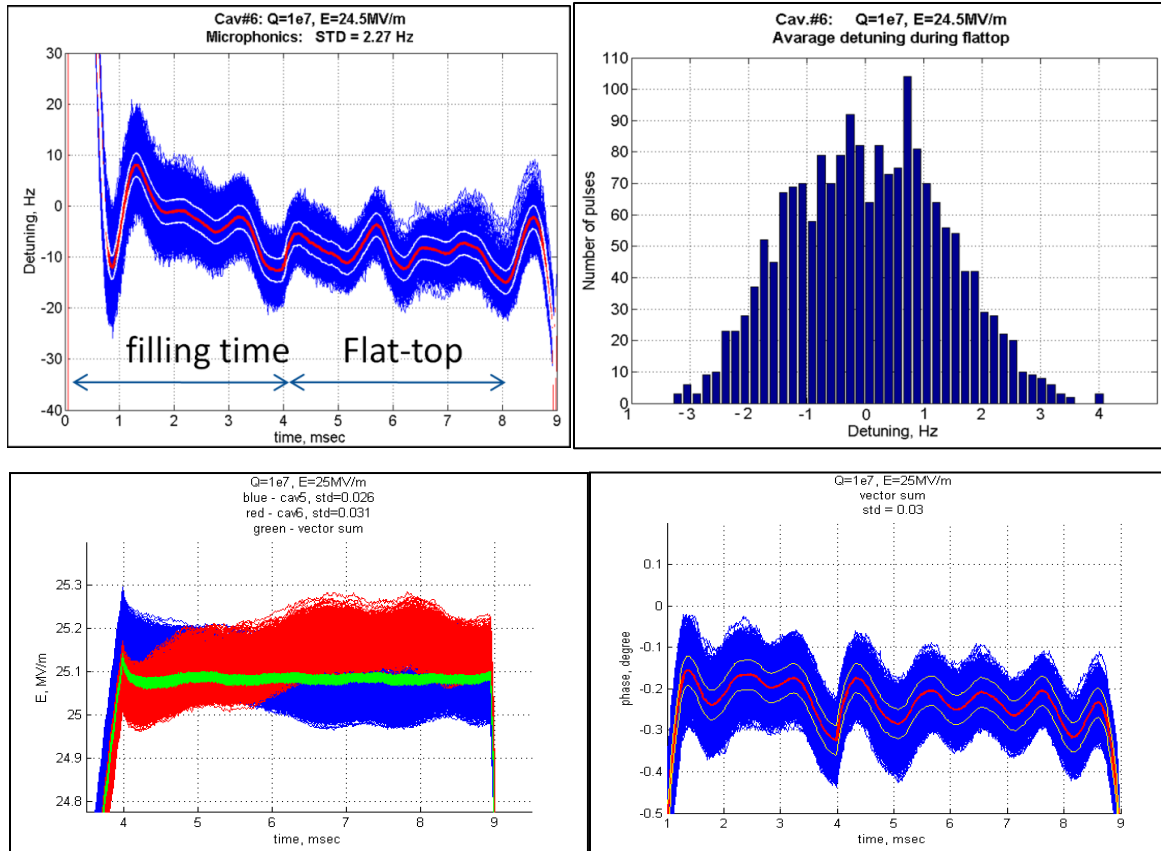


Figure III-43: (top-left): Residual cavity detuning after LFDC for 1800 pulses (microphonics included). (top-right): Histogram of average cavity detuning during the flat-top of the pulse. (bottom-left): Amplitude jitter in cavities (red and blue) and Vector sum signals. (bottom-right): Rms phase jitter in VS signal is ≈ 0.03 deg; rms phase jitter of individual cavities is ≈ 1 deg.

III.5 8 GeV Transport Line

III.5.1 Transport Line Requirements and Physics Design

Taking into account the large radius required to bend the 8 GeV H^- beam (≥ 1 km), the MI-10 straight section in the Main Injector/Recycler complex is identified as the preferred injection point (see Figure I-2). This straight section will be also used for extraction from the MI for LBNE; however because injection and extraction are bound to different machines which are vertically separated this is not expected to be an obstacle.

The new Recycler injection will be via a symmetric straight section with at least 20 meters between the doublets defining the straight. The straight section has zero dispersion and will

feature variable beta functions at the foil location. The condition $\alpha_x = \alpha_y \approx 0$ at the foil location will be applied to minimize the number of foil hits by the circulating beam.

The transport line will be designed to minimize losses due to all sources (discussed in the following) and maximize transmission. The transport line should match into the foil location with zero dispersion (in both planes) and should be able to adjust the spot size on the foil.

The elevation of transport line enclosure floor is expected to match the floor of the MI. The transport line must be optically matched to the new Recycler injection straight section with the additional civil constraint of minimizing the impact of new transport line enclosure on the MI and its tunnel. This is accomplished by adjusting the trajectory of the transport line to miss the “concrete nose” of the wide MI-8 tunnel intersection. The trajectory should be on the MI8 side of the “nose” which will help to minimize the impact to the MI enclosure during the tie-in of the new transport line. Figure III-44 shows the geometry.

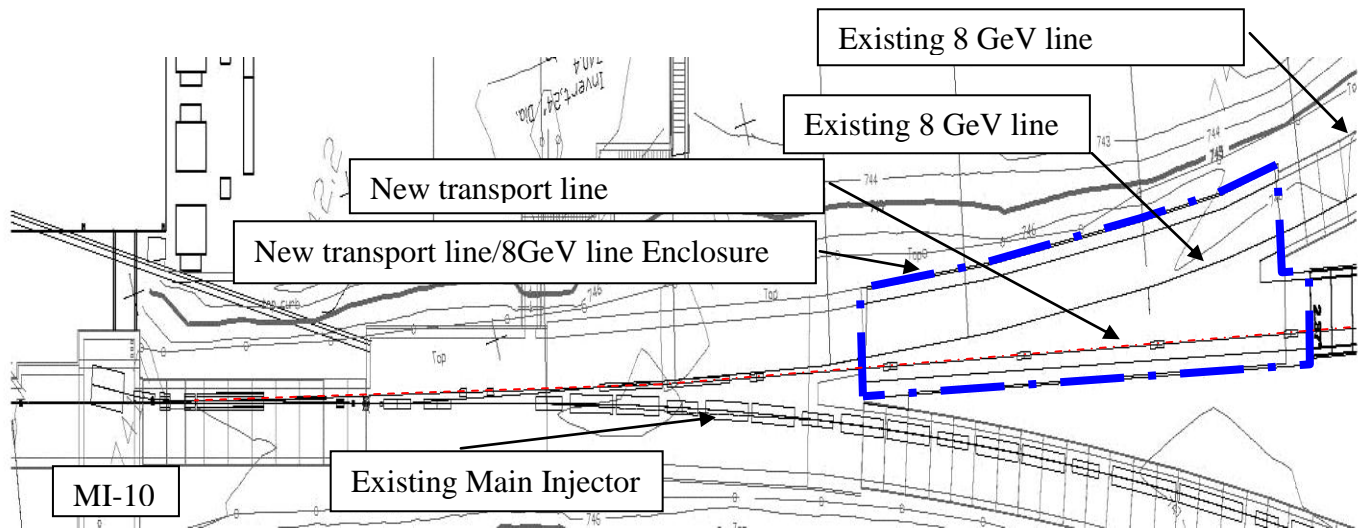


Figure III-44: Location of new 8 GeV H- transfer line approaching the MI-10 straight section.

III.5.2 Beam Loss

There are two major categories of beam loss. The first is directly related to the beam optics design and aperture limitations. It can be mitigated by correct choice of phase advances per period, avoiding non-adiabatic changes of Twiss functions, maximizing apertures (as

practical) and providing good orbit control. The latter requires a sufficient quantity of dipole correctors, beam position monitors and beam loss monitors. The second major category of beam loss is related to kinetic effects such as the beam-gas interactions and Lorentz stripping, stripping due to black-body radiation, and H⁻ intra-beam stripping. Each of these mechanisms has been described in detail in the previous sections (in particular see Section III.3.2.). All of these loss mechanisms may also be mitigated by design, *i.e.* by the vacuum level, limitations on magnetic fields, the interior temperature of the beam tube, and the strength of beam focusing. When operating with beam at the full 10 Hz pulsed linac capability, the beam power transported through the 8 GeV transport line will be 342 kW. Table III-8 summarizes the expected loss for the design choices of vacuum level, dipole field, beam tube temperature, and intra-beam stripping.

Loss Mechanism	8 GeV: 345 kW		
	Value	Loss/m	W/m
Blackbody	300 K	8×10^{-7}	0.3
Lorentz	500 G	5×10^{-10}	0.0002
Vacuum	1×10^{-8} Torr	1×10^{-8}	0.004
Total		8×10^{-7}	0.3
Residual activation bare beam pipe (mrem/hr)			15

Table III-8: Expected Beam loss contributions at 8 GeV

III.5.3 H⁻ Linac Dump

The design power for the H⁻ Linac dump is determined by assumptions on its utilization during the commissioning and operational phase as well as accident conditions. The initial design should be consistent with the maximum beam power expected during routine operation not only of Stage 3, but the ultimate utilization under Stage 4 as well, because once the enclosure and infrastructure are built and the dump absorber is installed and used, it becomes very difficult to make modifications to a highly radioactive component. The anticipated Stage 4 beam power is 4 MW at 8 GeV; however the design criteria for the dump is that it can absorb 10% of the total beam power implying a 400 kW capability. This is substantially less than the capability of the existing Main Injector dump. With an operational power during Stage 3 of 341 kW, this would imply that the dump absorber is capable of accommodating the entire linac beam power. However, we may wish to limit the beam directed to the dump to 34 kW based on requirements of components upstream of the absorber, for example the vacuum window at the absorber window. These evaluations will be completed as part of the more detailed dump design at the appropriate time.

III.5.4 H⁻ Transport to Recycler

The current version of the transport line between the 8 GeV pulsed Linac and the Recycler contains a single long achromatic arc to avoid the MI65 service building. With the location of the pulsed Linac on the Tevatron infield, the transport line must cross under the Tevatron and AP1 transport line tunnels, avoid the MI65 Service building, and merge into the MI8 transport line enclosure just upstream of the MI10 straight section. The current length of this transport line is on the order of 800 meters. This length could shrink or grow as the siting of the pulsed linac becomes firmer, but this will not significantly impact the basic design of the transport line. The basic structure of the transport line is a 90° FODO cell. It contains a matching section to both the Linac and Recycler, a transverse collimation section, a momentum collimation section, and a vertical bend section to match into the Recycler elevation. All bending sections shall be achromatic. Figure III-45 and Figure III-46 show respectively the lattice functions and dispersion of the present design. Note the collimation section (made up of 4 movable stripping foils and 4 movable jaw absorbers) is at the beginning of the line right after matching. The location of the collimators will be further optimized. The section with the vertical dipoles is not shown as the elevation of the pulsed Linac has not been firmed up. We do know that this vertical offset will comprise of 2 vertical dipoles separated by 360° such that the bend is achromatic. If the elevation of the Linac and transport line are the same as the Main Injector, the required elevation change is roughly 1.5m. This requires a bending angle of approximately 12 mrad which can be created with a 6 meter dipole at ~560 G. This will probably be located just before the horizontal arc.

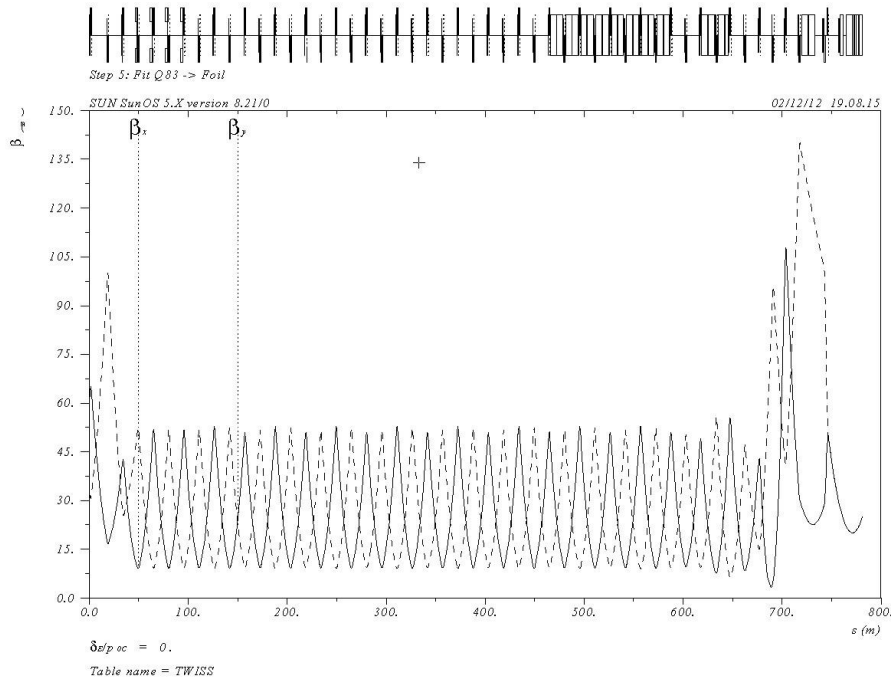


Figure III-45: Lattice functions of the 8 GeV H⁻ transport line directed to the Recycler.

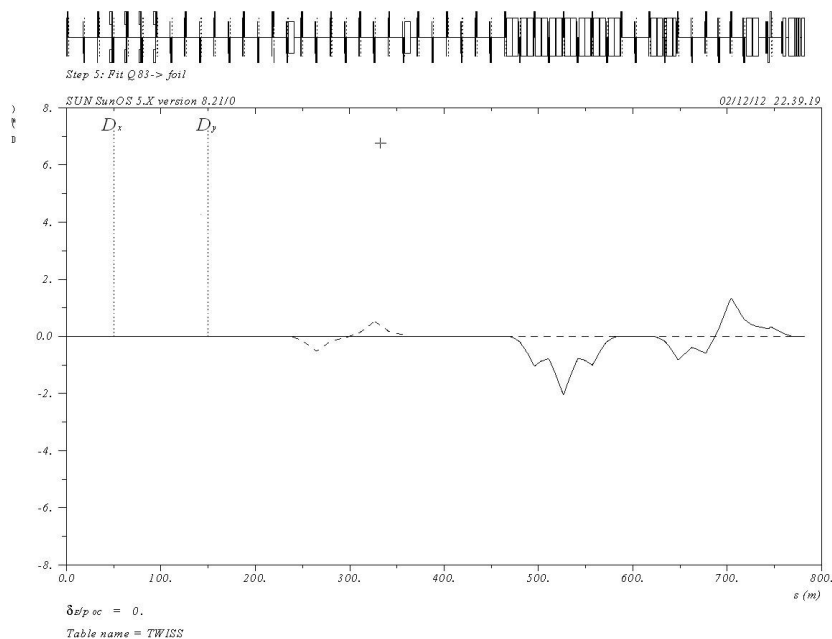


Figure III-46: Dispersion in the 8 GeV H⁻ transport line directed to the Recycler.

Since the transport line is matched to the permanent-magnet based Recycler it is likely that the line will be based on permanent magnets also. This is similar the existing Booster-to-MI 8 GeV transport line arrangement. The usual instrumentation and electromagnet correctors will be used.

III.6 Recycler/Main Injector

The Fermilab Recycler Ring is a fixed energy 8 GeV storage ring constructed with strontium ferrite permanent magnets and residing in the Main Injector tunnel. For the NOvA program, the Recycler is being converted from an antiproton storage ring to a proton accumulator, providing single turn injection into the Main Injector. In Project X the Recycler serves the same purpose, although at significantly higher intensities: boxcar stacking six 4.3 ms beam pulses from the linac via a multi-turn H⁻ stripping injection, capturing the beam in 53 MHz RF buckets, and performing a single turn extraction into the MI. The MI will receive 1.6×10^{14} protons from the Recycler in a single turn and will accelerate them to 120 GeV in 1.2 seconds. In general, both the Recycler and Main Injector operate in a similar mode to the NOvA operation [23].

III.6.1 Recycler Modifications

With a new injection insert in the Recycler, we anticipate the need for more flexibility in the lattice design. The Recycler is built with permanent magnet quadrupoles, permanent magnet combined function devices, powered dipole correctors, and a tune trombone of powered quadrupoles. The installation of new powered quad elements in the injection region allows for lattice flexibility.

III.6.2 Main Injector Modifications

In the present Main Injector, the injection energy is 8 GeV and maximum energy 120 GeV. Transition crossing is at $\gamma_t = 21.6$ GeV. Simulation shows that emittance dilution and beam loss will occur at high intensities. Furthermore, from experience at other machines (e.g., the AGS at BNL, the CERN PS, and the KEK PS), transition crossing could become a severe bottleneck in high intensity operation.

The design being considered is a first-order system employing local dispersion inserts at dispersion-free straight sections. The normal ramp rate of the MI is 240 GeV/s. In order to have an effective γ_t -jump, the jump rate should be at least an order of magnitude higher. The system was chosen to provide a $\Delta\gamma_t$ from +1 to -1 within 0.5 ms, a jump rate of 4000 GeV/s, about 17 times faster than the normal ramp rate. Details can be found in the Proton Driver Design study document [24].

III.6.3 Electron Cloud Mitigation

Electron cloud induced instabilities in either the Recycler or the MI could be an important limitation to the maximum proton flux. Ongoing studies in the Main Injector are investigating the generation of electron clouds and the performance of beam pipe coatings (e.g., TiN) in reducing the secondary electron yield. Simulations are being benchmarked to measurements [25]. Based on the measurements and simulations, it appears that a combination of beam pipe coating and damper upgrades should be sufficient to mitigate electron cloud instabilities.

III.6.4 RF System Modifications

Upgraded RF systems are required in both the Recycler and the Main Injector. The Recycler RF system is used solely for capture of the injected beam. With the higher intensity, the Main Injector needs more power than is currently available to accelerate the beam at 240 GeV/s. To minimize changes to the existing instrumentation (specifically BPM systems), the RF will operate at the same harmonic number of 588.

The peak beam current in the Main Injector is 2.25 A and 2.7 MV/turn are necessary to reach the desired acceleration rate. With a synchronous phase angle $\phi_s = 36^\circ$, 240 kV per cavity are required. From injection energy (8 GeV) to flattop (120 GeV), the frequency sweep is from 52.811 MHz to 53.104 MHz. A cavity design is under development, to be used in both the Recycler and the Main Injector.

To mitigate possible space charge effects, an increased bunching factor is desired. A frequency mismatch between the capture RF and the linac RF induces a parasitic longitudinal painting [26] but that is not enough. Studies have shown that a 2nd RF system operating at the 2nd harmonic and at half the voltage increase the bunching factor to ~ 0.35 , within the desired range to mitigate space charge effects.

IV Design Concepts of Major Subsystems

IV.1 CW Linac

IV.1.1 Ion source, LEBT, RFQ and MEBT

The Project X front end consists of an ion source, Low Energy Beam Transport (LEBT), Radio Frequency Quadrupole (RFQ), and Medium Energy Beam Transport (MEBT). The H⁺ beam originates from a nominally 5 mA (nominal, 10 mA peak) DC ion source and is transported through the LEBT to a CW normal-conducting RFQ, where it is bunched and accelerated to 2.1 MeV. In the MEBT a bunch-by-bunch chopper provides the required bunch patterns, removing 60-80% of bunches according to a pre-programmed timeline. To foresee possible upgrades, all elements of the front end are designed for beam currents of up to 10 mA. The beam energy of 2.1 MeV is chosen because it is below the neutron production threshold for most materials.

Ion Source

The ion source assembly is a DC, H⁺ source capable of delivering up to 10 mA of beam current at 30keV to the LEBT. The ion source specifications are listed in Ref. [27]. The present scenario assumes the volume cusp ion source presently commercially available from D-Pace Inc. ([28], Figure IV-1). This source is capable of delivering up to 15 mA with a satisfactory transverse emittance of $< 0.2 \mu\text{m}$ (rms, normalized), but its life time is relatively short. The main reason is the source's filament, which needs to be replaced every ~300 hours. To improve the beam uptime, two ion sources are planned to be installed (Figure III-2). Each source can be removed for repairs, installed back, and conditioned without interrupting the operation of another source.

Low Energy Beam Transport

The LEBT transports the beam from the exit of the ion source to the RFQ entrance and matches the optical functions to that of the RFQ. In addition, the LEBT forms a low-duty factor beam during commissioning and tuning of the downstream beam line and interrupts the beam as part of the machine protection system.

The functional requirement specifications are listed in [8], and its schematic is shown in Figure III-2. The LEBT includes 3 solenoids (for each leg), a slow switching dipole magnet, a chopper assembly (a kicker followed by a beam absorber), and diagnostics to characterize and to tune the beam. The length of the beam line, ~3 m, insures that the gas migration from the ion source to the RFQ is tolerable.

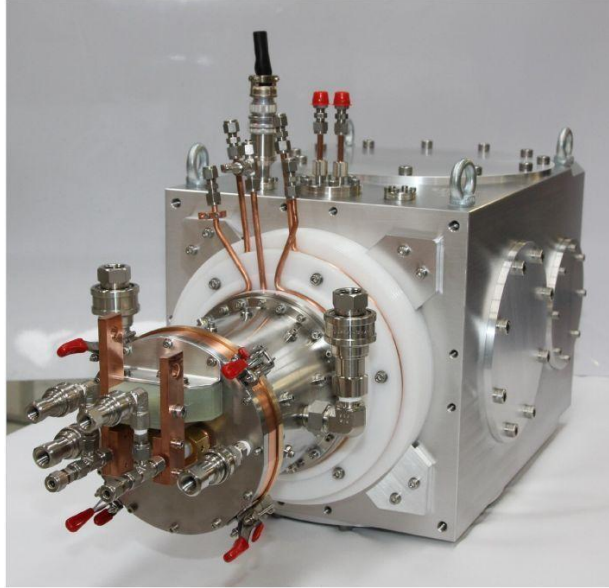


Figure IV-1: Photograph of the D-Pace ion source (foreground) with the vacuum chamber.

The beam diagnostics include an emittance scanner (see specifications in [29]) at the exit of each ion source, a DCCT, and a toroid. In addition, fixed electrically-insulated diaphragms are installed inside the solenoids. Moving the beam by dipole correctors, built into each solenoid and measuring the current to the downstream diaphragm allows estimating the beam size and its position. A scraper in front of the RFQ is a movable, electrically insulated, water-cooled plate that can be moved into three positions: completely removed; partially inserted so that a round opening in the plate is concentric with the RFQ entrance diaphragm; and fully inserted to completely intercept the beam. The scraper serves several purposes: the size of the opening is chosen to scrape the halo particles that otherwise would be lost in the RFQ or MEBT; the variation of beam current intercepted by the scraper while moving the beam across the opening with upstream dipole correctors gives information about the beam position and core size; and the fully inserted scraper works as a beam stop and an auxiliary beam current monitor.

Fast machine protection and pulsed beam operation are achieved via the chopper assembly, which comprises an electrostatic kicker followed by an absorber. In some scenarios, it can be used also as a pre-chopper to assist the MEBT chopping system. The primary machine protection mechanism is to disable the beam from the ion source by turning off its extraction and bias voltages, with the LEBT chopper serving as a fast beam switch during ion source turn-off.

For the Project X LEBT the optics design incorporates two regions (Figure III-3). First, the beam is nearly fully neutralized from the exit of the ion source to immediately upstream of the kicker. Further downstream, the beam can be either neutralized or un-neutralized. In the un-neutralized mode, the secondary ions created in that area are removed by a constant electric field on the kicker plates, and the ions from upstream are stopped by a positive voltage on the insulated diaphragm #2. In the neutralized mode, the kicker plates as well as the insulated diaphragm #2 have normally ground potential, while the insulated diaphragm #3 or the scraper is biased positively to prevent the ion escape longitudinally. The LEBT scheme is flexible enough to accommodate both versions by adjusting potentials and solenoid currents (see Figure III-4 for simulations of a fully neutralized transport case). The transport with an un-neutralized section is beneficial for decreasing the transition effects of the kicker pulse but results in an emittance increase. Relative benefits of each scenario can be clarified during PXIE experiments.

Radio-Frequency Quadrupole

The 162.5 MHz CW RFQ will accelerate an H^- ion beam with currents of up to 10 mA from 30 keV to 2.1 MeV (see Ref. 30 for specifications). Presently the Project X RFQ is assumed to be identical to that being developed for PXIE by LBNL [31]. This 4.45-m long, four-vane structure consists of four longitudinal modules and uses a 60 kV vane-to-vane voltage. Most of the RF input power is dissipated in the cavity walls to establish the needed RF field with ~12% beam loading. A series of 32 water-cooled pi-mode rods provides quadrupole mode stabilization, and a set of 80 evenly spaced fixed slug tuners is used for the final frequency adjustment and local field perturbation corrections. The design incorporates selected portions of the technology validated by the Spallation Neutron Source (SNS) Front End RFQ [32] designed and constructed at LBNL. An overall view of the full four-module RFQ is shown in Figure IV-2.

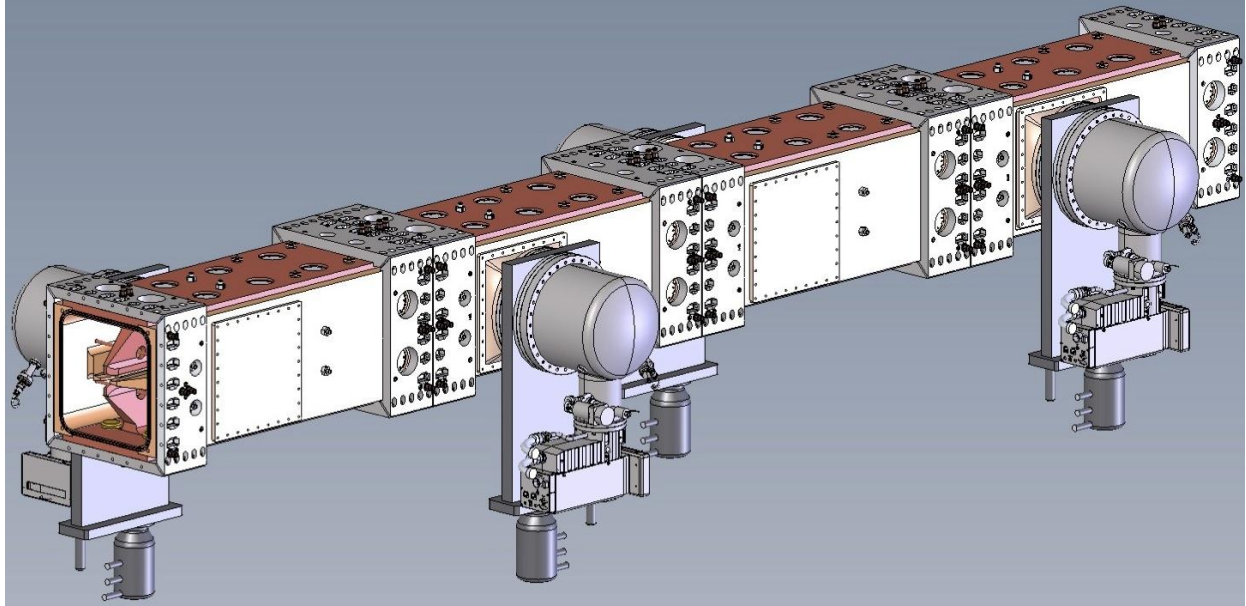


Figure IV-2: CAD model of the full four-module RFQ.

The beam dynamics design of the RFQ provides over 96% transmission for beam current from 1 to 15 mA. At 5 mA nominal current, 99.8% beam capture is achieved with transverse and longitudinal emittance (rms, norm) of 0.15π -mm-mrad and 0.64 keV-nsec, respectively. The RF design studies [33] include mode stabilization, field flatness, radial matching, and entrance and exit terminations. Table IV-1 summarizes the RF design results.

Parameter	Value
Frequency, MHz	162.493
Frequency of dipole mode, MHz	181.99
Q factor	14660
Max power density, W/cm ²	7.9
Total power loss, kW	74.6
Beam power @ 5mA, kW	10.5
Total RF power from source, kW	150

Table IV-1: Main parameters of the Project X RFQ electromagnetic design

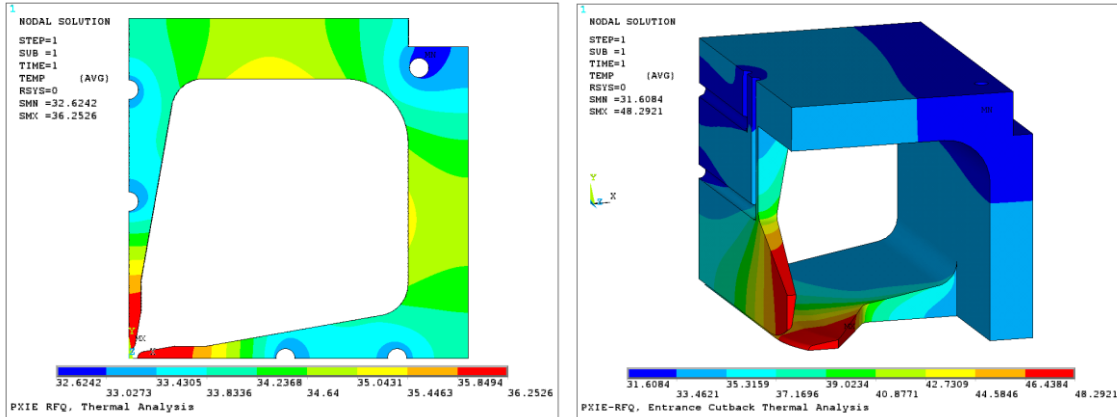


Figure IV-3: Temperature distribution in one RFQ quadrant body (left) and cut-back (right). The color scheme (degrees C) is at the bottom of each plot.

A series of RF and thermal finite-element models of the RFQ have been developed using ANSYS®. An example of the temperature contour plots for the cavity body and vane cutback region is shown in Figure IV-3. From the RF analysis, the average linear power density was determined to be 137 W/cm with a peak heat flux on the cavity wall of only 0.7 W/cm². With the 30°C water in the vane and wall cooling passages, the resulting temperature profile in the cavity body ranges between 32 and 37°C at full RF gradient.

Additional modeling that has been carried out includes stress and displacement analyses, thermal analyses of the tuners, pi-mode rods and vane cutbacks, and prediction of the frequency shift of the RFQ cavity due to thermal loading and changes in the cooling water temperature.

The RFQ cooling scheme will use differential water temperature control in the vane and wall passages. This technique provides active tuning of the RFQ by holding the wall water temperature constant and adjusting the vane water temperature up and down. The frequency of the RFQ can be shifted by -16.7 kHz for every 1°C rise in the vane cooling water temperature. For uniform water temperature control, the shift would only be -2.8 kHz/°C.

Medium Energy Beam Transport

The MEBT layout is given in Figure III-8 (reproduced in Figure IV-4). The MEBT generally provides beam transport and focusing (both transverse and longitudinal), beam chopping, chopped beam absorption, vacuum pumping, and diagnostics. Transverse focusing is provided primarily by equidistantly placed quadrupole triplets; the only exception is two doublets at the RFQ exit. Each triplet or doublet is followed by a pair of dipole correctors.

The specifications for the quadrupoles and correctors are listed in [34]. The spaces between neighboring triplets or doublets are referred to as MEBT sections, with each section providing a particular service. The section separation in the regular part of the MEBT is 1140 mm, which leaves a 650-mm long (flange-to-flange) space for various equipment (350 mm in the section between doublets labeled #0).

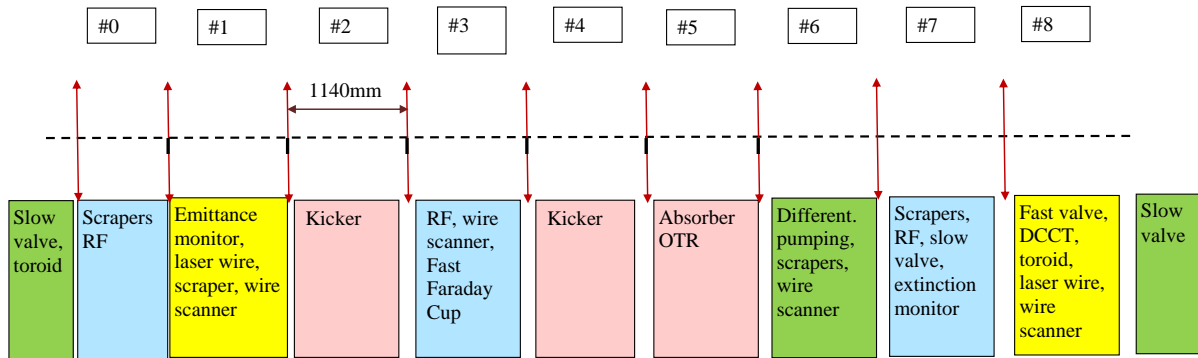


Figure IV-4: The MEBT structure. Sections are colored according to their main functions. The red vertical arrows schematically show the transverse focusing (doublets or triplets) elements.

The undesired beam bunches will be removed in the MEBT by a chopping system, represented in the figure by red boxes. The system consists of two identical 50 cm long kickers separated by a 180° transverse phase advance and an absorber (90° from the last kicker). In the broadband, travelling-wave kicker, the transverse electric field propagates with the phase velocity equal to the speed of H^- ions (~ 20 mm/ns, $\beta = 0.0668$) so that the ion vertical velocity changes sufficiently to push the ion bunches, designated to be removed, to the absorber. The separation between the kicker plates is 16 mm. The aperture is limited by protection plates on both sides of the kicker to 13 mm so that in the case of a mismatched transport, the intercepted beam current on these protection plates would trigger the beam turn-off. Detail specifications for the kicker can be found in Ref. [35]. The simulated transverse beam envelopes in the MEBT for both passing and chopped bunches are presented in Figure III-9.

Presently two versions of the kicker, which differ by the structure's impedance, are being investigated [16]. In the 50 Ohm version, the kicker plates are connected in vacuum by cable delay lines (Figure IV-5, purple loops). Compared to the helical structure discussed below, this arrangement considerably reduces coupling between neighboring turns and consequently dispersion. Each kicker is driven by two commercially available linear amplifiers. Signal distortion caused by the imperfections of the amplifier characteristics, cabling, and dispersion

in the structure are corrected by the corresponding pre-distortion of the amplifier's input signal.

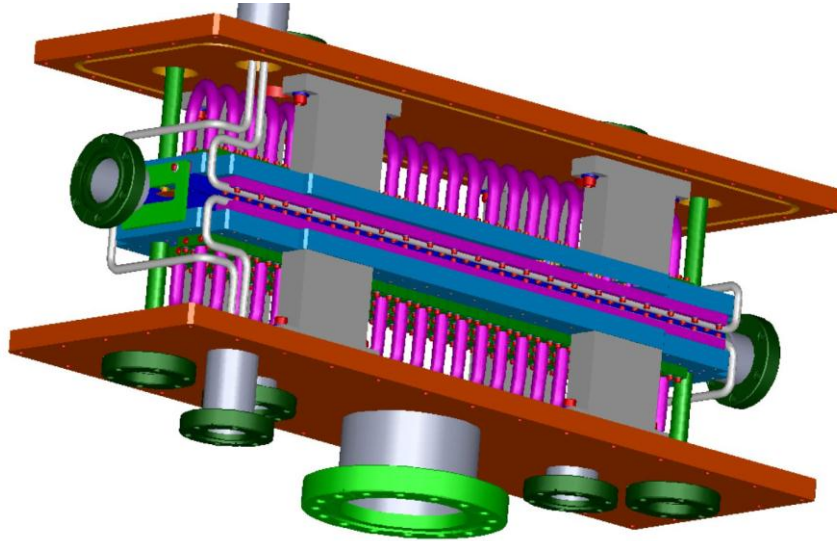


Figure IV-5: 3-D model of the 50-Ohm kicker structure (side walls of the vacuum box are removed for presentation purpose).

The 200-Ohm structure is comprised of two helical windings around grounded cylinders with plates attached to windings (Figure IV-6). In this scheme, the kicker driver is a fast switch being developed in-house. In addition, this scheme requires custom made feed-throughs, transmission lines, and current loads. While the 50 Ohm version has many elements commercially available and the design of its structure is more mature, the 200 Ohm is potentially less costly and has a lower power loss in the structure. The selection of the kicker technology for Project X will be based on beam tests at the PXIE.

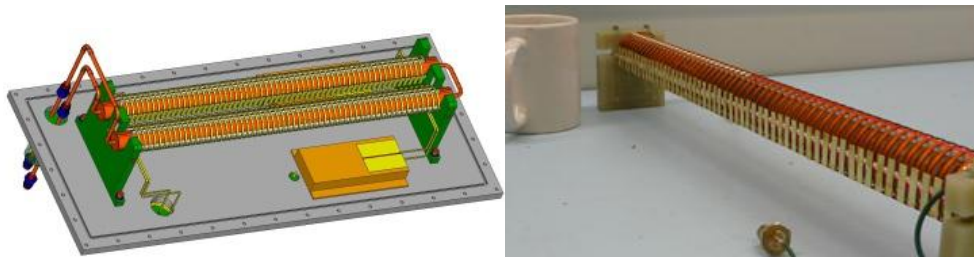


Figure IV-6: Conceptual design (left) and photograph (right) of a single-helix model of the 200 Ohm dual-helix kicker.

The undesired bunches are directed to an absorber, displaced vertically from the beam trajectory. To accommodate the entire beam that the upstream system is capable to deliver, the absorber is being designed for the maximum beam power of 21 kW that corresponds to a 10-mA beam completely diverted to the absorber (see specifications [36]). The power density in the beam with a ~ 2 mm rms radius exceeds by an order of magnitude what is technically possible to absorb without melting the surface. To decrease the surface power density, the absorber is positioned with a small angle, 29 mrad, with respect to the beam (Figure IV-7).

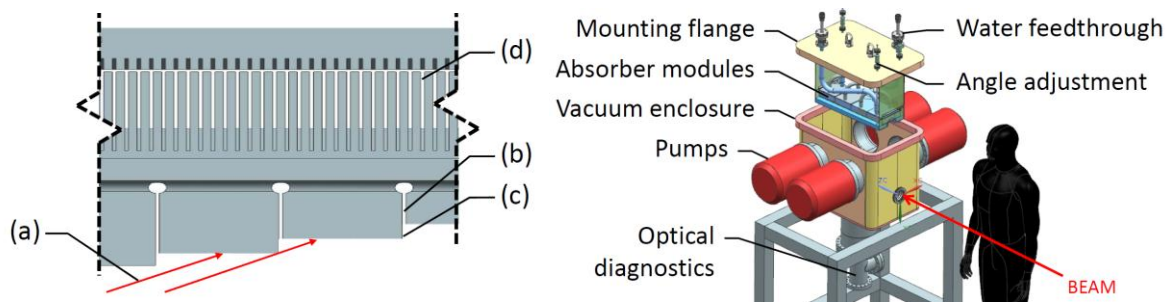


Figure IV-7: A conceptual design of the MEBT absorber. Left: a side-view of the absorber showing (a) beam incident on surface, (b) axial stress relief slits, (c) shadowing step increment (magnitude exaggerated), (d) 300 μ m wide by 1mm pitch water cooling channels. The horizontal scale is exaggerated. Right: an exploded view.

Challenges presented by the absorber design include maintaining vacuum quality, managing surface effects (sputtering and blistering), containing secondary particles, accommodating radiation effects, spreading energy deposition, and the survival at high temperatures and temperature-induced mechanical stresses. Presently the design choice is a monolithic absorber made from the molybdenum alloy TZM.

To keep the beam properly bunched and to match the longitudinal phase space to the first superconducting cryomodule, the MEBT includes 3 identical (room temperature) bunching cavities [37]. Each cavity is a quarter-wave 162.5 MHz resonator with the nominal accelerating voltage of 70 kV (at $\beta=0.0668$). A conceptual view of the cavity being designed for PXIE and some results of its simulations are shown in Figure IV-8.

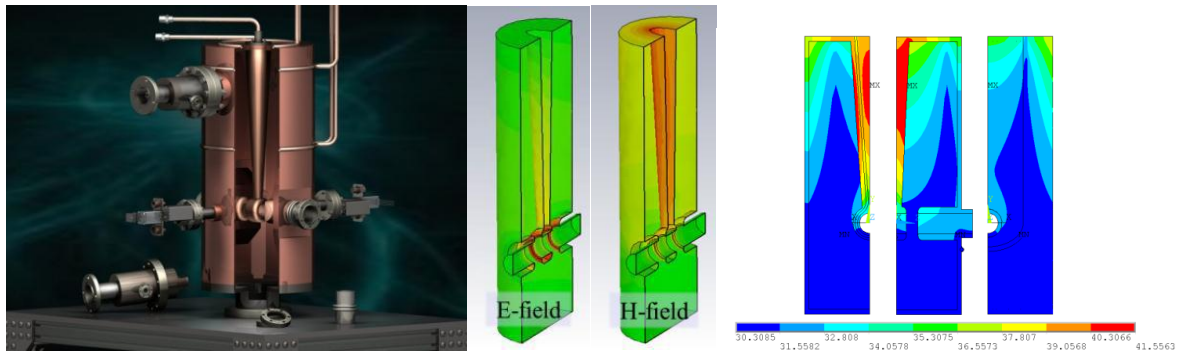


Figure IV-8: A conceptual design of the MEBT bunching cavity (left), simulated surface field distributions (center), and the temperature distribution (right) (from Ref. 38).

Each of the sections #0, 1, 6, and 7 in Figure IV-4 contains a set of 4 scrapers. Each of these 16 scrapers is envisioned as an electrically insulated, 100W-rated plate precisely movable across the half-aperture [39]. The scrapers will be used for several purposes: for beam halo measurements and removal; protection of downstream equipment from a beam loss caused by beam envelope and trajectory mismatches; as an auxiliary beam density distribution diagnostics in the pulse mode; and formation of a pencil H- beam for measurements downstream (in the pulse mode). The scraper sets in the upstream and downstream pairs are separated by $\sim 90^\circ$ of transverse phase advance to insure an effective removal of particles with large transverse actions.

The vacuum requirements for the MEBT are determined by the electron detachment in H-beam and by the necessity to have a low gas flow into the HWR cryomodule. Obviously, the electron detachment results in a loss of H⁻ beam intensity - an additional restrictive effect creating a flux of neutral hydrogen atoms that may reach the SRF cavities. For the conceptual design of the vacuum system it is convenient to choose a reasonable limit for the integral of the pressure over the distance along the MEBT axis. The selected value of 1×10^{-6} Torr·m corresponds to a relative loss of $\sim 10^{-4}$ and to an additional ~ 0.1 W heat load to the SRF by neutral atoms.

Gas flow from the room-temperature MEBT to the 2K HWR cryomodule can cause a gas deposition on the cryogenic surfaces, which negatively affects the cavity performance. To limit this effect to safe levels, the vacuum pressure upstream of the HWR cryomodule is specified to be below 1×10^{-9} Torr (hydrogen). To ensure this level, with a quite high gas load coming from the absorber, ~ 1 mTorr-l/s, the absorber section is followed by a differential pumping section and is separated from the SRF by two additional sections.

Most of diagnostics are listed in Figure IV-4 and will allow measuring beam properties at the RFQ exit (before sending it into the HWR cryomodule). In addition, each triplet and doublet

has a BPM inserted between quadrupoles. The BPMs will measure the transverse beam position and the bunch phase; functional requirements [40] foresee a capability of gating on a single bunch in the bunch train.

IV.1.2 CW Accelerating Structures Requirements

The parameters and requirements associated with all accelerating structures and cryomodules within the CW linac have been summarized in Table III-2, Table III-3, and Table III-4. This section describes design concepts for the cavity types required in the CW linac, and the associated cryomodules.

IV.1.3 Low-beta section (2.1-10 MeV, 162.5 MHz)

The original design of Project X included 325 MHz Single Spoke Cavities of type 0 (SSR0), to accelerate the H^- beam from 2.1 to 10 MeV. To maintain high beam quality, an adiabatic increase of the accelerating gradient in SSR0 cavities was necessary, and satisfying the adiabaticity condition required 3 cryomodules comprising 24 SSR0 cavities. After careful considerations, a design based on 162.5-MHz Half-Wave Resonator (HWR) cavities was selected instead. This design has several substantial advantages as compared to the 325 MHz SSR0 option:

- Only 8 HWRs are required to accelerate the beam to ~ 10 MeV while maintaining high beam quality.
- Reduced RF defocusing due to both the lower frequency and the lower synchronous phase angle results in a much faster energy gain without emittance growth.
- It opens the possibility to use 162.5 MHz re-bunchers in the MEBT to allow for longer drift spaces for the fast beam choppers.
- Significant cost reduction due to the reduced component count.

The beam dynamics optimization determines that a cavity beta of $\beta_{OPT}=0.112$ is optimal. The cavity design is based on recent advances in SRF technology for TEM-class structures being developed at ANL. Highly optimized EM parameters which maximize the real-estate gradient while maintaining low dynamic cryogenic loads and peak surface fields were achieved using a conical shape for both the inner and outer conductors. A “donut” shaped drift tube in the center conductor has been developed to minimize the undesirable quadrupole component of the electric field as is shown in Figure IV-9. Utilization of the HWR requires two major sub-systems: a 10 kW RF coupler and a slow tuner. A capacitive adjustable 10 kW RF coupler prototype has been designed, constructed, and is being prepared for testing. It will provide RF power through the port which is perpendicular to the beam axis in the center of the cavity (Figure IV-10). A pneumatically actuated mechanical slow tuner which

compresses the cavity along the beam axis is located outside of the helium vessel and will be attached to the SS beam port flanges shown in Figure IV-10. A fast tuner is not required for operations with a 4.9 kW RF power source (Stage II). This power supports 2 mA beam loading and has sufficient margin for amplifier control and suppression of microphonics (mainly related to helium pressure fluctuations). The required cavity bandwidth (loaded) is 49 Hz. Stage I has a 1 mA beam current. Consequently, the power can be reduced to about 3 kW. The main parameters of the HWR are shown in Table IV-2.

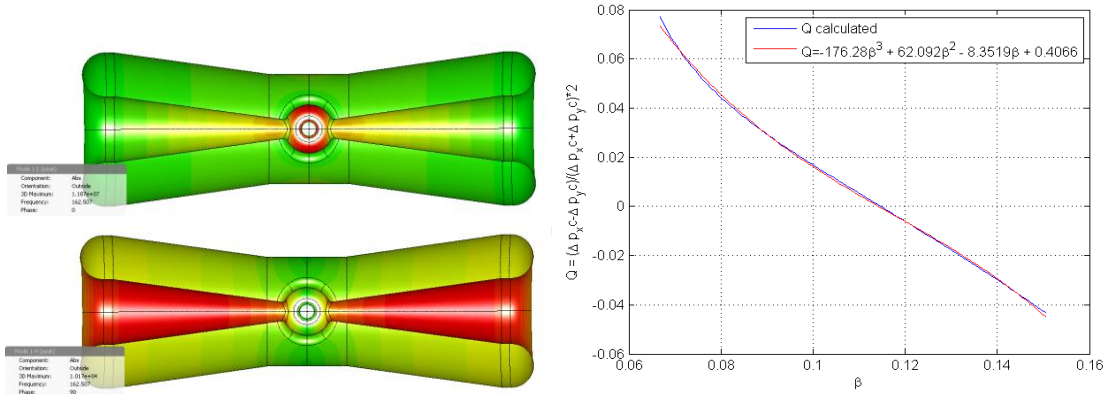


Figure IV-9: Left - Half-wave resonator model in Microwave Studio (MWS). The picture shows electric (top) and magnetic field (bottom) distributions on the surface. Red is high intensity and green is zero. Right - Quadrupole effect in the HWR cavity versus the particle velocity β in operating domain; red and blue line show simulation and approximation.

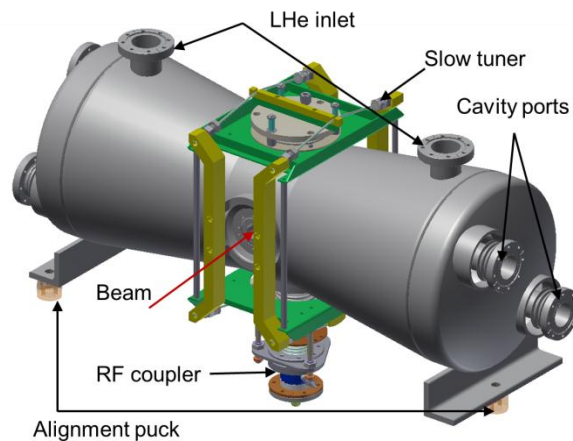


Figure IV-10: HWR cavity 3D model in INVENTOR

Extensive finite element analysis of the cavity included simulations to evaluate the integrity of the cavity per the Fermilab ES&H manual. The simulations include protection against plastic collapse, local failure, buckling, ratcheting and fatigue failure to ensure that the operating loads are below the maximum allowable limits. The maximum structural load is determined by the pressure set by the operation of the cryogenic system and the safety pressure relief valve. The evaluation was performed for 30 psig at room temperature and 60 psig at 2 Kelvin in the helium space of the cavity in compliance with the Fermilab requirements. In general, the over pressure condition could occur during the initial cryogenic cooling with the cavity structure at or near room temperature; since the room temperature strength limits (i.e., yield and ultimate) are lower than for cryogenic temperatures and the operating margin is smaller here, the room temperature limits were studied in more detail. The stress analysis was performed in the presence of the slow tuner and other appurtenance loads. The final design exceeds all evaluation criteria for the niobium and the stainless steel (SS) parts respectively.

HWR Cavity	Design Value	
Frequency	162.5	MHz
Geometric Beta (β_G)	0.094	
Optimum Beta (β_{OPT})	0.112	
Aperture (diameter)	33	mm
$L_{EFF} = \beta_{OPT}\lambda$	20.7	cm
R/Q_0	275	Ω
$G = Q_0R_S$	48	Ω
E_{max}/E_{acc}	4.65	
B_{max}/E_{acc}	5.0	mT/(MV/m)
Gradient	8.2	MV/m
Peak Surface Electric Field	38	MV/m
Peak Surface Magnetic Field	41	mT
Q_0	0.5	10^{10}
Operating Temperature	2	K

Table IV-2: HWR cavity requirements

Two methods have been studied for minimization of the cavity frequency sensitivity to fluctuations of the helium pressure: (1) adding gusseting to reduce the cavity deflections in the high magnetic and electric field regions and (2) varying the depth of the flat dish located opposite to the RF coupler port. The results of these studies showed that no gusseting is required; a minimal value of 1.4 kHz/atm was achieved by optimizing the dimensions of the flat dish penetration. Simulations of the slow tuner were performed by applying a force to the SS flanges of the helium jacket. For example, a 10 kN force results in a frequency shift of -120 kHz.

The primary operational parameters for the HWR are contained within Table IV-2, and are based on our recent experience with the ATLAS energy upgrade cryomodule and its long term operation. As is shown in Figure IV-11, recent tests of new 72 MHz Quarter Wave resonators (QWR) show just 2 nΩ residual resistance at 41 mT which readily supports design parameters of the HWRs. The peak fields shown in the table were taken directly from the CST MWS screen in simulations with ~200K tetrahedral mesh cells.

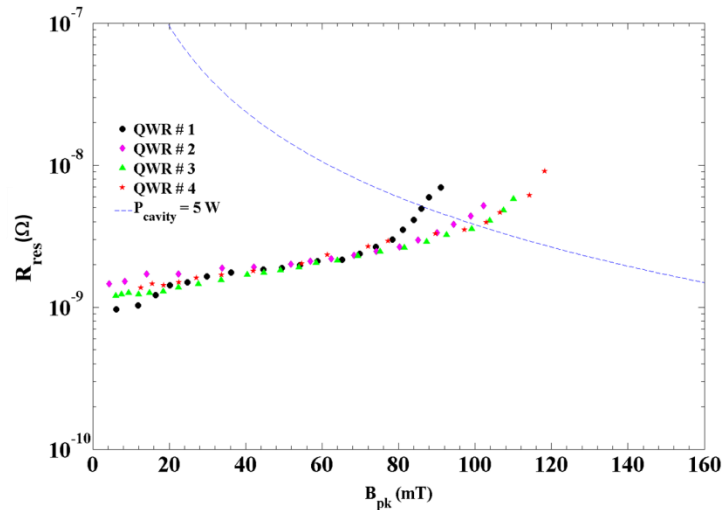


Figure IV-11: Cavity residual resistance measured in the ANL Intensity Upgrade QWR

The cryomodule designs all build upon past ANL experience with box cryomodules. Here the cryomodule is much wider due to the half-wave cavities being mounted on their sides. To keep the half-cylinder bottom would make the vacuum vessels unacceptably tall. We have arrived at making the vacuum vessel a box which appears to be a good compromise between fabrication cost, structural integrity and minimizing cryostat height. The radii of the rounded corners were chosen to fit the contents of the box minimizing overall height including the depth of the required gussets. Figure IV-12 shows the results of ANSYS calculations of the

structural deformations due to vacuum being pulled on the inside. Notice that the structure pulls in about 0.25” on average due to evacuation, the maxima are between 0.5” and 0.67”. Motion of the vacuum vessel wall moves the internal magnetic shielding and stresses the baton points which may degrade performance. Reducing the maximum displacement to less than 0.25” will avoid this but it adds the cost of additional gusseting. Future tests are planned here to evaluate the magnetic shielding.

The cryomodule houses 8 sets of identical components. Each set forms a focusing period and includes a resonator, a SC solenoid with 4 dipole coils and a Beam Position Monitor (BPM). Beam dynamics requires the solenoids to be aligned to better than ± 0.5 mm peak transversely with $\pm 0.1^\circ$ for all of the rotation angles with similar constraints on the cavities. The beam-line string length is 6 meters and will be supported and aligned on a cryomodule spanning titanium rail system, called the strong-back as shown in Figure IV-13. The strong-back is composed of 2 inch \times 8 inch grade 2 titanium plates formed into a box and supported by titanium hangers. Each component is mounted on top of the strong back with its own independent kinematic-alignment hardware.

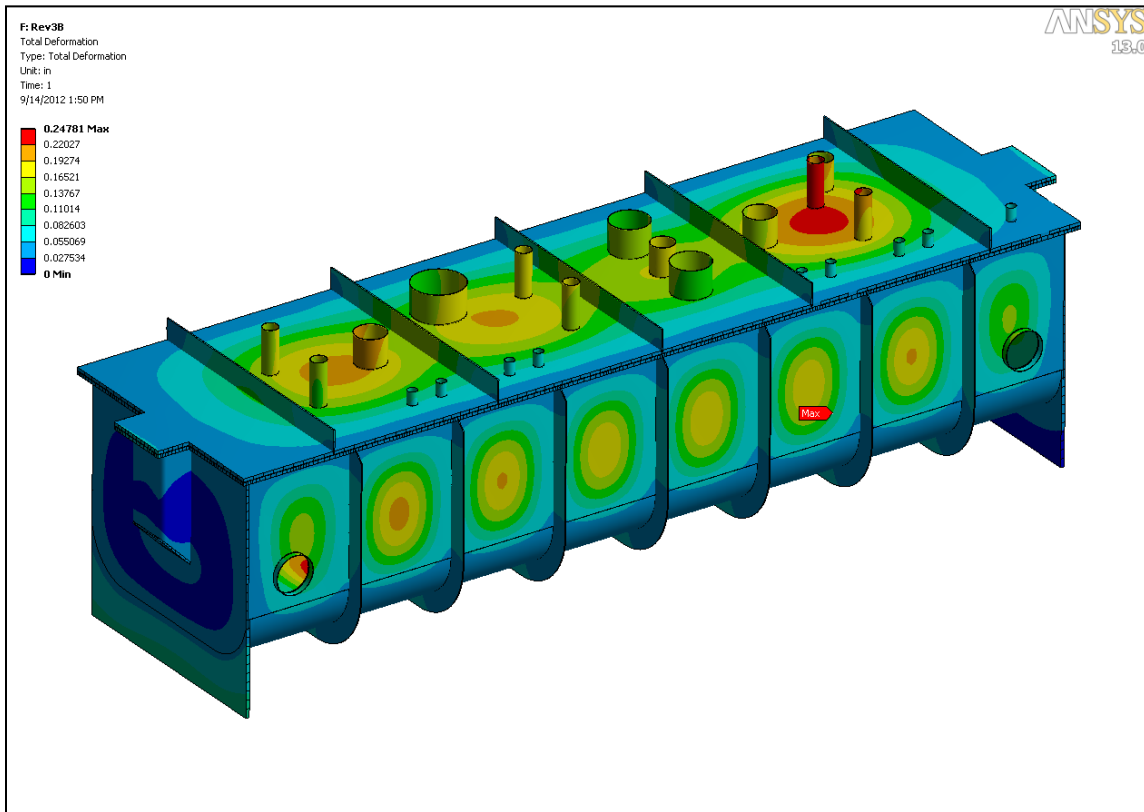


Figure IV-12: ANSYS results of the vacuum vessel deformation due to a 14.7 psi static pressure gradient across the walls. The red color corresponds to displacements greater than 0.6 inches with the maximum being 0.67 inches.

Table IV-3 summarizes the estimated static and dynamic heat loads to each temperature level in the cryomodule assembly (Figure IV-14) from all sources. The following sources were included in the calculation of 2K heat load: cavities, RF couplers, helium manifold, radiation from 70K to 2K, instrumentation, high current leads, strongback hangers, cavity and solenoid cooldown lines, vacuum manifold, slow tuners, and gate valves. Changing the operating voltages by + and -20% will result to 28W and 21 W total 2K heat load respectively. Currently two HWR prototypes are being fabricated. In addition, a high-power RF coupler, a BPM and SC solenoid have been built and are being cold tested now (spring 2013).

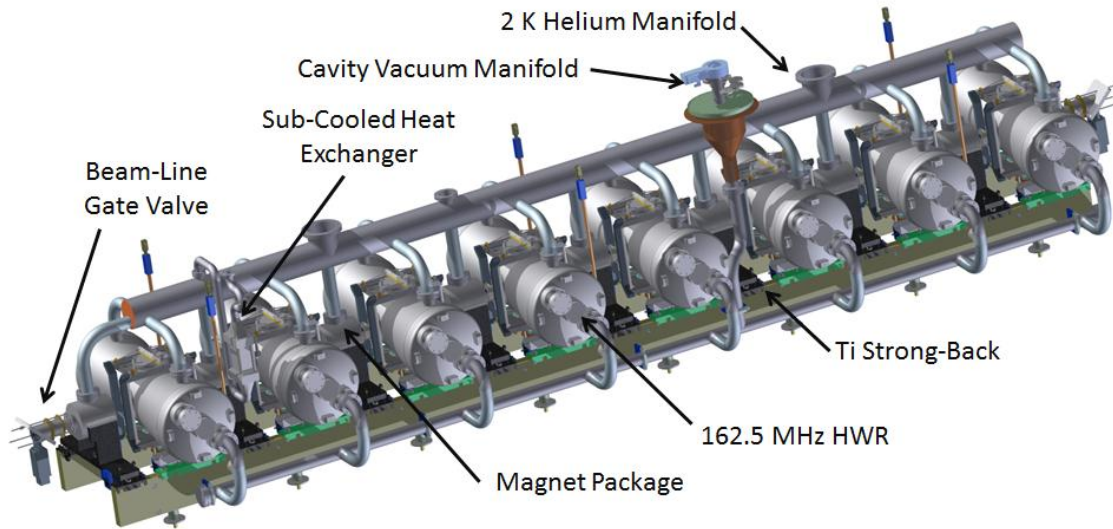


Figure IV-13: HWR Cavity String Assembly

Temperature	Load, W
2 K, static	14
2 K, dynamic	10*
5 K	60
70 K	250

*This value takes into account actual voltage distribution on the HWR cavities

Table IV-3: HWR Cryomodule Heat Load Estimate

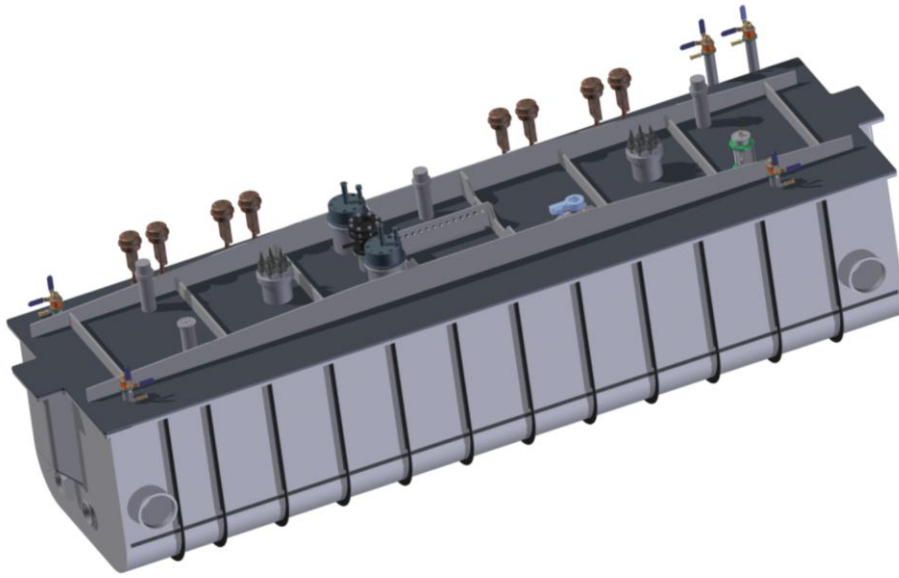


Figure IV-14: HWR cryomodule assembly.

IV.1.4 Low-beta section (10-160 MeV, 325 MHz)

Two cavity types are required to accelerate beam from 11 to 177 MeV ($\beta=0.15$ to 0.61). The general requirements on the sections containing these cavities are listed in Table III-3. All cavities are of the single spoke resonator (SSR) type. During the R&D phase, studies will be completed comparing the relative benefits of these and other possible low beta configurations.

SSR1 Cryomodule

Acceleration from 11 to 38 MeV utilizes superconducting SSR cavities with $\beta_{\text{opt}}=0.22$ (SSR1). The cavity has geometrical and electro-magnetic parameters shown in Table IV-4. A SSR1 cavity matching these requirements has been designed, fabricated, and tested with RF power as part of the HINS program. The mechanical design, including focusing elements, is displayed in Figure IV-15.

SSR1 Cavity	Design Value	
Frequency	325	MHz
Geometric Beta (β_G)	0.186	
Optimum Beta (β_{OPT})	0.222	
Aperture (diameter)	30	mm
$L_{EFF} = \beta_{OPT}\lambda$	20.5	cm
R/Q_0	242	Ω
$G = Q_0R_S$	84	Ω
E_{max}/E_{acc}	3.84	
B_{max}/E_{acc}	5.81	mT/(MV/m)
Gradient	10	MV/m
Peak Surface Electric Field	38	MV/m
Peak Surface Magnetic Field	58	mT
Q_0	0.5	10^{10}
Operating Temperature	2	K

Table IV-4: Requirements of the low-beta single spoke resonator (SSR1) cavities

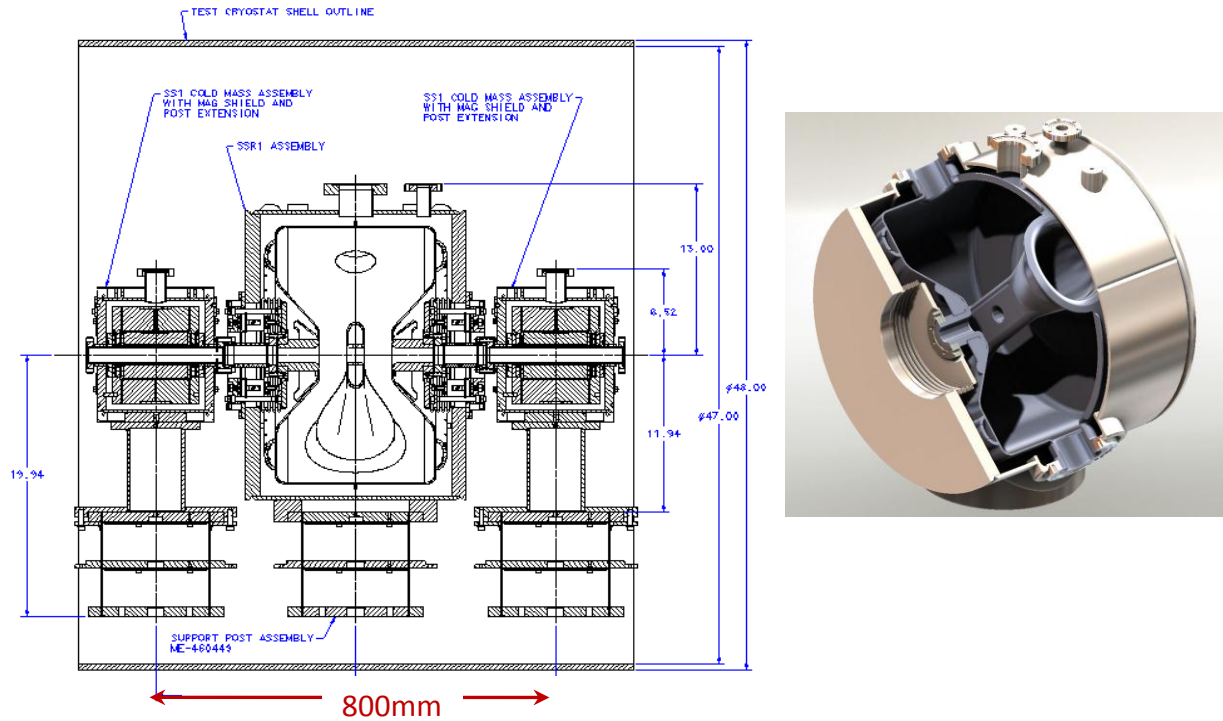


Figure IV-15: SSR1 cavity mechanical design and cutaway view.

Figure IV-16 shows the first(SSR1-02) cavity fabricated as part of the HINS program. The left photograph shows the bare cavity, the right a “dressed” cavity encased in its He jacket with ancillary slow and fast (piezo) tuners. To date an additional ten bare cavities were fabricated and delivered to Fermilab, (SSR1-05 – SSR1-14). Six have been tested with parameters suitable for operation in Project X. The measured performance at 2K of the bare cavity in a vertical test is displayed in Figure IV-17. Note that the cavities are made of Cabot niobium, which is not certified for high-gradient ILC operation, and demonstrated higher losses than material from certified vendors. However, all the cavities show a $Q_0 > 0.7 \times 10^{10}$ at the 2K at the operating gradient of 12 MeV/m, which is well above required value $> Q_0 > 0.5 \times 10^{10}$. Note that the cavity SSR1-02 made of certified material demonstrated a $Q_0 = 1.1 \times 10^{10}$ at 2K at the operating gradient. The measured surface resistance of this cavity as a function of temperature is shown in Figure IV-18. The cavity operational and test requirements are summarized in Table IV-5.



Figure IV-16: Photographs of the bare and dressed prototype SSR1 cavity

Parameter	Requirement
Max leak rate (room temp)	$< 10^{-10}$ atm-cc/sec
Operating gain per cavity	2.0 MeV
Maximum gain per cavity	2.4 MeV
Max. power dissipation per cavity at 2 K	5 W
Sensitivity to He pressure fluctuations df/dP	< 25 Hz/Torr
Field flatness	Within $\pm 10\%$
Multipacting	None within $\pm 10\%$ of operating grad.
Operating temperature	1.8-2.1 K
Operating pressure	16-41 mbar differential
MAWP	2 bar (RT), 4 bar (2K)
RF power input per cavity	6 kW (CW, operating)

Table IV-5: SSR1 cavity operational and test requirements.

A spoke cavity has no axial symmetry. Therefore its quadrupole component cannot be compensated over the entire range of cavity operation. Figure IV-19 presents the dependence of the quadrupole effect on the beam velocity. Due to engineering limitations, mainly related to the RF couplers, the cavities are rolled by 45° ; consequently, their quadrupole field is also rolled and is equivalent to a skew-quadrupole field. The cavity skew-quadrupole fields will be compensated by correction coils located inside nearby focusing solenoids capable to create dipole and skew-quadrupole fields.

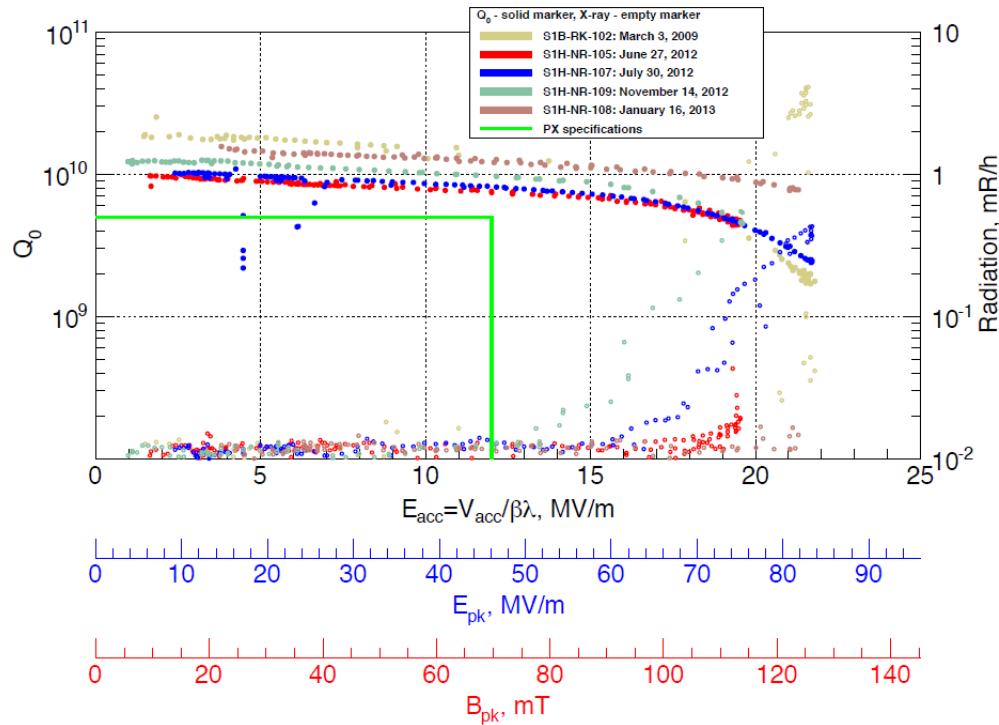


Figure IV-17: Q_0 vs. acceleration gradient from the cold test of the SSR1-02, SSR1-05, SSR1-07, SSR1-08, and SSR1-09 single-spoke cavities ($\beta = 0.22$). Maximal gain is 4.2 MeV @ 2K.

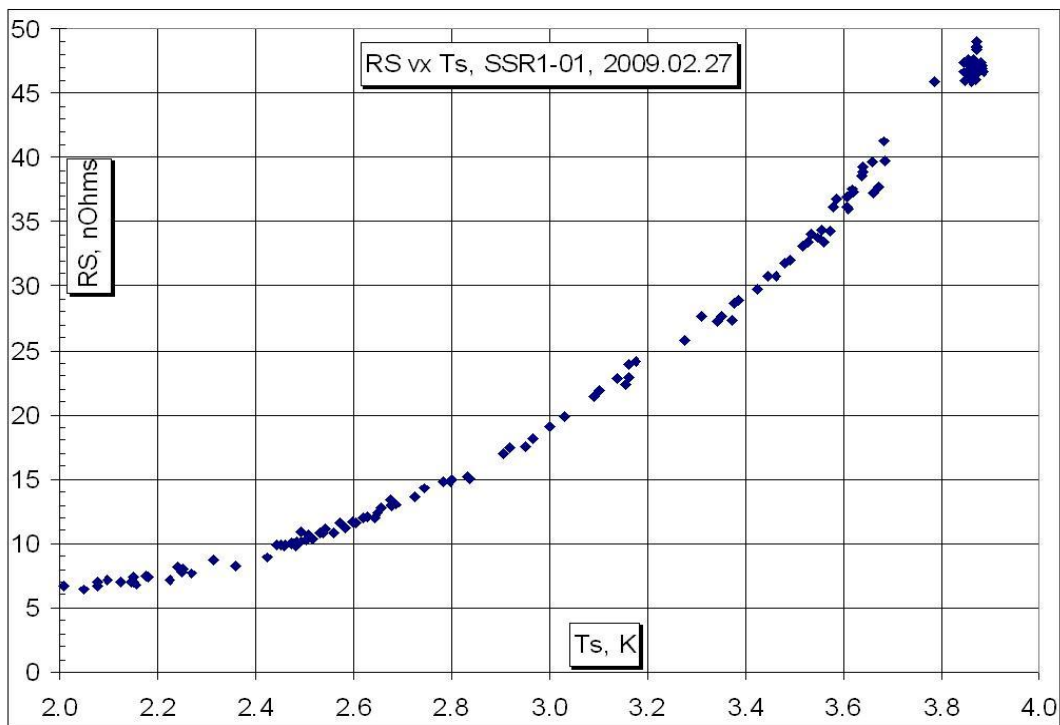


Figure IV-18: Temperature dependence of the surface resistance for SSR1 cavity.

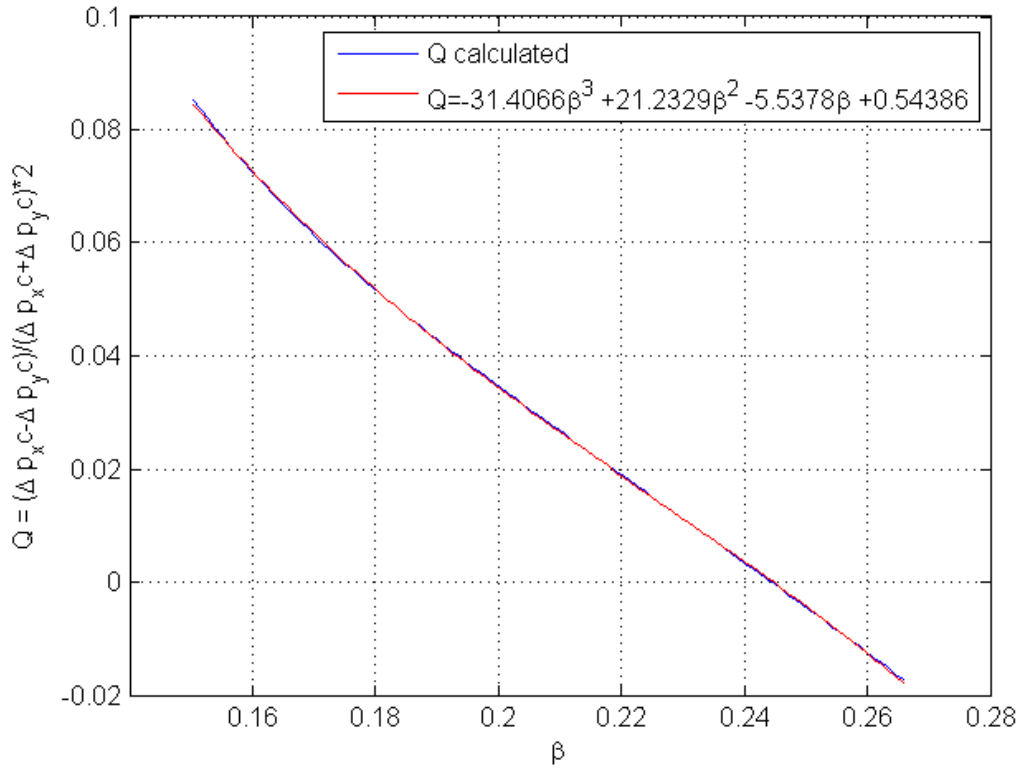


Figure IV-19: Quadrupole effect in SSR1 cavity versus the particle velocity β in the operating domain; blue and red line present simulation and approximation.

In order to attain the requirements for frequency range and resolution (Table IV-6), the tuning systems for cavities of narrow bandwidths such as SSR1 typically integrate a coarse and a fine mechanism engaged in series. The first normally utilizes a stepper motor with large stroke capability and limited resolution, the latter usually contains piezo-electric actuators with limited stroke but virtually infinite resolution.

	Requirement
Coarse frequency range	135 kHz
Coarse frequency resolution	20 Hz
Fine frequency range	1 kHz
Fine frequency resolution	≤ 2 Hz

Table IV-6: SSR1 tuning system requirements

The coarse tuner is predominantly used to achieve consistently the resonant frequency during the cool-down operations. The range necessary to compensate for the cool-down uncertainties is estimated to be 50 kHz. In the event that a cavity must be detuned as a result of a malfunction, the coarse tuning system must be able to shift the frequency away from resonance by at least 100 bandwidths which equal to ≈ 10 kHz, so that the beam is not disturbed. The requirement on the range was set arbitrarily considering a safety margin of 2.7. The requirement on the resolution of the coarse tuning system is set to a value that would allow operation in the event of a failure of the fine-tuning system. Based on other applications, it is believed that such resolution can be achieved with a coarse tuning system.

It is conservatively assumed that the coarse system cannot be operated during beam acceleration; it is thought that the vibration of a stepper motor may induce vibrations in the cavity severe enough to disrupt the operation. Thus, fine tuners shall be designed to compensate, at a minimum, the frequency shifts of the cavity induced by fluctuations of the helium bath pressure. The use of fine tuners will reduce considerably the hysteresis of the system by limiting the elements in motion during the tracking of the frequency. A particular design effort shall be dedicated to facilitate the access to all actuating devices of the tuning system from access ports on the vacuum vessel. All actuating devices must be replaceable from the ports, either individually or as a whole cartridge.



Figure IV-20: SSR1 cavity, helium vessel, and tuner

The Helium vessel will be fabricated from a non-magnetic stainless steel (e.g. 316L) designed to house a 2 K helium bath sufficient to remove up to 5 watts average dissipated power, with appropriately sized supply and return piping. It must meet the requirements of the Fermilab ES&H Manual for cryogenic pressure vessels and be rated at an MAWP

(Maximum Allowable Working Pressure) of no less than 2 bar at room temperature and 4 bar at 2 K. Every effort should be made to minimize the weight and physical size of the helium vessel in all dimensions. The cavity vessel with tuner system is shown in Figure IV-20.

SSR1 Input Coupler

The design of the input coupler is based on a 105 Ω coaxial line. It will be used for both SSR1 and SSR2 cryomodules. Its maximum power of 30 kW CW is determined by requirements for an eventual upgrade of Project X to 5 mA average beam current [7]. The coupler contains a single warm ceramic window that provides separation of the warm and cold coupler sections. During cryomodule fabrication, the cold section can be installed on the cavity in the cleanroom prior to assembly of the string. The warm section can then be installed from outside the vacuum vessel during final assembly. The inner conductor is solid copper with phosphor bronze bellows to accommodate motion due to misalignment and thermal contraction. The cold end of the outer conductor is 316L-stainless steel. The warm end is copper with phosphor bronze bellows. Heat load estimates don't suggest a significant penalty for not copper plating the outer conductor. A forced-air cooling tube is inserted into the inner conductor after assembly that supplies air to cool the coupler tip. The coupler parameters are shown in Table IV-7. Figure IV-21 shows the current coupler design.

	Requirement
CW Power	30 kW
Multipactor threshold	25 kW (Trav. Wave)
Passband	50 MHz
Input	3.125" coaxial
Input impedance	50 Ω
Output	3"× 0.5" coaxial
Output impedance	105 Ω

Table IV-7: Design parameters of SSR1 input coupler.

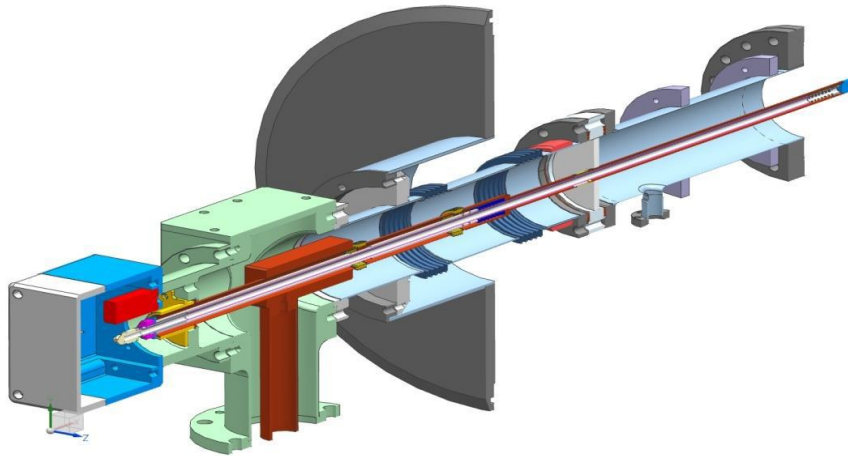


Figure IV-21: SSR1 input coupler.

SSR1 Current Leads

Each focusing element package contains five coils: the main solenoid, operating up to 100 A, and four coils which can be combined to serve as both x and y steering and skew-quadrupole correctors. Each coil can operate up to 50 A. A conduction cooled current lead design modeled after similar leads installed in the LHC at CERN is being developed for use in the SSR1 cryomodule. Thermal intercepts at 45-80 K and at 5 K help reduce the heat load to 2 K, nonetheless, these current leads represent a significant source of heat at the low temperature end. There will be one lead assembly for each magnetic element.

SSR1 Solenoid and Beam Position Monitor

The four magnet packages in the cryomodule each contain a focusing solenoid (lens) and four corrector coils all operating in a helium bath at 2 K. The general design requirements for the lenses in the SSR1 cryomodule are summarized in the list below:

Requirements essential for the beam dynamics in the linac:

- Integrated focusing strength of the lens must be not less than $4 \text{ T}^2\text{-m}$;
- Each lens must contain 4 coils which can be combined into two dipole correctors; bending strength of each corrector must be not less than 0.0025 T-m ;
- Clear aperture in the lens must be not less than 30 mm;

- Uncertainty of the location of the effective magnetic axis in the focusing solenoid of the lens relative to reference points on the outer surface of the device must be better than 0.1 mm rms.

Requirements essential for proper functioning of the cryomodule:

- Maximum current in the solenoid must be less than 100 A;
- Maximum current in the dipole correctors must be less than 50 A;
- LHe vessel must be used for cooling the windings down to 2 K;
- The lenses must be quench-protected; the energy deposited in the lenses after quenching must be as low as reasonably achievable;
- The LHe vessel must meet the requirements of the Fermilab's ES&H manual chapters for pressure vessel;
- The design of the LHe vessel must ensure reliable and reproducible mechanical connection to the alignment fixture of the cryomodule;
- Maximum magnetic field generated by lenses in the cryomodule in the area near the surface of the SSR1 superconducting cavities must not exceed the level that would result in more than two-fold reduction of the intrinsic quality factor after quench event at any point on the surface of the cavity.

The Project X lattice, especially the low-beta section, provides limited space along the beamline for beam diagnostics either inside individual cryomodules or between adjacent modules. In order to conserve axial space along the beamline a button-type beam position monitor (BPM) has been chosen for installation in the SSR cryomodules. For a non-relativistic beam they also generate larger signal than the strip-line BPMs. A total of four BPMs will be installed in the cryomodule, one near each magnetic element. These devices are compact and lend themselves well to incorporation right into the solenoid magnet package as shown below in Figure IV-22. The bellows in either end of the beam tube allow independent adjustment of each magnet.

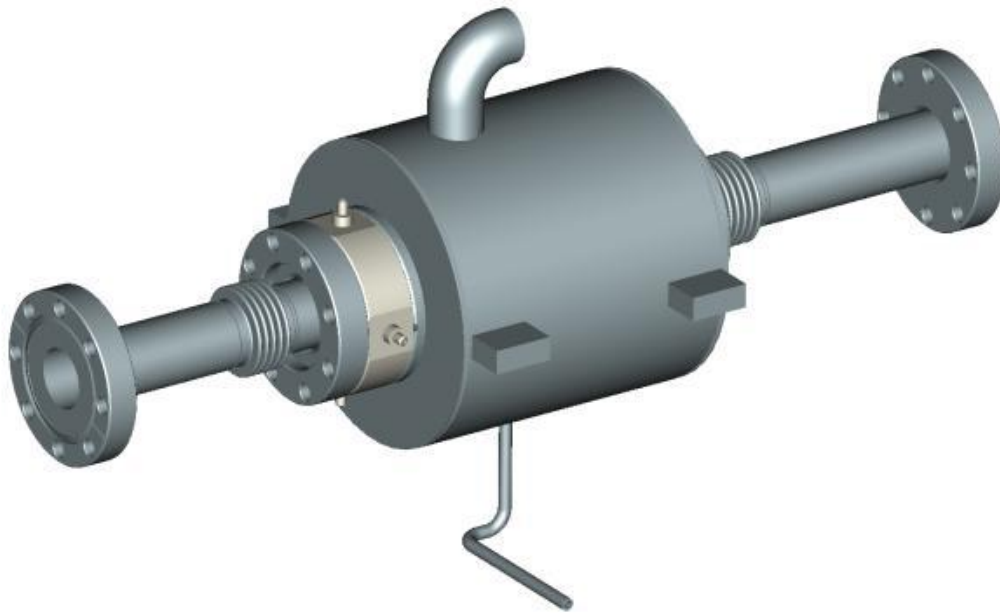


Figure IV-22: Solenoid and BPM assembly.

Final Assembly

The final assembly of the SSR1 cryomodule for SSR1 is shown in Figure IV-23 and Figure IV-24. Figure IV-23 shows the cavity string consisting of the cavities, solenoids, beam position monitors, and internal piping mounted on support posts that are in turn mounted to the strongback. Figure IV-24 shows the entire cryomodule assembly.

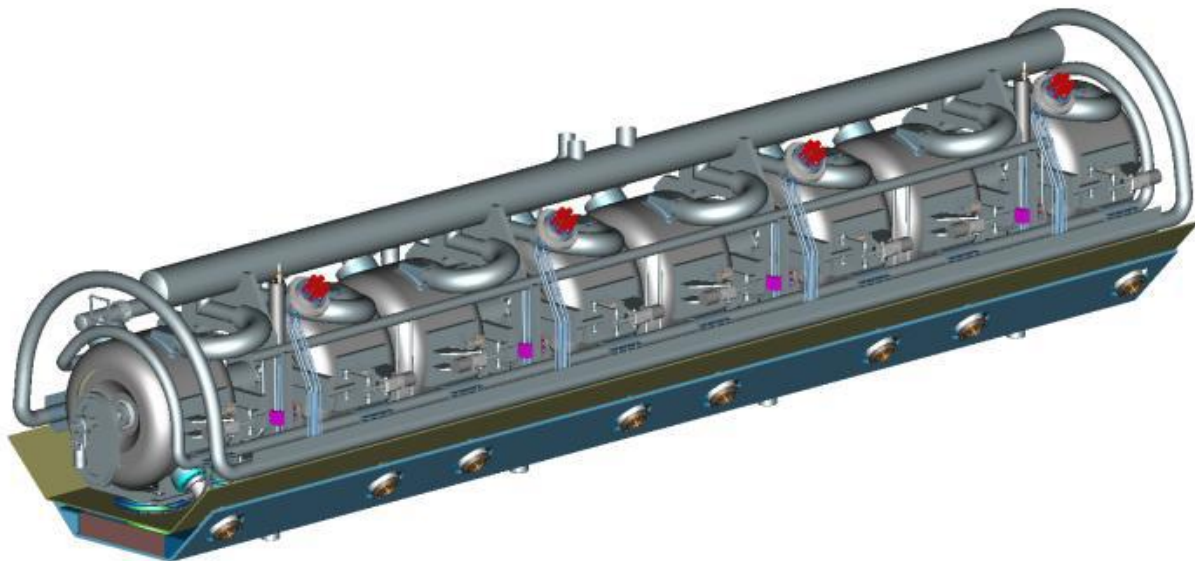


Figure IV-23: SSR1 cavity string assembly.

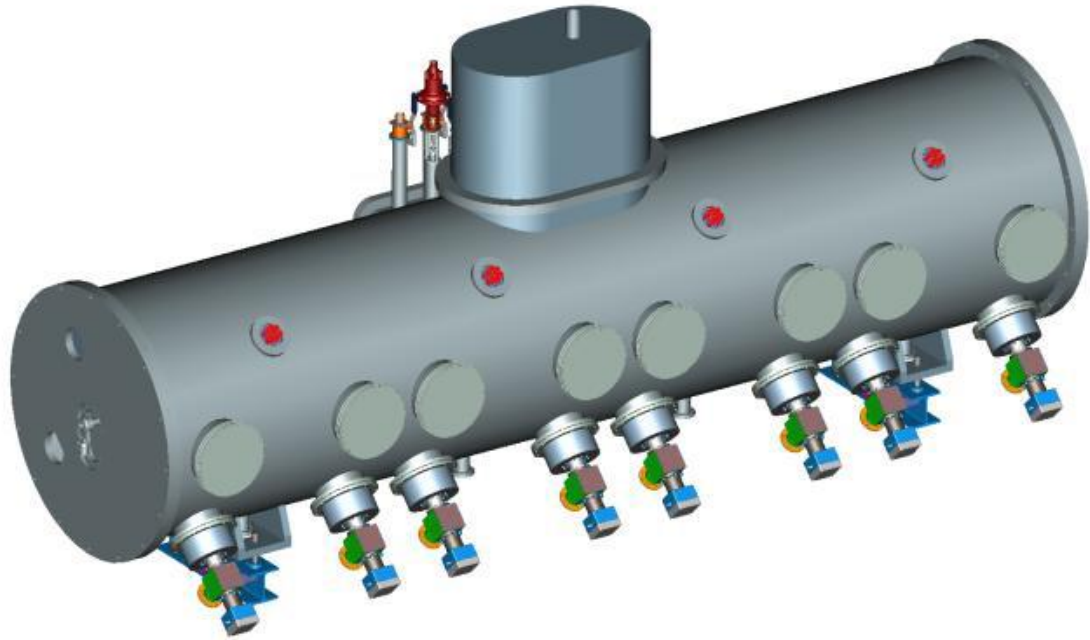


Figure IV-24: SSR1 cryomodule assembly

SSR1 Heat Load Estimate

Table IV-8 summarizes the estimated static and dynamic heat loads at each temperature level in the cryomodule assembly from the primary sources. As mentioned earlier, the nominal 80 K thermal shield and intercepts may operate anywhere between 45 and 80 K.

	Per Unit (W)			Units	Total (W)		
	80 K	5 K	2 K		70 K	5 K	2 K
Input coupler, static	5.4	2.8	0.5	8	43	23	4
Input coupler, dynamic	0	0	0.25	8	0	0	2
Cavity, dynamic	0	0	1.8	8	0	0	14
Support post	2.8	0.4	0.05	12	33	4	0.6
Conductor Lead Assembly	36.8	13.2	1.2	4	147	53	5
MLI (70 K + 2 K)	30.5	0	1.4	1	31	0	1
Cold-warm transition	0.7	0.1	0.01	2	1	0.2	0.02
TOTAL					255	80	27

Table IV-8: SSR1 Cryomodule Heat Load Estimates

SSR2 Cavities and Cryomodule

Acceleration from 38 to 177 MeV utilizes superconducting SSR cavities with $\beta_{\text{OPT}} = 0.51$ (SSR2). The cavity geometrical and electro-dynamic and mechanical design parameters are listed in Table IV-9 and Table IV-10. The cavity layout is shown in Figure IV-25. The electromagnetic optimization as well as mechanical design is complete, including the piezo tuner and helium vessel.

As in the SSR1 cryomodule, the quadrupole field is compensated by corrector coils which have independent leads. The SSR2 cavity has the same type of helium vessel as the SSR1 cavity, and the same type of tuners - coarse and fine. The input coupler is the same as for SSR1 cavity.

The SSR2 cryomodule design contains eight identical slots, which can accommodate both SSR2 dressed cavities and a focusing solenoid with a corrector package and BPM. The SSR2 cryomodule comprises 5 dressed cavities and 3 solenoids. The overall cryomodule length will be approximately 6.5 m. The vacuum vessel diameter will be 1.22 m (48 inches). Each cryomodule will be configured as a stand-alone unit, i.e. the vacuum vessel ends will be closed and cryogenic connections will be made at each module. Connections for cryogens and cryogenic control valves will be located in a mid-span vacuum vessel extension. The only module-to-module connection will be the beam line. The only beam instrumentation internal to the cryomodule assembly will be BPMs.

SSR2 Cavity	Design Value	
Frequency	325	MHz
Geometric Beta (β_G)	0.431	
Optimum Beta (β_{OPT})	0.515	
Aperture (diameter)	50	mm
$L_{EFF} = \beta_{OPT}\lambda$	47.5	cm
R/Q	275	Ω
$G = Q_0R_S$	118	Ω
E_{max}/E_{acc}	3.53	
B_{max}/E_{acc}	6.25	mT/(MV/m)
Gradient	11.2	MV/m
Peak Surface Electric Field	40	MV/m
Peak Surface Magnetic Field	70	mT
Max Energy Gain	5.3	MeV
Operating Temperature	2	K
Q_0 at 2 K	1.2	10^{10}
P_{diss} at Max Energy Gain	8.6	W

Table IV-9: Electro-dynamical requirements of the low-beta spoke cavities (SSR2)

	Requirements	
Mechanical	Radius, Length	280 mm, 540 mm
	He Vessel Material	Stainless Steel
	Maximum Allowable Pressure, MAWP	2 bar RT, 4 bar CT
	df/dp	≤ 25 Hz/mbar
Coupler	Max. design forward power	30 kW
Tuning	Coarse tuning range	135 kHz
	Fine tuning range	1000 Hz

Table IV-10: Mechanical parameters of the low-beta spoke cavities (SSR2)

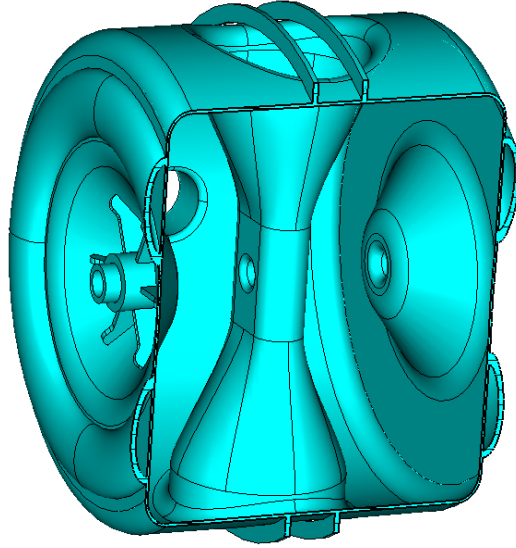


Figure IV-25: SSR2 cavity layout.

IV.1.5 Medium-beta section (160 – 3000 MeV, 650 MHz)

Acceleration from 177 MeV to 3 GeV will be provided by two families of the 5-cell elliptical cavities operating at 650 MHz and designed to $\beta_G = 0.61$ and $\beta_G = 0.9$. The cavity shape is optimized to decrease the field enhancement factors (magnetic and electric) in order to improve the interaction between the beam and the cavities. In order to do this, the cavity aperture should be as small as possible subject to the following considerations:

- field flatness,
- beam losses,
- mechanical stability,
- reliable surface processing.

The working gradient is chosen to provide the peak surface magnetic field that allows operation below high-field Q-slope, see Figure III-15. For a frequency of 650 MHz the peak magnetic field should be not greater than ~ 70 mT. In addition we require that the peak surface electric field be lower than 40 MV/m in order to avoid the risk of strong field emission.

Linear perturbation theory indicates that for a given relative error in the frequencies of cavity cells the field flatness is determined mainly by the distance, δf , between the operating

frequency and the frequency of the neighboring mode, $\pi(n-1)/n$. In terms of the coupling parameter, k , between the cavity cells and the number of cells one obtains:

$$\delta E/E \sim f_\pi/|f_\pi - f_{\pi(n-1)/n}| \equiv f_\pi/\delta f \approx (n-1)^2/k.$$

Thus, a cavity with fewer cells allows a smaller coupling coefficient, k , for a given field flatness. For example, the 9-cell ILC cavity has $\delta f/f_\pi$ of 6×10^{-4} ($k = 1.87\%$) and for the 5-cell 650 MHz cavity one can take the same $\delta f/f_\pi$ at least, yielding $k > 0.5\%$.

The aperture selected for the cavity represents a trade-off between requirements related to the cell-to-cell coupling and beam loss. The 805 MHz superconducting section of the SNS proton linac, which is close to Project X linac in average current, operates with cavities that have an aperture of 83 mm for low-beta part and 100 mm in high-beta part. Their experience is that these cavities operate with tolerable beam loss at these apertures. Thus, we have adopted these dimensions for the 650 MHz cavities of Project X. In addition, it appears that these apertures will also facilitate the required surface processing.

The 650 MHz cavities require sufficient wall thickness to minimize sagging caused by the overall weight. Figure IV-26 shows results of a simulation of the cavity sag caused by its weight as a function of wall thickness for the 650 MHz cavities and the ILC (1300 MHz) cavity. Note that stiffening rings are used for both the ILC and 650 MHz cavities to increase the rigidity of cavities. Requiring a maximum cavity sag of 120 μm (the same as ILC) results in a 4 mm wall thickness. A small cavity wall slope (designated by α in Figure IV-27) gives more freedom to decrease the field enhancement factors. However, the slope is limited by surface processing and mechanical stability requirements. For beta=0.9 we select the slope to be 5°. For beta=0.61 the slope is reduced to 2°, in order to maintain an acceptably low field enhancement.

Optimization of the two 650 MHz cavity shapes was done based on the constraints discussed above. Cavity performance parameters are summarized in Table IV-11. The physical description of the cavity shapes is displayed in Figure IV-27 and Table IV-12. Requirements for maximum cavity detuning amplitude and cavity sensitivity versus helium pressure fluctuations are discussed further in [41]. Note that the 650 MHz cavities have small beam loading, and thus microphonics mitigation is essential. In order to do this, the cavities are over-coupled; both active and passive means for microphonic compensation are planned to be used also [42]. Neither HB605 or LB650 cavities contain HOM dampers – they are not necessary for required beam current (see for example [43]).

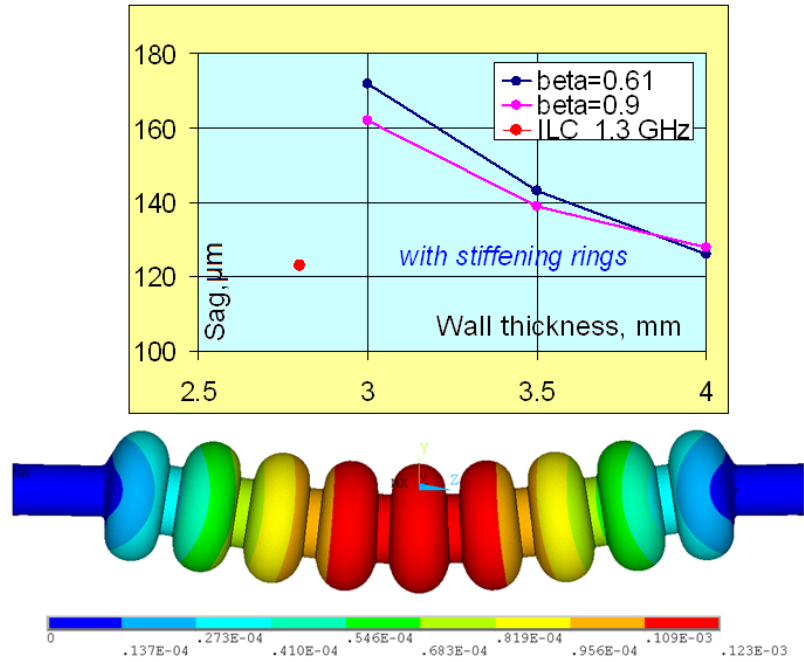


Figure IV-26: The cavity sag versus the wall thickness.

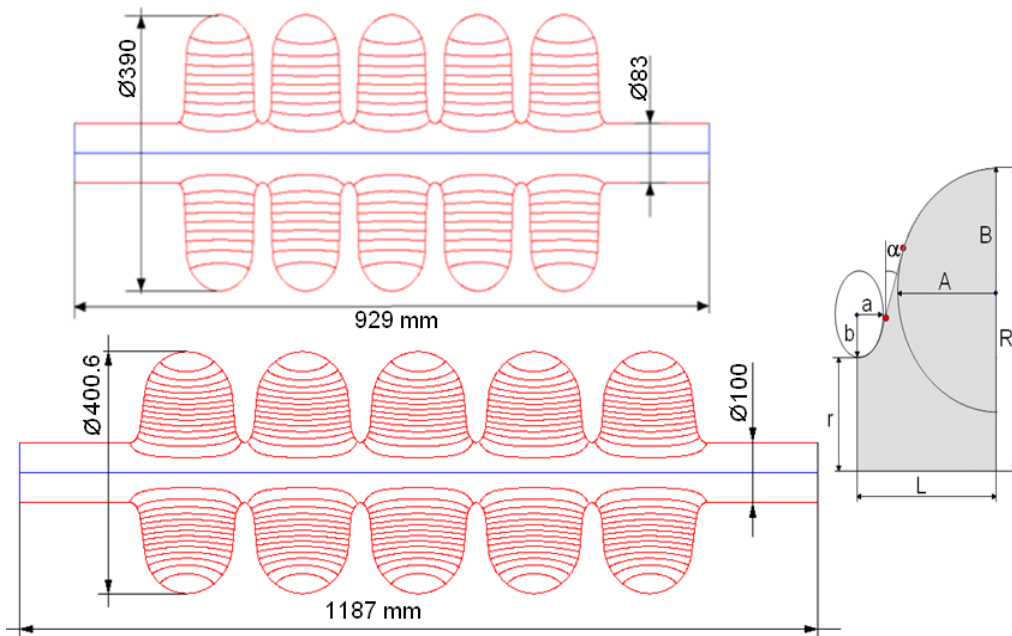


Figure IV-27: Layout of 650 MHz cavities. Beta=0.61(top) and beta=0.9 (bottom).

650 MHz Cavities	Design Value		
	Low Beta	High Beta	
Frequency	650	650	MHz
Geometric beta (β_G)	0.61	0.90	
Optimum Beta (β_{OPT})	0.64	0.95	
Aperture (diameter)	83	100	mm
Cells per Cavity	5	5	
Cavity Length	70	104	cm
R/Q ₀	378	638	Ω
G = Q ₀ R _S	191	255	Ω
E _{max} /E _{acc}	2.27	2.07	
B _{max} /E _{acc}	4.25	3.78	mT/(MV/m)
Gradient*	16.5	17	MV/m
Peak Surface Electric Field	37.5	35.2	MV/m
Peak Surface Magnetic Field	70	64	mT
Max. gain per cavity, MeV(on crest)	11.6	17.7	MeV
Operating temperature	2.0	2.0	K
Q ₀ at 2 K	1.5	1.5	10 ¹⁰
Cryogenic losses per cavity at 2 K	24	24	W
Peak detuning amplitude [♦]	<20	<20	Hz
Bandwidth [†]	45	45	Hz
Sensitivity to He pressure fluctuations df/dP	<25	<25	Hz/mbar
Beam current (Stage 1/Stage 2)	2	2/1	mA
Power consumed by the beam [♦]	23	35/17.5	kW
Maximal input RF power [†]	<34	<50/31	kW

* The gradient is taken for the optimal beta and normalized on the effective cavity length

[♦] The peak microphonics amplitude plus static detuning errors.

[†] Beam power plus the power overhead to account for waveguide losses, cavity detuning, etc.

Table IV-11: RF parameters of the 650 MHz cavities.

Dimension	Beta=0.61		Beta=0.9	
	Regular cell	End cell	Regular cell	End cell
r, mm	41.5	41.5	50	50
R, mm	195	195	200.3	200.3
L, mm	70.3	71.4	103.8	107.0
A, mm	54	54	82.5	82.5
B, mm	58	58	84	84.5
a, mm	14	14	18	20
b, mm	25	25	38	39.5
$\alpha, ^\circ$	2	2.7	5.2	7

Table IV-12: 650 MHz cavities dimensions (see Figure IV-27 for definition of dimensions).

A possible bunch structure required for muon, kaon, and nuclear experiments running in parallel at 3 GeV is shown in Figure IV-28. Average beam current in the 1-3 GeV linac in this mode is 1 mA. Figure IV-29 shows the spectrum for this beam structure, assuming very short bunches of equal charge and in the absence of timing jitter. The spectrum and (R/Q) values of the $\beta_G=0.9$ 650 MHz cavity are shown in Figure IV-30.

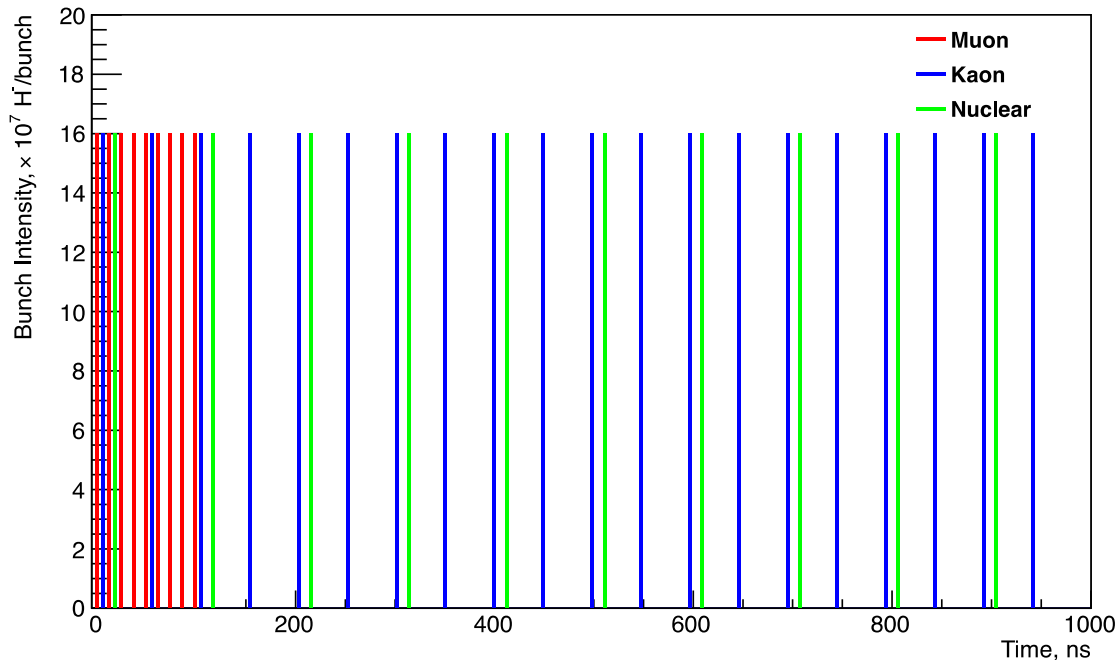


Figure IV-28: Beam structure for 3 GeV program.

The amplitude of an excited monopole HOM depends on the amplitude of the nearest beam spectrum line, I , the detuning δf , and the distance between the HOM frequency f and the beam spectrum line frequency. It can be estimated for a high Q resonance (assuming $\delta f/f \ll 1/Q$) as the following:

$$U_{HOM} \approx \frac{I(R/Q)}{4\sqrt{2}\delta f/f}.$$

If the high order mode is exactly at resonance,

$$U_{HOM} = \frac{1}{2}I(R/Q)Q_L,$$

where Q_L is the loaded quality factor of the mode. The cryogenic losses depend on square of HOM amplitude:

$$P_{loss} \approx \frac{U_{HOM}^2}{(R/Q)Q_0}.$$

Requiring that P_{loss} is much smaller than the sum of static heat load and cryogenic losses due to accelerating mode (20 W), and assuming that the intrinsic quality factor is $Q_0 = 5 \times 10^9$, the maximum allowable value of the monopole HOM loaded quality factor is obtained: $Q_L \ll 6 \times 10^7$.

Similarly, requiring that excitation of a monopole mode does not increase longitudinal emittance, $\varepsilon_z \gg U_{HOM}\sigma_z/c$, an estimation of the safe frequency detuning yields:

$$\delta f \gg f \frac{I(R/Q)\sigma_z}{4\sqrt{2}\varepsilon_z c}.$$

Here σ_z is the bunch length, and c is the speed of light. The worst case is at the beginning of $\beta_G = 0.9$ section, where the bunch length is at maximum ($\sigma_z/c = 7.7 \times 10^{-3}$ ns). Assuming the second pass-band monopole HOM (1241 MHz and $R/Q = 130$ Ohm) is the nearest beam spectrum line ($I = 1$ mA), and an emittance of $\varepsilon_z = 1.5$ keV ns, one obtains the following estimation for frequency detuning: $\delta f \gg 140$ Hz.

A more accurate estimation of coherent HOM excitation in the Project X linac is performed using statistical analysis based on the expected spread of data for the HOM parameters (frequency, impedance and quality factor). Errors of cavity shape introduced in manufacturing are taken into account by allowing random variations of cavity profile within 0.2 mm of ideal shape. In order to estimate probability of cryogenic losses, and relative change of longitudinal emittance, 10^5 random linacs were generated using predicted deviations of frequency, loaded quality factor and impedance values of monopole HOMs. It was found that the probability to have losses above 0.1 W per cryomodule is extremely small: 10^{-4} for an average beam current of 1 mA.

The beam structure, shown in Figure IV-28 consists of three main sub-components (1 MHz, 10 MHz and 20 MHz). The phase of the voltage of an HOM excited by the resonance with one of the beam components is random with respect to two other components of the beam. In case of a high- Q resonance such a HOM may introduce a significant energy variation and longitudinal emittance growth along the beam train. Results of statistical analysis show, that the probability of the emittance to double is 10^{-3} for the beam current 1 mA. Based on this analysis the conclusion is made that HOM couplers are not needed in 650 MHz cavities. More details can be found in Ref. [43].

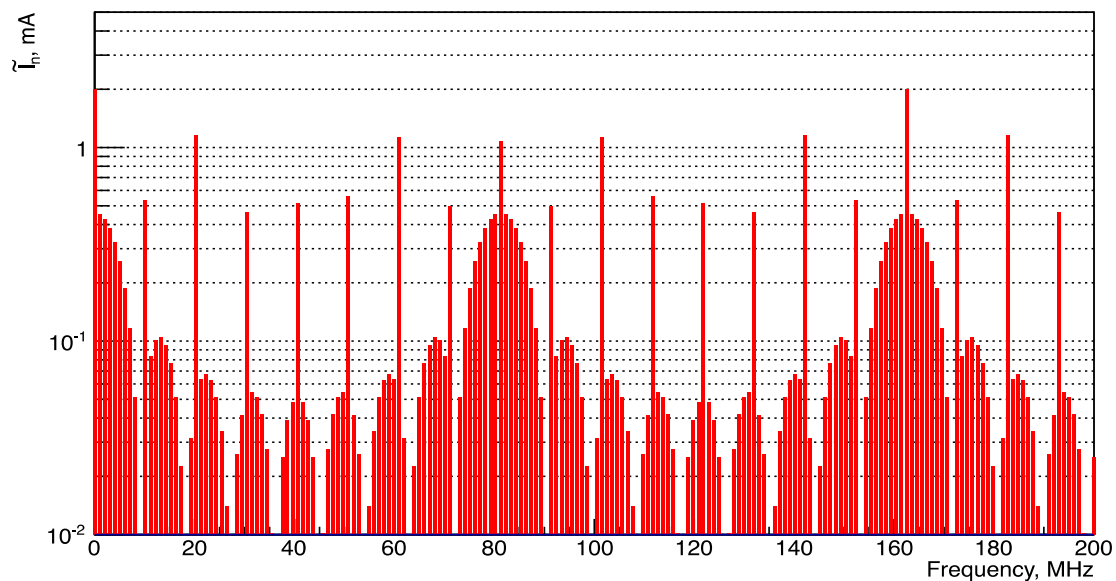


Figure IV-29: Beam spectrum of 3 GeV program.

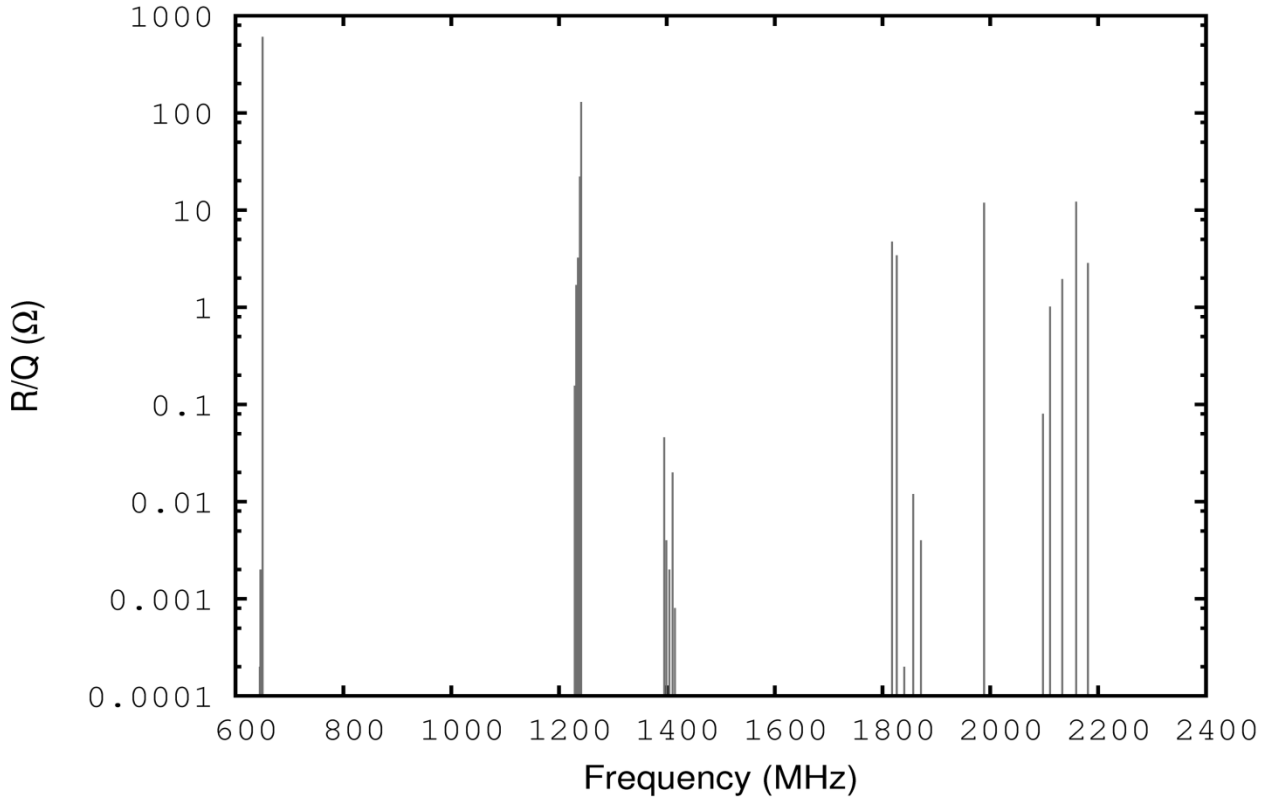


Figure IV-30: (R/Q) of the monopole HOMs in $\beta_G=0.9$ section of 650 MHz cavities.

Cryogenic losses in the cavities are determined by the R/Q value, G-factor and surface resistance. The surface resistance is in turn is a sum of residual resistance and BCS resistance. Modern surface processing technology may provide a residual resistance of ~ 5 n Ω [44]. BCS resistance as a function of the frequency f and temperature T may be estimated using the formula

$$R_{BCS} = 2 \cdot 10^{-4} \frac{1}{T} \left(\frac{f}{1.5} \right)^2 e^{-17.67/T}$$

which represents a good approximation to the value of BCS resistance. For 650 MHz one obtains ~ 3 n Ω for BCS and, thus, ~ 8 n Ω total. Assuming a medium field Q-slope at the peak field of 70 mT of about 30%, this gives a target for Q_0 value of the 650 MHz cavity of $\sim 2 \times 10^{10}$, and losses at the operating gradient (17.7 MeV/m) of ~ 30 W/cavity, or < 250 W/cryomodule. The preliminary mechanical design of the beta=0.9 cavity is shown in Figure IV-31.

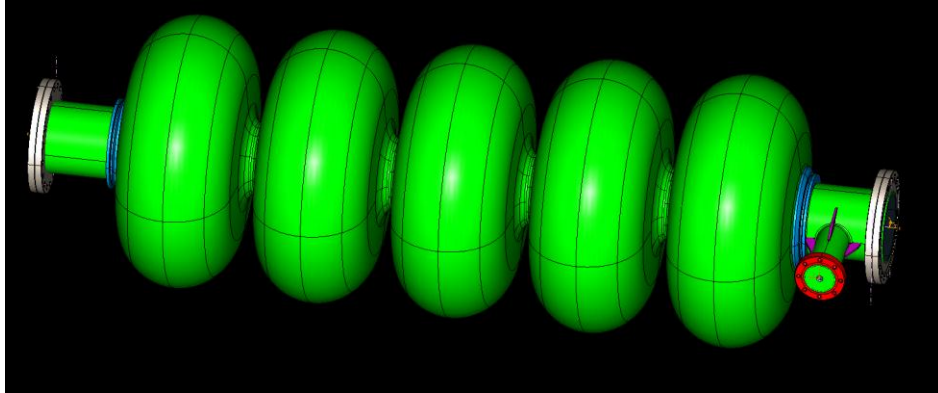


Figure IV-31: Preliminary mechanical design of the beta=0.9 cavity.

IV.1.6 RF power

There are more than 250 RF systems included in the CW linac. With the exception of the RFQ they are deployed as one amplifier per cavity. All RF systems – RFQ, buncher, half wave resonator (HWR), single spoke resonator (SSR1 & SSR2), low beta and high beta elliptical (LB650 & HB650) – will utilize continuous wave (CW) amplifiers. There are three frequencies of operation, 162.5 MHz (RFQ & HWR), 325 MHz (SSR1 & SSR2), and 650 MHz (LB650 & HB650). Power levels range from 4 kW to 150 kW. RF source requirements for the superconducting portion of the linac are listed in Table IV-13.

Section	Freq MHz	Microphonic amplitude Hz	Minimal bandwidth Hz	Maximal loaded Q	Max power per cavity kW
HWR	162.5	20	49	3.3×10^6	4.9
SSR1	325	20	56	5.8×10^6	5.5
SSR2	325	20	45	7.2×10^6	17
LB	650	20	45	1.4×10^7	34
HB1	650	20	45	1.4×10^7	50
HB2	650	20	45	1.4×10^7	31

Table IV-13: Maximum power consumption per cavity, tolerable microphonic amplitude, loaded Q and bandwidth.

The RFQ has two input ports and is driven by two 75 kW CW solid-state amplifiers. The beam energy at the RFQ output is 2.1 MeV. Three room temperature buncher cavities and one cryomodule containing eight superconducting HWRs at 162.5 MHz will have one solid-state amplifier each operating at power levels of 4 to 6 kW. Two cryomodules at 325 MHz will be populated with eight SSR1 cavities powered by 6 kW solid-state amplifiers. 7 kW solid-state amplifiers power seven SSR2 cryomodules with 5 cavities each. Five LB650s with 30 cavities and fifteen HB650s with 120 cavities will each be powered by a 35 kW IOT amplifier. Seven HB650s with 42 cavities in the 1 GeV linac will each be powered by a 50 kW IOT. It is possible that a solid-state or injection locked magnetron could be used at 650 MHz as R&D for those technologies mature.

The low level RF (LLRF) system will provide a drive signal on the order of 0 to +10 dBm for each RF power source. The amplifier(s) will provide sample signals of the pre-driver and final outputs. All amplifiers will be self-contained units complete with integral power supplies, protection circuits, and control interface. The RF distribution system for the CW linac will utilize rigid coax commensurate with system power levels, 6-1/8", 3-1/8", or 1-5/8" EIA flanged sections. The final connection to the cryomodules will utilize a section of flexible transmission line to minimize connector location tolerances. Each RF system will have a circulator and load to isolate the cavity from the power amplifier. This level of protection is essential in SRF systems due to full power reflection from the cavity in the absence of beam. Cavity and drive sample signals will be provided to the LLRF for vector regulation and frequency control of the cavities. All of the RF amplifiers will be water cooled to minimize the heat load to the building HVAC system.

While each amplifier has built in protection which includes, water flow, water temperature, pressure differential, and reflected power monitoring; a global interlock and hardware protection system will need to be designed for all RF systems. This will include water flow to loads and circulators, spark detection on cavity couplers, and RF leakage detection.

IV.1.7 RF Splitter

RF splitters are used to support a quasi-simultaneous beam delivery to multiple users. Presently we expect that two different splitter types will be used in the Project X. The first will split the "beam RF buckets" into two equal parts for bunch frequencies of 162.5 MHz. This requires operations at frequencies equal to $(n+1/2) \times 162.5$ MHz, where n is an integer. The splitter of the second type, to be used in Stage 2 at 3 GeV, splits the beam with 81.25 MHz bunch frequency into 3 parts, so that the non-deflected beam (crossing the splitter at the RF wave form zero crossing) would have 2 times larger number of buckets than two other

beams deflected in different directions (the corresponding bunches cross the splitter at maximum and minimum of the waveform). The frequency of this RF splitter has to be $(n+1/4) \times 81.25$ MHz.

The operating frequency of the deflecting RF structure is limited (i) by the bunch length – at high frequency and (ii) by the cavity transverse size – at low frequency. The cavity should have a reasonable aperture (a compromise between the deflecting properties and possible beam loss heating the cavity). The required deflecting kick is $\Delta pc/e \sim 7$ MV for both splitter types. It yields a total deflection angle of approximately ± 4 mrad at 1 GeV and ± 2 mrad at 3 GeV. A choice of RF frequency in vicinity of 400 MHz satisfies the above mentioned requirements and allows one to have very close designs for both splitters. The corresponding frequencies are 406.25 MHz = $(2+1/2) \times 162.5$ MHz and 426.5625 MHz = $(5+1/4) \times 81.25$ MHz. The cavities of these frequencies have sizes which fit existing cryogenic test facilities.

In order to provide this transverse kick, a two-cell version [45] of a ridge deflecting cavity [46,47] is suggested, see Figure IV-32. Parameters of the cavities are specified in Table IV-14.

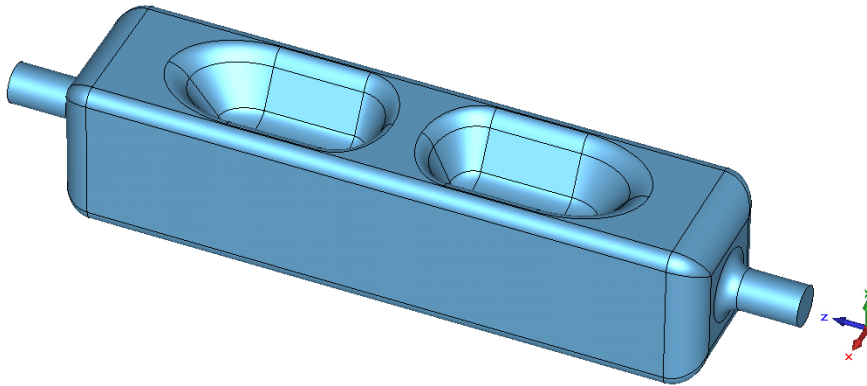


Figure IV-32: Two-cell ridge deflecting cavity.

Stage	I	II
Operating frequency, MHz	406.25	426.5625
Number of cells	2	2
Optimal beta	0.87	0.92
Transverse kick, MeV	7	7
Maximal surface electric field, MV/m	36	37
Maximal surface magnetic field, mT	50.5	52
R/Q*, Ohm	485	510
G-factor, Ohm	115	115
Dimensions, mm ³	270×270×1200	260×260×1150
Aperture, mm	70	65

* $R/Q = V_{kick}^2 / 2\omega W$, where W is the stored energy.

Table IV-14: Parameters of deflecting cavities

Input power requirements are determined mainly by the amplitude of microphonics δf . $P_{inp} < V_{kick}^2 / [(R/Q) \cdot f / \delta f]$. For a cavity operating at 7 MeV and for $\delta f = 15$ Hz, $P_{inp} < 4$ kW for both cases. Consequently, the cavity bandwidth should have the same order, or ~ 15 Hz. The microphonics amplitude is determined by expected helium pressure variations and df/dp value. Minimization of df/dp is one of the major goals during the cavity mechanical design. The helium pressure fluctuation budget is limited to 0.2 mbar rms. Thus, df/dp is to be about ~ 20 Hz/mbar taking into account the safety factor of 4.

IV.2 Collimators and Beam Dump

IV.2.1 8 GeV Collimators

A transverse collimation system is employed in the 8 GeV transfer line from the pulsed linac to the injection foil in the Recycler. Each collimation station system consists of a “thick” stripping foil, located just upstream of a quadrupole, and a downstream absorber. Large amplitude H⁻ ions that strike the foil are converted into protons which are defocused (in the collimation plane) by the downstream quad while the H⁻ remain focused. The protons receive a kick proportional to their offset in the quadrupole field such their amplitude is increased prior to being intercepted by an absorber placed just upstream of the next quadrupole to

intercept these particles. This technique has been successfully implemented at SNS. There they use a fixed aperture absorber. The Reference Design employs a movable jaw absorber to increase the efficiency of absorbing the stripped protons. This technique has been simulated in TRACK and the movable jaw absorber has been simulated in MARS. The technique is described in [48]. A conceptual description of the system is shown in Figure IV-33. The phase advance per cell in the 8 GeV transport line will be 90° , and therefore four stations (two in each plane) are required to cover the full phase space.

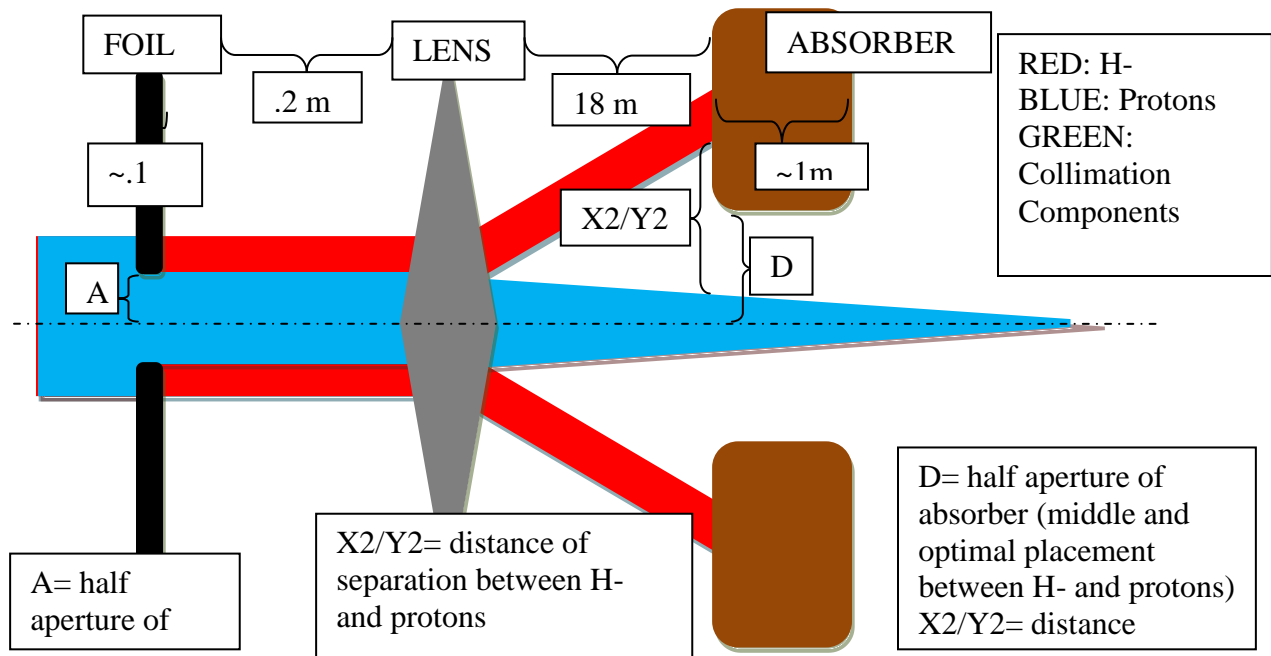


Figure IV-33: Concept of a horizontal H- transverse collimation station. A thin foil (black) intercepts large amplitude H- ions (blue). The focusing quadrupole (grey) defocuses the converted protons (red). The variable aperture absorber (brown) is adjusted to intercept the protons at an impact parameter that minimizes out-scattering.

Figure IV-34 displays the TRACK output for beam transport from the pulsed linac to the Recycler. The entrance to the transport line is on the left, and the figure ends with the injection stripping foil in the Recycler on the right. In this simulation 1 million particles were tracked through the beam line and the rms and 100% amplitudes are displayed: horizontal (blue) and vertical (red). The top figure displays the amplitudes when the collimation system is not engaged. The bottom figure displays the amplitude of the particles when the collimation system was set to intercept 1% of the particles. This particular simulation is

based on a prior version of the beamline containing six collimating stations (three horizontal and three vertical) and 60° cells. The effect of the six stations is readily seen in the maximum particle amplitudes on the left hand side of the plot. As can be seen the collimation system is effective in reducing the maximum particle amplitudes, with essentially no impact on the rms beam size. Figure IV-35 shows the resultant x-y beam distribution at the Recycler stripping foil location. In this figure, the width of the uncollimated beam distribution (shown in red) is almost a factor of three larger than the collimated distribution (shown in green). It is clear that this collimation scheme reduces the required injection foil size substantially, as well as minimizing the number of H^- in the tails that miss the injection foil. This will, in return, help reduce the activation in the injection area of the Recycler.

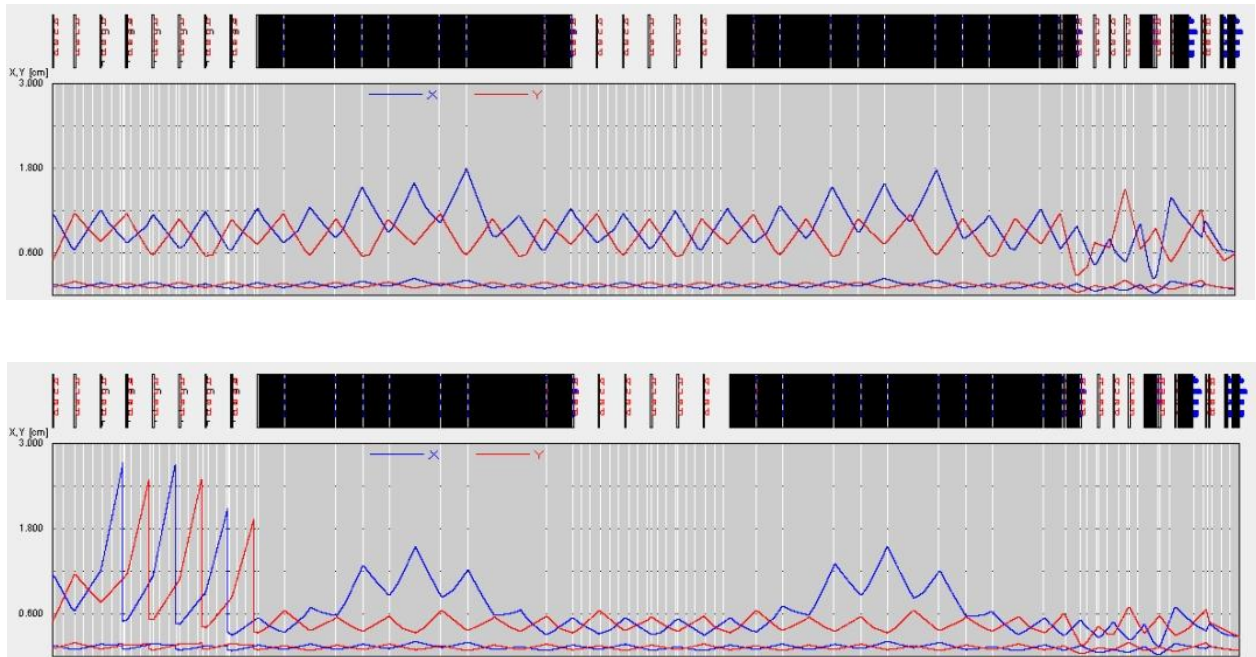


Figure IV-34: Comparison of maximum (100%) and rms particle amplitudes for no collimation (top) and collimation (bottom).

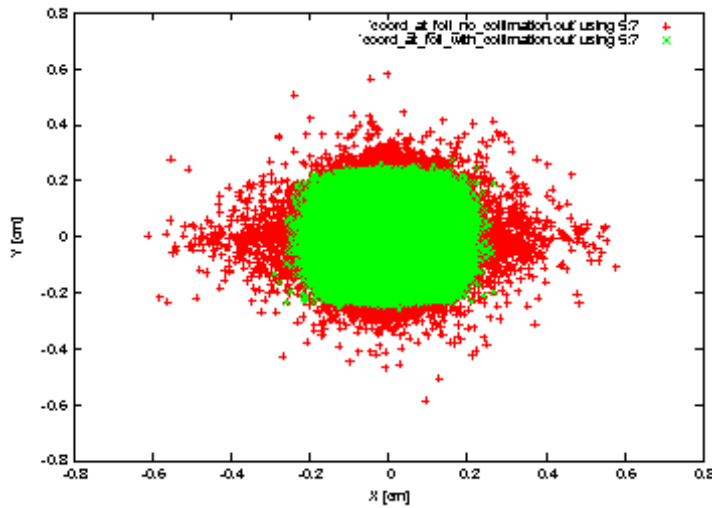


Figure IV-35: Beam distribution at the Recycler injection foil location, showing the impact of transverse collimation. Red is uncollimated and green is the collimated distribution.

The movable jaw absorbers were modeled in MARS to determine the requirements on the collimation system shielding which will meet Fermilab radiological requirements. Figure IV-36 shows the layout of the front face and top view of a horizontal absorber. The absorber consists of a 14×18×1 cm stainless steel vacuum chamber with two movable tungsten collimator jaws (magenta). The vacuum chamber is surrounded by 45 cm of steel and 10 cm of marble. The absorber jaws are 10 cm inside the front and rear face of the collimator. Also included in the model, but not shown, are the holes through the shielding for the motion control of the collimator jaws.

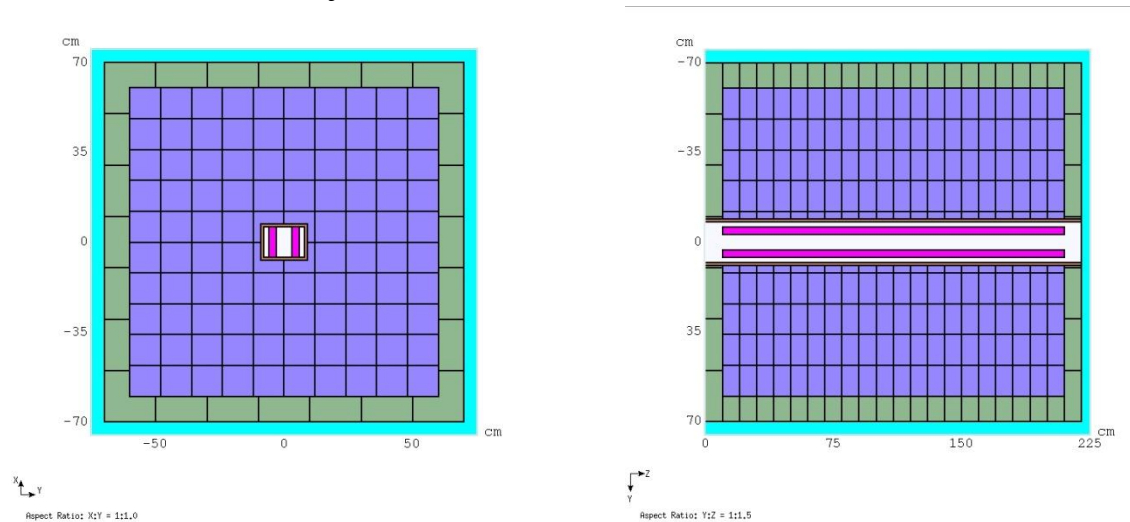


Figure IV-36: Geometry of the MARS model for a movable jaw transverse collimator.

Although this simulation is for 8 GeV transport, the same systems could also be installed in both 1 and 3 GeV transfer lines if it were deemed necessary. The expectation is that these will be installed in a straight section located in the 1 GeV transport line between exiting the Tevatron enclosure and entering the Booster enclosure. The utilization in the 3 GeV line requires further study.

IV.2.2 Recycler Injection Beam Absorber

The Recycler accumulates six pulses (spaced at 100 ms) containing 2.6×10^{13} protons each, every 1.2 seconds for the Main Injector 120 GeV neutrino program. This leaves six additional 10 Hz linac pulses that could be utilized for an 8 GeV program based off the pulsed linac or Recycler. The total injection beam power for the 120 GeV program is about 170 kW. If we assume all 10 Hz linac pulses were injected into the Recycler, the maximum delivered beam power from the pulsed linac would increase to approximately 350 kW.

The beam power delivered to the injection absorber under nominal operating conditions is due to 1) unstripped or partially stripped ions exiting the foil and 2) H^- ions missing the foil. Although the foil thickness would be sized to give greater than 99% stripping efficiency, we assume for these calculations that 2% of the injected H^- passing through the foil exit the foil as unstripped H^- or neutrals. Depending on the transverse tail distribution of the incoming H^- ions, a conservative approach is to assume that up to 3% of the beam in the tail could miss the foil and be directed to the absorber. Therefore, we assume 5% of the injected beam as a load on the injection absorber under normal operating conditions. The beam absorber is designed conservatively to accept 10% (which is consistent with designs at other facilities, in particular SNS) of the maximum beam power deliverable, i.e. 35 kW to allow for commissioning activities and abnormal injection conditions.

The design of the Recycler injection optics yields itself to a short dump line to the injection absorber. The current concept is to install the absorber in the MI-10 alcove and provide sufficient shielding to satisfy ALARA requirements. Although the goal is to utilize the existing alcove, it is recognized that some civil construction may be required to place the absorber farther from the ring centerline. The geometry of the absorber is shown in Figure IV-37. This particular layout is for a Main Injector absorber – Figure IV-38 compares the elevation of the absorber as utilized in the Recycler.

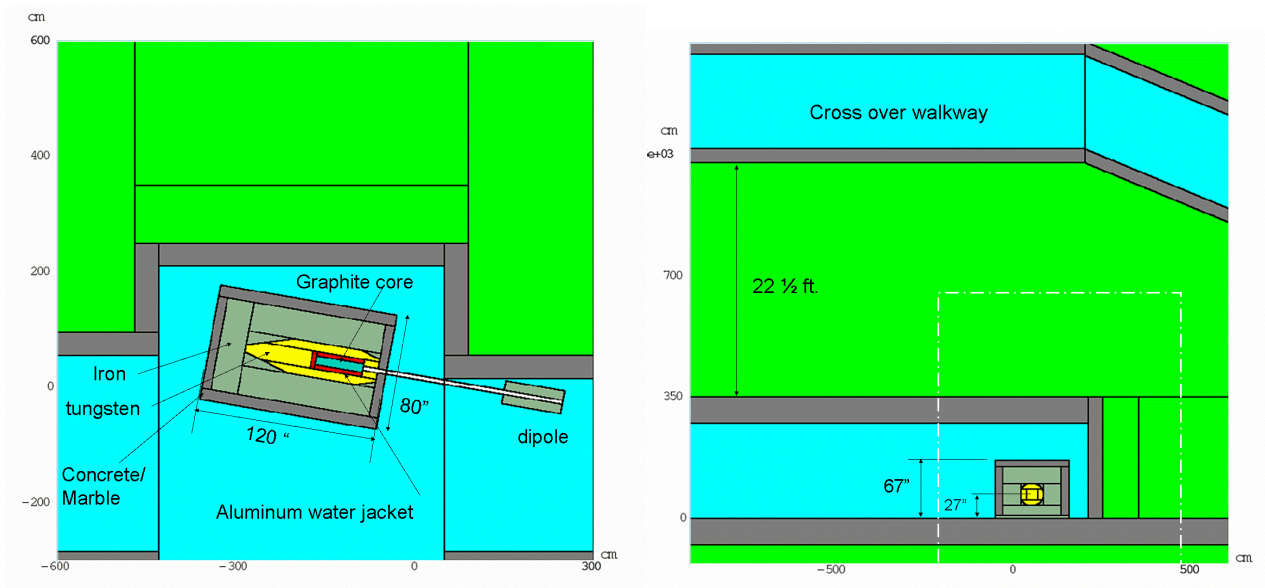


Figure IV-37: Mars model for injection absorber in the Main Injector.

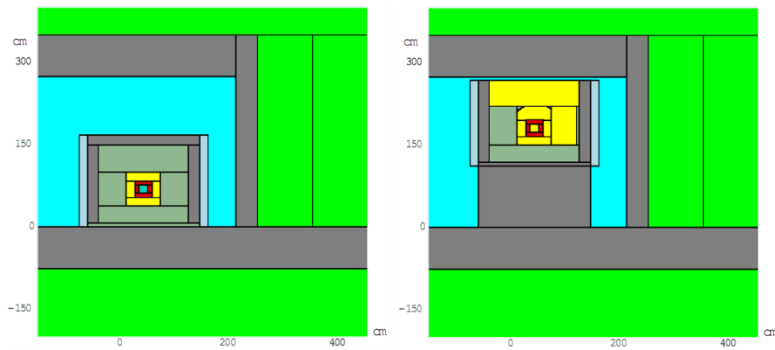


Figure IV-38: Comparison of potential absorber elevations for MI injection (left) and Recycler injection (right).

Much of the initial shielding design work was done with previous incarnations of Project X with the absorber located at the Main Injector elevation (Figure IV-37) with different injection scenarios and expected beam powers. These investigations showed that the prompt dose in the cross over walkway was ~ 0.002 mrem/hr for 6.5 kW on the beam absorber. The same simulation showed residual dosages (with 30-day irradiation and 1-day cool down) on

the outside of the marble to be less than 40 mrem/hr and the star density (for sodium and tritium production estimation) in the unprotected soil at the location of the sump drains to be a factor 10 less than the allowed levels [49]. Therefore, the conceptual design described in the reference easily met the radiological requirements for a beam power of 6.5 kW on the absorber.

With the current maximum beam power of 35 kW into the injection absorber, the previous results can roughly be scaled by the absorbed power. Using this scaling, the prompt dose rate in the crossover walkway is still 0.01 mrem/hr, still well below the limit of 0.05 mrem/hr for unrestricted access. Scaling the residual dose on the outside of the marble yields an unacceptable level of over 200 mrem/hr which will require additional attention. Scaling the star density in the soil still meets the requirements. Additional simulations for the Recycler installation and current expected injection scenario and beam powers are required.

With the LBNE plans to use the Main Injector straight section for extraction, the elevation of the injection absorber is raised to the Recycler elevation. It will be necessary to investigate changes in shielding for prompt dose in the walkway and star density in the unprotected soil. This analysis was completed in 2008 for the then assumed beam power of 10% of 1MW into the injection absorber. Figure IV-39 shows the star density surrounding the absorber in this configuration. This simulation showed that for 100 kW into the absorber the star density under the enclosure was at the limit for tritium and sodium production. Scaling these results to the present configuration, the star density is reduced to 35% of the limit.

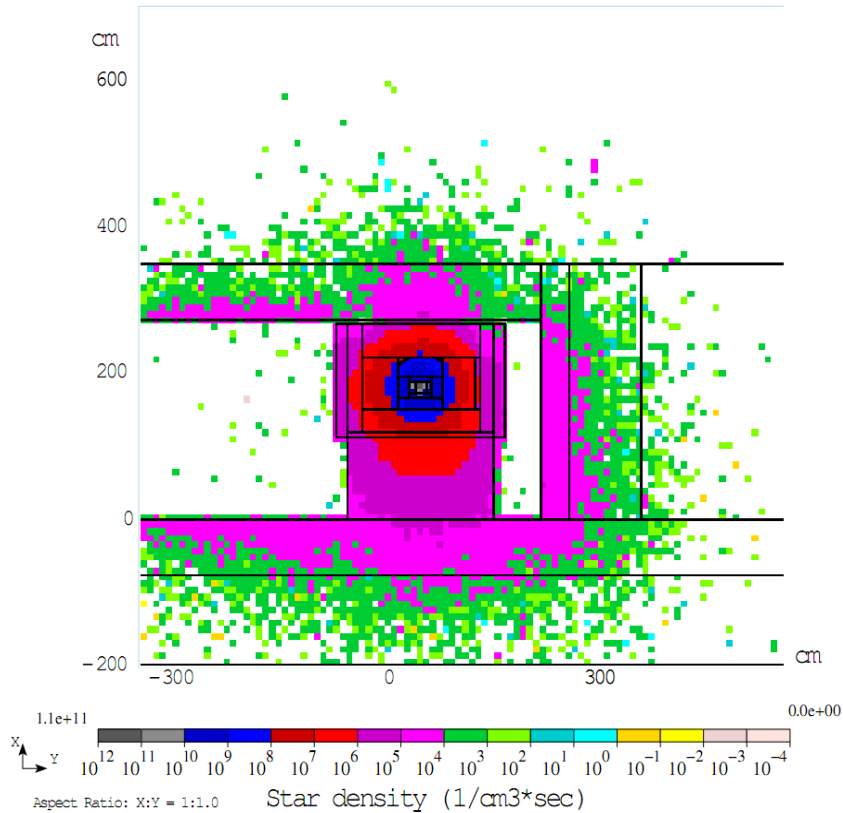


Figure IV-39: Star density around a Recycler injection absorber model with 100 kW into the absorber shows that the star density is at the radiological limit for surface water.

The initial injection absorber core design was patterned after the MI abort core, namely a graphite core surrounded by an aluminum water jacket. Simulations showed the maximum energy deposition localized outside the aluminum water jacket leading to heating of the shielding. In an effort to keep all the energy deposition within the aluminum water jacket (without lengthening the core) a sandwich core was investigated. This injection dump core design is shown in Figure IV-40. The core is a sandwich of alternating graphite and tungsten disks inside a sealed aluminum water jacket. The concept of alternating density of the core allows the energy deposition to be spread out over a larger distance thus reducing peak internal temperatures and forces. Further optimization of disk thicknesses is expected to reduce peak temperatures even further.

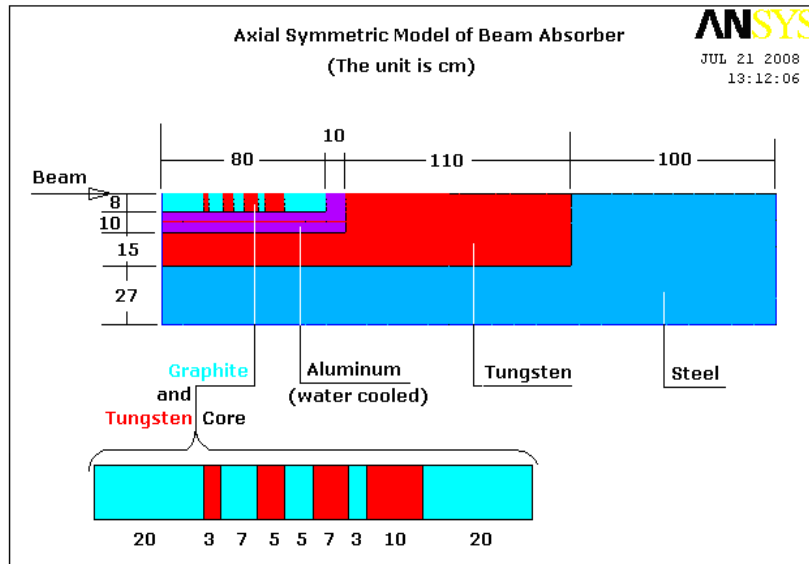


Figure IV-40: Geometry of the ANSYS model of Recycler injection absorber.

The thermal and stress simulations were completed at 36 kW. The design is robust against several failure modes (i.e. loss of cooling for 10 minutes and 2 full intensity pulses of 360 kW). Figure IV-41 and Figure IV-42 show results for 36 kW of steady state input power. Spreading out the energy deposition over a larger distance allows the absorber shielding to remain at room temperature. In addition, the stresses induced in the core from the increase in temperature, are well below the yield points of any of the materials. These studies indicate that under assumed operating conditions in the Reference Design the injection absorber provides a performance margin of between six and twelve. While these simulations indicate that the absorber concept is viable, more detailed simulation with more accurate assumptions on beam power will be pursued in the future.

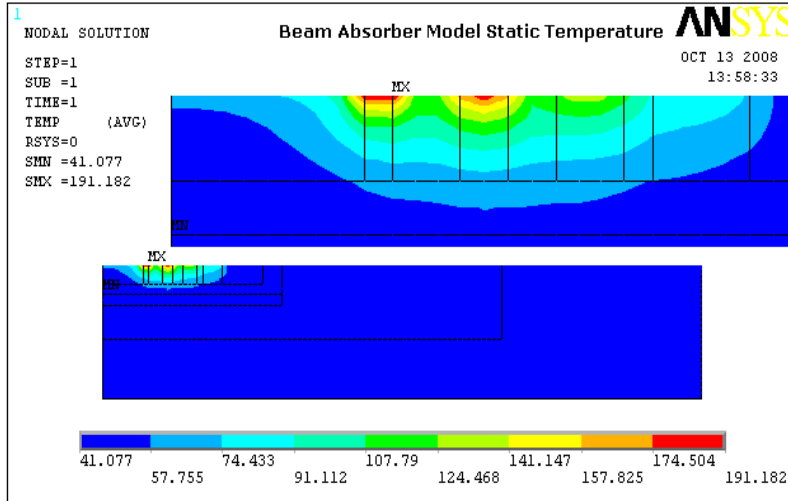


Figure IV-41: Steady state temperature in the absorber core for 36 kW incident beam power.

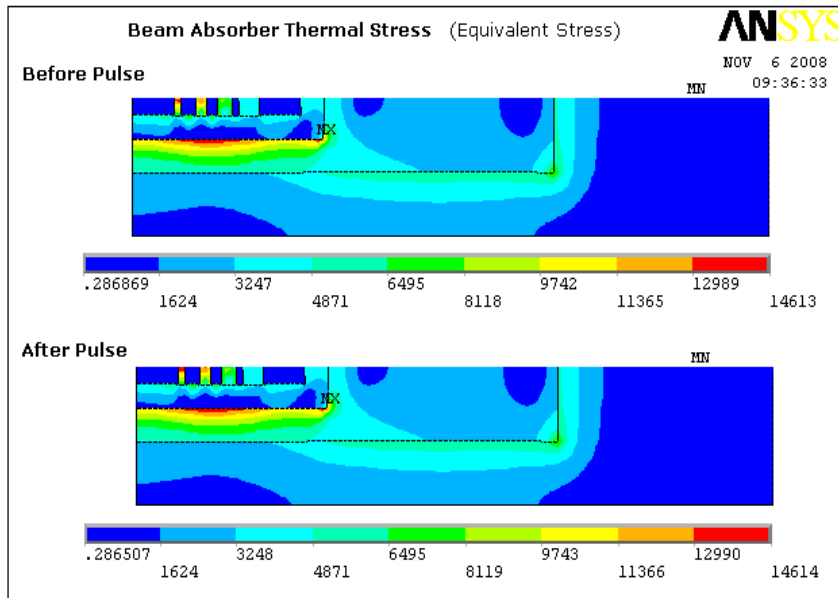


Figure IV-42: Thermal stress in the absorber core due to beam heating at 36 kW.

IV.3 3-8 GeV Pulsed Linac

IV.3.1 Accelerating Structures

Acceleration from 3 to 8 GeV in pulsed linac is provided by a $\beta=1.0$, 9-cell cavity operating at 1300 MHz. A photograph of the ILC 9-cell cavity is given in Figure IV-43 . Performance requirements for the 1300 MHz cavities are summarized in Table IV-15. The gradient is chosen to be 25 MV/m. For this gradient we expect a Q_0 that is at least 1.0×10^{10} – see Figure IV-44 where the test results for various TESLA/ILC type 9-cell cavities produced and tested at DESY and Americas region are summarized.

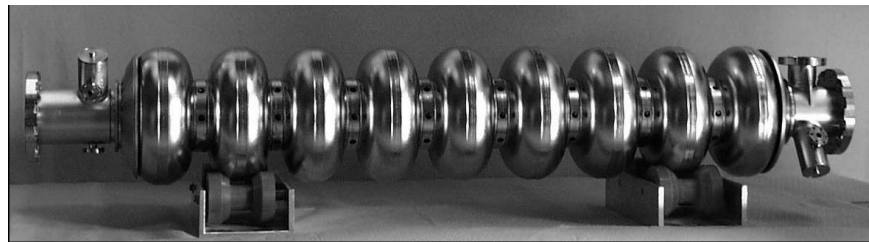


Figure IV-43: ILC 1300 MHz accelerating cavity

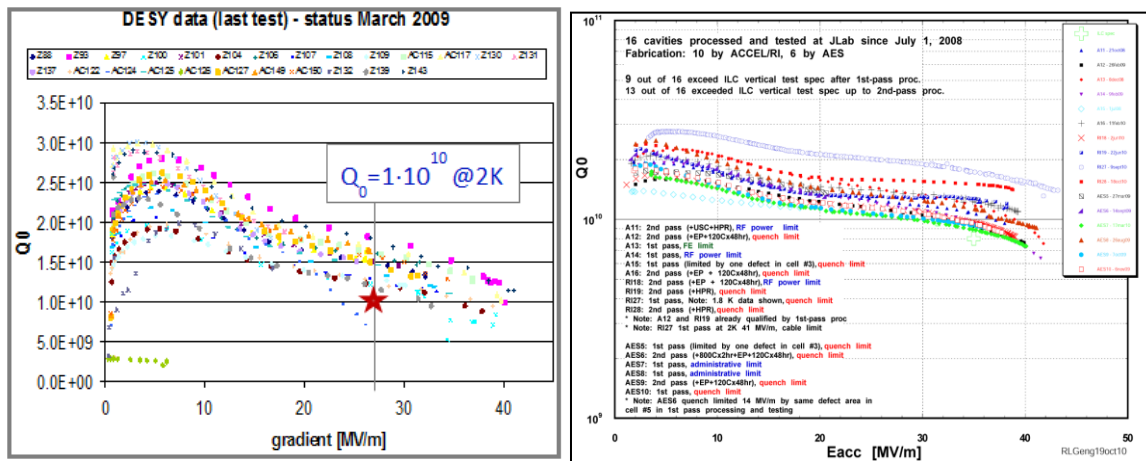


Figure IV-44: Data of Q measurements in latest cavities achieved at DESY (left) and Americas region (right)

1.3 GHz Cavity	Requirement	
Frequency	1300	MHz
Geometric Beta (β_G)	1.0	
Optimum Beta (β_{OPT})	1.0	
Iris diameter	70	mm
Cells/cavity	9	
Cavity Length	103.8	cm
R/Q ₀	1036	Ω
G = Q ₀ R _s	270	Ω
E _{max} /E _{acc}	2.0	
B _{max} /E _{acc}	4.2	mT/(MV/m)
Gradient	25	MV/m
Peak Surface Electric Field	50	MV/m
Peak Surface Magnetic Field	106	mT
Operating Temperature	2	K
Q ₀ at 2 K	1.0	10 ⁻¹⁰
Losses@2K	5	W
Pulse length	7.4	ms
Flat-top	4.3	ms
Rep. rate	10	Hz

Table IV-15: RF parameters of the ILC-type 1.3 GHz cavities.

The accelerating gradient and Q₀ shown in Table IV-15 are quite modest for that frequency. Recent progress in 9-cell 1.3 GHz cavity production and surface treatment supported by ILC and XFEL R&D programs push SRF technology up. As today more than 80% of cavities produced in Americas region demonstrated the accelerating gradient above 25 MV/m at the first test. Cavities not passing through 1st test were re-processed and tested again. After second test yield was increased up-to 90% as shown in Figure IV-45.

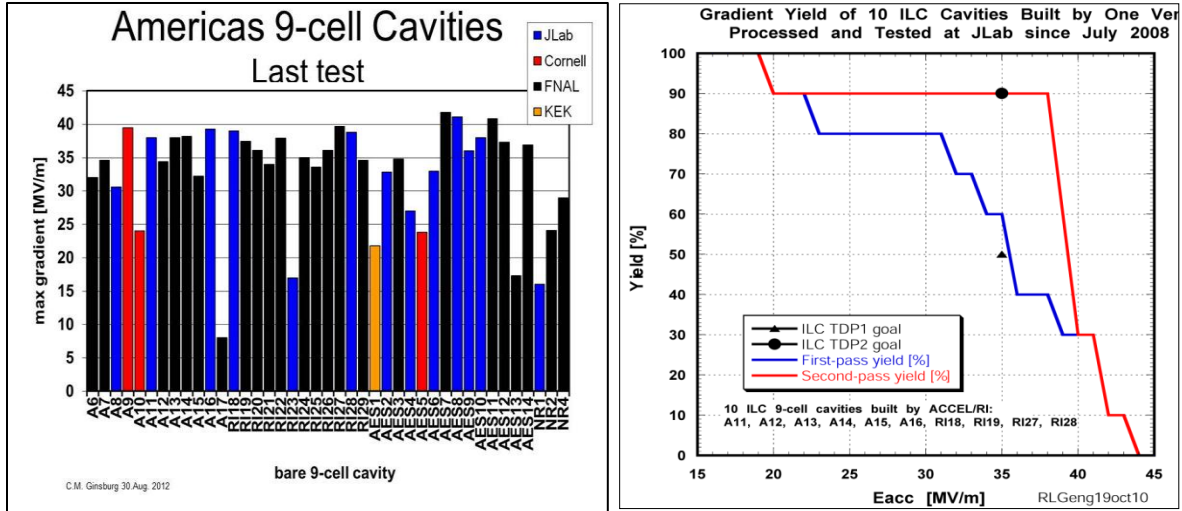


Figure IV-45: Maximum accelerating gradient achieved in American region (left) and gradient yield for 10 cavities build by one vendor (right).

A total of 224 cavities are required in the 1300 MHz section. These cavities are contained within 28 cryomodules. Each cryomodule contains 8 accelerating cavities and one focusing quadrupole. Figure IV-46 shows the ILC Type-4 cryomodule and schematically accompanied by the disposition of focusing elements within neighboring cryomodules. The requirements are summarized in Table IV-16.

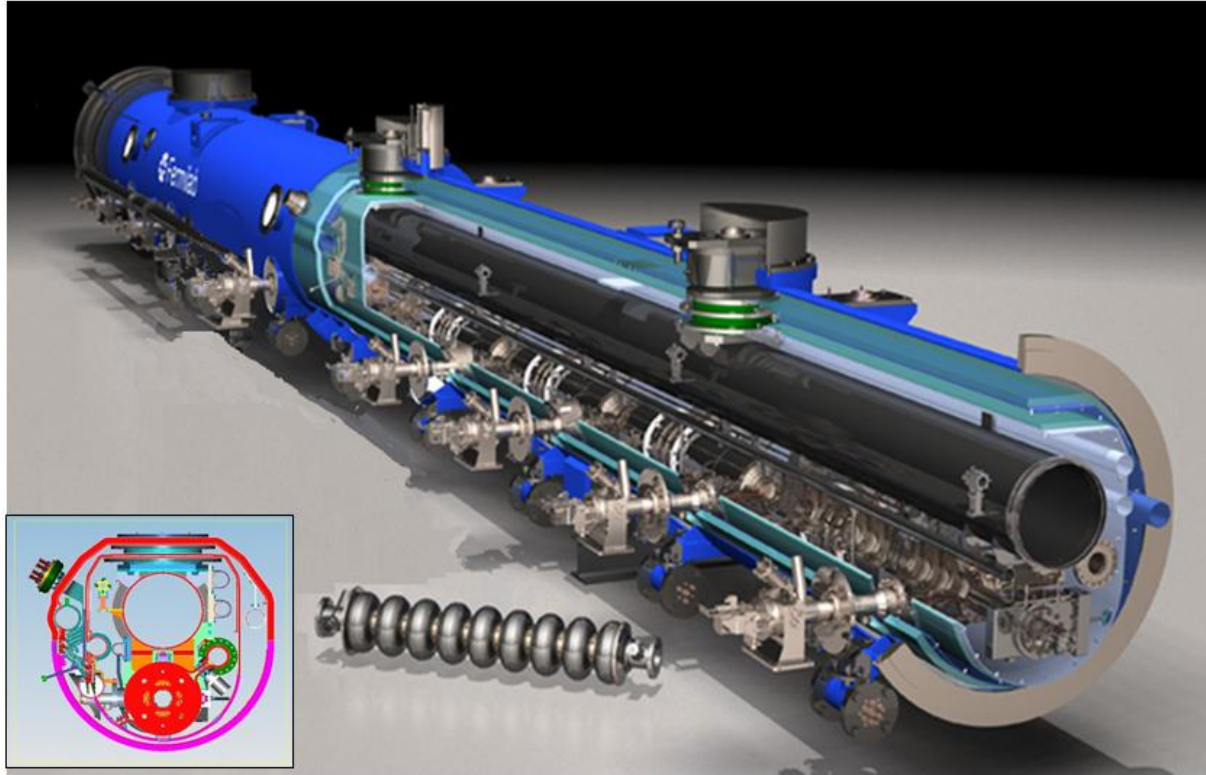


Figure IV-46: Type-4 ILC cryomodule (upper) and focusing schematics (lower).

	ILC-1.3 GHz	Units
Number of cavities	224	
Number of SC Quadrupoles	28	
Number of Cryomodules	28	
Total Length	~390	m
Period Length	25.23	m
Number of FODO periods	14	
Energy	3 - 8	GeV
Range of β	0.973 - 0.99	

Table IV-16: Summary table of 1.3 GHz cryomodules.

IV.3.2 RF Power

There are a total of 28 RF systems in the pulsed 3-8 GeV linac. These are distributed over 224 cavities in 28 cryomodules. The beta of the beam at the entrance to the pulsed linac is close to one; hence a single klystron power source can drive 8 cavities (one cryomodule). The RF power required for the cavity depends on loaded Q and cavity detuning as shown in Figure IV-47. The loaded Q of the cavity was chosen $Q_L=1 \times 10^7$, as a compromise between required power and cavity passband (Note: for an ideally tuned cavity the minimum power corresponds $Q_L=2.5 \times 10^7$ for 1 mA and 25 MV/m). Assuming control of microphonics and uncompensated Lorentz forces to limit detuning to less than 30 Hz maximum, the required RF power to a cavity is 35 kW. Taking into account the required power overhead for LLRF control and compensation of RF losses, the set power is 50 kW/cavity.

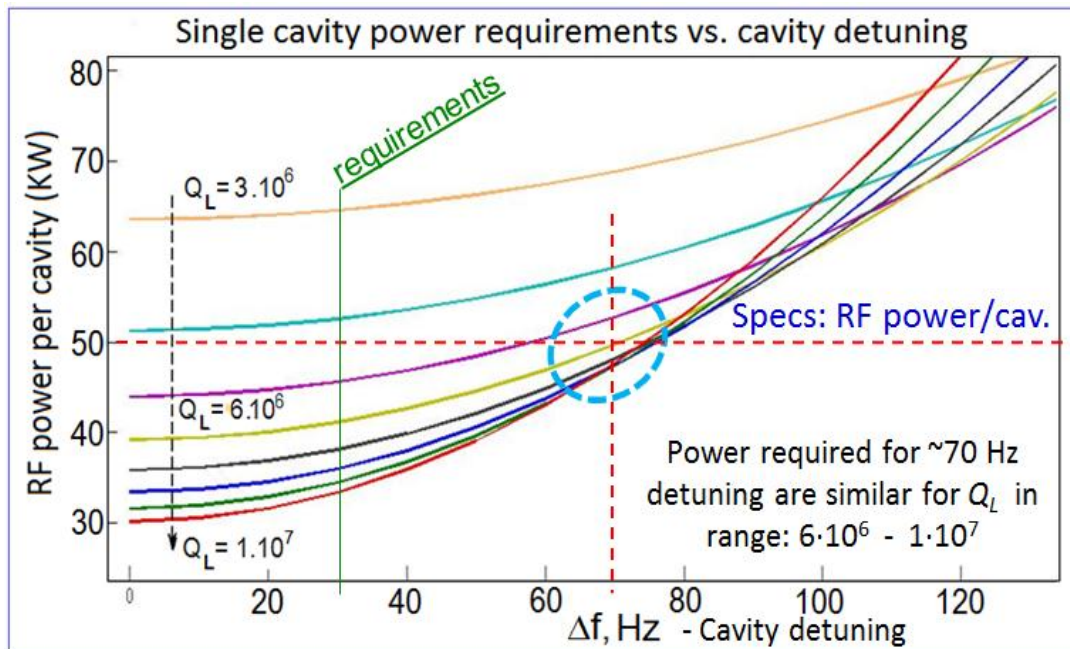


Figure IV-47: Required cavity RF power as function of cavity detuning for different loaded Q-values. Parameters: Gradient=25 MV/m, Beam current 1 mA.

In baseline configuration one RF station will feed one or two cryomodules. The RF power distribution scheme would be very similar to that of the XFEL, with a vector-sum feed-back control providing both phase and amplitude control. The required RF power source parameters for one cryomodule are shown in Table IV-17. Two possible types of power sources are considered: single-beam klystron (SBK) and multi-beam klystron (MBK). Klystron parameters are shown in Table IV-18.

Parameter	Recycler/MI	Direct Injection to MI	Units
Frequency	1.3	1.3	GHz
Loaded Q	1.e7	1.e7	
RF pulse width	7.4	30	ms
Cavity Gradient	25	25	MV/m
Beam current	1	1	mA
Repetition rate	10	10	Hz
Cavity RF power	32	32	kW
Cavity power + losses + regulation +EOL	50	50	kW
Power per Cryomodule	400	400	kW

Table IV-17: RF power requirements for a Pulsed Linac cryomodule

	Klystron per 1CM		Klystron per 2 CM's		Units
	SBK	MBK	SBK	MBK	
Klystron type	SBK	MBK	SBK	MBK	
Klystron power	400	400	800	800	kW
Voltage	54	33	71	44	kV
Current	12	20	19	30	A
Efficiency	60-62	62-64	60-62	62-64	%
Average Power	32	32	64	64	kW
Number of klystrons/linac	28	28	14	14	

Table IV-18: Klystrons parameters for the Pulsed Linac. Only the 800 kW SBK would require a modulator with oil.

One possible candidate for the pulsed linac power source is a MBK under development by Omega-P as a Small Business Innovative Research (SBIR) project (shown in Figure IV-48 with list of parameters in Table IV-19). As alternative solutions we considering source based on Injection locked 2-stage magnetron (SBIR proposal by Muons Inc). The schematic of magnetron station for 1 cryomodule is shown in Figure IV-49 with two 200 kW magnetrons per 1 cryomodule.

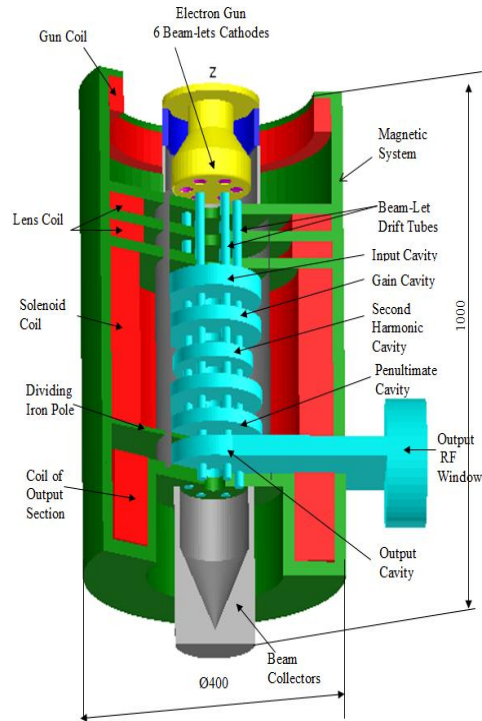


Figure IV-48: Multi-beam klystron proposed by Omega-P (SBIR project)

500 kW, 1.3 GHz MBK parameters		
Operating Frequency	GHz	1.3
Beam Voltage	kV	30
Number of Beam-lets		6
Beam-let / total Current	A	4.4 / 26.4
Beam-let / total perveance	10^{-6}	0.847 / 5.08
Cathode Loading	A/cm ²	2
Beam / RF Power	kW	792 / 515
Saturated Efficiency	%	65
Saturated Gain	dB	46
Pulse length	ms	8.4 / 30
Rep. rate	Hz	10 / 2
Brillouin / operating B_{solenoid}	Gs	400 / 800
Power of Magnetic System	kW	2.5
Max. collector power	kW	60

Table IV-19: Multi-beam klystron Parameters

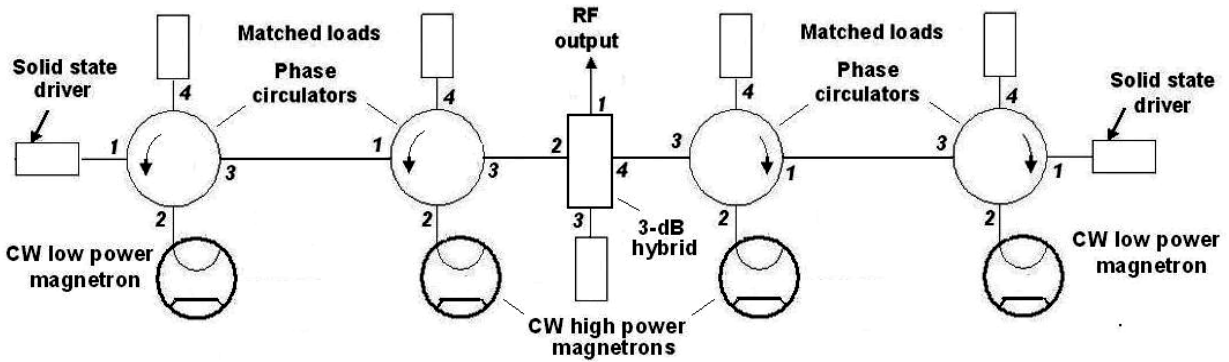


Figure IV-49: Schematic of a magnetron based RF source (SBIR proposal by Muons Inc.)

The low level RF (LLRF) system will provide a drive signal on the order of 0 to +10 dBm for each RF power source. The amplifier(s) will provide sample signals of the pre-driver and final outputs. All amplifiers will be self-contained units complete with integral power supplies, protection circuits, and control interface. The RF distribution system for the pulsed linac will use WR650 waveguide. The final connection to the cryomodels will utilize a section of flexible transmission line to minimize connector location tolerances. Each RF system will have a circulator and load to isolate the cavity from the power amplifier. This level of protection is essential in SRF systems due to full power reflection from the cavity in the absence of beam. Cavity and drive sample signals will be provided to the LLRF for vector regulation and frequency control of the cavities. All of the RF amplifiers will be water cooled to minimize the heat load to the building HVAC system.

While each amplifier has built in protection which includes, water flow, water temperature, pressure differential, and reflected power monitoring; a global interlock and hardware protection system will need to be designed for all RF systems. This will include water flow to loads and circulators, spark detection on cavity couplers, and RF leakage detection.

IV.4 MI/RR

The increased intensity provided by the Project X linac requires upgrades to several areas in the Recycler and Main Injector in order to achieve the performance goals listed in Table II-1. These upgrades are described below.

IV.4.1 H- Injection

Injection into the Recycler for the Neutrino program requires the accumulation of about 26 mA-ms. With the average pulsed Linac current of 1 mA the required injection time would be 26 ms. The current concept is to use six injections each of 4.3 ms in duration. With the revolution period of the Recycler being 11.2 μ s, this corresponds to approximately 388 turns injection time. With the Linac rep rate of 10 Hz, the total injection time into the Recycler is 0.6 seconds or 1 injection every 100 ms. There are two potential techniques that are under discussion for accomplishing the multi-turn H- injection into the Recycler, a standard carbon foil charge exchange technique and a new Laser Assisted H- stripping injection technique being pioneered at SNS. R&D for both techniques is being pursued and the salient features of each will be addressed. Currently, the carbon foil charge exchange is the default technique. Independent of stripping technique, transverse phase space painting must be utilized due to the difference in transverse emittance between the linac beam and final emittance of the circulating beam in the Recycler. Longitudinally, we will be utilizing micro bunch injection where individual linac micro bunches will be injected into already formed Recycler RF buckets. This will require accurate control of the phasing between the linac and Recycler RF.

The Recycler straight section 10 will be modified to be a symmetric straight for the purposes of H- injection. This has been discussed previously. Figure IV-50 and Figure IV-51 show the lattice functions of the modified Recycler and the layout of the injection chicane used for merging the H- onto the recycler closed orbit and transverse phase space painting. Both have zero dispersion and $D' = 0$ to eliminate targeting position of the H- on the foil due to changes in momentum.

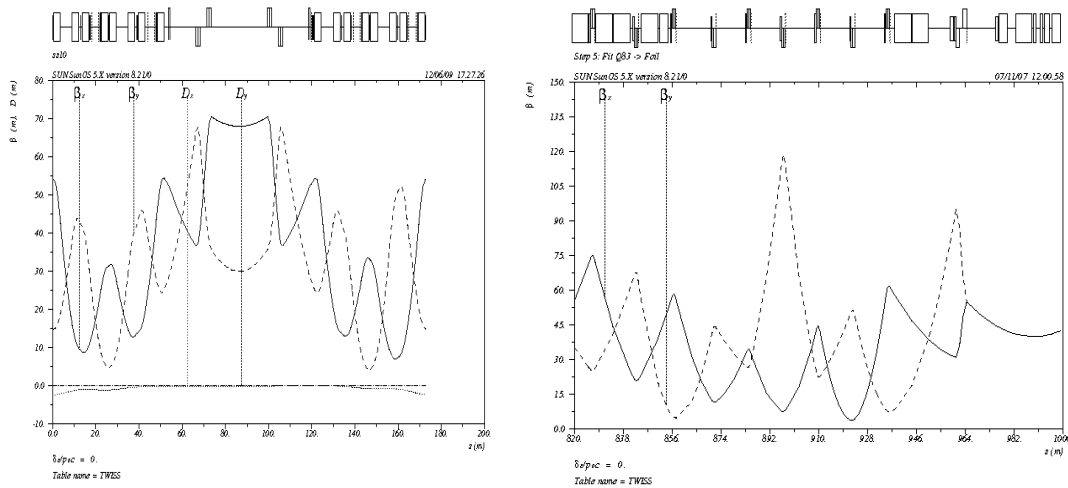


Figure IV-50: Lattice functions for of the modified Recycler straight section 10 for H- multi-turn injection (left) and the lattice functions of the end of the transport line (right). Note that both the ring and transport line have $\alpha=0$ at the foil location.

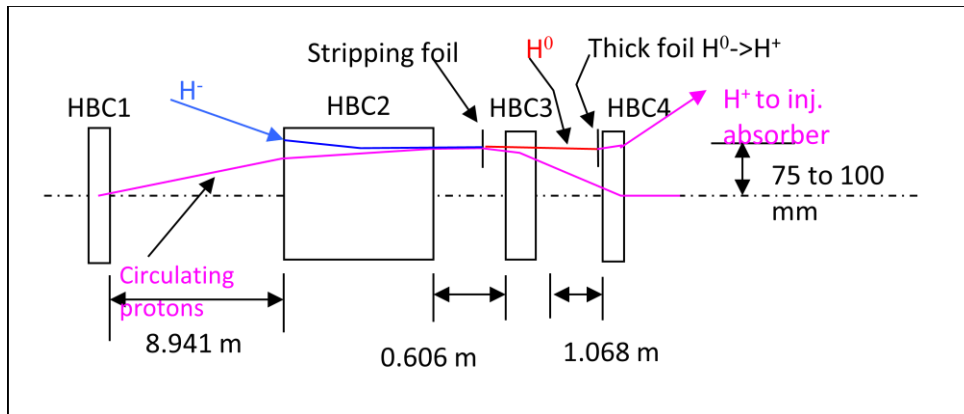


Figure IV-51: Layout of the recycler injection chicane showing the location of the “stripping foil” and the incoming H-, circulating proton, and waste beam trajectories.

In Figure IV-51 the “stripping foil” is the location where the H^- is converted into protons once the H^- have been merged onto the proton closed orbit. This conversion process could utilize either carbon foil or laser method of converting the H^- into protons. Any H^- that miss the foil or H^0 created in the foil will be completely stripped to protons for loss free transport to the injection absorber. The entire injection chicane is located within the doublets which form the symmetric straight section. Since the Recycler is used only as an accumulation ring and the accumulated charge will be transferred to the Main Injector immediately after the

sixth injection, it is not critical that the injection chicane magnets be ramped. It is envisioned that they are still electromagnets.

Transverse phase space painting involves the systematic moving of the ring closed orbit about the fixed “conversion point” of the incoming H⁻ ions. Figure IV-52 shows an example of this motion in the horizontal plane for a particular painting scenario. Here the green ellipse represents an empty circulating proton phase space determined by the final painted ring emittance. At the start of the painting injection process the proton closed orbit determined by the fast painting magnets (red) is bump to the outside of the ring and centered on the injection point for the H⁻. As the injection process proceeds the amplitude of the closed orbit is slowly collapsed with the painting magnets to the point of the red ellipse. This painting distance is equal to 3σ of the final painted ring emittance. In the figure a second step for removal of the circulating beam is shown. Here, the painting magnets are fully collapsed. It should be noted that the location of the purple ellipse is determined by the chicane dipoles.

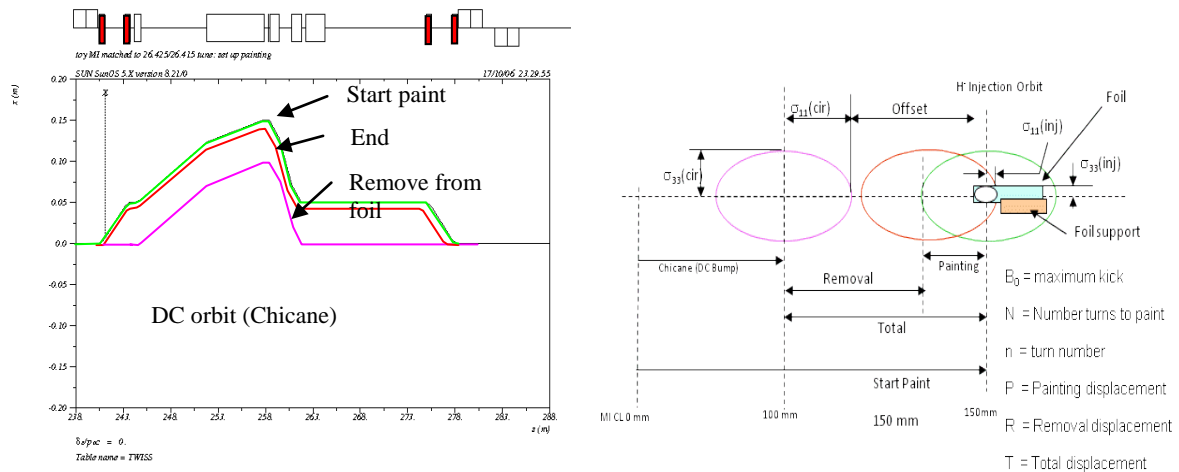


Figure IV-52: Example of movement of the circulating proton phase space for horizontal painting.

There are numerous transverse phase space painting scenarios that can be investigated, each with their own advantages and disadvantages. The injection chicane design would support any proposed painting scheme. The scheme considered at this stage is one that has been adopted by JPARC for their carbon charge exchange injection where they utilize an anti-correlated horizontal painting in the ring with vertical steering from the beam line (fixed y and varying y'). In this scheme, the foil is placed on the median plane where secondary

electrons are collected by an electron catcher on the side of the aperture. This painting scheme has been detailed elsewhere and results in a uniform distribution in x and y.

When considering foil injection, five main issues need to be addressed: 1) foil temperature and lifetime, 2) handling of secondary electrons, 3) minimizing secondary foil hits by circulating protons, 4) losses due to H^0 excited state produced by the incomplete stripping process and interactions with the foil, and 5) beam power directed to the injection absorber. Many of these can be addressed by design.

In injection the scenario considered here where the incoming H- beam current is low which requires longer injection periods (number of turns), the largest contribution to foil heating comes from circulating beam. This is in contrast to the injection of higher beam current and fewer turns, where the incoming beam is the major contribution to foil heating. Preliminary simulations [50] for six injection painting into the Recycler utilizing the J-PARC scenario for various injection times show peak temperatures approaching 2000°K during the last injection. Figure IV-53 shows peak temperature verses time. In addition, a single injection with a duration of approximately 26 ms is shown. Here, the peak temperature is close to 2500°K and the foil would not survive 1 pulse. A potential technique for reducing the peak temperature during the injection time is to move the foil during the injection time so the energy deposition is spread out over a larger area.

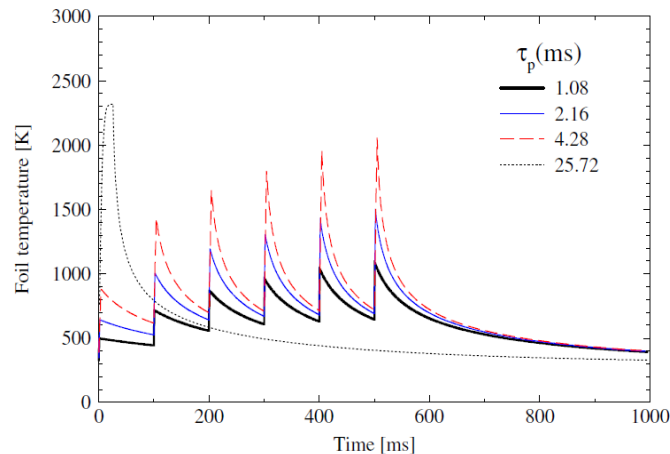


Figure IV-53: Peak temperature of foil during the injection of 26 mA-ms charge into the Recycler during various injection times.

A simulation was carried out in STRUCT to simulate a “rotating” foil by moving a linear foil in one dimension and the hit densities along the foil motion were accumulated. This hit density as a function of position and time was used to calculate a peak foil temperature. The

results of a stationary foil and two rotation periods were calculated. The results are shown in Figure IV-54.

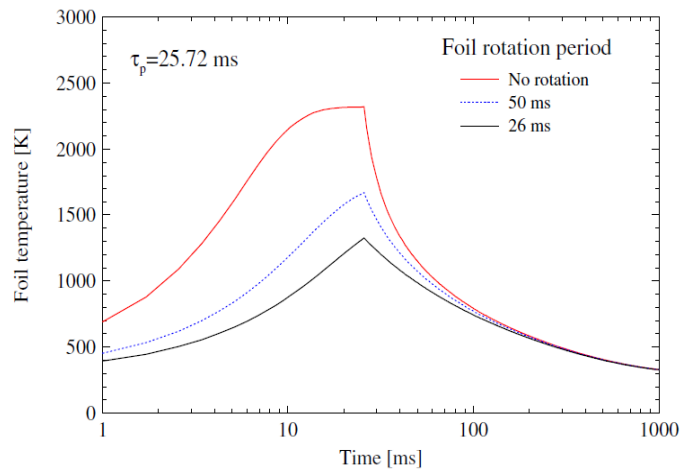


Figure IV-54: Temperature evolution during a single 26 ms injection period for a stationary foil (red) and two rotation periods.

Here it is clear that matching the rotation speed to the injection period reduced the peak hit density and thus the peak temperature. The amount of reduction is dependent not only on the speed but the area over which the energy is deposited. It should be clear that a moving foil does not address any issues with losses due to the interaction of the circulating beam with the foil. The concept of a rotating foil is depicted in Figure IV-55. Here, a thin Ultra Nano-Crystalline Diamond film is grown on a Silicon wafer. The outer 1 cm of wafer is removed exposing the UNCD diamond used for stripping. In figure, the green, red, and magenta ellipses represent the start and end of painting and circulating beam, respectively. This concept is being pursued to determine if this concept is feasible. Initial ANSYS simulations indicate that the rotational forces on the foil should be much smaller than the yield strength of the UNCD film. A thermal model was also modeled using ANSYS and indicates the same sort of temperature reductions as the STRUCT simulation. The first stage of the R&D program is to determine if this configuration can be commercially made and the steps involved in producing the foil. To this end we have contracted with several vendors to look at a UNCD and a graphene foil and make us some samples that can be tested. A rotational set up in the laboratory will be used to spin the foil at up to 2000 rpm and measure any deformations. A small spot on the foil will be heated with a laser or micro-torch while the foil is rotating to test the robustness of the foil and determine any deformation. Ultimately, a beam test and temperature measurement are planned. Currently SNS has a foil testing facility that could be potentially utilized for temperature and lifetime tests.

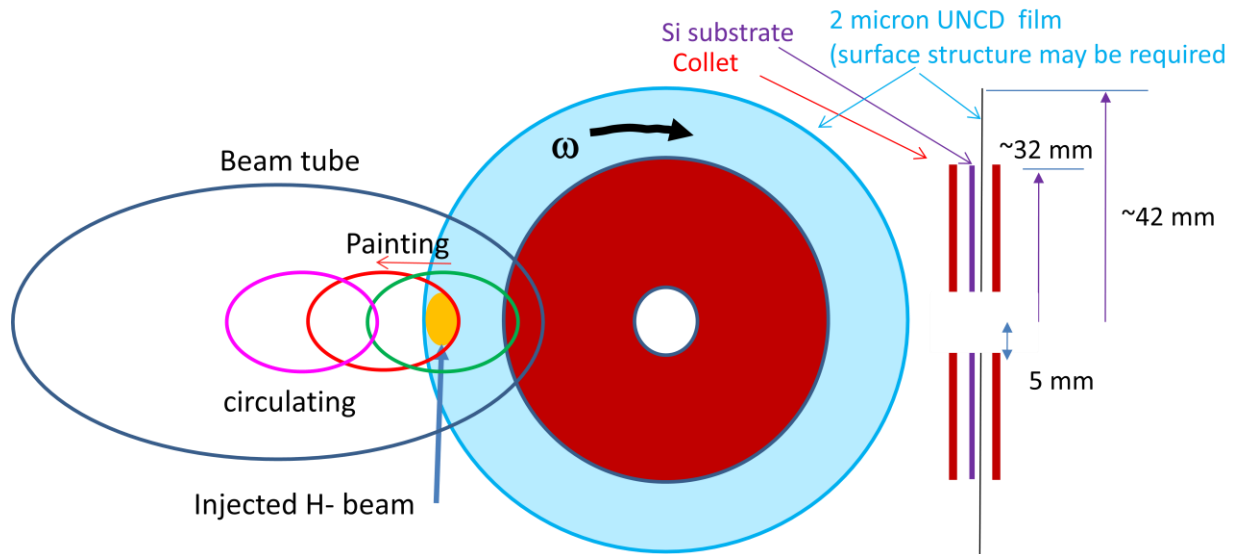


Figure IV-55: Concept for a rotating foil.

In addition to the development of a rotating foil system, we are collaborating with SNS on their next phase of laser stripping experiment. The proof of principal stripped a single 400 MHz bunch. The next stage will be to demonstrate stripping for a 10 us beam pulse. Final operational requirements require stripping a 1 ms beam pulse. SNS continues to develop the laser system required, the H- transport optical system, and the interaction chamber and hardware, for the next phase test. Due to the beam energy of 1 GeV at SNS, the energy of the photons needs to be 255 nm (UV). On the other hand FNAL injection into the Recycler at 8 GeV allows the use of 1064 nm (IR) photons. Many of the technical issues associated with UV are not present in the IR.

IV.4.2 Main Injector γ_t -jump

Designs for a γ_t -jump in Main Injector have been studied for the last 15 years. Details can be found in the Proton Driver Design Report [24]; a brief summary is included here. The system consists of 8 sets of pulsed quadrupole triplets. Each triplet has two quads in the arc and one of twice the integrated strength in the straight section, with a phase advance of π between each quadrupole. The perturbation to the original lattice is localized. In particular, the dispersion increase during the jump is small ($\Delta D_{max} \approx \pm 1$ m), which is the main advantage of a first-order jump system. Each triplet is optically independent from the others and provides roughly 1/8 of the total required jump amplitude (i.e., $\Delta\gamma_t \approx \pm 0.25$ per triplet).

The power supply uses a GTO as the fast switch and a resonant circuit with a 1 kHz resonant frequency. The beam pipe is elliptical and made of Inconel 718. It has low electrical conductivity and high mechanical strength so eddy current effects are relatively small. The eddy current effects scale as $\frac{1}{d}$, where d is the pipe wall thickness. The $\frac{1}{d}$ value of Inconel 718 is about four times lower than that of stainless steel.

The 8 pulsed triplet locations are summarized in Table IV-20. Since the original study was done, there have been changes to the Main Injector and these locations need to be revisited. A set of magnet design parameters has been developed and modeled (see Table IV-21).

Pulsed Triplet	Quad Locations
1	104, 108, 112
2	226, 230, 302
3	322, 326, 330
4	334, 338, 400
5	404, 408, 412
6	526, 530, 602
7	622, 626, 630
8	634, 638, 100

Table IV-20: Candidate γ_t quad triplet locations

	Requirement
Integrated Gradient	0.85 T
Vacuum pipe cross section (elliptical)	2.4 x 1.125 in
Field Quality, 1 inch radius	2%
Maximum length	17 in
Maximum Current	200 A
Maximum Voltage	As low as possible

Table IV-21: Pulsed quadrupole magnet parameters

IV.4.3 Electron Cloud Mitigation

Electron cloud generation could be a possible instability source for the intensities in the Recycler and Main Injector.

The best approach is to mitigate the generation of the cloud itself. There have been a series of measurements in the Main Injector, looking at secondary electron yield and cloud generation. A dedicated measurement setup now exists at MI-52, with newly developed RFA detectors. Both TiN and C coated beam pipes have been installed and measurements

made. Both coatings show significant reductions in secondary electron generation when compared to an uncoated stainless steel pipe. VORPAL simulations are being benchmarked against these measurements. Plan to install a SEY (Secondary Emission Yield) stand in MI in order to measure the effect of scrubbing in situ for different kinds of stainless steel. A picture of the SEY measuring stand is shown in Figure IV-56.

Research continues into the coating process. The Main Injector beam pipe is captured in the dipole magnets, so coating needs to take place in situ. We set up a coating (sputtering) facility in E4R and successfully coated with TiN a 6m long piece of round MI pipe and measured the coating thickness. It will be used to coat test coupons for SEY measurements in MI. The experience from our coating facility will be used to estimate the effort required to in-situ coat the MI beam pipe with TiN.

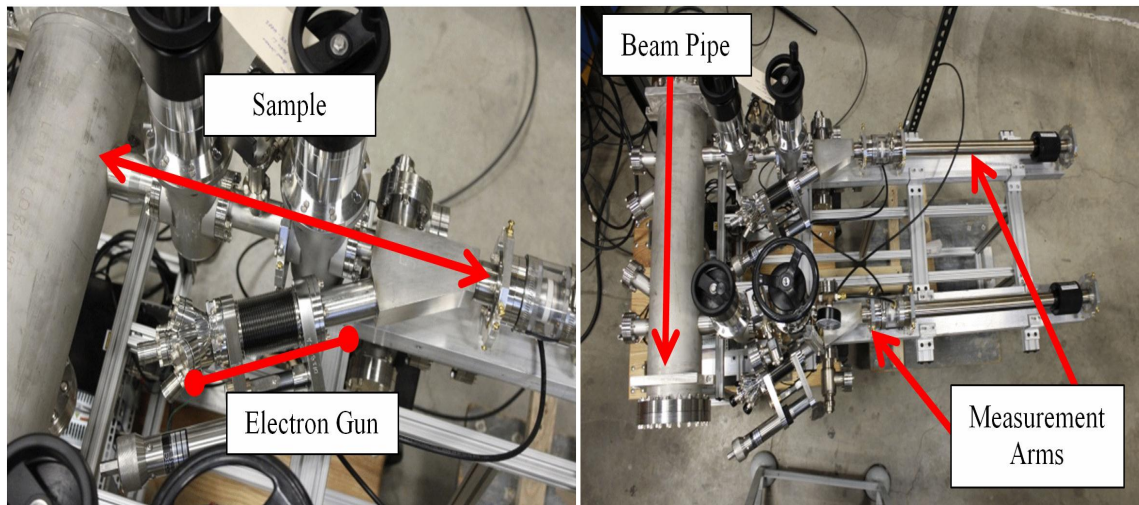


Figure IV-56: SEY Measuring Stand

IV.4.4 RF Systems

The Recycler and Main Injector need new 1st and 2nd harmonic RF cavities. The same cavities will be used in both machines. A cavity design has been developed, with perpendicular biased tuners and $R/Q \sim 30 \Omega$. A mechanical drawing of the cavity is in Figure IV-57. The cavity parameters are shown in Table IV-22. Higher Order Mode (HOM) Coaxial dampers for the 53 MHz cavities have been designed. The effect of the HOM dampers on the first 2 monopole cavity modes is shown in Figure IV-58. A mock-up of the first harmonic cavity has been constructed and a set of low level RF measurements were

taken. A preliminary design of the second harmonic cavity that is a scaled down version of the first harmonic has been completed.

The power source needs to provide greater than 550 kVA of total power and 4.65 A of current. To simplify operation and maintenance, the source should have enough bandwidth to power both the 1st and 2nd harmonic cavities. The EIMAC 8973 power tetrode amplifier has a maximum operating frequency of 110 MHz, output power capabilities greater than 1 MW, and plate dissipation of 1 MW. An 8973 tube has been purchased and a power test stand is being developed.

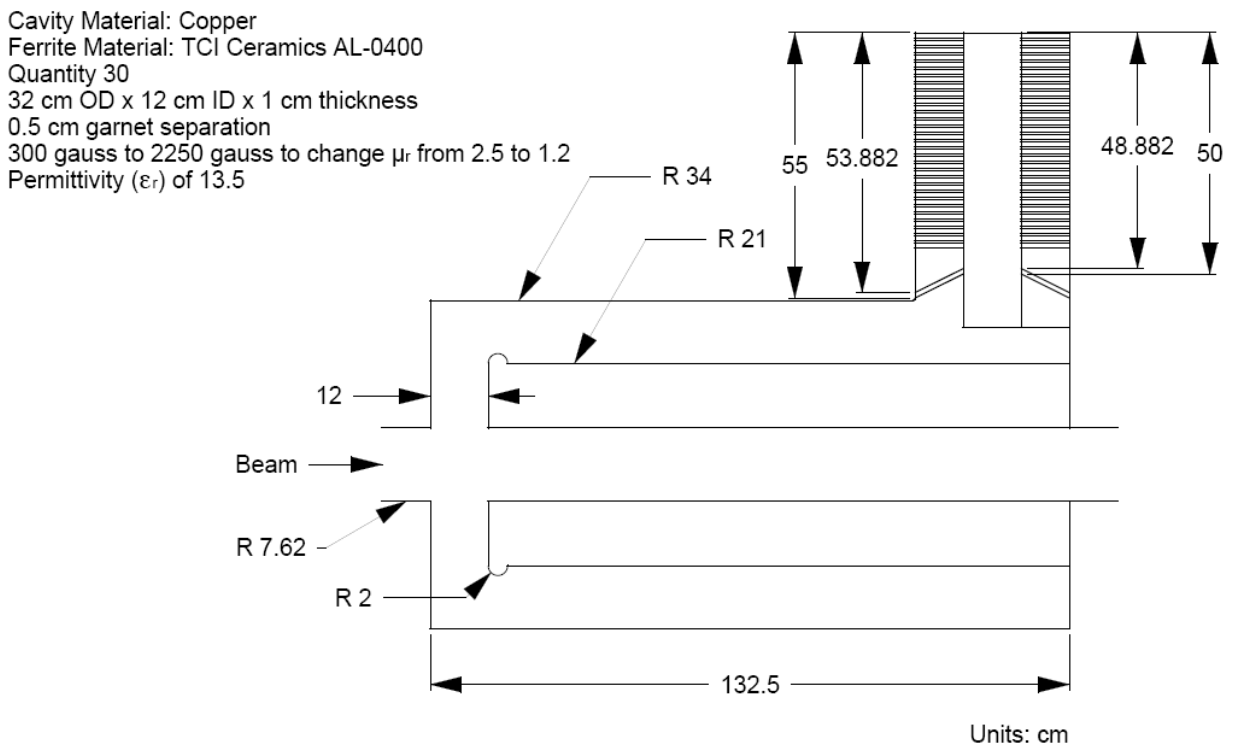


Figure IV-57: Mechanical dimensions of the 53 MHz cavity.

Tuner Intrusion 75 mm @ $V_{pk}=240$ kV	$\mu_r=1.2$	$\mu_r=2.5$	
R/Q	36.4	31.5	Ω
Q_0	12244	12023	
F	53.3047	52.6152	MHz
P_{wall}	64	76	kW
$P_{ferrite}$	6	42	kW
$P_{ceramic}$	0.2	0.6	kW

Table IV-22: Parameters of the new 53 MHz Cavity as a function of ferrite permeability.

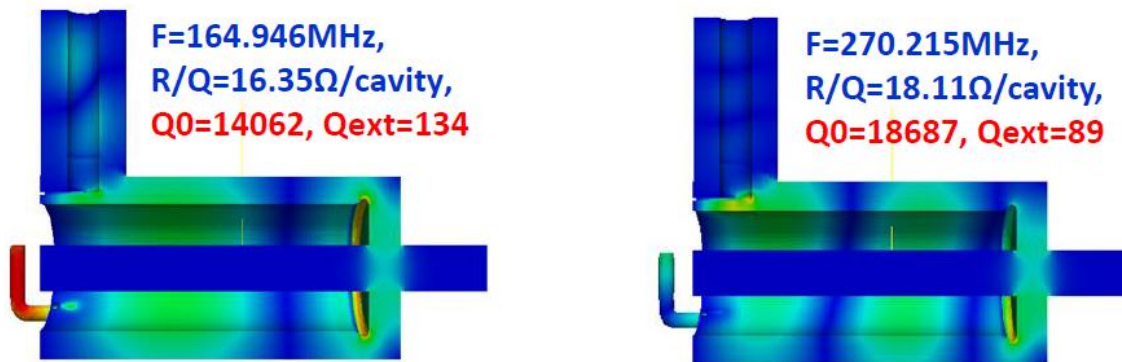


Figure IV-58: Effect of the 53 MHz cavity HOM dampers on the first two monopole modes.

IV.5 Cryogenics

The cryogenic system scope for Project X includes a new cryogenic plant, a cryogenic distribution system, and the necessary ancillary systems (purification system, cryogenic storage, etc.) to support the plant. A conceptual layout for the cryogenic system is shown in Figure IV-59.

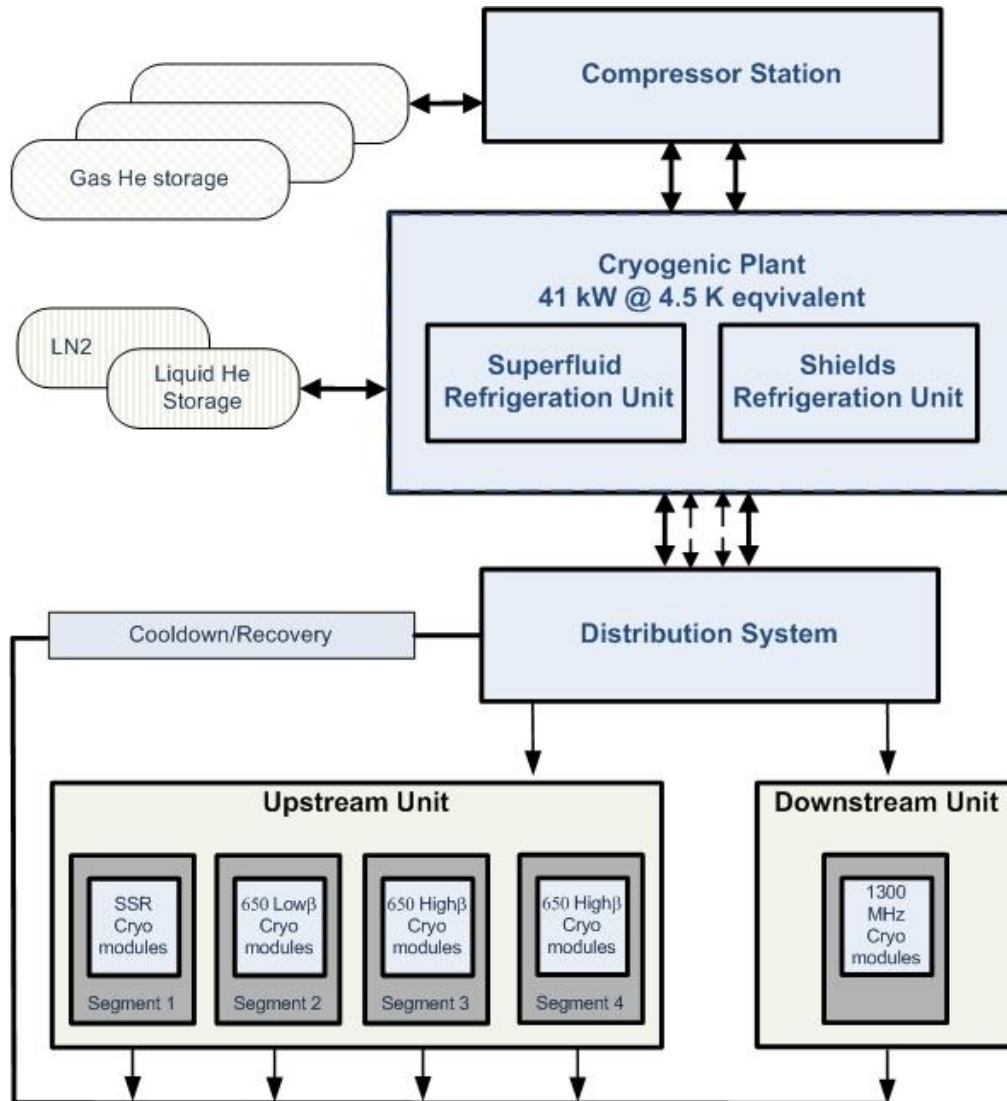


Figure IV-59: Conceptual Layout for the Project X Cryogenic System

The cryogenic distribution system accommodates a range of steady state and transient operating modes including RF on/RF off, cool down, and warm-up and fault scenarios. The system includes feed boxes, cryogenic transfer lines, bayonet cans, feed and end caps, string connecting and segmentation boxes, gas headers, etc. It will be capable of supporting operation of the linac within cool down and warm-up rate limits and other constraints imposed by accelerating SRF components. Protecting the superconducting RF cavities from over pressurization beyond the component's maximum allowable working pressure during fault conditions will be accommodated by the cryomodules and cryogenic distribution system. Components of the cryogenic distribution system contain cryogenic control and isolation valves, cryogenic instrumentation, safety valves, etc.

It is assumed that on the time scale of the Project X, a large portion of the Tevatron ancillary cryogenic components will be available for use by the project. These components include cryogenic nitrogen and helium dewars, gas storage tanks, purifier compressors, cryogenic transfer line and parts of the inventory management system.

SRF cavities are cooled by two-phase superfluid liquid helium. The cavities are grouped in 62 cryomodules of six different types, HWR, SSR-1, SSR-2, 650-low β , 650-high β , and 1300 MHz cryomodules. For cost estimating purposes, all cryomodules are divided into two cryogenic units. The cryogenic feed point is located between the upstream and downstream units. The upstream cryogenic unit consists of HWR, SSR-1, SSR-2, 650-low β and 650-high β , while the downstream unit contains 1300 MHz cryomodules.

The upstream unit contains 34 cryomodules and is subdivided into four (4) distinct cryogenic segments. The first segment contains ten cryomodules (one (1) HWR, two (2) SSR-1 and seven (7) SSR-2 cryomodules). The second segment comprises of five (5) 650 MHz Low β cryomodules. The third and fourth segments each contain eleven (11) 650 MHz High β cryomodules. A cryogenic transfer line runs along the upstream cryogenic unit and is used to distribute superfluid helium and helium gas for the thermal shields and intercepts to each segment.

The downstream unit contains twenty eight (28) 1300 MHz cryomodules divided into four segments. The TESLA concept is utilized for connecting 1300 MHz cryomodules within a segment.

Operation of Project X in a continuous wave mode results in very high dynamic heat loads to the cryogenic system. For SRF components, dynamic heat load (due to RF power dissipation) on average is an order of magnitude greater than the static heat load (due to conduction and thermal radiation).

A preliminary heat load estimate has been performed. For the design study, an additional 50% margin is applied to the estimated heat loads to ensure the system could meet all operational requirements. With this factor, the total equivalent design capacity at 4.5 K for the entire linac is approximately 41 kW. The physical size of a plant of this capacity is too large to house in a single cold box. As a result, two cold boxes are envisioned; one to support the superfluid loads and one to support the thermal shield loads.

A wide range of possible cryogenic plant design solutions that satisfy all requirements and constraints for Project X will be studied further. Combining effective use of the existing Fermilab infrastructure with commercially available components requires further study. The final solution will be based on a cycle with either cold compression alone or utilizing a hybrid approach (both cold and ambient temperature compression). Ease of operation, reliability, ability to operate efficiently over a wide range of loads, capital and operational costs, and other factors will be considered in selecting the technology for the Project X cryogenic plant.

A study will be performed to ensure that the Project X cavity operating temperature and segmentation layout are optimized to minimize the combined capital and operating cost while maintaining system reliability.

IV.6 Instrumentation

Various beam instrumentation and diagnostics systems are necessary to characterize the beam parameters and the performance in all Project X sub-accelerators. For startup and initial beam commissioning we need to provide, at a minimum, beam instruments in order to observe:

- Beam intensity
- Beam position / orbit
- Transverse beam profiles
- Beam phase / timing

The high beam intensity / power and the presence of superconducting technologies also require a reliable, fail safe machine protection system (MPS) to prevent quenches in cryogenic elements or damage due to an uncontrolled loss of the high power beam. This system will be based on beam loss monitors (BLM) and other beam intensity monitors (e.g. toroids).

Beside these core beam instrumentation systems, more specialized beam diagnostics need to be provided, e.g. to characterize the longitudinal bunch profile and tails, transverse beam halo, and more advanced beam emittance measures. Many types of beam monitors (e.g. BPMs, toroids, etc.) can be standardized. However many areas in Project X, such as the front-end (H⁻ source, RFQ and MEBT), the synchrotron, and injection/ejection sections, will demand dedicated beam diagnostics (Allison scanner, fast Faraday cup, e-beam scanner, vibrating-wire, etc.).

In order to develop this beam instrumentation, a complete set of “beam measurement requirements” has to be established. Each sub-accelerator (linac, transport lines, MI, Recycler) needs to address the operating modes with the nominal, as well as non-standard beam parameters, and all requirements for the different beam measurements (resolution, precision, dynamic range, etc.). We foresee the following general detectors and systems for beam instrumentation and diagnostics:

Beam Position Monitors

The beam orbit monitoring (i.e. transverse position and longitudinal phase) is the most fundamental measurement and the most powerful diagnostics tool in an accelerator. Project X requires a large number (~100) of new warm and cold beam position monitors (BPM), thus making it a complex and expensive measurement system. BPM pickups need high quality RF cables to transmit their low-power signals to the read-out hardware outside the accelerator tunnel. This requirement may impact the arrangement or layout of some conventional facilities. It is necessary to locate BPM pickups in cryogenic SCRF sections of the machine, which needs extra care to meet UHV, cryogenic and clean room requirements simultaneously.

Beam Monitoring in the SCRF Linac

The beam monitoring within the cryogenic environment is probably limited to beam orbit monitoring with BPMs. Other measurements such as beam profiling and other beam monitors, that may include moving parts, cannot operate in a cryogenic environment. Similar measurement systems would require a “warm” diagnostics section within the SCRF linac.

Beam Profile Monitors

Profile monitors are required in the transfer line for measuring emittance and matching between the linac and transfer line and the Recycler. Options for transverse profile monitors in the H- sections of Project X are the standard multi-wire monitor and the newer laser profile monitor. Laser-based profile monitors are intended as the primary technology choice with standard multi-wires as a fallback technology. . In addition, profile measurements in the rings will be made using ionization profile monitors and electron wire profile monitors.

Beam Loss Monitors

Typical fast ionization chambers with a large dynamic range will be utilized for most loss measurements. However, there may be instances where measurements of thermal neutrons or

machine activation during cooldown periods are desired. The loss monitors will be incorporated in a machine protection system.

Beam Current Monitors

To determine transport and injection efficiency, a combination of DCCTs and beam toroids will be used to obtain an accurate measure of beam current throughout the linac, transfer line, injection sections.

Special Monitors

Several types of special beam monitors and diagnostic tools are required to verify the beam quality and minimize beam losses. These include the monitoring of the transverse beam halo (e. g. vibrating wires, laser wires) and the detection of longitudinal tails (e. g. using optical sampling techniques with mode-locked laser wires). A list of special beam monitors and diagnostic tools is not complete but design of generic instrumentation ports in diagnostic sections will allow future instruments to be installed.

Data Acquisition and Timing

Most beam monitoring systems will use digital signal conditioning and processing methods to extract the wanted beam parameter(s). The generated output data needs to be “time stamped” with respect to the beam event, so beam and other recorded data can be cross-correlated throughout the entire Project X complex. This cross correlation will simplify diagnostics and trouble-shooting on the day-to-day operation.

Internal calibration systems, as well as data acquisition and transport cannot make use of a long pause in the beam pulse (there is none in CW operation). The integration times of some of the measured parameters, e.g. beam intensity, and their time stamping has to be discussed in detail.

Instrument Physical Space Issues

Sufficient physical space will be made available to accommodate the required beam detection elements. At some critical, real-estate limited locations, e.g. LEPT, MEPT, injection / extraction, and SRF areas, a compromise has to be worked out, which enables a decent way to sense the beam without compromising its quality in the diagnostic sections.

IV.7 Controls

The control system is responsible for control and monitoring of accelerator equipment, machine configuration, timing and synchronization, diagnostics, data archiving, and alarms. Project X will use an evolution of the Fermilab control system ACNET [51], this is the system that is used in the main accelerator complex and also at the NML/ASTA and PXIE test facilities [52]. ACNET (Figure IV-60) is fundamentally a three tiered system with front-end, central service, and user console layers. Front-end computers directly communicate with hardware over a wide variety of field buses. User console computers provide the human interface to the system. Central service computers provide general services such as a database, alarms, application management, and front-end support. Communication between the various computers is carried out using a connectionless protocol over UDP. Subsystems developed by collaborators based on the EPICS control system can be integrated into the main system.

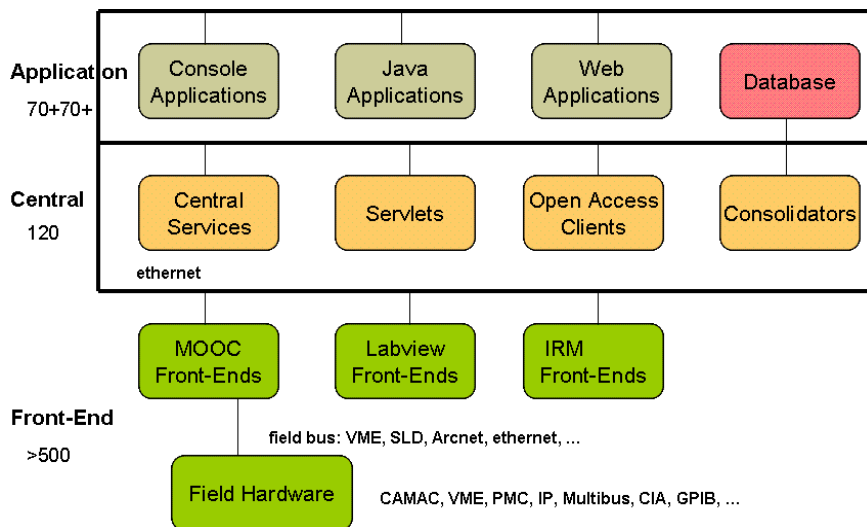


Figure IV-60: Project X Controls System architecture.

The scale of the control system is expected to be similar to that of the complex when the Tevatron was operating. The system should support up to 1M device properties. Time stamping must be provided so that all data from the CW linac and the pulsed linac can be properly correlated with that from the existing complex. The control system should contribute less than 1% to operational unavailability. The high beam power implies the need for a sophisticated machine protection system to avoid damage to the accelerator due to errant beam pulses. Furthermore, to minimize routine losses and activation of accelerator components a fast feedback system will be required to stabilize beam trajectories.

A new timing system will be developed that is a major enhancement over the TCLK and MDAT links in the main complex. A prototype has been developed based on a 1 Gbps data link that adds a data payload and cycle stamp to each clock event transmission. The latter will allow reliable correlation of data across different front-ends. The prototype design will be updated based on requirements for the CW linac.

It is highly desirable to have a single control system operating the entire complex rather than separate systems for the new linac(s) and older parts of the system. There should only be a single copy of core services such as alarms and data archiving. Software applications should be able to access any device in the system. This model simplifies development and operation and reduces long term maintenance costs of the complex. The Fermilab control system will be updated for the NOvA era and to support the NML and PXIE test facilities. This upgrade will include modernizing the application software environment as well as replacing obsolete hardware. Upgraded timing and machine protection systems will be developed for the Project X linac that will accommodate the legacy hardware in the existing parts of the complex. These systems as well as linac control software will be prototyped at NML and PXIE.

It is recognized that some equipment will be developed outside of Fermilab by institutions with expertise in the EPICS control system. Also it may be appropriate in some cases to use commercial hardware that comes with EPICS software. It is planned to support integration of EPICS front-ends and some core applications in the Fermilab control system. This has been demonstrated in several different ways at the HINS and NML test facilities. A gateway process between ACNET and EPICS based front-ends has been developed. The console environment also supports EPICS displays based on the EDM display manager.

The control system will specify standard interfaces between its internal components as well as with technical equipment. This will make integration, testing, and software development easier and more reliable and reduce the long term maintenance load. Also standard interfaces allow parts of the system to be more easily upgraded if required for either improved performance or to replace obsolete technologies. Only portions of the system need be changed while the core architecture of the control system remains the same.

IV.8 LLRF

The Low Level RF system encompasses the programming and regulation of the cavity field amplitude and phase as required by longitudinal beam dynamics in the machine. It also controls or interfaces to the ancillary equipment that is involved in the generation of RF. Hardware and software modules include Cavity Field Controllers, Resonance Controllers,

Master Oscillator, Phase Reference Line, LO distribution, transfer synchronization and the interface to interlocks, timing systems and the control system. This section will cover first the 3 GeV CW linac section operating at the frequencies; 162.5 MHz, 325 MHz and 650 MHz, followed by the pulsed 3-8 GeV 1300 MHz linac.

IV.8.1 LLRF for the CW 3 GeV SRF LINAC

The high level RF configuration for the CW linac provides a single power amplifier for each of the cavities. The beam current, cavity field gradients and worst-case microphonics determine the loaded cavity Qs and bandwidths. Analysis of the 1mA beam current and cavity gradients show that loaded Qs may be kept in the low 10^7 range where control of cavity microphonics will not create excessive RF power demands, nor large field disturbances. In addition, except for turn on, CW operation eliminates the dynamic effects of Lorentz force detuning and modulator droop. In many ways the CW linac will operate in a regime similar to the 12GeV upgrade of CEBAF. The largest disturbance to the cavity fields will be the beam structure produced by the beam chopper, particularly when the beam is turned off while ramping for injection into the Recycler. The LLRF system will provide the chop pattern for the MEBT and will therefore have the information required for accurate beam loading compensation.

For cost savings and hardware simplicity, the LLRF controllers will be grouped into stations that will cover two cryomodules (nominal 16 cavities) and the associated RF equipment. Fermilab has been extensively involved in SRF LLRF Control Systems for the ILC and ASTA. Two types of digital controllers have been developed and are in use, each of which could be modified to meet Reference Design requirements. RF and microwave hardware has also been developed for HINS and ILCTA that directly apply to Project X. Ongoing R&D will determine the details of the beam-based calibration and of the phase reference distribution system.

IV.8.2 LLRF for the Pulsed Linac

The 1300 MHz pulsed linac is implemented with cryomodules containing eight, nine-cell cavities. An RF station will contain one or two cryomodules with RF distributed from a single klystron. With a single RF source, individual cavity fields will vary within the group due to cavity resonance errors generated by Lorentz force detuning, microphonics and static cavity tuning errors. At 3 GeV and above, the beam is relativistic and longitudinally stiff so that field errors in individual cavities in a cryomodule will not cause energy errors, as long as the cavity field vector sum is maintained. The LLRF creates the vector sum of the calibrated baseband analytic signals from each cavity. This vector sum is then regulated by the digital

controller with a control bandwidth in the range of 100 kHz. The digital controller actuators are both the klystron RF drive signal and the piezo tuners on each cavity. Slow drifts in the resonant frequency errors are corrected by the motor tuner. There are a few noteworthy parameter differences of the pulsed linac section from ASTA or the ILC design such as an increase in Q from $3E6$ to $1E7$ and an increase in flattop length from 1 to 4 ms. Both of these differences are more challenging for Lorentz force compensation and therefore are part of ongoing studies at the ASTA facility.

IV.9 Safety and radiation shielding

Design requirements and radiation limits for accelerators and beam transport lines are provided by the Fermilab Radiological Controls Manual (FRCM). The manual requires that shielding designs shall be well-engineered to maintain occupational and environmental radiation exposures as low as reasonably achievable (ALARA) and compliant with applicable regulations and DOE Orders. The first choice for accelerator shielding designs are to be passive shielding elements designed to achieve areas external to shielding to be classified as minimal occupancy. Minimal occupancy is defined to mean any area which is not normally occupied by people more than 1 hour in 8 consecutive hours. Dose rates for potential exposure to radiological workers in areas without continuous occupancy shall be ALARA and such that individuals do not receive more than 20% of the applicable limits. The design goal for dose rates in areas of continuous occupancy is to be less than an average of 0.05 mrem/hr and as far below this and as low as is reasonably achievable (ALARA). Reliance on active systems such as radiation safety interlocks and/or beamline instrumentation to achieve radiation safety goals should be chosen only if passive elements cannot, in view of planned accelerator operations, reasonably achieve the level of protection required by the FRCM. Discharges of radioactive liquid to the environment should be kept ALARA. Materials and components should be selected to minimize the radiological concerns, both occupational and environmental. Where removable contamination might be associated with accelerator operations, provisions should be made in facility designs for the containment of such material. Internal radiation exposure is to be minimized in accordance with ALARA principles by the inclusion of engineered controls such as ventilation, containment, filtration systems, where practicable and with appropriate administrative procedures. Efficiency of maintenance, decontamination, operations, and decommissioning should be maximized.

The FRCM specifies the manner in which radiological posting requirements are to be determined. The maximum dose is that which can be delivered under the worst credible accident in that area, taking into consideration circumstances and controls, which serve to limit the intensity of the maximum beam loss and/or its duration. Some examples of accident

scenarios are (1) beam intensity significantly greater than the nominal beam intensity; (2) unanticipated beam losses; and (3) single pulse full machine loss on an element. The maximum dose is to be determined through the safety analysis, which shall document calculations and measurements of possible radiation exposures, radiation shielding, beam optics and other relevant information. The safety analysis must be reviewed and approved by the SRSO prior to construction and/or operation of the beam.

The FRCM specifies requirements for controls. Accelerator/beam line areas shall be posted and controlled for the normal operating conditions when the safety analysis documents that delivering the maximum dose to an individual is unlikely. Accelerator/beam line areas shall be posted and controlled for accident conditions when the safety analysis documents a scenario in which it is likely that the maximum dose may be delivered to an individual.

The application of the FRCM design requirements to Project X is described in the remainder of this section.

IV.9.1 Radiation Limits

Safety Analysis

Project X will be capable of the production and delivery of multi-megawatt beam power. Accelerator components such as cryomodules and beam pipes can be destroyed very quickly by beam power at this level. The Project X accelerators and associated beam lines require unprecedented control of beam orbit, beam optics, and beam losses in order to provide decades of safe operation for experimental programs. Consequently, the control of beam loss through a machine protection system is a primary design consideration for Project X.

Principal design features required for the control of beam loss include precision alignment of all accelerator components, precise control of beam focusing, elimination of RF jitter, and precision control of beam orbit. Operation of Project X accelerators and beam lines without precision controls could easily result in beam losses on the order of 100 W/m. Machine protection systems are required to ensure that all beam control features are functional and operating as intended. The loss of any precision control feature will cause the machine protection system to inhibit beam acceleration at the ion source, LEBT, or MEBT. The machine protection systems will be capable of limiting or stopping machine operation within a few microseconds of sensing an abnormal condition.

Project X accelerators and beam lines accelerate and transport H^- beams. Principal beam loss mechanisms are related to stripping electrons from H^- ions; the causes of stripping include H^-

ion collisions with residual gas, blackbody photon interactions, Lorentz force (magnetic stripping), and interbeam scattering. Beam loss due to these various mechanisms is dominated by interbeam scattering and has been determined to be about 0.1 W/m. Losses from the remaining mechanisms are $\ll 0.1$ W/m.

Facility Design Beam Loss Level

The conclusion of the Safety Analysis is that the average beam loss under normal conditions will be of the order of 0.1 W/m. Machine protection systems will monitor the performance of beam focusing, beam orbit, RF stability, and machine alignment. Machine protection systems will reduce accelerator beam power or inhibit accelerator operation in the event precision control of the accelerator control is lost. The reaction time of machine protection systems under consideration is on the order of a few microseconds. Therefore, only operation under normal conditions should be possible. For purposes of the facility design, it is assumed that the peak average beam loss will be 1 W/m, a factor of 10 higher than what is expected during nominal beam operating conditions.

Facility radiation level design goals

The design goals for Project X accelerators and beam lines are:

1. Permit unlimited occupancy for all service buildings, shielding berms, parking lots, control rooms, and associated areas. By design, radiation levels are to be kept below 0.05 mrem/hr in all accessible locations outside of the beam enclosures for normal operating conditions, based upon an assumed continuous beam loss of 1 W/m. The actual nominal beam loss condition described in the Safety Analysis is expected to be about 0.1 W/m.
2. Permit inspection and maintenance activities within tunnel enclosures while maintaining personnel radiation exposure due to residual activation of accelerator components and beam enclosures at levels as low as reasonably achievable.
3. Limit radiation exposure due to air activation both within the beam enclosure during inspection and maintenance activities and at the site boundary.
4. Limit ground water and surface water activation to levels well below regulatory standards.
5. Prevent the activation of beam component surfaces to avoid the generation of removable radioactivity.
6. Minimize the activation of accelerator components which can impact their useful service life

IV.9.2 Radiological Design Requirements and Consequences of Project X Radiation Limits

Nominal beam loss throughout the Project X accelerator and beam lines is expected to be about 0.1 W/m. Machine Protection Systems will limit or inhibit beam operations within microseconds of sensing a machine fault. The design requirements for radiation shielding discussed below are based upon an assumed continuous beam loss of 1 W/m. The consequences of the activation of accelerator components, enclosure structures, air, water, and removable contamination are discussed in terms of the expected nominal beam loss of 0.1 W/m as defined in the Safety Analysis.

Radiation Shielding

An early conceptual design of a Project X accelerator enclosure is shown in Figure IV-61. An enclosure height of 16 feet is indicated along with passive shielding of 24.5 feet. An option to transport 1 GeV beam from the 1 GeV Linac to the existing Booster accelerator is shown in Figure IV-62; a remnant of the Main Ring tunnel is used as a beam transport line. The tunnel height is 8 feet and the shield is approximately 20 feet. At this time, details of the Project X layout and facility design have not been finalized. It is necessary that the accelerator design precede the shield design, but some shielding design concepts for Project X are considered here.

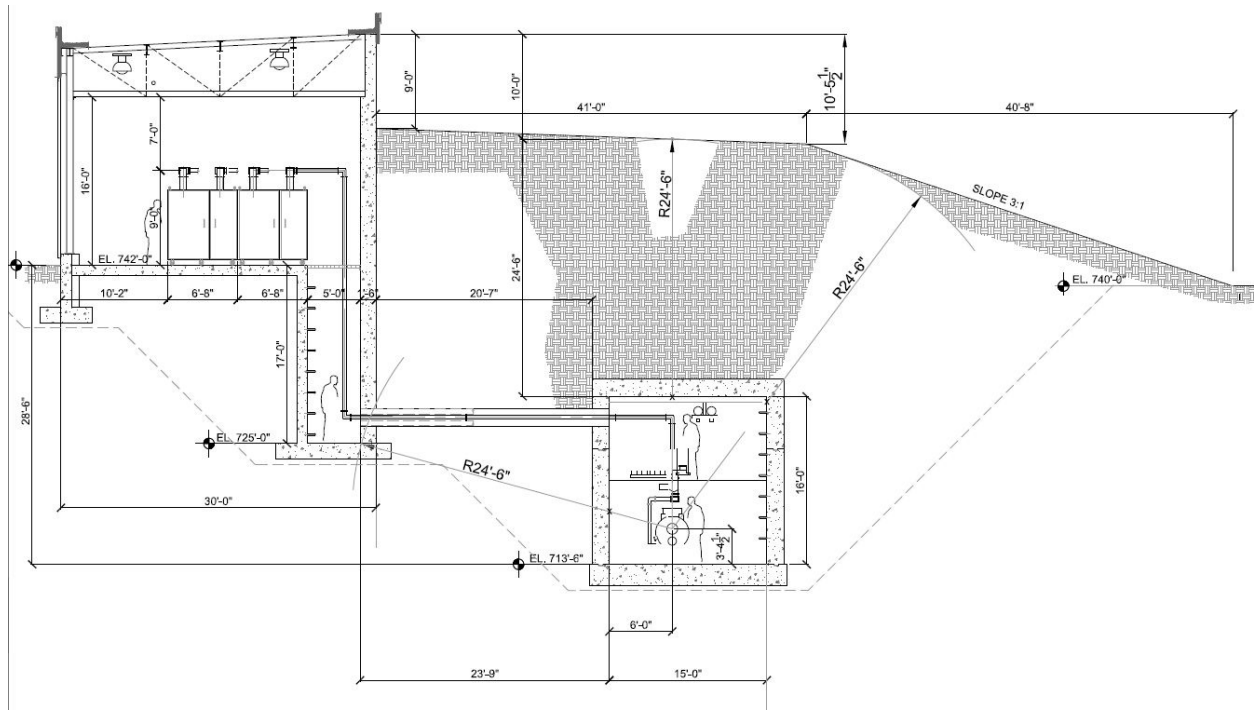


Figure IV-61: Early concept cross section of Project X linear accelerator enclosure

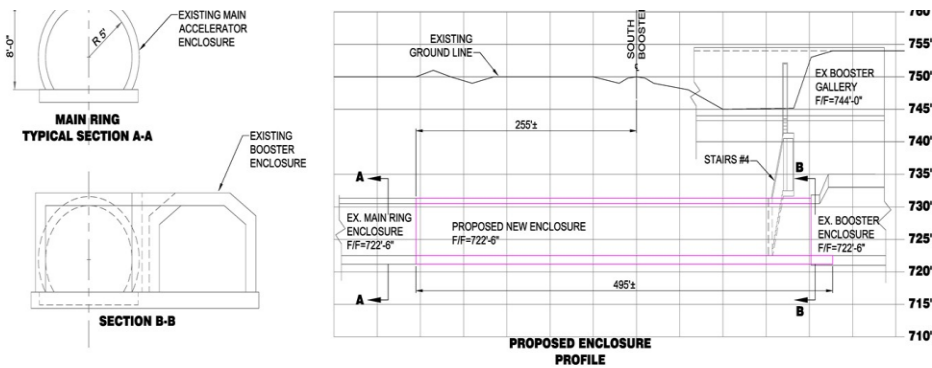


Figure IV-62: 1 GeV transport line to the Booster accelerator

An established parameterization [53] is used to determine the radiation dose equivalent rate as a function of energy (GeV), distance (feet), and angle with respect to incident beam direction (degrees) from a low energy proton beam (<1 GeV) incident upon a target:

$$S(E, r, \theta_s) = 2 \times 10^{-5} (1 + E^{0.6}) \left(\frac{1 - e^{-3.6E^{1.6}}}{\left(0.3048 r \left(\theta_s + \frac{40}{\sqrt{E}}\right)\right)^2} \right)$$

For neutron energies below 100 MeV, the attenuation length in concrete is significantly shorter than that for neutrons considered in higher beam energy based assessments. For example, for high energy shielding problems, 3 feet of concrete provides a reduction factor of 10 in radiation dose rate. The mean free path of low energy neutrons relative to the high energy asymptote has been parameterized [53]:

$$\frac{\lambda_{LE}}{\lambda_{HE}} = 1 - 0.8 e^{-5*E}$$

The reduction in radiation dose rate as a function of energy (GeV and concrete shield thickness (feet) is:

$$A(E, T_{conc}) = 10^{\frac{-T_{conc}}{3} / (1 - 0.8e^{-5*E})}$$

In the dose rate calculations, the peak neutron energy E (GeV), is taken to be equal to the beam energy. This simplification is conservative in that the actual neutron energies are necessarily lower and hence lead to better attenuation provided by the concrete shielding than indicated by calculations. In addition, the dose equivalent per neutron conversion factor is taken as a constant value of 40 fSv/n over the range of the neutron spectrum. The resulting shielding calculations are implicitly conservative.

Radiation shielding required to limit radiation dose rates to 0.05 mrem/hr for a 1 GeV linac and beam transport line assuming various beam levels of beam loss is shown in Figure IV-63. The shielding requirement varies with beam energy with the assumed maximum beam power loss for normal and accident conditions. The ultimate shielding thickness chosen will depend up a number of factors including the confidence level given to the Safety Analysis including consideration of the projected loss mechanisms and the machine protection system.

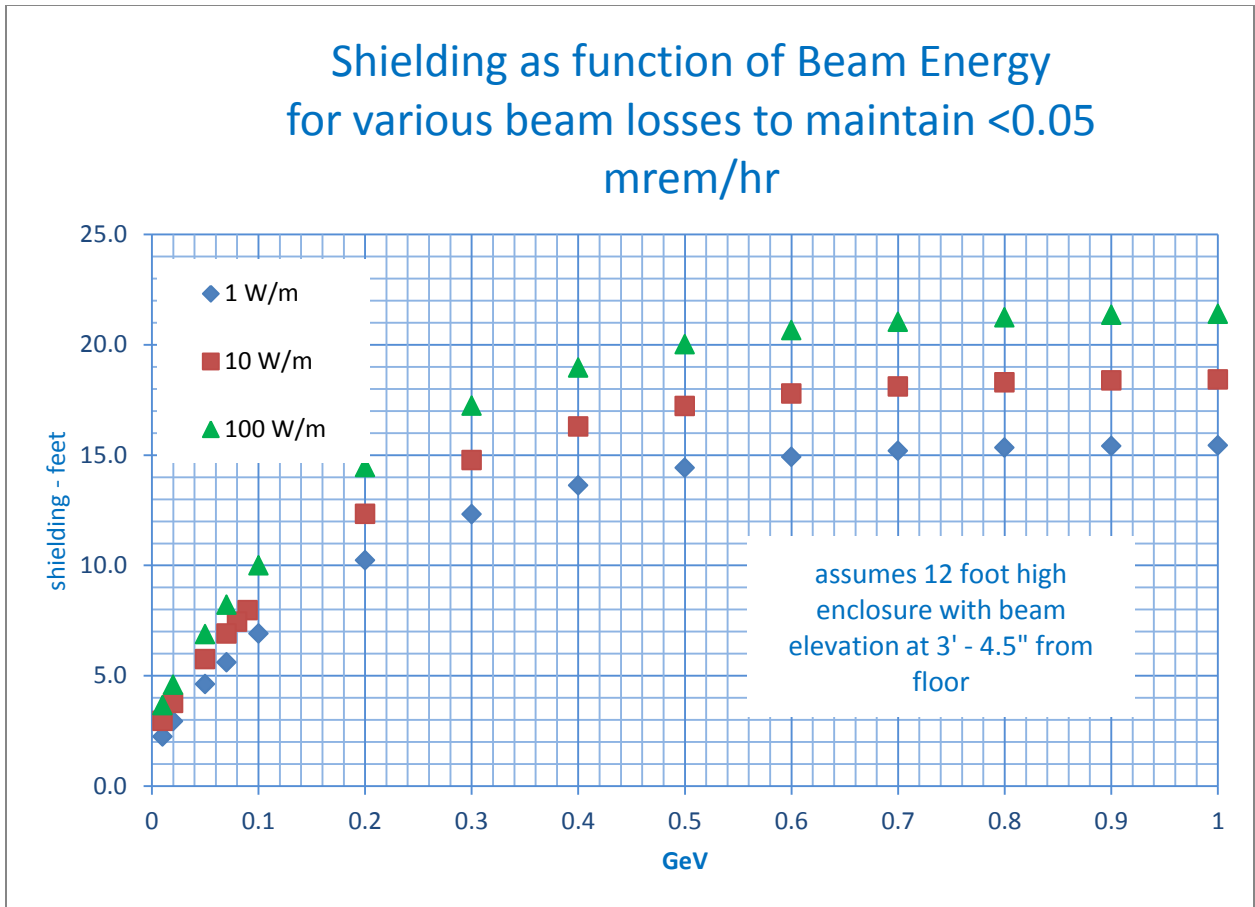


Figure IV-63: Radiation shielding requirements as a function of beam energy and beam power loss for a Project X beam enclosure

An active protection system, the Total Loss Monitor (TLM), currently under development, could be used to guarantee the limitation of any given beam power loss. The use of a TLM system could help to fix the level of beam power loss, and as a consequence, fix the amount of radiation shielding required.

The TLM is an argon gas filled ion chamber of variable length with an applied bias voltage. A beam loss in the vicinity of the ion chamber produces a charge whose magnitude is proportional to the amount of beam loss. The TLM response to an 8 GeV proton beam loss made under controlled conditions measured over a wide range of bias voltage and over two decades of beam intensity has been determined as shown in Figure IV-64. The response has been shown to be independent of the TLM length. At the nominal bias of 500 volts, the TLM response to 8 GeV proton beam loss is about 3 nC/E10 protons. Preliminary scaling laws, to be verified in further TLM development work, can be used to predict TLM response at other energies.

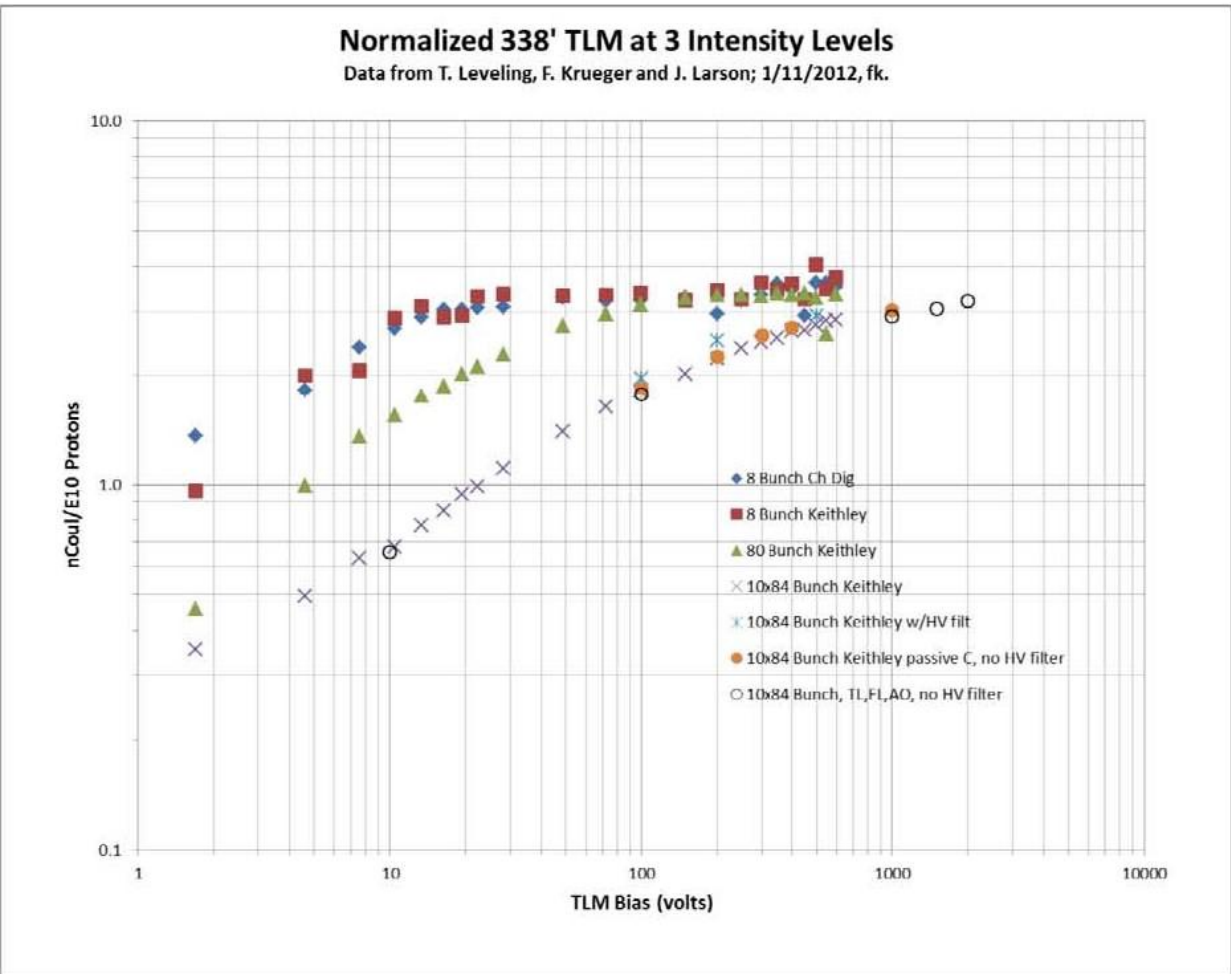


Figure IV-64: Response of 338 foot (103 meter) TLM as a function of applied bias voltage over 2 decades of beam intensity

The response can be scaled to beam energy down to 1 GeV by the relationship:

$$3 \frac{nC}{E10} \text{ protons} * \left(\frac{E}{8 \text{ GeV}} \right)^{0.8}$$

The response to beam energy below 1 GeV remains to be determined.

A feature of the TLM system is that an interlock trip level can be established to limit beam loss to 1 W/m or virtually any beam power loss. A TLM as presently conceived, does not distinguish between distributed losses and single point beam losses. The process to set TLM trip levels consists of two steps: 1. Establish the total charge to be collected for a distributed loss, e.g., 1 W/m. 2. Evaluate the shielding considering that the total charge can be deposited

at a single location. If the shielding is sufficient for the maximum charge collection rate at any location, then the TLM can effectively limit both the distributed beam loss and worst case single point beam loss.

Based upon preliminary TLM work, it should be possible to limit Project X beam loss with a TLM system beginning at the HW cryomodule and continuing through the entire accelerator and beam transport chain.

Residual Activation of accelerator components and structures

Residual radiation levels in beam transport lines and accelerators due to operational beam losses must be controlled in order to conduct maintenance activities while keeping personnel radiation exposure as low as reasonably achievable (ALARA). For 2-3 MW beam power, small fractions of a percent loss would result in very high residual radiation levels which would render beam enclosure access difficult and maintenance at loss points extraordinarily difficult. A sensitive machine protection system which inhibits beam operation when significant losses are present will be required to allow access and maintenance activity modes historically enjoyed at Fermilab.

For design purposes, a loss rate of 3 to 10 watts/meter results in a dose rate of about 100 mR/hr at one foot from beam line components such as magnets and accelerating cavities following a 30 day irradiation period and 1 day of cool down. A loss of 0.25 watts/meter results in a dose rate of about 100 mR/hr at one foot from low mass components such as beam pipes for the same irradiation/cooling period. Radiation levels are typically at least a factor of 5 less than these levels. For example, for a typical magnet beam loss location at 2 watts per meter, the fractional beam power loss is 1 ppm. A sensitive machine protection system will be required to quickly identify and suspend operation in the event such losses occur.

In the Safety Analysis, projected normal losses due to interbeam scattering and other loss mechanisms are about 0.1 W/m. The machine protection system as presently conceived should limit beam loss to < 1 W/m. Consequently, residual activation of the accelerator, beam line components, and tunnel structures should be comparable to or less than levels tolerated in existing and previous machines. While the machine protection system would serve to protect the accelerator and beam line components, the TLM system would serve in a parallel role as a personnel safety system to limit residual activation of accelerator components.

Air activation

Air activation must also be characterized due to projected Project X operations. Based upon the anticipated losses described in the safety analysis, the combination of anticipated normal beam loss and the machine protection system should serve to limit the total beam loss levels at or below those produced at existing facilities. Based upon projected losses from the Safety Analysis, no significant air activation is anticipated. While the machine protection system would serve to protect the accelerator and beam line components, the TLM system would serve in a parallel role as a personnel safety system to limit air activation within accelerator enclosures.

Water activation

The site chosen for the new Project X accelerator and beam line enclosures is presently at the center of the Tevatron beam enclosure. In order to evaluate surface and ground water activation, a geological survey (core borings) will be required to understand ground water migration rates at this site since no data presently exists. An estimate of surface and ground water activation is necessary in order to ensure compliance with regulatory requirements for surface and ground water. However, based upon losses projected by the Safety Analysis, no significant surface water or ground water activation is anticipated. The machine protection system would serve to limit the total beam loss that would also determine the level of surface water and ground water activation. The TLM system would serve a parallel, redundant role to also limit surface and ground water activation.

Radioactive surface contamination

Radioactive surface contamination results coincidentally with the activation of accelerator and beam line components. Maintenance activities are rendered more complicated when radioactive surface contamination is present due to prescriptions for the use of personnel protective equipment including coveralls, gloves, shoe covers, and other protective measures. It would be possible in megawatt beam power machines to produce very significant levels radioactive surface contamination at beam loss locations. However, as indicated in the Safety Analysis, nominal beam power losses are expected to be approximately 0.1 W/m, about a factor of 100 below the beam power loss required to produce the onset of measurable radioactive surface contamination. Consequently, radioactive surface contamination on accelerator, beam line components, and tunnel structures should be comparable to or less than levels tolerated in existing and previous machines.

Lifetime of machine components

Based upon the level of beam loss projected by the Safety Analysis and also upon experience with existing accelerator and beam line facilities, machine component lifetimes, in general, should be on the order of many decades.

IV.10 Machine Protection System

The Project X linac will accelerate 1mA of beam current at a CW duty cycle. While the peak current is relatively low compared to most HEP linacs, the average current will be equal or greater than any other HEP hadron linac. In order to protect the machine and associated diagnostics from beam induced damage and excessive radiation damage will require a robust Machine Protection System (MPS) that provides the requisite amount of protection for the entire system. The main goals of the MPS will be the following:

- Protect the accelerator from beam induced damage and operator damage.
- Manage and monitor the beam intensity.
- Safely switch off the beam in the case of failures.
- Determine the operational readiness of the machine.
- Manage and display alarms.
- Provide a comprehensive overview of the machine status.
- Provide high availability.
- Provide fail safe operation where possible.
- Provide post mortem analysis.

Several signals from devices or systems will be monitored and utilized as actuators to inhibit the beam at various stages of the accelerator. The main actuator for beam is the ion source power supply itself. In addition, signals from the LEBT/MEBT choppers, the Radio Frequency Quadrupole Amplifier (RFQ), cavity power amplifiers as well as beam stops and gate valves status will all contribute as additional control devices. A comprehensive overview of the entire machine will be obtained by carefully monitoring all relevant inputs from machine diagnostics and critical systems affecting safe or fail safe operation.

The protection system is modeled based on experience gained from commissioning and operating the SNS accelerator. Their peak current specifications are about 20× higher than the Project X peak beam current, but their average beam current is equivalent to Project X specifications due to the lower duty factor. Their copper to SC cavity transition occurs at 187 MeV. Above 200 MeV the Project X MPS hardware design and placement can be modeled after the SNS system. The Project X MPS system will not need response times as

stringent as SNS because of our low peak currents. The challenge for the Project X MPS comes from the low energy cryomodule protection (2.1 MeV – 150 MeV) where beam losses have difficulty penetrating the cryomodule and beam pipe.

IV.10.1 MPS Configuration

The MPS will be considered to be the collection of all subsystems involved in the monitoring and safe delivery of beam to the dump and not limited to any particular subsystem or diagnostic device. It has connections to several external devices and sub-systems. Figure IV-65 shows a conceptual overview diagram of the MPS. The top layer comprises signal providers such as beam loss monitors, beam position monitors, magnet power supplies etc. Systems at this level send alarms or status information to the MPS logic subsystems (permit system) which issues a permit based on the comprehensive overview of all inputs and request. Only simple digital signals (e.g. on-off, OK-alarm) are transmitted. All devices or subsystems that are determined to be pertinent to protecting the machine or necessary for machine configuration are included. The permit system layer of the MPS will be FPGA based and is thus fully programmable and handles complex logic task. The logic here will be designed to ensure safe operating conditions by monitoring operational input, chopper performance, the status of critical devices and by imposing limits on the beam power.

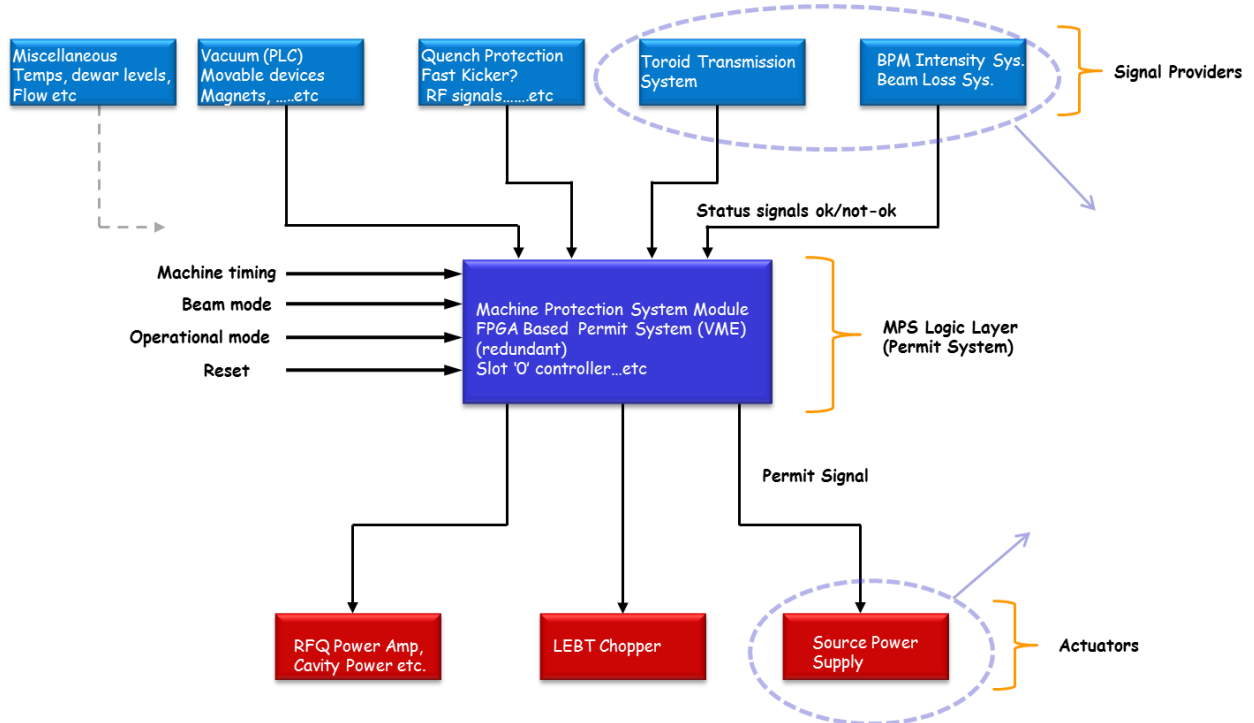


Figure IV-65: MPS Conceptual Layout

The final layer of the system shows the main actuators. This will comprise of all points where the MPS logic may act on the operation of the machine to prevent beam from being produced or transported. The entire protection system interfaces with the accelerator control system and machine timing system for configuration management, timing and post mortem analysis as shown in Figure IV-66. The operational modes, operational logic, reaction time and complexity of inputs will differ based on the machine configuration and damage potential at various stages of the accelerator complex.

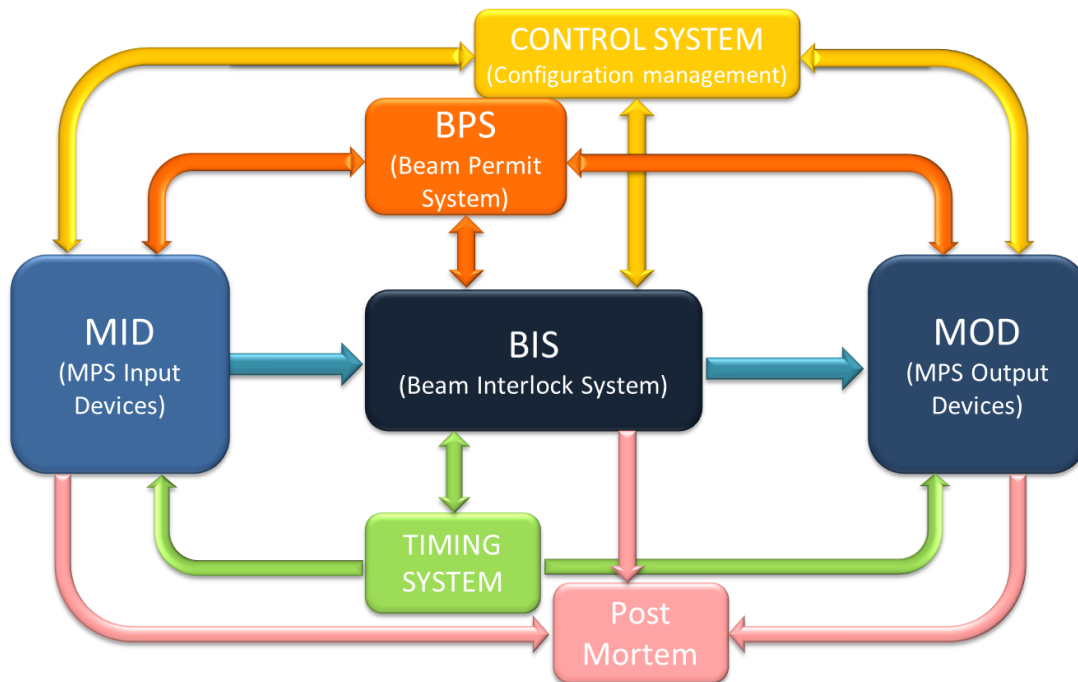


Figure IV-66: Conceptual layout integrated with control system

IV.10.2 Protection System R&D

Protecting the superconducting cavities from low energy protons losses where the particle energies are too low to produce significant detectable radiation will be a major part of the developmental work needed to effectively inject beam without quenches. To achieve this we will need to research sensitive means for measuring these losses and develop an effective feedback for machine protection. In addition we plan to achieve the following goals as a result of designing, constructing and operating the PXIE MPS:

- Understand and verify acceptable loss rates in the room temperature sections.
- Develop a strategy to monitor chopped beam from the MEFT.
- Estimate particle shielding effect of superconducting cavities and cryomodules.
- Develop effective algorithms for the FPGA based logic system.

- Demonstrate effective integration with controls/instrumentation and all subsystems.
- Understand dark current effects as it relates to protection issues.

In order to protect the accelerator from damage as the beam transitions from the room temperature sections of the machine to the superconducting sections, some specialized instrumentation may be developed at PXIE. Developing an effective algorithm to monitor the beam position as a feedback to machine protection will be of interest for both PXIE as well as Project X.

V Siting and Conventional Facilities

V.1 Siting Options

Ample space exists on the Fermilab site to construct all Project X related facilities within the site boundaries. Selection of the specific facility layout is based on an optimization of functionality, performance, interfaces with existing facilities, expandability, environmental impacts, and costs among other factors. In accordance with the latest funding guidance, a staged approach has been developed whereby the first 1 GeV is constructed in Stage 1, followed by 1-3 GeV in Stage 2 and finally 3-8 GeV in Stage 3. The layout of the facility must accommodate this staged approach and minimize cost in Stage 1.

The fundamental requirement of Stage 1 is to deliver 1 GeV beam to the existing Booster, Muon Campus (under construction), and a new Spallation Facility simultaneously. However, the Stage 1 layout must also consider future stages and their constraints. An important constraint is the location for 8 GeV injection into the Recycler (RR) for Stage 3. Transfer line radii become larger with energy and therefore there are limited options for routing the 8 GeV transfer line to the Main Injector (MI) tunnel. For this reason the layout designs originate at MI/RR and work backwards toward the front end. The favored location for injection is at MI-10 since the other symmetric 4 or 8 half-cell straight sections (MI-30, 40, 60) all include other major equipment (collimation and MI/RR transfer line, abort, RF). Since the beam is counter-clockwise in MI, the beam from Project X approaches MI-10 from the east and drives the location of the 3-8 GeV linac to the area inside the Tevatron ring.

Initial designs for a “one-shot” Project X in which all three stages are constructed concurrently had each accelerator in a linear arrangement as shown in Figure V-1. This is still a viable option should funding projections change but has some disadvantages in a staged scheme. An investment in conventional facilities would be required for all envisioned accelerators through 8 GeV to allow a path from the Stage 1 section to the Booster and Muon Campus. Also, it would not allow for concurrent construction of Stages 2 and 3 while Stage 1 is operating since they would share tunnels.

The layout designed for this report is shown in Figure V-2. It shows the Stage 1 1 GeV accelerator as the southernmost section, followed by the 3 GeV section to its north and finally the 3-8 GeV pulsed section. Locating the Stage 1 section south of F0 provides paths to the Booster by way of the Tevatron tunnel and to the Muon Campus through AP0 (see section III.2 for 1 GeV beam handling at F0). Connection from Tevatron tunnel to Booster is shown in Figure V-3. This layout allows for construction of Stages 2 and 3 concurrently with operation of Stage 1 and also provides flexibility for expansion beyond Project X. Figure V-

4 presents notable existing and planned facilities relevant to the construction of Project X Stage 1. The 3-8 GeV pulsed section could further be expanded to a muon accelerator as shown in Figure V-5.

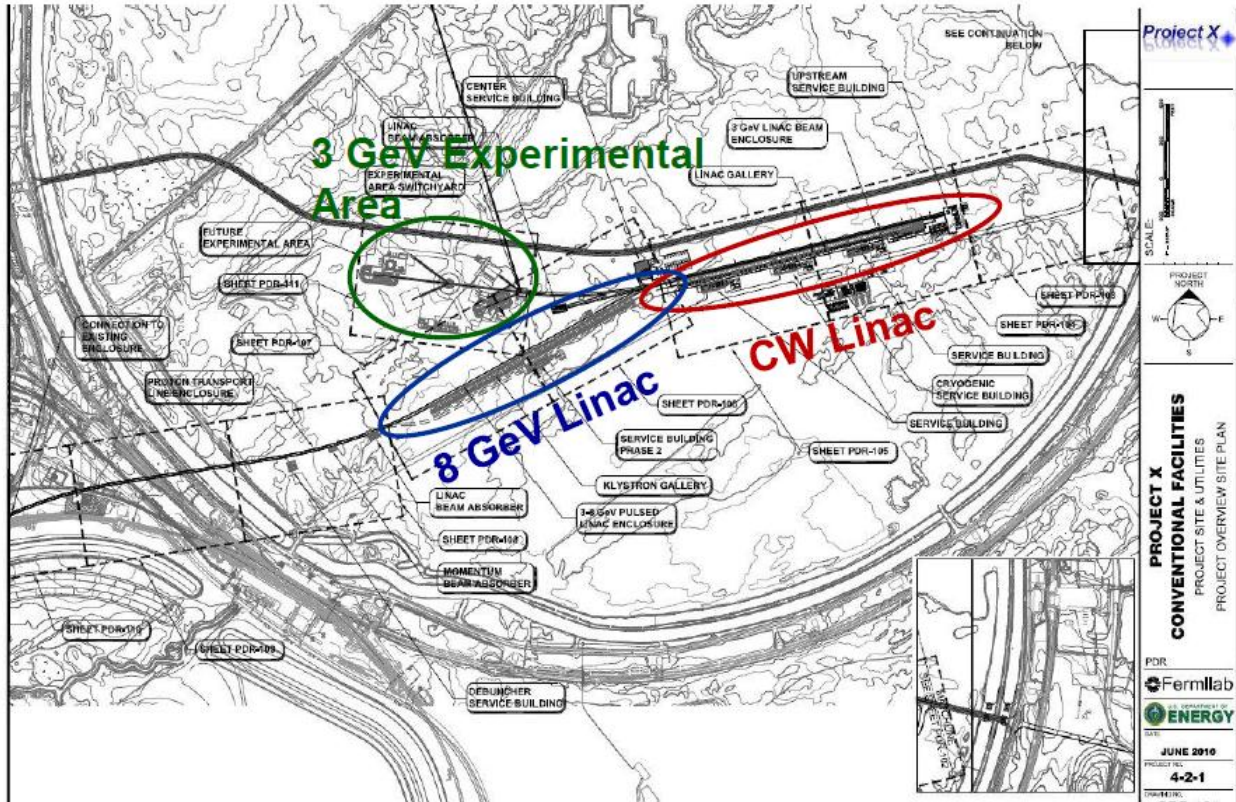


Figure V-1: "One-shot" Project X layout from 2010 Reference Design Report.

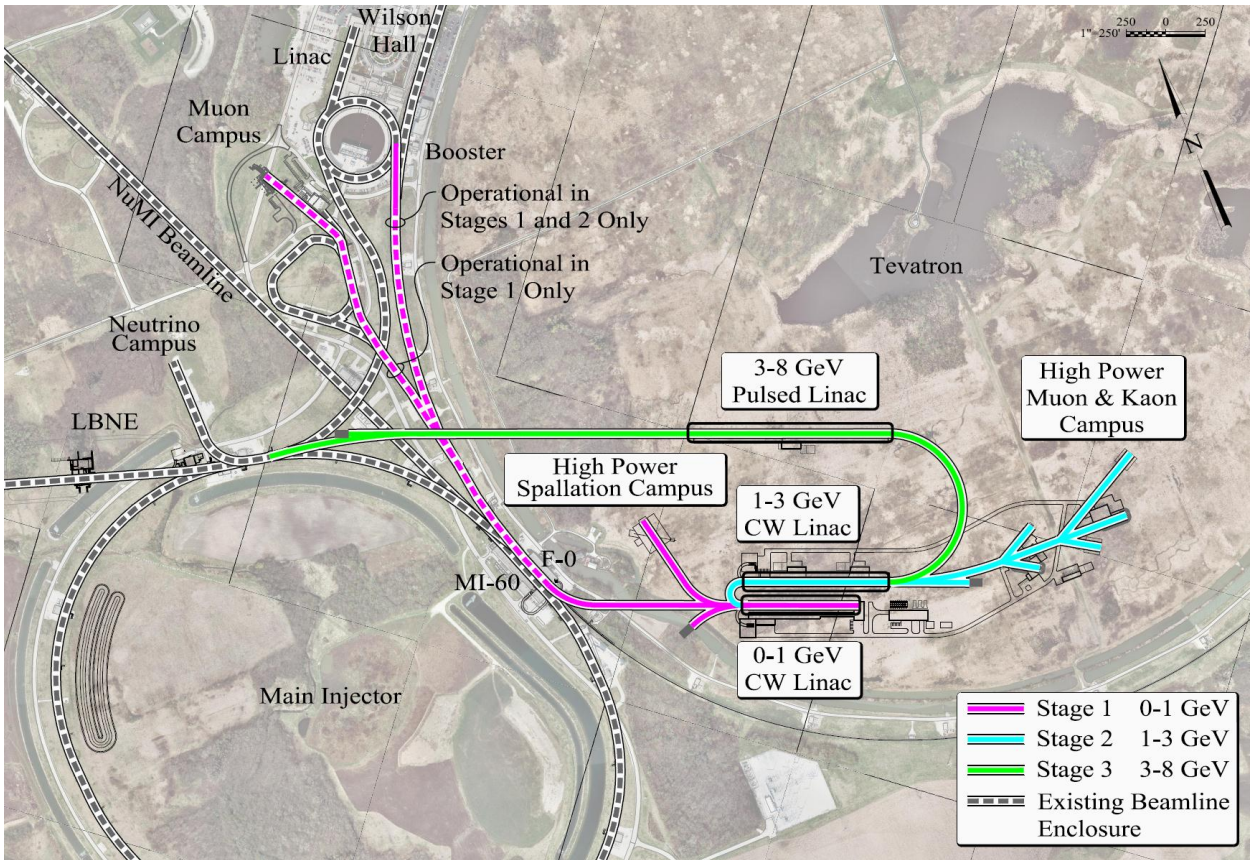


Figure V-2: Staged layout selected for the Reference Design

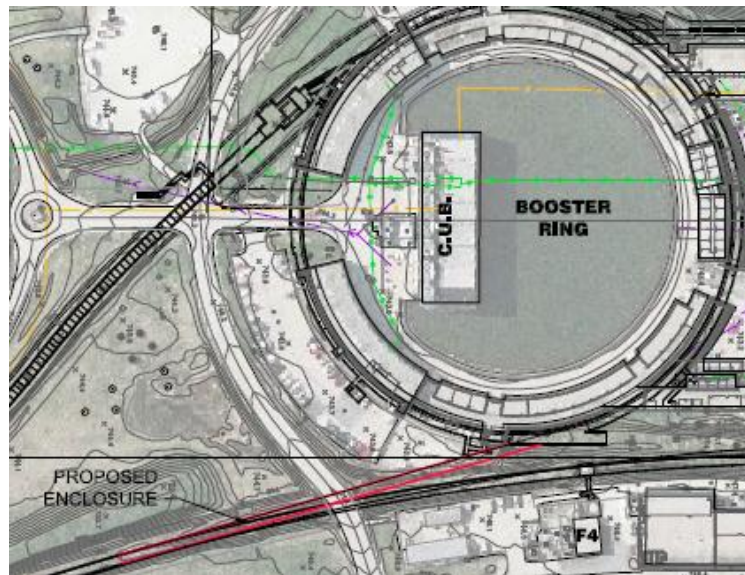


Figure V-3: New ~ 500 ft. tunnel section from Tevatron tunnel to Booster for Stage 1.



Figure V-4: Other notable existing and planned facilities relevant to Project X Stage 1 include the Booster, Muon Campus, and LBNE beamline.

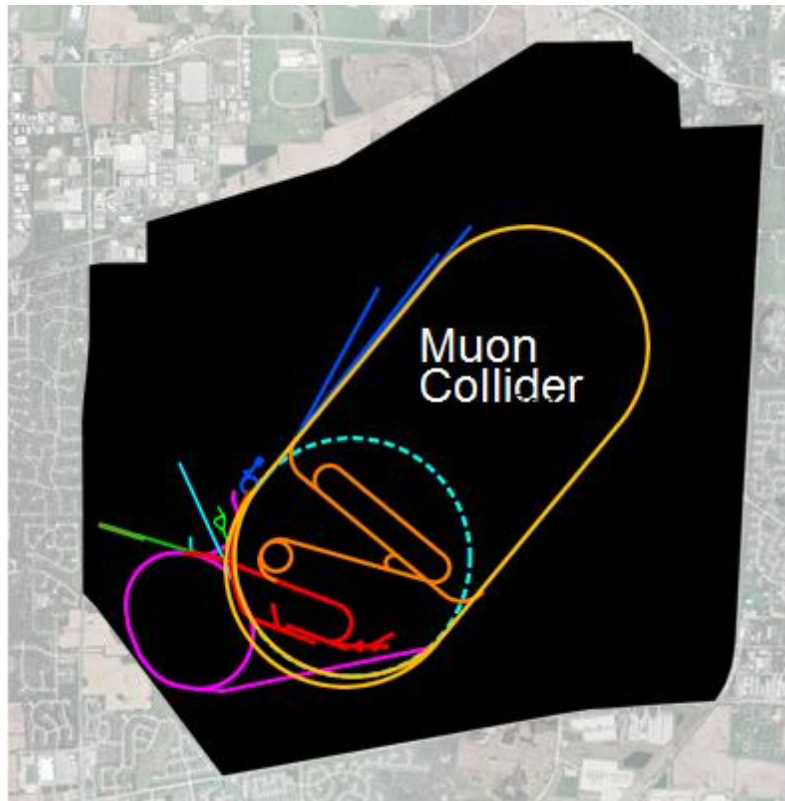


Figure V-5: Potential future facilities and their relation to Project X. Project X facilities in red, Muon Accelerator in orange, Muon Collider in yellow.

V.2 Conventional Facilities

This section outlines the conventional facilities required to house and support the 0 to 1-GeV CW Linac (Stage 1), 1 to 3-GeV CW Linac (Stage 2) and the 3 to 8-GeV pulsed Linac (Stage 3). Civil construction for the facility includes all below-grade beam-line enclosures. All above-grade buildings, roads, parking, utilities and services to accommodate the equipment for the operation of the facility on the Fermilab site are also included.

Construction of the below-grade linac(s) and beam transport lines as well as the above-grade service buildings are similar to previously utilized and proven construction methods previously executed at Fermilab. Construction of all below-grade enclosures consists of conventional open-cut type construction techniques. The architectural style of the new buildings reflects, and is harmonious with, the existing buildings. Currently, the layout has been optimized for the accelerator requirements. Future layouts will consider existing topography, sustainability, watersheds, vegetation, natural habitat, and wetlands. All the aspects will be thoroughly addressed in the Environmental Assessment for this project.

Site Construction

1. Site work

- a. Site Drainage will be controlled by ditches and culverts, preserving the existing watershed characteristics both during construction and subsequent operation.
- b. Road Construction includes a new temporary construction road providing access to Butterfield Road. This road will provide direct access for construction traffic during construction only – roadway will be restored to original condition upon completion of the project. New Service Road will provide permanent access to all service buildings and utility corridor.
- c. Landscaping includes the restoration of disturbed areas. Construction yards and stockpile areas will be removed after completion of the construction phase of the project. All disturbed areas will be returned to a natural state or landscaped in a similar manner as found at other Fermilab experimental sites. Erosion control will be maintained during all phases of construction.
- d. Wetlands Mitigation includes the avoidance or minimization of adverse impacts to wetlands in the project area. Environmental consultants would delineate wetlands, and a Clean Water Act permit application prepared for submittal to U.S. Army Corps of Engineers for impacts that cannot be completely avoided. Compensatory mitigation would be provided according to terms and conditions of the permit. This may be in the form of purchased wetland bank credits, restoration or enhancement of existing wetlands on site, or creation of new wetland areas. The permit would dictate the amount and type of mitigation, which must be in place prior to the initiation of construction. A Floodplain/Wetland Assessment pursuant to 10 CFR 1022 would be incorporated into the Environmental Assessment.

2. Utilities

The following utilities are required to support the operation of the facility. The list incorporates current assumptions and will require further refinement as the design process progresses.

- a. Electrical Power includes new duct banks and utilization of existing duct banks from two sources including Kautz Road Substation (KRS) and Master Substation (MSS). Separate high-voltage feeders with backup will be provided for conventional, machine and cryogenic power.
- b. Communications include new duct banks tied into the existing communication network along Kautz Road.
- c. Chilled Water (CHW & CHWR) for machine and building cooling will be supplied via new supply and return lines from the existing Central Utility Building (CUB).
- d. Low Conductivity Water (LCW) for machine cooling will be supplied via new supply and make-up water from the existing Main Injector ring LCW system.
- e. Industrial Cooling Water (ICW) for fire protection will be supplied via new supply and return lines from the existing site wide ICW system.

- f. Domestic Water Supply (DWS) for potable water and facilities will be supplied via new supply line from the existing site wide DWS system.
- g. Sanitary Sewer (SAN) for facilities will be supplied via new sewer main and lift station from to the existing site wide sanitary sewer system.
- h. Natural Gas (NGS) for building heating will be supplied via new supply lines from the existing site wide NGS system.

3. Facilities Construction

Conventional facilities will be constructed with future upgrade capabilities considered in the initial design phase. Equipment galleries, enclosures and surface buildings will be designed to accommodate future expansion of the technical components of the facility. See

Figure V-2 for a site map and facilities locations. The major elements for the conventional facilities are as follows:

- a) Below-Grade Construction
 - 0 to 1-GeV Continuous Wave (CW) Linac Enclosure
 - 1 to 3-GeV Continuous Wave (CW) Linac Enclosure
 - 3 to 8-GeV Pulsed Linac Enclosure
 - 3-GeV Experimental Area Switchyard
 - Various Transfer Line Enclosures
- b) Above-Grade Construction
 - 0 to 1-GeV Linac Gallery
 - 1 to 3-GeV Linac Gallery
 - 3 to 8-GeV Linac Gallery
 - Cryogenic Service Building

V.3 **Site Power Requirements**

An estimate of site power requirements for the linacs and beam transfer lines is given in Table V-1. Included on the various lines are:

CW Linac RF: RF power sources to accelerate 2 mA of beam to 1 GeV and 1 mA of beam from 1 GeV to 3 GeV. Also included are LLRF, protection circuits, RF controls, filament and bias supplies.

Pulsed Linac RF: RF sources, including modulators, to accelerate 1 mA of beam from 3 GeV to 8 GeV with a 4.4% duty factor. Also included are LLRF, protection circuits, RF controls, filament and bias supplies.

Cryogenic Systems: Based on the estimated cryomodule dynamic and static heat loads through both the CW and pulsed linacs, and system operation at 2 K. Because the heat load is overwhelmingly dynamic, the cryogenic system power associated with the CW linac is about 10.2 MW, while the pulsed linac is only about 1.0 MW.

LCW: The primary load is cooling of the RF sources.

ICW: Utilized for heat removal in the cryogenic systems.

HVAC: The primary loads are the 20% of RF power not removed by the LCW system and the removal of heat from equipment galleries.

Conventional Systems: Power required for other linac/beamline components (magnets, vacuum pumps), and for occupied spaces.

System	Wall-plug Power (MW)
CW Linac RF	16.4
Pulsed Linac RF	2.1
Cryogenic Systems	11.2
Low Conductivity Water	1.8
Industrial Chilled Water	1.0
HVAC	1.0
Conventional Systems	3.0
TOTAL SITE POWER	36.5

Table V-1: Estimated site-wide power requirements for the Project X Linacs

The total site-wide power of 36.5 MW supports operations with 1 MW of beam power at 1 GeV, 3 MW of beam power at 3 GeV, and 350 kW of beam power at 8 GeV. Thus the total system efficiency (beam power/wall-plug power) is about 12%.

Appendix I: Staging Scenarios

As described in the body of this report, the Reference Design provides a facility that will be unique in the world with unmatched capabilities for the delivery of very high beam power with flexible beam formats to multiple users. Financial and budgetary constraints have led to available funding have led to consideration of a staged approach to Project X. Development of a staging plan for Project X is based on application of the following principles:

- Each stage should have a cost significantly below \$1B.
- Each stage should present compelling physics opportunities.
- Each stage should utilize existing elements of the Fermilab complex to the extent possible.
- At the completion of the final stage the full vision of a world leading intensity frontier program at Fermilab should be realized.

I.1 Staging Scenario

A three stage approach to the Reference Design consistent with the above principles has been developed and is described below. The siting plan consistent with this approach has been presented in Figure I-1.

Stage 1

Stage 1 of Project X is comprised of a 1 GeV, CW, superconducting linac operating with an average current of 1 mA. A small fraction (~2%) of the beam will be injected into the existing Booster. Injection at 1 GeV is projected to result in a 50% increase in the per pulse proton intensity delivered from the Booster to the Main Injector complex, relative to current operations. Stage 1 thus establishes the potential for delivering up to 1200 kW onto a long baseline neutrino target (either NuMI or LBNE). Depending upon the operating energy of the Main Injector and the allocation of the Main Injector timeline between neutrino production and a possible rare kaon experiment, significant power could also be devoted a program based on 8 GeV protons. The balance of available linac beam can be delivered to the Muon Campus currently under development, providing a factor of ten increase in beam power available to the μ -to-e experiment, and/or to a newly developed experimental programs devoted to nuclear electric dipole moments (edm), ultra-cold neutrons, and possibly nuclear energy applications. An additional substantial benefit of Stage 1 is that the existing 400 MeV linac will be retired from service, removing a substantial operational risk within the Fermilab proton complex.

Stage 2

Stage 2 is based on extension of the CW linac to 3 GeV, with an average current of 1 mA accelerated to 3 GeV. Stage 2 thus provides 3 MW of beam power at 3 GeV, with the capability of delivering flexible beam formats to multiple experiments. It is anticipated that a Main Injector based kaon experiment would be relocated to the 3 GeV linac in Stage 2. Also accommodated are any number of muon and nuclei based experiments. Injection into the Booster at 1 GeV is retained, as will simultaneous delivery of 1 MW to the 1 GeV program established in Stage 1.

To support the Stage 2 performance the initial 1 GeV of the linac will be upgraded to 2 mA capability, with 1 mA available at 1 GeV and 1 mA transmitted into the 1-3 GeV linac section. In addition the Booster will be upgraded to 20 Hz capability.

Stage 3

Stage 3 completes the Reference Design via construction of the pulsed linac for acceleration of beam from 3 GeV to 8 GeV. This beam is delivered to the Recycler/Main Injector complex in support of the long baseline neutrino program. At Stage 3 >2MW of beam power is available at any energy between 60-120 GeV. Upgrades to the Recycler/Main Injector are required to support the increased beam power. Enhanced capability for delivery of 8 GeV beam, directly from the pulsed linac, is also created at this Stage. Beam capabilities at 1 and 3 GeV remain as in Stage 2.

In addition, with the completion of Stage 3 the existing 8 GeV Booster can be retired from service, taking the second substantial operating risk in the current program along with it.

Explanation of Tables

The tables below summarize the performance at all available beam energies at each stage. The organization of the tables is as follows:

- Each table describes beam performance in support of a particular program by Stage: Long Baseline Neutrino Program (Main Injector Fast Spill); 8 GeV Program (Booster in Stages 1 and 2, pulsed linac in Stage 3); 3 GeV Program; 1 GeV Program.
- Under each Stage there are two entries, corresponding to operations of the Main Injector at 120 GeV or at 60 GeV.
- There is a trade-off (proton economics) between beam power available for the Long Baseline Neutrino and 8 GeV program. The tables present a self-consistent set, based on the maximum beam power achievable in the Long Baseline Program and the

corresponding minimum in the 8 GeV program. Subsequent to the tables is a set of figures displaying the trade-offs between the two programs.

- The beam formats for the 3 GeV and 1 GeV programs are flexible, subject to certain constraints that are described at the end of this document.

**Long Baseline Neutrino Program
(Main Injector Fast Spill)**

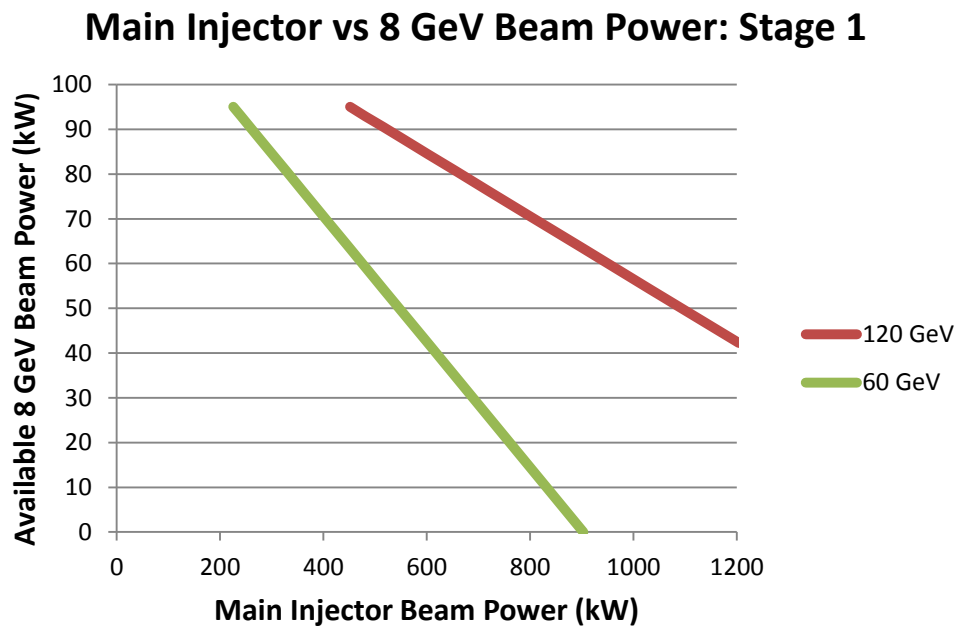
	Stage 1		Stage 2		Stage 3	
	120	60	120	60	120	60
Maximum Beam Power*	1200	900	1200	1200	2450	2450 kW
Protons per pulse	7.5×10^{13}	7.5×10^{13}	7.5×10^{13}	7.5×10^{13}	1.5×10^{14}	1.5×10^{14}
Pulse length	9.5	9.5	9.5	9.5	9.5	9.5 μ s
Number of bunches	504	504	504	504	504	504
Bunch spacing	18.9	18.9	18.9	18.9	18.9	18.9 ns
Bunch length (FWHM)	2	2	2	2	2	2 ns
Pulse repetition period	1.2	0.8	1.2	0.6	1.2	0.6 s

8 GeV Program

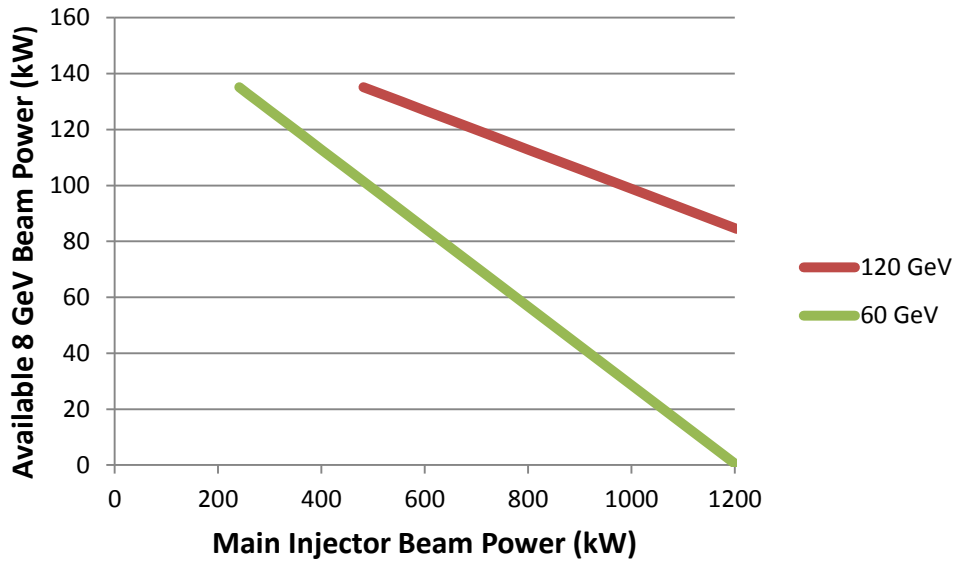
	Stage 1 (Booster)		Stage 2 (Booster)		Stage 3 (Pulsed Linac)	
	120	60	120	60	120	60
Minimum Beam Power*	42	0	84	0	172	0 kW
Protons per pulse	6.6×10^{12}	6.6×10^{12}	6.6×10^{12}	6.6×10^{12}	2.7×10^{13}	2.7×10^{13}
Pulse length	1.6	1.6	1.6	1.6	4300	4300 μ s
Number of bunches	81	81	81	81	140,000	140,000
Bunch spacing	18.9	18.9	18.9	18.9	30	30 ns
Bunch length (FWHM)	2	2	2	2	.04	.04 ns
Pulse repetition rate	15	15	20	20	10	10 Hz

Notes

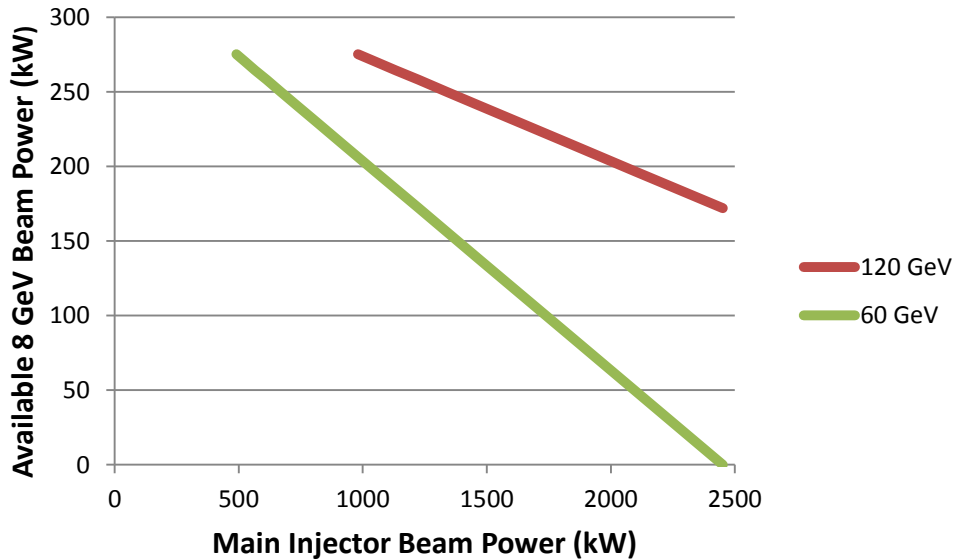
* Beam Power available from the Main Injector and at 8 GeV are dependent upon the disposition of protons provided at 8 GeV and the operational energy of the Main Injector. It is assumed that the disposition of protons will be a program planning decision based on the physics opportunities at the time. Below are presented the dependence upon available beam power at 8 GeV as a function of beam power available from the Main Injector, at each stage and for each of two operating energies.



Main Injector vs 8 GeV Beam Power: Stage 2



Main Injector vs 8 GeV Beam Power: Stage 3



** Independent bunch structures can be provided from the 1 and 3 GeV linac to three experimental areas simultaneously. The bunch pattern in any particular area must conform to the following requirements:

- Each bunch contains up to 1.9×10^8 particles (H⁻ ions);

- Bunches in each experimental area must be separated by either 12.4, 24.8, 49.6, or 99.2 ns (80, 40, 20, 10 MHz);
- The bunch patterns must repeat every 1.0 μ sec;
- The total current, summed over the three experimental areas, must be 1 mA averaged over the 1.0 μ s period.

An example is given in the body of this report (Figure II-2 and Figure II-3).

I.2 Booster Upgrades for Stage 1

The Booster synchrotron will require modification for its role in Project X Stage 1 where it acts to accelerate the 1 GeV beam to 8 GeV so it can be injected into the Recycler and ultimately the Main Injector. Major items of consideration are:

- The ultimate intensity limitations within the Booster.
- The new transfer line and injection insertion for bring the 1 GeV H⁻ beam into the Booster.
- Changes to the RF system to accelerate the increased beam current.
- Beam loss control and shielding to allow operation.
- Consideration of replacement of various components as they become aged or outdated.

The Booster accelerated its first beam to 8 GeV on May 21, 1971. When Project X begins operation it is likely that the Booster will be at least 50 years old. Many items in the Booster have been replaced over time, but several significant legacy systems remain including: the main magnets, much of the RF cavity system, the support girders, and the enclosure itself. Each of these items is an asset when considering the future, but also a liability.

The Project X Booster upgrades rely on previous upgrade programs to be completed successfully, the Accelerator and NuMI Upgrades (ANU) of the NOvA Project, and the Proton Improvement Plan (PIP). ANU is nearly complete (as of spring 2013) and concentrates on the Main Injector and Recycler. PIP is primarily concerned with the Proton Source, including the Booster and Linac. The PIP upgrades are a vital prerequisite for the Project X upgrades. PIP will act to significantly increase the repetition rate and intensity limits in the Booster; it will also address legacy issues, particularly the main RF cavities.

Booster Intensity Limitations

The ultimately achievable Booster beam intensity depends on several factors. The first and most apparent is the space charge limitation. The Booster beam experiences a force from its own electromagnetic field, distorting the optics in an intensity-dependent way. The primary impact is to cause an amplitude-dependent defocusing that results in a tune spread of the beam particles. This can be represented by a tune spread $\Delta\nu$

$$\Delta\nu = -\frac{\pi\lambda r_0 R}{2\varepsilon_N \beta\gamma^2}$$

where λ is the linear charge density, r_0 is the classical proton radius, R is the radius of the accelerator, ϵ_N is the normalized emittance of the beam, and β and γ are the relativistic parameters. The tune shift rapidly decreases with beam energy, so that a correspondingly larger line density (beam intensity) will result in the same tune shift. From this relationship we find that an intensity increase of a factor of 2.57 (157%) would result in the equivalent space charge tune shift at 1 GeV as at 400 MeV.

However, the above ratio does not fully determine the intensity limit. A larger tune shift at 1 GeV would also produce a larger tune shift through the remainder of the cycle, including crucial times such as transition crossing. Furthermore, the effects of space charge presently lead to beam loss at low energy which cannot be withstood at the Stage 1 injection energy. An equivalent relative loss with Project X would occur at a higher energy and greater proportional intensity. We believe these effects balance out with an increase of Booster intensity of 50% above current operations.

Existing Booster Injection Straight section

The Booster lattice contains 24 periods and can be described as a FoDoDoFo lattice utilizing gradient magnets with long straight sections (5.66 meters) between the defocusing gradient magnets and short straight sections (0.5 meters) between the F and D gradient magnets. Horizontal beta function varies from about 6 meters in the long straight to 33 m in the short straights while the vertical beta function varies from 20 m in the long straights to ~5.3 m in the short straights. The horizontal dispersion varies between approximately 1.8 (in the long straights) and 3.6 meters around the ring. The ring optics are shown in Figure 1.

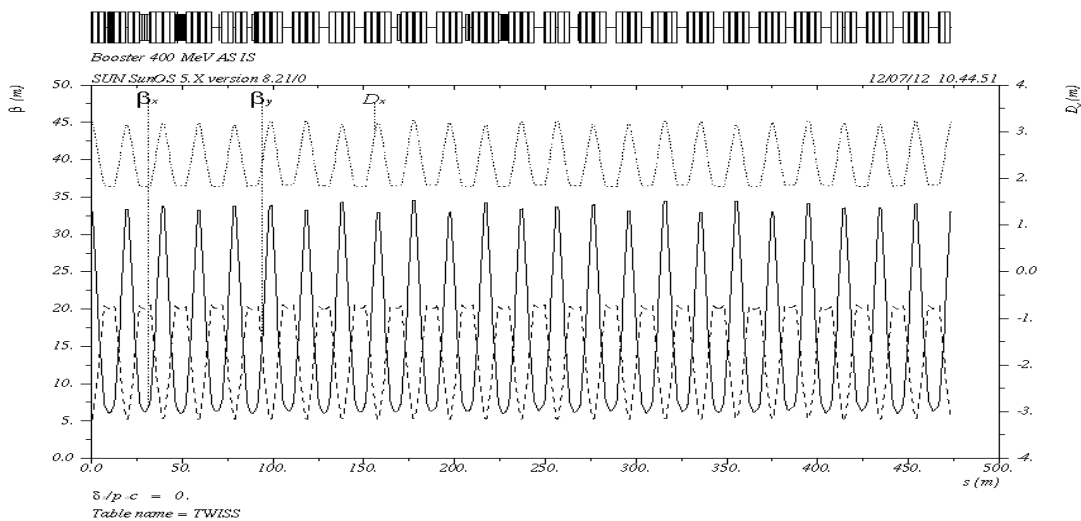


Figure 1: Lattice functions of the current Booster ring (MAD)

The injection straight section is located in the long straight section 01. A new injection design using a three dipole orbit bump magnet system (ORBUMP) was installed in 2006. The lattice functions and horizontal dispersion are shown in Figure 2 and listed in Table 1. The gradient magnets, ORBUMP magnets, and correctors are shown at the top of the figure. This new design, as compared to the original injection system with a septa and 4 chicane magnets, reduced the injection angle, the number of required dipoles, and the required strength of the dipoles by about a factor of two. The center dipole of this insert used to merge the incoming H- on the closed orbit produced by the three dipoles and runs at twice the field (current) as the outer dipoles. The injection foil is located immediately after the middle ORBUMP magnet. The current angle produced by the center dipole is approximately 44 mr which corresponds to an integrated field of 1.4 kG-m. Lorentz stripping in these magnets is not an issue at 400 MeV.

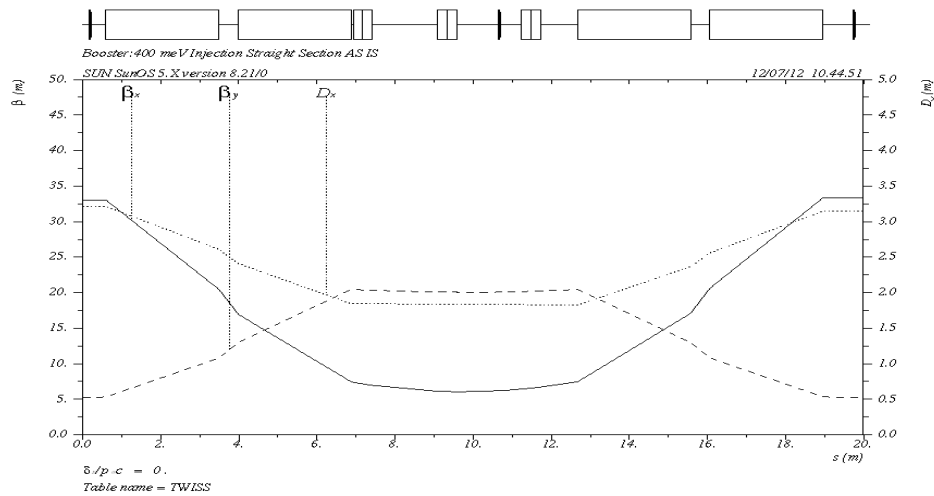


Figure 2: Lattice functions of the current Long 01 injection straight.

β_x	4.88m
α_x	0.049
β_y	18.52m
α_y	0.011
D_x	1.73
D'_x	-0.003

Table 1: The current lattice functions at the foil.

New pulsed ORBUMP magnets were designed to be capable of continuous operation at 15 Hz and at a peak/integrated dipole field of up to (at 15 kA excitation) 3 kG/1.676 kG-m. At 400 MeV this would produce a bend angle of 52.6 mr. A cross section of the magnet is shown in Figure 3.

The ORBUMP displaces the closed orbit during injection by approximately 45 mm at the location of the foil. The edge of the foil is placed at approximately 32 mm. Figure 4 shows a 6σ beam envelope for a normalized emittance of 16π -mm-mr. In the current design, the unstripped H-, protons, and neutrals follow the same trajectory until they enter the third ORBUMP magnet. This dipole places the protons on the Booster central trajectory while the H^0 continue undeflected until they hit the radial outside of the second downstream gradient magnet. The H- are initially deflected inward by the third dipole, but then deflected radially outward, crossing the closed orbit by the gradient magnets and are also deposited on the radially outside of the second gradient magnet.

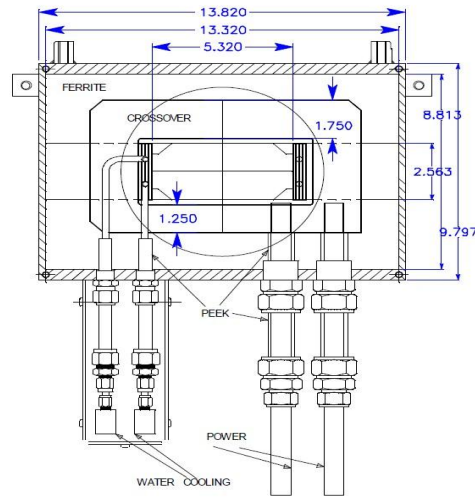


Figure 3: Cross section of the Booster pulsed ORBUMP magnet.

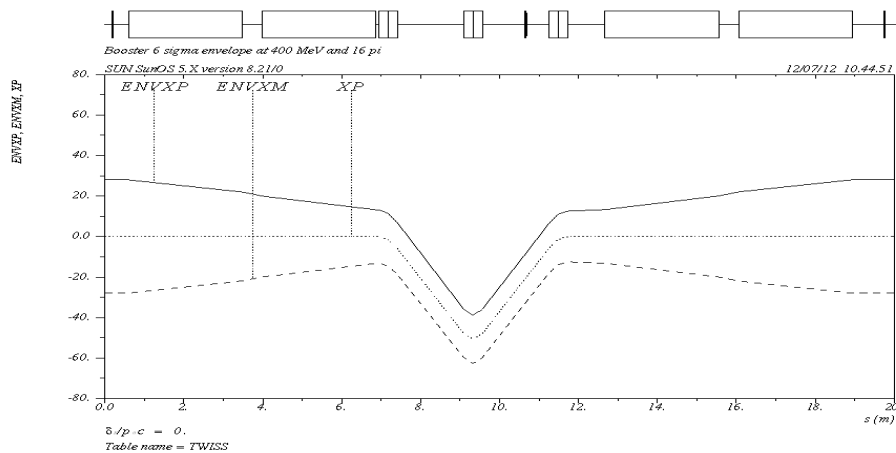


Figure 4: The horizontal 6σ beam envelope for a 16π -mm-mr 95% emittance showing the closed orbit due to the ORBUMP dipoles. The injection foil is located approximately 4.5 inches downstream of the middle bump magnet.

The injection foil changer, pictured in Figure 5, has the capability of holding up to 8 foils.

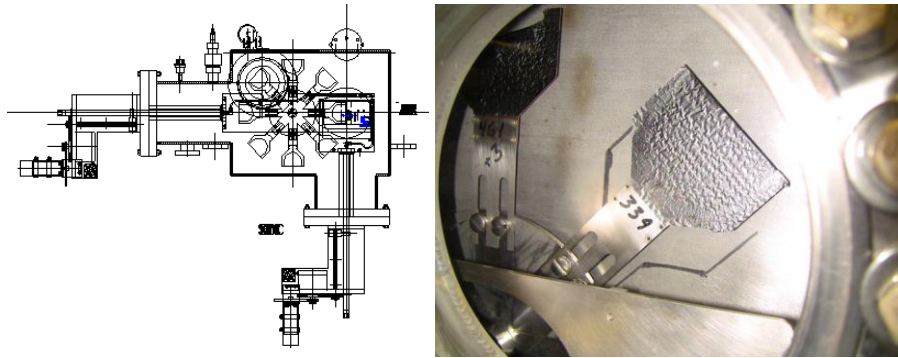


Figure 5: Current Booster injection foil changer and foil.

The expected stripping efficiency for the production of protons at 400 MeV, according to scaled Gulley parameters, for a carbon stripping foil of thickness $380 \mu\text{g}/\text{cm}^2$ ($\sim 1.15 \mu\text{m}$) is 99.9% which means that only 0.1% of the beam exits the foil as excited states of H^0 . The majority of these states will be in the lowest states, will not be stripped, and end being lost in the second downstream gradient magnet on the aisle side. In addition, any H^- leaving will get bent to the radial inside of the ring by the third ORBUMP magnet and any that enter the downstream gradient magnet will get bent to the outside of the ring and be lost in the downstream gradient magnets. Two loss points, one for H^- and the other for H^0 have been identified on the aisle side of the second gradient magnet downstream of the injection straight. With an average injection intensity of $5\text{E}12$ ions/cycle at a 7.5 Hz repetition rate the injected beam power is 2.43 kW. If 0.1% of the beam is lost due to incomplete stripping, this would correspond to approximately 2 W of beam loss at these two locations. Radiation surveys of these locations upon turning the Booster off show on the order of a few R “on-contact”. At the 1 GeV injection energy and a 15 Hz repetition rate and $7\text{E}12$ injected/cycle, the injected beam power rises to 16.8 kW and for 99% stripping efficiency and one is looking at a loss of 170 Watts or a factor of 8.5 increase in “on-contact” residual activity. A better solution for handling and safely disposing of the unstripped injected H^- will be incorporated into the new design.

The current injection into Booster utilizes a linac pulse length equivalent to 1-10 turns (~ 2.2 us/turn) and does not utilize any transverse phase space painting. The transport line is “matched” to the ring lattice functions and therefore the linac transverse emittance defines the “base” emittance of the beam in Booster. To this is added any emittance growth due to lattice, dispersion, or trajectory mismatch and scattering in the foil. The average scattering angle is only $33 \mu\text{r}$. The current 95% normalized emittance of the Booster beam at extraction is on the order 12 to $16 \pi\text{-mm-mr}$.

Injection at 1 GeV

Stage 1 of Project X will increase the injection energy of the current Booster to 1. The average current of the new CW linac is 1 mA over a period of 1 ms (Stage 1, rising to 2 mA over 0.5 ms in Stage 2).

To meet the proton intensity out of the MI/Recycler of $7.5E13/\text{cycle}$ requires Booster to provide $6.5E12/15\text{Hz}$ cycle, assuming a 95% slip stacking / acceleration efficiency in MI/RR. Assuming a 90% injection and acceleration efficiency in Booster, the linac must inject $7.3E12/15\text{Hz}$ cycle. If we assume a chopping factor of 50%, the peak linac current will be required 2 mA.

Booster Geometry for 1 GeV

We are currently evaluating utilization of the present long straight section in the Booster for injection at 1 GeV. It should be noted that the 1 GeV injection straight section for SNS is 12.5 m between quadrupoles and they utilize a 4 dipole chicane for injection. A secondary foil is utilized to convert any neutrals or H- that miss the foil to protons and transport them to an external dump. As noted above, the current Booster long straight section is 6 m between gradient magnets and does not contain an external dump for the neutrals or H- that miss the foil.

Two possible geometries for the injection chicane are a three dipole chicane, as in the current Booster implementation, and a four dipole chicane as utilized at SNS and the default design for H- injection into the Recycler. In addition there are two potential injection orientations, horizontal and vertical.

To determine if the existing ORBUMP magnets could be utilized for 1 GeV operation we scale the central ORBUMP magnetic field by the ratio $\beta\rho_{1G}/\beta\rho_{0.4G}$, and the required integrated dipole field of the central magnet becomes ~ 2.5 kG-m for the existing magnet steel length of 0.4823m (effective length of 0.5585m). This would correspond to a field of ~ 4.5 kG, about 50% greater than the current magnet design field. This indicates that the current three bump design would not work with the existing ORBUMP magnets. Increasing the (effective length) to roughly 1 m (physical length 0.86 meters) or using 2 of the existing ORBUMP magnets for the central bend brings the magnet strength back down to ~ 2.5 kG, well within the design parameters of the existing magnets. During the construction of the chicane magnets the asymmetry in stripline leads contribute to a significant quadrupole term such that the project should consider the construction of new dipoles.

A four-dipole design reduces the required strength of the center dipole as the chicane essentially consists of two “dog-leg” bumps with the stripping foil located between the two central dipoles. If the injection offset remains at 45 mm, then the required angles for all chicane magnets is roughly 22 mr. At 1 GeV this corresponds to an integrated strength of ~ 1.25 kG-m or a field of roughly 2.2 kG, well within the design of the existing magnets. In this scenario, the H^0 would

pass undeflected through the third chicane dipole and the unstripped H⁻ would be deflected in the opposite direction of the protons. This geometry requires the incoming H⁻ trajectory to be at an angle of 22 mrad with respect to the Booster straight section. This injection trajectory of the H⁻ entering the second ORBUMP magnet (for merging the H⁻ onto the circulating orbit) would need to miss the upstream gradient magnet which has a half-width of roughly 9 inches. Since this second magnet is only a few meters downstream of the gradient magnet a new strong septum magnet would be required for the injected beam to miss this gradient magnet.

Another consideration regarding the geometry of the injection is which injection plane would provide the fewest parasitic hits from the circulating beam on the foil. Current Booster injection is in the horizontal plane where the beta function is a factor of 3.8 smaller than that of the vertical plane. This will lead to a smaller orbit movement during painting injection, thus allowing more time for the already injected protons to impact the foil. In addition, the vertical size of the upstream gradient magnet is only 2/3 that of the horizontal which makes it easier to clear the upstream gradient magnet, in the case of a four dipole design. The selection of the injection plane would also impact the transport line design.

Magnetic Field and Lorentz stripping

At 1 GeV, dipole fields in the 2.5 to 3 kG range would lead to a loss rate due to Lorentz stripping in the range of 10⁻⁷ to 10⁻⁹/m, a negligible loss for the expected injection power of 16.8 kW. Figure 6 shows the loss rate/meter due to Lorentz stripping for 400 MeV and 1 GeV kinetic energies.

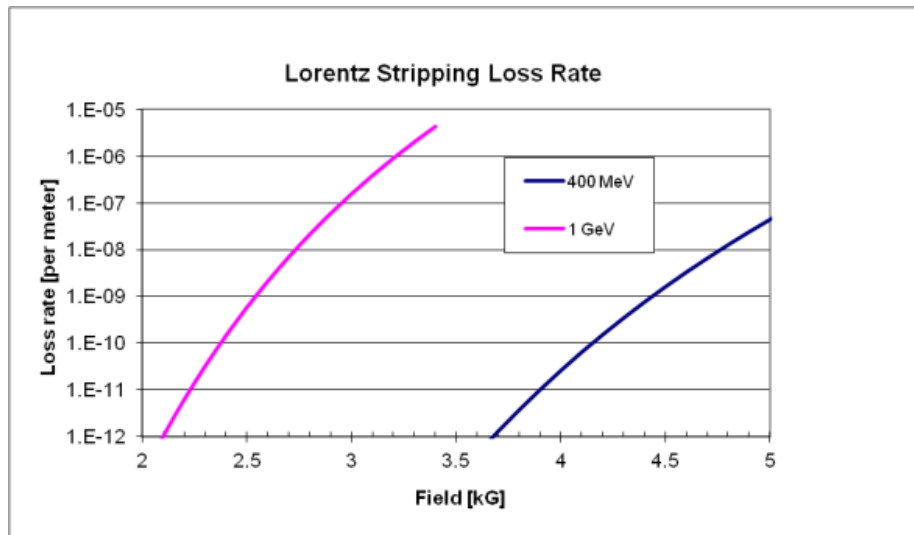


Figure 6: Loss rate due to Lorentz stripping for 400 MeV and 1 GeV H⁻ ions.

Booster straight section modifications

In order to minimize the activation of the downstream magnets by the unstripped H^- and H^0 , it is advantageous to install a well shielded absorber after the injection stripping foil, between the last ORBUMP dipole and the first gradient magnet. Currently, this is not feasible as the space is only $\sim 1/3$ meter in length. However, if the defocusing gradient magnets on either side of the injection straight can be shortened and the space occupied by ORBUMP can be slightly reduced, space can be opened up in which an absorber could be installed.

In order to create additional room for either injection scenario, the two gradient magnets were shortened by 25% (from 2.8896m to 2.167m) and the dipole field and gradients were increased by 25%, while keeping the bend center at the same point. This will increase the straight section by a modest 0.72m. This modification introduced an RMS variation in $\beta_x \sim 0.6\%$, $\beta_y \sim 4\%$, and D_x by $\sim 3\%$. The lattice with this modification is shown in Figure 7.

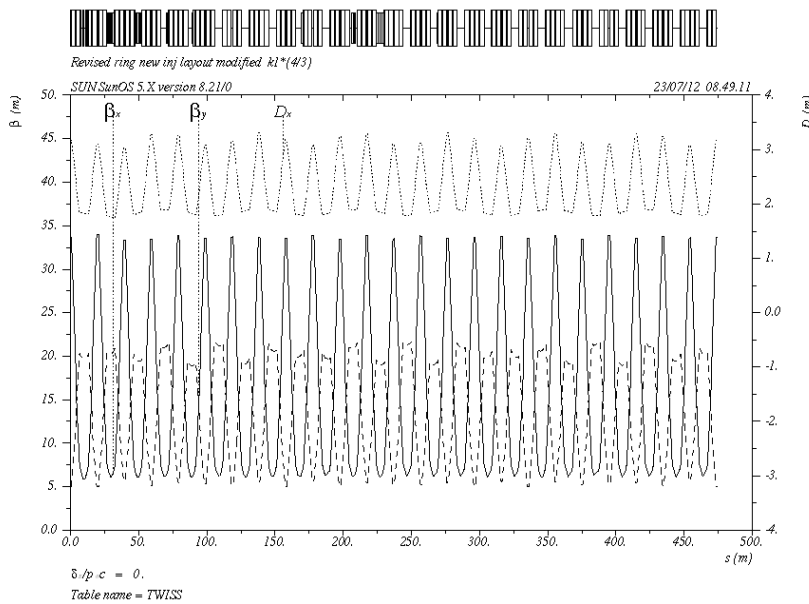


Figure 7: Lattice distortion due to shortening the two D gradient magnets on either side of the straight to $\frac{3}{4}$ length and increasing gradient by $\frac{4}{3}$ keeping bend center fixed.

These errors in $\Delta\beta_x$, $\Delta\beta_y$, ΔD_x may be corrected to a $\sim 1\%$ level by utilizing five quad correctors around the straight section, requiring only a few amps in each, however the correction at high field pushes the correctors close to their maximum. Another technique is to modify the gradient slightly in the two shorter gradient magnets. Reducing this to 98% of the scaled value corrects distortions in both beta functions, but there is a small residual dispersion distortion. These corrections are a first pass solution. Figure 8 shows the result of the lattice with only the ratio of the dipole and gradient adjusted.

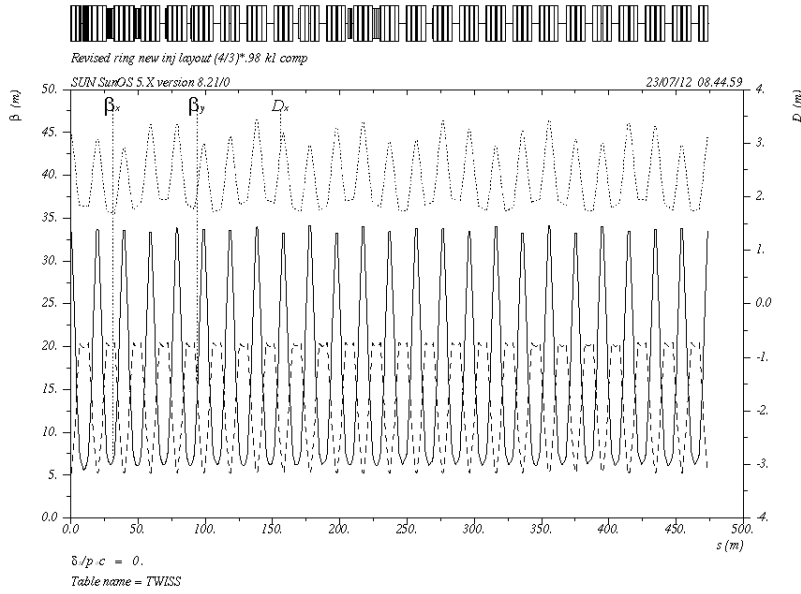


Figure 8: Lattice error from shortened magnet corrected by reducing gradient

Shortening the ORBUMP insert and shortening the adjacent gradient magnets allows the insertion of an absorber capable of shielding the downstream magnets from the unstripped neutral hydrogen atoms and the H^- missing the foil. Figure 9 shows an example of the new layout with the 6σ beam envelope for a 20π normalized emittance of a 1 GeV beam. The face of the absorber is approximately 0.95 m (~ 3 ns) downstream of the last ORBUMP magnet. The absorber with some downstream shielding is shown as a blue block in the figure. The H^0 and H^- trajectories are shown in blue.

According to PSTAR tables the projected range of 1 GeV protons in tungsten is 6.020 g/cm^2 which for a density of 19 g/cm^3 , yields a stopping range of 31.7 cm or 12.5 inches. The current Booster injection straight section was modified in MAD to reduce the adjacent gradient magnet length by 25% and shorten the ORBUMP insert which would allow the insertion of an absorber between the last ORBUMP magnet and the first gradient magnet. This absorber would have the dimensions of approximately 5 cm H x 6 cm W x 35 cm L with the inside edge at about 1.8 cm from the Booster centerline. This would still allow additional 30 cm shielding between the absorber and gradient magnet. Further refinement of the absorber geometry and a MARS simulation for the absorber assembly needs to be done.

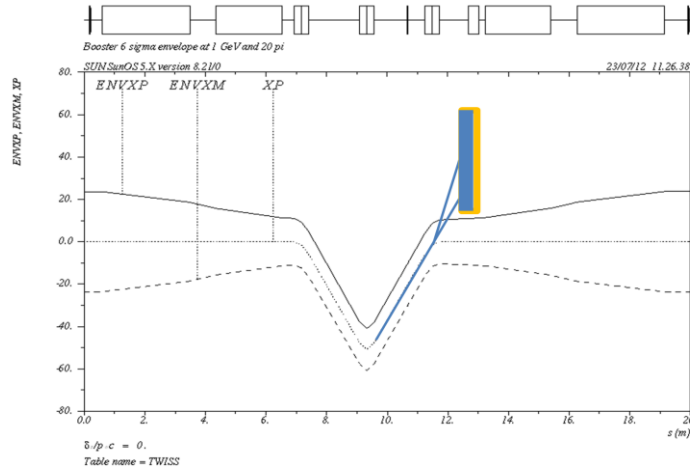


Figure 9: The potential location of an absorber for un-stripped neutrals and H⁻ missing the foil located between the last ORBUMP magnet and the first gradient magnet.

The efficiency for converting H⁻ ions into protons depends on the ion energy (velocity) and foil areal density (thickness). Figure 10 shows the yield of protons and the first two states of neutral hydrogen for 800 MeV and 1 GeV. The 1 GeV estimate is scaled from the 800 MeV predictions. The red curve contains the yield for the first three states of H⁰. Table 2 summarizes the values for a 500 $\mu\text{g}/\text{cm}^2$ carbon foil. The yield of states $n \geq 4$ is not tabulated here, but the $n=4$ state is roughly a factor of 2 less than $n=3$ and the yield of the higher order states drop rapidly. So, essentially only the first few excited states are of interest. All of these states are stable in the absence of an external magnetic field. In the proposed configuration the stripping foil is after ORBUMP 2 magnet, in the decaying field. The third ORBUMP magnet has a peak field of roughly 1.5 kG. Figure 11 shows the lifetime of the Stark States of neutral hydrogen as a function of magnetic field. We see that the field of 1.5 kG is in the middle of the $n=5$ stark states. All lower states will not be stripped. With the position of the absorber it will intercept all H⁰ and H⁻ (that miss the foil).

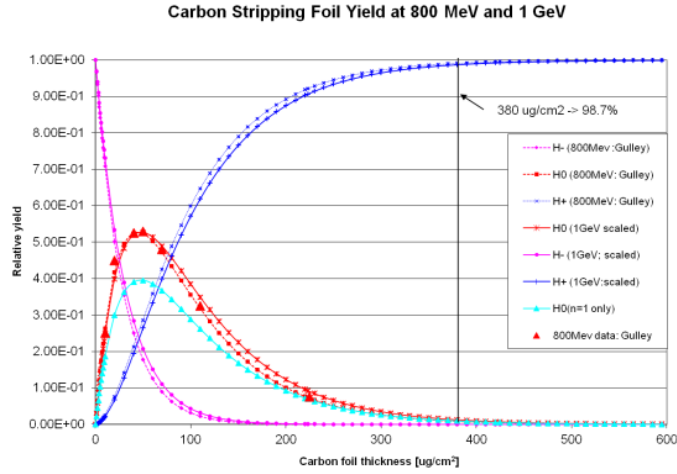


Figure 10: Stripping yield as a function of carbon foil thickness for 800 MeV data and scaled to 1 GeV.

State	Fraction
H ⁺	99.7%
H ⁻	9E-6%
H ₀ (n=1)	0.2%
H ₀ (n=2)	0.07%
H ₀ (n=3)	0.02%

Table 2: Estimates for production of the first few excited states of hydrogen from 1 GeV H-interacting with a carbon foil with thickness of 500 $\mu\text{g}/\text{cm}^2$.

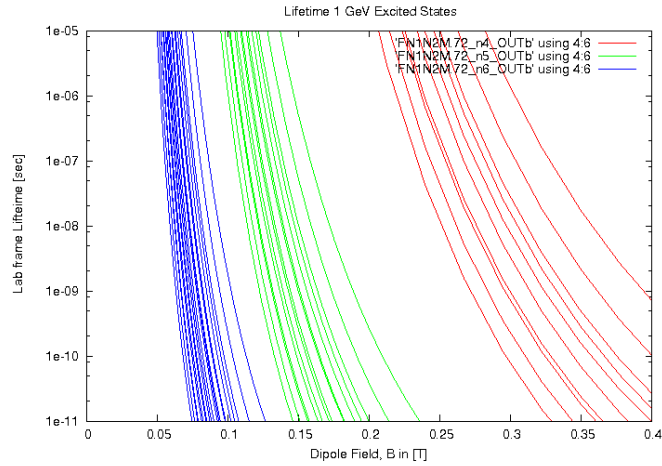


Figure 11: Lifetime of excited states with $n=4, 5,$ and 6 of hydrogen at 1 GeV.

Transverse phase space painting

The expected 95% normalized emittance of the 1 GeV linac is on the order of 1.7π -mm-mr. The design final emittance of the painted beam in the Booster is 20π -mm-mr or a ratio of 0.085 . There are two main options for performing transverse phase space painting into the Booster, painting in both dimensions in the ring and painting in one dimension in the ring and steering from the beam line in the other dimension. Both of these techniques are utilized in existing machines: SNS paints in both dimensions and JPARC paints and steers. In each of these scenarios the painting algorithms may be either correlated or anti-correlated in direction of painting of small to large or large to small amplitude. In addition, the functional form needs to be optimized to minimize over painting of the phase space as well as producing a KV-like distribution and minimizing the number of parasitic interactions between the circulating protons and the foil.

A Twiss parameter mismatch between the injection line and ring at the point of injection can be useful in minimizing the foil size as well as the number of parasitic hits by matching the orientation of the injected beam within the phase space of the circulating emittance. The first condition assures the injected beam is optimally positioned within the desired beam emittance of the ring and is given by:

$$\frac{\alpha_i}{\beta_i} = \frac{\alpha_r}{\beta_r} = \frac{X'_C - X'_o}{X_C - X_o}$$

where α and β are the standard lattice functions in the injection line (i) and ring (r) and X and X' are the beam position and angle for the injected beam centroid (C) and the closed orbit (o). This effectively demands that the orientation of the injected and circulating be matched as shown in the left hand plots in Figure 12.

The next condition assures the injected beam has the proper aspect ratio.

$$\frac{\beta_i}{\beta_r} \geq \left(\frac{\varepsilon_i}{\varepsilon_r}\right)^{1/3}$$

Given the expected linac 95% normalized emittance of $\sim 1.7\pi$ mm-mr, the final painted 95% normalized emittance in the Booster has been specified to be 20π mm-mr. This is a ratio of 0.085 and allows the definition of the transport lattice functions at the position of the foil to be $\beta_x = 2.1$ m and $\beta_y = 8.0$ m that are optimized for painting in both dimensions in the ring. For the paint/steer option the horizontal injected beam is matched as in the ring painting, but the vertical β for the injected beam needs to be increased to roughly 26m to get a better match. Note that in the paint/steer option that the vertical position of the injected beam remains constant while the angle is varied from large to small during the injection process, hence the vertical angle offset. The two cases are shown in Figure 12.

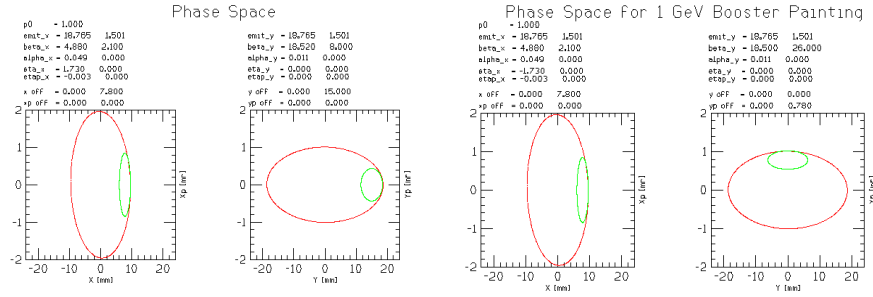


Figure 12: Two phase space painting options. Painting in both planes in the ring (left) and horizontal painting and vertical steering (right).

The usual injection orientation is to inject in the horizontal direction. However, in the Booster the horizontal beam size is about a factor of three smaller than the vertical. This implies that the rate the beam is removed from the foil is a factor three smaller for the horizontal direction than for the vertical, which leads to greater parasitic beam hits on the foil. The details of various painting options remain to be simulated.

Investigation of injection in the vertical plane using both a three bump chicane and four bump chicane indicate that vertical separation of the neutrals off the foil and the circulating protons is too small before the downstream gradient magnet to allow the insertion of an injection absorber. However, if the geometry of the injected beam can be arranged to miss the upstream ORBUMP magnet and gradient magnet, then this geometry would allow an injection absorber to be installed just upstream of the last chicane dipole. Here, we move the first and last chicane dipoles as far out as possible and center the central chicane dipoles with the foil between them.

Foil Issues

The thickness, geometry, mounting and orientation of the injection foil will be dependent on the particular painting scenario adopted.

The objective in selecting the foil thickness is to maximize the stripping probability while minimizing the losses due to secondary hits from the circulating protons. Thicker foils maximize the probability of stripping thus reducing the amount of unstripped H^0 that the injection absorber must dispose but increase losses from circulating beam hits. So the strategy will be to minimize losses due to each mechanism.

There are two classes of beam power related to foil heating. The first is where the linac injects a high current beam for a small number of turns and the second is where the linac current is low and requires many more turns to accumulate the required charge in the synchrotron. Stage 1 of the Project X will inject a low current (1 mA average) from a CW linac for 600 turns. In this scenario, most of the foil heating will be due to parasitic hits from the already circulating beam. The single pass injection will be only a small component. The parasitic hit density is determined by the specifics of the foil size and geometry and on the particular painting algorithm used. We can get an estimate of the minimum number of hits per proton by

$$h_{min} = \frac{1}{4} N_t \left(\frac{\varepsilon}{A} \right)^{\frac{4}{3}}$$

where N_t is the number of injection turns, ε is the injection beam emittance and A is the final painting emittance. For the given values of the injection and Booster emittance and assuming 600 turns, the minimum number of hits is 5.6/injected proton.

The injection beam power is 17.5 kW. If 1% of this beam remains un-stripped at injection, an average power of 175 W would be deposited into the injection absorber.

Booster Injection Energy

In order to accumulate the required intensity in Booster, the injection period needs to be on the order of 600 turns. At 1 GeV the revolution period is approximately 1.78 μ s which yields an

injection time of about 1.1 ms. Several scenarios have been discussed on how to handle this long injection time in a ring operated as a resonant circuit at 15 Hz. The current in the dipole bus, thus energy, goes as

$$I(t) = I_{inj} + dI \sin(2\pi ft)$$

where I_{inj} is the current at injection, dI is the differential current between injection and extraction, and f is the Booster repetition rate of 15 Hz. One option discussed is to start injection 500 μ s before the minimum field and end injection 500 μ s after, on the Booster ramp. Here the linac energy and Booster RF frequency would track the change in momentum due to the Booster ramp to keep the central orbit centered. The other option would create an injection front porch such that the energy remains constant during injection. An initial model of a single Booster magnet cell indicates that it is possible to flatten the injection front porch to on the order of a millisecond. This has not been applied to the model of the full ring and no design exists of such. This will require dedicated time for such activity.

Chopping patterns

At 1 GeV, the RF frequency in Booster for a harmonic $h = 84$ is 46.46 MHz. The ratio of the linac bunch frequency (162.5 MHz) to the Booster is 3.497. Figure 13 shows the Booster RF voltage as a function of time in red. The impulses (blue) represent the 162.5 MHz linac bunch spacing. The negative impulses represent empty linac beam buckets where the bunches have been removed by the chopper. Due to the harmonic ratio being close to half-integer (3.5), the filling pattern is constant during a single turn. Since we are attempting synchronous transfer we need to restrict the phase at which the bunches land within the Booster bucket to less than ± 90 degrees.

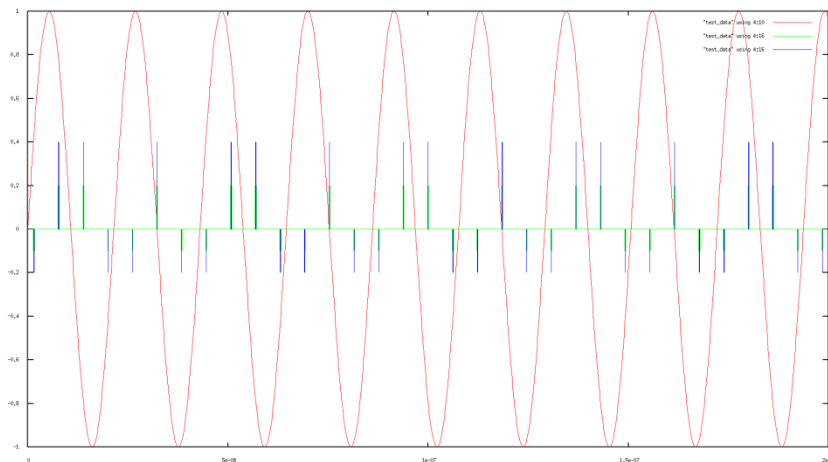


Figure 13: Booster RF and linac bunches injection scheme.

With this chopping pattern and an even harmonic number, alternate Booster buckets will be filled unevenly over the full injection time. To remedy this, the harmonic number of Booster, and

hence the Recycler and Main Injector may be changed by ± 1 such that Booster buckets will be filled alternately by one or two linac bunches on alternate turns which means that two turns would be needed to inject 3 bunches into each bucket (see Table 3). For a fixed number of injection turns the peak linac intensity would have to be increased by 3/2 above the 1 mA average. Longitudinal painting in phase would be required, on a turn by turn basis, in order to spread out the bunch distribution inside the Booster bucket.

Preliminary ESME simulations have been performed utilizing a stationary bucket for three RF configurations, fundamental frequency only, fundamental+2nd harmonic, and fundamental+3rd harmonic while restricting the phase at which linac bunches can be injected. The injected distributions are then accelerated. One finds that restricting the injection phase to $\pm 60^\circ$ allows 97% of the beam to survive to transition for the case of the fundamental + 2nd harmonic.

h	Booster			Recycler	
	E _{inj} [GeV]	f _{inj} [MHz]	f _{ext} [MHz]	f _{inj} [MHz]	f _{ext} [MHz]
83	1.075	46.421148	52.1775	52.182963	52.47129
84	0.995	46.426612	52.8061	52.81167	53.10348
85	0.925	46.421980	53.43479	53.44039	53.73566

Table 3: Impact of harmonic number choice on RF frequency

Harmonic RF Systems

The addition of a 2nd or 3rd harmonic RF cavity system will promote more efficient capture, acceleration, and transition-crossing in the Booster. Without increased efficiency of those processes the losses will be too great within the Booster enclosure. This section explores the application of these harmonic systems.

RF for Injection and ramping

Injection at 1 GeV in Project X stage 1 will take about 1 ms (613 turns) The Linac bunch frequency at injection is 162.5 MHz while the Booster RF frequency at 1 GeV is 46.47 MHz. Therefore, there must be three Linac bunches injected into one single Booster RF bucket at each turn in order to meet the intensity requirements. However, complications arise because the Linac RF and the Booster RF are not integer multiples and so phase locking is not possible. Each injection will be at a random Booster RF phase and so after 1 ms of continuous injections, the bucket will be completely full. To maintain the high injection efficiency and minimize losses, injection into a stationary Booster RF bucket is needed. Since the Booster has a continuous

sinusoidal ramp during injection, a stationary bucket can be created if the following relation is satisfied:

$$\frac{\dot{f}}{f} = \alpha \frac{\dot{B}}{B}$$

where f is the RF frequency and B is the magnetic field and the differentials \dot{f} and \dot{B} are with respect to the time variable t . For the Booster, the momentum compaction factor $\alpha = 0.072$. If the injection starts $500 \mu\text{s}$ before the minimum B field and finishes $500 \mu\text{s}$, then the RF frequency change is approximately:

$$\Delta f = \left[\left(\frac{B}{B_0} \right)^\alpha - 1 \right] f_0$$

If $B/B_0 \cong 1.004$, then $\Delta f \approx 13.36 \text{ kHz}$. And during this time, the synchronous radius changes by the following amount:

$$\Delta R \cong R_0 \alpha \frac{\dot{B}}{B_0} t$$

With $R_0 = 75.47 \text{ m}$, $\dot{B}/B_0 \cong 15.54$, $\Delta R \approx 42 \text{ mm}$, which means the average aperture needed is about 42 mm at injection. For stationary injection capture, the minimum RF voltage required for a given beam energy spread is shown in Figure 14. If the maximum injection energy error is $\pm 1 \text{ MeV}$, then the minimum voltage is about 40 KV .

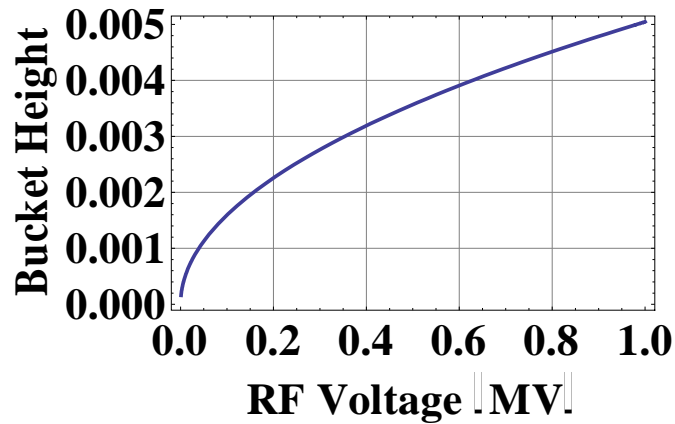


Figure 14: The minimum RF voltage required for given beam moment spread.

If the Linac can deliver over 3.6 mA peak current, chopping can be applied to the Linac beam so that two bunches are injected per bucket. However, bunch patterns will need to be programmed per turn so that each injected single or pair of bunches are within $\pm\theta$ degrees of the bucket. Figure 15 shows the injection distribution when one or two bunches are injected and confined to $\pm 90^\circ$ of the bucket. There is a double hump in the injected beam distribution because two bunch injections can only be supported in certain ranges of longitudinal phase. The beam distribution at the end of injection is shown in Figures 16-18.

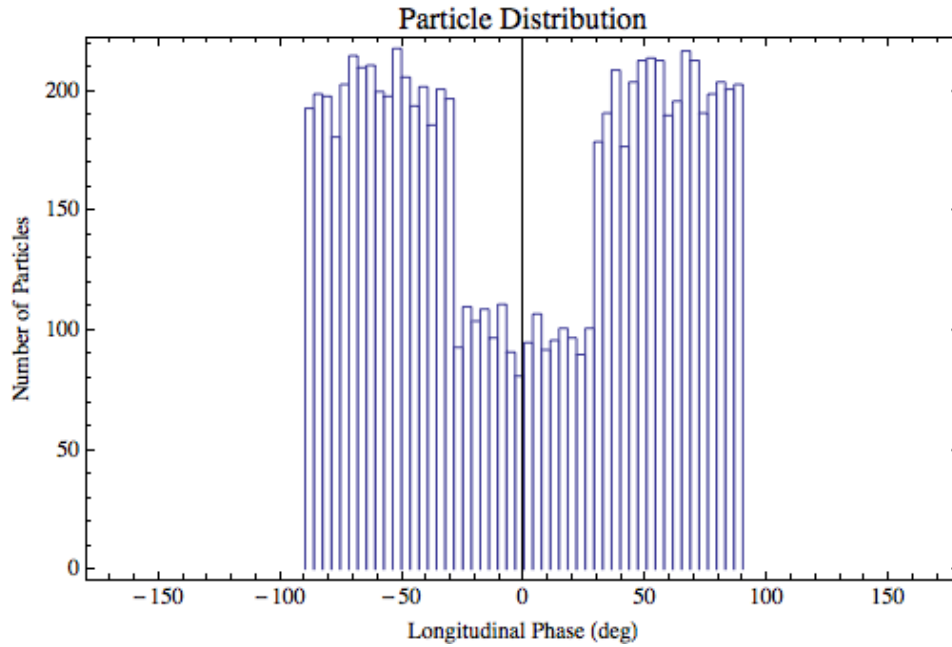


Figure 15: The longitudinal phase distribution that is injected into Booster. (Note: this is not the phase space projection onto the phase axis but is how the bunches will be injected). The chopped beam has been confined to $\pm 90^\circ$ of the bucket and each injection consists of either 1 or 2 bunches.

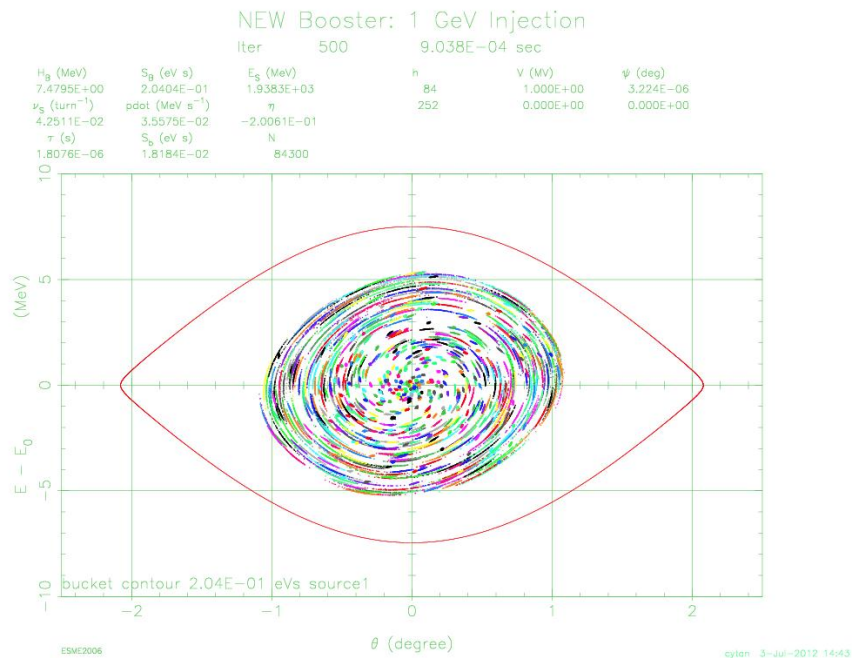


Figure 16: The phase space at the end of injection. The projections in longitudinal phase and energy are shown in Figures 17 and 18.

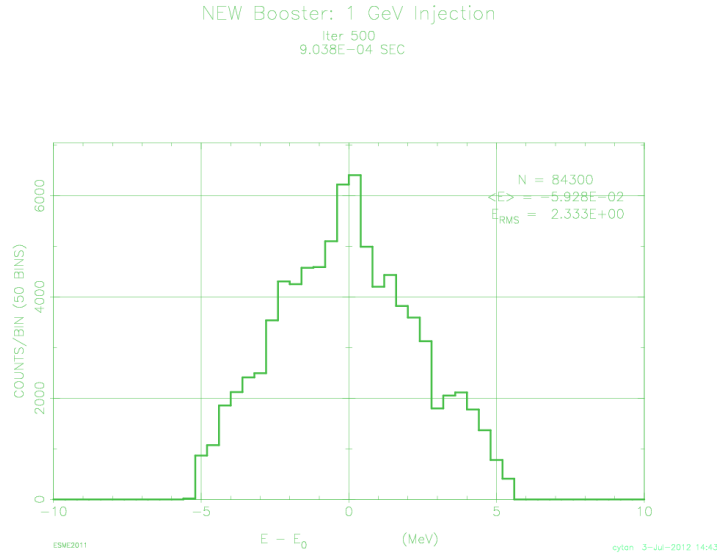


Figure 17: The particle distribution projected onto the energy axis.

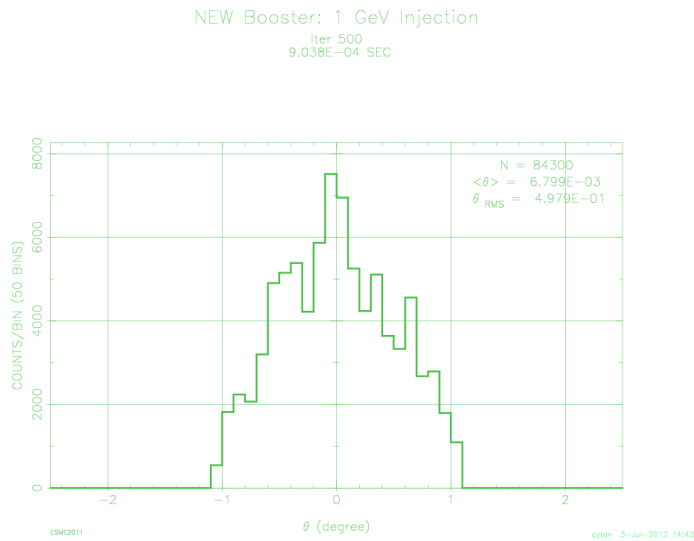


Figure 18: The particle distribution projected onto the phase axis.

2nd harmonic RF at injection

The addition of a 2nd harmonic RF system can be used to flatten the bucket so that the energy spread is reduced. Figure 19 shows the result of the flattened bucket with the second harmonic at 50% voltage and phase shifted by 180° with respect to the fundamental. The beam distribution is for ±90° chopped beam. Table 4 summarizes the transmission efficiency from the start of ramp to just before transition for different size chopped beam. The largest beam loss comes right at the

start of ramp because the stationary bucket is reduced by a factor of 6 when it transitions to an accelerating bucket.

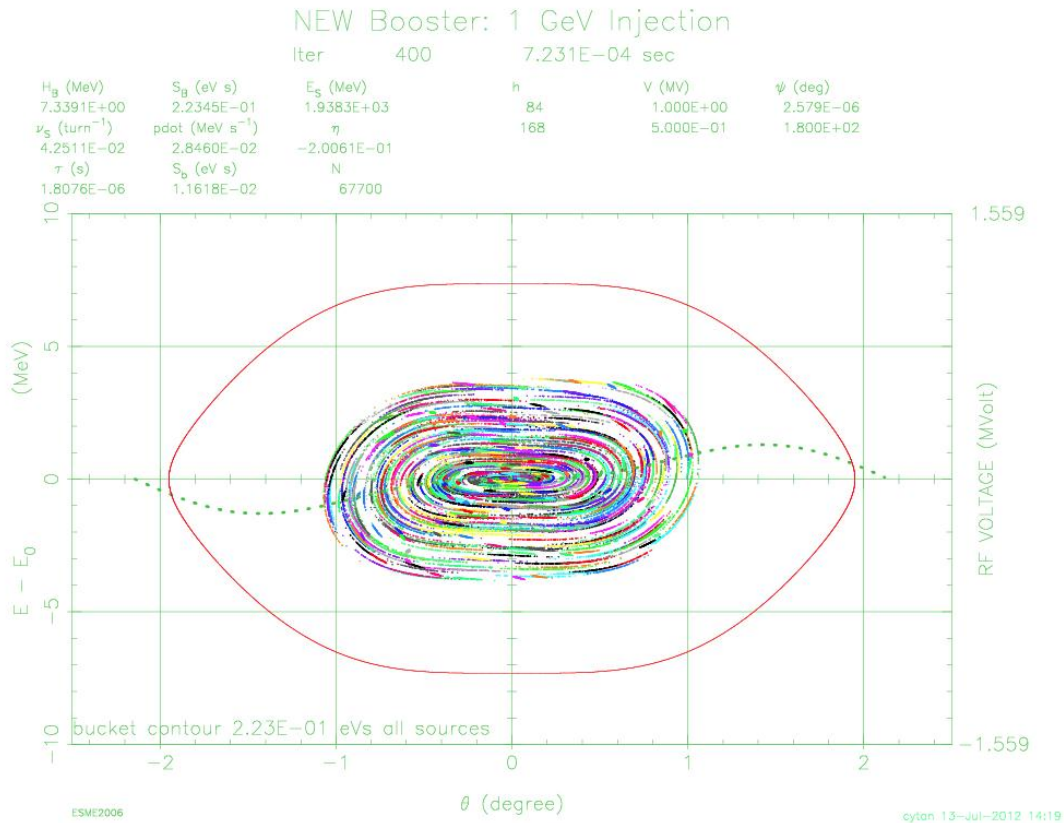


Figure 19: The addition of a 2nd harmonic at 50% of the voltage and 180° out of phase with respect to the fundamental flattens the bucket and compresses the energy spread of the beam as it evolves in the bucket during injection. The picture shown here is for ±90° chopped beam.

3rd harmonic RF at injection

A third harmonic RF system can be used instead of the 2nd harmonic to flatten the bucket. Compared to the 2nd harmonic, the transmission efficiency from the start of ramp to just before transition is worse. However, for ±60° chopped beam, the hit in efficiency is small – see Table 4. There are two advantages in using a 3rd harmonic system rather than a 2nd harmonic system

- The voltage required to flatten the bucket is 35% of the voltage of the fundamental compared to 50% of the voltage of the fundamental for the 2nd harmonic.
- If a 3rd harmonic system is required at transition then the cost of using it at injection is minimal.

Figure 20 shows the flattened bucket with a 3rd harmonic system at 35% and 180° out of the phase with respect to the fundamental. The beam distribution is for ±90° chopped beam.

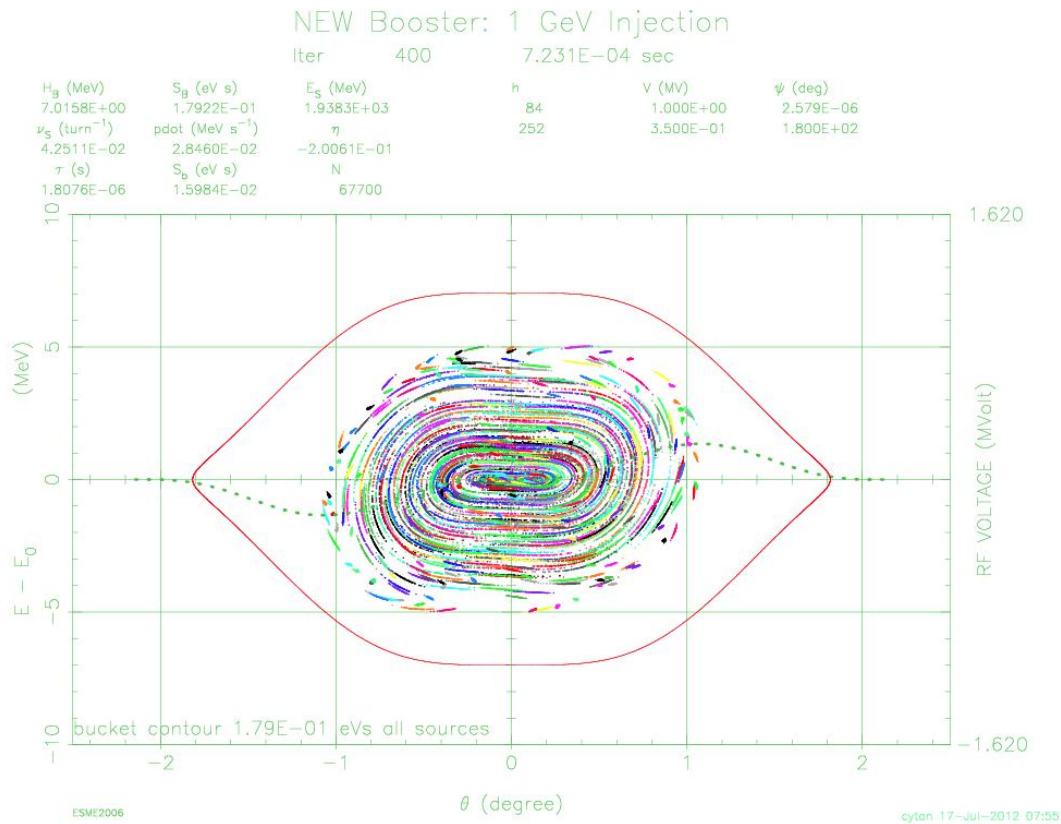


Figure 20: The addition of a 3rd harmonic at 35% of the voltage and 180° out of phase with respect to the fundamental. The bunch distribution is flattened but not to the extent as the 2nd harmonic system. The picture shown here is for ±90° chopped beam.

Transport efficiency from the start of ramp to the beginning of transition

The ramp used here is the biased sinusoid defined as KURVEB=3 in ESME. During the ramp, higher harmonics are turned off. In the simulation, beam falls out of the bucket at the start of ramp because the stationary bucket is much larger than the accelerating bucket. In this simulation, with the higher harmonics off, the bucket area just before the start of ramp is 0.2 eV-s, while at the start of ramp, the bucket area is 0.03 eV-s, i.e. more than a factor of 6 smaller.

Table 4 summarizes the results for the cases when only the fundamental RF, 2nd and 3rd harmonics are used at injection. In the case of the 2nd harmonic, it is set to 50% of the voltage and 180° out of phase with respect to the fundamental. In the 3rd harmonic case, it is set to 35% of the voltage and 180° out of phase with respect to the fundamental.

It is clear from this table that the beam must be chopped and that the 2nd harmonic has a better performance than the 3rd harmonic in terms of transmission efficiency. However, there are other considerations for using the 3rd harmonic, particularly transition crossing.

Size of chopped beam	Transmission Efficiency
Fundamental RF only	
±180°	30%
±90°	52%
±60°	84%
Fundamental + 2nd harmonic RF	
±180°	39%
±90°	71%
±60°	97%
Fundamental + 3rd harmonic RF	
±180°	35%
±90°	60%
±60°	94%

Table 4: Contrasting the ramp efficiencies for the various possible injection scenarios with and without higher order harmonics.

3rd Harmonic RF at Transition

In the Booster, transition crossing is strongly dominated by space charge forces. In this regime, the space charge force is defocusing before transition and focusing afterwards. This causes a mismatch to the bucket and as a consequence, there will be longitudinal emittance growth and beam loss.

Near transition energy in the Booster, partial loss of the focusing force in synchrotron motion can be alleviated by either temporally increase RF voltage just before the transition [54] or by flattening the RF wave [55] via the third harmonic RF system. In the flattened RF wave, all beam particles gain an equal amount of energy at each turn. This is called the focus free transition crossing method [56] and has been demonstrated in the Main Ring for preserving the beam intensity through transition crossing.

Figure 21 shows an ESME simulation carried out by using the FFTC scheme for the Booster transition crossing. In this simulation, the proton beam intensity is at the design value of 8.15E10/bunch with an initial longitudinal emittance of 0.02eV-s. In the figure, the beam emittance is larger for the FFTC scheme (0.059 eV-s) as in (c) than the normal transition without 3rd harmonic RF system (0.045eV-s) as in (a). However, more beam survived in the FFTC

transition (d) than the normal transition (beam survival rate of 96% in (d) compared to 80.5% in (b)).

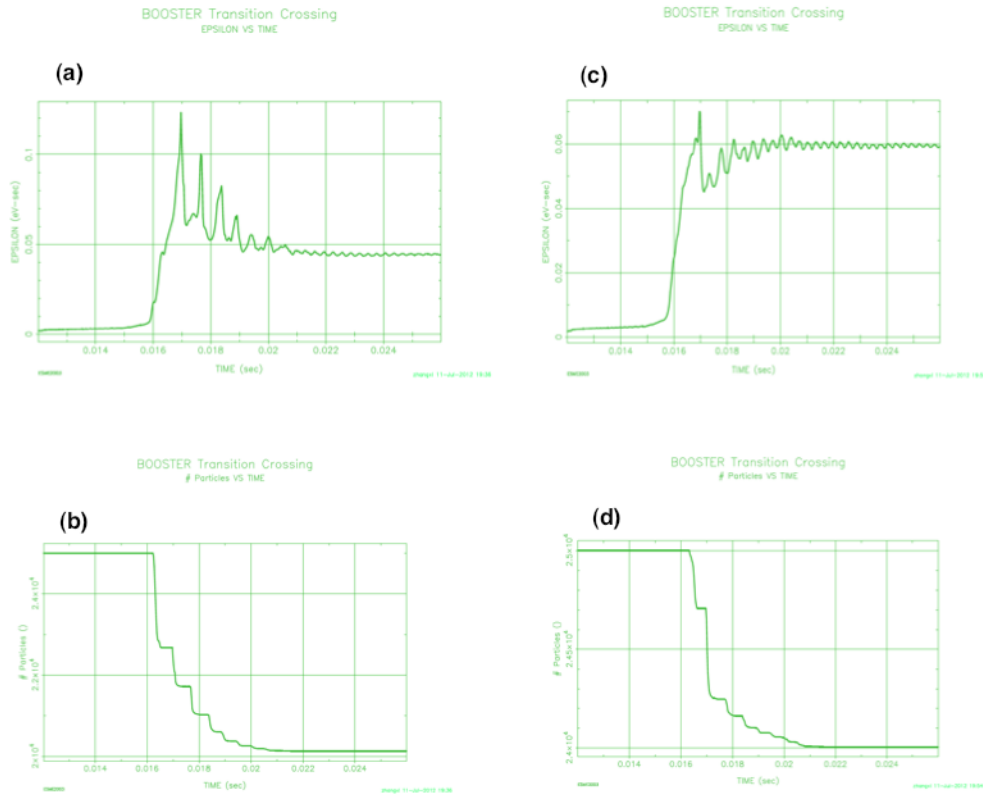


Figure 21: Comparison of the normal transition crossing shown in (a) and (b) with the FFTC scheme shown in (c) and (d).

The paper study was also done using RF voltage jumps for Booster operations with a lower beam intensity of $6E10$ proton/bunch in which the corrections of the beam to bucket mismatch were simulated. It shows that the mismatch can be reduced by two methods:

- 120 kV of 3rd harmonic voltage when applied before and during transition reduces the mismatch. See red traces of Figure 22 and Figure 23.
- At 60 kV, the voltage pattern shown in Figure 22 also reduces the mismatch. See green trace in Figures 22 and 23.

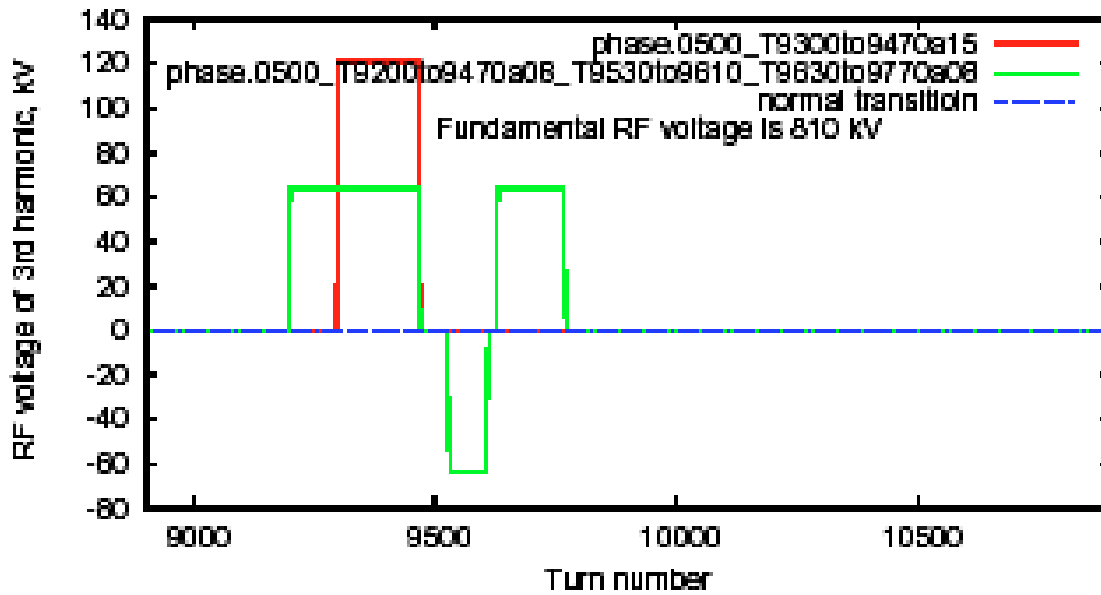


Figure 22: Voltage jumps used in the simulations. The red trace is for 120 kV of 3rd harmonic voltage. It is only applied before and during transition. The green trace is for 60 kV of 3rd harmonic voltage. It is applied before and after transition.

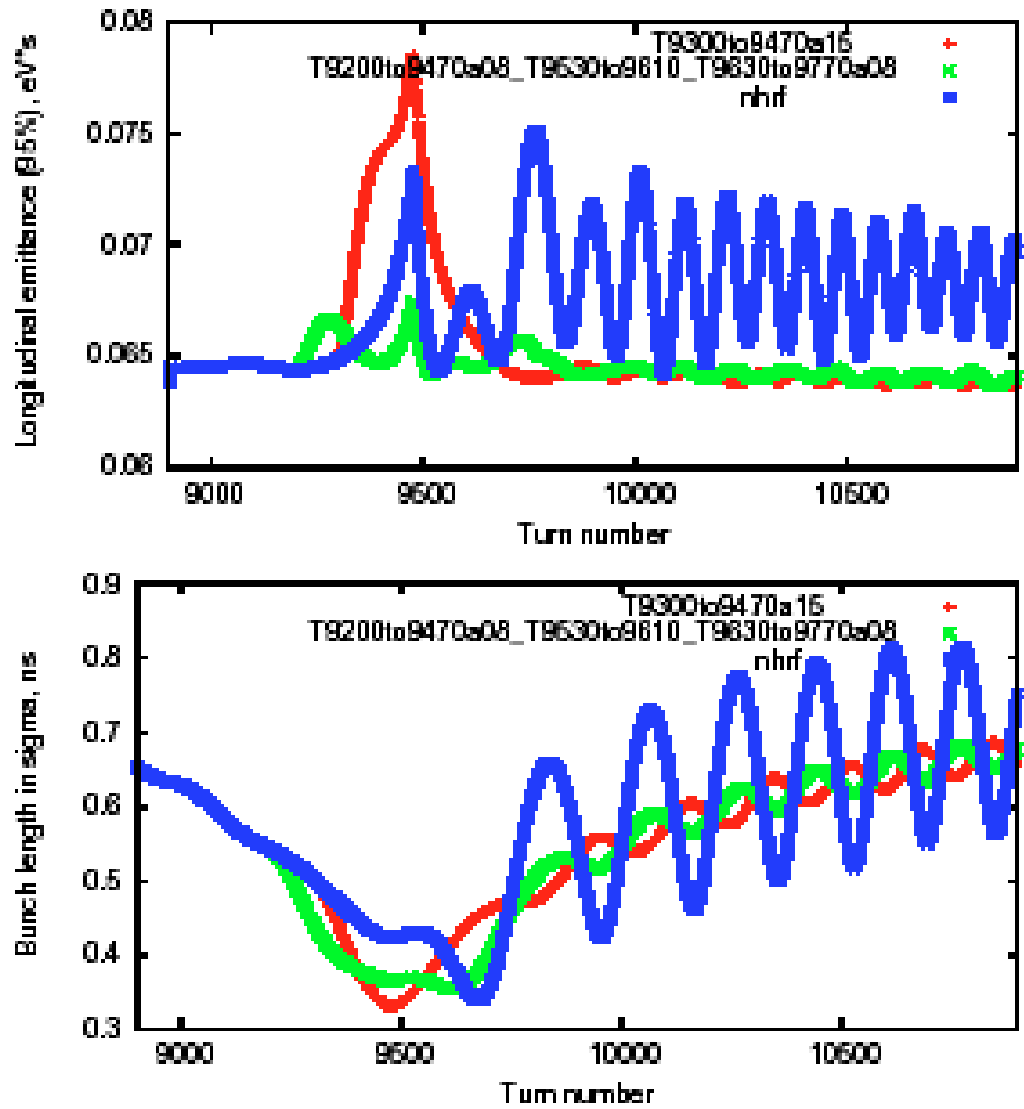


Figure 23: 3rd harmonic at 120 kV (red) and 60 kV (green) compared to no 3rd harmonic (blue). The top graph shows the effect on longitudinal emittance and the bottom graph shows the effect on bunch length.

Appendix II: Possible Performance/Scope Enhancements

Among the four Project X mission elements, the third is “provide a path toward a muon source for a possible future Neutrino Factory and/or a Muon Collider.” To produce the quantities of muons needed for these possible future facilities, 4 MW of proton beam power is required. Fortunately, the number of usable muons (collected by a muon capture system, cooled and accelerated) per unit beam power peaks near 8 GeV. Thus, it is natural to look at increasing the Project X pulsed linac output beam power to provide the proton beam for a possible future Neutrino Factory and/or a Muon Collider. The International Design Study for Neutrino Factory (IDS-NF) has provides a list of requirements [57]. Table 1 shows the IDS-NF proton beam requirements compared to Project X pulsed linac capabilities. The Muon Collider’s requirement [58] is nearly the same as IDS-NF and is also listed in Table 1.

	Project X Capabilities	IDS-NF (Muon Collider) Criteria
Particle	H minus	proton
Beam Energy (GeV)	8	5-15
Average Beam Power (kW)	320	4000
Repetition Rate (Hz)	10	50-60 (12-15)
Bunch Rate	162.5 MHz	--

Table 1: Project X pulsed linac capabilities compared to the IDS-NF and Muon Collider criteria for proton beam.

The final proton beam requirement for the Neutrino Factory and Muon Collider is for a single proton bunch with an rms length of less than or equal to 3 ns to hit the production target at the repetition rate.

II.1 High power at 8 GeV

The order of magnitude increase required in Project X beam power at 8 GeV can be addressed by

- increasing the particles per linac bunch;
- increasing the average beam current in the CW linac; and
- increasing the pulsed linac duty factor and repetition rate.

Table 2 shows how Project X parameters can be enhanced to achieve the greater beam power.

	Initial	Enhancement
# Particles/Linac Bunch (10^8)	1.9	3.8
Ion Source Current (mA)	5	10
Average Beam Current (mA)	1	5
Pulsed Linac Repetition Rate (Hz)	10	15
Pulsed Linac RF Period (ms)	100	66.7
Pulsed Linac Duty Cycle (%)	4.3	10
Pulsed Linac Beam Pulse Length (ms)	4.3	6.67
8 GeV Beam Power (kW)	320	4000

Table 2: Project X operational parameters: initial and enhancement.

The doubling of the number of particles per bunch is achieved by simply doubling the ion source current. The Project X ion source will be capable of delivering 10 mA. The rest of the front end is designed to transport 10 mA as well as the chopper system beam absorber is designed for 25 kW (see Section IV.1.1).

The increase of the ion source beam current is not enough to increase the average linac beam current by a factor of five. The medium energy beam transport section chopper system (see Section IV.1.1) will allow up to half of the beam to exit the front end. The Project X CW linac RF couplers (see Section IV.1.2) will be capable of handling the larger beam current; the couplers may be tuned in the future to optimize the amount of reflected beam power dependent upon the operational physics program that runs in conjunction with a high powered muon facility.

The increased repetition rate and duty factor of the pulsed linac will require more RF power. It is expected that providing the pulsed RF power for ~ 7.5 ms at 15Hz will require 125 kW per cavity. A straight forward solution is to provide each cavity its own Klystron. The pulsed linac RF couplers (see Section IV.3.1), located inside the cryogenic-modules, will have to be replaced with a 15 kW coupler.

The increased pulsed RF power along with increasing the number of RF power sources will have an impact upon the infrastructure concerning the Project X pulsed linac. The power sources will require more floor space; service buildings can be designed to fit the future power sources or so that the buildings can be expanded. More importantly, the RF power conductors will also increase, requiring more penetrations than will initially required; ideally, Project X will be

designed with enough penetrations for the larger number of power conductors. In addition, the increase number of pulsed RF power sources will need additional electrical power and water cooling; both utilities should initially be designed with the possibility of future expansion.

The increased RF pulsed power will also require more cryogenic cooling of the SRF. There will need to be an increase of 65% cryogenic cooling power. The cryogenic plant (see Section IV.5) and associated infrastructure should be designed with possible expansion as a criterion.

The linacs collimation systems and beam aborts will have to be designed (see Section IV.2.1), or replaced in the future, to handle the increased beam power.

II.2 Accumulator rings

If the enhancements to Project X outlined in the previous section are done, then a majority of the Neutrino Factory and Muon Collider criteria in Table 1 will be met. The output of the enhanced Project X pulsed linac will be 4 MW of H minus beam at 162.5 MHz. The ions need to be converted to protons and the linac bunches need to be combined to form a few intense bunches. An accumulation ring will be required.

At a point along the beam transport line between the pulsed linac and the Main Injector enclosure, a new switching magnet will direct the H minus beam into a new transport line. This 8 GeV H minus transport line will have the same physics considerations as the transport line exiting the Project X pulsed linac. The destination of this new transport line will be a new Accumulator Ring. Figure 1 shows a possible implementation of a new Accumulator Ring.

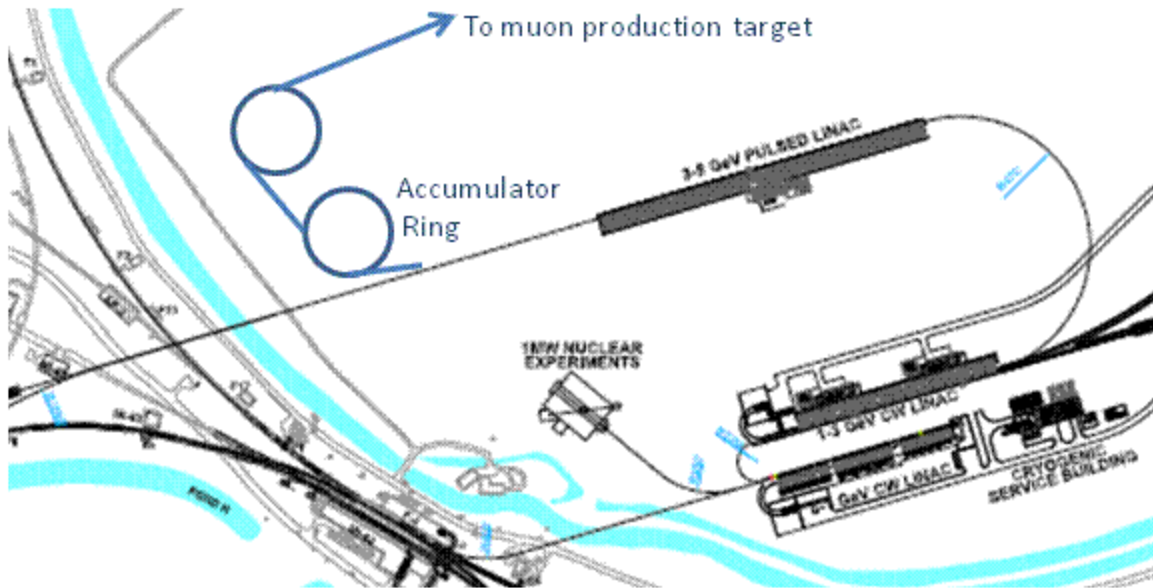


Figure 1: Possible layout of proton rings needed for future Neutrino Factory and/or Muon Collider

The Accumulator Ring will have ion stripping injection and will accumulate linac pulses into predefined RF bunches in the same manner as the Recycler. The main difference is that the ring will be much smaller with only four bunches. The front end chopper system will be programmed to allow half of the linac pulses through Project X and be synchronized to fill the RF buckets (similar to the scheme outlined earlier in II.2). An early design has the Accumulator Ring with a circumference of ~ 300 m [5911]. Initial calculations show the resulting intense proton bunches will be stable.

A challenge will be converting 4 MW of H minus beam into protons. Rotating foil and laser stripping systems will be investigated.

Even with the small circumference of the ring and small number of bunches, bunch rotation will need to be performed to achieve the very short (less than or equal to 3 nsec) bunch length desired for muon production and capture. A second accelerator ring is thought to be appropriate to perform this task as well as final proton beam collimation. The second ring would be located with the muon production and capture system; a proton beam transport system between the two rings would become necessary.

The Neutrino Factory and Muon Collider have different requirements for the repetition rate (see Table 2). The above enhancements result in the Accumulator Ring results in four proton bunches being formed at 15 Hz. Extraction from the Accumulator Ring and the delivery transport lines from the second ring are different for the Neutrino Factory and Muon Collider.

The Neutrino Factory requires proton bunches on target at a rate of 50-60 Hz. After the Accumulator Ring is filled, a single bunch is extracted to the second ring. The single bunch is then bunch rotated and then extracted to the target. At intervals of 16.7 ms, each of the remaining bunches are extracted from the Accumulator Ring, bunch rotated and sent to the muon production target. The resulting proton beam on target is at a rate of 60Hz, appropriate for a Neutrino Factory.

The 15 Hz repetition rate from the pulsed linac is appropriate for a Muon Collider. All four bunches will be extracted from the Accumulator Ring, bunch rotated in the second ring and then all four bunches will be extracted. Each bunch would be directed into a separate beam line. Each transport beam line would be a different length such that the four proton bunches would arrive simultaneously at the target (Figure 2).

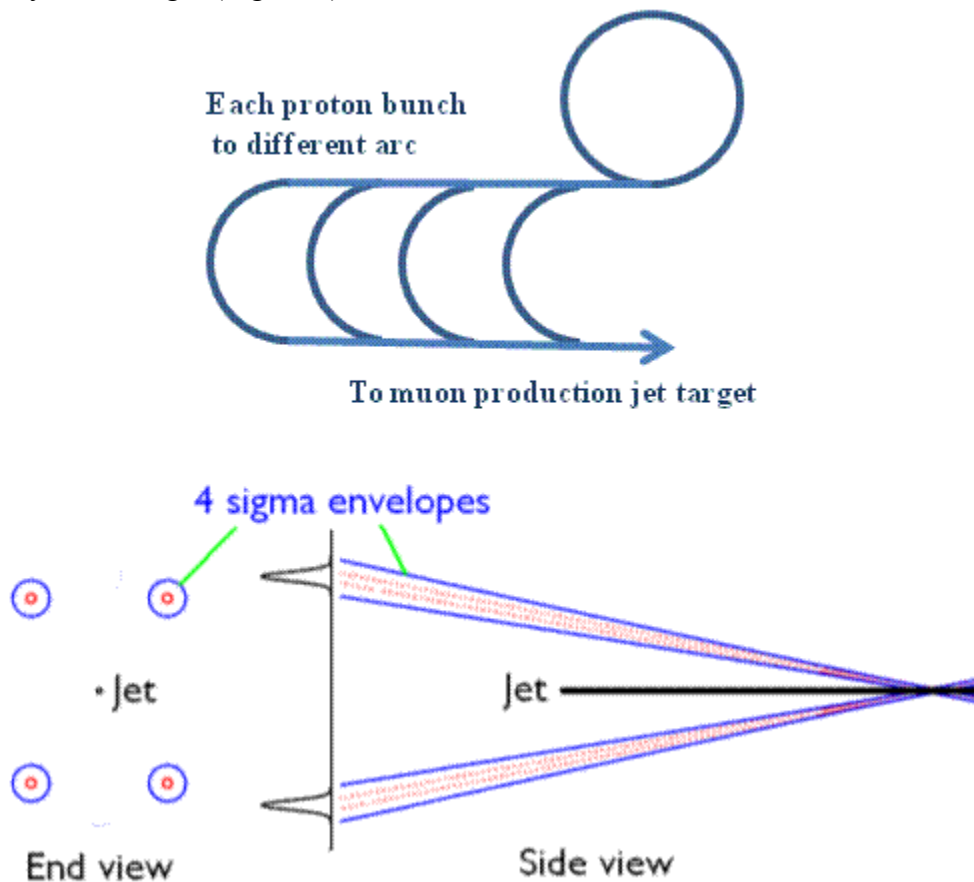


Figure 2: Top schematic shows a possible layout of four transport lines. The bottom shows four different beam trajectories to jet target for muon production.

References

1. “U.S. Particle Physics: Scientific Opportunities, A Strategic Plan for the Next Ten Years”, http://science.energy.gov/~media/hep/pdf/files/pdfs/p5_report_06022008.pdf
2. “Fermilab: A Plan for Discovery” https://www.fnal.gov/directorate/plan_for_discovery/
3. Henderson, S, Holmes, S, Kronfeld, A, and Tschirhart, R (editors), “Project X: Accelerator Reference Design, Physics Opportunities, Broader Impacts”, FERMILAB-TM-2557
4. McGinnis, D (editor), “Accelerator Issues of Project X”, <http://projectx-docdb.fnal.gov/cgi-bin/ShowDocument?docid=143>
5. Derwent, P (editor), “Project X Initial Configuration Document V1.1”, <http://projectx-docdb.fnal.gov/cgi-bin/ShowDocument?docid=83>
6. Derwent, P (editor), “Project X Initial Configuration Document–2”, <http://projectx-docdb.fnal.gov/cgi-bin/ShowDocument?docid=230>
7. Kephart, R (editor), “Project X Functional Requirements Specification,” <http://projectx-docdb.fnal.gov/cgi-bin/ShowDocument?docid=658>
8. Project X Document 912: “Project X LEBT: Functional Requirement Specifications”, <http://projectx-docdb.fnal.gov/cgi-bin/ShowDocument?docid=912>
9. Lebedev, V, “OptiM - Computer code for linear and non-linear optics calculations”, <http://www-bdnew.fnal.gov/pbar/organizationalchart/lebedev/OptiM/optim.htm>
10. Project X Document 1148: “PXIE Design Handbook”, <http://projectx-docdb.fnal.gov/cgi-bin/ShowDocument?docid=1148>
11. Ji, Q and Staples, J, Project X Document 897: “Project X H- Ion Source Acceptance Test and Future Plan”, <http://projectx-docdb.fnal.gov/cgi-bin/ShowDocument?docid=897>
12. Diebele, C and Aleksandrov A., “Experimental study of the SNS MEBT chopper performance”, in *Proc. of IPAC'10*, Kyoto, Japan, 2010, MOPD063
13. Project X Document 938: “PXIE MEBT Functional Requirements Specification”, <http://projectx-docdb.fnal.gov/cgi-bin/ShowDocument?docid=938>
14. Project X Document 933: “PXIE MEBT quadrupoles specifications”, <http://projectx-docdb.fnal.gov/cgi-bin/ShowDocument?docid=933>
15. Project X Document 977: “PXIE MEBT kicker specifications”, <http://projectx-docdb.fnal.gov/cgi-bin/ShowDocument?docid=977>

-
16. Lebedev, V, et al, “Progress with PXIE MEBT chopper”, in *Proc. of IPAC’12*, New Orleans, USA, 2012, WEPPD078
 17. Project X Document 1071: “FRS for Bunching cavity for PXIE MEBT”, <http://projectx-docdb.fnal.gov/cgi-bin/ShowDocument?docid=1071>
 18. Yakovlev, VP, “SRF Linac Technology Development”, to be published in *Proceedings of the XXVI Linac Conference (LINAC12)*, Tel-Aviv, 2012.
 19. Ciovati, G, “Review of High Field Q Slope, Cavity Measurements”, in *Proc. SRF2009*: 90 (2009)
 20. Reschke, D, “Analysis of the RF results of recent 9-cell cavities at DESY”, TTC-Report 2009-01, 2009
 21. Brunner, O, et al, “Assessment of the basic parameters of the CERN Superconducting Proton Linac”, PRSTAB 12, 070402, 2009
 22. Krivosheev, OE and Mokhov, NV ”Tolerable beam loss at High-Intensity Proton Machines”, Fermilab-Conf-00/185, Aug. 2000
 23. Ayres , DS, et al, “NOvA Technical Design Report”, Chapter 8, Fermilab-Design-2007-1, (October 2007)
 24. Foster, GW, Chou W, E. Malamud E (ed), “Proton Driver Study II”, Chapter 16, Fermilab-TM-2169, (May 2002).
 25. COMPASS SciDAC Collaboration (Paul L.G. Lebrun *et al.*), FERMILAB-CONF-10-091-CD, May 2010
 26. Yoon PS, Johnson DE, Chou W, “The Modeling of MicroBunch Injection into the Main Injector”, FERMILAB-TM-2398-AD-APC, (January 2008).
 27. Project X Document 968: “Project X and PXIE Ion Source Functional Requirement Specifications”, <http://projectx-docdb.fnal.gov/cgi-bin/ShowDocument?docid=968>
 28. Available at: <http://www.dehnel.com/index.html>
 29. Project X Document 1077: “PXIE LEBT Beam Transverse Emittance Station FRS”, <http://projectx-docdb.fnal.gov/cgi-bin/ShowDocument?docid=1077>
 30. Project X Document 894: “Project X RFQ functional physics requirements”, <http://projectx-docdb.fnal.gov/cgi-bin/ShowDocument?docid=894>

-
31. Virostek, S, et al, “Design and analysis of the PXIE CW Radio-Frequency Quadrupole (RFQ)”, in *Proc. of IPAC2012*, New Orleans, Louisiana, USA, 2012, THPPC034.
 32. Ratti, A, et al, “The Design of a High Current, High Duty Factor RFQ for the SNS”, in *Proc. of EPAC '00*, Vienna, Austria, 2000, pp. 495-497
 33. Romanov, G, et al, “Project X RFQ EM Design”, in *Proc. of IPAC'12*, New Orleans, Louisiana, USA, 2012, THPPP064
 34. Project X Document 933: “PXIE MEBT quadrupoles specifications”, <http://projectx-docdb.fnal.gov/cgi-bin/ShowDocument?docid=933>
 35. Project X Document 977: *PXIE MEBT kicker specifications*, <http://projectx-docdb.fnal.gov/cgi-bin/ShowDocument?docid=977>
 36. Project X Document 964: “Functional specifications for PXIE MEBT absorber”, <http://projectx-docdb.fnal.gov/cgi-bin/ShowDocument?docid=964>
 37. Project X Document 1071: “FRS for Bunching cavity for PXIE MEBT”, <http://projectx-docdb.fnal.gov/cgi-bin/ShowDocument?docid=1071>
 38. Romanov, G, et al, “CW room temperature re-buncher for the Project X front end” in *Proc. of IPAC'12*, New Orleans, USA, 2012, THPPP063
 39. Project X Document 1067: “Functional specifications for PXIE MEBT scrapers”, <http://projectx-docdb.fnal.gov/cgi-bin/ShowDocument?docid=1067>
 40. Project X Document 1043: “Specifications for PXIE MEBT BPMs”, <http://projectx-docdb.fnal.gov/cgi-bin/ShowDocument?docid=1043>
 41. Project X Document 827: “A Strategy for Cavity Resonance Control in the Project X CW Linac,” <http://projectx-docdb.fnal.gov/cgi-bin/ShowDocument?docid=827>
 42. Schappert, W, et al, “Microphonics Control for Project X,” *PAC2011*, New York, March 28, 2011, TUP086
 43. Yakovlev, V, et al, “HOMs in the Project-X CW Linac,” *International Workshop on Higher – Order Mode Damping in Superconducting RF Cavities*, Cornell University, October 11-13, 2010, http://www.lns.cornell.edu/Events/HOM10/rsrc/LEPP/Events/HOM10/Agenda/MA3_Yakovlev.pdf
 44. Project X Document 590: “Assumption about Q values in CW linac”, <http://projectx-docdb.fnal.gov/cgi-bin/ShowDocument?docid=590>

-
45. 1. Project X Document 826: “A compact cavity for the beam splitter of the Project X,” <http://projectx-docdb.fnal.gov/cgi-bin/ShowDocument?docid=826>
46. Delayen, JR, “Ridged Waveguide & Modified Parallel Bar,” *5th LHC Crab Cavity Workshop*, CERN, November 14-15, 2011, <http://indico.cern.ch/contributionDisplay.py?sessionId=0&contribId=3&confId=149614>
47. De Silva, SU, Delayen, JR, “Analysis of HOM Properties of Superconducting Parallel-Bar Deflecting/Crabbing Cavities”, *Proc. SRF2011*, Chicago IL USA, MOPO027 (2011).
48. Project X Document 537: “Conceptual Design Report of 8GeV H- Transport and Injection”, <http://projectx-docdb.fnal.gov/cgi-bin/ShowDocument?docid=537>
49. Johnson, DE, Chen, A, Rakhno I, “A Conceptual Design of an Internal Injection Absorber of 8 GeV H- Injection into the Fermilab Main Injector”, *Proceeding of the PAC07*, TUPA5018.
50. Drozhdin, AI, et al, “Modeling Multi-Turn Stripping Injection and Foil Heating for High Intensity Proton Drivers”, FN-0899-APC, 2011
51. Cahill, K, et al, “The Fermilab Accelerator Control System”, *ICFA Beam Dyn. Newslett.*47:106-124, 2008
52. Patrick, J and Lackey, S, “Control Systems for Linac Test Facilities at Fermilab”, *Proc. Linac08*, Victoria, BC, 2008
53. Sullivan, AH, “A Guide to Radiation and Radioactivity Levels Near High Energy Particle Accelerators”, Nuclear Technology Publishing, (1992).
54. X. Yang and W.A. Pellico, “Proposal of RF manipulation in Booster at injection and transition”, <https://beamdocs.fnal.gov/AD-private/DocDB/ShowDocument?docid=2686>
55. S. Y. Lee, *Accelerator Physics*, 2nd edition, pp309
56. C.M. Bhat et al, “Focus-Free Transition Crossing Studies with a 3rd Harmonic RF Cavity in the Fermilab Main Ring”, FERMILAB-PUB-95-409, 1995.
57. “IDS-NF Interim Design Report”, FERMILAB-PUB-11-581-APC, 19 October 2011
58. "Muon Colliders and Neutrino Factories," ICFA Beam Dynamics Newsletter No. 55, August 2011
59. Alexahin, Y, Neuffer, D, “Design of Accumulator and Compressor Rings for Project-X Based Proton Driver,” *Proceedings of IPAC12*, TUPPC043, (2012)

INSERT BLUE PAGE HERE

INSERT BLUE PAGE HERE

Project X: Physics Opportunities

Andreas S. Kronfeld, Robert S. Tschirhart
(Editors)

Usama Al-Binni, Wolfgang Altmannshofer, Charles Ankenbrandt, Kaladi Babu, Sunanda Banerjee, Matthew Bass, Brian Batell, David V. Baxter, Zurab Berezhiani, Marc Bergevin, Robert Bernstein, Sudeb Bhattacharya, Mary Bishai, Thomas Blum, S. Alex Bogacz, Stephen J. Brice, Joachim Brod, Alan Bross, Michael Buchoff, Thomas W. Burgess, Marcela Carena, Luis A. Castellanos, Subhasis Chattopadhyay, Mu-Chun Chen, Daniel Cherdack, Norman H. Christ, Tim Chupp, Vincenzo Cirigliano, Pilar Coloma, Christopher E. Coppola, Ramanath Cowsik, J. Allen Crabtree, Jean-Pierre Delahaye, Dmitri Denisov, Patrick deNiverville, André de Gouvêa, Ranjan Dharmapalan, Alexander Dolgov, Georgi Dvali, Estia Eichten, Jürgen Engelfried, Phillip D. Ferguson, Tony Gabriel, Avraham Gal, Franz Gallmeier, Kenneth S. Ganezer, Susan Gardner, Douglas Glenzinski, Stephen Godfrey, Elena S. Golubeva, Stefania Gori, Van B. Graves, Geoffrey Greene, Cory L. Griffard, Ulrich Haisch, Thomas Handler, Brandon Hartfiel, Ayman Hawari, Lawrence Heilbronn, James E. Hill, Patrick Huber, David E. Jaffe, Christian Johnson, Yuri Kamyshev, Daniel M. Kaplan, Boris Kerbikov, Brendan Kiburg, Harold G. Kirk, Andreas Klein, Kyle Knoepfel, Boris Kopeliovich, Vladimir Kopeliovich, Joachim Kopp, Wolfgang Korsch, Graham Kribs, Ronald Lipton, Chen-Yu Liu, Wolfgang Lorenzon, Zheng-Tian Lu, Naomi C. R. Makins, David McKeen, Geoffrey Mills, Rabindra Mohapatra, Nikolai V. Mokhov, Michael Mocko, Guenter Muhrer, Pieter Mumm, Lev Okun, David Neuffer, Mark A. Palmer, Robert Palmer, Robert W. Pattie Jr., David G. Phillips II, Vitaly Pronskikh, Kevin Pitts, Maxim Pospelov, Chris Quigg, Erik Ramberg, Amlan Ray, Paul E. Reimer, David G. Richards, Adam Ritz, Amit Roy, Arthur Ruggles, Robert Ryne, Utpal Sarkar, Andy Saunders, Yannis K. Semertzidis, Anatoly Serebrov, Hirohiko Shimizu, Robert Shrock, Pavel V. Snopok, William M. Snow, Arindam K. Sikdar, Aria Soha, Stefan Spanier, Sergei Striganov, Zhaowen Tang, Lawrence Townsend, Jon Urheim, Arkady Vainshtein, Richard J. Van Kooten, Richard Van de Water, Ruth S. Van de Water, Bernard Wehring, Lisa Whitehead, Robert J. Wilson, Elizabeth Worcester, Albert R. Young, William C. Wester III, and GERALYN Zeller

Argonne National Laboratory, Argonne, Illinois
University of Alabama, Tuscaloosa, Alabama
Brookhaven National Laboratory, Upton, New York
University of California, Davis, California
University of California, Irvine, California
California State University Dominguez Hills, Carson, California
Carleton University, Ottawa, Ontario, Canada
Columbia University, New York, New York
University of Chicago, Chicago, Illinois
University of Cincinnati, Cincinnati, Ohio
Colorado State University, Fort Collins, Colorado
University of Connecticut, Storrs, Connecticut

Fermi National Accelerator Laboratory, Batavia, Illinois
Hebrew University, Jerusalem, Israel
University of Houston, Houston, Texas
Illinois Institute of Technology, Chicago, Illinois
University of Illinois at Urbana-Champaign, Urbana, Illinois
Indiana University, Bloomington, Indiana
INFN, University of Ferrara, Ferrara, Italy
INFN, Gran Sasso National Laboratory, Assergi, Italy
Institute for Nuclear Research, Moscow, Russia
Institute for Nuclear Research, Troitsk, Russia
Institute of Theoretical and Experimental Physics, Moscow, Russia
Inter University Accelerator Centre, New Delhi, India
Jefferson Laboratory, Newport News, Virginia
University of Kentucky, Lexington, Kentucky
University of L'Aquila, L'Aquila, Italy
Lawrence Berkeley National Laboratory, Berkeley, California
Lawrence Livermore National Laboratory, Livermore, California
Los Alamos National Laboratory, Los Alamos, New Mexico
Ludwig-Maximilians Universität, Munich, Germany
University of Maryland, College Park, Maryland
University of Michigan, Ann Arbor, Michigan
University of Minnesota, Minneapolis, Minnesota
Novosibirsk State University, Novosibirsk, Russia
Muons Inc., Batavia, Illinois
Nagoya University, Nagoya, Japan
National Institute of Standards and Technology, Gaithersburg, Maryland
New York University, New York, New York
North Carolina State University, Raleigh, North Carolina
Northwestern University, Evanston, Illinois
Oak Ridge National Laboratory, Oak Ridge, Tennessee
Oklahoma State University, Stillwater, Oklahoma
University of Oxford, Oxford, United Kingdom
Physical Research Laboratory, Ahmedabad, India
Max-Planck-Institut für Kernphysik, Heidelberg, Germany
Universidad Autónoma de San Luis Potosí, San Luis Potosí, Mexico
Saha Institute of Nuclear Physics, Kolkata, India
SLAC National Accelerator Laboratory, Stanford, California
St. Petersburg Nuclear Physics Institute, Russia
State University of New York, Stony Brook, New York
Universidad Técnica Federico Santa María, Chile
University of Tennessee, Knoxville, Tennessee
Variable Energy Cyclotron Centre, Kolkata, India
University of Victoria, Victoria, British Columbia, Canada
Virginia Polytechnic Institute and State University, Blacksburg, Virginia
Washington University, St. Louis, Missouri

Contents

List of Figures	vii
List of Tables	viii
I Particle Physics with <i>Project X</i>	1
I.1 Themes	1
I.2 <i>Project X</i> Physics Stage by Stage	2
I.2.1 Stage 1	4
I.2.2 Stage 2	4
I.2.3 Stage 3	5
I.2.4 Stage 4: The Longer Term	5
I.3 Organization of the Physics Chapters	5
References	5
II Neutrino Experiments with <i>Project X</i>	6
II.1 Introduction	6
II.2 Long-baseline physics	9
II.2.1 Long-Baseline Neutrino Experiment	11
II.2.2 LBNE Mass Hierarchy Reach for Unfavorable Scenarios	13
II.2.3 Muon-based Neutrino Physics	19
II.3 Short-baseline physics	25
II.3.1 BooNE-X	26
II.3.2 LarLAr: A One-kiloton Liquid Argon Short Baseline Experiment	27
II.3.3 vStorm: Neutrinos from Stored Muons	28
II.3.4 Neutrinos from Stopped Kaons, Pions, and Muons	31
II.3.5 Dark Sector Physics at SBL Neutrino Experiments	31
II.3.6 Neutrino Scattering Physics Experiments	32
II.4 Summary	32
References	32

III Kaon Physics with <i>Project X</i>	37
III.1 Introduction	37
III.2 Rare Kaon Decays as Deep Probes of New Physics	38
III.2.1 The baseline: Rare Kaon Decays in the Standard Model	38
III.2.2 Beyond the Standard Model: Model-independent Considerations	43
III.2.3 The Minimal Supersymmetric Standard Model	47
III.2.4 The Randall-Sundrum Model	49
III.2.5 Beyond Rare Decays	51
III.3 Experiments	51
III.3.1 Experimental Landscape in This Decade	51
III.3.2 <i>Project X</i> Kaon Program	52
III.3.3 A $K_L^0 \rightarrow \pi^0 \nu \bar{\nu}$ Experiment at <i>Project X</i>	52
III.3.4 K^+ Experiments at <i>Project X</i>	54
III.4 Summary	54
References	55
IV Muon Experiments with <i>Project X</i>	60
IV.1 Introduction	60
IV.2 Physics Motivation	60
IV.2.1 Effective Theory Discussion	62
IV.2.2 Supersymmetry	63
IV.2.3 Neutrino Flavor Oscillations	64
IV.2.4 Extra Dimensions	64
IV.2.5 Connections between CLFV and the Muon Magnetic Moment	65
IV.3 Experiments	66
IV.3.1 $\mu \rightarrow e \gamma$	67
IV.3.2 Muon-to-electron Conversion	68
IV.3.3 $\mu \rightarrow 3e$	72
IV.3.4 Muonium-antimuonium Oscillations	73
IV.3.5 Muon Anomalous Magnetic Moment $g - 2$	76
IV.4 Summary	79
References	79

V	Measurements of EDMs with <i>Project X</i>	83
V.1	Introduction	83
V.2	Physics Motivation	84
V.2.1	Overview	84
V.2.2	EDMs of Atoms and Molecules	86
V.2.3	Rare Atom EDMs	87
V.2.4	EDMs of Light Nuclei	90
V.2.5	<i>CP</i> -Violating Sources at ~ 1 GeV	91
V.2.6	EDMs and New, TeV-Scale Sources of <i>CP</i> Violation	92
V.3	Experiments	97
V.3.1	Rare Atom EDM Experiments	98
V.3.2	SNS Neutron EDM	101
V.3.3	Storage Ring EDMs	102
V.4	Broader Possibilities	107
V.5	Summary	108
	References	109
VI	Neutron-Antineutron Oscillations with <i>Project X</i>	117
VI.1	Introduction	117
VI.2	Physics Motivation for n - \bar{n} Oscillation Searches	120
VI.2.1	Some Background Concerning Baryon Number Violation	121
VI.2.2	Some Models with n - \bar{n} Oscillations	121
VI.2.3	General Formalism for Analyzing n - \bar{n} Oscillations	123
VI.2.4	Operator Analysis and Estimate of Matrix Elements	126
VI.3	NNbarX: A Search for n - \bar{n} Oscillations with <i>Project X</i>	127
VI.3.1	Currently Existing Spallation Sources	129
VI.3.2	Increased Sensitivity of the NNbarX Experiment	129
VI.3.3	Requirements for an Annihilation Detector	132
VI.4	NNbarX Simulation	135
VI.5	The NNbarX Research and Development Program	136
VI.6	Summary	137
	References	137

VII New, Light, Weakly-coupled Particles with <i>Project X</i>	142
VII.1 Introduction	142
VII.1.1 Hidden Sectors	143
VII.1.2 Current Experimental Sensitivity	145
VII.2 Opportunities at Neutrino Facilities	147
VII.3 <i>Project X</i> Beam Parameters	149
VII.4 New Detector Technologies	149
VII.5 Summary	150
References	150
VIII Hadronic Structure with <i>Project X</i>	153
VIII.1 Introduction	153
VIII.2 Proton Spin Puzzle and Orbital Angular Momentum	153
VIII.2.1 Spin, Orbital Angular Momentum, and QCD	155
VIII.3 Polarized Drell-Yan: The Missing Spin Program	157
VIII.3.1 Measurement of the Sivers Sign Change with a Polarized Proton Beam	157
VIII.3.2 Polarized Beam Drell-Yan Measurements at Fermilab	159
VIII.3.3 OAM in the Sea	162
VIII.3.4 Polarized Target Drell-Yan Measurements at Fermilab	163
VIII.3.5 Improvements with <i>Project X</i> Luminosity	163
References	164
IX Hadronic Spectroscopy with <i>Project X</i>	167
IX.1 Hadron Spectroscopy	167
IX.1.1 Introduction	167
IX.1.2 Physics Motivation	167
IX.1.3 Experimental Setup	171
IX.1.4 Summary	173
References	174

X	Lattice-QCD Calculations for <i>Project X</i>	176
X.1	Physics Motivation	176
X.2	Introduction to Lattice QCD	177
X.3	Lattice QCD and <i>Project X</i> Experiments	180
X.3.1	Neutrino Experiments	180
X.3.2	Kaon Physics	182
X.3.3	Muon Experiments	186
X.3.4	Nucleon Matrix Elements and Fundamental Physics	190
X.3.5	Hadronic Physics	193
X.4	Computational Resources	196
X.5	Summary	197
	References	199

List of Figures

II-1	Predicted values of the CP phase δ_{CP} from neutrino sum rules	8
II-2	Values of the CP phase δ_{CP} for which a given 1σ precision can be achieved	11
II-3	LBNE mass hierarchy sensitivity for the worst-case value of $\delta_{CP} = +90^\circ$	14
II-4	CP violation sensitivity as a function of exposure	15
II-5	Measurement resolution of the CP phase δ_{CP} with <i>Project X</i> beam power	16
II-6	Expected sensitivity to θ_{23}	17
II-7	Non-standard interaction discovery reach in LBNE	18
II-8	Accuracy on the CP phase as a function of the true value of the CP phase	19
II-9	Muon accelerator timeline including the MAP feasibility-assessment period	24
II-10	Footprint of neutrino-factory and muon-collider facilities on the Fermilab site.	24
II-11	LSND and MiniBooNE anomalies	27
II-12	LarLAR sensitivity to the LSND anomaly in neutrino mode	28
II-13	Schematic of the ν Storm facility	30
II-14	Exclusion limits from a five year run of ν STORM	30
III-1	Z penguin, single- and double-photon penguin	39
III-2	Leading-order diagrams for $K \rightarrow \pi\nu\bar{\nu}$ in the SM	40
III-3	Leading-order mixing of current-current and penguin operators into Q_ν	41
III-4	Predictions for the $K \rightarrow \pi\nu\bar{\nu}$ branching ratios with Z -penguin dominance	45
III-5	Predictions for the $K_L \rightarrow \pi^0\ell^+\ell^-$ branching ratios with new physics	46
III-6	ϵ'_K/ϵ_K and $\text{BR}(K \rightarrow \pi\nu\bar{\nu})$ in Randall-Sundrum models.	50
III-7	Illustration of the KOPIO concept for <i>Project X</i>	53
III-8	K^+ momentum spectrum produced from 2.3 GeV protons	54
III-9	K^+ and K_L production yield at constant beam power	55
IV-1	Mass scale Λ vs. κ for selected CLFV experiments	61
IV-2	Stopped-muon yield in the current design of the Mu2e apparatus	71
IV-3	Stopped muons per GeV vs. incoming proton kinetic energy	72
IV-4	MACS apparatus at PSI	75
V-1	A flow chart for the analysis of EDMs	86

V-2	Representation of the shapes of ^{220}Rn and ^{224}Ra	90
V-3	Electron EDM and $h \rightarrow \gamma\gamma$ rate in a model with vector-like leptons of charge 2	93
V-4	Generic one-loop SUSY diagram giving rise to a fermion EDM or CEDM	94
V-5	Example two-loop Barr-Zee diagrams giving rise to a fermion EDM or CEDM	95
V-6	EDM contours for thallium and the neutron in supersymmetry	96
V-7	Proton EDM storage ring	105
VI-1	Configuration of the horizontal $n-\bar{n}$ search at ILL/Grenoble	119
VI-2	Initial NNbarX source design	128
VI-3	NNbarX layout and sensitivity	131
VI-4	ILL/Grenoble $n-\bar{n}$ detector	132
VI-5	Event display in Geant4 for a $\pi^+\pi^-2\pi^0$ annihilation event	135
VII-1	MiniBooNE cross section versus mass sensitivity to WIMP production	148
VIII-1	Tree-level hard-scattering processes relevant to TMD universality	154
VIII-2	Operator structures of the the eight leading-twist TMDs	155
VIII-3	Gauge-link topology of the one-gluon exchange forward scattering amplitudes	159
VIII-4	SeaQuest Spectrometer during the 2012 commissioning run	160
VIII-5	Single-spin asymmetry A_N as a function of x_f	161
VIII-6	Estimated statistical precision for the Drell-Yan sea-quark Sivers asymmetry	163
IX-1	Light isoscalar meson spectrum from lattice QCD	168
X-1	Hadron spectrum from many different lattice-QCD calculations	179
X-2	Lattice-QCD calculations of D -meson form factors compared with measurements	179
X-3	Hadronic vacuum polarization diagrams for muon $g-2$	188
X-4	Hadronic light-by-light diagrams for muon $g-2$	189
X-5	Elastic scattering phase-shift from lattice QCD for $\pi\pi$, $I = 1$, P -wave scattering	194

List of Tables

I-1	Physics opportunities for <i>Project X</i> by Stage	3
II-1	Neutrino-factory parameters	22
II-2	Muon-collider parameters	23
III-1	SM predictions and experimental limits for the four cleanest rare kaon decays	38
III-2	Comparison of the K_L production yield	53
IV-1	Beam requirements for muon experiments	66
IV-2	Protons required for single-event sensitivity $R_{\mu e} = 2.5 \times 10^{-18}$	70
V-1	Upper limits on EDMs from different experiments	84
V-2	Projected sensitivities at TRIUMF, FRIB, and <i>Project X</i>	99
V-3	Projected sensitivities for three scenarios	100
V-4	The required beam parameter values and the projected sensitivities	106
VI-1	Comparison of parameters in NNbarX simulations with existing practice.	131
VI-2	List of $n-\bar{n}$ annihilation modes	136
VIII-1	Planned polarized Drell-Yan experiments	161
IX-1	Properties of exotic hybrid mesons	170
X-1	Forecasts for lattice QCD	183

I Particle Physics with *Project X*

Andreas S. Kronfeld and Robert S. Tschirhart

This part of the book presents many aspects of the physics opportunities that become available with the *Project X* superconducting linac. As discussed in detail in Part I, the key features for physics are the high intensity, the flexible time structure, and the potential for mounting many experiments simultaneously. Many components of the *Project X* physics program complement each other: for example, neutrino experiments and searches for permanent electric dipole moments both aim to find new sources of CP violation, in two different sectors of particle physics. Some components of the physics program—from neutrino physics to hadron structure—are stalwarts of Fermilab fixed-target experiments. Others—searches for electric dipole moments and for baryon number violation via neutron-antineutron oscillations—address familiar themes, but the specific research would be new to Fermilab. The ability and flexibility to simultaneously run such a broad and rich experimental program is what makes the *Project X* accelerator such an attractive idea.

I.1 THEMES

Particle physics aims to understand the nature of matter, space, and time in their most fundamental guise. Some of the questions that propel our research are as follows:

- Are there new forces in nature?
- Do any new properties of matter help explain the basic features of the natural world?
- Are there any new (normal, or fermionic) dimensions to spacetime?

In pursuit of these themes, the mainstays of laboratory physics are high-energy colliding-beam experiments on the one hand, and intense beams on fixed targets on the other. Although one usually thinks of the first as the place to discover new particles, and the second as the place to tease out rare and unusual interactions, history provides several examples of precise measurements at high-energy colliders (for example, the mass of the W boson and the B_s oscillation frequency) and unexpected discoveries at high-intensity experiments (for example, flavor mixing in quarks and in neutrinos).

The *Project X* research program discussed in the following chapters addresses these deep questions in several ways:

- *New forces*: Experiments have established flavor-violating processes in quarks and neutrinos, so it seems conceivable that charged leptons violate flavor too. With *Project X*, one can search for these phenomena via muon-to-electron conversion and related processes. Many of the theoretical ideas unifying forces and flavor violation anticipate baryon-number violation, and *Project X* can extend the limits on neutron-antineutron oscillations by orders of magnitude. These same ideas posit measurable flavor-changing neutral currents, thereby mediating rare decays such as (charged and neutral) $K \rightarrow \pi\nu\bar{\nu}$.

- *New properties of matter:* According to the Sakharov conditions, the baryon asymmetry of the universe requires CP -violating interactions, but their strength in the Standard Model is insufficient to account for the observed excess. It is not known whether the missing CP violation takes place in the neutrino sector or the quark sector. *Project X* will aid both searches, by increasing the reach of neutrino oscillation experiments and by enabling a new suite of searches for nonzero electric dipole moments (EDMs). The latter program is broad, looking for an EDM of the neutron, proton, muon directly, and the electron, exploiting amplification in atoms such as ^{225}Ra , ^{223}Rn , and ^{211}Fr .
- *New dimensions:* Many extensions of the Standard Model introduce extra dimensions: in the case of supersymmetry, the dimensions are fermionic. The space of non-Standard interactions opens up possibilities for the interactions mentioned above: quark and neutrino CP violation and quark-flavor-changing neutral currents with supersymmetry, and flavor-changing neutral currents from a warped fifth spatial dimension. Rare kaon decays, EDMs, and neutron-antineutron oscillations are closely tied to these possibilities.

In addition to probing these fundamental questions, the *Project X* research program includes experiments that test and enrich our understanding of quantum chromodynamics and the electroweak theory. The following chapters spell out in detail the physics motivation and experimental techniques of this broad program.

The key to *Project X* is that it provides a platform for many experiments requiring high intensity. Not all of them are documented below, because, once the accelerator and experimental halls have been built, creative minds will generate new ideas that we cannot anticipate. Moreover, *Project X* can, in the farther future, lead to one or more of a neutrino factory, a muon ($\mu^+\mu^-$) collider, or a very high-energy proton collider with energy well beyond that of the LHC.

I.2 *Project X* PHYSICS STAGE BY STAGE

The *Project X* linac falls naturally into three stages. The first accelerates protons (technically H^- ions) to 1 GeV. It transports a continuous-wave beam, which means that many different time structures can be packed into the linacs. The Stage 1 linac, thus, not only drives the existing Booster and Main Injector at higher intensity, but also can distribute beam to other experiments with no interference to the Booster and Main Injector program. Interesting new experiments with a spallation target could be mounted, and muon-to-electron conversion could be studied without antiproton background. The second stage accelerates the beam (still H^-) to 3 GeV. The Booster and the Main Injector again become more powerful than before, and the 3-GeV linac itself increases the yield of muons (for flavor-violation experiments) and kaons (for ultrarare kaon decays). At this intensity, neutrino experiments driven by a 60-GeV Main Injector primary beam attain sufficiently high event rate to elucidate CP violation (see Sec. II.2) and the possibility of nonstandard sterile neutrinos (see Sec. II.3.3). The third stage is a pulsed linac that replaces the forty-year-old Booster, with a further power boost to the Main Injector, and no interruption to 1-GeV and 3-GeV operations.

The details of the accelerator staging are shown in Table I-1, which includes also the capability of the Fermilab accelerator complex following the 2013 shutdown (second column from left). In the rest of this section, we survey the highlights of each Stage of *Project X*, using this table as a guide.

Table I-1: Physics opportunities for *Project X* by Stage. The accelerator Reference Design (RDR) is described in Part I of this book and comprises Stages 1, 2, and 3. In all Stages, the intense beam is brought to the Main Injector (MI)—in Stages 1 and 2 to the original 8-GeV Booster as well. Examples of 8-GeV muon experiments include Mu2e and muon $g - 2$; an example of a 1–3-GeV muon experiment is an extension of Mu2e with optimized time structure and no antiproton background. Muon spin rotation (μ SR) and nuclear irradiation are broader impacts of *Project X* technology, discussed in Part III.

Program	Present		Project X Accelerator Reference Design				Beyond RDR
	NOVA operations		Stage 1	Stage 2	Stage 3	Stage 4	
MI neutrino	470–700 kW ^a		515–1200 kW	1200 kW	2450 kW	2450–4000 kW	
8 GeV neutrino	15–65 kW ^b		0–130 kW ^a	0–84 kW	0–172 kW	3000 kW	
8 GeV muon	20 kW		0–20 kW ^a	0–20 kW ^a	0–172 kW ^a	1000 kW	
1–3 GeV muon	—		80 kW	1000 kW	1000 kW	1000 kW	
Rare kaon decays	0–30 kW ^{b,c}		0–75 kW ^{b,d}	1100 kW	1870 kW	1870 kW	
Atomic EDMs	—		0–900 kW	0–900 kW	0–1000 kW	0–1000 kW	
Cold neutrons	—		0–900 kW	0–900 kW	0–1000 kW	0–1000 kW	
μ SR facility	—		0–900 kW	0–900 kW	0–1000 kW	0–1000 kW	
Irradiation facility	—		0–900 kW	0–900 kW	0–1000 kW	0–1000 kW	
Number of programs	4		8	8	8	8	
Total power	740 kW		2200 kW	4300 kW	6500 kW	12,000 kW	

^aOperating point in range depends on the MI proton beam energy for neutrino production.

^bOperating point in range depends on the MI slow-spill duty factor for kaon production.

^cWith less than 30% duty factor from Main Injector.

^dWith less than 45% duty factor from Main Injector.

I.2.1 Stage 1

As shown in the third column of Table I-1, Stage 1 of *Project X* will increase the Main Injector beam power for long-baseline neutrino experiments from 700 kW to 1200 kW. Simultaneously, it will provide substantial power in the 8-GeV Booster for short-baseline neutrino experiments. The extra power in the Main Injector would make it easier for ORKA, a proposal to accumulate 1000 events of the rare decay $K^+ \rightarrow \pi^+ \nu \bar{\nu}$, to reach its goals. In addition to the beam train to feed the Booster and Main Injector, the continuous-wave nature of Stage 1 means that the beam can be configured to support experiments based on a 1-GeV primary beam itself. A second beam train can be brought to the Mu2e experiment, increasing the available power from 8 kW to 80 kW. The lower energy is a further benefit to this experiment, because it produces no antiproton background. A third beam train, with aggregated power up to 900 kW, will strike spallation targets optimized for particle physics and the programs discussed in Part III. This facility will provide intense sources of cold neutrons for neutron-antineutron oscillations, ultracold neutrons for a next-generation neutron-EDM measurement, and isotopes such as ^{225}Ra , ^{223}Rn , and ^{211}Fr , which are well-suited for electron EDM measurements. A straightforward modification of the 1-GeV linac could create and accelerate polarized protons to a momentum of 0.7 GeV/ c , which is precisely that needed for a proton EDM experiment in an electrostatic storage ring. Note that the Standard-Model strong- CP contribution to the EDM changes sign from neutron to proton, whereas non-Standard contributions need not be of opposite sign. Thus, putting commensurate limits on both nucleon EDMs helps to constrain both kinds of CP violation.

I.2.2 Stage 2

Stage 2 of *Project X*, as shown in the fourth column of Table I-1, would support up to 1200 kW of power for long-baseline neutrino experiments over a wide range of Main Injector energy, down to 60 GeV from the usual 120 GeV. The lower initial energy allows the design of a neutrino beam whose energy spectrum is peaked at somewhat lower energies. With the high *Project X* intensity, the flux remains sufficient to study neutrino mixing. In fact, this setup enhances the sensitivity to neutrino mixing parameters, particularly the CP -violating phase of the mixing matrix that affects oscillations. The high power at 3 GeV can also serve to drive an early phase of a neutrino factory.

Stage 2 is the gateway for very high power for next generation muon and kaon experiments, up to 1000 kW per experiment. The energy, 3 GeV, has been chosen because it lies in the optimal ranges for muon and kaon yields. A third phase of Mu2e and related experiments (e.g., $\mu \rightarrow eee$ and oscillations between $\mu^+ e^-$ and $\mu^- e^+$ exotic atoms) will be mounted at the 3-GeV campus. The 3 GeV is also well suited to a long-recognized goal in kaon physics, the collection of 1000 events (at the Standard-Model rate) of the decay $K_L \rightarrow \pi^0 \nu \bar{\nu}$. Like its charged partner, it is a discovery mode. If new particles are found at the LHC, these measurements—on their own and in concert with other constraints from K , D , and B physics—lead to excellent discrimination among models of new physics. Note that these experiments run in parallel with the EDM and $n-\bar{n}$ experiments described in Stage 1. They all use different parts of the continuous-wave beam.

I.2.3 Stage 3

Stage 3, summarized in the fifth column of Table I-1, fully realizes the Reference Design. The total beam power of the Fermilab campus will now exceed 6000 kW, nearly ten times that available today. The beam power from the Main Injector alone will be 2450 kW, a three-fold increase. As in Stage 2, the Main Injector can be operated over a wide range of beam energy, 60–120 GeV, depending on physics needs. For long-baseline neutrino experiments, the benefit of high power is enormous: increasing the power by a factor of three increases the reach of an experiment just as much as tripling the detector mass. Short-baseline experiments at 8-GeV (primary) energy will at this stage have 180 kW of beam power available, which, again, ten times the current 8-GeV Booster. Once again, the higher power of Stage 3 at 8 GeV and at 60–120 GeV is a new resource. The experiments made possible by Stages 1 and 2 continue as before without interruption or penalty.

I.2.4 Stage 4: The Longer Term

These three Stages complete the *Project X* Reference Design, but the central idea of physics opportunities enabled by high beam power need not stop there. Appendix II of the Reference Design describes, and the right-most column of Table I-1 summarizes, a further upgrade to the entire Fermilab accelerator complex, known as Stage 4. The key additional capability of Stage 4 is much higher power, 3000–4000 kW at 8 GeV, for example, to drive more advanced accelerator concepts. In neutrino physics, these ideas include superbeams (e.g., simultaneous low and high energy neutrino beams illuminating the same large detector) and neutrino factories with beams produced in muon storage rings. Furthermore, Stage 4 lays the groundwork for future energy-frontier colliders, such as a multi-TeV muon collider or a very high energy hadron collider, which would need Stage-4 intensity at the front end.

I.3 ORGANIZATION OF THE PHYSICS CHAPTERS

In the following, Chapters II–VII flesh out the details of a broad attack on physics beyond the Standard Model, outlined above. Participants in the *Project X* Physics Study [1] explain, in turn, how the intense, flexible beam of the *Project X* accelerator can be used for neutrino physics, kaon physics, muon physics, electric dipole moments, neutron-antineutron oscillations, and experiments searching for new, light, weakly-coupled particles. The research program also has substantial components exploring hadronic structure and spectroscopy, which are described in Chapters VIII and IX. Chapter X describes enabling and supportive developments in lattice quantum chromodynamics that are important to both producing and interpreting measurements and associated scientific insights of the *Project X* research program.

References

- [1] “Project X Physics Study,” <https://indico.fnal.gov/event/projectxps12>

II Neutrino Experiments with *Project X*

*André de Gouvêa, Patrick Huber, Geoffrey Mills,
Charles Ankenbrandt, Matthew Bass, Mary Bishai, S. Alex Bogacz, Stephen J. Brice, Alan Bross,
Daniel Cherdack, Pilar Coloma, Jean-Pierre Delahaye, Dmitri Denisov, Estia Eichten,
Daniel M. Kaplan, Harold G. Kirk, Joachim Kopp, Ronald Lipton, David Neuffer,
Mark A. Palmer, Robert Palmer, Robert Ryne, Pavel V. Snopok, Jon Urheim, Lisa Whitehead,
Robert J. Wilson, Elizabeth Worcester, and GERALYN Zeller*

II.1 INTRODUCTION

Neutrino oscillations are irrefutable evidence for physics beyond the Standard Model of particle physics. The observed properties of the neutrino—the large flavor mixing and the tiny mass—could be consequences of phenomena which occur at energies never seen since the Big Bang, and they also could be triggered at energy scales as low as a few keV. Determining the energy scale of the physics responsible for neutrino mass is one of the primary tasks at the Intensity Frontier, which will ultimately require high-precision measurements. High precision is required because the telltale effects from either a low or high energy scale responsible for neutrino masses and mixing will be very small, either because couplings are very small, as in low-energy models, or the energy scales are very high and thus its effects are strongly suppressed.

The three flavor oscillation framework is quite successful in accounting for many results obtained in very different contexts: the transformation of ν_e into $\nu_{\mu,\tau}$ from the Sun [1]; the disappearance of ν_μ and $\bar{\nu}_\mu$ from neutrinos produced by cosmic ray interactions in the atmosphere; the disappearance of ν_μ and $\bar{\nu}_\mu$ [2,3] from neutrino beams over distances from 200–740 km [4–6]; the disappearance of $\bar{\nu}_e$ from nuclear reactors over a distance of about 160 km [7]; the disappearance of $\bar{\nu}_e$ from nuclear reactors over a distance of about 2 km [8–10]; and at somewhat lower significance also the appearance of ν_e [11,12] and, at even lower significance, the appearance of ν_τ [13] has been observed in experiments using man-made neutrino beams over 200–740 km distance. All these experimental results can be succinctly and accurately described by the oscillation of three active neutrinos governed by the following parameters of the Pontecorvo-Maki-Nakagawa-Sakata matrix [14,15], including their 1σ ranges [16]

$$\begin{aligned}\sin^2 \theta_{12} &= 3.07_{-0.16}^{+0.18} \times 10^{-1} \quad (16\%); & \Delta m^2 &= 2.43_{+0.1}^{-0.06} \times 10^{-3} \text{ eV}^2 \quad (3.3\%); \\ \sin^2 \theta_{23} &= 3.86_{-0.21}^{+0.24} \times 10^{-1} \quad (21\%); & \delta m^2 &= 7.54_{-0.22}^{+0.26} \times 10^{-5} \text{ eV}^2 \quad (3.2\%); \\ \sin^2 \theta_{13} &= 2.41 \pm 0.25 \times 10^{-1} \quad (10\%); & \delta &= 1.08_{-0.31}^{+0.28} \text{ rad} \quad (27\%); \end{aligned} \quad (\text{II.1.1})$$

where for all parameters whose value depends on the mass hierarchy, we have chosen the values for the normal mass ordering. The choice of parametrization is guided by the observation that for those parameters the χ^2 in the global fit is approximately Gaussian. The percentages given in parenthesis indicate the relative error on each parameter. For the mass splitting we reach errors of a few percent, however, for all of the mixing angles and the CP phase the errors are in the 10–30%

range. Therefore, while three flavor oscillation is able to describe a wide variety of experiments, it would seem premature to claim that we have entered the era of precision neutrino physics or that we have established the three flavor paradigm at a high level of accuracy. This is also borne out by the fact that there are significant hints at short baselines for a fourth neutrino [17]. Also, more general, so-called non-standard interactions are not well constrained by neutrino data; for a recent review on the topic see Ref. [18]. The issue of what may exist beyond three flavor oscillations, in particular the issue of sterile neutrinos, is discussed below in Sec. II.3.

Once one realizes that the current error bars are uncomfortably large, the next question is how well one wants to determine the various mixing parameters. The answer can be given on two, distinct levels. One is a purely technical one—if one wants to know X to a precision of x , one must know Y with a precision of y ; an example is given by Y taking to be θ_{13} and X the mass hierarchy. The other level is driven by theory expectations of the size of possible phenomenological deviations from the three flavor framework. In order to address the technical part of the question, one first has to define the target precision from a physics point of view. Looking at other fields of high-energy physics it is clear that the target precision evolves. For instance, predictions for the top quark mass, in hindsight, seem to have been always ahead by only a few GeV of the experimental capabilities, while at the time, there always was a valid physics argument for why the top quark is just around the corner. A similar evolution can be observed in B physics. Thus, any argument based on model-building inspired target precisions is always of a preliminary nature, as our understanding of models improves. With this caveat in mind, one argument for a target precision can be based on a comparison to the quark sector. Based on a theoretical preference for Grand Unification, one would expect that the answer to the flavor question should find an answer for leptons and quarks at same time (or energy scale) and therefore, a test of such a models should be most sensitive if the precision in the lepton and quark sector were nearly the same. For instance, the CKM angle γ , which is the exact analog of δ in the neutrino sector, is determined to $(70.4^{+4.3}_{-4.4})^\circ$ [19]. Thus, a precision target for δ of roughly 5° therefore follows.

Another argument for a similar level of precision can be made, based on the concept of so-called neutrino sum-rules [20]. Neutrino sum-rules arise in models where the neutrino mixing matrix has a certain simple form or texture at a high energy scale and the actual low-energy mixing parameters are modified by a non-diagonal charged lepton mass matrix. The simplicity of the neutrino mixing matrix is typically a result of a flavor symmetry, where the overall Lagrangian possesses an overall flavor symmetry G , which can be separated into two sub-groups G_ν and G_l for the neutrinos and charged leptons; it is the mismatch between G_ν and G_l that yields the observed mixing pattern, see, e.g., Ref. [21]. Typical candidates for G are given by discrete subgroups of $SU(3)$ which have a three-dimensional representation, e.g., A_4 . In a model-building sense, these symmetries can be implemented using so-called flavon fields, which undergo spontaneous symmetry breaking. This symmetry breaking picks the specific realization of G ; for a recent review see Ref. [22]. The idea of flavor symmetries is in stark contrast to the idea that neutrino mixing parameters are anarchic, i.e., random numbers with no underlying dynamics; for the most recent version of this argument, see Ref. [23]. To find out whether neutrino mixing corresponds to a symmetry or not should be one of the prime tasks of neutrino physics and furthermore, finding out which symmetry, should be attempted, as well.

In practice, flavor symmetries lead to relations between measurable parameters, whereas anarchy does not. For example, if the neutrino mixing matrix is of tri-bi-maximal form it predicts

$|U_{e3}| = 0$, which is clearly in contradiction to observations. In this case, a non-diagonal charged lepton mass matrix can be used to generate the right value of $|U_{e3}|$, leading to a sum-rule

$$\theta_{12} - \theta_{13} \cos \delta = \arcsin \frac{1}{\sqrt{3}} \quad (\text{II.1.2})$$

that can be tested if sufficiently precise measured values for the three parameters $\theta_{12}, \theta_{13}, \delta$ are available. Depending on the underlying symmetry of the neutrino mixing matrix different sum-rules arise. In Fig. II-1, several examples are shown and for each case the values of θ_{13} and θ_{12} or θ_{23} are drawn many times from a Gaussian distribution where the mean values and ranges are taken from Eq. (II.1.1). The resulting predictions of the value of the CP phase δ are histogrammed and shown as colored lines. The width of the distribution for each sum-rule arises from the finite experimental errors on θ_{12} or θ_{23} and θ_{13} . Two observations arise from this simple comparison, first the distance of the means of the distributions is as small as 15° and secondly the width of the distributions is significant compared to their separation and a reduction of input errors is mandated. The thin lines show the results if the errors are reduced to the value given in the plot which would be achieved by Daya Bay for $\sin^2 2\theta_{13}$, by Daya Bay II for $\sin^2 \theta_{12}$ and by NOVA for $\sin^2 \theta_{23}$. Assuming that the errors on θ_{12} , θ_{23} and θ_{13} are reduced to this level, the limiting factor is the natural spread between models, which is about 15° , which for a 3σ distinction between models translates into a target precision for δ of 5° . A measurement at this precision would allow to obtain valuable information on whether indeed there is an underlying symmetry behind neutrino mixing. Moreover, it is likely that is also allows to provide hints which specific class of symmetries is realized. This would constitute a major breakthrough in our understanding of flavor.

In Sec. II.2 we discuss long-baseline physics with subsections on LBNE and muon-based fa-

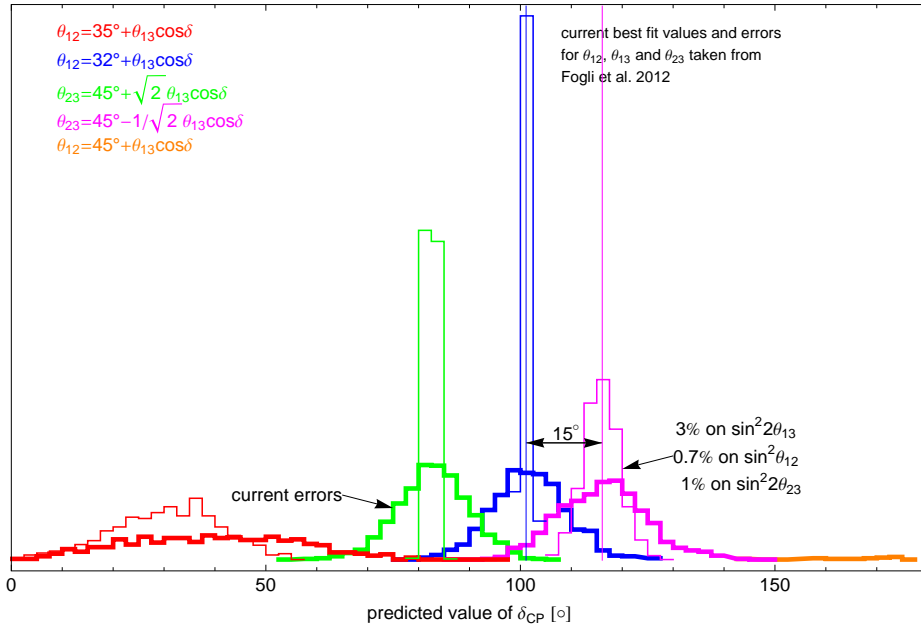


Figure II-1: Distributions of predicted values from δ_{CP} from various neutrino sum rules, as denoted in the legend and explained in the text.

cilities covering the gamut of measurements from atmospheric parameters over CP violation to non-standard interactions. The focus in Sec. II.2 is largely on the three flavor oscillation framework, how to test it and how to discover deviations from it. In Sec. II.3 the physics potential of experiments at a short baseline, i.e., less than a few kilometers, is highlighted. One of the major physics motivation for these experiments derives from existing experimental hints for a eV-scale sterile neutrino.

II.2 LONG-BASELINE PHYSICS

With the discovery of a large value for θ_{13} , the physics case for the next generation of long-baseline oscillation experiments has grown considerably stronger and one of the major uncertainties on the expected performance has been removed. The remaining questions are: the value of the leptonic CP phase and the quest for CP violation; the mass hierarchy; whether θ_{23} is maximal and if not, whether it is larger or smaller than $\pi/4$; and of course, the search for new physics beyond the three active neutrinos paradigm. Based on our current, incomplete understanding of the origin of neutrino mass and the observed flavor structure in general it is very hard to rank these question in their relative importance, but with the large value of θ_{13} it is feasible to design and build a long-baseline facility which can address all three questions with high precision and significance. Therefore, the question of relative importance can be avoided.

The error on θ_{13} will keep decreasing as the reactor measurements are refined and Daya Bay is expected to yield a precision which only would be surpassed by a neutrino factory. It is an important test of the three flavor oscillation model to see whether the value extracted from disappearance at reactors matches that from appearance in beams.

A combination of the existing experiments, T2K, NOvA and reactor data, allows to obtain a first glimpse on the mass hierarchy and with extended running and for favorable CP phases a 5σ determination is possible. Also, new atmospheric neutrino experiments like PINGU, ICAL at INO and Hyper-K have, in principle, some sensitivity to the mass hierarchy and the actual level of significance strongly depends on the obtainable angular and energy resolution for the incoming neutrino. There are also plans for a dedicated experiment, called Daya Bay 2, which would not rely on matter effects but aims at measuring the interference of the two mass squared differences at a distance of about 60 km from a nuclear reactor. It seems likely that global fits will be able to provide a $3\text{--}5\sigma$ determination of the mass hierarchy before the end of the next decade. It should be noted, that nonetheless a direct and precise method to test matter effects and to determine the mass hierarchy from a single measurement would be valuable even in this case.

One of the most commonly used frameworks to discuss physics beyond oscillations are so-called non-standard interactions (NSI). They can arise in many different models and their phenomenology is easy to capture in a model-independent way. For the measurement of NSI, the fact that θ_{13} is large means that interference of standard oscillation amplitudes proportional to $\sin 2\theta_{13}$ with NSI effects can enhance sensitivity substantially. If NSI are present, the extraction of the mass hierarchy from global fits is not likely to yield the correct result. Note, NSI are a straightforward mechanism to induce a difference between the reactor and beam measurements of θ_{13} . Longer baselines generally have more sensitivity to NSI and also allow a better separation of standard oscillation and NSI.

Given the likely status of the mass hierarchy measurement by the time *Project X* becomes active, the other very central physics goal is a measurement of the leptonic CP phase and potentially the discovery of CP violation in the lepton sector. It is important to distinguish these two goals—with large θ_{13} a measurement of the CP phase at a predetermined level of precision can be virtually guaranteed, whereas CP violation may or may not be present in the lepton sector. Therefore, we focus on the measurement of the CP phase and regard the sensitivity towards CP violation as secondary.¹ A determination of the CP phase requires to measure any two out of the following four transitions: $\nu_e \rightarrow \nu_\mu$, $\bar{\nu}_e \rightarrow \bar{\nu}_\mu$, $\nu_\mu \rightarrow \nu_e$, $\bar{\nu}_\mu \rightarrow \bar{\nu}_e$. However, due to the long baselines, there always will be also matter effects which yield a contribution to the CP asymmetries as well; it is necessary to separate this contribution from the genuine CP violation in the mixing matrix. This separation is greatly facilitated by exploiting L/E information, ideally spanning a wide enough L/E interval so that more than one node of the oscillation can be resolved. This requirement, in combination with limitations of neutrino sources and detectors translates into the need for baselines longer than 1,000 km [24–26]. This is also clearly borne out in the discussion of the LBNE reconfiguration—shorter baselines like those available in the existing NuMI beamline, require generally a larger exposure to reach the same parametric CP sensitivity, in absence of external information.

For superbeam experiments, the control of systematic errors will be a major issue, since neither the detection cross sections nor beam fluxes are known within the required precision. Near detectors, together with hadron production data, will play an important role. However, this alone will not be sufficient to obtain per cent level systematics, since the beam at the near detector is composed mostly of ν_μ and hence a measurement of the ν_e cross section is not possible, but in the far detector the signal are ν_e , see e.g., Ref. [27]. Unfortunately, there are no strong theory constraints on the ratio of muon-to-electron neutrino cross sections either [28]. Here, a facility like ν STORM maybe helpful, which is described in detail in Sec. II.3.3. Also, better theory calculations of neutrino-nucleon interactions will certainly be required. As described in Chapter X, such calculations are possible with lattice QCD and will be carried out over the next several years. In this context, these calculations will help disentangle hadronic from nuclear effects in neutrino-nucleus scattering.

In Fig. II-2, a comparison of the CP precision for various facilities, as explained in the legend, is shown. Clearly, the neutrino factory (blue line, labeled LENF) is the only facility which approaches the CKM precision, and it has the potential to go even further. For the superbeams, 2020, LBNE, LBNO, and T2HK, we note that they span a very wide range of precision, which demonstrates the crucial importance of achieving sufficient statistics. The number of events is determined by the product of beam power, detector mass and running time and each of these ingredients can vary easily within an order of magnitude. LBNO has recently submitted an expression of interest [30] to CERN which outlines a much smaller detector and lower beam power which would put its CP precision somewhere close to any of the reconfigured LBNE options. Obtaining a sufficient number of events is crucial and clearly, here *Project X* can help with increasing the beam power at 60 GeV. The sensitivity of these results to the assumptions made about systematics is not shown in this plot—but a clear difference does exist, and T2HK exhibits a very strong sensitivity to the assumed level of systematics [29] and thus is significantly more at risk of running into a systematics limitation. Both LBNE and LBNO due to their long baselines and resultant wide L/E coverage are quite safe from systematics [29]. Note, at the current stage all these experiments have to rely on assumptions

¹This is an operational statement, which does not imply that CP violation is less interesting. Rather, in practice one will have to measure the phase and then one knows whether CP is violated or not.

about their systematics. In any comparison as presented in Fig. II-2 the relative performance can vary greatly depending on these assumptions. In the end, *both* sufficient statistics combined with small systematics will be required to perform a precise measurement of the CP phase.

II.2.1 Long-Baseline Neutrino Experiment

The Long-Baseline Neutrino Experiment (LBNE) [31] plans a comprehensive program that will fully characterize neutrino oscillation phenomenology using a high-intensity accelerator muon-neutrino beam and a massive liquid-argon time-projection chamber (LAr TPC) as a far detector sited for a 1300-km baseline. The goals for this program are the determination of leptonic CP violation, the neutrino mass hierarchy, precision measurements of neutrino mixing and interactions, as well as underground physics, including the exploration of proton decay and supernova neutrino bursts. The LBNE program assumes a 700 kW Main Injector (MI) proton beam power, however the beam line and target station are designed to be able to exploit *Project X* beam power up to 2.3 MW.

For the program of testing and constraining the three-flavor mixing paradigm underlying neu-

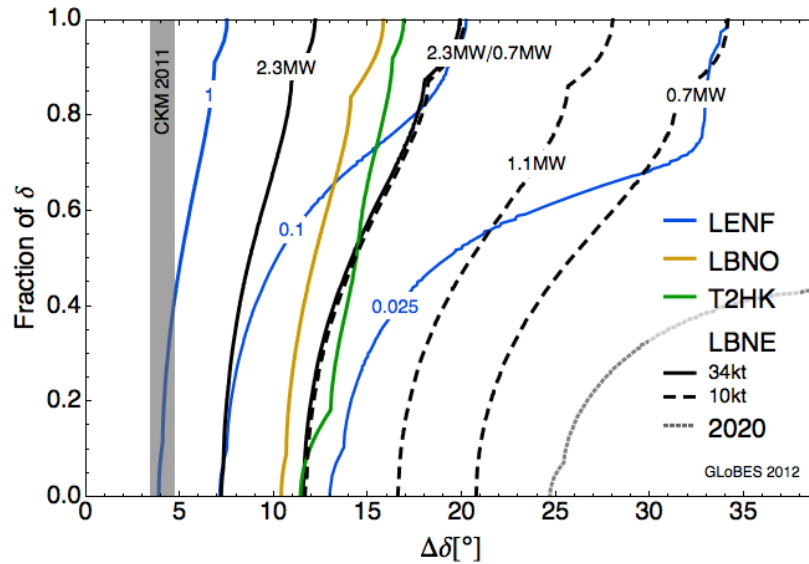


Figure II-2: Fraction of values of the CP phase δ_{CP} for which a given 1σ precision $\Delta\delta$ can be achieved. The various lines are for different setups as indicated in the legend. The vertical gray shaded area, labeled “CKM 2011”, indicates the current errors on the CP phase in the CKM matrix. This calculation includes near detectors and assumes consistent flux and cross section uncertainties across different setups. The setups are: LBNF—a 10-GeV neutrino factory with 1.4×10^{22} useful muon decays, which corresponds to 4-MW proton beam power for 10^8 s, 2,000 km baseline and a 100 kt magnetized iron detector; LBNO—uses a 100 kt LAr detector at a baseline of 2,300 km and 10^{22} POT at 50 GeV, which translates into about 800 kW of beam power for 10^8 s; T2HK—a 560 kt water Cherenkov detector at 295 km using a 1.66 MW beam for 5×10^7 s, which is equivalent to 1.2×10^8 s at 700 kW; LBNE—using LAr detectors of either 10 kt or 34 kt at a distance of 1,300 km with different beam powers as indicated in the legend for 2×10^8 s; 2020—results obtain from a combined fit to nominal runs of T2K, NOvA and Daya Bay. All detector masses are fiducial. Plot courtesy P. Coloma [29].

trino oscillation phenomenology, the key observables for conventional horn-focused long-baseline neutrino beam experiments are the survival probabilities of the ν_μ and $\bar{\nu}_\mu$ beam components (in operation with the respective horn-current polarities), and the corresponding appearance probabilities for ν_e (and $\bar{\nu}_e$). In its simplest form, the measurements can be reduced to four numbers. However, as an on-axis experiment, the LBNE detectors will be exposed to a broad neutrino energy spectrum, with flux at both the first and second oscillation maxima. The interplay of matter effects and both the CP -conserving and CP -violating contributions associated with the phase δ present within the standard three-flavor mixing picture, lead to complex energy dependencies of the ν_e and $\bar{\nu}_e$ appearance probabilities. Detailed analysis of these energy dependencies will enable untangling of overlapping effects, for example, ambiguities presented by the unknown octant and the currently limited precision on θ_{23} . The 1300 km baseline is nearly optimal for resolving the picture of neutrino mixing: by virtue of the very long baseline, matter effects are enhanced to the point that ambiguities between leptonic CP violating effects and the CP -asymmetry induced by interactions with electrons as the neutrinos propagate are well separated.

The significant effort to construct an experiment like LBNE with a massive, highly sensitive detector and very long baseline is aimed at minimizing systematic uncertainties to the extent possible. As a result, many LBNE measurements are expected to be statistics limited. To fully capitalize on the LBNE physics potential, it is essential that investment also be made in the delivery of a neutrino beam with the highest intensity possible.

Project X can provide a significant enhancement to the LBNE neutrino program. A staged increase in the MI proton beam power will increase the neutrino flux proportionately, thus reducing the time required to reach the science goals and may reduce certain systematic uncertainties. Stages 2 and 3 of *Project X* would also support further optimization of the LBNE neutrino energy spectrum while maintaining high beam power. In the following we provide a few specific examples of how the science reach of LBNE is substantially accelerated by the available of different stages of *Project X*.

II.2.1.1 Assumptions, Scope and Organization of this Discussion

In the following discussion, the reach of LBNE toward its neutrino oscillation physics goals is cast in a context that enables visualization of the impact of *Project X*. LBNE has recently received DOE CD-1 approval as a phased program, with a far detector fiducial mass of at least 10 kt in the initial phase. For the full LBNE program, a far detector complex with fiducial mass of at least 34 kt would be deployed. The actual evolution of the far detector complex will depend on domestic funding scenarios as well as contributions from international partners. For this reason, sensitivities are plotted as a function of exposure in kt-years. Thus, a 20-kt far detector, operating for 5 years in neutrino mode and 5 years in antineutrino mode with a 700 kW beam would have an exposure of 200 kt-years. Operating at 2.1 MW beam power, as would be possible with Stage 3 of *Project X*, for that same duration would then correspond to an exposure of 600 kt-years at 700 kW. Or as indicated above, it would decrease by a factor of three the time needed to reach a given physics goal relative to that indicated in these plots. For a number of the plots we explicitly show a scenario in which beam power is increased at specific intervals from 700 kW to 1.1 MW to 2.3 MW, as the different *Project X* stages begin operation.

Additionally, optimization of the beam line configuration, including length of the decay volume and energy (nominally 120 GeV) of the primary MI beam extracted onto the hadron production target, is still under development. Consequently, for illustration purposes, a number of the plots presented here show sensitivity ranges that correspond to different beam line configurations, ranging from that documented in the 2012 LBNE Conceptual Design Report [32] to more optimized configurations including MI operation at 80 GeV and a longer decay volume (250 m, instead of the nominal 200 m length).

In this discussion, we focus on the ν_e appearance and ν_μ disappearance measurements that are the mainstay of the LBNE program. First, while there is a good chance that determination of the neutrino mass hierarchy will not require *Project X*, there are scenarios where the combination of LBNE and *Project X* will be needed, and this is illustrated briefly in Sec. II.2.2. On the other hand, LBNE sensitivity to CP violation and the value of the CP phase in the mixing matrix δ_{CP} depends strongly on the beam power and neutrino energy spectrum, and is where *Project X* is most critical. This is demonstrated in Sec. II.2.2.1. With regard to ν_μ disappearance, we first report in Sec. II.2.2.2 the dependence of the sensitivity to θ_{23} , and specifically its possible departure from $\pi/4$. We then describe in Sec. II.2.2.3 the sensitivity of LBNE to the presence of non-standard interactions that would modify the energy-dependence of the ν_μ survival probability. Finally, comments on the potential impact on precision physics with a highly capable near detector complex are given in Sec. II.2.2.4.

II.2.2 LBNE Mass Hierarchy Reach for Unfavorable Scenarios

Unambiguous determination of whether the mass hierarchy (MH) is normal or inverted is one of the most important questions to be addressed by the current and next generation of neutrino experiments, including the initial phase of LBNE. Yet, it is conceivable that neutrino-mixing parameter values will be unfavorable, and additional sensitivity that could be provided by *Project X* will be needed. Figure II-3 shows the MH determination significance as function of exposure (the product of far detector fiducial mass and beam time) for a 700 kW proton beam for the worst case scenario where the unknown phase in the mixing matrix δ_{CP} is $+90^\circ$. The bands represent the range for two proton beam configurations, as described earlier: The lower edge of the band is for the nominal 120 GeV proton beam described in the 2012 Conceptual Design Report [32]; the upper edge is for an enhanced beam with an 80 GeV MI beam energy of the same power. The higher beam power of *Project X* effectively compresses the exposure scale so, for example, a 5σ measurement that would take 5 years with the 80 GeV/700 kW beam, would be reduced to a little over three years with a 1.1 MW beam. Earlier knowledge of the correct mass hierarchy would allow better optimization of the run strategy for other oscillation parameter measurements.

II.2.2.1 LBNE Reach in CP Violation

A primary goal of LBNE is observation of CP violation in the neutrino sector. Through measurement of the energy-dependent probabilities for electron-neutrino (antineutrino) appearance in a muon-neutrino (antineutrino) beam with its source at a distance of 1300 km, LBNE will be sensitive to terms involving the CP phase δ_{CP} that appears in the standard form of the three-flavor mixing

matrix. If δ_{CP} is zero or π radians, there is no CP violating term in the matrix, and hence deviations from these values would constitute evidence for CP violation.

The two plots in Fig. II-4 illustrate the significance of a non-zero (or π) measurement for different exposures scenarios with increasing beam power successively from the nominal LBNE 700 kW, through 1.1 MW (*Project X* Stage 1), to 2.3 MW (*Project X* Stage 2). Here, significance is defined as the square-root of the difference in χ^2 between the electron-neutrino spectrum predicted for some the value of δ_{CP} and that for a value of 0 or π radians. The left plot shows the significance as a function of δ_{CP} itself. (If the MH were unknown and not measured in the same experiment, as it is for LBNE, ambiguities would make this distribution asymmetric.) The plot on the right shows the exposure, with *Project X* beam power epochs indicated, for which the CP violation significance is that value or higher for 50% of the full δ_{CP} range. For example, a 100 kt-year exposure with a 700 kW beam, followed by a 44 kt-year exposure with a 1.1 MW beam would yield a 3σ or better CPV significance for half of the δ_{CP} range. For a 35-kt LBNE this corresponds to a little over 4 years.

Figure II-5 shows the accuracy in the determination of δ_{CP} and θ_{13} . In the left plot, the bold crosses indicate three different true values of δ_{CP} with the same true value of $\sin^2 2\theta_{13} = 0.1$. The

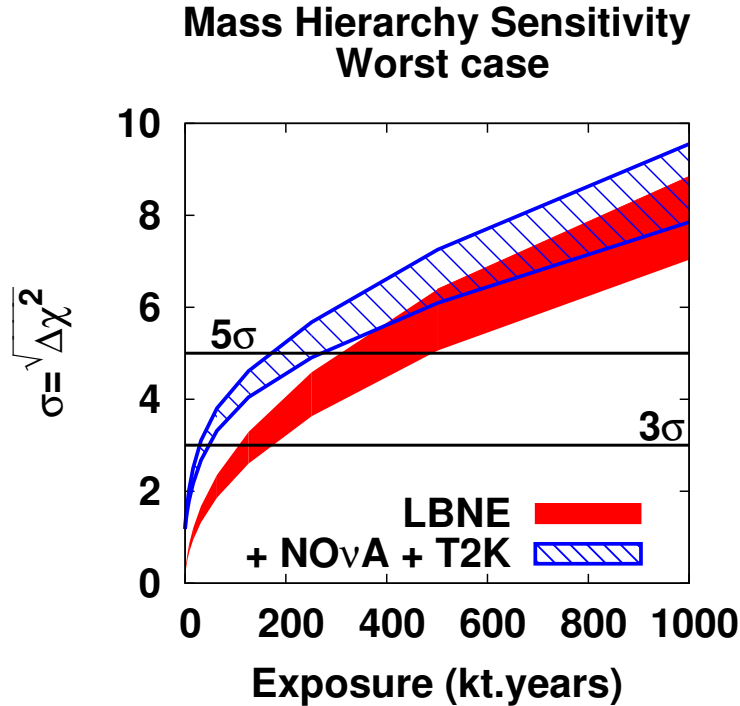


Figure II-3: LBNE mass hierarchy sensitivity for the worst-case value of $\delta_{CP} = +90^\circ$. The bands represent ranges delimiting the two 700 kW beam configurations described in the text. For δ_{CP} less than zero there is only a small sensitivity difference between LBNE alone and when combined with T2K and NOVA; greater than 5σ determination is achieved with an exposure of 100 kt-years. For higher beam power correspondingly less time is needed to reach the same overall exposure.

colored solid lines show how the 1σ contours shrink by the end of the three successive beam power phases. The right-hand plot shows the 1σ resolution on the CP phase as a function of its true value. The width of the band illustrates the variation due to beam design alternatives, as in Fig. II-3.

II.2.2.2 LBNE Reach with Muon Neutrino Disappearance

LBNE capabilities for ν_μ disappearance measurements will enable precision measurement of the mixing angle θ_{23} . To obtain maximal sensitivity to both the deviation of $\sin^2 2\theta_{23}$ from unity and the θ_{23} octant it is necessary to simultaneously analyze the ν_μ disappearance and ν_e appearance signals [33]. In Fig. II-6 we show the significance (plotted here for $\Delta\chi^2$, rather than $\sqrt{\Delta\chi^2}$ used earlier) to determine the octant of θ_{23} as a function of its true value. The range of θ_{23} values hinted (at the 1σ level) by the analysis of existing data by Fogli *et al.* [16] is indicated by the hatched vertical band for illustrative purposes. It is important to note, however, that experimental precision on θ_{23} itself has a strongly non-linear dependence on the actual value as one approaches maximal mixing (45°). This non-linearity is further illustrated in the plot on the right in Fig. II-6 for the case of a 10-kt Far Detector, with pre-Project-X beams. Nevertheless, over a considerable range of plausible θ_{23} values, the addition of capability from beam upgrades associated with *Project X* stages can be transformative for distinguishing θ_{23} from 45° .

II.2.2.3 Sensitivity to Matter Effects from Nonstandard Interactions

Flavor-dependent non-standard interactions (NSI) of neutrinos as they propagate through matter have been proposed as a way of altering the pattern of neutrino oscillations without requiring the

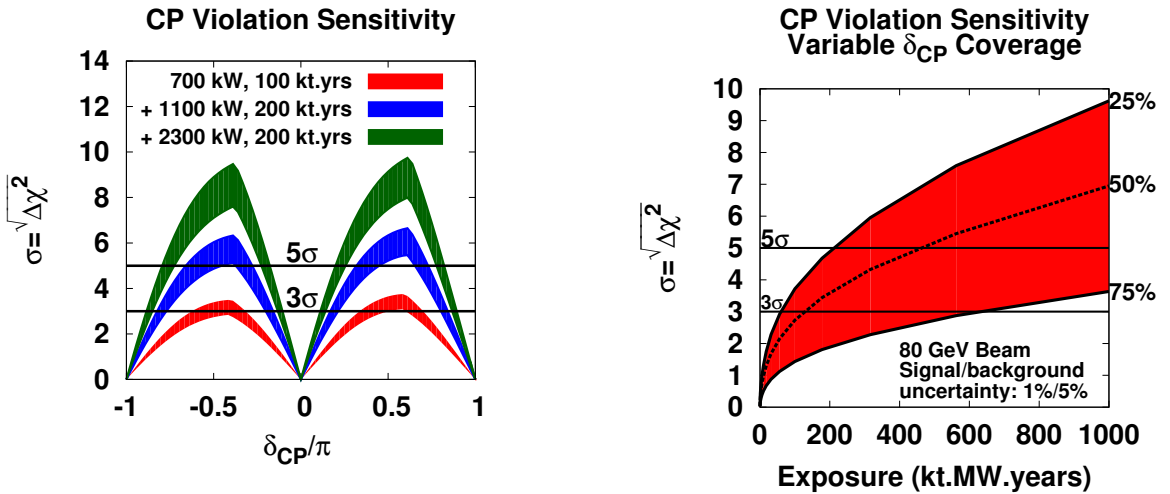


Figure II-4: CP violation sensitivity as a function of exposure (far detector mass times beam power times run time) at the indicated proton beam power (corresponding to a straw man *Project X* development scenario). Significance of non-zero value of δ_{CP} over the full δ_{CP} range (left); CP violation sensitivity for 50% coverage (central dotted line) of the full δ_{CP} range (right). The red shaded region in the right hand panel indicates CP fractions from 25% - 75%.

introduction of additional neutrino species. In general, charged-current (CC) and neutral-current (NC) interactions are possible, and these could either be flavor-changing or flavor-conserving. Long-baseline experiments have especially strong sensitivity to NC NSI-induced effects, since it is the forward scattering of neutrinos (including ν_μ and ν_τ) that would give rise to MSW-like distortions of the survival probability for beam ν_μ 's as a function of energy. By virtue of the 1300 km baseline, LBNE has a unique advantage in this area compared to other long-baseline experiments, except atmospheric-neutrino experiments, which may, however, be limited by systematic effects.

Following Ref. [33], NC NSI can be parameterized as new contributions to the MSW matrix in the neutrino-propagation Hamiltonian:

$$H = U \begin{pmatrix} 0 & & \\ & \Delta m_{21}^2/2E & \\ & & \Delta m_{31}^2/2E \end{pmatrix} U^\dagger + \tilde{V}_{\text{MSW}}, \quad (\text{II.2.1})$$

with

$$\tilde{V}_{\text{MSW}} = \sqrt{2}G_F N_e \begin{pmatrix} 1 + \epsilon_{ee}^m & \epsilon_{e\mu}^m & \epsilon_{e\tau}^m \\ \epsilon_{e\mu}^{m*} & \epsilon_{\mu\mu}^m & \epsilon_{\mu\tau}^m \\ \epsilon_{e\tau}^{m*} & \epsilon_{\mu\tau}^{m*} & \epsilon_{\tau\tau}^m \end{pmatrix} \quad (\text{II.2.2})$$

Here, U is the leptonic mixing matrix, and the ϵ -parameters give the magnitude of the NSI relative to standard weak interactions. For new physics scales of few $\times 100$ GeV, $|\epsilon| \lesssim 0.01$ is expected.

To assess the sensitivity of LBNE to NC NSI, the NSI discovery reach is defined in the following way: After simulating the expected event spectra, assuming given ‘‘true’’ values for the NSI

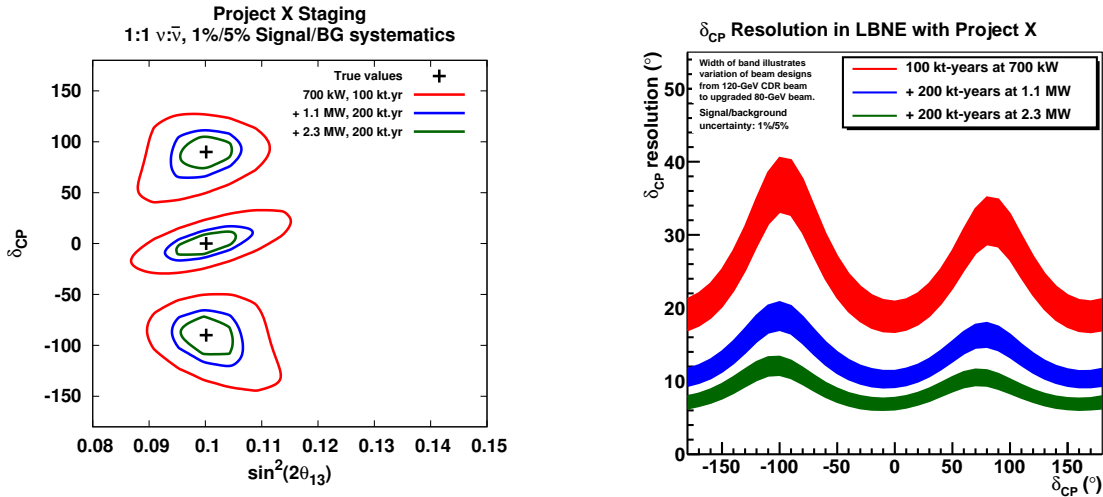


Figure II-5: Measurement resolution of the CP phase δ_{CP} , for a program scenario that includes an evolution of the proton beam as upgraded via *Project X*. Each time period comprises equal exposure for neutrinos and antineutrinos. Normalization uncertainties of 1% for signal and 5% for background are assumed. At left, 1σ δ_{CP} resolution contours are plotted for three values of δ_{CP} (-90° , 0° , $+90^\circ$), each with $\sin^2\theta_{13} = 0.1$. At right, the 1σ resolution on δ_{CP} is plotted as a function of δ_{CP} .

parameters, one attempts a fit assuming no NSI. If the fit is incompatible with the simulated data at a given confidence level, one would say that the chosen “true” values of the NSI parameters are within the experimental discovery reach. Figure II-7 shows the NSI discovery reach of LBNE for the case where only one of the $\epsilon_{\alpha\beta}^m$ parameters at a time is non-negligible [33]. Even with a 10 kt detector and 700 kW beam power, LBNE can explore substantial new regions of parameter space. Enhancing the program with a combination of detector mass and beam power would extend the discovery reach correspondingly.

II.2.2.4 LBNE Reach in Precision Neutrino Physics

A highly capable neutrino detector to measure the unoscillated neutrino fluxes and their interactions at the near site will significantly enhance the core scientific capability of LBNE. It would enable a very rich short-baseline physics program with more than a hundred unique physics and engineering Ph. D. topics. Among the broad physics goals of this program [37,38] are to: (1) measure the absolute and relative flux of all four neutrino species (ν_{μ}, ν_e and corresponding antineutrinos), including the energy scales of neutrinos and antineutrinos, as required to normalize the oscillation signals at the Far Detector; (2) measure the cross section of neutrino- and antineutrino-induced inclusive and exclusive processes in nuclear targets across a large energy range (0.5–50 GeV) to 3% precision, to aid in the interpretation of the oscillation signals in the Far Detector; (3) measure the yield of particles produced in neutrino interactions such as neutral and charged pions/kaons, which are the dominant backgrounds to oscillation signals; and (4) measure precisely the fundamental electroweak and strong interaction parameters that are accessible to neutrino physics; and (5) perform sensitive searches for new physics, such as sterile neutrinos. While these physics goals will also surely be enhanced with increased fluxes afforded by *Project X*, detailed studies of sensitivities are ongoing at this point.

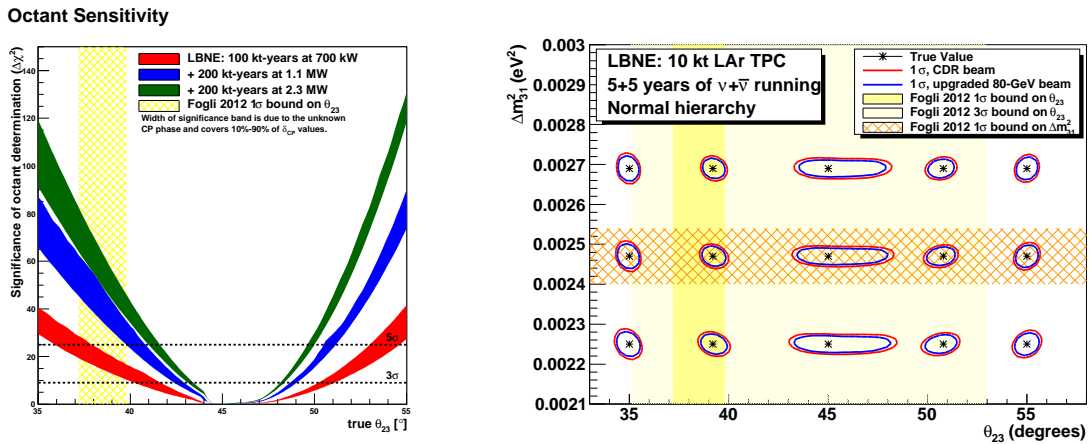


Figure II-6: Left: Sensitivity of determination of the octant of mixing angle θ_{23} from ν_{μ} disappearance and ν_e appearance signals, with the same scenario for beam power evolution and detector exposure assumed in the ν_e appearance analyses above. Right: Projected precision on the atmospheric Δm^2 and $\sin^2 2\theta_{23}$ for the case of a 10-kt far detector operating for 10 years at 700 kW.

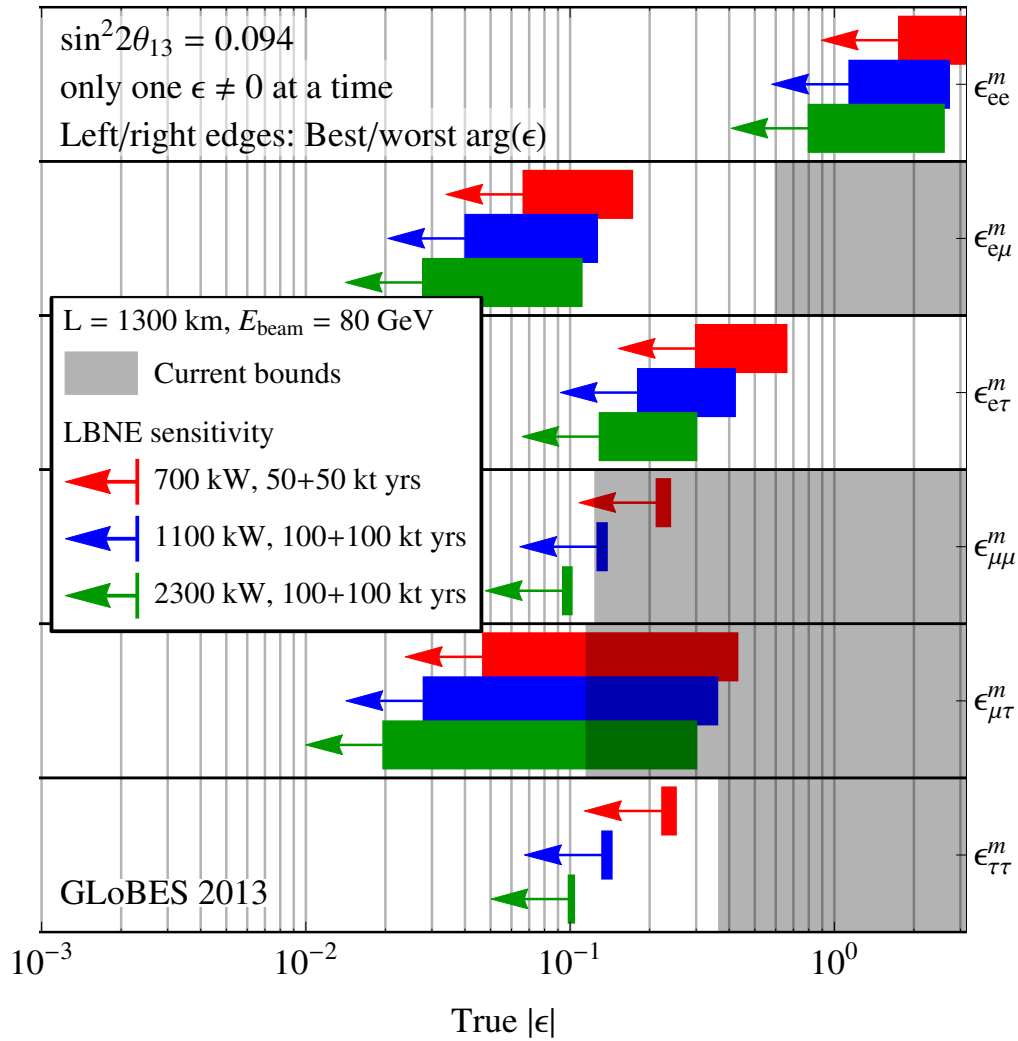
NC NSI discovery reach (3σ C.L.)

Figure II-7: Non-standard interaction discovery reach in LBNE at various phases in the evolution of detector mass and beam power. The left and right edges of the error bars correspond to the most favorable and the most unfavorable values for the complex phase of the respective NSI parameters. The gray shaded regions indicate the current model-independent limits on the different parameters at 3σ [34–36]. This study takes $\sin^2 2\theta_{13} = 0.094$. From J. Kopp.

II.2.3 Muon-based Neutrino Physics

The questions of leptonic CP violation and the completeness of the three-flavor picture, can only be addressed by very high precision measurements of neutrino and antineutrino oscillation probabilities, specifically including channels where the initial and final flavor of neutrino are different. Several neutrino sources have been conceived to reach high sensitivity and to allow the range of measurements necessary to remove all ambiguities in the determination of oscillation parameters. The sensitivity of these facilities is well beyond that of the presently approved neutrino oscillation program. Studies so far have shown that, even for the measured large value of θ_{13} , the neutrino factory, an intense high-energy neutrino source based on a stored muon beam, gives the best performance for CP measurements over the entire parameter space. Its time-scale and cost, however, remain important question marks. Second-generation super-beam experiments using megawatt proton drivers may be an attractive option in certain scenarios, but eventually the issue of systematics control may limit this technology. It should be noted that once detailed plans are considered, the fiscal and time scales of true super-beams are very large as well.

In response to the measurement of large θ_{13} , the neutrino factory design has been reoptimized to a stored muon energy of 10 GeV and a single baseline of 2000 km using a 100 kt magnetized iron detector. It is possible to further reduce the energy to around 5 GeV and concomitantly the baseline to 1300 km without an overall loss in performance if one changes the detector technology to improve efficiency around 1–2 GeV; possible choices could be a magnetized liquid argon detector or a magnetized fully active plastic scintillator detector. If one of these technology choices can be shown to be feasible, there currently appears to be no strong physics performance reason to favor the 10 GeV over the 5 GeV option, or vice versa. The low-energy option seems attractive due to its synergies with planned super-beams like LBNE and because the detector technology would allow for a comprehensive physics program in atmospheric neutrinos, proton decay and supernova detection. Within the low-energy option detailed studies of luminosity staging have been carried out, which indicate that at even at 1/20th of the full-scale beam intensity and starting with a 10 kt

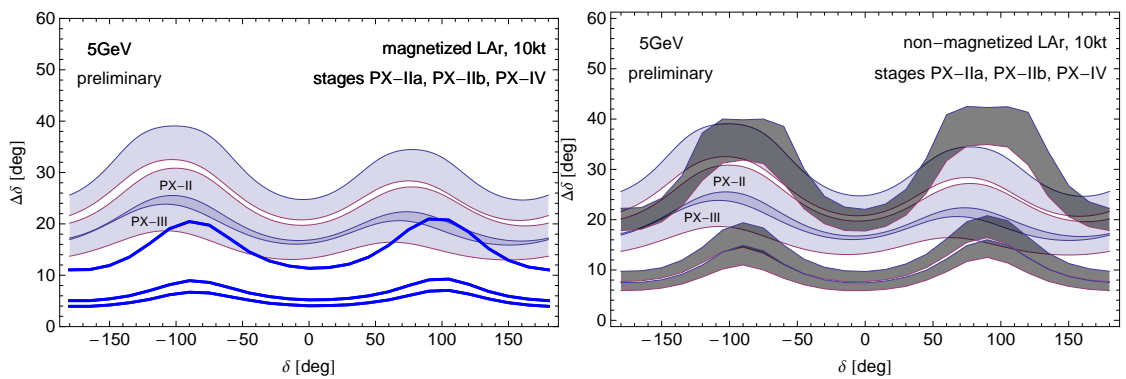


Figure II-8: Accuracy on the CP phase δ as a function of the true value of the CP phase at 1σ confidence level. The light blue bands depict the accuracy as expected from LBNE using the various beams *Project X* can deliver. In the left hand panel, the thick blue lines represent what a neutrino factory beam can do using a magnetized LAr detector. In the right hand panel, the gray bands illustrate the accuracy of a neutrino factory using a non-magnetized detector. The neutrino factory beam intensities can be found in Table II-1. Adapted from Ref. [39].

detector significant physics gains beyond the initial phases of a pion-decay based beam experiment, like LBNE, can be realized [39]. At full beam luminosity and with a detector mass in the range of 10–30 kt, a 5 GeV neutrino factory offers the best performance of any conceived neutrino oscillation experiment, which is shown in Fig. II-8. The gray bands in the right hand panel illustrate the performance using a LAr detector without a magnetic field, where the charge identification is performed statistically and not on an event-by-event basis, as explained in detail in Ref. [40].

Muon accelerators offer unique potential for the U.S. high-energy physics community. In 2008, and subsequently in 2010, the U.S. Particle Physics Project Prioritization Panel (P5) [41,42] recommended that a world-class program of Intensity Frontier science be pursued at Fermilab as the Energy Frontier program based on the Tevatron reached its conclusion. Accordingly, Fermilab has embarked on the development of a next generation neutrino detector with LBNE and a next generation proton source with *Project X*. However, looking towards the fruition of these efforts, we must also consider how to provide the next generation of capabilities that would enable the continuation of a preeminent Intensity Frontier research program. Building on the foundation of *Project X*, muon accelerators can provide that next step with a high intensity and precise source of neutrinos to support a world-leading research program in neutrino physics. Furthermore, the infrastructure developed to support such an Intensity Frontier research program can also enable the return of the U.S. high energy physics program to the Energy Frontier. This capability would be provided in a subsequent stage of the facility that would support one or more muon colliders, which could operate at center-of-mass energies from the Higgs resonance at 125 GeV up to the multi-TeV scale. Thus, muon accelerators offer the unique potential, among the accelerator concepts being discussed for the 2013 Community Summer Study process, to provide world-leading experimental support spanning physics at both the Intensity and Energy Frontiers.

The U.S. Muon Accelerator Program (MAP) has the task of assessing the feasibility of muon accelerators for neutrino factory (NF) and Muon Collider (MC) applications. Critical path R&D items, which are important for the performance of one or more of these facilities, include

- Development of a high power target station capable of handling 4 MW of power. Liquid metal jet technology has been shown to be capable of handling this amount of power. However, a complete engineering design of a multi-MW target station with a high field capture solenoid (nominal 20 T hybrid normal and superconducting magnet with ~ 3 GJ stored energy) requires considerable further work. While challenging, target stations with similar specifications are required for other planned facilities (e.g., spallation sources), and our expectation is that many of the critical engineering issues will be addressed by others over the next several years.
- Muon cooling is required in order to achieve the beam parameters for a high performance NF and for all MC designs under consideration. An ionization cooling channel requires the operation of RF cavities in Tesla-scale magnetic fields. Promising recent results from the MuCool Test Area (MTA) at Fermilab point towards solutions to the breakdown problems of RF cavities operating in this environment [43–47].
- High-intensity and low-energy beams (~ 200 MeV, optimal for muon ionization cooling) are susceptible to a range of potential collective effects. Evaluating the likely impact of these effects on the muon beams required for NF and MC applications, through simulation and

experiment, is an important deliverable of the MAP feasibility assessment. These results will be crucial for an informed community decision on muon accelerator facilities. Furthermore, the proposed staging plan enables confirming R&D to be performed at each stage for the next stage in the plan, thus enabling a well-informed decision process moving forward.

- For the MC, a new class of backgrounds from muon decays impacts both the magnet/shielding design for the collider itself and the backgrounds in the detector. It has been found that the detector backgrounds can be managed by means of pixelated detectors with good time resolution [48,49]. Thus, this issue appears to present no impediment to moving forward with full detector studies and machine design efforts.

In the context of the proposed staging plan, baseline parameter specifications have been developed for a series of facilities, each capable of providing cutting edge physics output, and at each of which the performance of systems required for the next stage can be reliably evaluated. The plan thus provides clear decision points before embarking upon each subsequent stage. The staging plan builds on, and takes advantage of, existing or proposed facilities, specifically: *Project X* at Fermilab as the MW-class proton driver for muon generation; Homestake as developed for the LBNE detector, which could then house the detector for a long baseline neutrino factory. The performance characteristics of each stage provide unique physics reach

- *vSTORM*: a short baseline neutrino factory enabling a definitive search for sterile neutrinos, see Sec. II.3.3, as well as neutrino cross-section measurements that will ultimately be required for precision measurements at any long baseline experiment.
- *L3NF*: an initial long baseline neutrino factory, optimized for a detector at Homestake, affording a precise and well-characterized neutrino source that exceeds the capabilities of conventional superbeam technology.
- *NF*: a full intensity neutrino factory, upgraded from *L3NF*, as the ultimate source to enable precision *CP* violation measurements in the neutrino sector.
- *Higgs Factory*: a collider whose baseline configurations are capable of providing between 5,000 and 40,000 Higgs events per year with exquisite energy resolution.
- *Multi-TeV Collider*: if warranted by LHC results, a multi-TeV Muon Collider likely offers the best performance and least cost for any lepton collider operating in the multi-TeV regime.

Nominal parameters for a short baseline *NF*, *vSTORM* [50] and two stages of a long baseline *NF* optimized for a detector located at Homestake are provided in Table II-1. *MC* parameters for two stages of a *Higgs Factory* as well as 1.5 TeV and 3.0 TeV colliders are provided in Table II-2. All of these machines would fit readily within the footprint of the Fermilab site. The ability to deploy these facilities in a staged fashion offers major benefits:

1. the strong synergies among the critical elements of the accelerator complex maximize the size of the experimental community that can be supported by the overall facility;

Table II-1: Muon Accelerator Program baseline neutrino-factory parameters for ν STORM and two phases of a neutrino factory located on the Fermilab site and pointed towards a detector at Homestake. For comparison, the parameters of the IDS-NF are also shown.

System	Parameters	Unit	ν STORM	L3NF	NF	IDS-NF
Performance	stored μ^+ or μ^- /year		8×10^{17}	2×10^{20}	1.25×10^{21}	1×10^{21}
	ν_e or ν_μ^* to detectors/yr		3×10^{17}	9.4×10^{19}	5.6×10^{20}	5×10^{20}
Detector	Far Detector	Type		Mag LAr	Mag LAr	Super-Bind
	Distance from ring	km	1.5	1300	1300	2000
	Mass	kT	1.3	10	30?	100
	magnetic field	T	2	0.5?	0.5?	1-->2 ?
	Near Detector	Type	Liquid Ar	Liquid Ar	Liquid Ar	Liquid Ar
	Distance from ring	m	50	100	100	100
Mass	kT	0.1	1	2.7	2.7	
	magnetic field	T	No	No	No	No
Neutrino Ring	Ring Momentum P_μ	GeV/c	3.8	4	4	10
	Circumference C	m	350	1190	1190	1190
	Straight section Length	m	150	470	470	470
	Arc Length	m	25	125	125	125
Acceleration	Initial Momentum	GeV/c	3.8	0.22	0.22	0.22
	single pass Linac	GeV	None	0.9	0.9	0.9
	4.5-pass RLA	GeV	None	4	4	4
	NS-FFAG Ring	GeV	None	None	None	10
	SRF frequency	MHz	None	201	201	201
	Number of cavities		None	50 + 26	50 + 26	50 + 26 + 25
	Total Arc Length	m	50	550	550	550 + 200
Cooling			No	No	4D	4D
Proton Source	Proton Beam Power	MW	0.2	1	3	4
	Proton Beam Energy	GeV	60	3	3	10
	protons/year	1×10^{21}	0.2	41	125	25
	Repetition Frequency	Hz	1.25	70	70	50

- the staging plan reduces the investment required for individual steps between stages to levels that will hopefully fit within the future budget profile of the U.S. high energy physics program.

ν STORM's capabilities could be deployed now. The NF options and initial Higgs Factory could be based on the 3 GeV proton source of *Project X* Stage 2 operating with 1 MW and, eventually, 3 MW proton beams. This opens the possibility of launching the initial NF, which requires no cooling of the muon beams, within the next decade. Similarly, the R&D required for a decision on a collider could be completed by the middle of the next decade.

This timeline is summarized in Fig. II-9, which projects an informed decision on proceeding with an NF by the end of this decade, and a similar decision point on the first muon collider by the middle of the next decade. An MC in the multi-TeV range would offer exceptional performance due to the absence of synchrotron radiation effects, no beamstrahlung issues at the interaction point, and anticipated wall power requirements at the 200 MW scale, well below the widely accepted 300 MW maximum affordable power requirement for a future high energy physics facility. Figure II-10 shows the potential footprint of a sequence of facilities beginning with ν STORM and followed by

Table II-2: Muon Accelerator Program baseline muon-collider parameters for both Higgs factory and multi-TeV energy-frontier colliders. An important feature of the staging plan is that collider activity could begin with *Project X* Stage 2 beam capabilities at Fermilab.

Muon Collider Baseline Parameters					
Parameter	Units	Higgs Factory		Multi-TeV Baselines	
		Initial Cooling	Upgraded Cooling/Combiner		
CoM Energy	TeV	0.126	0.126	1.5	3.0
Avg. Luminosity	$10^{34} \text{cm}^{-2} \text{s}^{-1}$	0.0017	0.008	1.25	4.4
Beam Energy Spread	%	0.003	0.004	0.1	0.1
Circumference	km	0.3	0.3	2.5	4.5
No. of IPs		1	1	2	2
Repetition Rate	Hz	30	15	15	12
β^*	cm	3.3	1.7	1 (0.5-2)	0.5 (0.3-3)
No. muons/bunch	10^{12}	2	4	2	2
No. bunches/beam		1	1	1	1
Norm. Trans. Emittance, ϵ_{TN}	mm-rad	0.4	0.2	0.025	0.025
Norm. Long. Emittance, ϵ_{LN}	mm-rad	1	1.5	70	70
Bunch Length, σ_s	cm	5.6	6.3	1	0.5
Beam Size @ IP	μm	150	75	6	3
Beam-beam Parameter / IP		0.005	0.02	0.09	0.09
Proton Driver Power	MW	4 [#]	4	4	4

[#] Could begin operation with Project X Phase 2 beam

a neutrino factory and Higgs Factory at Fermilab, which could be based on the *Project X* Stage 2 configuration.

To summarize, muon accelerators can enable a broad and world-leading high energy physics program which can be based on the infrastructure of the single remaining U.S high energy physics laboratory, Fermilab. While any decision to move forward with muon accelerator based technologies rests on the evolving physics requirements of the field, as well as the successful conclusion of the MAP feasibility assessment later this decade, the ability of muon accelerators to address crucial questions on both the Intensity and Energy Frontiers, as well as to provide a broad foundation for a vibrant U.S. HEP program, argues for a robust development program to continue. This will enable a set of informed decisions by the U.S. community starting near the end of this decade.

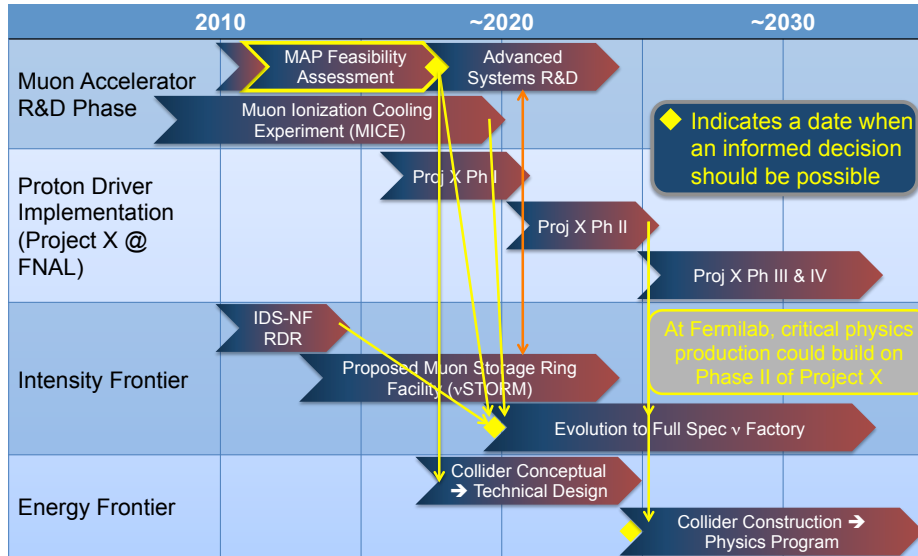


Figure II-9: Muon accelerator timeline including the MAP feasibility-assessment period. It is anticipated that decision points for moving forward with a neutrino factory project supporting intensity-frontier physics efforts could be reached by the end of this decade, and a decision point for moving forward with a muon collider physics effort supporting a return to the energy frontier with a U.S. facility could be reached by the middle of the next decade. These efforts are able to build on *Project X* Stage 2 capabilities as soon as they are available. It should also be noted that the development of a short baseline neutrino facility, i.e., *vSTORM*, would significantly enhance MAP research capabilities by supporting a program of advanced systems R&D.

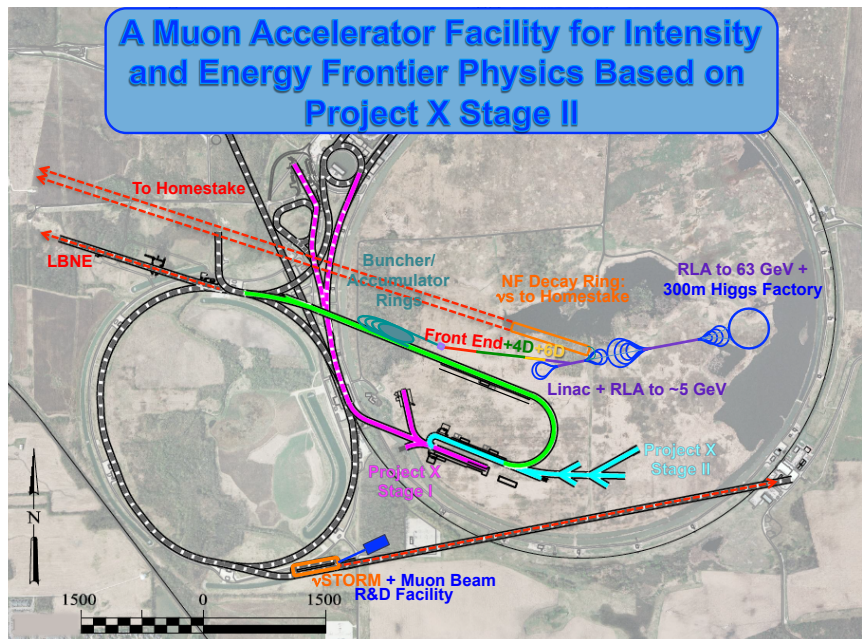


Figure II-10: Footprint of neutrino-factory and muon-collider facilities, including an initial muon collider Higgs factory, on the Fermilab site.

II.3 SHORT-BASELINE PHYSICS

Short-baseline oscillation physics in the context of *Project X* deals with flavor conversion and disappearance phenomena which take place at L/E values which are considerably smaller than those associated with the mass-squared splittings of atmospheric and solar neutrino oscillations. This area has seen an increased scientific interest, stimulating several workshops and documents, notably the sterile neutrino white paper [17] and the report of the short baseline focus group at Fermilab [51]. The LSND [52] and now MiniBooNE [53] results indicate a possible flavor conversion of $\bar{\nu}_\mu$ to $\bar{\nu}_e$ at the level of about 0.003. At the same time, MiniBooNE has seen a low energy excess of events which may or may not be related to their primary signal and LSND. The results from calibrations of low energy radio-chemical solar neutrino experiments using the reaction $\text{Ga} + \nu_e \rightarrow \text{Ge} + e^-$ based on artificial, mono-energetic neutrino sources (^{51}Cr and ^{37}Ar) [54] seem to show a deficit in count rate of about 25% with an error bar of about 10%. The so-called reactor anomaly [55] indicates a 6% deficit of ν_e emitted from nuclear reactors at baselines less than 100 m. Interestingly, this is entirely based on the re-analysis of existing data; the deficit is caused by three independent effects which all tend to increase the expected neutrino event rate. There have been two re-evaluations of reactor antineutrino fluxes [56,57] both see an increase of flux by about 3%. The neutron lifetime decreased from 887–899 s to 885.7 s [58] and thus the inverse β -decay cross section increased by a corresponding amount. The contribution from long-lived isotopes to the neutrino spectrum was previously neglected and enhances the neutrino flux at low energies.

All these hints have a statistical significance around 3σ and may be caused by one or more sterile neutrinos with masses of roughly 0.5 eV to 4 eV. The results of the PLANCK [59] satellite mission data when compared with the measured value of the Hubble constant hint at new light degrees of freedom in the universe, possibly sterile neutrinos.

Resolving those anomalies will require a new series of experiments. More specifically, the short baseline focus group [51] recommends that Fermilab pursue accelerator-based experiments which can definitively address these anomalies on a short timescale. In conjunction with the global efforts on sterile neutrinos, many of which do not rely on a large accelerator infrastructure, it seems plausible and highly likely that, by the time *Project X* starts its physics program, there will have been either a discovery of sterile neutrinos, or more generally new physics at short baselines, or stringent new limits which significantly contradict the current indications. In the latter case, there will be no short-baseline program at FNAL in the *Project X* era. In the case of an unambiguous discovery, the task of *Project X* would be to deliver high intensities at energies around 8 GeV to allow detailed studies of the newly discovered sterile neutrino(s), or whatever new physics effect is behind the short-baseline anomalies.

Several proposals exist, both a Fermilab (MiniBooNE II [60] and LAr1 [61]) and at CERN (ICARUS/NESSIE [62]), to use, as MiniBooNE did, pion decay-in-flight beams. The crucial difference to MiniBooNE would be the use of a near detector, and potentially the use of LAr TPCs instead of Cherenkov detectors. While these new proposals would constitute a significant step beyond what MiniBooNE has done, especially in terms of systematics control, it remains to be proven that a beam which has a 1% level contamination of ν_e can be used to perform a high precision study of a sub-percent appearance effect. Therefore, not all proposals are able to take full advantage of the beam intensities *Project X* will deliver.

One proposal to resolve the LSND puzzle is OscSNS [63,64], which aims to repeat the LSND measurement while avoiding the shortcomings of LSND. The idea is to build a liquid scintillator detector at a powerful 1–3 GeV proton source to exploit kaon, pion, and muon decay-at-rest. A high beam power of more than 1 MW and a short duty cycle of less than 10^{-5} are key to improve on LSND’s performance. OscSNS is the most direct test of LSND conceivable and, thus, is entirely model independent and could be central to resolving the short baseline anomalies.

Another proposed technology is to use a stored muon beam, called ν STORM. Here, the neutrinos are produced by the purely leptonic, and therefore well understood, decay of muons. Thus, the neutrino flux can be known with sub-percent precision. The signals are wrong-sign muons which can be identified quite easily in a magnetized iron detector. The precise knowledge of the neutrino flux and the expected very low backgrounds for the wrong-sign muon search allow one to reduce systematic effects to a negligible level, hence permitting precise measurements that would shed light on the new physics that may be behind the short-baseline anomalies.

II.3.1 BooNE-X

MiniBooNE has enjoyed 10 years of smooth operation, during which an astounding 6.46×10^{20} protons on target (POT) have been delivered in neutrino mode, and an even more astounding 1.14×10^{21} POT have been delivered in antineutrino mode. The results of those data are compared to the LSND data in Fig.II-11 in the context of an oscillation phenomena. The neutrino mode data has yielded an excess of $162.0 \pm 28.1_{\text{stat}} \pm 38.7_{\text{syst}}$ events at reconstructed neutrino energies below 475 MeV. That excess is not described well by a simple two-neutrino model, but can be accommodated by an extended 3 active + 2 sterile neutrino model, fit to the world’s relevant neutrino data. While the statistical significance of the excess is 6σ , the overall significance is limited to 3.4σ by the systematic error in the estimation of the background. That systematic error is related to the error in the detector acceptance or efficiency for π^0 background events, and to a lesser extent, the flux of neutrinos, and the neutrino-nucleus cross sections. Similarly, an excess of is observed in antineutrino mode of $78.4 \pm 20.0_{\text{stat}} \pm 20.3_{\text{syst}}$ events, consistent with the neutrino-mode data.

Given the success of the MiniBooNE program, we believe that constructing a MiniBooNE detector (reusing the mineral oil, electronics, and PMTs from MiniBooNE if necessary) at a new location ~ 200 meters from the Booster Neutrino Beam proton target, will be the most expedient way understand whether or not the excess events observed by MiniBooNE are caused by an oscillation process. The primary motivation for a near detector, rather than a detector further away, is that the neutrino interaction rate will be over seven times larger, and the measurement will precisely determine the neutrino-related backgrounds within six months of running. The combination of the present MiniBooNE neutrino-mode data, plus a 4-month (1×10^{20} POT or $\sim 700,000$ neutrino events) neutrino-mode run with the BooNE [60] detector, would result in a 5σ sensitivity to whether or not the excess is an oscillation effect.

In the *Project X* era, the linac will enable a much brighter Booster Neutrino Beam (BNB), and if oscillation phenomena are indeed verified, a detailed exploration of oscillations would be possible with the addition of a third detector at a distance of 1–2 km from the BNB proton target. The BooNE-X detector with a mass of 2–5 kT would be suitable with the higher neutrino flux available. The MiniBooNE technology costs scale with $(\text{mass})^{2/3}$, which is favorable compared with liquid

argon costs, which scale with (mass)¹. Measurements of a precision of 6σ would be possible with such a three-detector system.

II.3.2 LarLAr: A One-kiloton Liquid Argon Short Baseline Experiment

An interesting and powerful way to probe the MiniBooNE/LSND anomalies would be to combine the MicroBooNE detector with another, larger, liquid-argon time projection chamber (LAr TPC) in a near/far configuration. A near/far configuration, dubbed LAr1, would considerably reduce the systematic errors, while the size of the second detector would increase statistics significantly, which are expected to be the limiting factor for a MicroBooNE-only search. With a two detector system, a definite statement regarding oscillations could be made.

The LBNE collaboration is currently designing a 1 kt LArTPC as an engineering prototype. It has been pointed out that this detector could be instrumented and placed in the BNB at Fermilab to study short-baseline oscillations. Several configurations have been considered for this experiment. The MicroBooNE detector, used as the near detector, could be located either at 200 m or 470 m from the BNB. The far detector, LarLAr, could be placed either at 470 m or 700 m. Note that no further optimization has been done on the chosen detector locations, which leaves room for improvement. In the sensitivity studies presented here, the fiducial volumes assumed for MicroBooNE and LarLAr are 61.4 t and 347.5 t respectively. A flat 80% efficiency was assumed. All

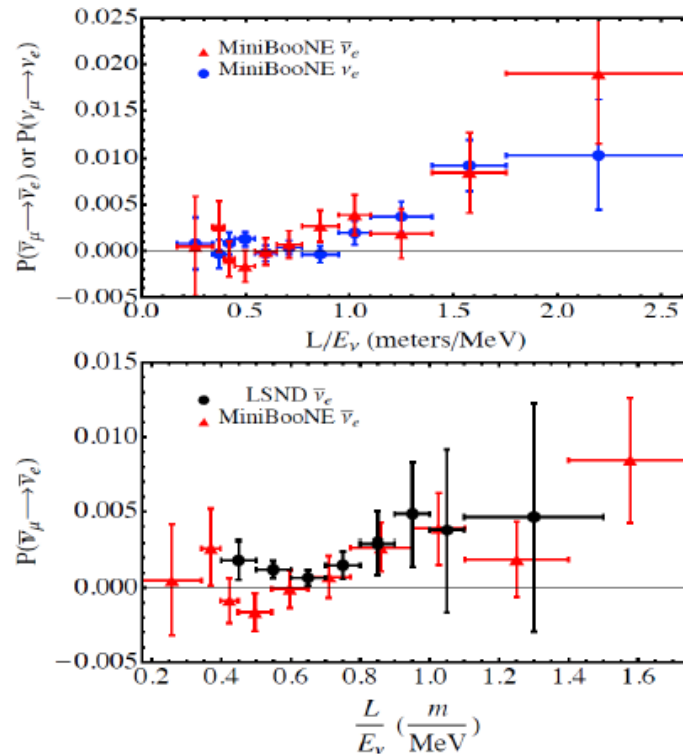


Figure II-11: LSND and MiniBooNE anomalies as an oscillation probability vs. L/E . The interpretation of the anomalies as an oscillation effect is consistent with the data.

results shown below are for statistical errors only, which are assumed to be the dominant source of uncertainty. Fig. II-12 shows sensitivity curves to a 3+1 neutrino model, for different configurations with both MicroBooNE and LarLAr detectors combined in neutrino and antineutrino modes, for a total of 6.6×10^{20} POT in each mode. Such a sample is achievable in two years under an improved-linac *Project X* scenario. It is clear from these studies that combining two LAr detectors is a very powerful way to probe short-baseline oscillations. If systematic uncertainties can be reasonably mitigated, this two LAr-detector experiment would offer definitive measurements (at the 5σ level) of the Mini-BooNE/LSND anomalies in both neutrino and antineutrino modes. Note that in the antineutrino case, more than 6.6×10^{20} POTs would be required to reach the 5σ level for the whole allowed parameter space.

II.3.3 ν Storm: Neutrinos from Stored Muons

The idea of using a muon storage ring to produce a high-energy ($\simeq 50$ GeV) neutrino beam for experiments was first discussed in 1974 by Koshkarev [65]. A detailed description of a muon storage ring for neutrino oscillation experiments was first produced in 1980 by Neuffer [66]. In his paper, Neuffer studied muon decay rings with E_μ of 8, 4.5 and 1.5 GeV. With his 4.5 GeV ring design, he achieved a figure of merit of $\simeq 6 \times 10^9$ useful neutrinos per 3×10^{13} protons on target. The facility

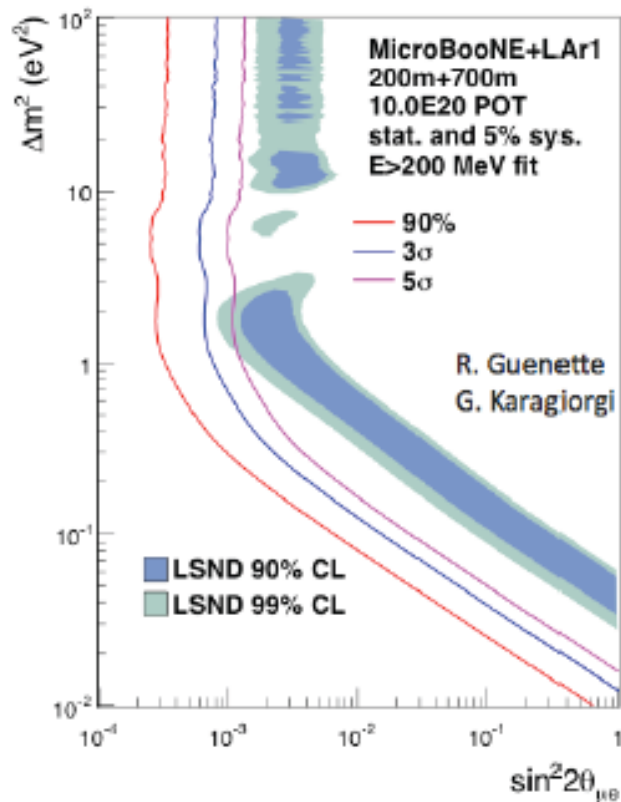


Figure II-12: LarLAr sensitivity to the LSND anomaly in neutrino mode.

we describe here—vSTORM [50]—is essentially the same facility proposed in 1980 and would use a 3–4 GeV/c muon storage ring to study eV-scale oscillation physics and, in addition, could add significantly to our understanding of ν_e and ν_μ cross sections. In particular the facility can

1. address the large Δm^2 oscillation regime and make a major contribution to the study of sterile neutrinos;
2. make precision ν_e and $\bar{\nu}_e$ cross-section measurements;
3. provide a technology (μ decay ring) test demonstration and μ beam diagnostics test bed;
4. provide a precisely understood ν beam for detector studies.

See Fig. II-13 for a schematic of the facility.

The facility is the simplest implementation of the neutrino-factory concept [67]. In our case, 60 GeV/c protons are used to produce pions off a conventional solid target. The pions are collected with a focusing device (horn or lithium lens) and are then transported to, and injected into, a storage ring. The pions that decay in the first straight of the ring can yield a muon that is captured in the ring. The circulating muons then subsequently decay into electrons and neutrinos. We are starting with a storage ring design that is optimized for 3.8 GeV/c muon momentum. This momentum was selected to maximize the physics reach for both oscillation and the cross section physics.

It would also be possible to create a $\pi \rightarrow \mu$ decay channel and inject the muons into the decay ring with a kicker magnet. This scheme would have the advantage that the transport channel could be longer than the straight in the decay ring and thus allow for more π decays to result in a useful μ . This does complicate the facility design, however, due to the need for the kicker magnet and the desire to use single-turn extraction from the Main Injector.

Muon decay yields a neutrino beam of precisely known flavor content and energy. For example for positive muons: $\mu^+ \rightarrow e^+ + \bar{\nu}_\mu + \nu_e$. In addition, if the circulating muon flux in the ring is measured accurately (with beam-current transformers, for example), then the neutrino beam flux is also accurately known. Near and far detectors are placed along the line of one of the straight sections of the racetrack decay ring. The near detector can be placed at 20–50 meters from the end of the straight. A near detector for disappearance measurements will be identical to the far detector, but only about one tenth the fiducial mass. It will require a μ catcher, however. Additional purpose-specific near detectors can also be located in the near hall and will measure neutrino-nucleon cross sections. vSTORM can provide the first precision measurements of ν_e and $\bar{\nu}_e$ cross sections which are important for future long-baseline experiments. A far detector at $\simeq 2000$ m would study neutrino oscillation physics and would be capable of performing searches in both appearance and disappearance channels. The experiment will take advantage of the “golden channel” of oscillation appearance $\nu_e \rightarrow \nu_\mu$, where the resulting final state has a muon of the wrong-sign from interactions of the $\bar{\nu}_\mu$ in the beam. In the case of μ^+ s stored in the ring, this would mean the observation of an event with a μ^- . This detector would need to be magnetized for the wrong-sign muon appearance channel, as is the case for the current baseline neutrino factory detector [68]. A number of possibilities for the far detector exist. However, a magnetized iron detector similar to that used in MINOS [69] is likely to be the most straight forward approach for the far detector design. We believe that it will meet the performance requirements needed to reach our physics goals. For the

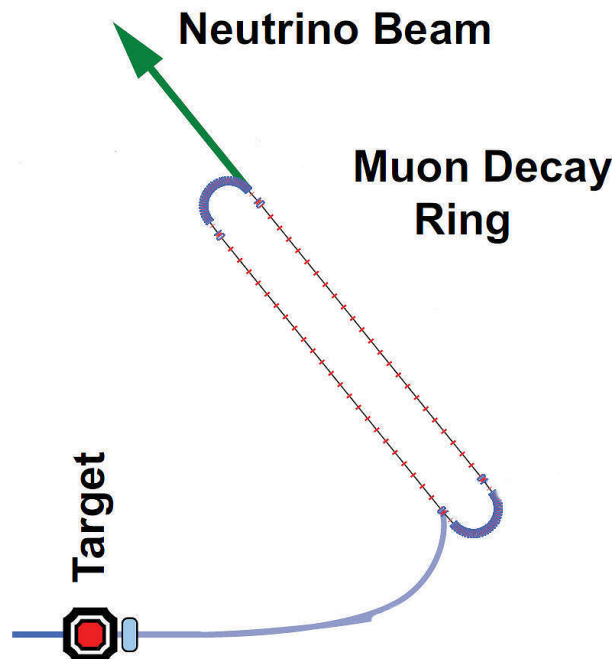


Figure II-13: Schematic of the vStorm facility.

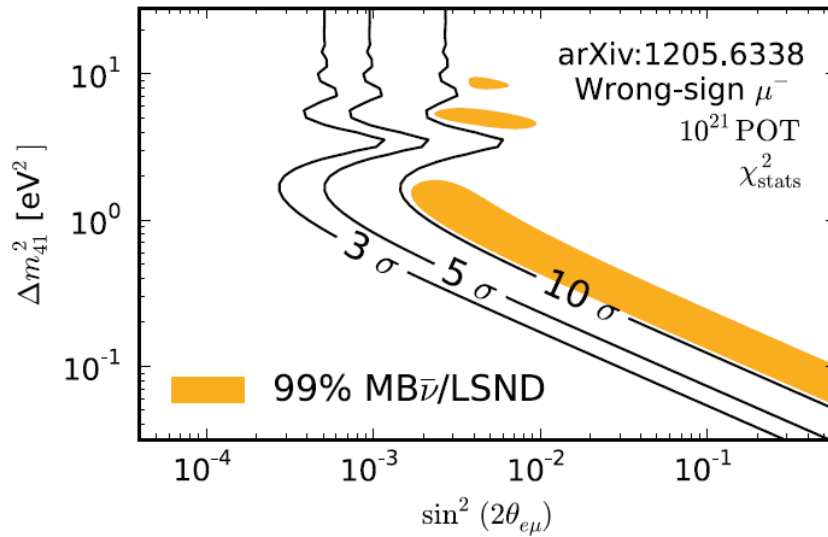


Figure II-14: Exclusion limits (statistical uncertainties only) from a five year run of vSTORM. The orange-shaded areas show the combined 99% CL allowed region from MiniBooNE and LSND.

purposes of the vSTORM oscillation physics, a detector inspired by MINOS, but with thinner plates and much larger excitation current (larger B field) is assumed.

II.3.4 Neutrinos from Stopped Kaons, Pions, and Muons

The *Project X* facility provides a unique opportunity for US science to perform a definitive search for sterile neutrinos. The MW beam power of *Project X* is a prodigious source of neutrinos from the decay of K^+ , π^+ and μ^+ at rest. These decays produce a well specified flux of neutrinos via $K^+ \rightarrow \mu^+ \nu_\mu$, $\tau_K = 1.2 \times 10^{-8}$ s, $\pi^+ \rightarrow \mu^+ \nu_\mu$, $\tau_\pi = 2.7 \times 10^{-8}$ s, and $\mu^+ \rightarrow e^+ \nu_e \bar{\nu}_\mu$, $\tau_\mu = 2.2 \times 10^{-6}$ s. With the *Project X* RCS option, the low duty factor is more than 1000 times less than LAMPF, and this smaller duty factor reduces cosmic backgrounds and allows the induced events from π^+ decay to be separated from the ν_e and $\bar{\nu}_\mu$ induced events from μ^+ decay.

The detector would be based on the LSND and MiniBooNE detector technologies, similar to the OscSNS proposal [64] and would consist of an ~ 1 kT tank of mineral oil, covered by approximately 3500 8-inch phototubes, and located about 60 m from the production target. The K^+ decays provide a mono-energetic ν_μ which can be seen via charged current reactions. A direct measurement of oscillations can be made by measuring their rate as a function of flight path. The experiment will use the mono-energetic 29.8 MeV to investigate the existence of light sterile neutrinos via the neutral-current reaction $\nu_\mu {}^{12}\text{C} \rightarrow {}^{12}\text{C}^*(15.11 \text{ MeV})$, which has the same cross section for all active neutrinos but is zero for sterile neutrinos. An oscillation of this reaction, with a known neutrino energy, is direct evidence for sterile neutrinos. The experiment can also carry out a unique and decisive test of the LSND appearance $\bar{\nu}_e$ signal. In addition, a sensitive search for ν_e disappearance can be made by searching for oscillations in the detector of the reaction $\nu_e {}^{12}\text{C} \rightarrow e^+ {}^{12}\text{N}(gs)$, where the $\text{N}(gs)$ is identified by its beta decay. It is important to note that all of the cross sections involved are known to a few percent or better. The existence of light sterile neutrinos would be the first major extension of the Standard Model, and sterile neutrino properties are central to dark matter, cosmology, astrophysics, and future neutrino research. An experiment at *Project X* would be able to prove whether sterile neutrinos can explain the existing short-baseline anomalies.

II.3.5 Dark Sector Physics at SBL Neutrino Experiments

Finally, short-baseline neutrino oscillation experiments are also ideal tools to search for more exotic physics [70]. The production of other weakly interacting particles—such as axions, dark gauge bosons, and WIMP particles—is in many cases expected to be detectable in SBL neutrino experiments. The “portal” to the dark sector is dark-photon mixing with normal photons, and π^0 and η decays to photons produce the dark-sector particles: $\pi^0, \eta \rightarrow \gamma V$, $V \rightarrow \tilde{\chi}\chi$. As an example, the 3σ anomaly in the muon $g - 2$ could be explained by such a model and account for the dark matter observed in the universe. Indeed, MiniBooNE has already proposed [71] to test some or those models with a run where the beam is steered off-target to suppress neutrino production. For further discussion, see Chapter VII.

II.3.6 Neutrino Scattering Physics Experiments

In general, the higher intensity beams offered by *Project X* would enable more precise measurements of Standard-Model processes. They include leptonic processes span the range from $\nu e \rightarrow \nu e$ at a stopped $K/\pi/\mu$ neutrino source, all the way up to the deep-inelastic scattering of neutrinos off of nuclei in the many-GeV energy range. Those measurements can probe non-standard interactions and yield important information about nuclear physics. Neutrino-nucleus scattering data is essential for interpreting precision long-baseline oscillation experiments. For example, a detector in the LBNE neutrino beam, if designed properly, could make dramatic progress on further understanding of those processes with the high event rates of a *Project X* beam. As discussed above, a better understanding of neutrino-nucleon form factors, obtained via lattice QCD, will also help.

II.4 SUMMARY

For the short-baseline program, *Project X* most likely will play a role after a discovery has been made and in that case, the goal would be a precise measurement of the parameters of the newly discovered physics. If there is no discovery in the short-baseline program prior to *Project X*, it is doubtful that this program would be pursued in the *Project X* era. The only technology which seems to have a clear upgrade path to high precision short-baseline physics without running into systematics issues is vSTORM. vSTORM would profit considerably from increased beam power at 120 GeV.

The LBNE experiment is strong motivation for *Project X* in order to fully capitalize on the considerable investment made on a large underground detector and new beamline. The currently approved LBNE Project scope includes a new beamline capable of accepting all the beam power *Project X* can deliver. However, the initial detector mass is rather small, 10 kt, and on the surface, which may require a further effective reduction of fiducial mass to cope with cosmogenic backgrounds. The initial small detector mass and the risk of it becoming effectively smaller with surface operations is strongly motivating the LBNE collaboration grow in number and resources in order to place the initial detector underground, and with a mass greater than 10 kT.

A staged muon-based program starting with vSTORM can evolve in various, adjustable steps to a full neutrino factory, which, eventually, sets the stage for a muon collider. This pathway seems to be a very attractive option, producing outstanding physics with every step. At the same time, it crucially requires *Project X* and, thus, could be one of the most compelling motivations for *Project X*. Obviously, going beyond vSTORM requires a vigorous R&D effort, which in the form of the IDS-NF and MAP is already ongoing, but would benefit from increased funding.

References

- [1] B. Aharmim *et al.* (SNO Collaboration), “Combined analysis of all three phases of solar neutrino data from the Sudbury Neutrino Observatory,” (2011), arXiv:1109.0763 [nucl-ex]
- [2] R. Wendell *et al.* (Super-Kamiokande Collaboration), Phys. Rev. **D81**, 092004 (2010), [arXiv:1002.3471 [hep-ex]]

- [3] K. Abe *et al.* (Super-Kamiokande Collaboration), Phys. Rev. Lett. **107**, 241801 (2011), [arXiv:1109.1621 [hep-ex]]
- [4] M. H. Ahn *et al.* (K2K Collaboration), Phys. Rev. **D74**, 072003 (2006), [arXiv:hep-ex/0606032 [hep-ex]]
- [5] P. Adamson *et al.* (MINOS Collaboration), Phys. Rev. Lett. **108**, 191801 (2012), [arXiv:1202.2772 [hep-ex]]
- [6] K. Abe *et al.* (T2K Collaboration), Phys. Rev. **D85**, 031103 (2012), [arXiv:1201.1386 [hep-ex]]
- [7] S. Abe *et al.* (KamLAND Collaboration), Phys. Rev. Lett. **100**, 221803 (2008), [arXiv:0801.4589 [hep-ex]]
- [8] Y. Abe *et al.* (Double Chooz Collaboration), Phys. Rev. **D86**, 052008 (2012), [arXiv:1207.6632 [hep-ex]]
- [9] J. K. Ahn *et al.* (RENO Collaboration), Phys. Rev. Lett. **108**, 191802 (2012), [arXiv:1204.0626 [hep-ex]]
- [10] F. P. An *et al.* (Daya Bay Collaboration), Phys. Rev. Lett. **108**, 171803 (2012), [arXiv:1203.1669 [hep-ex]]
- [11] P. Adamson *et al.* (MINOS Collaboration), Phys. Rev. Lett. **107**, 181802 (2011), [arXiv:1108.0015 [hep-ex]]
- [12] K. Abe *et al.* (T2K Collaboration), Phys. Rev. Lett. **107**, 041801 (2011), [arXiv:1106.2822 [hep-ex]]
- [13] N. Agafonova *et al.* (OPERA Collaboration), Phys. Lett. **B691**, 138 (2010), [arXiv:1006.1623 [hep-ex]]
- [14] B. Pontecorvo, Sov. Phys. JETP **6**, 429 (1957)
- [15] Z. Maki, M. Nakagawa, and S. Sakata, Prog. Theor. Phys. **28**, 870 (1962)
- [16] G. L. Fogli *et al.*, Phys. Rev. **D86**, 013012 (2012), [arXiv:1205.5254 [hep-ph]]
- [17] K. N. Abazajian *et al.*, “Light sterile neutrinos: A white paper,” (2012), arXiv:1204.5379 [hep-ph]
- [18] T. Ohlsson, Rep. Prog. Phys. **76**, **044201**, 044201 (2013), [arXiv:1209.2710 [hep-ph]]
- [19] A. Lenz *et al.* (CKMFitter Group), Phys. Rev. **D86**, 033008 (2012), [arXiv:1203.0238 [hep-ph]]
- [20] S. F. King, JHEP **0508**, 105 (2005), [arXiv:hep-ph/0506297 [hep-ph]]
- [21] G. Altarelli and F. Feruglio, Rev. Mod. Phys. **82**, 2701 (2010), [arXiv:1002.0211 [hep-ph]]
- [22] S. F. King and C. Luhn, Rept. Prog. Phys. **76**, 056201 (2013), [arXiv:1301.1340 [hep-ph]]

- [23] A. de Gouvêa and H. Murayama, “Neutrino mixing anarchy: Alive and kicking,” (2012), arXiv:1204.1249 [hep-ph]
- [24] M. Diwan *et al.*, “Proposal for an experimental program in neutrino physics and proton decay in the Homestake Laboratory,” Fermilab-BNL Joint Study on Long-baseline Neutrino Oscillations (2006), arXiv:hep-ex/0608023 [hep-ex]
- [25] V. Barger, P. Huber, D. Marfatia, and W. Winter, Phys. Rev. **D76**, 053005 (2007), [arXiv:hep-ph/0703029 [hep-ph]]
- [26] V. Barger *et al.*, “Report of the US long-baseline neutrino experiment study,” (2007), arXiv:0705.4396 [hep-ph]
- [27] P. Huber, M. Mezzetto, and T. Schwetz, JHEP **0803**, 021 (2008), [arXiv:0711.2950 [hep-ph]]
- [28] M. Day and K. S. McFarland, Phys. Rev. **D86**, 053003 (2012), [arXiv:1206.6745 [hep-ph]]
- [29] P. Coloma, P. Huber, J. Kopp, and W. Winter, “Systematics in long-baseline neutrino oscillations for large θ_{13} ,” (2012), in preparation
- [30] A. Rubbia *et al.*, “Expression of interest for a very long baseline neutrino oscillation experiment (LBNO),” (2012), CERN-SPSC-2012-021, SPSC-EOI-007
- [31] LBNE Collaboration, http://lbne.fnal.gov/collaboration/collab_main.shtml
- [32] LBNE Collaboration, “LBNE conceptual design report,” (March 2012), <https://sharepoint.fnal.gov/project/lbne/LBNE%20at%20Work/SitePages/Reports%20and%20Documents.aspx>
- [33] P. Huber and J. Kopp, JHEP **1103**, 013 (2011), [arXiv:1010.3706 [hep-ph]]
- [34] S. Davidson, C. Peña-Garay, N. Rius, and A. Santamaria, JHEP **0303**, 011 (2003), [arXiv:hep-ph/0302093 [hep-ph]]
- [35] M. C. Gonzalez-Garcia and M. Maltoni, Phys. Rept. **460**, 1 (2008), [arXiv:0704.1800 [hep-ph]]
- [36] C. Biggio, M. Blennow, and E. Fernández-Martínez, JHEP **0908**, 090 (2009), [arXiv:0907.0097 [hep-ph]]
- [37] T. Akiri *et al.* (LBNE Collaboration), “The 2010 interim report of the Long-Baseline Neutrino Experiment Collaboration physics working groups,” (2011), arXiv:1110.6249 [hep-ex]
- [38] “Physics research goals of the LBNE project,” <http://lbne2-docdb.fnal.gov/cgi-bin/ShowDocument?docid=3056>
- [39] E. Christensen, P. Coloma, and P. Huber, “Physics performance of a low-luminosity low energy neutrino factory,” (2013), arXiv:1301.7727 [hep-ph]
- [40] P. Huber and T. Schwetz, Phys. Lett. **B669**, 294 (2008), [arXiv:0805.2019 [hep-ph]]

- [41] Particle Physics Project Prioritization Panel, “U.S. particle physics: Scientific opportunities, a plan for the next ten years,” (May 2008)
- [42] Particle Physics Project Prioritization Panel, “Recommendations on the extended Tevatron run,” (October 2010)
- [43] K. Yonehara *et al.*, Conf. Proc. **C1205201**, 208 (2012)
- [44] M. R. Jana *et al.*, Conf. Proc. **C1205201**, 217 (2012)
- [45] B. Freemire *et al.*, “Study of electronegative gas effect in beam induced plasma,” (2012), FERMILAB-CONF-12-249-APC, IPAC-2012-MOPPC040
- [46] D. L. Bowring *et al.*, “Progress on a cavity with beryllium walls for muon ionization cooling channel R&D,” (2012), IPAC-2012-THPPC033
- [47] Z. Li, L. Ge, C. Adolphsen, D. Li, and D. Bowring, “Improved RF design for an 805 MHz pillbox cavity for the U.S. MuCool program,” (2012), IPAC-2012-THPPC040
- [48] A. Conway and H. Wenzel, “Higgs measurements at a muon collider,” (2013), arXiv:1304.5270 [hep-ex]
- [49] A. Mazzacane, in *Higgs Factory Muon Collider Workshop* (UCLA, 2013)
- [50] P. Kyberd *et al.* (nuSTORM Collaboration), “nuSTORM: Neutrinos from STORed Muons,” (2012), arXiv:1206.0294 [hep-ex]
- [51] S. J. Brice *et al.*, *Short-Baseline Neutrino Focus Group Report*, Tech. Rep. (Fermilab, 2012) FERMILAB-FN-0947, <http://lss.fnal.gov/archive/test-fn/0000/fermilab-fn-0947.shtml>
- [52] A. Aguilar-Arevalo *et al.* (LSND Collaboration), Phys. Rev. **D64**, 112007 (2001), [arXiv:hep-ex/0104049 [hep-ex]]
- [53] A. A. Aguilar-Arevalo *et al.* (MiniBooNE Collaboration), Phys. Rev. Lett. **110**, 161801 (2012), [arXiv:1207.4809 [hep-ex]]
- [54] C. Giunti and M. Laveder, Phys. Rev. **C83**, 065504 (2011), [arXiv:1006.3244 [hep-ph]]
- [55] G. Mention *et al.*, Phys. Rev. **D83**, 073006 (2011), [arXiv:1101.2755 [hep-ex]]
- [56] P. Huber, Phys. Rev. **C84**, 024617 (2011), (E) Phys. Rev. **C85** 029901, [arXiv:1106.0687 [hep-ph]]
- [57] T. A. Mueller *et al.*, Phys. Rev. **C83**, 054615 (2011), [arXiv:1101.2663 [hep-ex]]
- [58] J. Beringer *et al.* (Particle Data Group), Phys. Rev. **D86**, 010001 (2012)
- [59] P. A. R. Ade *et al.* (Planck Collaboration), “Planck 2013 results. XVI. Cosmological parameters,” (2013), arXiv:1303.5076 [astro-ph.CO]

- [60] G. B. Mills *et al.*, “A proposal to build a MiniBooNE near detector: BooNE,” (2011), http://www.fnal.gov/directorate/program_planning/Dec2011PACPublic/BooNE_Proposal.pdf
- [61] H. Chen *et al.*, “A letter of intent for a neutrino oscillation experiment on the Booster Neutrino Beamline: LAr1,” (2012), FERMILAB-PROPOSAL-1030
- [62] A. Antonello *et al.*, “Search for anomalies in the neutrino sector with muon spectrometers and large LArTPC imaging detectors at CERN,” (2012), arXiv:1208.0862 [physics.ins-det]
- [63] G. T. Garvey *et al.*, Phys. Rev. **D72**, 092001 (2005), [arXiv:hep-ph/0501013 [hep-ph]]
- [64] W. Louis *et al.* (OscSNS Collaboration), “OscSNS: a precision neutrino oscillation experiment at the SNS,” (2013), arXiv:1305.4189 [hep-ex]
- [65] D. G. Koshkarev, “Proposal for a decay ring to produce intense secondary particle beams at the SPS,” (1974)
- [66] V. Barger and D. Cline, eds., *Design Considerations for a Muon Storage Ring* (Conference on Neutrino Mass, 1980)
- [67] S. Geer, Phys. Rev. **D57**, 6989 (1998), (E) Phys. Rev. **D59** 039903, [arXiv:hep-ph/9712290 [hep-ph]]
- [68] S. Choubey *et al.*, “International design study for the neutrino factory, interim design report,” arXiv:1112.2853 [hep-ex]
- [69] E. Ables *et al.* (MINOS Collaboration), “P-875: A long baseline neutrino oscillation experiment at Fermilab,” (1995)
- [70] J. L. Hewett, H. Weerts, *et al.*, *Fundamental Physics at the Intensity Frontier* (U.S. Department of Energy, Germantown, MD, 2012) arXiv:1205.2671 [hep-ex]
- [71] R. Dharmapalan *et al.* (MiniBooNE Collaboration), “Low mass WIMP searches with a neutrino experiment: A proposal for further MiniBooNE running,” (2012), arXiv:1211.2258 [hep-ex]

III Kaon Physics with *Project X*

Vincenzo Cirigliano, David E. Jaffe, Kevin Pitts,
Wolfgang Altmannshofer, Joachim Brod, Stefania Gori, Ulrich Haisch, and Robert S. Tschirhart

III.1 INTRODUCTION

Kaon decays have played a key role in the shaping of the Standard Model (SM) [1–3] from the discovery of kaons [4] until today. Prominent examples are the introduction of internal flavor quantum numbers (strangeness) [5,6], parity violation ($K \rightarrow 2\pi, 3\pi$ puzzle) [7,8], quark mixing [9,10], meson-antimeson oscillations, the discovery of CP violation [11], suppression of flavor-changing neutral currents (FCNC) and the Glashow-Iliopoulos-Maiani (GIM) mechanism [12]. Kaon properties continue to have a high impact in constraining the flavor sector of possible extensions of the SM. As we explain in this chapter, their influence will extend into the *Project X* era.

In the arena of kaon decays, a prominent role is played by the FCNC modes mediated by the quark-level processes $s \rightarrow d(\gamma, \ell^+ \ell^-, \nu\bar{\nu})$, and in particular the four theoretically cleanest modes $K^+ \rightarrow \pi^+ \nu\bar{\nu}$, $K_L \rightarrow \pi^0 \nu\bar{\nu}$, $K_L \rightarrow \pi^0 e^+ e^-$, and $K_L \rightarrow \pi^0 \mu^+ \mu^-$. Because of the peculiar suppression of the SM amplitude (loop level proportional to $|V_{us}|^5$) which in general is not present in SM extensions, kaon FCNC modes offer a unique window on the flavor structure of SM extensions. This argument by itself already provides a strong and model-independent motivation to study these modes, even while the TeV-scale is probed at the LHC: rare K decays can teach us about the flavor structure of SM extensions at much, much higher energies. For further discussion of the role of quark and lepton flavor physics in the search for new phenomena, see the recent review in Ref. [13].

The discovery potential of rare decays depends on how well we can calculate their rates in the SM, how strong the constraints from other observables are, and how well we can measure their branching ratios (BRs). State-of-the-art predictions are summarized in Table III-1 and show that we currently know the BRs $K^+ \rightarrow \pi^+ \nu\bar{\nu}$ at the 10% level, $K_L \rightarrow \pi^0 \nu\bar{\nu}$ at the 15% level, while $K_L \rightarrow \pi^0 e^+ e^-$, and $K_L \rightarrow \pi^0 \mu^+ \mu^-$ at the 25–30% level. Note that the charged and neutral $K \rightarrow \pi \nu\bar{\nu}$ modes are predicted with a precision surpassing any other FCNC process involving quarks.

Within a general effective field theory (EFT) analysis of new physics effects, $K \rightarrow \pi \nu\bar{\nu}$ probe a number of leading dimension-six operators. A subset of these operators is essentially unconstrained by other observables, and therefore on general grounds one can expect sizable deviations from the SM in $K \rightarrow \pi \nu\bar{\nu}$ (both modes), depending on the flavor structure of the Beyond the Standard Model (BSM) scenario. Moreover, an analysis of the correlations among various rare K decay modes allows one to disentangle the size of different BSM operators, thus enhancing our model-discriminating power and making the case for building a broad K physics program, that involves all rare FCNC decays.

If one restricts the analysis to the subset of Z -penguin BSM operators, which are the dominant in several explicit models of new physics, a number of constraints on $K \rightarrow \pi \nu\bar{\nu}$ emerges. In fact, Z -penguin operators affect a large number of kaon observables ($K \rightarrow \pi \ell^+ \ell^-$, ε_K , ε'/ε , and in the case

Table III-1: Summary of current SM predictions and experimental limits for the four cleanest rare kaon decays. In the SM predictions, the first error is parametric, the second denotes the intrinsic theoretical uncertainty.

Mode	Standard Model	Experiment
$K^+ \rightarrow \pi^+ \nu \bar{\nu}$	$7.81(75)(29) \times 10^{-11}$	$(1.73^{+1.15}_{-1.05}) \times 10^{-10}$ E787/949
$K_L \rightarrow \pi^0 \nu \bar{\nu}$	$2.43(39)(6) \times 10^{-11}$	$< 2.6 \times 10^{-8}$ E391a
$K_L \rightarrow \pi^0 e^+ e^-$	$(3.23^{+0.91}_{-0.79}) \times 10^{-11}$	$< 28 \times 10^{-11}$ KTEV
$K_L \rightarrow \pi^0 \mu^+ \mu^-$	$(1.29^{+0.24}_{-0.23}) \times 10^{-11}$	$< 38 \times 10^{-11}$ KTEV

of one operator $K \rightarrow \pi \ell \nu$ through SU(2) gauge invariance). Figure III-4 illustrates that currently the strongest constraints on $K \rightarrow \pi \nu \bar{\nu}$ arise from direct CP violation in $K \rightarrow \pi \pi$ decays, which excludes order-of-magnitude deviations in $K_L \rightarrow \pi^0 \nu \bar{\nu}$ while still allowing for dramatic effects in $K^+ \rightarrow \pi^+ \nu \bar{\nu}$. While this is true only in models in which the Z-penguin dominates contributions to $K \rightarrow \pi \nu \bar{\nu}$, we think this constraint should be used as a target for future “discovery” searches in $K_L \rightarrow \pi^0 \nu \bar{\nu}$ at *Project X*. As discussed in detail later in this chapter, there is strong evidence to support a Day-1 *Project X* $K_L^0 \rightarrow \pi^0 \nu \bar{\nu}$ experiment with ~ 1000 SM event sensitivity, which would retain plenty of discovery potential even in presence of the constraint from ϵ'/ϵ .

This chapter is organized as follows. Section III.2 elaborates further on the physics case supporting the search for rare FCNC K decays well into the next decade. We begin with a review of the SM predictions (Sec. III.2.1) and we then discuss the physics reach, first in a model-independent effective theory framework (Sec. III.2.2), then within supersymmetric models (Sec. III.2.3), and last within Randall-Sundrum models of warped extra dimensions (Sec. III.2.4). We briefly comment on the reach of other decay modes in Sec. III.2.5. In Sec. III.3 we first summarize the landscape of kaon experiments in this decade (Sec. III.3.1), and then discuss the opportunity and impact of rare kaon decay measurements at *Project X* (Sec. III.3.2). We summarize in Section. III.4.

III.2 RARE KAON DECAYS AS DEEP PROBES OF NEW PHYSICS

Rare kaon decays are severely suppressed in the Standard Model (SM). Therefore they are highly sensitive to possible new physics (NP) effects. Given the high precision of the SM predictions—in particular those of the “golden modes” $K \rightarrow \pi \nu \bar{\nu}$ (charged and neutral)—as well as the expected future experimental sensitivities, even deviations from the SM predictions as small as 20–30% could allow to establish the existence of NP. Moreover, visible deviations from the SM predictions are possible within many well motivated NP models like the Minimal Supersymmetric Standard Model (MSSM) and in Randall-Sundrum (RS) Models. In the following we give more details on the SM predictions of rare K decays and their sensitivity to the flavor structure of SM extensions.

III.2.1 The baseline: Rare Kaon Decays in the Standard Model

The decays $K^+ \rightarrow \pi^+ \nu \bar{\nu}$, $K_L \rightarrow \pi^0 \nu \bar{\nu}$, $K_L \rightarrow \pi^0 e^+ e^-$ and $K_L \rightarrow \pi^0 \mu^+ \mu^-$ proceed dominantly through heavy-quark induced flavor-changing neutral currents (FCNC). Within the standard model, the elec-

troweak processes inducing the rare K decays arise first at the one-loop level and are of three types: Z penguin and W box, single photon penguin, and double photon penguin, each being a function of the ratios m_q^2/M_W^2 (see Fig. III-1). Here m_q , $q = u, c, t$, are the up-type quark masses, and M_W is the W boson mass. (The GIM mechanism cancels the constant part of the loop functions when summing over the three up-quark flavors.)

The relative importance of each type of process contributing to the rare K decays can be neatly understood in terms of the limit of the loop functions for large or small quark masses. The Z penguin, as well as the CP -violating single-photon penguin, are dominated by short-distance physics (top- and charm-quark), due to the powerlike breaking of the Glashow-Iliopoulos-Maiani (GIM) mechanism. On the contrary, the CP -conserving photon penguins are fully dominated by the long-distance up-quark contribution, arising from the logarithmic behavior of the corresponding loop functions.

Theory predictions for the decay rates are obtained using an effective theory framework, which allows us to separate the different energy scales involved in the decay processes and to use appropriate methods of calculation [14]. The short-distance part is encoded explicitly into the Wilson coefficients of the weak effective Hamiltonian. However, computing the hadronic matrix elements of operators involving quark fields is a nontrivial problem, which can be addressed with lattice QCD (see Chapter X) or other nonperturbative methods based on symmetries and dispersion relations.

III.2.1.1 $K^+ \rightarrow \pi^+ \nu \bar{\nu}$ and $K_L \rightarrow \pi^0 \nu \bar{\nu}$

For the the decays $K^+ \rightarrow \pi^+ \nu \bar{\nu}$ and $K_L \rightarrow \pi^0 \nu \bar{\nu}$ short-distance physics dominates because of the absence of photon penguins. The effective Hamiltonian for the $K^+ \rightarrow \pi^+ \nu \bar{\nu}$ decay involves, to a good approximation, only the operator $Q_V = (\bar{s}d)_{V-A}(\bar{\nu}\nu)_{V-A}$. Its Wilson coefficient, induced at leading order by the SM box and penguin diagrams shown in Fig. III-2, contains two terms proportional to λ_t and λ_c , respectively, where $\lambda_i \equiv V_{id}V_{is}^*$. We have used the CKM unitarity relation $\lambda_u = -\lambda_c - \lambda_t$ to eliminate λ_u . The leading behavior of the top-quark contribution X_t , proportional to λ_t , is given by m_t^2/M_W^2 . The smallness of λ_t compensates the effect of the large top-quark mass and makes it comparable in size to the charm-quark contribution P_c , proportional to λ_c , with the leading behavior $(m_c^2/M_W^2) \ln(m_c^2/M_W^2)$. The appearance of the large logarithm is related to the bilocal mixing of current-current and penguin operators into Q_V through charm-quark loops shown in Fig. III-3. This introduces large scale uncertainties, which have been removed by computing the next-to-next-to-leading order (NNLO) QCD corrections to P_c in renormalization-group (RG) improved perturbation theory [15]. In addition, the electroweak corrections are known. They sum the LO and next-to-leading order (NLO) QED logarithms to all orders and fix the renormalization

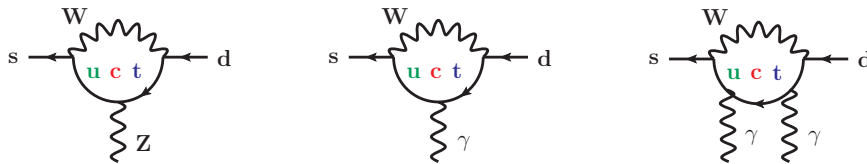


Figure III-1: Z penguin, single- and double-photon penguin.

scheme of the electroweak input parameters in the charm-quark sector, leading to the final prediction $P_c = 0.368(25)$ [16].

The top-quark contribution X_t does not contain a large logarithm and can be computed in fixed-order perturbation theory. The NLO QCD corrections have been known for a long time [17,18], and also the full two-loop electroweak corrections to X_t have been computed recently, fixing the renormalization scheme of the electroweak input parameters also in the top-quark sector and rendering the remaining scale and scheme dependence essentially negligible [19]. The final result is $X_t = 1.465(17)$, where the error is largely due to the remaining QCD scale uncertainty.

The branching ratio of the charged mode is given by

$$\text{BR}_{\text{ch}} = \kappa_+ (1 + \Delta_{\text{EM}}) \left[\left(\frac{\text{Im}\lambda_t}{\lambda^5} X_t \right)^2 + \left(\frac{\text{Re}\lambda_c}{\lambda} (P_c + \delta P_{c,u}) + \frac{\text{Re}\lambda_t}{\lambda^5} X_t \right)^2 \right]. \quad (\text{III.2.1})$$

Here, the quantity $\kappa_+ = 0.5173(25) \times 10^{-10}$ [20] contains the hadronic matrix element of Q_V . It has been determined from the full set of $K_{\ell 3}$ data using isospin symmetry, including NLO and partially NNLO corrections in chiral perturbation theory (χ PT) and QED radiative corrections [20]. The quantity $\Delta_{\text{EM}} = -0.3\%$ [20] accounts for the effects of real soft photon emission. Moreover, the CKM parameter $\lambda = |V_{us}| = 0.2255(7)$ [21].

The effects of soft charm and up quarks as well as of higher-dimensional operators have been estimated in χ PT and are lumped into $\delta P_{c,u} = 0.04(2)$, which enhances the branching ratio by roughly 6% [22]. The error on $\delta P_{c,u}$ could in principle be reduced by a lattice-QCD calculation [23].

Using $m_t(m_t) = 163.7(1.1)\text{GeV}$ [24], $m_c(m_c) = 1.279(13)\text{GeV}$ [25], and the remaining input from Ref. [26,27], we find the following numerical prediction:

$$\text{BR}_{\text{ch}} = (7.81 \pm 0.75 \pm 0.29) \times 10^{-11}, \quad (\text{III.2.2})$$

where the first error is related to the uncertainties of the input parameters, and the second error quantifies the remaining theoretical uncertainty. The parametric error is dominated by the uncertainty in the CKM inputs $|V_{cb}|$ (56%) and $\bar{\rho}$ (21%) and could be reduced significantly in the future by better determinations of these parameters. The main contributions to the theoretical uncertainty are ($\delta P_{c,u} : 46\%$, $X_t : 24\%$, $P_c : 20\%$, $\kappa_+^+ : 7\%$), respectively. The branching ratio has been measured

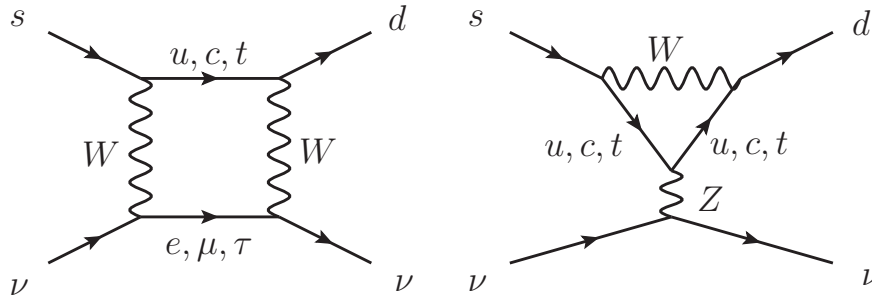


Figure III-2: Leading-order diagrams contributing to the decay amplitude for $K \rightarrow \pi \nu \bar{\nu}$ in the SM.

with a value $\text{BR}_{\text{ch}} = (1.73^{+1.15}_{-1.05}) \times 10^{-10}$ [28], consistent with the SM prediction within the (still large) experimental error.

The neutral mode $K_L \rightarrow \pi^0 \nu \bar{\nu}$ is purely CP -violating [29,30], so only the top-quark contribution is relevant for the decay rate because of the smallness of $\text{Im} \lambda_c$. It is given by the same function X_t as for the charged mode.

The branching ratio is given by

$$\text{BR}_{\text{neutr}} = \kappa_L \left(\frac{\text{Im} \lambda_t}{\lambda^5} X_t \right)^2, \quad (\text{III.2.3})$$

where $\kappa_L = 2.231(13) \times 10^{-10}$ comprises the hadronic matrix element of Q_ν has been extracted from the $K_{\ell 3}$ decays, as for the charged mode [20]. There are no further long-distance contributions, which is the reason for the exceptional theoretical cleanness of this mode.

Including also a factor taking into account the small ($\approx -1\%$) effect of indirect CP violation [31], we find for the branching ratio

$$\text{BR}_{\text{neutr}} = (2.43 \pm 0.39 \pm 0.06) \times 10^{-11}, \quad (\text{III.2.4})$$

using the same input as for the charged mode. Again, the first error corresponds to the parametric and the second to the theoretical uncertainty. Here, the parametric uncertainty is dominated by the error in the CKM parameters V_{cb} (54%) and $\bar{\eta}$ (39%) and could again be reduced in the future by better determinations of these parameters. The main contributions to the second, theoretical uncertainty are (X_t : 73%, κ_V^L : 18%), respectively. All errors have been added in quadrature.

The neutral mode has not been observed yet; an upper bound for the branching ratio is given by $\text{BR}_{\text{neutr}} < 6.7 \times 10^{-8}$ (90% CL) [32].

III.2.1.2 $K_L \rightarrow \pi^0 \ell^+ \ell^-$

Unlike the neutrino modes, the $K_L \rightarrow \pi^0 \ell^+ \ell^-$ modes, $\ell = e, \mu$, have sizeable long-distance contributions. Although these contributions are difficult to calculate, these processes are relevant because they are sensitive to helicity-suppressed contributions, which allows the disentangling scalar and

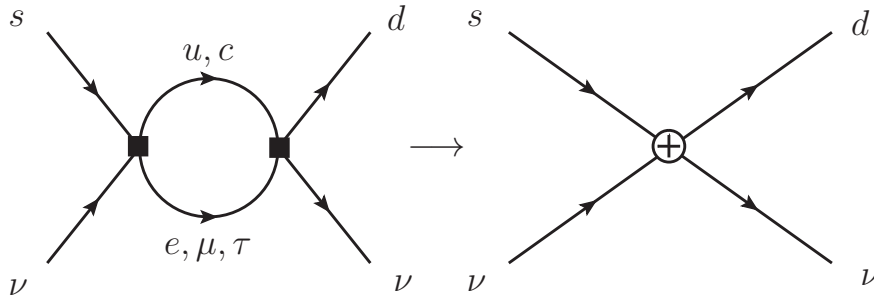


Figure III-3: Leading-order mixing of current-current and penguin operators into Q_ν .

pseudoscalar operators from vector and axial-vector operators [33]. It can be exploited because of the good theoretical control over the individual contributions to the branching ratios, which we now consider in turn:

1. The direct CP -violating contribution (DCPV) is contained in two Wilson coefficients C_{7V} and C_{7A} induced by Z and γ penguins, which are known at NLO QCD [34]. The matrix elements of the corresponding operators $Q_{7V} = (\bar{s}d)_{V-A}(\ell^+\ell^-)_V$ and $Q_{7A} = (\bar{s}d)_{V-A}(\ell^+\ell^-)_A$ can be extracted from $K_{\ell 3}$ decays in analogy to the neutrino modes [20].
2. The indirect CP -violating contribution (ICPV) is related via $K^0-\bar{K}^0$ mixing to the decay $K_S \rightarrow \pi^0\ell^+\ell^-$. It is dominated by a single χ PT coupling a_S [35], whose absolute value can be extracted from the experimental $K_S \rightarrow \pi^0\ell^+\ell^-$ decay rates to give $|a_S| = 1.2(2)$ [36].

Both ICPV and DCPV can produce the final lepton pair in a 1^{--} state, leading to interference between the two amplitudes. Whether the interference is constructive or destructive is determined by the sign of a_S , which is unknown at the moment (see also [37–39]). It can be determined by measuring the $K_L \rightarrow \pi^0\mu^+\mu^-$ forward-backward asymmetry [33]. In addition, lattice QCD calculations of these modes will be able to determine the relative sign of the two amplitudes in the next few years; see discussion in Chapter X.

The purely long-distance CP -conserving contribution is induced by a two-photon intermediate state $K_L \rightarrow \pi^0\gamma^*\gamma^* \rightarrow \pi^0\mu^+\mu^-$ and produces the lepton pair either in a phase-space suppressed 2^{++} or in a helicity suppressed 0^{++} state. The former is found to be negligible [38], while the latter is only relevant for the muon mode because of helicity suppression. It can be extracted within χ PT from experimental information on the $K_L \rightarrow \pi^0\gamma\gamma$ decay [40].

The prediction for the branching ratio is [41]

$$\begin{aligned} \text{BR}_{e^+e^-} &= 3.23_{-0.79}^{+0.91} \times 10^{-11} \quad (1.37_{-0.43}^{+0.55} \times 10^{-11}), \\ \text{BR}_{\mu^+\mu^-} &= 1.29_{-0.23}^{+0.24} \times 10^{-11} \quad (0.86_{-0.17}^{+0.18} \times 10^{-11}), \end{aligned} \quad (\text{III.2.5})$$

for constructive (destructive) interference. The error of the prediction is completely dominated by the uncertainty in a_S and could be reduced by better measurements of the $K_S \rightarrow \pi^0\ell^+\ell^-$ modes [33]. Experimental upper limits for the two decays [42,43] are

$$\begin{aligned} \text{BR}_{e^+e^-} &< 28 \times 10^{-11} \quad (90\% \text{ CL}), \\ \text{BR}_{\mu^+\mu^-} &< 38 \times 10^{-11} \quad (90\% \text{ CL}), \end{aligned} \quad (\text{III.2.6})$$

which lie still one order of magnitude above the SM predictions.

III.2.1.3 Future Improvements

Over the next decade, we expect improvements in lattice-QCD calculations combined with progress in B meson measurements (LHCb and Super-Belle) to allow one to reduce the parametric uncertainty on both $K \rightarrow \pi\nu\bar{\nu}$ to the 5% level. Substantial improvements in $K_L \rightarrow \pi^0\ell^+\ell^-$ will have to rely on lattice QCD computations, requiring the evaluation of bi-local operators. Exploratory

steps exist in this direction, but these involve new techniques and it is hard to forecast the level of uncertainty that can be achieved, even in a ten-year timescale. Therefore, from a theory perspective, the golden modes remain both $K \rightarrow \pi\nu\bar{\nu}$ decays, because they suffer from small long-distance contamination, indeed negligible in the CP violating K_L case.

III.2.2 Beyond the Standard Model: Model-independent Considerations

New-physics searches in rare kaon decays can be approached using a top-down or a bottom-up approach. In the former case one starts with a concrete NP model and predicts the observables and their correlations, while in the latter case one maps classes of models onto an effective theory with the goal to get insights free from personal taste and prejudices. In this subsection we give a concise review of the bottom-up approach to kaon physics.

The starting point to obtain an effective description is to make the reasonable assumption that the scale Λ associated to the new dynamics is sufficiently above the weak scale v , which in turn allows for a systematic expansion in powers of $v/\Lambda \ll 1$. If one furthermore assumes that SM particles are weakly coupled to the NP sector (a technical assumption which could be relaxed), then one may classify the new interactions in terms of $SU(2)_L \times U(1)_Y$ invariant operators of increasing dimension.

Our discussion here parallels the one given in Ref. [44]. To leading order in v/Λ , six operators can affect the $K \rightarrow \pi\nu\bar{\nu}$ decays. Three of these are four-fermion operators and affect the $K \rightarrow \pi\ell^+\ell^-$ decays as well (one of these operators contributes to $K \rightarrow \pi\ell\nu$ by $SU(2)$ gauge invariance). The coefficients of these operators are largely unconstrained by other observables, and therefore one can expect sizable deviations from the SM in $K \rightarrow \pi\nu\bar{\nu}$ (both modes) and $K \rightarrow \pi\ell^+\ell^-$.

The other leading operators contributing to $K \rightarrow \pi\nu\bar{\nu}$ involve the Higgs doublet ϕ and reduce, after electroweak symmetry breaking, to effective flavor-changing Z -boson interactions, with both left-handed (LH) and right-handed (RH) couplings to quarks. These Z -penguin operators (both LH and RH) are the leading effect in many SM extensions, and affect a large number of kaon observables ($K \rightarrow \pi\ell^+\ell^-$, ε_K , ε'/ε , and in the case of one operator $K \rightarrow \pi\ell\nu$ through $SU(2)$ gauge invariance), so we discuss them in some detail. The set of dimension-6 operators with a ϕ field include

$$Q = (\phi^\dagger \overleftrightarrow{D}_\mu \phi) (\bar{D}_L \gamma^\mu S_L), \quad \tilde{Q} = (\phi^\dagger \overleftrightarrow{D}_\mu \phi) (\bar{d}_R \gamma^\mu s_R), \quad (\text{III.2.7})$$

where D_L, S_L (d_R, s_R) are $SU(2)_L$ quark doublets (singlets) and $\overleftrightarrow{D}_\mu = D_\mu - \overleftarrow{D}_\mu$ with D_μ denoting the electroweak covariant derivative. After electroweak symmetry breaking, one has

$$Q \rightarrow \bar{d}_L \gamma_\mu s_L Z^\mu + \bar{u}_L \gamma_\mu c_L Z^\mu + \dots, \quad \tilde{Q} \rightarrow \bar{d}_R \gamma_\mu s_R Z^\mu + \dots, \quad (\text{III.2.8})$$

where the ellipses represent additional terms that are irrelevant for the further discussion. We see that Q induces the left-handed (LH) Z -penguin well-known from the minimal supersymmetric SM (MSSM), Randall-Sundrum (RS) models, *etc.*, while \tilde{Q} leads to a right-handed (RH) Z -penguin, which is highly suppressed in the SM by small quark masses. The results (III.2.8) hence imply that flavor-changing Z -boson interactions relevant for kaon physics can be parameterized to leading order in v/Λ by

$$\mathcal{L}_{\text{eff}} \propto (\lambda_\nu C_{\text{SM}} + C_{\text{NP}}) \bar{d}_L \gamma_\mu s_L Z^\mu + \tilde{C}_{\text{NP}} \bar{d}_R \gamma_\mu s_R Z^\mu, \quad (\text{III.2.9})$$

where $\lambda_q = V_{qs}^* V_{qd}$ with V_{qp} denoting the elements of the quark mixing matrix and $C_{\text{SM}} \approx 0.8$ encodes the SM contribution to the LH Z-penguin.

In terms of the effective NP couplings C_{NP} and \tilde{C}_{NP} , the branching ratios of the $K \rightarrow \pi v \bar{v}$ decays take a simple form, namely

$$\begin{aligned} \text{BR}(K_L \rightarrow \pi^0 v \bar{v}) &\propto (\text{Im} X)^2, \\ \text{BR}(K^+ \rightarrow \pi^+ v \bar{v}(\gamma)) &\propto |X|^2, \end{aligned} \quad (\text{III.2.10})$$

with

$$X = X_{\text{SM}} + \frac{1}{\lambda^5} \left(C_{\text{NP}} + \tilde{C}_{\text{NP}} \right), \quad (\text{III.2.11})$$

where $X_{\text{SM}} \approx 1.2e^{2.9i}$ represents the SM contribution and $\lambda \approx 0.23$ denotes the Cabibbo angle. Treating the magnitude and phase of C_{NP} (\tilde{C}_{NP}) as free parameters one can then determine the possible deviations in the $K \rightarrow \pi v \bar{v}$ branching ratios in a model-independent fashion. The outcome of such an exercise is shown in Fig. III-4. Here the yellow, orange, and red shaded contours correspond to $|C_{\text{NP}}| \leq \{0.5, 1, 2\} |\lambda_r C_{\text{SM}}|$, and the magenta band indicates the 68% confidence level (CL) limit on $\text{BR}(K^+ \rightarrow \pi^+ v \bar{v}(\gamma))$ from the combination of the E787 and E949 results [45]. The gray area is inaccessible because, cf. Eqs. (III.2.10), $|X|^2 \geq (\text{Im} X)^2$ for any X , a constraint known as the Grossman-Nir bound [46]. It is evident from the figure that O(1000%) enhancements of $\text{BR}(K_L \rightarrow \pi^0 v \bar{v})$ are in principle possible without violating the experimental constraint on $\text{BR}(K^+ \rightarrow \pi^+ v \bar{v})$, if NP were to generate large CP -violating effects in the LH Z-penguin. Since (III.2.11) is symmetric under the exchange of C_{NP} and \tilde{C}_{NP} , the same conclusions hold in the case of the RH Z-penguin.

The situation changes dramatically if one restricts oneself to scenarios of minimal-flavor violation (MFV), where the effective couplings satisfy $C_{\text{NP}} \propto \lambda_r C_{\text{SM}}$ and $\tilde{C}_{\text{NP}} \approx 0$ by definition. The subspace accessible to MFV models is indicated by the blue parabola in Fig. III-4. As one can see the pattern of deviations is very restricted in this class of models, which implies that precision measurements of both $K \rightarrow \pi v \bar{v}$ modes provide a unique way to test and to possibly refute the MFV hypothesis. Still one has to bear in mind that explicit MFV realizations such as the MSSM predict effects that do not exceed O(10%) [47], which sets the benchmark for the precision that upcoming kaon experiments should aim for.

The number of operators that can leave an imprint in the $K_L \rightarrow \pi^0 \ell^+ \ell^-$ ($\ell = e, \mu$) decays is larger than the one in the case of $K \rightarrow \pi v \bar{v}$. Besides (axial-)vector operators resulting from Z- and photon-penguin diagrams also (pseudo-)scalar operators associated to Higgs exchange can play a role [33]. In a model-independent framework, one hence should consider

$$Q_A = (\bar{d}\gamma^\mu s)(\bar{\ell}\gamma_\mu\gamma_5\ell), \quad Q_V = (\bar{d}\gamma^\mu s)(\bar{\ell}\gamma_\mu\ell), \quad Q_P = (\bar{d}s)(\bar{\ell}\gamma_5\ell), \quad Q_S = (\bar{d}s)(\bar{\ell}\ell). \quad (\text{III.2.12})$$

In Fig. III-5 we depict the accessible parameter space corresponding to various classes of NP. The blue parabola illustrates again the predictions obtained by allowing only for a contribution C_{NP} with arbitrary modulus and phase. We see that in models with dominance of the LH Z-penguin the deviations in $K_L \rightarrow \pi^0 \ell^+ \ell^-$ are strongly correlated. A large photon-penguin can induce significant corrections in C_V , which breaks this correlation and opens up the parameter space as illustrated by the dashed orange parabola and the yellow shaded region. The former predictions are obtained by employing a common rescaling of $C_{A,V}$, while in the latter case the coefficients $C_{A,V}$ are allowed to take arbitrary values. If besides $Q_{A,V}$ also $Q_{P,S}$ can receive sizable NP corrections a further

relative enhancement of $\text{BR}(K_L \rightarrow \pi^0 \mu^+ \mu^-)$ compared to $\text{BR}(K_L \rightarrow \pi^0 e^+ e^-)$ is possible. This feature is exemplified by the light blue shaded region that corresponds to the parameter space that is compatible with the constraints on $C_{P,S}$ arising from $K_L \rightarrow \mu^+ \mu^-$.

In many explicit SM extensions such as RS scenarios [49,50], little Higgs models [51], *etc.* the pattern of deviations in the $K_L \rightarrow \pi^0 \ell^+ \ell^-$ channels is however less spectacular than suggested by Figure III-5. In fact, this is a simple consequence of the relations

$$C_A \propto -\frac{1}{s_w^2} (C_{\text{NP}} - \tilde{C}_{\text{NP}}), \quad C_V \propto \left(\frac{1}{s_w^2} - 4 \right) (C_{\text{NP}} + \tilde{C}_{\text{NP}}), \quad C_{P,S} \propto m_s m_\ell, \quad (\text{III.2.13})$$

where the factors $-1/s_w^2 \approx -4.4$ and $1/s_w^2 - 4 \approx 0.4$ arise from the axial-vector and vector coupling of the Z-boson to charged leptons, while the mass factors $m_{s,\ell}$ reflect the helicity suppression of pseudoscalar and scalar interactions. To overcome this suppression requires the presence of an

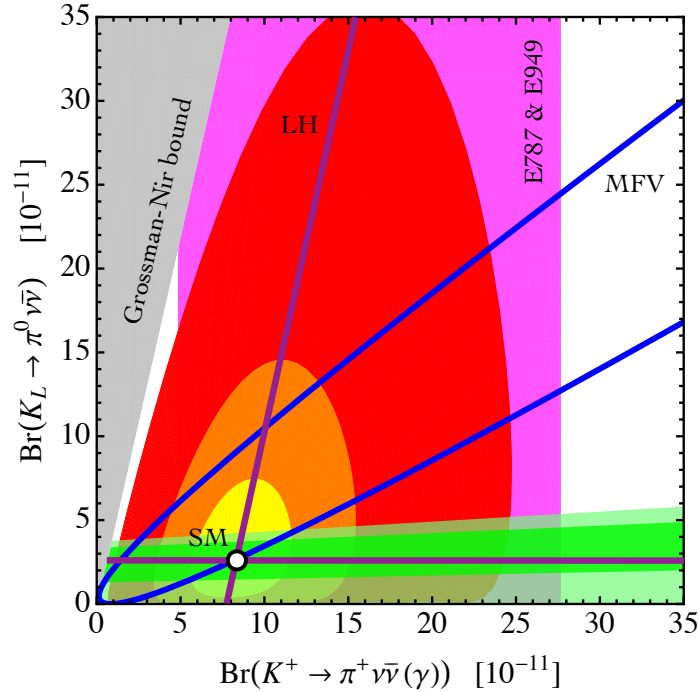


Figure III-4: Predictions for the $K \rightarrow \pi \nu \bar{\nu}$ branching ratios assuming dominance of the Z-penguin operators, for different choices of the effective couplings $C_{\text{NP}}, \tilde{C}_{\text{NP}}$. The SM point is indicated by a white dot with black border. The yellow, orange, and red shaded contours correspond to $|C_{\text{NP}}, \tilde{C}_{\text{NP}}| \leq \{0.5, 1, 2\} |\lambda_r C_{\text{SM}}|$; the magenta band indicates the 68% confidence level (CL) constraint on $\text{BR}(K^+ \rightarrow \pi^+ \nu \bar{\nu}(\gamma))$ from experiment [45]; and the gray area is theoretically inaccessible. The blue parabola represents the subspace accessible to MFV models. The purple straight lines represent the subspace accessible in models that have only LH currents, due to the constraint from ϵ_K [48]. The green band represents the region accessible after taking into account the correlation of $K_L \rightarrow \pi^0 \nu \bar{\nu}$ with ϵ'_K/ϵ_K : the (light) dark band corresponds to predictions of ϵ'_K/ϵ_K within a factor of (5) 2 of the experimental value, using central values for the hadronic matrix elements. See text for additional details.

extended gauge and/or Higgs sector. Explicit NP models that produce such pronounced effects in $K_L \rightarrow \pi^0 \ell^+ \ell^-$ as shown in Fig. III-5 have not been built.

So far we have only considered NP in rare kaon decays. It is, however, also important to consider how effects in $K \rightarrow \pi \nu \bar{\nu}$ and $K_L \rightarrow \pi^0 \ell^+ \ell^-$ are linked to deviations in well-measured kaon observables like ε_K and $\varepsilon'_K/\varepsilon_K$. In fact, CP violation in kaon mixing provides the most stringent constraint on possible new flavor structures in many non-MFV scenarios. This is a consequence of the strong chiral and renormalization group enhancement of the left-right operator $Q_{LR} = (\bar{d}_{RS_L})(\bar{d}_{LS_R})$ relative to the SM contribution $Q_{LL} = (\bar{d}_L \gamma^\mu s_L)(\bar{d}_L \gamma_\mu s_L)$. For NP scales $\Lambda = O(1 \text{ TeV})$, one has approximately

$$\varepsilon_K \propto \text{Im}(97C_{LR} + C_{LL}), \quad (\text{III.2.14})$$

with $C_{LR,LL}$ denoting the effective coupling of $Q_{LR,LL}$. Concerning ε_K , SM extensions fall, hence, into two classes: those with currents of only one chirality (LH or RH) and those with both (LH and RH). In the former case it can be shown [48] that under mild assumptions there are stringent correlation between $\Delta S = 2$ and $\Delta S = 1$ observables, while no such link exists in the latter case. For $K \rightarrow \pi \nu \bar{\nu}$ this model-independent correlation leads to two branches of solutions, one parallel to the $\text{BR}(K^+ \rightarrow \pi^+ \nu \bar{\nu})$ axis and one parallel to the Grossman-Nir bound. These two branches are indicated in Fig. III-4 by purple lines. Certain little Higgs [51] and Z' models [52], in fact, show this

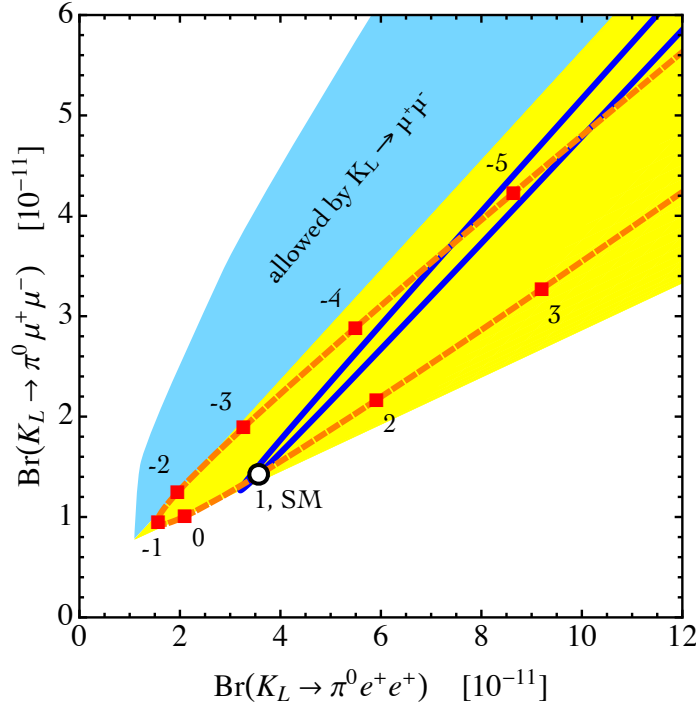


Figure III-5: Predictions for the $K_L \rightarrow \pi^0 \ell^+ \ell^-$ branching ratios assuming different types of NP contributions. The SM point is indicated by a white dot with black border. The blue parabola represents the region accessible by allowing only for C_{NP} with arbitrary modulus and phase. The subspace accessible when $C_{V,A} \neq 0$ is represented by the dashed orange parabola (common rescaling of $C_{A,V}$) and the yellow shaded region (arbitrary values of $C_{A,V}$). The subspace accessible when $C_{S,P} \neq 0$ (compatibly with $K_L \rightarrow \mu^+ \mu^-$) is represented by the light blue shaded region.

distinctive pattern, while in the generic MSSM [53] and the RS framework [49,50] the correlation is completely washed out. The ε_K constraint thus does not restrict the $K \rightarrow \pi\nu\bar{\nu}$ decay rates in general.

A second kaon observable that is known [47,50,51,54,55] to bound NP in the $K \rightarrow \pi\nu\bar{\nu}$ modes is the ratio of the direct and indirect CP violation in $K_L \rightarrow \pi\pi$ as measured by $\varepsilon'_K/\varepsilon_K$. The reason for this correlation is simple to understand from the approximation

$$\frac{\varepsilon'_K}{\varepsilon_K} \propto -\text{Im} \left[\lambda_t (-1.4 + 13.8R_6 - 6.6R_8) + (1.5 + 0.1R_6 - 13.3R_8) (C_{\text{NP}} - \tilde{C}_{\text{NP}}) \right], \quad (\text{III.2.15})$$

where the first (second) term in brackets encodes the SM (NP) contribution. Typical values of the hadronic matrix elements $R_{6,8}$ quoted in the literature are $R_6 \in [0.8, 2]$ and $R_8 \in [0.8, 1.2]$. The current status and prospects for lattice-QCD calculations of $K \rightarrow \pi\pi$ matrix elements are discussed in Chapter X: a complete three-flavor lattice-QCD calculation of $\varepsilon'_K/\varepsilon_K$ is expected in a couple of years, with a total error as small as $\sim 20\%$.

The hierarchy of the numerical coefficients multiplying $R_{6,8}$ in Eq. (III.2.15) is explained by recalling that while the QCD- (R_6) and Z -penguins (R_8) are both strongly enhanced by renormalization-group effects, the former correction results mainly from the mixing of the current-current operators $Q_{1,2}$ into the QCD-penguin, which is essentially free from NP. In contrast, mixing with $Q_{1,2}$ plays only a minor role in the case of the Z -penguins, so that any NP contribution to the initial conditions in this sector directly feeds through into $\varepsilon'_K/\varepsilon_K$. This implies that a strong cancellation of QCD- and Z -penguins is present only within the SM, but not beyond. The coefficients C_{NP} and \tilde{C}_{NP} hence have in general a considerable impact on both $K \rightarrow \pi\nu\bar{\nu}$ and $\varepsilon'_K/\varepsilon_K$ and this leads to a stringent model-independent correlation between the observables. This feature is illustrated by the (light) green band in Fig. III-4, which corresponds to predictions of $\varepsilon'_K/\varepsilon_K$ within a factor of (5) 2 of the experimental value. One observes that even under mild theoretical assumptions, the constraint on $\varepsilon'_K/\varepsilon_K$ disfavors order of magnitude enhancements of the CP -violating channel $K_L \rightarrow \pi^0\nu\bar{\nu}$, while it has little impact on the CP -conserving $K^+ \rightarrow \pi^+\nu\bar{\nu}$ mode. Let us add that $\varepsilon'_K/\varepsilon_K$ can also receive large contributions from chromomagnetic-dipole operators [50,55]. Since these effects are in general not linked to those associated to the Z -penguins, the aforementioned correlation between $\varepsilon'_K/\varepsilon_K$ and $K_L \rightarrow \pi^0\nu\bar{\nu}$ is expected to be robust, in that it can be evaded only by cancellations among different contributions to $\varepsilon'_K/\varepsilon_K$.

III.2.3 The Minimal Supersymmetric Standard Model

Supersymmetric extensions of the SM contain several new sources of flavor violation. In particular, the bilinear and trilinear soft SUSY breaking terms, which lead to the masses of the squarks, are not necessarily aligned in flavor space with the quark masses. The result are flavor and CP violating gluino-squark-quark interactions that can induce large NP effects in various low energy flavor observables. Indeed, the good agreement of the experimental data on FCNC processes with the SM predictions leads to strong constraints on the new sources of flavor violation in the MSSM. Interestingly, rare kaon decays can give important complementary information on the flavor structure of the MSSM. In the following we focus on the clean $K \rightarrow \pi\nu\bar{\nu}$ decays.

III.2.3.1 Minimal Flavor Violation

Assuming completely generic flavor mixing among the squarks leads to excessively large contributions to several well measured FCNC processes, unless the masses of the SUSY particles are well beyond the reach of the LHC. One way to avoid the strong experimental flavor constraints, is to assume that the SM Yukawa couplings are the only sources of flavor violation, the so-called Minimal Flavor Violation (MFV) Ansatz. In such a framework, FCNCs are suppressed by the same small CKM matrix elements as in the SM, and experimental bounds can be naturally avoided.

One finds that in the MSSM with MFV, the corrections to the branching ratios of the $K_L \rightarrow \pi^0 \nu \bar{\nu}$ and $K^+ \rightarrow \pi^+ \nu \bar{\nu}$ decays are generically tiny and can only reach $O(10\%)$ [56]. Moreover, this is only possible if stops and charginos are extremely light with masses below 200 GeV. Given the expected experimental and theoretical uncertainties, an observation of one of the $K \rightarrow \pi \nu \bar{\nu}$ decays, with a branching ratio that differs significantly from the SM prediction, would therefore not only rule out the SM, but would also be strong evidence for sources of flavor violation beyond MFV. Note that this statement holds in the context of the MSSM. In general, the MFV framework does allow for sizable NP contributions to both branching ratios that are strongly correlated.

III.2.3.2 Beyond Minimal Flavor Violation

Within the MSSM, sizable non-Standard effects in the $K \rightarrow \pi \nu \bar{\nu}$ decays can only be generated if the soft SUSY breaking terms have a non-MFV structure. The leading amplitudes that can give rise to large effects are generated by: (i) charged-Higgs–top-quark loops [57] and (ii) chargino–up-squark loops [58,59].

In the case (i), deviations from the SM can be generated in the large $\tan\beta$ regime by non-MFV terms in the soft masses of the right-handed down squarks. The recently improved bounds on the branching ratios of the rare decays $B_s \rightarrow \mu^+ \mu^-$ and $B_d \rightarrow \mu^+ \mu^-$, however, put strong constraints on such flavor structures.

In the case (ii), large effects can be induced if the trilinear couplings of the up squarks contain new sources of flavor violation beyond MFV. This provides the exciting opportunity to probe flavor violation in the *up sector* with rare kaon decays. Interestingly enough, the required up squark flavor structures are only mildly constrained by current flavor data, with the strongest constraints coming from ϵ_K and ϵ'/ϵ [55]. However, as these observables are also highly sensitive to other, independent, flavor violating sources, huge effects in the $K \rightarrow \pi \nu \bar{\nu}$ decays cannot be excluded. Large flavor violating entries in the up squark trilinear couplings are well motivated. They are for example required in certain models of radiative flavor violation [60] and can also provide a NP explanation of the surprisingly large observed difference in the direct *CP* asymmetries in $D \rightarrow K^+ K^-$ and $D \rightarrow \pi^+ \pi^-$ decays [61]. Generically, one can expect uncorrelated $O(1)$ corrections to both $K \rightarrow \pi \nu \bar{\nu}$ branching ratios in these models, but even enhancements by an order of magnitude cannot be excluded [53]. Note that extreme enhancements, however, require considerably fine tuning to avoid the constraints from ϵ_K and ϵ'/ϵ . Even neglecting fine tuned scenarios, extremely valuable information on the MSSM flavor sector can be obtained from $K \rightarrow \pi \nu \bar{\nu}$, thanks to the high precision of the envisioned future experiments.

III.2.3.3 Very Light Neutralinos

The MSSM allows the interesting possibility that the mass of the lightest neutralino χ is so small that the $K \rightarrow \pi\chi\chi$ decays become possible [62]. As neither neutrinos nor neutralinos are detected in experiment, the signature is the same: $K \rightarrow \pi + \cancel{E}$. The decay with neutralinos in the final state can have appreciable rates only if beyond-MFV flavor structures in the down squark sector are present which allow the $K \rightarrow \pi\chi\chi$ decay already at the tree level. Interestingly, a small finite mass of the neutralinos of $O(100 \text{ MeV})$ would lead to a considerable distortion of the pion momentum spectrum, allowing to disentangle $K \rightarrow \pi\nu\bar{\nu}$ and a possible $K \rightarrow \pi\chi\chi$ contribution.

III.2.4 The Randall-Sundrum Model

Randall-Sundrum models, in which all SM fields are allowed to propagate in the bulk, represent a very exciting alternative to more traditional extensions of the SM, like the MSSM. The model contains important new sources of flavor violation beyond the MFV framework. The explanation of the hierarchies of the SM fermion masses and mixings leads to non universal shape functions of the SM fermions in the bulk and therefore to nonuniversalities in the interactions of the Kaluza-Klein (KK) and SM gauge bosons with SM fermions. This implies FCNCs at the tree level mediated by the several gauge bosons and by the Higgs. However, the tree level flavor violating couplings are proportional to the mass splitting between the two fermions, hence leading to a suppression of the flavor transitions involving the first two generation fermions, through the so called RS-GIM mechanism [63]. Additionally, it has been shown that enlarging the bulk gauge symmetry to $SU(3)_c \times SU(2)_L \times SU(2)_R \times U(1)$ guaranties the protection of the Z boson flavor changing (and flavor conserving) couplings with left handed quarks and a not too large NP contribution to the T parameter even for low KK scales [64–66]. The latter model is the so called RS model with custodial protection. In spite of these protection mechanisms, the flavor structure of the RS model is very rich and it generically leads to too large NP contributions to ϵ_K [67]. In the following we will focus on the discussion of several kaon rare decays in the subspace of parameter space that predicts ϵ_K compatible with the experimental constraints.

III.2.4.1 The $K \rightarrow \pi\nu\bar{\nu}$ Decays

The most important NP contribution to the $K \rightarrow \pi\nu\bar{\nu}$ rare decays arises from tree level electroweak (EW) penguin diagrams. In general enhancements of the neutral $K_L \rightarrow \pi^0\nu\bar{\nu}$ decay by almost an order of magnitude are possible even for a multi-TeV KK scale [50]. The NP contributions to $K^+ \rightarrow \pi^+\nu\bar{\nu}$ are in general uncorrelated with those entering the neutral decay and can also be sizable: the model can predict enhancements of the branching ratio of $K^+ \rightarrow \pi^+\nu\bar{\nu}$ by a factor 2, sufficient to reach the central value of the present measurement of the charged kaon decay [49].

However, EW penguins generically give also the dominant correction to the direct CP violation in $K \rightarrow \pi\pi$, as discussed in Section III.2.2. This results in a strong anti-correlation between $K_L \rightarrow \pi^0\nu\bar{\nu}$ and the CP violating observable ϵ' . Imposing the constraint from ϵ'/ϵ disfavors large deviations of the branching ratio of $K_L \rightarrow \pi^0\nu\bar{\nu}$ from its SM prediction. Sizable NP effects in $K^+ \rightarrow \pi^+\nu\bar{\nu}$ are instead unconstrained by ϵ'/ϵ , since in general there is no correlation between the

charged CP conserving kaon decay and direct CP violation in $K \rightarrow \pi\pi$. These points are illustrated in Fig. III-6.

III.2.4.2 The $K_L \rightarrow \pi^0 \ell^+ \ell^-$ and $K_L \rightarrow \mu^+ \mu^-$ Decays

The CP violating $K_L \rightarrow \pi^0 \ell^+ \ell^-$ decays are not as clean as the $K \rightarrow \pi\nu\bar{\nu}$ modes. However they offer the opportunity to constrain additional $\Delta F = 1$ effective operators that are not entering in the neutrino decay modes. In the RS model the dominant NP effect arises from the tree level exchange of a Z-boson with axial-vector couplings to the SM fermions. This results in a direct correlation between the branching ratios $\text{BR}(K_L \rightarrow \pi^0 e^+ e^-)$ and $\text{BR}(K_L \rightarrow \pi^0 \mu^+ \mu^-)$ and also between $K_L \rightarrow \pi^0 \ell^+ \ell^-$ and the CP violating process $K_L \rightarrow \pi^0 \nu\bar{\nu}$. This implies that: (i) too large NP contributions to $K_L \rightarrow \pi^0 \ell^+ \ell^-$ are disfavored by the constraint from ϵ'/ϵ and (ii) a precise measurement of both decays, $K_L \rightarrow \pi^0 \mu^+ \mu^-$ and $K_L \rightarrow \pi^0 \nu\bar{\nu}$, would test the operator structure of the model.

The NP contributions to the leptonic CP conserving $K_L \rightarrow \mu^+ \mu^-$ decay are encoded by the same effective Hamiltonian describing the $K_L \rightarrow \pi^0 \ell^+ \ell^-$ decays. However, contrary to the latter decays, the short distance (SD) contribution to $K_L \rightarrow \mu^+ \mu^-$ is by far dominated by the absorptive contribution with two internal photon exchanges. Consequently, the SD contribution constitutes only a small fraction of the branching ratio. Nonetheless this decay can lead to interesting constraints in the RS model. The correlation between $K^+ \rightarrow \pi^+ \nu\bar{\nu}$ and $K_L \rightarrow \mu^+ \mu^-$ offers in fact a clear test of the handedness of the NP flavor violating interactions. The former decay is sensitive to the vector component of the flavor violating $Zs\bar{d}$ coupling, while the latter measures its axial-vector component. Therefore, since the SM flavor changing Z penguin is purely left-handed, in the original RS model,

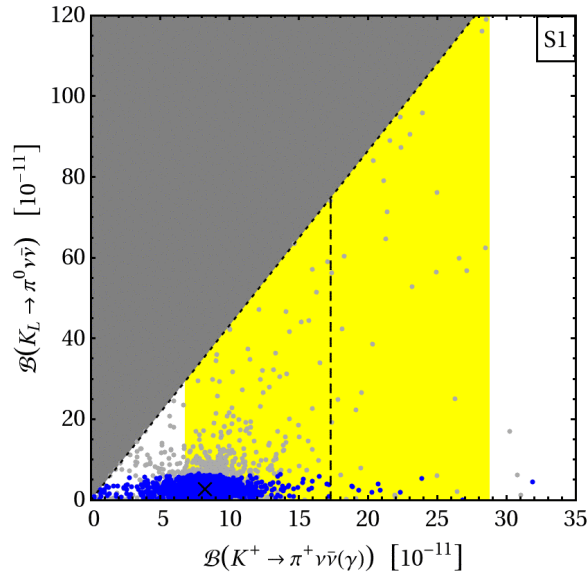


Figure III-6: Impact of ϵ'_K/ϵ_K on $K \rightarrow \pi\nu\bar{\nu}$ branching ratios in Randall-Sundrum models. The blue (light gray) scatter points are consistent (inconsistent) with the measured value of ϵ'_K/ϵ_K . Plot taken from Ref. [50].

in which the NP contributions to these decay are dominated by left-handed Z couplings, the two decay modes show a direct correlation [50]. On the contrary, in the RS model with custodial protection where the main NP effect in $K_L \rightarrow \mu^+ \mu^-$ arises from right-handed Z couplings, the correlation has been found to be an inverse one [49].

III.2.5 Beyond Rare Decays

While the main focus of this chapter was on the FCNC probes, it is worth mentioning that kaons provide as well unique probes of the charged-current (CC) sector of SM extensions. Two prominent examples involve precise measurements of the ratio $R_K = \Gamma(K \rightarrow e\nu)/\Gamma(K \rightarrow \mu\nu)$, which test lepton universality, and measurements of the transverse muon polarization P_μ^T in the semileptonic decay $K^+ \rightarrow \pi^0 \mu^+ \nu_\mu$, which is sensitive to BSM sources of CP violation in scalar CC operators. In both cases there is a clean discovery window provided by the precise SM theoretical prediction of R_K [68] and by the fact that in the SM P_μ^T is generated only by small and theoretically known final state interactions [69,70].

III.3 EXPERIMENTS

III.3.1 Experimental Landscape in This Decade

NA62. The NA62 experiment [71] at CERN is an in-flight measurement of $K^+ \rightarrow \pi^+ \nu \bar{\nu}$. The experiment will have a commissioning run with a partial detector later in 2012. Full commissioning followed by a physics run will begin in 2014. The NA62 goal is a measurement of the $K^+ \rightarrow \pi^+ \nu \bar{\nu}$ branching ratio with 10% precision. The NA62 experiment anticipates a very robust and diverse kaon physics program beyond the primary measurement.

KOTO. The KOTO experiment [72] at JPARC is an in-flight measurement of $K_L^0 \rightarrow \pi^0 \nu \bar{\nu}$. Significant experience and a better understanding of the backgrounds to this rare decay mode were obtained in E391a, the predecessor of KOTO. The anticipated sensitivity of the experiment is a few signal events (assuming the SM branching ratio) in three years of running with 300 kW of beam. A commissioning run will occur later in 2012, but the longer term performance of the experiment will depend upon the beam power evolution of the JPARC accelerator.

TREK. The TREK Experiment (E06) at JPARC [73] will search for T violation in charged kaon decays by measuring the polarization asymmetry in $K^+ \rightarrow \pi^0 \mu^+ \nu_m$ decays. TREK needs at least 100 kW (proposal assumes 270 kW) for this measurement. While the accelerator is running at lower power, collaborators have proposed P36, which will use much of the TREK apparatus to perform a search for lepton flavor universality violation through the measurement of $\Gamma(K \rightarrow e\nu)/\Gamma(K \rightarrow \mu\nu)$ at the 0.2% level. The P36 experiment requires only 30 kW of beam power and will be ready to run in 2015. The uncertainty of the JPARC beam power profile and potential conflicts for beamline real estate make the long term future of the TREK experiment unclear.

ORKA. The ORKA experiment [74], is proposed to measure $K^+ \rightarrow \pi^+ \nu \bar{\nu}$ with 1000 event sensitivity at the Main Injector later this decade. ORKA is a stopped kaon experiment that builds on the

experience of the E787/949 experiments at Brookhaven. Like NA62, ORKA offers a wide variety of measurements beyond the $K^+ \rightarrow \pi^+ \nu \bar{\nu}$ mode.

Let us look at the experimental landscape at the end of this decade under optimistic assumptions. The NA62 experiment will have measured the $K^+ \rightarrow \pi^+ \nu \bar{\nu}$ branching ratio to 10% precision. The KOTO will have measured the $K_L^0 \rightarrow \pi^0 \nu \bar{\nu}$ mode with standard model sensitivity. The P36 experiment will have improved precision on lepton flavor universality. The ORKA and TREK experiments would be in progress. Even under the optimistic scenario spelled out above, we would be far from exploring the full physics reach of kaons. Therefore, there are significant opportunities for important measurements in the kaon sector at *Project X*.

III.3.2 *Project X* Kaon Program

The flagship measurement of the *Project X* kaon era would be an experiment to measure the $K_L^0 \rightarrow \pi^0 \nu \bar{\nu}$ branching ratio with 5% precision. This effort will need to build upon the KOTO experience, benefit from significant detector R&D and take advantage of the beam power and flexibility provided by Stage 2 of *Project X*. Based upon the $K_L^0 \rightarrow \pi^0 \nu \bar{\nu}$ experience at JPARC, it seems likely that an effort to achieve this ultimate sensitivity will take two generations. Depending upon the outcome of the TREK experiment at JPARC, a T violation experiment would be an excellent candidate for *Project X*, as would a multi-purpose experiment dedicated to rare modes that involve both charged and neutral particles in the final state. This experiment might be able to pursue $K_L \rightarrow \pi^0 \ell^+ \ell^-$ as well as many other radiative and leptonic modes.

III.3.3 A $K_L^0 \rightarrow \pi^0 \nu \bar{\nu}$ Experiment at *Project X*

Several years ago, the KOPIO initiative [75] proposed to measure $K_L^0 \rightarrow \pi^0 \nu \bar{\nu}$ with a SM sensitivity of 100 events at the BNL AGS as part of RSVP (Rare Symmetry Violating Processes) project. The experimental technique and sensitivity were well-developed and extensively reviewed. KOPIO was designed to use a neutral beam at 42° targeting angle produced by 24 GeV protons from the BNL AGS. The produced neutral kaons would have an average momentum of 800 MeV/ c with a range from 300 to 1200 MeV/ c . A low momentum beam was critical for the Time-Of-Flight (TOF) strategy of the experiment.

The TOF technique is well-matched to the kaon momentum that would be produced by a proton beam of 3 GeV kinetic energy at *Project X*. Performance of the TOF strategy was limited by the design bunch width of 200 ps at the AGS. The *Project X* beam pulse timing, including target time slewing, is expected to be less than 50 ps and would substantially improve the momentum resolution and background rejection capability of the $K_L^0 \rightarrow \pi^0 \nu \bar{\nu}$ experiment driven with *Project X* beam. The KOPIO concept for *Project X* is illustrated in Fig. III-7.

The Fermilab Accelerator Physics Center has recently developed a comprehensive simulation module in the LAQGSM/MARS (MARS15) framework [76] for particle production in the challenging T_p region of 1–4 GeV. Kaon production in this module is treated as a sum of well measured exclusive channels with little tuning. The simulations have been benchmarked against the high

Table III-2: Comparison of the K_L production yield. The BNL AGS kaon and neutron yields are taken from RSVP reviews in 2004 and 2005. The *Project X* yields are for a thick target, fully simulated with LAQGSM/MARS15 into the KOPIO beam solid angle and momentum acceptance.

	Beam energy	Target (λ_I)	$p(K)$ (MeV/c)	K_L/s into $500 \mu\text{sr}$	$K_L : n (E_n > 10 \text{ MeV})$
BNL AGS	24 GeV	1.1 Pt	300-1200	60×10^6	$\sim 1 : 1000$
<i>Project X</i>	3 GeV	1.0 C	300-1200	450×10^6	$\sim 1 : 2700$

quality data sets from the COSY/ANKE experiment [77]. One such benchmark, shown in Fig. III-8, is an absolute prediction of forward K^+ production yield on carbon and is in excellent agreement with COSY/ANKE data. The estimated (LAQGSM/MARS15) kaon yield at constant beam power (yield/ T_p) is shown in Fig. III-9. The yield on carbon saturates at about 5 GeV, and the $T_p = 3.0$ GeV yield is about a factor of about two times less than the peak yield in the experimentally optimal angular region of 17–23 degrees which mitigates the high forward flux of pions and neutrons. The 3.0 GeV operational point is a trade-off of yield with accelerator cost. The enormous beam power of *Project X* more than compensates for operation at an unsaturated yield point.

The comparative K_L production yields from thick targets fully simulated with LAQGSM/MARS15 are shown in Table III-2.

The AGS K_L yield per proton is 20 times the *Project X* yield; however, *Project X* compensates with a 0.5 mA proton flux that is 150 times the RSVP goal of 10^{14} protons every 5 seconds. Hence the neutral kaon flux would be eight times the AGS flux goal into the same beam acceptance. The nominal five-year *Project X* run is 2.5 times the duration of the KOPIO AGS initiative and hence the reach of a *Project X* $K_L^0 \rightarrow \pi^0 \nu \bar{\nu}$ experiment could be 20 times the reach of the RSVP goals.

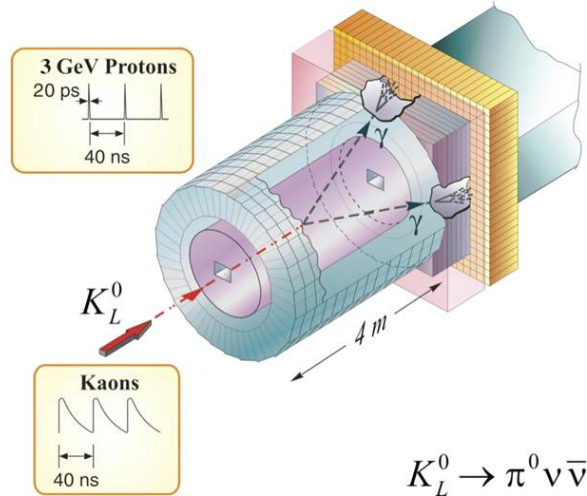


Figure III-7: Illustration of the KOPIO concept for *Project X*. Precision measurement of the photon arrival time through time-of-flight techniques is critical. Good measurement of the photon energies and space angles in a high rate environment is also critical to controlling backgrounds.

A TOF-based $K_L^0 \rightarrow \pi^0 \nu \bar{\nu}$ experiment driven by *Project X* would need to be re-optimized for the *Project X* K_L momentum spectrum, TOF resolution and corresponding background rejection. It is likely that this optimization would be based on a smaller neutral beam solid angle which would simply the detector design, increase the acceptance and relax the requirement to tag photons in the fierce rate environment of the neutral beam. Optimizing the performance will probably require a proton pulse train frequency of 20-50 MHz and an individual proton pulse timing of ~ 20 ps. Based on the E391a and KOTO experience, a careful design of the target and neutral beam channel is required to minimize the neutron halo. The optics from a long (~ 39 cm) carbon target (Table III-2) may be inconsistent with the neutron halo requirements. A shorter and denser target would have to be engineered to handle the beam power while maintaining the kaon flux. The high K_L beam flux, the potential of break-through TOF performance and improvements in calorimeter detector technology support the plausibility of a Day-1 $K_L^0 \rightarrow \pi^0 \nu \bar{\nu}$ experiment with ~ 1000 SM event sensitivity.

III.3.4 K^+ Experiments at *Project X*

In the case where a significant non-SM result were observed by ORKA [74], the $K^+ \rightarrow \pi^+ \nu \bar{\nu}$ decay mode could be studied with higher statistics with a K^+ beam driven by *Project X*. The high-purity, low-momentum K^+ beam designed for ORKA could also serve experiments to precisely measuring the polarization asymmetry in $K^+ \rightarrow \pi^0 \mu^+ \nu_m$ decays and to continue the search for lepton flavor universality violation through the measurement of $\Gamma(K \rightarrow e \nu)/\Gamma(K \rightarrow \mu \nu)$ at high precision.

III.4 SUMMARY

Rare kaon decays are extremely sensitive probes of the flavor and CP -violating sector of any SM extension. The $K \rightarrow \pi \nu \bar{\nu}$ golden modes have great discovery potential: (i) sizable ($O(1)$) deviations

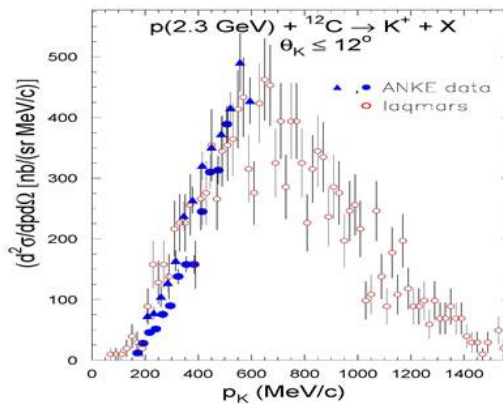


Figure III-8: LAQGSM/MARS (MARS15) simulation [76] of the K^+ momentum spectrum produced from 2.3 GeV protons (kinetic) on a thin carbon target (open circles). Absolutely normalized measurements (closed circles and triangles) from the ANKE experiment [77] are overlaid indicating excellent validation of the simulation in this production region.

from the SM are possible; (ii) even small deviations can be detected due to the precise theoretical predictions. Next generation searches should aim for a sensitivity level of 10^3 SM events (few %) in both K^+ and K_L modes, so as to maximize discovery potential. We foresee the search for $K_L \rightarrow \pi^0 \nu \bar{\nu}$ as the flagship measurement of the kaon program at *Project X*, with the potential to uncover novel BSM sources of CP violation. But we also stress the importance of pursuing the broadest possible set of measurements, so as to enhance the model discriminating power of *Project X*.

The *Project X* kaon program will benefit greatly from an ongoing R&D effort to produce hermetic, highly efficient low-energy calorimetry; high precision calorimetric timing; particle identification for π/μ and π/K separation at low energies; and very low mass tracking with excellent momentum and spatial resolution. Although R&D can move forward in the near term, there is a significant concern that domestic expertise in kaon physics will be completely depleted if there is no near-term kaon program in the U.S. As a consequence, the ORKA experiment at the Main Injector is an absolutely integral part of the *Project X* kaon program. If ORKA does not run this decade, there will be little hope of carrying out the extremely challenging kaon program that the science motivates and *Project X* can facilitate.

References

- [1] S. L. Glashow, Nucl. Phys. **22**, 579 (1961)
- [2] A. Salam, Conf. Proc. **C680519**, 367 (1968)
- [3] S. Weinberg, Phys. Rev. Lett. **19**, 1264 (1967)
- [4] G. D. Rochester and C. C. Butler, Nature **160**, 855 (1947)

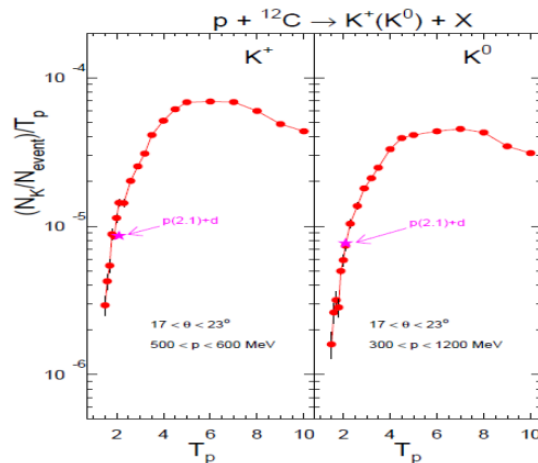


Figure III-9: LAQGSM/MARS (MARS15) simulation [76] of the K^+ and K_L production yield at constant beam power (yield/ T_p) for experimentally optimal angular and energy regions as a function of beam kinetic energy T_p (GeV).

- [5] A. Pais, Phys. Rev. **86**, 663 (1952)
- [6] M. Gell-Mann, Phys. Rev. **92**, 833 (1953)
- [7] R. H. Dalitz, Phys. Rev. **94**, 1046 (1954)
- [8] T. D. Lee and C.-N. Yang, Phys. Rev. **104**, 254 (1956)
- [9] N. Cabibbo, Phys. Rev. Lett. **10**, 531 (1963)
- [10] M. Kobayashi and T. Maskawa, Prog. Theor. Phys. **49**, 652 (1973)
- [11] J. H. Christenson, J. W. Cronin, V. L. Fitch, and R. Turlay, Phys. Rev. Lett. **13**, 138 (1964)
- [12] S. L. Glashow, J. Iliopoulos, and L. Maiani, Phys. Rev. **D2**, 1285 (1970)
- [13] A. J. Buras and J. Girrbach, “Towards the identification of new physics through quark flavor-violating processes,” (2013), arXiv:1306.3775 [hep-ph]
- [14] G. Buchalla, in *Kaon 2011: International Conference on CP Violation*, edited by F. Costantini *et al.* (2001) arXiv:hep-ph/0110313 [hep-ph]
- [15] A. J. Buras, M. Gorbahn, U. Haisch, and U. Nierste, Phys. Rev. Lett. **95**, 261805 (2005), [arXiv:hep-ph/0508165 [hep-ph]]
- [16] J. Brod and M. Gorbahn, Phys. Rev. **D78**, 034006 (2008), [arXiv:0805.4119 [hep-ph]]
- [17] G. Buchalla and A. J. Buras, Nucl. Phys. **B548**, 309 (1999), [arXiv:hep-ph/9901288 [hep-ph]]
- [18] M. Misiak and J. Urban, Phys. Lett. **B451**, 161 (1999), [arXiv:hep-ph/9901278 [hep-ph]]
- [19] J. Brod, M. Gorbahn, and E. Stamou, Phys. Rev. **D83**, 034030 (2011), [arXiv:1009.0947 [hep-ph]]
- [20] F. Mescia and C. Smith, Phys. Rev. **D76**, 034017 (2007), [arXiv:0705.2025 [hep-ph]]
- [21] M. Antonelli *et al.*, Eur. Phys. J. **C69**, 399 (2010), [arXiv:1005.2323 [hep-ph]]
- [22] A. F. Falk, A. Lewandowski, and A. A. Petrov, Phys. Lett. **B505**, 107 (2001), [arXiv:hep-ph/0012099 [hep-ph]]
- [23] G. Isidori, G. Martinelli, and P. Turchetti, Phys. Lett. **B633**, 75 (2006), [arXiv:hep-lat/0506026 [hep-lat]]
- [24] Tevatron Electroweak Working Group (CDF and DØ Collaborations), “Combination of CDF and DØ results on the mass of the top quark using up to 5.6 fb⁻¹ of data,” (2010), arXiv:1007.3178 [hep-ex]
- [25] K. G. Chetyrkin *et al.*, Phys. Rev. **D80**, 074010 (2009), [arXiv:0907.2110 [hep-ph]]
- [26] J. Charles *et al.* (CKMfitter Group), Eur. Phys. J. **C41**, 1 (2005), [arXiv:hep-ph/0406184 [hep-ph]]

- [27] K. Nakamura *et al.* (Particle Data Group), J. Phys. **G37**, 075021 (2010)
- [28] A. V. Artamonov *et al.* (E949 Collaboration), Phys. Rev. Lett. **101**, 191802 (2008), [arXiv:0808.2459 [hep-ex]]
- [29] L. S. Littenberg, Phys. Rev. **D39**, 3322 (1989)
- [30] G. Buchalla and G. Isidori, Phys. Lett. **B440**, 170 (1998), [arXiv:hep-ph/9806501 [hep-ph]]
- [31] G. Buchalla and A. J. Buras, Phys. Rev. **D54**, 6782 (1996), [arXiv:hep-ph/9607447 [hep-ph]]
- [32] J. K. Ahn *et al.* (E391a Collaboration), Phys. Rev. Lett. **100**, 201802 (2008), [arXiv:0712.4164 [hep-ex]]
- [33] F. Mescia, C. Smith, and S. Trine, JHEP **0608**, 088 (2006), [arXiv:hep-ph/0606081 [hep-ph]]
- [34] G. Buchalla, A. J. Buras, and M. E. Lautenbacher, Rev. Mod. Phys. **68**, 1125 (1996), [arXiv:hep-ph/9512380 [hep-ph]]
- [35] G. D’Ambrosio, G. Ecker, G. Isidori, and J. Portoles, JHEP **9808**, 004 (1998), [arXiv:hep-ph/9808289 [hep-ph]]
- [36] J. R. Batley *et al.* (NA48/1 Collaboration), Phys. Lett. **B576**, 43 (2003), [arXiv:hep-ex/0309075 [hep-ex]]
- [37] C. Bruno and J. Prades, Z. Phys. **C57**, 585 (1993), [arXiv:hep-ph/9209231 [hep-ph]]
- [38] G. Buchalla, G. D’Ambrosio, and G. Isidori, Nucl. Phys. **B672**, 387 (2003), [arXiv:hep-ph/0308008 [hep-ph]]
- [39] S. Friot, D. Greynat, and E. De Rafael, Phys. Lett. **B595**, 301 (2004), [arXiv:hep-ph/0404136 [hep-ph]]
- [40] G. Isidori, C. Smith, and R. Unterdorfer, Eur. Phys. J. **C36**, 57 (2004), [arXiv:hep-ph/0404127 [hep-ph]]
- [41] P. Mertens and C. Smith, JHEP **1108**, 069 (2011), [arXiv:1103.5992 [hep-ph]]
- [42] A. Alavi-Harati *et al.* (KTeV Collaboration), Phys. Rev. Lett. **93**, 021805 (2004), [arXiv:hep-ex/0309072 [hep-ex]]
- [43] A. Alavi-Harati *et al.* (KTeV Collaboration), Phys. Rev. Lett. **84**, 5279 (2000), [arXiv:hep-ex/0001006 [hep-ex]]
- [44] S. Jäger, “Rare K decays: model-independent studies,” <http://indico.cern.ch/getFile.py/access?contribId=5&resId=0&materialId=slides&confId=65927>
- [45] S. Adler *et al.* (E787 and E949 Collaborations), Phys. Rev. **D77**, 052003 (2008), [arXiv:0709.1000 [hep-ex]]
- [46] Y. Grossman and Y. Nir, Phys. Lett. **B398**, 163 (1997), [arXiv:hep-ph/9701313 [hep-ph]]

- [47] A. J. Buras, P. Gambino, M. Gorbahn, S. Jäger, and L. Silvestrini, Nucl. Phys. **B592**, 55 (2001), [arXiv:hep-ph/0007313 [hep-ph]]
- [48] M. Blanke, Acta Phys. Polon. **B41**, 127 (2010), [arXiv:0904.2528 [hep-ph]]
- [49] M. Blanke, A. J. Buras, B. Duling, K. Gemmler, and S. Gori, JHEP **0903**, 108 (2009), [arXiv:0812.3803 [hep-ph]]
- [50] M. Bauer, S. Casagrande, U. Haisch, and M. Neubert, JHEP **1009**, 017 (2010), [arXiv:0912.1625 [hep-ph]]
- [51] M. Blanke, A. J. Buras, S. Recksiegel, C. Tarantino, and S. Uhlig, JHEP **0706**, 082 (2007), [arXiv:0704.3329 [hep-ph]]
- [52] C. Promberger, S. Schatt, and F. Schwab, Phys. Rev. **D75**, 115007 (2007), [arXiv:hep-ph/0702169 [HEP-PH]]
- [53] A. J. Buras, T. Ewerth, S. Jäger, and J. Rosiek, Nucl. Phys. **B714**, 103 (2005), [arXiv:hep-ph/0408142 [hep-ph]]
- [54] A. J. Buras and L. Silvestrini, Nucl. Phys. **B546**, 299 (1999), [arXiv:hep-ph/9811471 [hep-ph]]
- [55] A. J. Buras, G. Colangelo, G. Isidori, A. Romanino, and L. Silvestrini, Nucl. Phys. **B566**, 3 (2000), [arXiv:hep-ph/9908371 [hep-ph]]
- [56] G. Isidori, F. Mescia, P. Paradisi, C. Smith, and S. Trine, JHEP **0608**, 064 (2006), [arXiv:hep-ph/0604074 [hep-ph]]
- [57] G. Isidori and P. Paradisi, Phys. Rev. **D73**, 055017 (2006), [arXiv:hep-ph/0601094 [hep-ph]]
- [58] Y. Nir and M. P. Worah, Phys. Lett. **B423**, 319 (1998), [arXiv:hep-ph/9711215 [hep-ph]]
- [59] G. Colangelo and G. Isidori, JHEP **9809**, 009 (1998), [arXiv:hep-ph/9808487 [hep-ph]]
- [60] A. Crivellin, L. Hofer, U. Nierste, and D. Scherer, Phys. Rev. **D84**, 035030 (2011), [arXiv:1105.2818 [hep-ph]]
- [61] G. F. Giudice, G. Isidori, and P. Paradisi, JHEP **1204**, 060 (2012), [arXiv:1201.6204 [hep-ph]]
- [62] H. K. Dreiner *et al.*, Phys. Rev. **D80**, 035018 (2009), [arXiv:0905.2051 [hep-ph]]
- [63] K. Agashe, G. Perez, and A. Soni, Phys. Rev. **D71**, 016002 (2005), [arXiv:hep-ph/0408134 [hep-ph]]
- [64] K. Agashe, A. Delgado, M. J. May, and R. Sundrum, JHEP **0308**, 050 (2003), [arXiv:hep-ph/0308036 [hep-ph]]
- [65] C. Csáki, C. Grojean, L. Pilo, and J. Terning, Phys. Rev. Lett. **92**, 101802 (2004), [arXiv:hep-ph/0308038 [hep-ph]]

- [66] K. Agashe, R. Contino, L. Da Rold, and A. Pomarol, *Phys. Lett.* **B641**, 62 (2006), [arXiv:hep-ph/0605341 [hep-ph]]
- [67] C. Csáki, A. Falkowski, and A. Weiler, *JHEP* **0809**, 008 (2008), [arXiv:0804.1954 [hep-ph]]
- [68] V. Cirigliano and I. Rosell, *Phys. Rev. Lett.* **99**, 231801 (2007), [arXiv:0707.3439 [hep-ph]]
- [69] A. R. Zhitnitsky, *Sov. J. Nucl. Phys.* **31**, 529 (1980)
- [70] V. P. Efrosinin, I. B. Khriplovich, G. G. Kirilin, and Y. G. Kudenko, *Phys. Lett.* **B493**, 293 (2000), [arXiv:hep-ph/0008199]
- [71] NA62 Collaboration, <http://na62.web.cern.ch/na62/>
- [72] KOTO Collaboration, <http://koto.kek.jp/>
- [73] TREK Collaboration, <http://trek.kek.jp/>
- [74] J. Comfort *et al.* (ORKA Collaboration), “ORKA: Measurement of the $K^+ \rightarrow \pi^+ \nu \bar{\nu}$ decay at Fermilab,” (2011)
- [75] KOPIO Collaboration, “KOPIO Experiment Proposal,” (2005), <http://www.bnl.gov/rsvp/KOPIO.htm>
- [76] K. K. Gudima, N. V. Mokhov, and S. I. Striganov, in *Applications of High Intensity Proton Accelerators*, edited by R. Raja and S. Mishra (2009) <http://lss.fnal.gov/archive/preprint/fermilab-conf-09-647-apc.shtml>
- [77] M. Büscher *et al.*, *Eur. Phys. J.* **A22**, 301 (2004), [arXiv:nucl-ex/0401031 [nucl-ex]]

IV Muon Experiments with *Project X*

*Robert Bernstein, Graham Kribs,
André de Gouvêa, Vincenzo Cirigliano, Douglas Glenzinski, Brendan Kiburg,
Kyle Knoepfel, Nikolai V. Mokhov, Vitaly S. Pronskikh and Robert S. Tschirhart*

IV.1 INTRODUCTION

The fundamental origin of flavor in the Standard Model remains a mystery. Despite the roughly eighty years since Rabi asked “Who ordered that?” upon learning of the discovery of the muon, we have not understood the reason that there are three generations or, more recently, why the quark and neutrino mixing matrices are so different. The solution to the flavor problem would give profound insights into physics beyond the Standard Model (BSM) and tell us about the couplings and the mass scale at which the next level of insight can be found. Rare muon decays provide exceptional probes of flavor violation beyond the Standard Model physics. The observation of charged lepton flavor violation (CLFV) is an unambiguous signal of new physics and muons, because they can be made into intense beams, are the most powerful probe. Experiments at *Project X* using charged lepton flavor violation can probe mass scales up to $O(10^4)$ TeV/c^2 .

Project X's unique combination of intensity and flexibility of time structure make it possible to envisage a range of experiments. Searches for $\mu \rightarrow e\gamma$ and $\mu \rightarrow 3e$ are stopped muon experiments that require as low, constant instantaneous rates as are practical. Muon-to-electron conversion experiments use captured muons, and current designs benefit more from a pulsed beam structure. The spacing between pulses and the requirements on the width of pulses depends on the Z of the element in which the capture occurs, and a range of elements is often required to either map out or exclude a given BSM interaction. Certainly if a signal is observed before *Project X* a systematic study of different Z materials is required with pulse separations varying by an order of magnitude from hundreds of nanoseconds to a few microseconds.

The ability to switch the time structure of the beam to fit the needs of an individual experiment is as much a part of the strength of *Project X* as is the raw intensity: if you can't use the intensity because of the time structure, you can't do the physics.

IV.2 PHYSICS MOTIVATION

As is well known, Yukawa couplings in the quark and lepton sectors break the global flavor symmetries of the Standard Model to $U(1)_B \times U(1)_\ell$ (with Dirac neutrino masses) or just $U(1)_B$ (with Majorana neutrino masses). Parameterizing the flavor mixing as CKM [1,2] and PMNS [3,4] mixing for the quark and neutrino sectors very successfully accommodates all experimental observations to date.

Rare muon decays provide exceptional probes of flavor violation beyond the Standard Model physics. This is because the predicted rates for $\mu \rightarrow e$ processes in the Standard Model resulting from a neutrino mass mixing insertion are unobservably small [5–9]

$$\text{BR}(\mu \rightarrow e\gamma) = \frac{3\alpha}{32\pi} \left| \sum_{i=2,3} U_{\mu i}^* U_{ei} \frac{\Delta m_{i1}^2}{M_W^2} \right|^2 < 10^{-54}, \quad (\text{IV.2.1})$$

where $U_{\alpha i}$ are elements of the PMNS neutrino mixing matrix and Δm_{ij}^2 are the neutrino mass-squared differences. Hence, the observation of charged lepton flavor violation (CLFV) is an unambiguous signal of new physics.

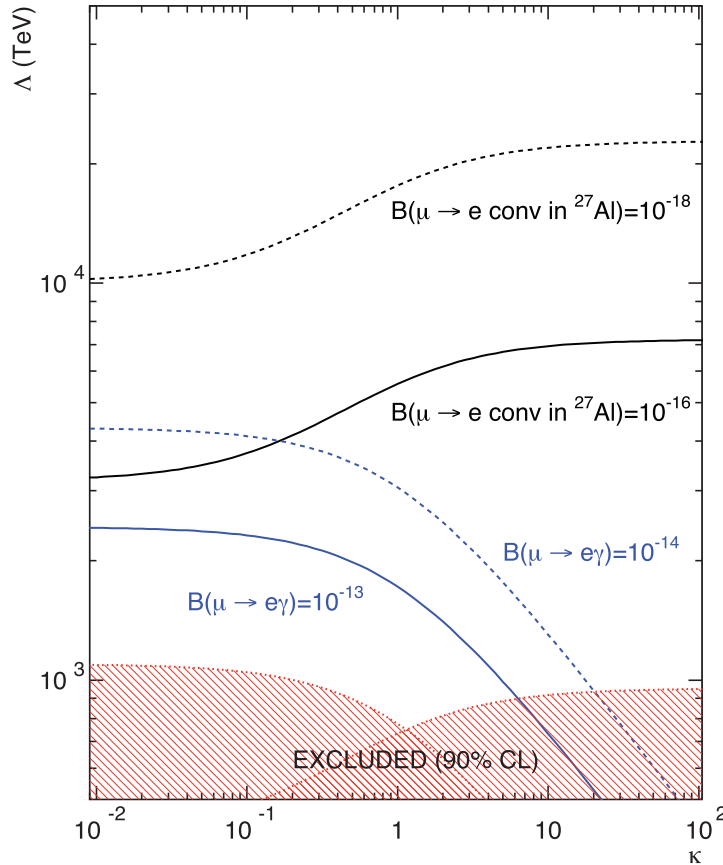


Figure IV-1: Mass scale Λ vs. κ for selected experiments. The left-hand side of the plot for small κ can be probed by experiments such as MEG looking for $\mu \rightarrow e\gamma$. The right-hand side can be tested by $\mu N \rightarrow eN$. Comparing and contrasting measurements and limits pins down or constrains new physics more powerfully than either experiment alone. A similar plot can be made for the $\mu \rightarrow 3e$ process, but the meaning of κ would be different. From Ref. [10].

IV.2.1 Effective Theory Discussion

Physics beyond the Standard Model generically can lead to new sources of flavor violation that far exceed the Standard Model values. A simple model-independent approach to CLFV is to simply write the effective operators that mediate the lepton flavor-violating processes, including [11,12]

$$\mathcal{L}_{CLFV} = \frac{m_\mu}{(1+\kappa)\Lambda^2} \bar{\mu}_R \sigma_{\mu\nu} e_L F^{\mu\nu} + \frac{\kappa}{(1+\kappa)\Lambda^2} \bar{\mu}_L \gamma_\mu e_L \bar{f}_L \gamma^\mu f_L. \quad (\text{IV.2.2})$$

These are parameterized by $1/\Lambda^2$ with a coefficient κ that weights the relative importance of the “magnetic moment” type operator versus the four-fermion interaction. Specific scenarios of physics beyond the Standard Model will lead to different combinations of these and additional operators, such as scalar and tensor [13–15] (as well as different relative weights for the four-fermion interactions as the other fermion f varies). There are basically two classes of possibilities:

- models that directly impact electroweak symmetry breaking, such as supersymmetry
- models that directly impact the flavor puzzle, such as ones that attempt to *explain* the flavor mixings and mass hierarchy

Constraints in the κ - Λ plane from current and potential limits on $\mu \rightarrow e\gamma$ and $\mu N \rightarrow eN$ are shown in Fig. IV-1.

In the context of a general effective theory analysis [13–15], it has been shown that information about the relative strength of the different four-fermion operators that mediate CLFV can be obtained by studying $\mu \rightarrow e$ conversion on different target nuclei. There are three types of effective operators that contribute to the coherent $\mu \rightarrow e$ conversion process: the dipole, the vector, and the scalar operators. Using the nonrelativistic approximation for the muon wave function, the three operators give the same form of overlapping integrals among the wave functions of the initial muon and the final electron and the nucleon density in the target nuclei. However, as the relativistic and finite nuclear size effects become important for heavy nuclei [14,16,17], the transition amplitudes for the three operators show different dependences on the atomic number Z . The relative numbers of neutrons and protons also change as Z increases: this fact allows one to find out if the LFV operators couples to up-type or down-type quarks again by looking at the target atom dependence. The theoretical uncertainties of such an analysis arise predominantly from the nucleon “sigma terms” $\langle N | m_q \bar{q}q | N \rangle$ ($q = u, d, s$). These uncertainties can be largely reduced with input from lattice QCD (see Sec. X.3.3.1 and Ref. [18]) and do not constitute a limiting factor in discriminating models where one or at most two underlying operators (dipole, scalar, vector) provide the dominant source of lepton flavor violation. A realistic discrimination among underlying mechanisms requires a measurement of the ratio of conversion rates at the 5% level (in the case of two light nuclei) or at the 20% level (in the case of one light and one heavy nucleus) [15].

Operators besides those in Eq. (IV.2.2) can also signal new physics. One possibility is muonium-antimuonium oscillations, where $\mu^+ e^-$ oscillates into $\mu^- e^+$ via four-fermion interactions such as

$$\frac{\bar{\mu}_R \gamma_\mu e_R \bar{\mu}_R \gamma^\mu e_R}{\Lambda^2} + \text{H.c.} \quad (\text{IV.2.3})$$

and other chiralities. This type of interaction was considered in a recent paper on flavor-violating Higgs couplings to leptons [19]. Reinterpreting their limit, which used the MACS experimental result [20], one obtains the bound $\Lambda \gtrsim 1.6$ TeV. It is also possible to change lepton flavor and charge through scattering off nuclei, $\mu^\pm N \rightarrow e^\mp N'$, which proceeds through further higher dimensional operators.

In the LHC era, the motivations for the continued search for new sources of flavor violation should be clear: if new physics is discovered at the LHC, searches for and measurements of charged lepton flavor violation can have enormous discriminating power in differentiating among models. On the other hand, if no direct evidence of new physics is found, experiments at *Project X* using charged lepton flavor violation can probe mass scales up to $O(10^4)$ TeV, far beyond the reach of any planned collider. In this chapter, based largely on the ideas discussed at the meeting of the Project X Physics Study [21], we discuss several examples where large flavor violation arises in the lepton sector.

IV.2.2 Supersymmetry

Weak scale supersymmetry remains an intriguing possibility to understand the stability of the electroweak scale. In the minimal supersymmetric standard model (MSSM), the Higgs mass is constrained to be very light, less than about 130 GeV (a value computed long ago; see, for example, S.P. Martin’s classic “Supersymmetry Primer” [22]). The observation at the LHC of a particle consistent with being a Higgs boson of about 126 GeV is, thus, a tantalizing clue that a *weakly* coupled description of electroweak symmetry breaking is a viable possibility. The lack of evidence for superpartners at the LHC challenges the supersymmetry paradigm, but a version of supersymmetry called “natural supersymmetry,” with Higgsinos and stops of order the electroweak scale and gluinos not too heavy remains viable, and is only now being probed [23,24].

The MSSM contains slepton mass matrices that are otherwise undetermined. Arbitrary slepton mixing would lead to a huge rate for CLFV [25–31]. Instead, the nonobservation of $\mu \rightarrow e$ processes can be used to constrain the slepton flavor mixing, often parameterized by $\delta_{XY}^\ell \equiv \delta m_{XY}^2/m^2$ where δm_{XY}^2 is the off-diagonal (12)-entry appearing in the sfermion mass matrix connecting the X -handed slepton to the Y -handed slepton, and m^2 is the average slepton mass. Reference [31] found $\delta_{LR}^\ell \lesssim 3 \times 10^{-5}$, while $\delta_{LL}^\ell \lesssim 6 \times 10^{-4}$, over a scan of the mSUGRA parameter space. Similarly strong bounds on δ_{RR}^ℓ can also be found, though cancellations between diagrams in the amplitude can in some cases allow for much larger mixing [29–31].

One of the interesting developments over the past five years is the possibility that slepton flavor mixing may *not* lead to such large rates for $\mu \rightarrow e$, when the MSSM is extended to include an approximate R -symmetry [32]. Unlike the MSSM, the most important constraint is not necessarily $\mu \rightarrow e\gamma$ [33]. This is easily seen by inspection of the R -symmetric flavor-violating operators: $\mu \rightarrow e\gamma$ requires a chirality-flip via a muon Yukawa coupling, whereas $\mu \rightarrow e$ conversion has no such requirement. We find that $\mu \rightarrow e$ conversion rules out maximal mixing throughout the right-handed slepton mixing parameter space for sub-TeV superpartner masses. This is complementary to $\mu \rightarrow e\gamma$, where we find cancellations between the bino and Higgsino diagrams, analogous to what was found before in the MSSM [29–31]. For left-handed slepton mixing, we find possible cancellations in the amplitudes for $\mu \rightarrow e$ conversion, and instead $\mu \rightarrow e\gamma$ provides generally the strongest constraint.

Finally, we find that $\mu \rightarrow 3e$ provides the weakest constraint on both left-handed and right-handed slepton mixing throughout the parameter space considered.

IV.2.3 Neutrino Flavor Oscillations

The right-handed neutrino mass matrix that is central to the understanding of small neutrino masses via the seesaw mechanism can arise either (1) from renormalizable operators or (2) from nonrenormalizable or super-renormalizable operators, depending on the symmetries and the Higgs content of the theory beyond the Standard Model. In Ref. [34], lepton flavor violating (LFV) effects were studied in the first class of seesaw models wherein the ν_R Majorana masses arise from renormalizable Yukawa couplings involving a $B - L = 2$ Higgs field. In this model, detailed predictions for $\tau \rightarrow \mu\gamma$ and $\mu \rightarrow e\gamma$ branching ratios were found after taking the-then neutrino oscillation data into account. In minimal supergravity models, a large range of MSSM parameters (suggested by the relic abundance of neutralino dark matter and that was consistent with Higgs boson mass and other constraints) have radiative decays are in the range accessible to planned experiments. This compares with predictions of lepton flavor violation in the second class of models that arise entirely from the Dirac Yukawa couplings. The ratio $r \equiv \text{BR}(\mu \rightarrow e\gamma)/\text{BR}(\tau \rightarrow \mu\gamma)$ provided crucial insight into the origin of the seesaw mechanism for neutrino mass generation.

In Ref. [35], the predictions for $\text{BR}(\mu \rightarrow e\gamma)$ and $\text{BR}(\tau \rightarrow \ell\gamma)$, $\ell = \mu, e$, were studied in a class of horizontal $\text{SU}(2)$ models that lead to a 3×2 seesaw model for neutrino masses. Two such models were considered that obtained the correct pattern for the PMNS matrix. In these models, the effective low energy theory below the $\text{SU}(2)_H$ scale is the MSSM. Assuming a supersymmetry breaking pattern as in the minimal SUGRA models (with consistency to $g - 2$, $b \rightarrow s\gamma$ and WMAP dark matter constraints on the parameters of the model), the $\text{BR}(\mu \rightarrow e\gamma)$ prediction was expected to be accessible to the MEG experiment. Given that Ref. [35] is nearly ten years old, it remains interesting to update the theoretical analysis with the latest constraints (including the Higgs mass) and determine the impact of future CLFV experiments in this class of models.

IV.2.4 Extra Dimensions

In Ref. [36], a detailed calculation of the $\mu \rightarrow e\gamma$ amplitude in a warped Randall-Sundrum (RS) model was presented using the mixed position/momentum representation of 5D propagators and the mass insertion approximation, where the localized Higgs VEV was assumed to be much smaller than the Kaluza-Klein (KK) masses in the theory. The calculation reveals potential sensitivity to the specific flavor structure known as “anarchic Yukawa matrices.” While generic flavor bounds can be placed on the lepton sector of RS models, one can systematically adjust the structure of the Y_e and Y_ν matrices to alleviate the bounds while simultaneously maintaining anarchy. In other words, there are regions of parameter space which can improve agreement with experimental constraints without fine tuning. Conversely, one may generate anarchic flavor structures which—for a given KK scale—cannot satisfy the $\mu \rightarrow e\gamma$ constraints for *any* value of the anarchic scale Y_* . Over a range of randomly generated anarchic matrices the KK scale may be pushed to 4 TeV. It is interesting to consider the case where $M_{\text{KK}} = 3$ TeV where KK excitations are accessible to the LHC. The minimal model suffers a $\text{O}(10)$ tension between the tree-level lower bound, $Y_* > 4$ and the loop-level upper bound $Y_* < 0.5$. This tension is slightly alleviated in the custodial model, where the tree-level lower bound,

$Y_* > 1.25$ and the loop-level upper bound $Y_* < 0.3$. Thus, even for $M_{\text{KK}} = 3 \text{ TeV}$, some mild tuning in the relative sizes of the 5D Yukawa matrix is required. Now, anarchic models generically lead to small mixing angles. This feature fits the observed quark mixing angles well, but is in stark contrast with the lepton sector where neutrino mixing angles are large, pointing to additional flavor structure in the lepton sector. For example in [37] a bulk A_4 non-Abelian discrete symmetry is imposed on the lepton sector. This leads to a successful explanation of both the lepton mass hierarchy and the neutrino mixing angles (see also [38]) while all tree-level lepton number-violating couplings are absent, so the only bound comes from the $\mu \rightarrow e\gamma$ amplitude.

In Ref. [39], LFV processes were studied in 5D gauge models that are related to neutrino mass generation. Two complete models which generate neutrino masses radiatively were examined. They give rise to different neutrino mass patterns thus, it is not surprising that they give different prediction for LFV rates. The first model, with a low unification scale, makes essential use of bileptonic scalars. It also contains characteristic doubly-charged gauge bosons. In this model, the rare τ decays are much more enhanced compare to their counterpart μ decays. Among the $\tau \rightarrow \ell\gamma$ decays the largest mode is the $\mu\gamma$, at a level $< 10^{-14}$. The second model, by contrast, has a high unification scale (a 5D orbifold version of the usual GUT). The important ingredient for LFV and neutrino masses is using an symmetric representation under the GUT [**15** under $SU(5)$] for the Higgs bosons. In this model, $\mu \rightarrow e$ conversion in nuclei can be within the experimental capability of future experiments. As in the first model, $\mu \rightarrow e\gamma$ will not be observable. This is very different from conventional four-dimensional unification models. It was also noticed [39] that the split fermion model has the characteristic of $L \rightarrow 3l$ and $\mu \rightarrow e$ conversion dominating over $L \rightarrow l\gamma$.

IV.2.5 Connections between CLFV and the Muon Magnetic Moment

In Sec. IV.3.5, the current experimental and theoretical status of the muon anomalous magnetic moment, along with expectations for the near and intermediate futures, is discussed. In a nutshell, the world's most precise measurement of the anomalous magnetic moment, $g - 2$, of the muon disagrees with the world's best standard model estimate for this observable at around the 3.6σ level. The existence of new, heavy degrees of freedom may be responsible for the observed discrepancy.

It is useful to compare, in a model-independent way, new physics that could mediate CLFV to that which may have manifested itself in precision measurements of the muon anomalous magnetic moment. Similar to the discussion in Sec. IV.2.1, new, heavy physics contributions to the muon $g - 2$ are captured by the effective Lagrangian

$$\mathcal{L}_{g-2} \supset \frac{m_\mu}{\Lambda^2} \bar{\mu}_R \sigma_{\mu\nu} \mu_L F^{\mu\nu} + h.c.. \quad (\text{IV.2.4})$$

Current $g - 2$ data point to $\Lambda \sim 8 \text{ TeV}$. Equation (IV.2.4) is, however, very similar to Eq. (IV.2.2) in the limit $\kappa \ll 1$, keeping in mind that Λ in Eq. (IV.2.4) need not represent the same quantity as Λ in Eq. (IV.2.2) in the limit $\kappa \ll 1$.

We can further relate the effective $g - 2$ effective new physics to that of charged-lepton flavor violating processes as follows: $(\Lambda_{\text{CLFV}})^{-2} = \theta_{e\mu} (\Lambda_{g-2})^{-2}$. Here the parameter $\theta_{e\mu}$ measures how well the new physics conserves flavor. For example, if $\theta_{e\mu} = 0$, the new physics is strictly flavor conserving, while if the new physics is flavor-indiferent, $\theta_{e\mu} \sim 1$. In either case, a lot can be inferred

Table IV-1: Summary of beam requirements for muon experiments.

Process	Time Structure	Capture or stop	Accepted muons	Muon KE
$\mu \rightarrow 3e$	continuous	stop	$O(10^{19})$	surface
$\mu \rightarrow e\gamma$	continuous	stop	$O(10^{19})$	surface
$\mu^- N \rightarrow e^- N$	pulsed	capture	$O(10^{19})$	≤ 50 MeV
$\mu^- N \rightarrow e^+ N(A, Z - 2)$	pulsed	capture	$O(10^{19})$	≤ 50 MeV
$\mu^+ e^- \rightarrow \mu^- e^+$	pulsed	stop	$O(10^{13})$	surface

regarding whether new physics has manifested itself in the muon $g - 2$, and what properties this new physics ought to have. If $\theta_{e\mu} \sim 1$, negative searches for $\mu \rightarrow e\gamma$ already preclude a new physics interpretation to the muon $g - 2$ results, since, as discussed earlier, these constrain $\Lambda \gtrsim 1000$ TeV. On the other hand, if the muon $g - 2$ discrepancy is real evidence for new physics, current searches for $\mu \rightarrow e\gamma$ already reveal that flavor violation in the new-physics sector is highly suppressed: $\theta_{e\mu} < 10^{-4}$. A similar analysis can be carried out for $\kappa \gg 1$. In this case, the relative sensitivity of the most relevant charged-lepton flavor violating processes (either $\mu \rightarrow e$ -conversion or $\mu \rightarrow eee$) is much higher.

The comparison of data on the anomalous magnetic moment of the muon is, of course, also quite powerful when it comes to concrete models. A detailed analysis of quite generic versions of the MSSM allows one to directly related the branching ratio for $\mu \rightarrow e\gamma$ to the supersymmetric contributions to the muon $g - 2$ [40].

IV.3 EXPERIMENTS

Searches for CLFV using for muons changing into electrons have been the most important for several reasons. First, as soon as the muon was realized to be a heavier version of the electron, there was every reason to ask why it did not decay into its lighter relative, and the discovery of the muon long predates the discovery of the tau. Second, we can make muon beams but not tau beams. Even today, in the era of flavor factories, the intensity of muon beams makes up for the (usually) smaller smaller per-particle effect. The kaon CLFV processes are also not as powerful as muon-based searches. Therefore, muon-based CLFV experiments have dominated the field. There is an active program to improve muon-based limits by four orders-of-magnitude in key processes (so roughly an order of magnitude in mass reach) and remain ahead of the competition from other channels. There are three important muon-based searches: muon-to-electron conversion, $\mu^- N \rightarrow e^- N$, $\mu \rightarrow e\gamma$, and $\mu \rightarrow 3e$. A fourth process that is ripe for improvement and of increasing interest is $\mu^- N(A, Z) \rightarrow e^+ N(A, Z - 2)$. Finally, the muonium-antimuonium transition provides a unique window into BSM physics, and it may be possible to improve the searches by two orders of magnitude.

The experiments and their beam requirements are summarized in Table IV-1.

IV.3.1 $\mu \rightarrow e\gamma$

IV.3.1.1 Current Status

MEG at the Paul Scherrer Institute (PSI) in Zurich, Switzerland, has just reached a limit of 5.7×10^{-13} at 90% CL with 3.6×10^{14} stopped muons [41]. The experiment is now background limited. An upgrade proposal to reach a limit of 6×10^{-14} has been approved at PSI [42]. Here, we provide an equation from Ref. [42], explained in Ref. [43], which gives the relationship among resolutions and the level at which the experiment observes background:

$$\mathcal{B} \propto \frac{R_\mu}{D} \Delta t_{e\gamma} \frac{\Delta E_e}{m_\mu/2} \left(\frac{\Delta E_\gamma}{15m_\mu/2} \right)^2 \left(\frac{\Delta\theta_{e\gamma}}{2} \right)^2, \quad (\text{IV.3.1})$$

where \mathcal{B}^{-1} is the number of muons collected in order to reach one background event. The factors are the muon stop rate divided by the beam duty factor, R_μ/D ; the detector time resolution, $\Delta t_{e\gamma}$; the positron energy resolution, ΔE_e ; the photon energy resolution, ΔE_γ ; and the angular resolution, $\Delta\theta_{e\gamma}$. Improving the vertex determination lowers the background quadratically through the last factor.

IV.3.1.2 Next Steps

The MEG upgrade proposes to use either a surface muon beam with momentum $\approx 29 \text{ MeV}/c$ or subsurface muon beam at $\approx 25 \text{ MeV}/c$, along with the thinnest possible stopping target. The use of a subsurface beam is motivated by reducing the range straggling to stop muons. Hence the thinnest target gives the best constraints on the event vertex in the reconstruction of the back-to-back e and γ in $\mu \rightarrow e\gamma$. The straggling in range is given by

$$\Delta R \propto P^{3.5} \sqrt{((0.09)^2 + (3.5\Delta P/P)^2)}, \quad (\text{IV.3.2})$$

where P is the momentum and ΔP its spread, so a reduction in beam momentum gives a rapid decrease in the distance over which the muon stops [42].

There are two choices for going beyond the MEG upgrade proposal. MEG did not convert the photon, and its approved upgrade continues to use this method to achieve a ten-fold improvement in the limit. MEG is also considering an active target, although this is still an option rather than part of the baseline design. With photon conversion, a thin converter is needed so that multiple scattering and energy loss do not spoil the resolution. Then, however, the statistical power suffers, because only a small fraction of the photons can be converted, although the remaining events have the superior resolution of tracking, relative to calorimetry. How to resolve the conflict between statistics and resolution requires further study.

IV.3.1.3 Beam Requirements

Since the background is effectively a function of the square of the instantaneous intensity, as continuous a beam as possible, with minimal instantaneous fluctuation, is required. The beam should either be surface or slightly subsurface as explained above.

IV.3.2 Muon-to-electron Conversion

Muon-to-electron conversion experiments [43] bring negative muons to rest by stopping them in a target. The muons fall into orbit around an atomic nucleus. The muons can then (1) decay while in orbit (known as either DIO or MIO in the literature), (2) undergo nuclear capture, or (3) convert into electrons. The first process is a background; the second, the normalization for the signal; the third, the signal itself: a mono-energetic electron at an energy of the muon mass minus binding and recoil energy. Typical signal energies for the converted electrons therefore close to 100 MeV, depending on Z . The nucleus recoils coherently in the process and does not change state. One might think that muon decays would not be a significant background since the peak and upper limit of the muon free-decay Michel spectrum is at 52.8 MeV, far from the 100 MeV signal energy. The spectrum of a muon decaying from an atomic orbital differs from the free decay spectrum because the outgoing electron can exchange a photon with the nucleus. The endpoint now becomes the conversion energy. This is simple to understand: transform to the rest frame of the outgoing neutrinos. Then neglecting the tiny neutrino mass, the final state is an outgoing electron recoiling against a nucleus, precisely the same state as the conversion signal. Modern evaluations of the spectrum can then be combined with realistic resolutions and other effects to extract an expected amount of background [44]. Improving the resolution and minimizing energy loss in the apparatus (a stochastic process that increases the δ -function signal width, increasing all backgrounds) are therefore central to both improving existing limits and future *Project X* experiments.

The other major background comes from radiative pion capture, in which $\pi^- N \rightarrow \gamma N$ and the photon either internally or externally converts and produces an electron indistinguishable from signal. By spacing the beam pulses further part, one can use the pion lifetime to reduce the background. Pulsed beams, with (for Mu2e) 10^{-10} protons between pulses per protons in pulses, are therefore a key ingredient in the next generation of experiments; this suppression is known as extinction. A related source of background is antiproton production. Fermilab Booster experiments use 8 GeV kinetic energy protons and thus are above \bar{p} production threshold. Antiprotons do not decay (so far as we know) and move slowly, with kinetic energies of ~ 5 MeV; therefore much of the time information associated with the beam pulse is lost. Antiprotons can therefore evade the extinction requirements. If they reach the stopping target, they will then annihilate in the same material used to capture muons and produce pions that then undergo radiative pion capture. Experiments must then absorb in the beam to annihilate the \bar{p} s before they reach the stopping target. The absorber also stops muons, lowering the flux on the stopping target. The need to reduce the antiproton rate to an acceptable level without an unacceptable loss of muons is a limitation of the upcoming generation of experiments. *Project X*, with 1–3 GeV proton beams instead of 8 GeV, will produce negligible numbers of antiprotons and eliminate this problem.

IV.3.2.1 Current Status

The best existing searches for muon-to-electron conversion have been performed at PSI by the SINDRUM-II collaboration. SINDRUM-II used a variety of materials; the best limits were set on Au, with $R_{\mu e} < 7 \times 10^{-13}$ at 90% CL. The SINDRUM-II series had three relevant limitations:

1. the time between beam pulses at PSI is just under 20 ns, which leaves the experiments vulnerable to backgrounds from radiative pion capture since the pulse separations approximately

- the pion lifetime;
2. only $O(10^8)$ muons/s were available;
 3. the $\pi e5$ area at PSI required SINDRUM-II to use a degrader and beam vetoes.

IV.3.2.2 Next Steps

Fermilab’s Mu2e experiment at the Booster will reach 6×10^{-17} at 90% CL for conversions on Al, a four order-of-magnitude improvement over SINDRUM-II. There are two possibilities: (1) Mu2e sees a signal, or (2) it does not. If it does not, a huge part of SUSY parameter space, and that of other models, will be ruled out up to mass scales near 10^4 TeV/ c^2 . *Project X* can improve the statistical power by as much as two orders of magnitude. If a signal *is* seen, then Mu2e’s aluminum target needs to be changed to other elements in order to probe the nature of the new physics. However, as Z increases the lifetime of the μN muonic atom decreases until the conversion is obscured by the beam flash and backgrounds. The *Project X* flexible time structure and short beam pulses can be used to mitigate the experimental difficulties. Other, new technologies, such as FFAGs or helical cooling channels might be used as well. In either case, study a signal or improve a limit, the intensity provided at *Project X* would be required to advance.

It should be noted that the current beam timeline for Mu2e uses only one third of the available time because of details of the beam structure that are irrelevant for this discussion. In principle one could immediately gain a factor of three, but then with no other changes the background would be approximately one event or more from cosmic-ray induced events and the decay-in-orbit process. The increase in delivered protons may also cause a problem from increased radiation damage to the solenoids requiring more frequent warm-ups to anneal the Al-stabilized superconductor.

Recent studies have concentrated on a ten-fold improvement using the current Mu2e tripartite solenoid design [45]. The goal is to have an experiment with a single-event sensitivity 2.5×10^{-18} with fewer than 1 background event. The experiment would use the lower energy proton beams at 1 or 3 GeV from *Project X*. Enumerating the assumptions:

1. proton pulses with a full-base width of 100 ns;
2. duty factor of 90%;
3. intrinsic extinction from the machine of $\leq 10^{-6}$ followed by an additional $\leq 10^{-6}$ as in Mu2e through the “extinction dipole”;
4. protons at 1 or 3 GeV to eliminate antiproton-induced RPC backgrounds;
5. a beam transport system to the current Mu2e beam line.

These studies have found that either an Al or Ti stopping target seemed workable. The yield was 1.4×10^{-4} stopped muons/proton at 1 GeV and 6.7×10^{-4} at 3 GeV, compared to 1.6×10^{-3} , an order-of-magnitude higher at the Booster’s 8 GeV. Straightforward calculations then lead to the requirements in Table IV-2 (for Al; Ti is similar).

Table IV-2: Protons required to achieve a single-event sensitivity of $R_{\mu e} = 2.5 \times 10^{-18}$ at three different energies.

Proton energy	Protons on target	Beam power	Protons/pulse
8 GeV	3.6×10^{21}	80 kW	1.0×10^8
3 GeV	8.6×10^{21}	72 kW	2.5×10^8
1 GeV	40×10^{21}	112 kW	1.2×10^9

The rates are approximately 3–4 times the Mu2e rates, which will likely require upgrades to the detector but does not seem an unachievable goal. Mu2e at the Booster is designed for 8 kW on the proton target. There are then at least two immediate challenges:

1. the increased power requires additional shielding to the production solenoid; radiation damage to the Al-stabilized superconductor will cause quenching and although Al-stabilized superconductor can be annealed the loss of data will be too great;
2. the number of neutrons will scale along with the protons and beam power, and those neutrons can fire the cosmic ray veto, punch through to the detector, or cause other problems.

We show two relevant graphs from Ref. [46]. The first, Fig. IV-2, shows that in fact the muon yield, with the current Mu2e solenoid design, not only can be maintained but it can be *higher* at 3 GeV and about equal at 1 GeV, holding power fixed. This result is far from obvious, since the collection efficiency of the Mu2e solenoids were optimized for the Booster-era 8 GeV protons.

The second problem is that of radiation damage in the Al stabilizers for the solenoid coils, addressed in Fig. IV-3. A figure of merit (FOM) is defined as the number of stopped muons per GeV (so for 1 kW fixed beam power) per peak radiation damage. The radiation damage in metals is measured in displacements per atom (DPA), which is simply the number of times an atom is displaced from its site in the crystal lattice, per unit fluence (fluence is the flux per unit area, integrated over time). It is a standard metric for radiation damage [47]. The plot shows that the FOM peaks at about 1 GeV: the number of DPAs at the peak radiation damage location is small, driving the FOM upwards. The peak DPA drops in part because a lower energy proton beam will produce more isotropic secondaries, driving the peak DPA to smaller values as the energy decreases. The current Mu2e heat-shield design corresponds to the curve labeled “bronze HRS.” The “tungsten HRS” would be a better absorber, but tungsten is more expensive.

IV.3.2.3 Beam Requirements

There are three general requirements:

1. A pulsed beam. In a Mu2e-style experiment on Al or Ti, pulses no longer than 50 ns would be best.

2. A variable time separation between pulses. The requirement on the time separation between pulses is governed by the experimental details and the lifetime of muonic atoms in the converting nucleus: too short, and the detector may be overwhelmed by the beam flash; too long, and the muons will decay away. For Au, one would want about 100–200 ns between pulses.
3. As little beam as possible between pulses. The issue here is often referred to as extinction. The RPC background is suppressed by waiting for pions to decay after the pulse. A proton arriving between pulses restarts the clock and removes the suppression factor.

While an order-of-magnitude improvement seems plausible, if Mu2e sees no signal it will be difficult to take full advantage of *Project X* intensities for a $\times 100$ improvement. Backgrounds from cosmic rays and the absolute calibration of the momentum scale (related to separating the decay-in-orbit background from the signal) would limit the experiment in its current design. In the case of a signal, it would be imperative to measure the conversion rate on heavy nuclei such as Au. These backgrounds would likely not preclude the measurement but would likely be significant limitations. Nor would it be straightforward to improve the limit switching from Al to heavy nuclei, where one might expect the signal to be larger and a limit therefore better. The first two beam-related requirements above will be difficult to meet simultaneously in a Mu2e-style experiment. With a pion lifetime of 26 ns and a muonic lifetime of 72.6 ns, combined with a beam pulse of order 1 ns,

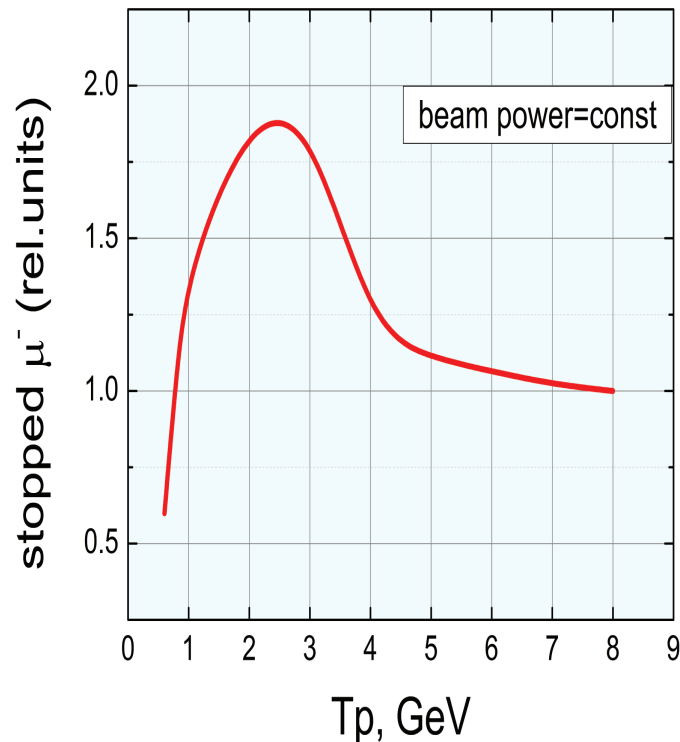


Figure IV-2: Stopped-muon yield in the current design of the Mu2e apparatus as a function of proton kinetic energy T_p , normalized to unity at the Booster-era Mu2e of 8 GeV kinetic energy. Note the 1 GeV yield is slightly better than the 8 GeV yield, and the 3 GeV yield is almost twice as high. Beam power is kept constant as the proton energy varies.

the radiative pion backgrounds cannot be suppressed even with extinction methods: the muonic lifetime is just too short. There are next-generation concepts that form circulating beams in which the pions can decay, effectively creating a long flight path before forming the final muon beam. [48] These reduce the radiative pion capture background sufficiently. They also manage the prompt background and beam flash, allowing the experiment to access short-lifetime capture materials such as Au.

IV.3.3 $\mu \rightarrow 3e$

IV.3.3.1 Current Status

A new measurement should strive to set a limit $< O(10^{-16})$ to be competitive with existing limits and other planned measurements. The current limit in SINDRUM is $BR(\mu \rightarrow 3e) < 1.0 \times 10^{-12}$ at 90% CL [49]. Therefore a factor of 10^4 improvement is required. With a one-year run, one then requires 10^9 – 10^{10} decays/s, before acceptances, etc., are included. The current $\pi e5$ (MEG) beamline yields about 10^9 muons/s, barely enough. A spallation neutron source at PSI (called SINQ, <http://www.psi.ch/sinq/>) could provide 5×10^{10} muons/s, probably an effective minimum requirement.

Existing experiments have used stopped muons and muon decay-at-rest. In that case the outgoing electron and positrons can be tracked and the kinematic constraints $\sum \mathbf{p} = \mathbf{0}$ and $\sum E = m_e$,

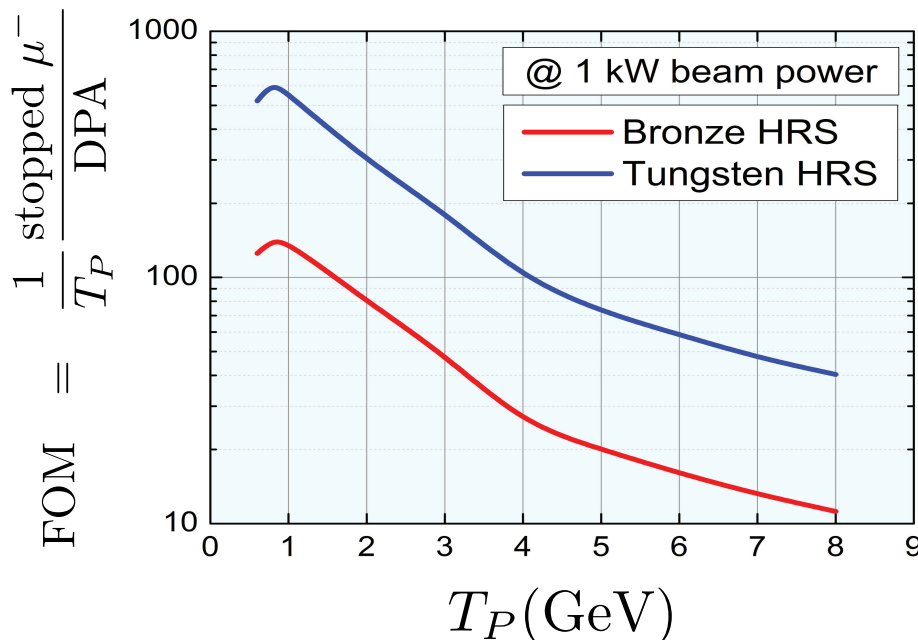


Figure IV-3: Figure of merit FOM, defined as stopped muons per GeV per peak DPA for 1 kW beam power in the current Mu2e solenoid, plotted against the kinetic energy of the incoming proton. Two heat and radiation shields (HRS) are shown; the bronze HRS is close to the current Mu2e design, and the tungsten shield is a more effective, but more expensive, variant.

along with timing, can then be used to identify the rare decay.

Unfortunately, this mode suffers from many of the same problems as $\mu \rightarrow e\gamma$. Because it is a decay, unlike muon-to-electron conversion, $\mu \rightarrow 3e$ electrons are in the same momentum range as ordinary Michel decays. Therefore there are accidental backgrounds from Michel positrons that coincide with e^+e^- pairs from γ conversions or from other Michel positrons that undergo Bhabha scattering. (One could cut on the opening angle between the positrons and each of the electrons, since conversions tend to have a small opening angle, but if the $\mu \rightarrow 3e$ process occurs through processes with a photon, one then loses acceptance.)

IV.3.3.2 Next Steps

A new $\mu \rightarrow 3e$ experiment using monolithic active pixel sensors; the experiment has just received approval at PSI [50]. As described in Ref. [51], the proponents plan to overcome the difficulties above by making the tracking material so thin that multiple scattering is small and backgrounds from radiative muon decay ($\mu^+ \rightarrow e\nu\bar{\nu}\gamma$ with a subsequent photon conversion) are negligible. The location of the experiment is a matter of logistics, time-sharing with MEG, etc. A first-round would achieve 10^{-15} with eventual improvements in the beam (possibly moving to a spallation neutron source at PSI) and the detector yielding a potential limit of 10^{-16} . Potential limits on the experiment from the decay $\mu^+ \rightarrow e^+e^-e^+\nu_e\bar{\nu}_\mu$ are discussed in Ref. [52]; the phase space for accepting such decays and their being indistinguishable from a $\mu \rightarrow 3e$ signal may be the ultimate limitation of these experiments.

IV.3.3.3 Beam Requirements

The beam requirements are quite similar to MEG: a nearly monochromatic beam with a high stopping rate over a small volume. The experiment will use a high-intensity surface beam with small emittance and a momentum-bite of $\leq 10\%$. The initial phase for the PSI run will be 10^7 – 10^8 muons/s rising closer to 10^8 for the second phase.

The second phase of $\mu \rightarrow 3e$ hopes to reach $O(10^{-16})$. An unpleased stopping rate of order GHz is then required. PSI's HiMB project could supply the necessary intensity in the current experimental area, about 2×10^9 stops/s, and a detailed feasibility study of HiMB has just started as of this writing. Assuming the HiMB area is built and successful, then 10^7 μ/s (for perfect acceptance) are needed to reach the sensitivity at which the radiative decay background limits the experiment in a few-year run.

IV.3.4 Muonium-antimuonium Oscillations

Hydrogenic bound states of μ^+e^- (muonium, or “Mu”) can convert through a $\Delta L = 2$ process to μ^-e^+ ($\overline{\text{Mu}}$). This process is analogous to $K^0\bar{K}^0$ mixing; Pontecorvo [53] suggested the process could proceed through an intermediate state of two neutrinos. Part of the calculation is performed in Ref. [54]. One typically states the result of a search as an upper limit on an effective coupling analogous to G_F : $G_{\text{Mu}\overline{\text{Mu}}}$, where the exchange is mediated by such particles as a doubly charged Higgs, a dileptonic gauge boson, heavy Majorana neutrinos, or a supersymmetric τ -sneutrino. The

new interaction leads to a splitting of the otherwise degenerate energy levels (recall the coupling is $V - A$). Such a new interaction would break the degeneracy by an amount

$$\frac{\delta}{2} = \frac{8 G_F}{\sqrt{2} n^2 \pi a_o^3} \left(\frac{G_{\text{Mu}\overline{\text{Mu}}}}{G_F} \right), \quad (\text{IV.3.3})$$

where n is the principal quantum number and a_o is the Bohr radius of the muonium atom. For $n = 1$,

$$\delta = 2.16 \times 10^{-12} \frac{G_{\text{Mu}\overline{\text{Mu}}}}{G_F} \text{ eV}. \quad (\text{IV.3.4})$$

Assuming an initially pure $\mu^+ e^-$ state, the probability of transition is given by:

$$\mathcal{P}(t) = \sin^2 \left(\frac{\delta t}{2\hbar} \right) \lambda_\mu e^{-\lambda_\mu t}, \quad (\text{IV.3.5})$$

where λ_μ is the muon lifetime. Modulating the oscillation probability against the muon lifetime tells us the maximum probability of decay as antimuonium occurs at $t_{\text{max}} = 2\tau_\mu$. The overall probability of transition is

$$P_{\text{total}} = 2.5 \times 10^{-3} \left(\frac{G_{\text{Mu}\overline{\text{Mu}}}}{G_F} \right). \quad (\text{IV.3.6})$$

Normally the experiments quote a limit on $G_{\text{Mu}\overline{\text{Mu}}}$. Experimentally, of course, no such thing is measured; one measures a probability of transition. The limit is set assuming an interaction of $(V \pm A) \times (V \pm A)$ although one can also set limits on masses of, for example, dileptonic gauge bosons. We follow the practice of quoting a limit on the ratio of coupling constants.

The experimental signature of antimuonium decay is an energetic electron from normal muon decay in coincidence with an approximately 13.5 eV kinetic energy positron (the Rydberg energy in the $1s$ state). Because the negative muon can be captured, the signal rate is suppressed by the capture fraction (depending on Z , around a factor of two for $(V \mp A) \times (V \pm A)$ processes). This measurement suffers rate-dependent backgrounds not dissimilar to those found in $\mu \rightarrow e\gamma$ and $\mu \rightarrow 3e$, from accidentals and radiative decay processes:

1. The rare decay mode $\mu^+ \rightarrow e^+ e^+ e^- \nu_e \bar{\nu}_\mu$ with a branching ratio of $(3.4 \pm 0.4) \times 10^{-5}$ (from the 2008 PDG). If one of the positrons has low kinetic energy and the electron is detected, this channel can fake a signal.
2. The system starts as muonium, hence $\mu^+ \rightarrow e^+ \nu_e \bar{\nu}_\mu$ yields a positron. If the e^+ undergoes Bhabha scattering, an energetic electron can be produced. Background results from the coincidence of that scattering with a scattered e^+ .

IV.3.4.1 Current Status

Modern experiments rely on the coincident detection of the muon and positron; the most recent experiment is described in Ref. [55]. A subsurface μ^+ at ≈ 20 MeV/c is passed into SiO_2 powder (the material provides stopping power with voids for the muonium system to escape). The apparatus could detect the decay of both muonium and antimuonium. Decay positrons or electrons were observed in a spectrometer at right angles to the beam and after passing through a pair of MWPCs were detected in NaI. Atomic electrons (or positrons) were electrostatically collected, focused, and accelerated to 5.7 keV. A dipole then charge- and momentum-selected the particles, which were finally detected by an MCP. The advantages of observing the thermal muonium are obvious: one can verify the experimental method and calibrate the detectors, study acceptances with reversed polarities, etc. The most recent experiment set a limit $G_{\text{Mu}\bar{\text{Mu}}}/G_F < 3.0 \times 10^{-3}$ at 90% CL [55].

IV.3.4.2 Next Steps

It is interesting to consider placing the muonium system in a magnetic field, since the muonium energy levels will be split. We refer the reader to Refs. [56,57] for a fuller discussion of the physics. Because the spectrometers used to detect and measure electron momenta require a magnetic field, this effect must be included in the calculation of the transition rate. In this more general case,

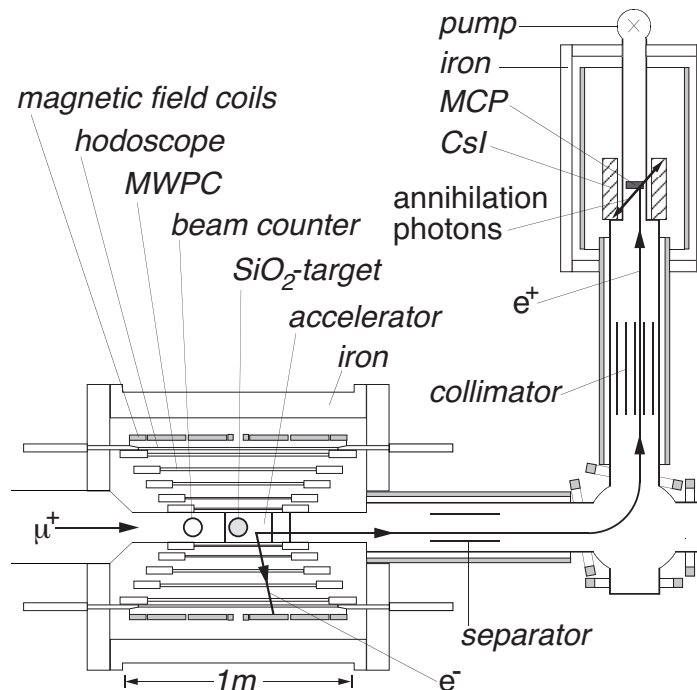


Figure IV-4: MACS apparatus at PSI. The signature requires the energetic E^- from the μ^- decay of $\bar{\text{Mu}}$ in a magnetic spectrometer, in coincidence with the atomic shell e^+ , which is accelerated and magnetically guided onto a microchannel plate; at least one annihilation photon is then detected in a CsI calorimeter. From Ref. [55].

$\delta \rightarrow \sqrt{\delta^2 + \Delta^2}$. The effect is significant even for a weak (~ 0.1 T) field because of the Zeeman splitting of the energy levels. The reduction factor for fields of about 0.1 Gauss to 0.1 Tesla is nearly flat at a factor of two, but [58] shows the reduction becomes rapidly more suppressed at higher fields.

The technology of earlier experiments is now obsolete. One significant limit was the rate capabilities of the available MWPCs. New technologies could certainly improve on 1998-style methods. The best existing experiment used CsI; modern scintillating crystals such as LYSO have much better rate capabilities.

IV.3.4.3 Beam Requirements

A pulsed beam seems a necessity to reduce backgrounds from the $\mu^+ \rightarrow e^+ e^+ e^- \nu_e \bar{\nu}_\mu$ muon decay. The intensity should be commensurate with a few order-of-magnitude improvement in the limit. The efficiency for muonium formation is already about 60%, and the earlier experiments ran for ≈ 210 hours with 1.4×10^9 decaying muonium atoms [54].

IV.3.5 Muon Anomalous Magnetic Moment $g - 2$

IV.3.5.1 Current Status

A concrete plan is in place to probe new physics at the TeV scale by improving the precision on the measurement of the anomalous magnetic moment of the muon, $a_\mu \equiv (g_\mu - 2)/2$. Within the framework of the Dirac equation, g_μ is expected to equal 2. However, quantum loop corrections associated with QED, electroweak, and QCD processes lead to a deviation from this value. These SM loop corrections have been calculated with a precision of 420 ppb (part-per-billion) [59]:

$$a_\mu^{\text{SM}} = 116591802(49) \times 10^{-11}. \quad (\text{IV.3.7})$$

The largest contributor to the theoretical uncertainty stems from two hadronic effects. The first, with larger error on a_μ , is hadronic vacuum polarization, which can, however, be extracted from $e^+ e^- \rightarrow$ hadrons and from hadronic τ decays. The second, with smaller but less solid error, come from the hadronic light-by-light process. The prospects for calculating both hadronic contributions with lattice QCD and, thereby reducing and solidifying the uncertainties, is discussed in Sec. X.3.3.2.

The most precise experimental determination of a_μ was conducted at Brookhaven by the E821 experiment. Muons with a momentum of 3.094 GeV/c are injected into an ≈ 7 m-radius magnetic storage ring. Precise measurements of both the 1.45 T magnetic field and the precession frequency of the muons in that field allows the anomaly to be determined to 540 ppb [60]:

$$a_\mu^{\text{E821}} = 116592089(63) \times 10^{-11}. \quad (\text{IV.3.8})$$

The comparison between the standard model prediction and the measurement is $\Delta a_\mu = 287(80) \times 10^{-11}$, which amounts to a 3.6σ deviation. To highlight one example, if supersymmetry exists there would be new contributions to a_μ via supersymmetric particle loops, analogous to the standard model QED, weak, and QCD loops. This current discrepancy between the experimental observation and the standard model could be a hint that such contributions actually exist.

IV.3.5.2 Next Steps

The Brookhaven E821 experiment finished statistics-limited. In the near future, the Fermilab E989 Collaboration aims reduce the experimental uncertainty on a_μ to 140 ppb [61]. This relies on a factor 20 increase in the statistics and a variety of improvements in the measurements of the magnetic field and the decay electrons' energies and times. The proposal has received Mission Need (CD-0) from the Department of Energy, and the storage ring is being transported to Fermilab. Slated to start taking data in 2016, the New $g - 2$ Experiment will accumulate the necessary statistics using a μ^+ beam in about two years. If the central value remains the same, i.e., $a_\mu^{\text{E989}} = a_\mu^{\text{E821}}$, the improved experimental precision will result in a 5.5σ deviation with the standard model. Further expected improvements in theory could increase this significance to 8σ , which would amount to a discovery of new physics.

At that point, a natural followup would be to try to run with the same configuration and a higher intensity beam at *Project X*. Several experimental components are well-suited to handle additional beam rate. Each calorimeter is segmented into 54 lead fluoride crystals, which would be critical for resolving pileup at *Project X* beam rates. The data acquisition system for E989 is designed to digitize all calorimeter channels continuously during the beam spills. This means that the incoming raw data rate is determined by the chosen digitization frequency rather than the instantaneous decay electron rate. The data is then processed to identify electrons and read out during the 800 ms period when the Booster batches are being delivered to the NOVA experiment. Assuming some reasonably similar proton economics occurs in the LBNE era, the E989 detector system will be able to handle the additional rate.

However the biggest challenges for handling additional beam would come from the pion production target station. E989 will use the Inconel production target that was used for antiproton production at the end of the Tevatron Run II. Four booster batches will be redistributed into 16 bunches during each 1.33 s main injector cycle. A lithium lens that collects the pions has been developed to handle the increased pulse rate of 12 Hz, up from 0.45 Hz during Tevatron running. With an increased repetition rate, the cooling capacity of the lens is a significant issue. Care must be taken to avoid the reaching the melting point of lithium (453.75 K). The lithium lens has been simulated in ANSYS to understand the thermal constraints. These simulations were validated with a test stand that pulsed the lens with 12 Hz repetition rates. Additional preliminary simulations have been performed to model the lens performance at higher repetition rates. The studies determined that running with lens in the current configuration was not feasible at rates greater than 21 Hz due to the reaching the melting point of lithium. Rates of 15 Hz and 18 Hz were not ruled out, but more work is needed to understand how we would accommodate any additional pulses heading into the *Project X* era.

When the secondary production target is upgraded to accept additional rate, the systematic errors of E989 could be further reduced by modifying the experiment to use a smaller beam aperture. In the current configuration, the magnetic field must be highly uniform – and precisely measured – over the storage aperture radius of 4.5 cm. With the higher beam flux, the collimators could be reduced to a few centimeters where the magnetic field gradients are smallest, reducing the systematic contribution from the knowledge of the field.

Another interesting possibility would be to switch the beam polarity to deliver negative muons. The μ^- production rate is about 2.5 times lower than for μ^+ [62], so a μ^- measurement with com-

parable statistics would take a prohibitive amount of time in the pre-*Project X* era. The target considerations above would still be an issue with the μ^- beam. Running with μ^- requires flipping the polarity of the storage ring magnet, which would help demonstrate that the field-related systematics are under control. Almost all aspects of the current design would be appropriate for a measurement of $g - 2$ of the negative muon. However, the electric quadrupole plates that provide vertical beam focusing in the muon storage ring would need to be upgraded for running with μ^- . This is because the electrons can get trapped in the high field regions near the quadrupole plates, whereas the positrons produced during μ^+ running disappear at the surfaces. This necessitates an order of magnitude more stringent vacuum requirements and an improved design of the plate surfaces.

Another possible outcome of the E989 μ^+ running could be that the discrepancy between experimental and Standard-Model values of a_μ disappears. In this event, the path to reusing the storage ring to significantly higher precision is not immediately clear. E821 was designed to have sensitivity to the electroweak contribution to the anomalous magnetic moment, $a_\mu^{\text{EW}} = 154(1) \times 10^{-11}$ (or 130 ppb). If the current anomaly disappears then the next contribution within the Standard Model would be the two-loop Higgs terms, $a_\mu^{\text{H}} \approx 4 \times 10^{-11}$ [63]. This contribution of ≈ 35 ppb is an additional factor of four beyond the proposed sensitivity of E989 (140 ppb). Assuming that advances in lattice QCD lead to improvements in the uncertainties of the leading hadronic terms over the next decade, a next generation muon $g - 2$ experiment could continue to probe the standard model.

A new approach to measure a_μ to 100 ppb with an ultracold muon beam has been proposed at J-PARC [64,65]. The basic strategy is to bring 3 GeV protons to a production target and collect surface muons (μ^+). These muons are then stopped in a secondary target where they form muonium and diffuse. Lasers are used to remove the electrons from the muonium, resulting in ultracold muons with a kinetic energy of around 25 mV. These muons would then be accelerated to 300 MeV/ c and injected into a 66 cm diameter, 3 Tesla storage ring via a novel three-dimensional injection spiral scheme.

The success of such a proposal relies on an ultrahigh intensity surface muon beam. To reach a precision of 100 ppb in about a year of running, 10^6 ultra cold muons per second must be produced. The expected efficiency of converting surface muons to ultracold muons is on the order of 10^{-5} to 10^{-3} , implying a surface muon beam rate requirement of 10^9 to 10^{11} muons per second. The lower end of this range is comparable to the current rates produced at PSI.

IV.3.5.3 Beam Requirements

The extension of the muon $g - 2$ storage ring experiments require a muon beam with a momentum of 3.094 GeV/ c . A high intensity μ^- beam would be the natural extension to the current experiment. The beam should be pulsed with bunch spacings no smaller than 10 ns to allow adequate time for muon decay and data acquisition. The beam pulses should be no longer than 120 ns so that the leading edge of the pulse does not lap the trailing edge during injection into the storage ring. Additional muons per bunch can be utilized by the existing $g - 2$ experimental design. However, the number of booster batches delivered to the pion production target is not easily accommodated by the lithium collection lens.

The small storage ring experiments would utilize a high intensity surface muon beam with required rates of 10^9 – 10^{11} μ^+ per second. Significant technology advances in laser ionization to

produce ultra cold muons is required. A novel 3-dimensional injection spiral scheme into a tabletop scale 3 T cyclotron would also need to be developed.

IV.4 SUMMARY

Studies of charged lepton flavor violation with muons are of paramount importance. If the LHC experiments discover new physics, these processes can discriminate and distinguish among models. If the mass scale of BSM physics is beyond that accessible at the LHC then charged lepton flavor violation can probe up to $10^4 \text{ TeV}/c^2$. Since such probes are indirect, regardless of the LHC results, one experiment will not suffice. *Project X* offers an opportunity to perform the key experiments required in one place in a staged manner.

There are five processes that are essential to this campaign, namely, $\mu^+ \rightarrow e^+\gamma$, $\mu^+ \rightarrow e^+e^+e^-$, $\mu^-N \rightarrow e^-N$, $\mu^-N \rightarrow e^+N$, and $\mu^+e^- \leftrightarrow \mu^-e^+$. The first two “decay experiments” require a very different time structure from the next two “capture” experiments involving conversion in the field of a nucleus, and the last, muonium-antimuonium oscillations, requires yet another time structure. All require intense beams at megawatts of power at 1–3 GeV proton kinetic energy. *Project X* has the flexibility of time structure required and can supply the requisite intensity for a full set of measurements. Initial studies of the conversion experiments are promising: it is plausible that an order-of-magnitude improvement over the Booster-era Mu2e is achievable. The $\mu \rightarrow e\gamma$ and $\mu \rightarrow 3e$ experiments are being pursued at PSI, with an approved upgrade to MEG to reach $\text{BR}(\mu \rightarrow e\gamma) < 6 \times 10^{-14}$ at 90% CL and an approved experiment for $\mu \rightarrow 3e$ at roughly 10–16. Progressing past these experiments will require new experimental techniques since they are likely to be background-limited. One likely requirements is hard cuts on the data to eliminate backgrounds, and here the *Project X* intensity can make up for acceptance loss. In muonium-antimuonium, a two-order of magnitude improvement is likely possible, and the both the flexible time structure and intensity are essential. Finally, the $g-2$ anomaly can be probed as well for the opposite sign of muons, permitting CPT tests and systematic cross-checks presuming the current anomaly survives the Booster experiment and improvements in the lattice calculations. If new physics is seen, further investigation will be required.

References

- [1] N. Cabibbo, Phys. Rev. Lett. **10**, 531 (1963)
- [2] M. Kobayashi and T. Maskawa, Prog. Theor. Phys. **49**, 652 (1973)
- [3] B. Pontecorvo, Sov. Phys. JETP **6**, 429 (1957)
- [4] Z. Maki, M. Nakagawa, and S. Sakata, Prog. Theor. Phys. **28**, 870 (1962)
- [5] W. J. Marciano and A. I. Sanda, Phys. Lett. **B67**, 303 (1977)
- [6] S. M. Bilenky, S. T. Petcov, and B. Pontecorvo, Phys. Lett. **B67**, 309 (1977)

- [7] T.-P. Cheng and L.-F. Li, Phys. Rev. **D16**, 1425 (1977)
- [8] B. W. Lee, S. Pakvasa, R. E. Shrock, and H. Sugawara, Phys. Rev. Lett. **38**, 937 (1977)
- [9] B. W. Lee and R. E. Shrock, Phys. Rev. **D16**, 1444 (1977)
- [10] A. de Gouvêa and P. Vogel, “Lepton flavor and number conservation, and physics beyond the Standard Model,” Fundamental Symmetries in the Era of LHC (2013), arXiv:1303.4097 [hep-ph]
- [11] A. de Gouvêa, AIP Conf. Proc. **721**, 275 (2004)
- [12] A. de Gouvêa and J. Jenkins, Phys. Rev. **D77**, 013008 (2008), [arXiv:0708.1344 [hep-ph]]
- [13] Y. Kuno and Y. Okada, Rev.Mod.Phys. **73**, 151 (2001), [arXiv:hep-ph/9909265 [hep-ph]]
- [14] R. Kitano, M. Koike, and Y. Okada, Phys.Rev. **D66**, 096002 (2002), [arXiv:hep-ph/0203110 [hep-ph]]
- [15] V. Cirigliano, R. Kitano, Y. Okada, and P. Tuzon, Phys.Rev. **D80**, 013002 (2009), [arXiv:0904.0957 [hep-ph]]
- [16] O. U. Shanker, Phys.Rev. **D20**, 1608 (1979)
- [17] A. Czarnecki, W. J. Marciano, and K. Melnikov, AIP Conf.Proc. **435**, 409 (1998), [arXiv:hep-ph/9801218 [hep-ph]]
- [18] A. S. Kronfeld, Ann.Rev.Nucl.Part.Sci. **62**, 265 (2012), [arXiv:1203.1204 [hep-lat]]
- [19] R. Harnik, J. Kopp, and J. Zupan, JHEP **1303**, 026 (2013), [arXiv:1209.1397 [hep-ph]]
- [20] L. Willmann *et al.*, Phys. Rev. Lett. **82**, 49 (1999), [arXiv:hep-ex/9807011]
- [21] “Project X Physics Study,” <https://indico.fnal.gov/event/projectxps12>
- [22] S. P. Martin, “A supersymmetry primer,” (1997), arXiv:hep-ph/9709356
- [23] ATLAS Collaboration, “Search for direct top squark pair production in final states with one isolated lepton, jets, and missing transverse momentum in $\sqrt{s} = 8$ TeV pp collisions using 21 fb⁻¹ of ATLAS data,” (2013), <http://cds.cern.ch/record/1532431>
- [24] S. Chatrchyan *et al.* (CMS Collaboration), “Search for supersymmetry in hadronic final states with missing transverse energy using the variables α_t and b -quark multiplicity in pp collisions at $\sqrt{s} = 8$ TeV,” (2013), arXiv:1303.2985 [hep-ex]
- [25] I.-H. Lee, Nucl. Phys. **B246**, 120 (1984)
- [26] I.-H. Lee, Phys. Lett. **B138**, 121 (1984)
- [27] J. Hisano, T. Moroi, K. Tobe, and M. Yamaguchi, Phys. Rev. **D53**, 2442 (1996), [arXiv:hep-ph/9510309 [hep-ph]]
- [28] J. Hisano and D. Nomura, Phys. Rev. **D59**, 116005 (1999), [arXiv:hep-ph/9810479 [hep-ph]]

- [29] I. Masina and C. A. Savoy, Nucl. Phys. **B661**, 365 (2003), [arXiv:hep-ph/0211283 [hep-ph]]
- [30] P. Paradisi, JHEP **0510**, 006 (2005), [arXiv:hep-ph/0505046 [hep-ph]]
- [31] M. Ciuchini *et al.*, Nucl. Phys. **B783**, 112 (2007), [arXiv:hep-ph/0702144]
- [32] G. D. Kribs, E. Poppitz, and N. Weiner, Phys. Rev. **D78**, 055010 (2008), [arXiv:0712.2039 [hep-ph]]
- [33] R. Fok and G. D. Kribs, Phys. Rev. **D82**, 035010 (2010), [arXiv:1004.0556 [hep-ph]]
- [34] K. S. Babu, B. Dutta, and R. N. Mohapatra, Phys. Rev. **D67**, 076006 (2003), [arXiv:hep-ph/0211068 [hep-ph]]
- [35] B. Dutta and R. N. Mohapatra, Phys. Rev. **D68**, 056006 (2003), [arXiv:hep-ph/0305059 [hep-ph]]
- [36] C. Csáki, Y. Grossman, P. Tanedo, and Y. Tsai, Phys. Rev. **D83**, 073002 (2011), [arXiv:1004.2037 [hep-ph]]
- [37] C. Csáki, C. Delaunay, C. Grojean, and Y. Grossman, JHEP **0810**, 055 (2008), [arXiv:0806.0356 [hep-ph]]
- [38] F. del Aguila, A. Carmona, and J. Santiago, JHEP **1008**, 127 (2010), [arXiv:1001.5151 [hep-ph]]
- [39] W.-F. Chang and J. N. Ng, Phys. Rev. **D71**, 053003 (2005), [arXiv:hep-ph/0501161 [hep-ph]]
- [40] J. Hisano and K. Tobe, Phys. Lett. **B510**, 197 (2001), [arXiv:hep-ph/0102315 [hep-ph]]
- [41] J. Adam *et al.* (MEG Collaboration), “New constraint on the existence of the $\mu^+ \rightarrow e^+ \gamma$ decay,” (2013), arXiv:1303.0754 [hep-ex]
- [42] A. M. Baldini *et al.*, “MEG upgrade proposal,” (2013), arXiv:1301.7225 [physics.ins-det]
- [43] R. H. Bernstein and P. S. Cooper, “Charged lepton flavor violation: An experimenter’s guide,” To be published in Phys. Rept. C
- [44] A. Czarnecki, X. Garcia i Tormo, and W. J. Marciano, Phys. Rev. **D84**, 013006 (2011), [arXiv:1106.4756 [hep-ph]]
- [45] K. Knoepfel *et al.* (2013), to be submitted to the Proceedings of Snowmass 2013
- [46] D. Glenzinski, K. Knoepfel, N. V. Mokhov, V. S. Pronskikh, and R. Tschirhart, “On optimal beam energy for the Mu2e experiment for Project X stages,” FERMILAB-TM-2559-APC-PPD
- [47] M. Li, “Moving from DPA to changes in materials properties,” (2012), <https://indico.fnal.gov/getFile.py/access?contribId=23&sessionId=3&resId=0&materialId=slides&confId=4982>
- [48] Y. Kuno, PoS NFACT08, 111 (2008)

- [49] U. Bellgardt *et al.*, Nucl. Phys. **B299**, 1 (1988)
- [50] N. Berger, J. Phys. Conf. Ser. **408**, 012070 (2013), [arXiv:1110.1504 [hep-ex]]
- [51] A. Blondel *et al.* ($\mu 3e$ Collaboration), “Letter of intent for an experiment to search for the decay $\mu \rightarrow eee$,” (2012), http://www.physi.uni-heidelberg.de/Forschung/he/mu3e/documents/LOI_Mu3e_PSI.pdf
- [52] R. M. Djilkibaev and R. V. Konoplich, Phys. Rev. **D79**, 073004 (2009)
- [53] B. Pontecorvo, Sov. Phys. JETP **6**, 429 (1957)
- [54] L. Willmann and K. Jungmann, Lect. Notes Phys. **499**, 43 (1997), [arXiv:hep-ex/9805013]
- [55] L. Willmann *et al.*, Phys. Rev. Lett. **82**, 49 (1999)
- [56] Y. Kuno and Y. Okada, Rev. Mod. Phys. **73**, 151 (2001), [arXiv:hep-ph/9909265 [hep-ph]]
- [57] G. Feinberg and S. Weinberg, Phys. Rev. **123**, 1439 (1961)
- [58] W.-S. Hou and G.-G. Wong, Phys. Lett. **B357**, 145 (1995), [arXiv:hep-ph/9505300]
- [59] J. Beringer *et al.* (Particle Data Group), Phys. Rev. **D86**, 010001 (2012)
- [60] G. W. Bennett *et al.* (Muon $g - 2$ Collaboration), Phys. Rev. **D73**, 072003 (2006)
- [61] R. M. Carey *et al.*, “The new $g - 2$ experiment: A proposal to measure the muon anomalous magnetic moment to ± 0.14 ppm precision,” (2009), http://www.fnal.gov/directorate/program_planning/Mar2009PACPublic/Proposal_g-2-3.0Feb2009.pdf
- [62] O. B. van Dyck *et al.*, IEEE Trans. Nucl. Sci. **26**, 3197 (1979)
- [63] A. Czarnecki, B. Krause, and W. J. Marciano, Phys. Rev. Lett. **76**, 3267 (1996), [arXiv:hep-ph/9512369 [hep-ph]]
- [64] T. Mibe (J-PARC $g - 2$ collaboration), Chin. Phys. **C34**, 745 (2010)
- [65] H. Iinuma (J-PARC $g - 2$ collaboration), J. Phys. Conf. Ser. **295**, 012032 (2011)

V Measurements of Electric Dipole Moments with *Project X*

*Tim Chupp, Susan Gardner, Zheng-Tian Lu,
Wolfgang Altmannshofer, Marcela Carena, Yannis K. Semertzidis*

V.1 INTRODUCTION

A permanent electric dipole moment (EDM) \mathbf{d} of a nondegenerate system is proportional to its spin \mathbf{S} , and it is nonzero if the energy of the system shifts in an external electric field, in a manner controlled by $\mathbf{S} \cdot \mathbf{E}$. Such an interaction breaks the discrete symmetries of parity P and time reversal T . According to the CPT theorem, it reflects the existence of CP violation, i.e., of the product of charge conjugation C and parity P , as well. A nonzero EDM has yet to be established, and the existing experimental limits, as we report for a variety of systems in Table V-1, are extremely sensitive probes of new physics, probing the existence of new particles and new sources of CP violation beyond the TeV scale. While the discovery of a nonzero EDM in any system must be our first and foremost goal, increasingly sensitive EDM measurements in a variety of systems are also essential to constraining and ultimately determining the nature of any new sources of CP violation found.

EDM searches of enhanced experimental sensitivity are a key step in the exploration of the fundamental nature of our Universe, particularly in regards to the manner in which it came to have such a markedly large baryon asymmetry of the universe (BAU). Sakharov tells us that particle physics is capable of a microscopic explanation of the BAU, but baryon number, C , and CP violation are all required in concert with a departure from thermal equilibrium in order to realize a nonzero result [1]. Interestingly, all the necessary ingredients appear in the Standard Model (SM), but numerical assessments of the BAU in the SM fall far short of the observed value [2–7]. This motivates the ongoing hunt for new sources of CP violation. Currently we know as a result of the experiments at the B -factories, with key input from the Tevatron, that the Cabibbo-Kobayashi-Maskawa (CKM) mechanism serves as the dominant source of flavor and CP violation in flavor-changing processes [8,9]. Nevertheless, these definite conclusions do not end our search because we have not yet understood the origin of the BAU.

Searches for EDMs have a particularly high priority in the LHC era. If new physics is discovered at the LHC, then EDMs offer a unique window on its nature. EDMs act as exquisitely sensitive probes of the existence of possible new CP -violating phases beyond those present in the SM. In particular, EDMs are uniquely suitable to probing additional sources of CP violation in the Higgs sector. On the other hand, in the absence of any direct new physics signals at the LHC, increasingly sensitive searches for EDMs provide access to energy scales well beyond our direct reach, probing new physics at *much* higher scales as long as the new physics is assumed to contain sizable sources of CP violation.

Table V-1: Upper limits on EDMs ($|d|$) from different experiments. For the “Nucleus” category, the EDM values are of the ^{199}Hg atom that hosts the nucleus. No *direct* limit yet exists on the proton EDM, though such could be realized through a storage ring experiment, possible at *Project X* and elsewhere; see Sec. V.3. Here we report the best inferred limit in brackets, which is determined by asserting that the ^{199}Hg limit is saturated by d_p exclusively.

Category	Limit ($e\text{ cm}$)	Experiment	Standard Model Value ($e\text{ cm}$)
Electron	1.0×10^{-27} (90% C.L.)	YbF molecules in a beam [10]	10^{-38}
Muon	1.9×10^{-19} (95% C.L.)	Muon storage ring [11]	10^{-35}
Neutron	2.9×10^{-26} (90% C.L.)	Ultracold neutrons in a bottle [12]	10^{-31}
Proton	$[7.9 \times 10^{-25}]$	Inferred from ^{199}Hg [13]	10^{-31}
Nucleus	3.1×10^{-29} (95% C.L.)	^{199}Hg atoms in a vapor cell [13]	10^{-33}

In the next section we explore these ideas in greater detail, describing the experimental observables, the theoretical frameworks to analyze them, and the windows opened on TeV scale physics and beyond. In subsequent sections, we offer a broad overview of the current and planned experiments, showing how the program at *Project X* can both complement and enhance current plans. Finally we turn to a discussion of the broader opportunities the *Project X* concept offers for the study of new sources of CP violation and close with a summary.

V.2 PHYSICS MOTIVATION

V.2.1 Overview

In complex systems, the observation of a violation of a symmetry (or symmetries) of the SM constitutes evidence for physics beyond the Standard Model (BSM). Searches for permanent EDMs are being developed in a variety of systems, including nuclei, atoms, molecules, and solids, and are particularly prominent examples of such tests. Although CP is not a symmetry of the SM, EDM searches are null tests nevertheless, because observing a nonzero EDM at current levels of sensitivity would attest to the existence of physics beyond the electroweak SM. The SM without neutrino masses nominally has two sources of CP violation: through a single phase δ in the Cabibbo-Kobayashi-Maskawa (CKM) matrix, as well as through the T -odd, P -odd product of the gluon field strength tensor and its dual, the latter product being effectively characterized in the full SM by the parameter $\bar{\theta}$. The CKM mechanism of CP violation does give rise to nonzero EDMs; however, the first nontrivial contributions to the quark and charged lepton EDMs come in three- and four-loop order, respectively, so that for the down quark $|d_d| \sim 10^{-34} e\text{ cm}$ [14,15], whereas for the electron $|d_e| \sim 10^{-38} e\text{ cm}$ [16] with massless neutrinos. In the presence of neutrino mixing, the lepton EDMs can become much larger, though they are still orders of magnitude beyond experimental reach [17]. Turning to the neutron EDM, d_n , a plurality of nonperturbative enhancement mechanisms can act. There is a well-known chiral enhancement, under which the neutron EDM is estimated to be $|d_n| \sim 10^{-31}\text{--}10^{-33} e\text{ cm}$ [18–20], making it several orders of magnitude below current experimental sensitivity nonetheless—and likely experimentally inaccessible for decades.

A distinct enhancement arising from the nucleon’s intrinsic flavor structure may also operate [21]. The second mechanism, known as strong CP violation, appears with an operator of mass dimension four; consequently, it is unsuppressed by any mass scale and need not be small, though it is bounded experimentally to be $\bar{\theta} < 10^{-10}$ [13], assuming no other sources of CP violation are present. The lack of an established explanation for the small size of $\bar{\theta}$ is known as the “strong CP problem.” Possible explanations must be compatible, too, with $\delta \sim O(1)$, which experimental measurements of CP -violating observables in B -meson decays demand [22–24]. The manner of its resolution can also impact the possible numerical size of non-CKM sources of CP violation, see Ref. [25] for a discussion. If the Peccei-Quinn mechanism operates, so that there is indeed a new continuous symmetry [26] which is spontaneously and mechanically broken at low energies, then we could win on two counts. There would be a new particle, the *axion* [27,28], which we may yet discover [29,30], and non-CKM sources of CP violation could also be of $O(1)$ in size. This particular resolution of the strong CP violation problem would also imply that a nonzero EDM speaks to the existence of physics beyond the SM. In Sec. V.4, we consider how *Project X* capacities for EDM searches could be adapted to a new sort of axion search [30].

The electric dipole moment d and magnetic moment μ of a nonrelativistic particle with spin \mathbf{S} is defined via

$$\mathcal{H} = -d \frac{\mathbf{S}}{S} \cdot \mathbf{E} - \mu \frac{\mathbf{S}}{S} \cdot \mathbf{B}, \quad (\text{V.2.1})$$

noting $\mathbf{d} \equiv d\mathbf{S}/S$ as well as $\boldsymbol{\mu} \equiv \mu\mathbf{S}/S$. This expression in itself suggests an experimental method: a nonzero d is present if the energy splitting of the spin states in a magnetic field is altered upon the reversal of an applied electric field—and this method has been the basis of EDM searches for decades [31]. The $\mathbf{S} \cdot \mathbf{E}$ interaction for a spin 1/2 particle has the following relativistic generalization

$$\mathcal{L} = -d \frac{i}{2} \bar{\Psi} \boldsymbol{\sigma}^{\mu\nu} \gamma_5 \Psi F_{\mu\nu}, \quad (\text{V.2.2})$$

if CPT symmetry is assumed. Such a dimension-five operator can be generated in a variety of well-motivated extensions of the SM, giving rise to EDMs substantially in excess of the predictions of the CKM model [25,32]. We suppose that the SM is the low-energy limit of a more fundamental theory in which new particles appear at some energy scale Λ . At energies below that scale, the new degrees of freedom no longer appear, but their presence can still be felt through the appearance of effective operators of dimension D , with $D > 4$, which augment the SM. The new effective operators, constructed from SM fields, are suppressed by a factor of Λ^{D-4} , and, moreover, respect the $SU(3)_C \times SU(2)_L \times U(1)$ gauge symmetry of the SM. Upon imposing $SU(2)_L \times U(1)$ gauge invariance this chirality-changing, dimension-five operator becomes of dimension-six in numerical effect. Under naive dimensional analysis, the EDM of a fermion with mass m_f can be estimated as $d_f \sim e \sin \phi_{CP} m_f / \Lambda^2$, where ϕ_{CP} is a CP -violating phase [33]. To give a sense of the sensitivity of the existing experiments, we note that the currently best measured limit of the neutron EDM is $|d_n| < 2.9 \times 10^{-26}$ e-cm [12], whereas that of the electron is $|d_e| < 1.05 \times 10^{-27}$ e-cm [10]—we report both limits at 90% CL. If $\sin \phi_{CP} \sim 1$, as $\sin \delta$ is in the CKM mechanism, then the current experimental limits on the electron and neutron imply that $\log_{10}[\Lambda(\text{GeV})] \sim 5$, where we employ a light quark mass $m_f = m_q \sim 10 \text{ MeV}$ in the neutron case. Including a loop suppression factor of $\alpha/4\pi \sim 10^{-3}$, we estimate, crudely, that energy scales of some 3 TeV are probed by current experiments, with the next generation of EDM experiments, anticipating a factor of 100 in increased sensitivity, improving the energy reach by a factor of 10.

We have considered the new-physics reach of an EDM measurement in simple systems, but the greatest experimental sensitivities can be found in complex systems, most notably in atoms, molecules, and solids (crystals). The connection between the empirical EDM limits in such systems and new sources of CP violation at the TeV scale is made indirectly, through multiple theoretical frameworks, each with its own range of validity tied to a particular energy scale. Tracking the manner in which TeV-scale sources of CP violation emerge in the low-energy theoretical frameworks appropriate to the descriptions of nuclei, atoms, and molecules is a richly complex task; we illustrate it, schematically and incompletely, in Fig. V-1 and refer to Ref. [32] for a recent review. In the following discussion, we start at the energy scales of the systems in question and evolve upward, ending with a discussion of the models which evince new TeV-scale sources of CP violation.

V.2.2 EDMs of Atoms and Molecules

Atoms and molecules differ from fundamental particles such as electrons, muons, and taus, as well as from neutrons, protons, deuterons, and indeed nuclei, in that their composite nature guarantees that their EDMs vanish in the point-like, nonrelativistic limit even if their constituents have nonzero EDMs—this is the so-called Schiff theorem [35]. This effect suppresses the visibility of an EDM in an experimental measurement, but enhancements also arise because the cancellation can be strongly violated by relativistic and finite-size effects. The former effect can give such an atomic experiment sensitivity to d_e , whereas the latter effect can give rise to a nonzero atomic EDM through P -odd, T -odd nuclear moments, of which the “Schiff moment” is typically the driving contribution. If the electrons have nonzero total spin, then a magnetic quadrupole moment (MQM) can also contribute [34]. The precise role of the mechanisms in realizing a nonzero EDM depends on the nature

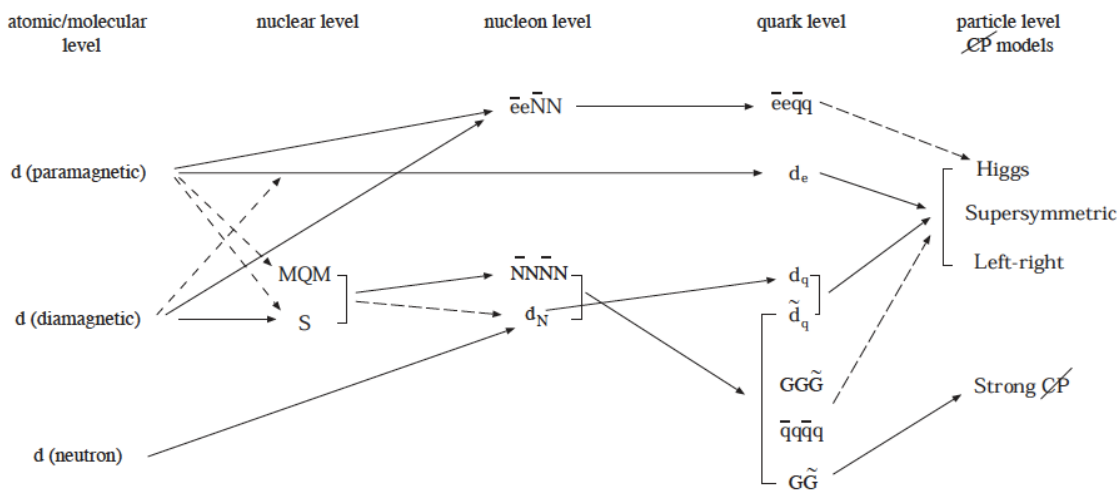


Figure V-1: A flow chart for the analysis of EDMs, connecting new sources of CP violation at the TeV scale through the parameters of effective Lagrangians at ever lower energy scales to give rise finally to nonzero lepton, nucleon, nuclear, atomic, molecular, and solid-state EDMs. Empirical limits on EDMs in various systems in turn constrain different CP -violating sources, as indicated by arrows; dashed, as opposed to solid, lines note the existence of weaker constraints. From Ref. [34].

of the particular atom in question. Atoms are broadly classified as either paramagnetic or diamagnetic. In paramagnetic atoms, the atomic electrons have an unpaired spin, and in this case relativistic effects are most important, making EDMs in paramagnetic atoms or molecules sensitive to d_e , strikingly so in heavy atoms with atomic number Z , scaling as $Z^3\alpha^2$ [36,37]. This enhancement can be interpreted in terms of an enhanced, “effective” electric field. Polar diatomic molecules, such as TlF or YbF, can evince even larger enhancements of the effective electric field [34,38]. Paramagnetic systems are also sensitive to P -odd, T -odd electron-nucleon interactions. In contrast, diamagnetic atoms have only paired electronic spins, so that the EDMs of these systems are particularly sensitive to the tensor P -odd, T -odd electron-nucleon interactions, which can act to unpair electrons in a closed shell. However, once hyperfine effects are included, other P -odd, T -odd electron-nucleon interactions, as well as d_e , can also contribute to the EDM [34,39]. As we have noted, atomic EDMs can also be induced by P -odd, T -odd nuclear moments, whose effects operate in both diamagnetic and paramagnetic atoms, though the effects are much less difficult to probe in diamagnetic systems. Moreover, nuclear deformation and atomic state mixing can give rise to marked enhancements. For example, in a heavy diamagnetic atom of a rare isotope, for which the nucleus has octupole strength [40,41] or a permanent octupole deformation [42–44], the T -odd, P -odd charge distribution in the nucleus, characterized by the Schiff moment, is predicted to be significantly enhanced relative to ^{199}Hg . We refer to Refs. [32,34,45] for detailed treatments of all these issues.

V.2.3 Rare Atom EDMs

In what follows we focus on the systems of immediate relevance to experiments at the first stage of *Project X*: atoms with rare nuclear isotopes, for which their EDMs can be markedly enhanced, and neutrons. In connecting experimental limits on atomic EDMs to fundamental sources of CP violation, multiple layers of theoretical analysis are required, as we have noted. Specifically, it is the task of atomic theory to compute an atomic EDM in terms of nuclear inputs, such as the P -odd, T -odd nuclear moments, and it is the task of nuclear theory to compute these nuclear moments in terms of the nucleon EDMs and P -odd, T -odd nucleon-nucleon interactions. We postpone, for the moment, discussion of the connection of these hadronic inputs to quantities realized in terms of quark and gluon degrees of freedom—and return to them in the next section, in which we discuss the neutron EDM as well. To illustrate the connections explicitly, yet concisely, we consider a CP -odd, effective Lagrangian in hadron degrees of freedom, at the nuclear scale, which can generate both the Schiff moments and the germane P -odd, T -odd electron-nucleon interactions. Namely [25],

$$\mathcal{L}_{\text{eff}}^{\text{nuclear}} = \mathcal{L}_{e\text{-edm}} + \mathcal{L}_{eN} + \mathcal{L}_{\pi NN}, \quad (\text{V.2.3})$$

where $\mathcal{L}_{e\text{-edm}} = -i(d_e/2)\bar{e}(F\sigma)\gamma_5 e$,

$$\begin{aligned} \mathcal{L}_{eN} = & C_S^{(0)} \bar{e}i\gamma_5 e \bar{N}N + C_P^{(0)} \bar{e}e \bar{N}i\gamma_5 N + C_T^{(0)} \epsilon_{\mu\nu\alpha\beta} \bar{e}\sigma^{\mu\nu} e \bar{N}\sigma^{\alpha\beta} N \\ & + C_S^{(1)} \bar{e}i\gamma_5 e \bar{N}\tau^3 N + C_P^{(1)} \bar{e}e \bar{N}i\gamma_5 \tau^3 N + C_T^{(1)} \epsilon_{\mu\nu\alpha\beta} \bar{e}\sigma^{\mu\nu} e \bar{N}\sigma^{\alpha\beta} \tau^3 N, \end{aligned} \quad (\text{V.2.4})$$

and

$$\begin{aligned} \mathcal{L}_{\pi NN} = & -(i/2)\bar{N}(F\sigma)(d^{(0)} + d^{(1)}\tau^3)\gamma_5 N + \bar{g}_{\pi NN}^{(0)} \bar{N}\tau^a N \pi^a + \bar{g}_{\pi NN}^{(1)} \bar{N}N \pi^0 \\ & + \bar{g}_{\pi NN}^{(2)} (\bar{N}\tau^a N \pi^a - 3\bar{N}\tau^3 N \pi^0) + \dots, \end{aligned} \quad (\text{V.2.5})$$

noting that the superscripts indicate interactions of isoscalar (0), isovector (1), or isotensor (2) character and that $d^{(0)} + d^{(1)}$ and $d^{(0)} - d^{(1)}$ contribute to d_p and d_n , respectively. In recent years the construction of $\mathcal{L}_{\pi NN}$ has been revisited within the context of heavy-baryon chiral perturbation theory (HBChPT), a low-energy, effective field theory in which the nucleons are nonrelativistic and a momentum expansion effected in the context of interactions which respect the chiral symmetry of QCD serves as an organizing principle, where we refer to Ref. [46] for a review. The result of this analysis [47–49] yields terms which map to those articulated in Eq. (V.2.5), as well as explicit T -odd and P -odd contact interactions which capture the most important of the short-range NN interactions [32]. Employing Eq. (V.2.5), we note that the EDM of thallium atom, which is paramagnetic, is given by [25]

$$d_{205\text{Tl}} = -585d_e - e(43\text{GeV}) \times (C_S^{(0)} - 0.2C_S^{(1)}), \quad (\text{V.2.6})$$

though we caution the reader that the ultimate relative role of the terms is sensitive to the precise BSM model. The experimental limit of $|d_{205\text{Tl}}| \leq 9.4 \times 10^{-25} e\text{cm}$ at 90% C.L., which is currently the most stringent limit in any paramagnetic atom, yields $|d_e| \leq 1.6 \times 10^{-27} e\text{cm}$ at 90% C.L. [50] if one assumes the atomic EDM is saturated by d_e . Table V-1 reveals that the recent EDM limit from YbF [10] is somewhat stronger, but the possibility that the study of ^{211}Fr at *Project X*, which we discuss in Sec.V.3.1.3, could yield an improved sensitivity of $\sim 10^3$ to d_e tantalizes.

For diamagnetic atoms, such as ^{129}Xe , ^{199}Hg , ^{223}Rn , or ^{225}Ra , there are two main contributions to the atomic EDM, as we have mentioned—a tensor electron-nucleon interaction [51], controlled by $C_T^{(0)}$, and the P -odd and T -odd nuclear moments, of which the Schiff moment \mathcal{S} appears in leading order in an expansion about the point-like limit. Indeed, it is the only T -odd, P -odd nuclear moment which generates an EDM in the current context. Typically we can characterize the EDM of a diamagnetic atom, d_{dia} , in the following parametric way:

$$d_{\text{dia}} = d_{\text{dia}}(\mathcal{S}[\bar{g}_{\pi NN}^{(i)}, d^{(i)}], C_S^{(i)}, C_P^{(i)}, C_T^{(i)}, d_e). \quad (\text{V.2.7})$$

The Schiff moment \mathcal{S} tends to play a driving role, and this can be understood in the following way. The contribution of \mathcal{S} to the T -odd, P -odd nuclear electrostatic potential generates, in essence, an effective electric field in the nucleus that has a permanent projection along \mathbf{I} , the total nuclear angular momentum, and which is naturally T -odd and P -odd. This effective electric field polarizes the atomic electrons and thus gives rise to an atomic EDM [34]. For an effective pion-mediated nucleon-nucleon interaction, the contributions to the Schiff moment can be decomposed into isospin components given by [52]

$$\mathcal{S} = g(a_0\bar{g}_{\pi NN}^{(0)} + a_1\bar{g}_{\pi NN}^{(1)} + a_2\bar{g}_{\pi NN}^{(2)}), \quad (\text{V.2.8})$$

where g is the usual, CP -conserving πNN coupling constant, $g \equiv 13.5$, and the P -odd, T -odd physics is contained in $\bar{g}_{\pi NN}^{(0,1,2)}$, which are dimensionless. We note that the latter contribute to $d_{n,p}$ as well. In general the a_i , in units of $e\text{fm}^3$, represent the polarization of the nuclear charge distribution by a specific isospin component of the P -odd, T -odd interaction and can reflect intricate cancellations. The Schiff moment in ^{199}Hg has been computed by different groups [34,53], employing Skyrme effective interactions and, most recently, fully self-consistent mean field (Hartree-Fock-Bogoliubov) computations with core-polarization effects included in a unified way [53]. A dispersion of the results with different Skyrme interactions is reflective of the theoretical systematic error [54]. Beyond this, some dispersion in the collected results exists [34,53]. It is crucial to note, however, that

large collective enhancements of the Schiff moment, relative to the single-particle contributions, can occur under special conditions. For nuclei with strong octupole collectivity, the Schiff moment may be significantly enhanced relative to ^{199}Hg due to the large intrinsic dipole moment and, for permanently deformed nuclei, the closely spaced, opposite parity levels that arise. In this picture, the enhanced Schiff moment for deformed systems can be written [43]

$$S \approx 0.05e \frac{\beta_2 \beta_3^2 Z A^{2/3} r_0^3 \eta}{E_+ - E_-}, \quad (\text{V.2.9})$$

where E_+ and E_- are the energies of opposite parity states and η is the matrix element of the effective T -odd and P -odd interaction between nucleons. In the presence of rigid octupole deformation, the computation of this latter quantity is expected to be more robust [32]. Here β_2 and β_3 are the quadrupole and octupole deformation parameters—and are experimentally accessible as we shall detail.

V.2.3.1 Octupole Deformation and Schiff Moment Enhancements

Experimental programs in two important octupole-enhanced systems, ^{225}Ra and $^{221/223}\text{Rn}$ are underway, and the experimental details are presented in section V.3. For ^{225}Ra , with a half-life of 14.9 days, a great deal has been studied regarding its nuclear structure, including the 55 keV spacing of the ground $1/2^+$ state and the lowest $1/2^-$ state of the negative parity band, suggesting that ^{225}Ra is octupole deformed [55]. Calculations including work by Engel and collaborators, who estimate the $a_{0,1,2}$, confirm that these quantities are indeed enhanced [52]. Experimental studies also indicate that ^{226}Ra is octupole deformed [56]. Recently the first direct evidence of octupole deformation with a determination of β_3 in ^{224}Ra has been established through measurements of Coulomb excitation of 2.85 MeV/a.m.u. rare-isotope beams at REX-ISOLDE (CERN) [57], strengthening the confidence in the size of the Schiff moment. Though a precise estimate of the enhancement relative to ^{199}Hg or ^{129}Xe is hampered by the difficulty of accurately calculating the a_i , particularly for ^{199}Hg [53,54], as a rough estimate we take $a_0 = 0.01$ for ^{199}Hg and $a_0 = 5$ for ^{225}Ra indicating an enhancement of 500 for the isoscalar contributions. Similar enhancements are expected for a_1 and a_2 . In work at REX-ISOLDE [57], octupole collectivity was also determined for ^{220}Rn indicating a similar β_3 compared to ^{224}Ra , but as evidence of octupole vibrations and not of permanent octupole deformation. In this case, the formula of Eq. (V.2.9) would not apply; nevertheless, enhancements of the Schiff moment may occur [40,41]. Though the spins and parities for ^{221}Rn have not been determined for any states, three new gamma-ray lines between 200 keV and 300 keV excitation were identified in a subsequent experiment at REX-ISOLDE. Further measurements are necessary to determine the nature of ^{223}Rn .

Although the EDMs of atomic systems, notably ^{199}Hg [13], can be measured with much higher precision than that of the neutron, these results currently probe the underlying physics at a level crudely commensurate to that of the neutron EDM limit, to the extent that they are comparable. This is simply a concrete consequence of the Schiff theorem in ^{199}Hg and need not hold generally. Indeed, one can be optimistic in regards to the prospects for EDM studies in ^{225}Ra and other deformed systems. A measurement of the EDM in ^{225}Ra of much less sensitivity than that of ^{199}Hg can probe the underlying physics to a comparable level, with improvements to the sensitivity of the current ^{199}Hg limit yielding new-physics sensitivity well beyond that.

V.2.4 EDMs of Light Nuclei

Advances in storage ring technology make sensitive EDM experiments of electrically charged particles possible. The possible candidate systems include not only the proton and the muon, but also light nuclei, such as the deuteron and ^3He . At *Project X* the first two possibilities are more readily realizable, though there are plans afoot to realize the latter elsewhere. We refer to Sec. V.3.3 for a description of the basic empirical concepts as well as an overview of the possibilities.

The study of light nuclei appeal because the combination of chiral and isospin symmetry serve as powerful tools in distinguishing the various possible CP -violating interactions which appear in Eq. (V.2.5). It has been known for some time that the deuteron EDM is a particularly sensitive discriminant of its CP -violating source, notably $g_{\pi NN}^{(1)}$ [58], where we refer to Ref. [32] for a review. Recently the deuteron EDM has been revisited [59,60], affirming the earlier arguments. In HBChPT, the EDMs of the proton, neutron, and light nuclei can be analyzed within a single framework. Consequently, exploiting the distinct way the various CP -violating sources appear in leading-order HBChPT, it has been shown that a systematic program of EDM measurements in these systems could potentially disentangle their CP -violating sources [60,61]. A proton storage ring EDM experiment would be a significant step along this path.

We discuss the physics implications of a muon EDM experiment of improved sensitivity at the close of Sec. V.2.6.

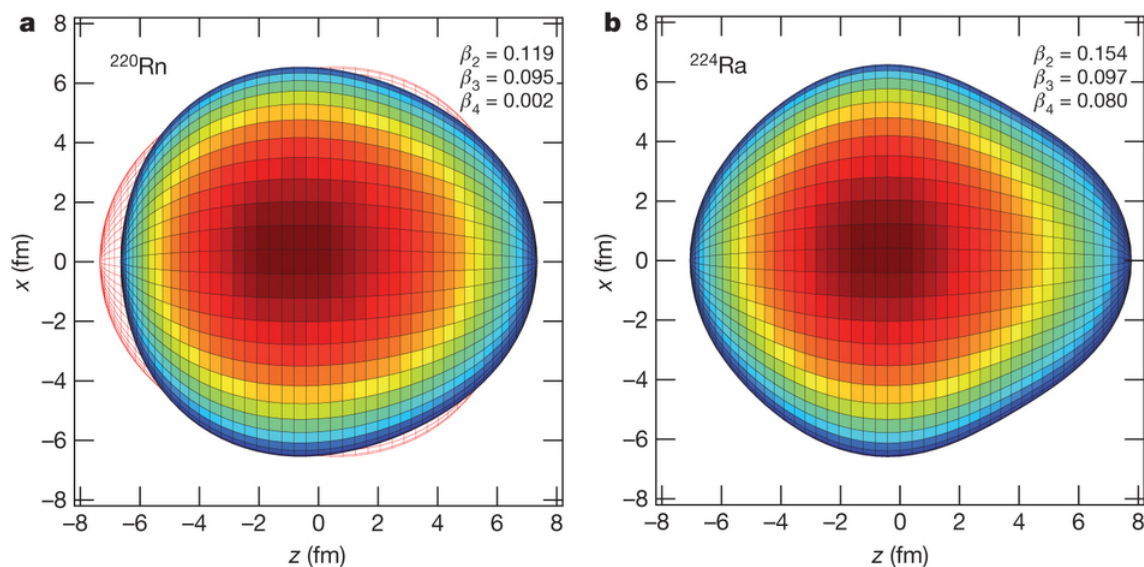


Figure V-2: Representation of the shapes of ^{220}Rn and ^{224}Ra . The left panel depicts vibrational motion between two surfaces, the second indicated by the red hatched line. The right panel denotes static deformation in the intrinsic frame. The color scale, from blue to red, represents the y -values of the surface. From Ref. [57], to which we refer for all details.

V.2.5 CP -Violating Sources at ~ 1 GeV

In this section we consider the connection between the low-energy constants of $\mathcal{L}_{\pi NN}$, detailed in Eq. (V.2.5), to underlying quark and gluon degrees of freedom, where we wish to consider low-energy sources of CP violation beyond the SM. Thinking broadly and systematically we organize the expected contributions in terms of the mass dimension of the possible CP -violating operators appearing in an effective field theory with a cutoff of ~ 1 GeV [25]:

$$\begin{aligned} \mathcal{L}_\Lambda = & \frac{\alpha_s \bar{\theta}}{8\pi} \varepsilon^{\alpha\beta\mu\nu} F_{\alpha\beta}^a F_{\mu\nu}^a - \frac{i}{2} \sum_i d_i \bar{\psi}_i F_{\mu\nu} \sigma^{\mu\nu} \gamma_5 \psi_i - \frac{i}{2} \sum_{i \in u,d,s} \tilde{d}_i \bar{\psi}_i F_{\mu\nu}^a t^a \sigma^{\mu\nu} \gamma_5 \psi_i \\ & + \frac{1}{3} w f^{abc} F_{\mu\nu}^a \varepsilon^{\nu\rho\delta} F_{\rho\delta}^b F_{\beta}^{\mu,c} + \sum_{i,j} C_{ij} (\bar{\psi}_i \psi_i) (\bar{\psi}_j i \gamma_5 \psi_j) + \dots \end{aligned} \quad (\text{V.2.10})$$

with $i, j \in u, d, s, e, \mu$ unless otherwise noted—all heavier degrees of freedom have been integrated out. The leading term is the dimension-four strong CP term, proportional to the parameter $\bar{\theta}$. Even in the presence of axion dynamics, a higher dimension operator could *induce* a nonzero value of $\bar{\theta}$ [25,62]; thus we retain it explicitly. The balance of the terms are the nominally dimension-five fermion EDMs d_i and quark chromo-EDMs (CEDM) \tilde{d}_i , though they are effectively of dimension 6 once $SU(2)_L \times U(1)$ symmetry is imposed. Moreover there are the dimension-six Weinberg three-gluon operator, w , and CP violating 4 fermion operators, C_{ij} . This list is not exhaustive even within the restricted operator dimensions we have considered. To see this we consider the leading dimension set of operators in SM fields under $SU(2)_L \times U(1)$ gauge invariance at the electroweak scale, prior to electroweak symmetry breaking. Turning to Ref. [63], one finds that there are in total 19 dimension-six operators in terms of gauge, Higgs, and fermion degrees of freedom which can contribute to an EDM.¹ After electroweak symmetry breaking, certain of the terms becomes those enumerated in Eq. (V.2.10); the balance are largely four-fermion operators which functionally become contributions of dimension 8 under $SU(2)_L \times U(1)$ gauge invariance. We refer to Ref. [32] for an exhaustive analysis. Various extensions of the SM can generate the low-energy constants which appear, so that, in turn, EDM limits thereby constrain the new sources of CP violation which appear in such models. In connecting the Wilson coefficients of these operators and hence models of new physics to the low-energy constants of $\mathcal{L}_{\pi NN}$, Eq. (V.2.5), requires the computation of nonperturbative hadron matrix elements. Parametrically, we have [25]

$$\begin{aligned} d_n &= d_n(\bar{\theta}, d_i, \tilde{d}_i, w, C_{ij}) \\ \bar{g}_{\pi NN}^{(i)} &= \bar{g}_{\pi NN}^{(i)}(\bar{\theta}, d_i, \tilde{d}_i, w, C_{ij}). \end{aligned} \quad (\text{V.2.11})$$

Several computational aspects must be considered in connecting a model of new physics at the TeV scale to the low-energy constants of Eq. (V.2.10). After matching to an effective theory in SM degrees of freedom, there are QCD evolution and operator mixing effects, as well as flavor thresholds, involved in realizing the Wilson coefficients at a scale of ~ 1 GeV. Beyond this, the hadronic matrix elements must be computed. We refer the reader to a detailed review of all these issues, including recent technical developments in this area [32]. Typically QCD sum rule methods, or a $SU(6)$ quark model, have been employed in the computation of the matrix elements [25].

¹In Ref. [63], certain operators are of the same form for $f \in u, d, e$, making our tally consistent with Ref. [32].

For the neutron, we note Ref. [64] for a comparative review of different methods. Lattice gauge theory can also be used to compute the needed proton and neutron matrix elements, and the current status and prospects for lattice-QCD calculations are presented in Sec. X.3.4.1. So far lattice-QCD methods have only been used to compute the matrix element associated with $\bar{\theta}$, but calculations of the dimension-six operators needed to make predictions for BSM theories are also underway.

To give a concrete yet simple example, for the neutron we note the estimate [25]

$$d_n^{\text{est}} = \frac{8\pi^2 |\langle \bar{q}q \rangle|}{M_n^3} \left[\frac{2\chi m_*}{3} e(\bar{\theta} - \theta_{\text{ind}}) + \frac{1}{3}(4d_d - d_u) + \frac{\chi m_0^2}{6}(4e_d \tilde{d}_d - e_u \tilde{d}_u) \right], \quad (\text{V.2.12})$$

where terms which are naively of dimension 6 and higher have been neglected and θ_{ind} is given in terms of \tilde{d}_q [25,62]. The study of the EDM of ^{225}Ra , in contrast, brings in sensitivity to $\bar{g}_{\pi NN}^{(1)}$ and thus to the combination $\tilde{d}_u - \tilde{d}_d$. We refer to Ref. [25] for all details. We note in passing that d_n and d_p have also been analyzed in chiral perturbation theory employing the sources of Eq. (V.2.5), where we refer to Ref. [32] for a review, as well as in light-cone QCD [65].

The electron-nucleon couplings, $C_{S,P,T}^{(i)}$, also play a role in atomic EDMs; they receive contributions from semileptonic, four-fermion couplings C_{qe} . The hadronic matrix element which connects these quantities can be computed using low-energy theorems for the matrix element of quark bilinears in the nucleon [25].

V.2.6 EDMs and New, TeV-Scale Sources of *CP* Violation

A variety of well-motivated extensions of the SM can generate EDMs substantially in excess of the predictions of the CKM model [25,32]. This includes models with an extended Higgs sector, with manifest left-right symmetry at sufficiently high energy scales, with extra spacetime dimensions, and with weak-scale supersymmetry, that can generate EDMs through dimension-five operators, though, as we have noted, they are of dimension-six in numerical effect. Models with weak-scale supersymmetry are particularly appealing in that they can potentially resolve a variety of theoretical problems at once, yielding a cosmic baryon asymmetry through an electroweak phase transition more efficiently than in the SM [66,67], as well as providing a dark-matter candidate [68,69]. These models have and have had significant implications for flavor physics. Furthermore, limits from the nonobservation of EDMs and, more generally, of new interactions, constrain the appearance of new degrees of freedom [9,70]. In the LHC era, it has been possible to search for the predicted new degrees of freedom directly, and all searches have yielded null results thus far—though the campaign is far from over. As we have noted, EDMs retain their interest even if no new physics signals are observed at the LHC since, modulo theoretical uncertainties and assumptions, a discovery would reveal the energy scale of new physics beyond LHC reach.

The discovery of a Higgs-like boson at the LHC [72,73] is a milestone in our understanding of the mechanism of electroweak symmetry breaking, and provides a consistent mathematical formulation of the SM of particle physics. Given the absence of any direct signals of new physics at the LHC, as yet, attention is being focused on the study of the properties of the Higgs-like boson. At current sensitivities, the accessible production modes and decay rates are overall in reasonable agreement with the predictions of the SM Higgs. In particular, there is strong experimental evidence that the newly discovered particle decays with an appreciable branching fraction to ZZ^* , in spite of

the very strong phase space suppression. Hence, that indicates that the particle couples to the Z gauge boson at tree level as expected. Previous hints of an enhanced $h \rightarrow \gamma\gamma$ rate persist in the ATLAS data [74], but are not confirmed by the latest CMS analysis [75]. Detailed studies of the decays of the newly discovered particle into 4 leptons show kinematic distributions consistent with a spin zero particle. An assignment of spin 2 cannot be conclusively excluded but would demand a tuning of the tensor couplings to fit current data. Moreover, first studies of the CP properties of the Higgs-like boson in the $h \rightarrow ZZ$ channel strongly favor the scalar over the pseudoscalar hypothesis [76,77], as predicted by the SM.

It is of great importance to use all possible experimental handles to test possible departures from SM properties of the newly discovered particle. Observing evidence of departures would conclusively show that, even if the new Higgs-like particle is the one responsible for electroweak symmetry breaking, the SM is an effective theory that requires extensions. EDM experiments give complementary indirect information on the CP properties of the Higgs-like boson. In particular, the current experimental limits put strong constraints on possible CP violation in the $h \rightarrow \gamma\gamma$ and also the $h \rightarrow Z\gamma$ decays assuming that the couplings of the Higgs-like boson to light fermions are SM-like [71,78,79]. EDM limits imply—barring accidental cancellations—that possible new physics which modifies the $h \rightarrow \gamma\gamma$ and $h \rightarrow Z\gamma$ rates has to be approximately CP conserving. Simple extensions of the SM, which can modify the diphoton rate, are models with extra vector-like fermions. Such models contain a physical CP violating phase that can induce fermion EDMs at the two-loop level, through Barr-Zee diagrams. In regions of parameter space that lead to visible new physics effects in $h \rightarrow \gamma\gamma$, this phase is constrained to be below $\lesssim 0.1$ (see Fig. V-3). Moreover, EDMs give also the opportunity to obtain indirect information on the couplings of the Higgs-like boson to

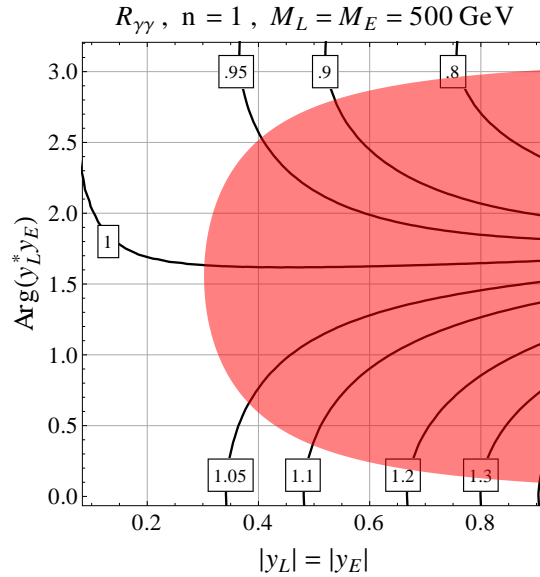


Figure V-3: Electron EDM and $h \rightarrow \gamma\gamma$ rate in a model with exotic vector-like leptons of charge 2. Possible modifications of the $h \rightarrow \gamma\gamma$ rate are shown in the plane of the Yukawa couplings of the exotic leptons versus the relevant CP -violating phase. Note that curves of fixed $R_{\gamma\gamma}$, defined as the modified $h \rightarrow \gamma\gamma$ rate in units of the SM $h \rightarrow \gamma\gamma$ rate, are shown as solid black lines. The red region is excluded by the experimental limit on the electron EDM. From Ref. [71].

the first generation of SM fermions, which are not directly experimentally accessible. For example, current EDM limits already constrain possible imaginary parts in the couplings to electrons, up quarks, and down quarks to be at most one order of magnitude below the corresponding SM Yukawa couplings.

Despite the absence of direct evidence for supersymmetric particles at the LHC, models of supersymmetry (SUSY) remain among the most well-motivated and popular extensions of the Standard Model. Besides direct searches, there exist various ways to probe SUSY models indirectly with low energy observables. The minimal supersymmetric extension of the Standard Model (MSSM) generically contains numerous new sources of CP violation. Parameterizing the soft SUSY breaking terms in the most general way, one finds $O(50)$ new CP violating phases in the MSSM. Most of them are connected to new sources of flavor violation, but even in the limit of completely flavor-blind soft SUSY breaking terms, one is still left with 6 physical CP phases that can be probed with EDMs. We discuss first the flavor blind case and come back to “flavored EDMs” at the end of the section.

In the flavor blind case, the relevant CP phases are the invariants $\arg(M_i \mu B_\mu^*)$ and $\arg(A_f \mu B_\mu^*)$, where μ is the Higgsino mass, B_μ is the soft Higgs mixing parameter, $M_{1,2,3}$ are the bino, wino, and gluino masses, and $A_{u,d,\ell}$ are universal trilinear couplings of the up-type squarks, down-type squarks, and sleptons, respectively. These phases can induce contributions to all the operators in Eq. (V.2.10) [25,80,81]. In the following, we assume that a Peccei-Quinn symmetry takes care of the $\bar{\theta}$ term which appears in dimension-four, so that we need not consider that operator further. However, a nonzero $\bar{\theta}$ term can be induced through the appearance of an appropriate higher-dimension operator; though we will not consider this possibility further as we have no explicit axion dynamics [25,62]. Generically, the largest SUSY effect comes from fermion EDMs, d_i , and CEDMs \tilde{d}_i , that can be induced at the one-loop level by sfermion-gaugino and sfermion-higgsino loops. A generic Feynman diagram is shown in Fig. V-4. In the illustrative case of a degenerate SUSY spectrum at the scale M_{SUSY} , and only two CP phases θ_μ (the phase of the higgsino mass), and θ_A (the universal phase of the trilinear couplings) one finds [25]

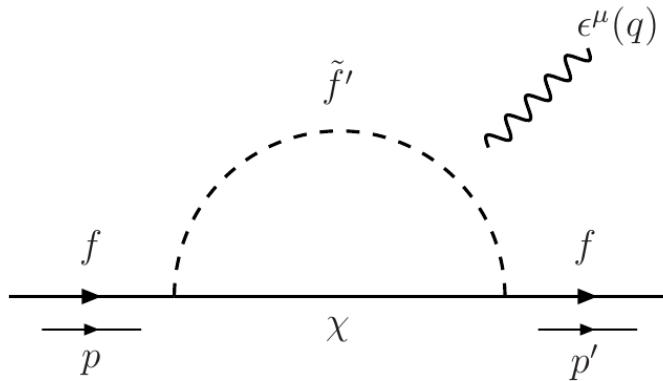


Figure V-4: Generic one-loop SUSY diagram giving rise to a fermion EDM or CEDM. From Ref. [80].

$$\frac{d_e}{e\kappa_e} \simeq \frac{g_1^2}{12} \sin\theta_A + \left(\frac{5g_2^2}{24} + \frac{g_1^2}{24} \right) \sin\theta_\mu \tan\beta, \quad (\text{V.2.13})$$

$$\frac{d_q}{e_q\kappa_q} \simeq \frac{2g_3^2}{9} \left(\sin\theta_\mu R_q - \sin\theta_A \right), \quad (\text{V.2.14})$$

$$\frac{\tilde{d}_q}{\kappa_q} \simeq \frac{5g_3^2}{18} \left(\sin\theta_\mu R_q - \sin\theta_A \right), \quad (\text{V.2.15})$$

where $R_q = \tan\beta$ for down quarks, and $R_q = \cot\beta$ for up quarks, and

$$e\kappa_i \simeq \frac{m_i}{1 \text{ MeV}} \left(\frac{1 \text{ TeV}}{M_{\text{SUSY}}} \right)^2 \times 1.3 \times 10^{-25} e \text{ cm}. \quad (\text{V.2.16})$$

If the SUSY CP phases are assumed to be generically of $O(1)$, the masses of first generation scalar fermions have to be at least several TeV to avoid the constraints from the current EDM limits. If the first two generations of sfermions have mass far above the TeV scale and, hence are decoupled, as, e.g., in the "more minimal supersymmetric Standard Model" scenario [82], two-loop contributions to the fermion (C)EDMs can become very important. In particular, two-loop Barr-Zee type diagrams [83] can access the light third generation of sfermions (see the left diagram in Fig. V-5) and can typically lead to strong constraints on the CP phases. Only in scenarios where the only sizable phase comes from the bino mass M_1 , the constraints are still rather weak as shown in Fig. V-6. In such frameworks, electroweak baryogenesis remains possible in the MSSM, but demands very large splitting between the two top scalar partners, and that the lightest supersymmetric particle be a neutralino with mass close to half of the Higgs mass value to avoid LHC constraints on the production and decay rates of the 125 GeV Higgs-like boson [84,85]. An explanation of the matter-antimatter asymmetry (BAU) in this framework leads to lower bounds on EDMs that are only about 2 orders of magnitude below the current experimental limits [86–88]. The sensitivities that can be achieved with *Project X* will allow one to probe essentially the entire parameter range of that framework. Even if all SUSY scalars are completely decoupled, as in models of split SUSY [89–91], two-loop Barr-Zee type diagrams that contain gauginos and Higgsinos (see the right diagram in Fig. V-5) can lead to effects in EDMs that will be accessible with improved experimental sensitivity [92].

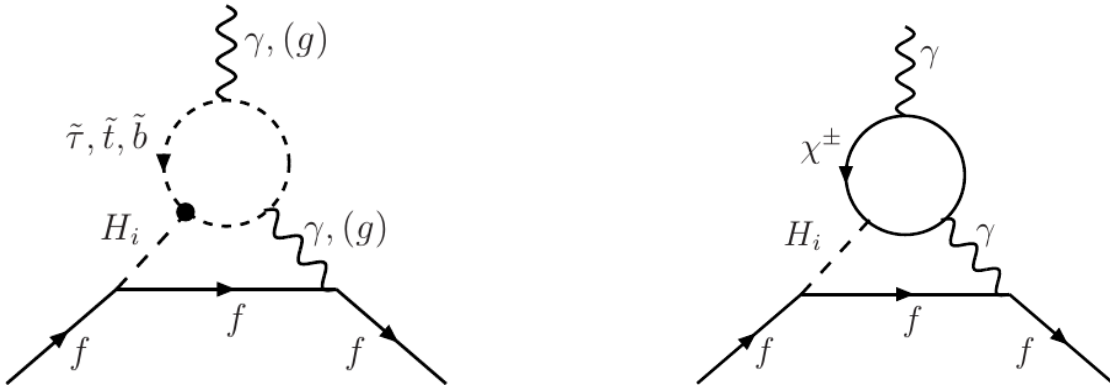


Figure V-5: Example two-loop Barr-Zee diagrams giving rise to a fermion EDM or CEDM. From Ref. [80].

In SUSY scenarios with large $\tan\beta$, very important contributions to EDMs can also come from CP -violating 4 fermion operators [93,94]. The coefficients C_{ij} can be generated at the one-loop level by neutral Higgs boson mixing and by complex Yukawa threshold corrections and scale with the third power of $\tan\beta$. It is important to note that these contributions do not decouple with the scale of the SUSY particles, but with the mass of the heavy Higgs bosons. Finally, the Weinberg three-gluon operator w receives contributions at the two-loop level by squark gluino loops, and at the three-loop level by diagrams involving the Higgs bosons. For a TeV-scale SUSY spectrum, the induced effects on EDMs are typically small.

Going beyond the MSSM, EDMs remain highly sensitive to additional sources of CP violation. In particular, SUSY models with extended Higgs sectors, like the next-to-minimal supersymmetric standard model (NMSSM) [95] or the effective beyond the MSSM (BMSSM) setup [96], can contain CP phases in the Higgs sector already at tree level. Existing and expected limits on EDMs lead to strong constraints on such phases [97–99]. Nonetheless, electroweak baryogenesis can be made compatible with EDM constraints in such models [97,100–108], and at the same time a light dark matter candidate can be viable [109].

EDMs are highly sensitive probes of additional sources of CP violation beyond those present already in the SM. On the other hand, new CP violating phases could in principle also modify the SM predictions for CP violation in meson mixing or in rare B -meson decays. Given the strong constraints from flavor observables on possible new sources of flavor violation at the TeV scale [9], an often adopted assumption is the principle of minimal flavor violation (MFV) [110], which states that the SM Yukawa couplings remain the only sources of flavor violation even in extensions of the SM. It is important to stress, that MFV does not forbid the existence of additional flavor diagonal sources of CP violation [111–113]. While MFV ensures that flavor constraints are generically under control for new physics at the TeV scale, EDM experiments probe flavor diagonal CP phases of $O(1)$, up to tens of TeV, as discussed above. In concrete new physics models, however, both EDMs and CP asymmetries in rare B -meson decays can have comparable sensitivity to new physics at the TeV scale and give complementary information on the model parameters (see [111] for a corresponding study in the MSSM with MFV).

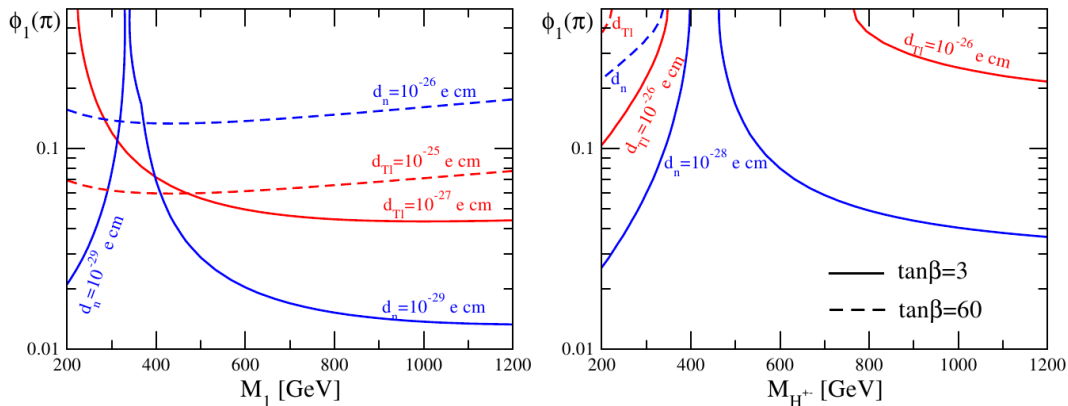


Figure V-6: Curves of constant values for the thallium (red) and neutron (blue) EDM as function of the bino mass M_1 and the charged Higgs mass M_{H^\pm} in the case of heavy first two generations for sfermions. From Ref. [81].

If new physics introduces generic new sources of flavor violation, then flavor constraints push the new physics spectrum far above the TeV scale. Nonetheless, EDMs can provide important constraints in such frameworks. Due to the generic flavor mixing, the EDMs of first generation fermions can become proportional to the masses of the third generation. These large enhancements allow to probe scales of 1000 TeV with EDMs. An explicit example of such a case is given by the mini-split SUSY framework [114–117], where squarks and sleptons in a range from ~ 100 –10,000 TeV allow to accommodate a 125 GeV Higgs mass in an “effortless” way. Current EDM bounds already probe 100 TeV squarks in this framework [118,119]. Future improved sensitivities will allow to probe squarks at 1000 TeV and above.

In the future, if a nonzero EDM is discovered in one particular system, the measurement of EDMs of other types is essential to resolving the underlying mechanisms of CP violation. The neutron and heavy atom EDMs are thought to be most sensitive to different CP -violating sources [34]. In addition, the recently proposed storage ring EDM experiments of the proton and deuteron aim to probe combinations of CP -violating contributions which differ from those in the neutron EDM. In contrast, experiments with paramagnetic atoms or molecules are sensitive to the EDM of the electron and a possible new CP -violating electron-quark interaction.

On a separate tack, a muon EDM of improved sensitivity probes other aspects of new-physics models. Recalling the simple dimensional estimate $d_f \sim e \sin \phi_{CP} m_f / \Lambda^2$, one might think that a muon EDM d_μ would need to be no more than a factor of 100 less stringent than the electron EDM to probe interesting new physics. This is not the case; several authors have discussed the size of d_μ within supersymmetric scenarios [120,121], finding that d_μ could be as large as $d_\mu \sim 10^{-22} e\text{cm}$, which is easily within the reach of planned, future dedicated initiatives. Such a large EDM could speak to the structure of flavor breaking at the Planck scale [121].

V.3 EXPERIMENTS

The high-energy, high-intensity, high-power proton beam envisioned for *Project X* provides a number of exciting experimental opportunities for EDM measurements that can be separated into three categories distinguished by system and technical aspects:

1. Rare-atom EDM experiments with ^{225}Ra , ^{223}Rn , and ^{211}Fr that would make use of the Th-target concept for rare-isotope production.
2. A neutron EDM experiment, for example using the apparatus being developed for the SNS experiment, which would take advantage of the superior neutron flux from a spallation target powered by the high-power proton beam.
3. Storage ring EDM experiments, specifically a dedicated muon experiment and a proton-EDM experiment that uses developments in polarized proton beams and polarimetry.

EDM experiments are a unique mix of atomic, low-energy-nuclear and accelerator-physics techniques, which, for the most part, are stand-alone efforts that only require the isotope or neutron production facilities anticipated at *Project X*. Unlike other *Project X* physics activities, no facility-wide detectors would be employed. For example, the rare-isotope EDM experiments derive beam

from the Th target concept for isotope production, which uses the 1 GeV beam exclusively. Without doubt, *Project X*, already at Stage 1, would be a tremendous enabler for the planned nuclear studies. The Project X Injector Experiment (PXIE) with proton beams of 40 MeV at 1 mA may also provide useful yields of isotopes for fundamental physics research, but this is still under study. This set of results could potentially unravel the various sources of CP violation encoded in the low-energy constants associated with CP -violating effective operators at low energies. Such systematic studies would be key were an EDM discovered in any system; the highly leveraged nature of the enhancements in ^{225}Ra make this system an excellent example of the opportunities presented by *Project X*.

V.3.1 Rare Atom EDM Experiments

Rare-atom experiments use short-lived isotopes with half lives varying from 3 min for ^{211}Fr to 24 min for ^{223}Rn to 14 days for ^{225}Ra . For the two-week ^{225}Ra , it is practical to use separated isotope derived from a ^{229}Th (7340 yr) source for development at the first EDM measurements; however in order to reach the 10^{-29} level, an isotope production facility must be used. FRIB is a promising source of ^{225}Ra , however the potential of *Project X* would ultimately provide the largest sample. For the shorter lived Fr and Rn, *Project X* would also provide unprecedented rates for rare-isotope production; however these would require an on-line style experiment. As discussed in section V.2.3.1, octupole collectivity of nuclei with $Z \approx 88$ and $N \approx 134$ leads to a charge distribution in the body frame which is polarized or aligned with the spin by the isospin-dependent CP -violating contributions. Permanent octupole deformation also leads to closely spaced opposite parity levels that enhance the polarizability, for example in ^{225}Ra and possibly ^{223}Rn . The recent REX-ISOLDE work [57] suggests that the enhancement in ^{225}Ra may be an order of magnitude greater than for ^{221}Rn . For francium, the unpaired electron is subject to P -odd, T -odd forces due to the interaction of the electron EDM with the electric field of the nucleus as a consequence of relativistic effects as well as of the existence of a contact interaction with the nucleus mediated by a P -odd, T -odd scalar current.

V.3.1.1 Radon-221, 223

The promise of an EDM experiment in radon arises for several reasons. Most importantly, precision measurements with polarized noble gases in cells have demonstrated the feasibility of an EDM experiment. For ^{129}Xe , it was measured that $d = 0.7 \pm 3.4 \times 10^{-27} e \text{ cm}$ [122]. A number of techniques have been developed including spin-exchange-optical-pumping (SEOP) using rubidium, construction of EDM cells and wall coatings that reduce wall interactions, in particular for spins greater than $1/2$. The Radon-EDM collaboration has developed an experiment (S-929) at TRIUMF's ISAC, an on-line isotope separator-facility, which has been approved with high priority. The experimental program includes development of on-line techniques including collection of rare-gas isotopes and transfer to a cell, and techniques for detection of spin precession based on gamma-ray anisotropy, beta asymmetry and laser techniques.

For polarized rare-isotope nuclei, the excited states of the daughter nucleus populated by beta decay are generally aligned, leading to a $P_2(\cos\theta)$ distribution of gamma-ray emission. The gamma anisotropy effect has been used to detect nuclear polarization in ^{209}Rn [123,124] and ^{223}Rn [123].

Table V-2: Projected sensitivities for $^{221/223}\text{Ra}$ and the corresponding sensitivities in ^{199}Hg at TRIUMF, FRIB, and *Project X*.

Facility	TRIUMF-ISAC	FRIB (^{223}Th source)	<i>Project X</i>
Rate	$2.5 \times 10^7 \text{ s}^{-1}$	$1 \times 10^9 \text{ s}^{-1}$	$3 \times 10^{10} \text{ s}^{-1}$
# atoms	3.5×10^{10}	1.4×10^{12}	4.2×10^{13}
EDM Sensitivity	$1.3 \times 10^{-27} \text{ e cm}$	$2 \times 10^{-28} \text{ e cm}$	$5 \times 10^{-29} \text{ e cm}$
^{199}Hg equivalent	$1.3 \times 10^{-29} \text{ e cm}$	$2 \times 10^{-30} \text{ e cm}$	$5 \times 10^{-31} \text{ e cm}$

At TRIUMF, the large-coverage HPGe gamma-detector array TIGRESS or the new GRIFFIN array may be used. Alternatively, the beta asymmetry can be used to detect nuclear polarization with a higher efficiency. Both the gamma-anisotropy and beta-asymmetry detection techniques have an analyzing power expected to be limited to 0.1–0.2. The sensitivity of the EDM measurement is proportional to the analyzing power, thus laser-based techniques are also under investigation. A newly conceived two-photon magnetometry for ^{129}Xe , which may also be useful as a co-magnetometer in neutron-EDM measurements, is under development. The analyzing power for two-photon transitions can be close to unity as long as the density is sufficient.

EDM measurements in radon isotopes will ultimately be limited by production rates. The *Project X* isotope separator scenario is projected to produce 1–2 orders of magnitude more than current facilities and provides a promising alternative to extracting rare-gas isotopes from the FRIB beam dump as indicated in Table V-2.

V.3.1.2 Radium-225 Atomic EDM

The primary advantage of ^{225}Ra is the large enhancement [44,53,125], approximately a factor of 1000, of the atomic EDM over ^{199}Hg that arises from both the octupole deformation of the nucleus and the highly relativistic atomic electrons. This favorable case is being studied at both Argonne National Laboratory [126] and Kernfysisch Versneller Instituut (KVI) [127]. The scheme at Argonne is to measure the EDM of ^{225}Ra atoms in an optical dipole trap (ODT) as first suggested in Ref. [128]. The ODT offers the following advantages: $\mathbf{v} \times \mathbf{E}$ and geometric phase effects are suppressed, collisions are suppressed between cold fermionic atoms, vector light shifts and parity mixing induced shifts are small. The systematic limit from an EDM measurement in an ODT can be controlled at the level of 10^{-30} e cm [128].

The Argonne collaboration has completed the development of a multi-step process that prepares cold, trapped ^{225}Ra atoms, and has observed the nuclear spin precession of ^{225}Ra atoms in an optical dipole trap. In the next step of an EDM measurement, the precession frequency and its dependence on a strong electric field will be studied. A linear dependence would signify the existence of a nonzero EDM. In the experiment, ^{225}Ra atoms are first chemically reduced in a hot oven and physically evaporated into a collimated atomic beam. Transverse cooling is applied to enhance the forward atomic beam flux by a factor of 100. The atoms are slowed and are captured into a magneto-optical trap (MOT) [126]. The trapped atoms are then transferred to a movable optical dipole trap (ODT) that is controlled by a lens mounted on a translation stage. The ODT carries the

Table V-3: Projected sensitivities for ^{225}Ra and their ^{199}Hg -equivalent values for three scenarios.

Phase	Phase 1	Phase 2	FRIB after upgrade, <i>Project X</i>
Ra (mCi)	1-10	10	> 1000
$d(^{225}\text{Ra})$ ($10^{-28}e\text{cm}$)	100	10	1
equiv. $d(^{199}\text{Hg})$ ($10^{-30}e\text{cm}$)	10	1	0.1

cold ^{225}Ra atoms into a neighboring measurement chamber, and hands the atoms off to a stationary, standing-wave ODT [129]. With the observation of nuclear precession in the standing-wave ODT, the collaboration is poised to begin the first phase of the EDM measurement at the sensitivity level of $10^{-26}e\text{cm}$, which should be competitive with $10^{-29}e\text{cm}$ for ^{199}Hg in terms of sensitivity to T -violating physics. For phase 2 of this experiment, the collaboration plans to upgrade the optical trap. In the present MOT, the slower and trap laser operate at 714 nm where there is a relatively weak atomic transition rate. In phase 2, they would upgrade the trap to operate at 483 nm where a strong transition can be exploited for slowing and trapping.

In the first and second phases, a typical experimental run will use 1-10 mCi of ^{225}Ra presently available. The next-generation isotope facility, such as FRIB after upgrade or *Project X*, is expected to produce more than 10^{13} ^{225}Ra atoms/s [130]. In this case it should be possible to extract more than 1 Ci of ^{225}Ra for use in the EDM apparatus. This would lead to a projected sensitivity of $10^{-28}e\text{cm}$ for ^{225}Ra , competitive with $10^{-31}e\text{cm}$ for ^{199}Hg . Table V-3 summarizes the projected sensitivities.

V.3.1.3 Electron EDM with Francium

For paramagnetic systems including alkali atoms, the EDM of the atom arises predominantly due to the electron EDM and due to CP -violating components of the electron-nuclear interaction. In particular, the electron EDM induces an atomic EDM that is approximately proportional to $Z^3\alpha^2$, and for heavy atoms, the atomic EDM is enhanced relative to the electron EDM. Francium is an extremely promising system in which to study the electron EDM [131], and for ^{211}Fr , the large nuclear spin and magnetic dipole moment allow efficient laser cooling. Systematic effects, including a magnetic field that arises due to leakage currents resulting from the applied electric field can couple to the magnetic moment producing a false EDM, and the motional magnetic field $\mathbf{B}_{\text{mot}} = (\mathbf{v} \times \mathbf{E})/c^2$ leads to systematic effects linear in \mathbf{E} . For an experiment in zero magnetic field, the atom is quantized along the electric field, and these effects can be removed in first order and residual magnetic fields are small. Remaining systematic effects scale as $1/E^n$, with $n > 2$. Consequently, the ratio of systematic effect sensitivity to electron EDM sensitivity in ^{211}Fr is two orders of magnitude smaller than in any lighter alkalis. An ISOL source at *Project X* would have proton beam currents about two orders of magnitude larger than TRIUMF and ISOLDE, and may produce 10^{13} Fr s^{-1} , which would be sufficient to lower the electron EDM upper limit by a factor of up to 1000.

V.3.2 SNS Neutron EDM

A large effort is underway to develop the SNS nEDM experiment with the goal of achieving a sensitivity $< 3 \times 10^{-28}$ e cm, two orders of magnitude beyond the current experimental limits. The SNS is a dedicated accelerator-based neutron source utilizing a high-powered 1 GeV proton beam at 1.4-3 MW incident on the liquid-mercury spallation target. A cold moderator provides neutrons to the Fundamental-Neutron-Physics-Beamline (FNPB). The nEDM experiment will use 8.9 Å neutrons which are converted to ultra-cold neutrons (velocity less than ≈ 8 m/s) in superfluid helium in the nEDM experiment. The rate of neutron production is limited by the power of the proton beam and practical considerations of the target and moderators. Since the FNPB is a multipurpose cold beam, the nEDM experiment will take what it can get. The possibility of developing a significantly more intense source of 8.9 Å neutrons for the nEDM experiment by utilizing the higher powered *Project X* proton beam may provide unprecedented sensitivity to the neutron EDM.

The nEDM experiment, based on Ref. [132], uses a novel polarized ^3He co-magnetometer and will detect the neutron precession via the spin-dependent neutron capture on ^3He . The capture reaction produces energetic proton and triton, which ionize liquid helium and generate scintillation light that can be detected. Since the EDM of ^3He is strongly suppressed by electron screening in the atom it can be used as a sensitive monitor of the ~ 30 mGauss magnetic field. High densities of trapped UCNs are produced via phonon production in superfluid ^4He which can also support large electric fields, and ~ 70 kV/cm is anticipated.

The nEDM technique allows for a number of independent checks on systematics including:

1. Studies of the temperature dependence of false EDM signals in the ^3He .
2. Measurement of the ^3He precession frequency using SQUIDS.
3. Cancellation of magnetic field fluctuations by matching the effective gyromagnetic ratios of neutrons and ^3He with the “spin dressing” technique [132].

Key R&D developments underway in preparation of the full experiment include:

1. Maximum electric field strength for large-scale electrodes made of appropriate materials in superfluid helium below a temperature of 1 K.
2. Magnetic field uniformity for a large-scale magnetic coil and a superconducting Pb magnetic shield.
3. Development of coated measurement cells that preserve both neutron and ^3He polarization along with neutron storage time.
4. Understanding of polarized ^3He injection and transport in the superfluid.
5. Estimation of the detected light signal from the scintillation in superfluid helium.

The experiment will be installed at the FNPB (Fundamental Neutron Physics Beamline) at the SNS and construction is likely to take at least five years, followed by hardware commissioning and data taking. Thus first results could be anticipated by the end of the decade.

Regarding next generation neutron EDMs, a spallation source optimized for ultra-cold neutrons (UCNs) could substantially improve the sensitivity of next generation neutron EDM experiments, which in the case of the US nEDM experiment, will be statistically limited at the SNS. A key metric for these experiments is the density of UCNs provided to or in the experiment, which can be much higher per incident beam proton in an optimized UCN source. There are several paths *Project X* can provide to improve the statistical reach of the nEDM after completion of running at FNPB. For example, a cold neutron source envisioned for a neutron-antineutron oscillation experiment early in *Project X* (NNbarX) could provide increased cold neutron flux for UCN production in the nEDM experiment as well. Alternatively, one can implement an optimized UCN source at *Project X* and couple it “externally” to a nEDM experiment. Such a source should also be compatible with NNbarX and is projected to provide substantial gains in available UCN density for nEDM.

V.3.3 Storage Ring EDMs

The EDM of the muon was measured as part of the muon $g - 2$ measurement [11] in a magnetic storage ring and has led to the idea of measuring the EDM of charged particles in storage rings with magnetic, electric, or a combination of fields. With stable particles combined with proton polarization and polarimetry, the storage ring method brings a revolution in statistics to the field. *Project X* will fulfill the need for intense low emittance beams that enable longer storage times, narrower line widths and therefore the promise to extend EDM sensitivity to the 10^{-30} e cm range. But perhaps more crucial is adding the direct measurement of the proton-EDM to the set of EDM results, which will provide new information, specifically on the isovector contributions to the nucleon EDMs. In addition, the expertise in accelerator physics that will concentrate with *Project X* will provide the storage ring method with a highly instrumented ring with the most sensitive equipment, and it will be a testing ground for many notions regarding accelerators and storage rings. In turn, innovative solutions can be applied to *Project X* accelerators to understand it better and improve their performance.

Stage 1 of *Project X* can be configured in a straightforward manner to provide the necessary polarized protons with the required energy, emittance, and flux. High power is not required, and it is true that the existing Fermilab linac could be reconfigured, at substantial expense, to drive the experiment. If Stage 1 of *Project X* is built to drive many new experiments, then this is definitely the most cost effective approach to include the elements of the accelerator required for the proton EDM experiment (e.g. polarized proton source). There are “frozen spin” muon EDM concepts proposed at JPARC and developed for PSI that are dedicated configurations for EDM sensitivity that could operate in Stage 1 of *Project X*, and can thus have much higher sensitivity than the EDM measurement parasitic to the $g - 2$ measurement.

Storage Ring EDM methods also provide a unique set of systematic errors and solutions. Since the particles are stored in a ring, information regarding their position can reveal systematic-error sources. Storing particles in clock-wise (CW) and counter-clock-wise (CCW) directions, in alternating fills, reveals the main systematic error source, i.e., a net radial magnetic field (a menace in EDM experiments). The difference in particle positions and EDM-like signals is a powerful tool against the main systematic errors. In addition, for particles with a positive anomalous magnetic moment, it is possible to use an all-electric-field ring to store the particles for an EDM experiment.

Storing particles in CW and CCW directions simultaneously (possible in an all-electric ring), further simplifies combating the main systematic errors. Finally, another systematic error, the so-called geometrical phase, can also be revealed by a) looking at the EDM-like signal as a function of the azimuthal location of the ring, b) compare the beam position around the azimuth to its “ideal” closed orbit, etc. These standard techniques for a storage ring eliminate the geometrical phase error as well. Clearly, the storage ring EDM methods can substantially advance the quest for ever greater sensitivity with the high intensity beams available even today, e.g., protons and deuterons and by applying well developed beam storage techniques, e.g., for protons, deuterons, muons, etc.

V.3.3.1 Measurement Principle

The interaction energy for a particle at rest with a magnetic dipole moment (MDM), $\boldsymbol{\mu}$, and electric dipole moment (EDM), \boldsymbol{d} , in magnetic and electric fields is given by Eq. (V.2.1), i.e., magnetic dipole moments couple only to magnetic fields and electric dipole moments couple only to electric fields. The spin precession rate for rectilinear motion is given by

$$\frac{d\boldsymbol{s}}{dt'} = \boldsymbol{\mu} \times \mathbf{B}' + \boldsymbol{d} \times \mathbf{E}', \quad (\text{V.3.1})$$

where t' , \mathbf{E}' , and \mathbf{B}' are evaluated in the particle rest frame. We note \boldsymbol{s} is the rest-frame particle spin vector, with $\boldsymbol{\mu} = g(q/2m)\boldsymbol{s}$, yielding $\mu = (1+a)q\hbar/2m$ with $a = (g-2)/2$ the anomalous magnetic moment. Correspondingly, $\boldsymbol{d} = \eta(e/2mc)\boldsymbol{s}$, with η a dimensionless parameter that plays a similar role to the EDM that g plays for the MDM. In storage rings, the momentum precession is given by

$$\frac{d\boldsymbol{\beta}}{dt} = \frac{q}{m\gamma} \left[\frac{\mathbf{E}}{c} + \boldsymbol{\beta} \times \mathbf{B} - \frac{(\boldsymbol{\beta} \cdot \mathbf{E}) \boldsymbol{\beta}}{c} \right], \quad (\text{V.3.2})$$

where $\boldsymbol{\beta} = \mathbf{v}/c$ is the particle velocity divided by the speed of light. We emphasize that t , \mathbf{E} , and \mathbf{B} are all laboratory frame quantities. frame and consider the Thomas precession, if applicable. The spin precession rate due to the magnetic and electric fields including Thomas precession is given by [133,134]

$$\begin{aligned} \frac{d\boldsymbol{s}}{dt} = \frac{q}{m} \boldsymbol{s} \times & \left[\left(\frac{g}{2} - 1 + \frac{1}{\gamma} \right) \mathbf{B} - \left(\frac{g}{2} - 1 \right) \frac{\gamma}{\gamma+1} (\boldsymbol{\beta} \cdot \mathbf{B}) \boldsymbol{\beta} - \left(\frac{g}{2} - \frac{\gamma}{\gamma+1} \right) \frac{\boldsymbol{\beta} \times \mathbf{E}}{c} \right] \\ & + \frac{\eta q}{2m} \left[\frac{\mathbf{E}}{c} - \frac{\gamma}{1+\gamma} \frac{\boldsymbol{\beta} \cdot \mathbf{E}}{c} + \boldsymbol{\beta} \times \mathbf{B} \right], \end{aligned} \quad (\text{V.3.3})$$

where the last term is due to the EDM.

One way to determine the so-called $g-2$ precession rate is to compute the time-dependence of the scalar product between the velocity unit vector, $\hat{\boldsymbol{\beta}}$, and spin vector, \boldsymbol{s} . When $\boldsymbol{\beta} \cdot \mathbf{B} = \boldsymbol{\beta} \cdot \mathbf{E} = 0$, it can also be estimated using

$$\boldsymbol{\Omega} = \boldsymbol{\omega}_a + \boldsymbol{\omega}_{\text{EDM}} = -\frac{q}{m} \left[a\mathbf{B} - \left(a - \left(\frac{mc}{p} \right)^2 \right) \frac{\boldsymbol{\beta} \times \mathbf{E}}{c} \right] - \frac{\eta q}{2m} \left[\frac{\mathbf{E}}{c} + \boldsymbol{\beta} \times \mathbf{B} \right] \quad (\text{V.3.4})$$

showing that while the so-called g-2 precession rate (ω_a) is mostly in the horizontal plane there is also a small precession in the out of plane direction for a nonzero EDM.² This causes a small tilt in the g-2 precession plane. The dedicated EDM method, developed by the Storage Ring EDM Collaboration, optimizes the EDM sensitivity by minimizing the horizontal precession and maximizing the vertical one. Since the EDM precession is in the vertical direction, where there is no acceleration, there is no Thomas precession involved and the EDM precession is directly proportional to η and not to $\eta - 2$ as it is correspondingly in the horizontal plane.

V.3.3.2 EDM Optimization

As we have noted, the traditional way to search for an EDM is to place a neutral system in a weak magnetic field region and observe the interaction energy of the magnetic moment of the system with the magnetic field. Then apply a very strong electric field and look for a change in the interaction energy when the electric field direction is reversed. If there is an energy shift proportional to the applied electric field, it would signal a permanent electric dipole moment along the MDM of the system. A charged system would be accelerated out of the electric field region and get lost in a very short time. However, charged particles in a storage ring are regularly stored for hours in very large numbers without any special difficulty. This fact provides a special opportunity to look for an optimization process in probing the charged particle EDMs.

The out-of-plane or “vertical” polarization change as a function of time is an indication of an EDM signal. The vertical polarization is given by

$$\Delta P_V = P_L \frac{\omega_{\text{EDM}}}{\Omega} \sin(\Omega t + \theta_0) \quad (\text{V.3.5})$$

with $\Omega = \sqrt{(\omega_a^2 + \omega_{\text{edm}}^2)}$, and P_L the longitudinal polarization. Setting $\omega_a = 0$ maximizes the sensitivity to the EDM of the stored particles. Here are two distinct ways we can achieve this goal:

1. Use a special combination of dipole magnetic and radial electric fields to cancel the horizontal spin precession. The radial electric field required is equal to

$$E_r = \frac{aBc\beta\gamma^2}{1 - a\beta^2\gamma^2} \approx aBc\beta\gamma^2 \quad (\text{V.3.6})$$

This method was used for the muon EDM LOI to J-PARC and the deuteron EDM proposal at BNL. The advantage of this method is that the ring can be quite small, and the sensitivity quite large since the equivalent electric field in the particle rest frame is equal to $\mathbf{v} \times \mathbf{B}$, equal to 300 MV/m for a relativistic particle in a 1 T magnetic field. The disadvantage is that it requires the development of a combined system with a dipole magnetic field and a radial electric field in the same region. Systematic error sources are any net vertical electric field average around the ring, requiring frequent clock-wise (CW) and counter-clock-wise (CCW) storage. During that rotation, the dipole magnetic field is flipped but the radial electric field remains constant.

²In the absence of electric fields, ω_a is independent of γ .

- Use $\mathbf{B} = \mathbf{0}$, by eliminating every possible source of magnetic fields. Then use a special momentum value at which the horizontal spin precession is equal to the momentum precession, i.e., $\vec{\omega}_a = 0$, as is shown in Fig. V-7. The special particle momentum is equal to $p = mc/\sqrt{a}$. The particle momentum is equal to 3.08 GeV/c for the muon and 0.7 GeV/c for the proton. The advantage of this method is the simplicity of the electric ring. In addition, simultaneous CW and CCW beam storage is possible, enabling the detection of spurious B fields by probing the *relative* displacements of the counter-rotating beams. The disadvantage is that the ring real estate is large because the maximum electric fields available are still small compared to the equivalent magnetic fields. Furthermore, the ring needs to be shielded to first order from spurious magnetic fields adding to the cost. Obviously this method cannot be applied to particles with negative anomalous magnetic moment values, e.g., the deuteron, ^3He , etc.

The required parameters for the polarized beams are given in Table V-4.

V.3.3.3 Plans

The Storage Ring EDM Collaboration has proposed a proton EDM experiment sensitive to 10^{-29} ecm [135,136]. With an upgrade, applying stochastic cooling to the stored proton beam, it may be possible to achieve another order of magnitude in sensitivity for the proton, down to 10^{-30} ecm. The proposal requires highly polarized protons with an intensity of more than 10^{10} particles per cycle of 15– minutes. The method uses polarized protons at the so-called “magic” momentum of 0.7 GeV/c in an all-electric storage ring with a radius of ~ 40 m. At this momentum, the proton spin and momentum vectors precess at the same rate in any transverse electric field. When the spin is kept along the momentum direction, the radial electric field acts on the EDM vector causing the proton spin to precess vertically. The vertical component of the proton spin builds up for the

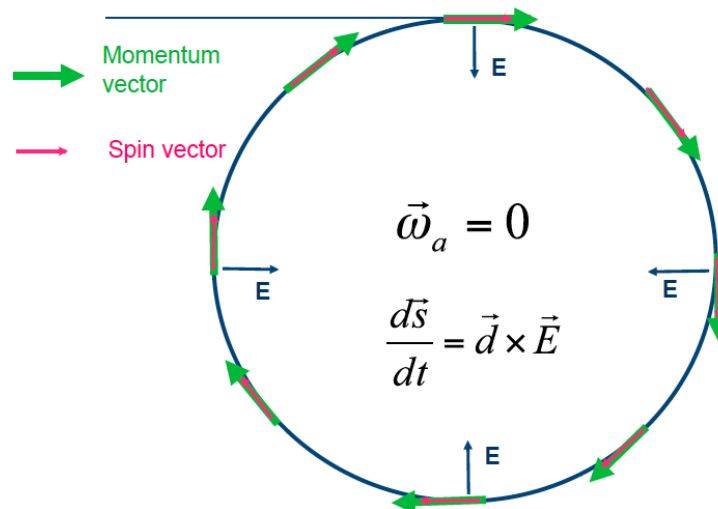


Figure V-7: At the magic momentum the particle spin and momentum vectors precess at the same rate in an electric storage ring, i.e., the so-called $g - 2$ precession rate is zero. That allows the spin to precess in the vertical direction if the particle EDM is nonzero.

Table V-4: The required beam parameter values and the projected sensitivities

Particle	Beam intensity, polarization, NP^2	Horizontal, vertical emittance 95%, normalized [mm-mrad], dp/p	Momentum [GeV/c]	Projected Sensitivity [e cm]
Protons	4×10^{10} , > 80%	2, 6, 2×10^{-4} rms	0.7	10^{-29} , 10^{-30}
Deuterons	2×10^{11} , > 80%	3, 10, 10^{-3}	1	10^{-29}
^3He	TBD, > 80%	TBD	TBD	$< 10^{-28}$
Muons	$NP^2 = 5 \times 10^{16}$ total	800, 800, 2% max	0.5	10^{-24}

duration of the storage time, which is limited to 10^3 s by the estimated horizontal spin coherence time (hSCT) of the beam within the admittance of the ring. This spin coherence time can be further prolonged by various techniques, e.g., stochastic cooling or sextupoles placed at special locations around the ring.

The strength of the storage ring EDM method comes from the fact that a large number of highly polarized particles can be stored for a long time, a large hSCT can be achieved and the transverse spin components can be probed as a function of time with a high sensitivity polarimeter. The polarimeter uses elastic nuclear scattering off a solid carbon target placed in a straight section of the ring serving as the limiting aperture. The collaboration over the last few years has developed the method and improved their understanding and confidence in it. Some notable accomplishments are listed below:

1. Systematic errors, the efficiency and analyzing power of the polarimeter has been studied. The polarimeter systematic errors, caused by possible beam drifting, are found to be much lower than the statistical sensitivity [137].
2. A tracking program has been developed to accurately simulate the spin and beam dynamics of the stored particles in the all-electric ring. Several aspects of the beam and spin dynamics have been developed analytically, so it is possible to compare with precision simulations [138]. The required ring parameters are readily available at BNL with current capabilities. At Fermilab we would need a polarized proton source. There is no need for a siberian snake since the acceleration to the required kinetic energy (233 MeV) is done in the LINAC.
3. The required radial E-fields (≈ 100 kV/cm) can be achieved using technology developed as part of the international linear collider (ILC) and energy recovery linacs (ERL) R&D efforts [139]. Tests at J-Lab indicate that much higher than 100 kV/cm across a 3 cm plate separation can be achieved [140].
4. The geometrical phase effect can be reduced to a level lower than the statistical sensitivity based on a position tolerance of commonly achievable ~ 0.1 mm in the relative positioning of the E-field plates around the ring.

V.4 BROADER POSSIBILITIES

In this section we consider broader prospects in regards to the quest for new sources of CP violation at low energies.

As we have discussed, one possible resolution of the strong CP problem implies that a new particle, an axion, exists—this is well-motivated new physics which does not in any way rely on the notion of naturalness and new physics at the weak scale. In particular, the dynamical relaxation of the axion potential solves the strong CP problem, where the essential components of the axion Lagrangian are [25]

$$\mathcal{L}_a = \frac{1}{2} \partial_\mu a \partial^\mu a + \frac{a(x)}{f_a} \frac{\alpha_s}{8\pi} F_{\mu\nu}^a \tilde{F}^{\mu\nu a}. \quad (\text{V.4.1})$$

The mass of the axion is controlled by its mixing with the neutral pion; current algebra techniques [141,142] yield $m_a \approx f_\pi m_\pi / f_a$ where f_π is the usual pion decay constant. Consequently, for large values of the Peccei-Quinn scale f_a , the axion is very light. Current searches place the limit $f_a > 10^{10}$ GeV [29]. Cosmological constraints on f_a have also been thought to operate, requiring that $f_a \lesssim 10^{12}$ GeV so that the axion contribution to the closure energy density today, Ω_a , is less than unity [143–145]. The cosmological constraints, however, are not compelling; they can be evaded [146], most notably, if f_a is in excess of the inflation energy scale [147]. Moreover, much larger values of f_a can have a ready origin: a string/M-theory QCD axion in which gauge unification arises from four-dimension renormalization group running has f_a which is naturally of the grand unification scale, $f_a \sim 10^{16}$ GeV [146]. This window of parameter space has not been probed directly, previously; however, as suggested in Refs. [30,148], the axion can give rise to a time-dependent EDM, which potentially can be identified using NMR techniques. Current plans [148] consider such a search in the context of a solid-state EDM experiment, or, more precisely, of an experiment building on the technical capacities developed in such contexts. We offer a brief view of the status of such experiments in what follows.

In solid-state systems, the EDM of the unpaired electrons is detectable either through the magnetic field produced when the electron EDMs are aligned by the strong internal electric field ($\mathbf{B}_{\text{ind}} \cdot \mathbf{E}$) or through the electric field induced when the electron magnetic moments are polarized by a strong magnetic field ($\mathbf{E}_{\text{ind}} \cdot \mathbf{B}$) [149–153]. For example, in PbTiO_3 , a ferroelectric crystal, sensitivity to the electron EDM is enhanced due to the large number of electrons in the solid and due to the strong internal electric field in a cooled crystal [154]. A similar measurement in gadolinium-gallium garnet is under way [149]. Another approach using ferromagnetic gadolinium-iron garnet would detect the electric field produced by the electron EDMs aligned with the magnetically polarized spins [155].

It should be possible to employ the NMR techniques we have mentioned to the study of time-dependent EDMs in other systems, possibly in rare atom experiments at *Project X*.

As a second possibility we consider the possibility of probing spin-*independent* sources of CP violation at low energies. Radiative β decay, e.g., offers the opportunity of studying T -odd correlations which do not appear in ordinary β decay. That is, a triple-product momentum correlation among the final-state particles in that process is both parity P - and naively time-reversal T -odd but independent of the particle spin. Its spin independence renders it distinct from searches for permanent electric-dipole-moments (EDMs) of neutrons and nuclei. The inability of the Standard Model

(SM) to explain the cosmic baryon asymmetry prompts the search for sources of CP violation which do not appear within it and which are not constrained by other experiments. Here, too, T -violation is linked to CP violation through the CPT-theorem. A decay correlation, however, can be, by its very nature, only “pseudo” T -odd, so that it can be mimicked by final-state effects without fundamental T or CP violation; in beta decay, these final-state interactions are electromagnetic in nature and wholly calculable at the needed levels of precision [156,157]. Such a calculation is crucial to establishing a baseline in the search for new sources of CP -violation in such processes. It is motivated in large part by the determination, due to Harvey, Hill, and Hill, that pseudo-Chern-Simons terms appear in $SU(2)_L \times U(1)$ gauge theories at low energies—and that they can impact low-energy weak radiative processes involving baryons [158,159]. In the SM such pseudo-Chern-Simons interactions are CP -conserving, but considered broadly they are not, so that searching for the P - and T -odd effects that CP -violating interactions of pseudo-Chern-Simons form would engender offers a new window on physics beyond the SM, specifically on new sources of CP violation mediated by the weak vector current, probing the CP structure of particular hidden sector models [160]. The ultraheavy atoms we have considered in the context of EDM searches would not do here; the value of Z cannot be too large, or the computation of the SM background from FSI is not controlled. Rather, lighter nuclei, such as ^{35}Ar , are better choices [157,160], so that these studies may be better suited to the FRIB facility.

V.5 SUMMARY

EDM searches of enhanced experimental sensitivity give us sensitive probes of new physics beyond the SM, potentially giving insight on the energy scale of new physics, irrespective of developments at the LHC.

The first stage of the *Project X* accelerator gives us unprecedented sensitivity to rare atom EDMs, particularly ^{225}Ra and ^{211}Fr , giving us the opportunity to sharpen constraints on low-energy sources of CP violation in chirality-changing interactions by orders of magnitude. The experimental capacities involved can be extended to the study of broader prospects as well, using CP violation to probe the nature of dark matter and possibly leading to the discovery of the axion. Moreover, a storage ring EDM experiment offers the possibility of probing the proton EDM directly and with high sensitivity for the very first time.

At anticipated levels of experimental sensitivity, there is little doubt that a nonzero EDM would be Nature’s imprimatur of the existence of physics beyond the SM. However, to go beyond this, theory must make strides in order to take advantage of such experimental developments. There are different issues to consider. The interpretation of the EDM of a complex system such as ^{225}Ra —beyond discovery—involves hadronic, nuclear, and atomic computations. Lattice gauge theory methods may well be able to redress limitations in current computations of hadronic matrix elements. Ultimately the interpretability of possible EDMs in terms of underlying sources of CP violation may prove sharpest in simple systems such as the neutron and proton, and in these systems as well *Project X* can open new decades of sensitivity.

References

- [1] A. D. Sakharov, *Pisma Zh. Eksp. Teor. Fiz.* **5**, 32 (1967)
- [2] M. B. Gavela, P. Hernandez, J. Orloff, and O. Pene, *Mod. Phys. Lett.* **A9**, 795 (1994), [arXiv:hep-ph/9312215 [hep-ph]]
- [3] M. B. Gavela, P. Hernandez, J. Orloff, O. Pene, and C. Quimbay, *Nucl. Phys.* **B430**, 382 (1994), [arXiv:hep-ph/9406289 [hep-ph]]
- [4] P. Huet and E. Sather, *Phys. Rev.* **D51**, 379 (1995), [arXiv:hep-ph/9404302 [hep-ph]]
- [5] V. A. Kuzmin, V. A. Rubakov, and M. E. Shaposhnikov, *Phys. Lett.* **B155**, 36 (1985)
- [6] M. E. Shaposhnikov, *Nucl. Phys.* **B287**, 757 (1987)
- [7] G. R. Farrar and M. E. Shaposhnikov, *Phys. Rev. Lett.* **70**, 2833 (1993), [arXiv:hep-ph/9305274 [hep-ph]]
- [8] J. Charles *et al.* (CKMfitter Group), *Eur. Phys. J.* **C41**, 1 (2005), [arXiv:hep-ph/0406184 [hep-ph]]
- [9] G. Isidori, Y. Nir, and G. Perez, *Ann. Rev. Nucl. Part. Sci.* **60**, 355 (2010), [arXiv:1002.0900 [hep-ph]]
- [10] J. J. Hudson, D. M. Kara, I. J. Smallman, B. Sauer, M. Tarbutt, *et al.*, *Nature* **473**, 493 (2011)
- [11] G. W. Bennett *et al.* (Muon (g-2) Collaboration), *Phys. Rev.* **D80**, 052008 (2009), [arXiv:0811.1207 [hep-ex]]
- [12] C. A. Baker, D. D. Doyle, P. Geltenbort, K. Green, M. van der Grinten, *et al.*, *Phys. Rev. Lett.* **97**, 131801 (2006), [arXiv:hep-ex/0602020 [hep-ex]]
- [13] W. C. Griffith *et al.*, *Phys. Rev. Lett.* **102**, 101601 (2009)
- [14] I. B. Khriplovich, *Phys. Lett.* **B173**, 193 (1986)
- [15] A. Czarnecki and B. Krause, *Phys. Rev. Lett.* **78**, 4339 (1997), [arXiv:hep-ph/9704355 [hep-ph]]
- [16] M. E. Pospelov and I. B. Khriplovich, *Sov. J. Nucl. Phys.* **53**, 638 (1991)
- [17] D. Ng and J. N. Ng, *Mod. Phys. Lett.* **A11**, 211 (1996), [arXiv:hep-ph/9510306 [hep-ph]]
- [18] M. B. Gavela, A. Le Yaouanc, L. Oliver, O. Pene, J. Raynal, *et al.*, *Phys. Lett.* **B109**, 215 (1982)
- [19] I. B. Khriplovich and A. R. Zhitnitsky, *Phys. Lett.* **B109**, 490 (1982)
- [20] X.-G. He, B. H. J. McKellar, and S. Pakvasa, *Int. J. Mod. Phys.* **A4**, 5011 (1989)
- [21] T. Mannel and N. Uraltsev, *Phys. Rev.* **D85**, 096002 (2012), [arXiv:1202.6270 [hep-ph]]

- [22] K. Abe *et al.* (Belle Collaboration), Phys. Rev. Lett. **87**, 091802 (2001), [arXiv:hep-ex/0107061 [hep-ex]]
- [23] B. Aubert *et al.* (BaBar Collaboration), Phys. Rev. Lett. **87**, 091801 (2001), [arXiv:hep-ex/0107013 [hep-ex]]
- [24] B. Aubert *et al.* (BaBar Collaboration), Phys. Rev. Lett. **89**, 201802 (2002), [arXiv:hep-ex/0207042 [hep-ex]]
- [25] M. Pospelov and A. Ritz, Annals Phys. **318**, 119 (2005), [arXiv:hep-ph/0504231 [hep-ph]]
- [26] R. D. Peccei and H. R. Quinn, Phys. Rev. Lett. **38**, 1440 (1977)
- [27] S. Weinberg, Phys. Rev. Lett. **40**, 223 (1978)
- [28] F. Wilczek, Phys. Rev. Lett. **40**, 279 (1978)
- [29] S. J. Asztalos *et al.* (ADMX Collaboration), Phys. Rev. Lett. **104**, 041301 (2010), [arXiv:0910.5914 [astro-ph.CO]]
- [30] P. W. Graham and S. Rajendran, Phys. Rev. **D84**, 055013 (2011), [arXiv:1101.2691 [hep-ph]]
- [31] N. F. Ramsey, Rept. Prog. Phys. **45**, 95 (1982)
- [32] J. Engel, M. J. Ramsey-Musolf, and U. van Kolck, Prog. Part. Nucl. Phys.(2013), [arXiv:1303.2371 [nucl-th]]
- [33] A. De Rujula, M. B. Gavela, O. Pene, and F. Vegas, Nucl. Phys. **B357**, 311 (1991)
- [34] J. S. M. Ginges and V. V. Flambaum, Phys. Rept. **397**, 63 (2004), [arXiv:physics/0309054 [physics]]
- [35] L. I. Schiff, Phys. Rev. **132**, 2194 (1963)
- [36] P. G. H. Sandars, Phys. Lett. **B14**, 194 (1965)
- [37] P. G. H. Sandars, Phys. Lett. **B22**, 290 (1966)
- [38] P. G. H. Sandars, Phys. Rev. Lett. **19**, 1396 (1967)
- [39] I. B. Khriplovich and S. Lamoreaux, *CP Violation without Strangeness: Electric Dipole Moments of Particles, Atoms, and Molecules* (Springer, Berlin, 1997)
- [40] J. Engel, J. L. Friar, and A. C. Hayes, Phys. Rev. **C61**, 035502 (2000), [arXiv:nucl-th/9910008 [nucl-th]]
- [41] V. V. Flambaum and V. G. Zelevinsky, Phys. Rev. **C68**, 035502 (2003), [arXiv:nucl-th/0208073 [nucl-th]]
- [42] N. Auerbach, V. V. Flambaum, and V. Spevak, Phys. Rev. Lett. **76**, 4316 (1996), [arXiv:nucl-th/9601046 [nucl-th]]
- [43] V. Spevak, N. Auerbach, and V. V. Flambaum, Phys. Rev. C **56**, 1357 (1997)

- [44] J. Dobaczewski and J. Engel, Phys. Rev. Lett. **94**, 232502 (2005), [arXiv:nucl-th/0503057 [nucl-th]]
- [45] V. A. Dzuba and V. V. Flambaum, Int. J. Mod. Phys. **E21**, 1230010 (2012), [arXiv:1209.2200 [physics.atom-ph]]
- [46] V. Bernard, Prog. Part. Nucl. Phys. **60**, 82 (2008), [arXiv:0706.0312 [hep-ph]]
- [47] E. Mereghetti, W. H. Hockings, and U. van Kolck, Annals Phys. **325**, 2363 (2010), [arXiv:1002.2391 [hep-ph]]
- [48] C. M. Maekawa, E. Mereghetti, J. de Vries, and U. van Kolck, Nucl. Phys. **A872**, 117 (2011), [arXiv:1106.6119 [nucl-th]]
- [49] J. de Vries, E. Mereghetti, R. G. E. Timmermans, and U. van Kolck, “The effective chiral Lagrangian from dimension-six parity and time-reversal violation,” (2012), arXiv:1212.0990 [hep-ph]
- [50] B. C. Regan, E. D. Commins, C. J. Schmidt, and D. DeMiller, Phys. Rev. Lett. **88**, 071805 (2002)
- [51] A.-M. Martensson-Pendrill, Phys. Rev. Lett. **54**, 1153 (1985)
- [52] J. Dobaczewski and J. Engel, Phys. Rev. Lett. **94**, 232502 (2005)
- [53] S. Ban, J. Dobaczewski, J. Engel, and A. Shukla, Phys. Rev. **C82**, 015501 (2010), [arXiv:1003.2598 [nucl-th]]
- [54] J. deJesus and J. Engel, Phys. Rev. C **72**, 045503 (2005)
- [55] R. G. Helmer, M. A. Lee, C. W. Reich, and I. Ahmad, Nucl. Phys. **A474**, 1357 (1997)
- [56] J. F. C. Cocks *et al.*, Nucl. Phys. **A645**, 61 (1997)
- [57] L. P. Gaffney *et al.*, Nature **497**, 199 (2013)
- [58] V. V. Flambaum, I. B. Khriplovich, and O. P. Sushkov, Sov. Phys. JETP **60**, 873 (1984)
- [59] O. Lebedev, K. A. Olive, M. Pospelov, and A. Ritz, Phys. Rev. **D70**, 016003 (2004), [arXiv:hep-ph/0402023 [hep-ph]]
- [60] J. de Vries, E. Mereghetti, R. G. E. Timmermans, and U. van Kolck, Phys. Rev. Lett. **107**, 091804 (2011), [arXiv:1102.4068 [hep-ph]]
- [61] J. de Vries, R. Higa, C.-P. Liu, E. Mereghetti, I. Stetcu, *et al.*, Phys. Rev. **C84**, 065501 (2011), [arXiv:1109.3604 [hep-ph]]
- [62] I. I. Y. Bigi and N. G. Uraltsev, Nucl. Phys. **B353**, 321 (1991)
- [63] B. Grzadkowski, M. Iskrzynski, M. Misiak, and J. Rosiek, JHEP **1010**, 085 (2010), [arXiv:1008.4884 [hep-ph]]

- [64] S. Narison, Phys. Lett. **B666**, 455 (2008), [arXiv:0806.2618 [hep-ph]]
- [65] S. J. Brodsky, S. Gardner, and D. S. Hwang, Phys. Rev. **D73**, 036007 (2006), [arXiv:hep-ph/0601037 [hep-ph]]
- [66] M. S. Carena, M. Quiros, and C. E. M. Wagner, Phys. Lett. **B380**, 81 (1996), [arXiv:hep-ph/9603420 [hep-ph]]
- [67] D. Delepine, J. M. Gerard, R. Gonzalez Felipe, and J. Weyers, Phys. Lett. **B386**, 183 (1996), [arXiv:hep-ph/9604440 [hep-ph]]
- [68] G. Jungman, M. Kamionkowski, and K. Griest, Phys. Rept. **267**, 195 (1996), [arXiv:hep-ph/9506380 [hep-ph]]
- [69] C. Balazs, M. S. Carena, A. Menon, D. Morrissey, and C. Wagner, Phys. Rev. **D71**, 075002 (2005), [arXiv:hep-ph/0412264 [hep-ph]]
- [70] W. Buchmuller and D. Wyler, Nucl. Phys. **B268**, 621 (1986)
- [71] W. Altmannshofer, M. Bauer, and M. Carena(2013), in preparation
- [72] G. Aad *et al.* (ATLAS Collaboration), Phys. Lett. **B716**, 1 (2012), [arXiv:1207.7214 [hep-ex]]
- [73] S. Chatrchyan *et al.* (CMS Collaboration), Phys. Lett. **B716**, 30 (2012), [arXiv:1207.7235 [hep-ex]]
- [74] ATLAS Collaboration, “Measurements of the properties of the Higgs-like boson in the two photon decay channel with the ATLAS detector using 25 fb⁻¹ of proton-proton collision data,” (2013), ATLAS-CONF-2013-012
- [75] CMS Collaboration, “Updated measurements of the Higgs boson at 125 GeV in the two photon decay channel,” CMS-PAS-HIG-13-001
- [76] ATLAS Collaboration, “Measurements of the properties of the Higgs-like boson in the four lepton decay channel with the ATLAS detector using 25 fb⁻¹ of proton-proton collision data,” (2013), ATLAS-CONF-2013-013
- [77] CMS Collaboration, “Properties of the Higgs-like boson in the decay $H \rightarrow ZZ \rightarrow 4\ell$ in pp collisions at $\sqrt{s} = 7$ and 8 TeV,” CMS-PAS-HIG-13-002
- [78] D. McKeen, M. Pospelov, and A. Ritz, Phys. Rev. **D86**, 113004 (2012), [arXiv:1208.4597 [hep-ph]]
- [79] J. Fan and M. Reece, “Probing charged matter through Higgs diphoton decay, gamma ray lines, and EDMs,” (2013), arXiv:1301.2597 [hep-ph]
- [80] J. R. Ellis, J. S. Lee, and A. Pilaftsis, JHEP **0810**, 049 (2008), [arXiv:0808.1819 [hep-ph]]
- [81] Y. Li, S. Profumo, and M. Ramsey-Musolf, JHEP **1008**, 062 (2010), [arXiv:1006.1440 [hep-ph]]

- [82] A. G. Cohen, D. B. Kaplan, and A. E. Nelson, *Phys. Lett.* **B388**, 588 (1996), [arXiv:hep-ph/9607394 [hep-ph]]
- [83] S. M. Barr and A. Zee, *Phys. Rev. Lett.* **65**, 21 (1990)
- [84] M. Carena, G. Nardini, M. Quiros, and C. Wagner, *Nucl. Phys.* **B812**, 243 (2009), [arXiv:0809.3760 [hep-ph]]
- [85] M. Carena, G. Nardini, M. Quiros, and C. E. Wagner, *JHEP* **1302**, 001 (2013), [arXiv:1207.6330 [hep-ph]]
- [86] D. E. Morrissey and M. J. Ramsey-Musolf, *New J. Phys.* **14**, 125003 (2012), [arXiv:1206.2942 [hep-ph]]
- [87] V. Cirigliano, S. Profumo, and M. J. Ramsey-Musolf, *JHEP* **0607**, 002 (2006), [arXiv:hep-ph/0603246 [hep-ph]]
- [88] V. Cirigliano, Y. Li, S. Profumo, and M. J. Ramsey-Musolf, *JHEP* **1001**, 002 (2010), [arXiv:0910.4589 [hep-ph]]
- [89] N. Arkani-Hamed and S. Dimopoulos, *JHEP* **0506**, 073 (2005), [arXiv:hep-th/0405159 [hep-th]]
- [90] G. F. Giudice and A. Romanino, *Nucl. Phys.* **B699**, 65 (2004), [arXiv:hep-ph/0406088 [hep-ph]]
- [91] N. Arkani-Hamed, S. Dimopoulos, G. F. Giudice, and A. Romanino, *Nucl. Phys.* **B709**, 3 (2005), [arXiv:hep-ph/0409232 [hep-ph]]
- [92] G. F. Giudice and A. Romanino, *Phys. Lett.* **B634**, 307 (2006), [arXiv:hep-ph/0510197 [hep-ph]]
- [93] O. Lebedev and M. Pospelov, *Phys. Rev. Lett.* **89**, 101801 (2002), [arXiv:hep-ph/0204359 [hep-ph]]
- [94] D. A. Demir, O. Lebedev, K. A. Olive, M. Pospelov, and A. Ritz, *Nucl. Phys.* **B680**, 339 (2004), [arXiv:hep-ph/0311314 [hep-ph]]
- [95] U. Ellwanger, C. Hugonie, and A. M. Teixeira, *Phys. Rept.* **496**, 1 (2010), [arXiv:0910.1785 [hep-ph]]
- [96] M. Dine, N. Seiberg, and S. Thomas, *Phys. Rev.* **D76**, 095004 (2007), [arXiv:0707.0005 [hep-ph]]
- [97] K. Blum, C. Delaunay, M. Losada, Y. Nir, and S. Tulin, *JHEP* **1005**, 101 (2010), [arXiv:1003.2447 [hep-ph]]
- [98] W. Altmannshofer, M. Carena, S. Gori, and A. de la Puente, *Phys. Rev.* **D84**, 095027 (2011), [arXiv:1107.3814 [hep-ph]]
- [99] W. Altmannshofer and M. Carena, *Phys. Rev.* **D85**, 075006 (2012), [arXiv:1110.0843 [hep-ph]]

- [100] S. J. Huber, T. Konstandin, T. Prokopec, and M. G. Schmidt, Nucl. Phys. **B757**, 172 (2006), [arXiv:hep-ph/0606298 [hep-ph]]
- [101] M. Pietroni, Nucl. Phys. **B402**, 27 (1993), [arXiv:hep-ph/9207227 [hep-ph]]
- [102] A. T. Davies, C. D. Froggatt, and R. G. Moorhouse, Phys. Lett. **B372**, 88 (1996), [arXiv:hep-ph/9603388 [hep-ph]]
- [103] S. J. Huber and M. G. Schmidt, Nucl. Phys. **B606**, 183 (2001), [arXiv:hep-ph/0003122 [hep-ph]]
- [104] J. Kang, P. Langacker, T.-J. Li, and T. Liu, Phys. Rev. Lett. **94**, 061801 (2005), [arXiv:hep-ph/0402086 [hep-ph]]
- [105] A. Menon, D. E. Morrissey, and C. E. M. Wagner, Phys. Rev. **D70**, 035005 (2004), [arXiv:hep-ph/0404184 [hep-ph]]
- [106] P. Kumar and E. Pontón, JHEP **1111**, 037 (2011), [arXiv:1107.1719 [hep-ph]]
- [107] S. J. Huber, T. Konstandin, T. Prokopec, and M. G. Schmidt, Nucl. Phys. **A785**, 206 (2007), [arXiv:hep-ph/0608017 [hep-ph]]
- [108] S. Profumo, M. J. Ramsey-Musolf, and G. Shaughnessy, JHEP **0708**, 010 (2007), [arXiv:0705.2425 [hep-ph]]
- [109] M. Carena, N. R. Shah, and C. E. Wagner, Phys. Rev. **D85**, 036003 (2012), [arXiv:1110.4378 [hep-ph]]
- [110] G. D’Ambrosio, G. F. Giudice, G. Isidori, and A. Strumia, Nucl. Phys. **B645**, 155 (2002), [arXiv:hep-ph/0207036 [hep-ph]]
- [111] W. Altmannshofer, A. J. Buras, and P. Paradisi, Phys. Lett. **B669**, 239 (2008), [arXiv:0808.0707 [hep-ph]]
- [112] L. Mercolli and C. Smith, Nucl. Phys. **B817**, 1 (2009), [arXiv:0902.1949 [hep-ph]]
- [113] P. Paradisi and D. M. Straub, Phys. Lett. **B684**, 147 (2010), [arXiv:0906.4551 [hep-ph]]
- [114] L. J. Hall and Y. Nomura, JHEP **1201**, 082 (2012), [arXiv:1111.4519 [hep-ph]]
- [115] M. Ibe and T. T. Yanagida, Phys. Lett. **B709**, 374 (2012), [arXiv:1112.2462 [hep-ph]]
- [116] A. Arvanitaki, N. Craig, S. Dimopoulos, and G. Villadoro, JHEP **1302**, 126 (2013), [arXiv:1210.0555 [hep-ph]]
- [117] N. Arkani-Hamed, A. Gupta, D. E. Kaplan, N. Weiner, and T. Zorawski, “Simply unnatural supersymmetry,” (2012), arXiv:1212.6971 [hep-ph]
- [118] D. McKeen, M. Pospelov, and A. Ritz, Phys. Rev. **D87**, 113002 (2013), [arXiv:1303.1172 [hep-ph]]
- [119] W. Altmannshofer, R. Harnik, and J. Zupan(2013), in preparation

- [120] A. Romanino and A. Strumia, Nucl. Phys. **B622**, 73 (2002), [arXiv:hep-ph/0108275 [hep-ph]]
- [121] G. Hiller, K. Huitu, T. Ruppell, and J. Laamanen, Phys. Rev. **D82**, 093015 (2010), [arXiv:1008.5091 [hep-ph]]
- [122] M. A. Rosenberry and T. E. Chupp, Phys. Rev. Lett. **86**, 22 (2001)
- [123] M. Kitano *et al.*, Phys. Rev. Lett. **60**, 2133 (1988)
- [124] E. R. Tardiff *et al.*, Phys. Rev. **C77**, 052501(R) (2008)
- [125] V. Spevak, N. Auerbach, and V. V. Flambaum, Phys. Rev. **C56**, 1357 (1997), [arXiv:nucl-th/9612044 [nucl-th]]
- [126] J. R. Guest *et al.*, Phys. Rev. Lett. **98**, 093001 (2007)
- [127] S. De, U. Dammalapati, K. Jungmann, and L. Willmann, Phys. Rev. **A79**, 041402(R) (2009)
- [128] M. V. Romalis and E. N. Fortson, Phys. Rev. **A59**, 4547 (2009)
- [129] R. H. Parker *et al.*, Phys. Rev. **C86**, 065503 (2012)
- [130] B. Mustapha and J. A. Nolen, Nucl. Instrum. Meth. A **521**, 59 (2004)
- [131] J. L. Hewett, H. Weerts, *et al.*, *Fundamental Physics at the Intensity Frontier* (U.S. Department of Energy, Germantown, MD, 2012) arXiv:1205.2671 [hep-ex]
- [132] R. Golub and K. Lamoreaux, Phys. Rept. **237**, 1 (1994)
- [133] J. D. Jackson, *Classical Electrodynamics*, 3rd ed. (John Wiley, New York, 1998)
- [134] V. Bargmann, L. Michel, and V. L. Telegdi, Phys. Rev. Lett. **2**, 435 (1959)
- [135] F. J. M. Farley *et al.*, Phys. Rev. Lett. **93**, 052001 (2004), [arXiv:hep-ex/0307006 [hep-ex]]
- [136] Storage Ring EDM Collaboration, <http://www.bnl.gov/edm/>
- [137] N. P. M. Brantjes *et al.*, Nucl. Instrum. Meth. A **664**, 49 (2012)
- [138] Y. Orlov, private communication.
- [139] B. M. Dunham *et al.*, “Performance of a very high voltage photoemission electron gun for a high brightness, high average current erl injector,” Proceedings of PAC07, TUPMS021
- [140] M. Bastani Nejad *et al.*, Phys. Rev. STAB **15**, 083502 (2012)
- [141] W. A. Bardeen and S.-H. H. Tye, Phys. Lett. **B74**, 229 (1978)
- [142] J. Kandaswamy, P. Salomonson, and J. Schechter, Phys. Rev. **D17**, 3051 (1978)
- [143] J. Preskill, M. B. Wise, and F. Wilczek, Phys. Lett. **B120**, 127 (1983)
- [144] L. F. Abbott and P. Sikivie, Phys. Lett. **B120**, 133 (1983)

- [145] M. Dine and W. Fischler, Phys. Lett. **B120**, 137 (1983)
- [146] P. Fox, A. Pierce, and S. D. Thomas, “Probing a QCD string axion with precision cosmological measurements,” (2004), arXiv:hep-th/0409059 [hep-th]
- [147] S. Thomas, private communication.
- [148] P. Graham, “Axion detection with NMR,” SnowDARK (2013), <http://www.physics.utah.edu/snowpac/index.php/snowdark-2013/snowdark-2013-talks-slides>
- [149] C. Y. Liu and S. K. Lamoreaux, Mod. Phys. Lett. A **19**, 1235 (2004)
- [150] F. L. Shapiro, Soviet Physics Uspekhi **11**, 345 (1968)
- [151] S. Y. Buhmann, V. A. Dzuba, and O. P. Sushkov, Phys. Rev. **A66**, 042109 (2002)
- [152] A. O. Sushkov, S. Eckel, and S. K. Lamoreaux, Phys. Rev. A **79**, 022118 (2009)
- [153] A. O. Sushkov, S. Eckel, and S. K. Lamoreaux, Phys. Rev. A **81**, 022104 (2010)
- [154] T. N. Mukhamedjanov and O. P. Sushkov, Phys. Rev. A **72**, 034501 (2005)
- [155] B. J. Heidenreich *et al.*, Phys. Rev. Lett. **95**, 253004 (2005)
- [156] S. Gardner and D. He, Phys. Rev. **D86**, 016003 (2012), [arXiv:1202.5239 [hep-ph]]
- [157] S. Gardner and D. He, “ T -odd momentum correlation in nuclear radiative β decay,” (2013), in preparation
- [158] J. A. Harvey, C. T. Hill, and R. J. Hill, Phys. Rev. Lett. **99**, 261601 (2007), [arXiv:0708.1281 [hep-ph]]
- [159] J. A. Harvey, C. T. Hill, and R. J. Hill, Phys. Rev. **D77**, 085017 (2008), [arXiv:0712.1230 [hep-th]]
- [160] S. Gardner and D. He, Phys. Rev. **D88**, to appear (2013), [arXiv:1302.1862 [hep-ph]]

VI Neutron-Antineutron Oscillations with *Project X*

Yuri Kamyshkov, Chris Quigg, William M. Snow, Albert R. Young,
Usama Al-Binni, Kaladi Babu, Sunanda Banerjee, David V. Baxter, Zurab Berezhiani,
Marc Bergevin, Sudeb Bhattacharya, Stephen J. Brice, Thomas W. Burgess, Luis A. Castellanos,
Subhasis Chattopadhyay, Mu-Chun Chen, Christopher E. Coppola, Ramanath Cowsik,
J. Allen Crabtree, Alexander Dolgov, Georgi Dvali, Phillip D. Ferguson, Tony Gabriel,
Avraham Gal, Franz Gallmeier, Kenneth S. Ganezer, Elena S. Golubeva, Van B. Graves,
Geoffrey Greene, Cory L. Griffard, Thomas Handler, Brandon Hartfiel, Ayman Hawari,
Lawrence Heilbronn, James E. Hill, Christian Johnson, Boris Kerbikov, Boris Kopeliovich,
Vladimir Kopeliovich, Wolfgang Korsch, Chen-Yu Liu, Rabindra Mohapatra, Michael Mocko,
Nikolai V. Mokhov, Guenter Muhrer, Pieter Mumm, Lev Okun, Robert W. Pattie Jr.,
David G. Phillips II, Erik Ramberg, Amlan Ray, Amit Roy, Arthur Ruggles, Utpal Sarkar,
Andy Saunders, Anatoly Serebrov, Hirohiko Shimizu, Robert Shrock, Arindam K. Sikdar,
Aria Soha, Stefan Spanier, Sergei Striganov, Zhaowen Tang, Lawrence Townsend,
Robert S. Tschirhart, Arkady Vainshtein, Richard J. Van Kooten, and Bernard Wehring

VI.1 INTRODUCTION

An observation of neutron-antineutron ($n-\bar{n}$) transformation would constitute a discovery of fundamental importance for cosmology and particle physics. It would provide the first direct experimental evidence for baryon number (\mathcal{B}) violation, and would qualitatively change our ideas of the scales relevant for quark-lepton unification and neutrino mass generation. If seen at rates achievable in next-generation searches, $n-\bar{n}$ transformation must be taken into account for any quantitative understanding of the baryon asymmetry of the universe. A discovery of this process would also prove that all nuclei are ultimately unstable. In fact, a search for $n-\bar{n}$ oscillations using free neutrons at *Project X* possesses excellent potential in exploring the stability of matter. A limit on the free-neutron oscillation time $\tau_{n-\bar{n}} > 10^{10}$ s, which appears to be within the range of the next generation of experiments described in this chapter, would correspond to a limit on matter stability of $T_A = 1.6 - 3.1 \times 10^{35}$ yrs [1,2].

Project X presents an opportunity to probe $n-\bar{n}$ transformation with free neutrons with an unprecedented improvement in sensitivity. Improvements would be achieved by creating a unique facility, combining a high-intensity cold-neutron source *dedicated* to particle physics experiments with advanced neutron-optics technology and detectors which build on the demonstrated capability to detect antineutron annihilation events with zero background. Existing slow-neutron sources at research reactors and spallation sources possess neither the required space nor the degree of access to the cold source needed to take full advantage of advanced neutron-optics technology which enables a greatly improved free $n-\bar{n}$ transformation search experiment. Therefore, a dedicated source devoted exclusively to fundamental neutron physics, such as would be available at *Project X*, repre-

sents an exciting tool to explore not only $n-\bar{n}$ oscillations, but also other Intensity Frontier questions accessible through slow neutrons.

The current best limit on $n-\bar{n}$ oscillations comes from the Super-Kamiokande experiment, which determined an upper bound on the free-neutron oscillation time of $\tau_{n-\bar{n}} > 3.5 \times 10^8$ s from $n-\bar{n}$ transformation in ^{16}O nuclei [2,3]. An important point for underground detector measurements is that these experiments are already limited in part by atmospheric neutrino backgrounds. Because only modest increments in detector mass over Super-Kamiokande are feasible and the atmospheric neutrino backgrounds will scale with the detector mass, dramatic improvements in the current limit will be challenging for underground experiments.

Experiments that utilize free neutrons to search for $n-\bar{n}$ oscillations have a number of remarkable features. The basic idea for these experiments (we go into much greater detail in Sections VI.2 and VI.3) is to prepare a beam of slow (below room temperature) neutrons which propagate freely from the exit of a neutron guide to a distant annihilation target. During the time in which the neutron propagates freely, a \mathcal{B} -violating interaction can produce oscillations from a pure “ n ” state to one with an admixture of “ n ” and “ \bar{n} ” amplitudes. Antineutron appearance is sought through annihilation in a thin target, which generates a star pattern of several secondary pions seen by a tracking detector situated around the target. This signature strongly suppresses backgrounds. We note that, to observe this signal, the “quasi-free” condition must hold, in which the n and \bar{n} are effectively degenerate in energy. This creates a requirement for low pressures (below roughly 10^{-5} Pa for *Project X*) and very small ambient magnetic fields (between 1 and 10 nT for *Project X*) in order to prevent level splittings between the neutron and antineutron from damping the oscillations. Advantages of a new $n-\bar{n}$ oscillation search experiment at *Project X* would include:

- detection of annihilation events with zero background (see discussion next paragraph), maximizing the discovery potential for these experiments,
- a systematic cross-check of a non-zero $n-\bar{n}$ signal is possible by a modest increase in the magnetic field, which damps out oscillations,
- and orders of magnitude improvement in sensitivity over the current free-neutron limit through the use of cutting-edge neutron optics, greatly increasing the neutron integrated flux and average transit time to the annihilation target.

These advantages provide a strong motivation to search for $n-\bar{n}$ oscillations as a part of *Project X*.

The current best limit for an experimental search for free $n-\bar{n}$ oscillations was performed at the ILL in Grenoble in 1994 [4] (see Fig. VI-1). This experiment used a cold neutron beam from their 58 MW research reactor with a neutron current of 1.25×10^{11} n/s incident on the annihilation target and gave a limit of $\tau_{n-\bar{n}} > 0.86 \times 10^8$ s [4]. The average velocity of the cold neutrons was ~ 600 m/s and the average neutron observation time was ~ 0.1 s. A vacuum of $P \simeq 2 \times 10^{-4}$ Pa maintained in the neutron flight volume and a magnetic field of $|\mathbf{B}| < 10$ nT satisfied the quasi-free conditions for oscillations to occur. Antineutron appearance was sought through annihilation with a $\sim 130\text{-}\mu\text{m}$ thick carbon-film target that generated at least two tracks (one due to a charged particle) in the tracking detector with a total energy above 850 MeV in the surrounding calorimeter. In one year of operation the ILL experiment saw zero candidate events with zero background.

An $n-\bar{n}$ oscillation search experiment at *Project X* (NNbarX) is conceived of as a two-stage experiment. The neutron spallation target/moderator/reflector system and the experimental apparatus need to be designed together in order to optimize the sensitivity of the experiment. The target system and the first-stage experiment can be built and start operation during the commissioning of the first-stage of *Project X*, which is based on a 1-GeV proton beam Linac operating at 1 mA. The first-stage of NNbarX will be a horizontal experiment with configuration similar to the ILL experiment performed in the 1990s, but employing modernized technologies that include an optimized slow-neutron target/moderator/reflector system and an elliptical supermirror neutron-focusing reflector. Our very conservative baseline goal for a first-stage experiment is a factor of 30 improvement of the sensitivity (probability of appearance) for $n-\bar{n}$ oscillations beyond the limits obtained in the ILL experiment. This level of sensitivity would also surpass the $n-\bar{n}$ oscillation limits obtained in the Super-Kamiokande, Soudan-II, and SNO intranuclear searches [3,5,6]. In fact, although still in progress, our optimization studies indicate that this horizontal geometry is capable of improvements of a factor of 300 or more in 3 years of operation at *Project X*. A future, second stage of an NNbarX experiment can achieve higher sensitivity by exploiting a vertical layout and a moderator/reflector system that can make use of colder neutrons and ultracold neutrons (UCN) for the $n-\bar{n}$ search. This experimental arrangement involves new technologies that will require a dedicated R&D campaign, but the sensitivity of NNbarX should improve by another factor of ~ 100 with this configuration, corresponding to limits for the oscillation time parameter $\tau_{n-\bar{n}} > 10^{10}$ s.

In what follows we present a more detailed analysis of the theoretical formalism and motivation for measurements of $n-\bar{n}$ oscillations. We then proceed to a more detailed description of our

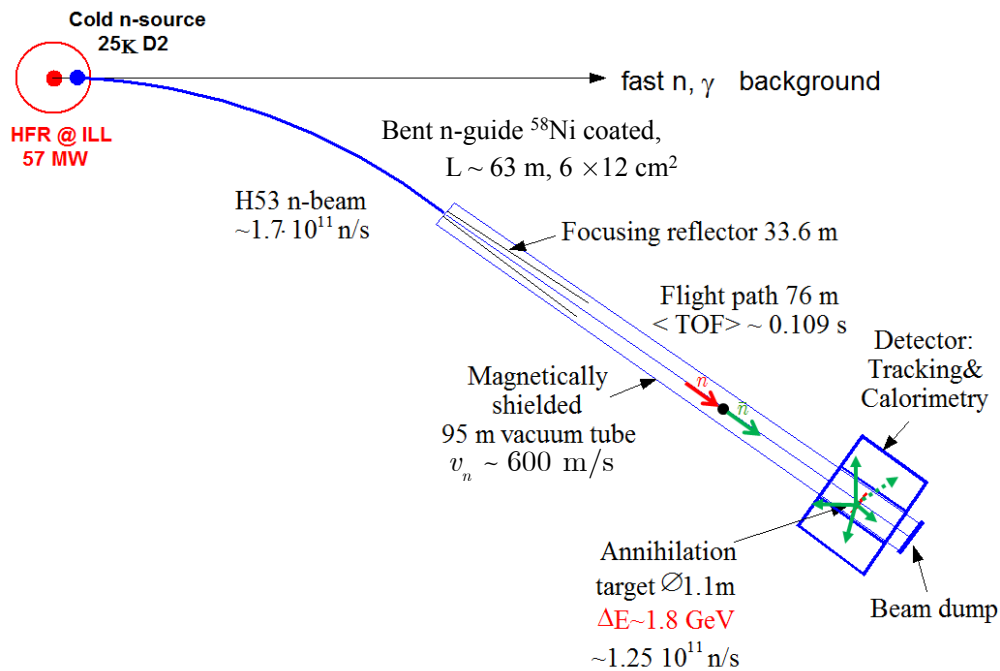


Figure VI-1: Configuration of the horizontal $n-\bar{n}$ search experiment at ILL/Grenoble [4], published in 1994.

VI.2 PHYSICS MOTIVATION FOR n - \bar{n} OSCILLATION SEARCHES

The search for neutron–antineutron oscillations [7–9] may illuminate two of the great mysteries of particle physics and cosmology: the great stability of ordinary matter and the origin of the preponderance of matter over antimatter in the universe. Processes that violate baryon number and lepton number must be highly suppressed, but they must be present if the observed matter excess evolved from an early universe in which matter and antimatter were in balance [10–12]. The primitive interactions of quantum chromodynamics and the electroweak theory conserve baryon number \mathcal{B} and lepton number \mathcal{L} , but we have not identified a dynamical principle or symmetry that compels conservation of either baryon number or lepton number.

Indeed, grand unified theories (GUTs) [13,14] and nonperturbative effects in the Standard Model itself lead to baryon number violation [15–17]. The baryon-number–violating effects in all these models appear with a very weak strength so that stability of atoms such as hydrogen, helium, etc., is not significantly affected on the time scale of the age of the universe. The discovery that neutrino species mix, which demonstrates that individual (e, μ, τ) lepton numbers are not conserved, leaves open the possibility that overall lepton number is conserved. The observation of neutrinoless double-beta decay would establish \mathcal{L} nonconservation. Once we accept the possibility that baryon number is not a good symmetry of nature, there are many questions that must be explored to decide the nature of physics associated with \mathcal{B} -violation:

- Is (a nonanomalous extension of) baryon number, \mathcal{B} , a global or local symmetry?
- Does baryon number occur as a symmetry by itself or does it appear in combination with lepton number, \mathcal{L} , i.e. $\mathcal{B} - \mathcal{L}$, as the Standard Model (SM) would suggest?
- What is the scale of baryon-number violation and the nature of the associated physics that is responsible for it? For example, is this physics characterized by a mass scale not too far above the TeV scale, so that it can be probed in experiments already searching for new physics in colliders as well as low energy rare processes?
- Are the details of the physics responsible for baryon-number violation such that they can explain the origin of matter ?

Proton-decay searches probe baryon-number violation due to physics at a grand unified scale of $\sim 10^{15}$ - 10^{16} GeV. In contrast, the baryon-number–violating process of n - \bar{n} oscillation, where a free neutron spontaneously transmutes itself into an anti-neutron, has very different properties and probes quite different physics; for one thing it violates baryon number by two units and is caused by operators that have mass dimension nine so that it probes new physics at mass scales ~ 1 TeV and above. Therefore it can be probed by experiments searching for new physics at this scale. Secondly, it may be deeply connected to the possibility that neutrinos may be Majorana fermions, a natural expectation. A key question for experiments is whether there are theories that predict n - \bar{n} oscillations at a level that can be probed in currently available facilities such as reactors or in contemplated ones such as *Project X* at Fermilab, with intense neutron fluxes. Equally important to know is what conclusion can be drawn about physics beyond the Standard Model if no signal appears after the free-neutron oscillation time is improved by two orders of magnitude above the current limit of $\sim 10^8$ s.

VI.2.1 Some Background Concerning Baryon Number Violation

Early on, it was observed that in a model with a left-right symmetric electroweak group, $G_{\text{LR}} = \text{SU}(2)_{\text{L}} \times \text{SU}(2)_{\text{R}} \times \text{U}(1)_{\mathcal{B}-\mathcal{L}}$, baryon and lepton numbers in the combination $\mathcal{B} - \mathcal{L}$ can be gauged in an anomaly-free manner. The resultant $\text{U}(1)_{\mathcal{B}-\mathcal{L}}$ can be combined with color $\text{SU}(3)$ in an $\text{SU}(4)$ gauge group [18], giving rise to the group $G_{422} = \text{SU}(4) \times \text{SU}(2)_{\text{L}} \times \text{SU}(2)_{\text{R}}$ [18–20]. A higher degree of unification involved models that embed either the Standard Model gauge group $G_{\text{SM}} = \text{SU}(3)_{\text{c}} \times \text{SU}(2)_{\text{L}} \times \text{U}(1)_{\text{Y}}$ or G_{422} in a simple group such as $\text{SU}(5)$ or $\text{SO}(10)$ [13,14]. The motivations for grand unification theories are well known and include the unification of gauge interactions and their couplings, the related explanation of the quantization of weak hypercharge and electric charge, and the unification of quarks and leptons. While the gauge couplings do not unify in the Standard Model, they do unify in a minimal supersymmetric extension of the Standard Model. Although supersymmetric particles have not been discovered in the 7-TeV and 8-TeV data at the Large Hadron Collider, they may still be observed at higher energy. Supersymmetric grand unified theories thus provide an appealing possible ultraviolet completion of the Standard Model. The unification of quarks and leptons in grand unified theories (GUTs) generically leads to the decay of the proton and the decay of neutrons that would otherwise be stably bound in nuclei. These decays typically obey the selection rule $\Delta\mathcal{B} = -1$ and $\Delta\mathcal{L} = -1$. However, the general possibility of a different kind of baryon-number violating process, namely the $|\Delta\mathcal{B}| = 2$ process of $n-\bar{n}$ oscillations, was suggested [7] even before the advent of GUTs. This was further discussed and studied after the development of GUTs in [8,9] and in a number of subsequent models [21–39]. Recently, a number of models have been constructed that predict $n-\bar{n}$ oscillations at levels within reach of an improved search, e.g. [29,30,33,38]. We proceed to discuss some of these.

VI.2.2 Some Models with $n-\bar{n}$ Oscillations

It was pointed out in 1980 that a class of unified theories for Majorana neutrino mass in which the seesaw mechanism operates in the TeV mass range predicts $n-\bar{n}$ oscillation transition times that are in the accessible range being probed in different experiments [23]. This model was based on the idea that $\mathcal{B} - \mathcal{L}$ is a local rather than a global symmetry. This idea is incorporated in the electroweak gauge group G_{LR} and accommodates right-handed neutrinos and an associated seesaw mechanism. The Majorana neutrino mass terms are $|\Delta\mathcal{L}| = 2$ operators and hence, in the context of the $\text{U}(1)_{\mathcal{B}-\mathcal{L}}$ gauge symmetry, it is natural that they are associated with baryon number violation by $|\Delta\mathcal{B}| = 2$. Thus, $n-\bar{n}$ oscillations are an expected feature of this model. Detailed analysis of the model shows that it naturally predicts the existence of TeV-scale color-sextet Higgs particles that can be probed at the LHC.

The question of how restrictive the range of neutron oscillation time is in this class of models has recently been investigated by requiring that the model also explain the observed matter-anti-matter asymmetry. The basic idea is that since $n-\bar{n}$ oscillations are a TeV-scale \mathcal{B} -violating phenomenon, they will remain in equilibrium in the thermal plasma down to very low temperatures in the early universe. Hence, in combination with Standard-Model baryon-number-violating processes they will erase any pre-existing baryon asymmetry in the universe. Therefore in models with observable $n-\bar{n}$ oscillation, one must search for new ways to generate a matter-antimatter asymmetry near or below the weak scale. Such a mechanism was proposed in a few recent papers [32,35,37], where it was

shown that high-dimensional operators that lead to processes such as neutron oscillation can indeed generate a baryon asymmetry via a mechanism called post-sphaleron baryogenesis. This mechanism specifically applies to the class of G_{422} models for neutron oscillation discussed in Ref. [23], as well as to other models for neutron oscillation.

Because of quark-lepton unification, the field responsible for the seesaw mechanism now has color-sextet partners. The neutral scalar field, which breaks $\mathcal{B} - \mathcal{L}$ gauge symmetry to generate neutrino masses has couplings to these colored scalars and decays slowly to the six-quark states via the exchange of virtual color sextet fields. This decay in combination with CP violation is ultimately responsible for baryogenesis. Due to its slowness, the decay cannot, however, compete with the Hubble expansion until the universe cools below the weak scale. The cosmological requirements for baryogenesis then impose strong constraints on the parameters of the model and predict that there must be an *upper limit* on the free-neutron oscillation time of 5×10^{10} s [38], while for most of the parameter range it is below 10^{10} s. Essentially what happens is that if the neutron oscillation time exceeds this bound, then the magnitude of the baryon asymmetry becomes smaller than the observed value or the color symmetry of the model breaks down, neither of which is acceptable for a realistic theory. It may therefore be concluded that if the search for $n-\bar{n}$ oscillation up to a transition time of 10^{10} s comes out to be negative, this class of interesting neutrino mass models will be ruled out.

A different type of model that predicts $n-\bar{n}$ oscillations at a rate close to current limits involves an extra-dimensional theoretical framework [30]. Although current experimental data are fully consistent with a four-dimensional Minkowski spacetime, it is useful to explore the possibility of extra dimensions, both from a purely phenomenological point of view and because the main candidate theory for quantum gravity—string theory—suggests the existence of higher dimensions. Ref. [30] focuses on theories in which standard-model fields can propagate in extra dimensions and the wave functions of standard-model fermions have strong localization at various points in this extra-dimensional space. The effective size of the extra dimension(s) is denoted L ; the associated mass parameter $\Lambda_L = L^{-1}$ can be $\sim 50\text{--}100$ TeV. Such models are of interest partly because they can provide a mechanism for obtaining a hierarchy in fermion masses and quark mixing. In generic models of this type, excessively rapid proton decay can be avoided by arranging that the wavefunction centers of the u and d quarks are separated far from those of the e and μ . However, as was pointed out in Ref. [30], this does not guarantee adequate suppression of $n-\bar{n}$ oscillations. Indeed, for typical values of the parameters of the model, it was shown that $n-\bar{n}$ oscillations occur at levels that are in accord with the current experiment limit but not too far below this limit. One of the interesting features of this model is that it is an example of a theory in which proton decay is negligible, while $n-\bar{n}$ oscillations could be observable at levels close to current limits. Other models of this type have recently been studied in [39]. These models have scalar fields in two representations of $SU(2) \times SU(2) \times U(1)$ and violate baryon number by two units. Some of the models give rise to $n-\bar{n}$ oscillations, while some also violate lepton number by two units. The range of scalar masses for which $n-\bar{n}$ oscillations are measurable in the next generation of experiments is also discussed in [39]. In extra dimensional models with low scale gravity, neutron-antineutron oscillations are predicted to occur 1–2 orders of magnitude less frequently than current experimental limits [40].

We conclude that there is strong motivation to pursue a higher-sensitivity $n-\bar{n}$ oscillation search experiment that can achieve a lower bound of $\tau_{n-\bar{n}} \gtrsim 10^9\text{--}10^{10}$ s.

VI.2.3 General Formalism for Analyzing n - \bar{n} Oscillations

VI.2.3.1 Oscillations in a Field-Free Vacuum

We denote the effective Hamiltonian that is responsible for n - \bar{n} oscillations as H_{eff} . This has the diagonal matrix elements

$$\langle n|H_{\text{eff}}|n\rangle = \langle \bar{n}|H_{\text{eff}}|\bar{n}\rangle = m_n - \frac{i\lambda}{2}, \quad (\text{VI.2.1})$$

where $\lambda^{-1} = \tau_n = 0.88 \times 10^3$ s is the mean life of a free neutron. Here we assume CPT invariance, so that $m_n = m_{\bar{n}}$. The transition matrix elements are taken to be real and are denoted

$$\langle \bar{n}|H_{\text{eff}}|n\rangle = \langle n|H_{\text{eff}}|\bar{n}\rangle \equiv \delta m. \quad (\text{VI.2.2})$$

Consider the 2×2 matrix

$$\mathcal{M}_{\mathcal{F}} = \begin{pmatrix} m_n - i\lambda/2 & \delta m \\ \delta m & m_n - i\lambda/2 \end{pmatrix} \quad (\text{VI.2.3})$$

Diagonalizing this matrix $\mathcal{M}_{\mathcal{F}}$ yields the mass eigenstates

$$|n_{\pm}\rangle = \frac{|n\rangle \pm |\bar{n}\rangle}{\sqrt{2}} \quad (\text{VI.2.4})$$

with mass eigenvalues

$$m_{\pm} = (m_n \pm \delta m) - \frac{i\lambda}{2}. \quad (\text{VI.2.5})$$

Hence, if one starts with a pure $|n\rangle$ state at $t = 0$, then there is a finite probability P for it to be an $|\bar{n}\rangle$ at $t \neq 0$ given by

$$P_{\bar{n} \leftarrow n}(t) = |\langle \bar{n}|n(t)\rangle|^2 = \sin^2(t/\tau_{n-\bar{n}})e^{-\lambda t}, \quad (\text{VI.2.6})$$

where

$$\tau_{n-\bar{n}} = \frac{1}{|\delta m|}. \quad (\text{VI.2.7})$$

Neutron–antineutron oscillations would likewise be inhibited by a neutron–antineutron mass difference. Should oscillations be observed, $\tau_{n-\bar{n}}$ can also be interpreted as a limit on $|m_n - m_{\bar{n}}|$, and so test CPT invariance [41].

Current lower limits on the oscillation lifetime, $\tau_{n-\bar{n}} \gtrsim 10^8$ s, greatly exceed the lifetime for β -decay of the free neutron.

VI.2.3.2 Oscillations in a Magnetic Field

We next review the formalism for the analysis of n - \bar{n} oscillations in an external magnetic field [23, 24]. This formalism is relevant for an experiment searching for n - \bar{n} oscillations using neutrons that propagate some distance in a vacuum pipe, because although one must use degaussing methods to greatly reduce the magnitude of the magnetic field in the pipe, it still plays an important role in

setting the parameters of the experiment. This formalism is relevant for both the ILL experiment at Grenoble and NNbarX.

The n and \bar{n} interact with the external \mathbf{B} field through their magnetic dipole moments, $\boldsymbol{\mu}_{n,\bar{n}}$, where $\mu_n = -\mu_{\bar{n}} = -1.9\mu_N \approx 6 \times 10^{-14}$ MeV/Tesla. Hence, the matrix \mathcal{M}_B now takes the form

$$\mathcal{M}_B = \begin{pmatrix} m_n - \boldsymbol{\mu}_n \cdot \mathbf{B} - i\lambda/2 & \delta m \\ \delta m & m_n + \boldsymbol{\mu}_n \cdot \mathbf{B} - i\lambda/2 \end{pmatrix} \quad (\text{VI.2.8})$$

Diagonalizing this mass matrix yields mass eigenstates

$$|n_1\rangle = \cos\theta |n\rangle + \sin\theta |\bar{n}\rangle \quad (\text{VI.2.9})$$

and

$$|n_2\rangle = -\sin\theta |n\rangle + \cos\theta |\bar{n}\rangle, \quad (\text{VI.2.10})$$

where

$$\tan(2\theta) = -\frac{\delta m}{\boldsymbol{\mu}_n \cdot \mathbf{B}}. \quad (\text{VI.2.11})$$

The eigenvalues are

$$m_{1,2} = m_n \pm \sqrt{(\boldsymbol{\mu}_n \cdot \mathbf{B})^2 + (\delta m)^2} - \frac{i\lambda}{2}. \quad (\text{VI.2.12})$$

Experiments typically reduced the magnitude of the magnetic field to $|\mathbf{B}| \sim 10^{-4}$ G = 10^{-8} T, so $|\boldsymbol{\mu}_n \cdot \mathbf{B}| \simeq 10^{-21}$ MeV. Since one knows from the experimental bounds that $|\delta m| \lesssim 10^{-29}$ MeV, which is much smaller than $|\boldsymbol{\mu}_n \cdot \mathbf{B}|$, it follows that $|\theta| \ll 1$. Thus,

$$\Delta E \equiv m_1 - m_2 = 2\sqrt{(\boldsymbol{\mu}_n \cdot \mathbf{B})^2 + (\delta m)^2} \simeq 2|\boldsymbol{\mu}_n \cdot \mathbf{B}|. \quad (\text{VI.2.13})$$

The transition probability is then

$$P_{\bar{n} \leftarrow n}(t) = \sin^2(2\theta) \sin^2[(\Delta E)t/2] e^{-\lambda t}. \quad (\text{VI.2.14})$$

In a free propagation experiment, one arranges that the neutrons propagate for a time t such that $|\boldsymbol{\mu}_n \cdot \mathbf{B}|t \ll 1$ and also $t \ll \tau_n$. Then,

$$P_{\bar{n} \leftarrow n}(t) \approx (2\theta)^2 \left(\frac{\Delta E t}{2}\right)^2 \simeq \left(\frac{\delta m}{\boldsymbol{\mu}_n \cdot \mathbf{B}}\right)^2 \left(\boldsymbol{\mu}_n \cdot \mathbf{B} t\right)^2 = [(\delta m)t]^2 = (t/\tau_{n-\bar{n}})^2. \quad (\text{VI.2.15})$$

Then the number of \bar{n} 's produced by the n - \bar{n} oscillations is given essentially by $N_{\bar{n}} = P_{\bar{n} \leftarrow n}(t)N_n$, where N_n is the number of neutrons observed. The sensitivity of the experiment is proportional to the square of the propagation time t , so, with adequate magnetic shielding, one wants to maximize t , subject to the condition that $|\boldsymbol{\mu}_n \cdot \mathbf{B}|t \ll 1$.

VI.2.3.3 Oscillations in Matter

To put the proposed free propagation n - \bar{n} oscillation experiment in perspective, it is appropriate to review limits that have been achieved in the search for n - \bar{n} oscillations in matter, using large nucleon-decay detectors. In matter, the matrix \mathcal{M}_A takes the form

$$\mathcal{M}_A = \begin{pmatrix} m_{n\text{eff}} & \delta m \\ \delta m & m_{\bar{n}\text{eff}} \end{pmatrix} \quad (\text{VI.2.16})$$

with

$$m_{n\text{eff}} = m_n + V_n, \quad m_{\bar{n}\text{eff}} = m_n + V_{\bar{n}}. \quad (\text{VI.2.17})$$

The nuclear potential V_n is practically real, $V_n = V_{nR}$, but $V_{\bar{n}}$ has an imaginary part representing the $\bar{n}N$ annihilation,

$$V_{\bar{n}} = V_{\bar{n}R} - iV_{\bar{n}I}, \quad (\text{VI.2.18})$$

with [1,2,26]

$$V_{nR}, V_{\bar{n}R}, V_{\bar{n}I} \sim \text{O}(100) \text{ MeV}. \quad (\text{VI.2.19})$$

The mixing is thus strongly suppressed; $\tan(2\theta)$ is determined by

$$\frac{2\delta m}{|m_{n\text{eff}} - m_{\bar{n}\text{eff}}|} = \frac{2\delta m}{\sqrt{(V_{nR} - V_{\bar{n}R})^2 + V_{\bar{n}I}^2}} \ll 1. \quad (\text{VI.2.20})$$

Using the upper bound on $|\delta m|$ from the ILL reactor experiment, this gives $|\theta| \lesssim 10^{-31}$. This suppression in mixing is compensated for by the large number of nucleons in a nucleon decay detector such as Soudan-2 [5] or Super-Kamiokande [3] e.g., $\sim 10^{33}$ neutrons in the (fiducial part of the) Super-Kamiokande detector.

The eigenvalues of \mathcal{M}_A are

$$m_{1,2} = \frac{1}{2} \left[m_{n\text{eff}} + m_{\bar{n}\text{eff}} \pm \sqrt{(m_{n\text{eff}} - m_{\bar{n}\text{eff}})^2 + 4(\delta m)^2} \right]. \quad (\text{VI.2.21})$$

Expanding m_1 for the mostly- n mass eigenstate $|n_1\rangle \simeq |n\rangle$, one obtains

$$m_1 \simeq m_n + V_n - i \frac{(\delta m)^2 V_{\bar{n}I}}{(V_{nR} - V_{\bar{n}R})^2 + V_{\bar{n}I}^2}. \quad (\text{VI.2.22})$$

The imaginary part leads to matter instability via annihilation of the \bar{n} , producing mainly pions (with mean multiplicity $\langle n_\pi \rangle \simeq 4 - 5$). The rate for this is

$$\Gamma_m = \frac{1}{\tau_m} = \frac{2(\delta m)^2 |V_{\bar{n}I}|}{(V_{nR} - V_{\bar{n}R})^2 + V_{\bar{n}I}^2}. \quad (\text{VI.2.23})$$

Thus, $\tau_m = 1/\Gamma_m \propto (\delta m)^{-2}$. Writing

$$\tau_m = R \tau_{n-\bar{n}}^2, \quad (\text{VI.2.24})$$

one has

$$R \simeq 100 \text{ MeV}, \quad (\text{VI.2.25})$$

i.e.,

$$R \simeq 1.5 \times 10^{23} \text{ s}^{-1} . \quad (\text{VI.2.26})$$

The lower bound on $\tau_{n-\bar{n}}$ from $n-\bar{n}$ searches in reactor experiments yields a lower bound on τ_m and vice versa. With estimated inputs for V_{nR} , $V_{\bar{n}R}$, and $V_{\bar{n}l}$ from nuclear calculations, $\tau_{n-\bar{n}} > 0.86 \times 10^8$ s yields $\tau_m \gtrsim 2 \times 10^{31}$ yr.

Limits on matter instability due to $n-\bar{n}$ oscillations have been reported by several nucleon decay experiments [42]. The signature is the emission of an energy of $2m_n \simeq 2$ GeV, mainly in the form of pions. However, these are emitted from a point within the nucleus (oxygen in a water Cherenkov detector and mainly iron in the Soudan detector), and interact as they propagate through the nucleus. Thus, modeling this process is complicated. In 2002, the Soudan experiment reported the bound [5]

$$\tau_m > 0.72 \times 10^{32} \text{ yr (90\% CL)} . \quad (\text{VI.2.27})$$

Using the relation

$$\tau_{n-\bar{n}} = \sqrt{\frac{\tau_m}{R}} , \quad (\text{VI.2.28})$$

this is equivalent to $\tau_{n-\bar{n}} \gtrsim 1.3 \times 10^8$ s. In 2011, the Super-Kamiokande experiment reported a limit [3]

$$\tau_m > 1.9 \times 10^{32} \text{ yr (90\% CL)} , \quad (\text{VI.2.29})$$

equivalent to $\tau_{n-\bar{n}} \gtrsim 2.4 \times 10^8$ s [1], or $\tau_{n-\bar{n}} \gtrsim 3.5 \times 10^8$ s [2].

The envisioned free neutron propagation experiment has the potential to improve substantially on these limits. Achieving sensitivities of $\tau_{n-\bar{n}} \sim 10^9$ s to 10^{10} s would be roughly equivalent to

$$\tau_m \simeq (1.6 - 3.1 \times 10^{33} \text{ yr}) \left(\frac{\tau_{n-\bar{n}}}{10^9 \text{ s}} \right)^2 . \quad (\text{VI.2.30})$$

A field-theoretic approach to the $n-\bar{n}$ transition in nuclei yields results very close to the results of the potential approach [43], and further studies of the suppression in matter are under way [44].

VI.2.4 Operator Analysis and Estimate of Matrix Elements

At the quark level, the $n \rightarrow \bar{n}$ transition is $(udd) \rightarrow (u^c d^c d^c)$. This is mediated by six-quark operators O_i , so the effective Hamiltonian is

$$H_{\text{eff}} = \int d^3x \mathcal{H}_{\text{eff}} , \quad (\text{VI.2.31})$$

where the effective Hamiltonian density is

$$\mathcal{H}_{\text{eff}} = \sum_i c_i O_i . \quad (\text{VI.2.32})$$

In four-dimensional spacetime, this six-quark operator has Maxwellian dimension 9 in mass units, so the coefficients have dimension -5 . We write them generically as

$$c_i \sim \frac{\kappa_i}{M_X^5} \quad (\text{VI.2.33})$$

If the fundamental physics yielding the n - \bar{n} oscillation is characterized by an effective mass scale M_X , then, with $c_i \sim O(1)$ (after absorbing dimensionless numerical factors into the effective scale M_X), then the transition amplitude is

$$\delta m = \langle \bar{n} | H_{\text{eff}} | n \rangle = \frac{1}{M_X^5} \sum_i c_i \langle \bar{n} | O_i | n \rangle \quad (\text{VI.2.34})$$

Hence,

$$\delta m \sim \frac{\kappa \Lambda_{\text{QCD}}^6}{M_X^5}, \quad (\text{VI.2.35})$$

where κ is a generic κ_i and $\Lambda_{\text{QCD}} \approx 200$ MeV arises from the matrix element $\langle \bar{n} | O_i | n \rangle$. For $M_X \sim \text{few} \times 10^5$ GeV, one has $\tau_{n-\bar{n}} \simeq 10^9$ s.

The operators O_i must be color singlets and, for M_X larger than the electroweak symmetry breaking scale, also $SU(2)_L \times U(1)_Y$ -singlets. An analysis of these (operators) was carried out in [25] and the $\langle \bar{n} | O_i | n \rangle$ matrix elements were calculated in the MIT bag model. Further results were obtained varying MIT bag model parameters in [27]. These calculations involve integrals over sixth-power polynomials of spherical Bessel functions from the quark wavefunctions in the bag model. As expected from the general arguments above, it was found that

$$|\langle \bar{n} | O_i | n \rangle| \sim O(10^{-4}) \text{ GeV}^6 \simeq (200 \text{ MeV})^6 \simeq \Lambda_{\text{QCD}}^6. \quad (\text{VI.2.36})$$

A calculation of the n - \bar{n} transition matrix elements at ~ 10 – 20% precision would be highly informative. In the near future, lattice QCD can provide a first-principles calculation of the complete set of n - \bar{n} transition matrix elements with controlled uncertainties. Exploratory results for n - \bar{n} matrix elements presented at the *Project X* Physics Study [45] are consistent, at the order-of-magnitude level, with dimensional expectations. For more discussion, see Sec. X.3.4.3.

Another interesting, successful way to describe baryons is as Skyrmions, topological configurations that are permitted in the chiral Lagrangian once a stabilizing term is added [46,47]. Being topological objects, pure Skyrmions are forbidden from decaying and are therefore not a useful laboratory for studying baryon-number-violating processes. The chiral bag model, in which the center of the Skyrmion is replaced with a volume of free massless quarks, joins the exact chiral symmetry of the Skyrme picture with a more accurate short-distance description of QCD. This modification relaxes the topological selection rule that would forbid proton decay or n - \bar{n} oscillations, but Martin and Stavenga have argued [48,49] that an important inhibition remains. They estimate a $\times 10^{-10}$ suppression of the n - \bar{n} oscillation rate. This line of reasoning requires further examination.

VI.3 NNbarX: A SEARCH FOR n - \bar{n} OSCILLATIONS WITH *Project X*

As mentioned in Sec. VI.1, the search for n - \bar{n} oscillations using free neutrons (as opposed to neutrons bound in nuclei) requires intense beams of very low energy (meV) neutrons. Such neutron beams are available at facilities optimized for condensed matter studies focused on neutron scattering. These sources may be based on high flux reactors such as the ILL or the High Flux Isotope Reactor (Oak Ridge) or on accelerator based spallation sources such as the SNS, the JSNS in Japan,

or SINQ (Switzerland). Indeed, as stated in Sec. VI.1, the best limit to date for $n-\bar{n}$ oscillation times was set at the ILL in 1991. Existing neutrons sources are designed and optimized to serve a large number of neutron scattering instruments that each require a relatively small beam. A fully optimized neutron source for an $n-\bar{n}$ oscillation experiment would require a beam having a very large cross section and large solid angle. There are no such beams at existing sources as these attributes would preclude them from providing the resolution necessary for virtually all instruments suitable for materials research. The creation of such a beam at an existing facility would require very major modifications to the source/moderator/shielding configuration that would seriously impact the its efficacy for neutron scattering. In point of fact, the reason there has been no improvement in the limit on free neutron $n-\bar{n}$ oscillations since the ILL experiment of 1991 is that no substantial improvement is possible using existing sources (or any likely future source devoted to materials research).

From Sec. VI.2.3.2, the figure of merit for the sensitivity of a free $n-\bar{n}$ search experiment is $N_n \cdot t^2$, where N_n is the number of free neutrons observed and t is the neutron observation time. A schematic of the ILL $n-\bar{n}$ experiment [4] is shown in Fig. VI-1. The initial intensity of the neutron source was determined in the ILL experiment by the brightness of the liquid deuterium cold neutron source and the transmission of the curved neutron guide. Although, in principle, one expects the sensitivity to improve as the average velocity of neutrons is reduced, it is not practical to use very cold (velocity below 200 m/s) and ultracold neutrons UCN (below 7 m/s) with a horizontal layout for the $n-\bar{n}$ search due to effects of Earth's gravity, which will not allow free transport of very slow neutrons over significant distances in the horizontal direction.

Only modest improvements in the magnetic field and vacuum levels reached for the ILL experiment would still assure satisfaction of the quasi-free condition for the horizontal experiment planned at *Project X*, but in our ongoing optimizations we will investigate limits of $|\mathbf{B}| \leq 1$ nT in the whole free flight volume and vacuum better than $P \sim 10^{-5}$ Pa in anticipation of the more stringent requirements for the vertical experiment. The costs of realizing these more stringent goals will be considered in our ongoing optimization of the experimental design.

The *Project X* spallation target system will include a cooled spallation target, reflectors and cold

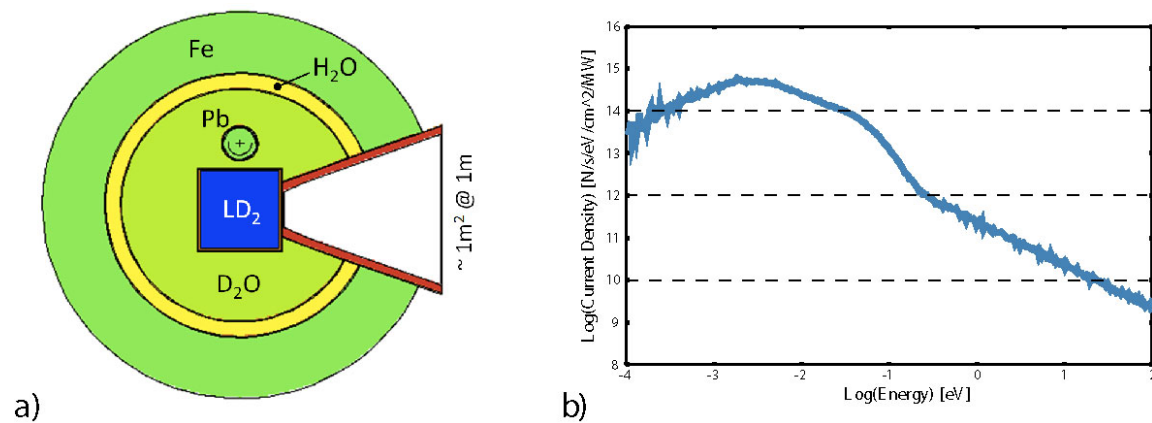


Figure VI-2: Initial NNbarX source design. Panel (a) depicts the layout of a baseline cold neutron source geometry and (b) depicts an MCNP simulation of the cold neutron spectrum entering the neutron optical system.

source cryogenics, remote handling, nonconventional utilities, and shielding. The delivery point of any high-intensity beam is a target which presents technically challenging issues for optimized engineering design, in that optimal neutron performance must be balanced by effective strategies for heat removal, radiation damage, remote handling of radioactive target elements, shielding, and other aspects and components of reliable safe operation.

The NNbarX baseline design incorporates a spallation target core which can be cooled by circulating water or heavy water and will be coupled to a liquid deuterium cryogenic moderator with optimized size and performance (see Fig. VI-2). As we point out below, existing, operating spallation sources provide an excellent starting point for an optimized target design, as several such sources exist and would be perfectly adequate for the NNbarX experiment at Fermilab. In the next three sections, we review some of the specifications for operating 1 MW spallation neutron sources, our strategy to increase the number of neutrons we direct to the annihilation target, and the sensitivity improvements relative to the ILL experiment.

VI.3.1 Currently Existing Spallation Sources

Domestic and international 1 MW spallation sources include the Spallation Neutron Source (SNS) at ORNL and the PSI SINQ [50,51] source in Villigen, Switzerland. The SNS at ORNL [52] uses a liquid mercury target running at 1.0 MW with a proton energy of 825 MeV, and a frequency of 60 Hz. The time-averaged flux of neutrons with kinetic energies below 5 meV at a distance of 2 m from the surface of the coupled moderators is $1.4 \times 10^9 \text{ n cm}^{-2} \text{ s}^{-1}$ at 1 MW [53,54]. A similar source, JSNS, is running at JPARC in Japan [55].

The SINQ source is currently the strongest operating continuous mode spallation neutron source in the world. It receives a continuous (51 MHz) 590 MeV proton beam at a current up to 2.3 mA. Under normal operation the beam current is typically 1.5 mA. The SINQ source uses a *cannelloni* target made of an array of Zircaloy clad lead cylinders. The cold neutron beam contains a flux of $2.8 \times 10^9 \text{ n cm}^{-2} \text{ s}^{-1}$ at 1MW and a distance of 1.5 m from the surface of the Target 8 coupled moderators [56,57]. These facilities demonstrate that the substantial engineering challenges of constructing a 1 MW spallation target/moderator/reflector (TMR) system can be overcome. However, as noted earlier, none of these existing multipurpose facilities is a suitable host for the next generation $n-\bar{n}$ experiment due to constraints imposed on their TMR designs by their materials research missions.

VI.3.2 Increased Sensitivity of the NNbarX Experiment

A higher sensitivity in the NNbarX experiment compared to the previous ILL experiment [4], can be achieved by employing various improvements in neutron optics and moderation [58]. Conventional moderator designs can be enhanced to increase the yield of cold neutrons through a number of neutronics techniques such as a reentrant moderator design [59], use of reflector/filters [60], super-mirror reflectors [61], and high-albedo materials such as diamond nanoparticle composites [62–64]. Although potentially of high positive impact for an $n-\bar{n}$ experiment, some of these techniques are not necessarily suitable for multipurpose spallation sources serving a materials science user community (where sharply defined neutron pulses in time may be required, for example).

Supermirrors based on multilayer coatings can greatly increase the range of reflected transverse velocities relative to the nickel guides used in the ILL experiment. In the following discussion, m , denotes the increased factor for near-unity reflection above nickel. Supermirrors with $m = 4$, are now mass-produced and supermirrors with up to $m = 7$, can be produced [61].

To enhance the sensitivity of the $n-\bar{n}$ search the supermirrors can be arranged in the shape of a truncated focusing ellipsoid [65] as shown in Fig. VI-3a. The focusing reflector with a large acceptance aperture will intercept neutrons within a fixed solid angle and direct them by single reflection to the target. The cold neutron source and annihilation target will be located in the focal planes of the ellipsoid. The geometry of the reflector and the parameter m of the mirror material are chosen to maximize the sensitivity $N_n \cdot t^2$ for a given brightness of the source and a given size of the moderator and annihilation target. Elliptical concentrators of somewhat smaller scale have already been implemented for a variety of cold neutron experiments [66]. Critically, the plan to create a *dedicated* spallation neutron source for particle physics experiments creates a unique opportunity to position the NNbarX neutron optical system to accept a huge fraction of the neutron flux, resulting in large gains in the number of neutrons directed to the annihilation target. Because such a strategy makes use of such a large fraction of the available neutrons for a single beamline, it would be incompatible with a typical multi-user materials science facility. The NNbarX collaboration contains specialists in neutronics design, moderator development and spallation target construction and design (including leaders of the design and construction team for the SNS and the Lujan Mark III systems). Initial steps towards an optimized design have been taken, with an NNbarX source design similar to the SINQ source modeled and vetted vs. SINQ source performance (see Fig. VI-2), and a partially optimized elliptical neutron optics system shown in Fig. VI-3(a).

MCNPX [67] simulation of the performance of the cold source shown in Fig. VI-2 produced a flux of cold neutrons emitted from the face of cryogenic liquid deuterium moderator into forward hemisphere with the spectrum shown in Fig. VI-2. Only a fraction of the integrated flux is accepted by the focusing reflector to contribute to the sensitivity at the annihilation target.

For sensitivity ($N_n \cdot t^2$) calculations, neutrons emitted from the surface of neutron moderator were traced through the detector configuration shown in Fig. VI-2 with gravity taken into account and with focusing reflector parameters that were adjusted by a partial optimization procedure. The flux of cold neutrons impinging on the annihilation detector target located at the distance L from the source was calculated after reflection (mostly single) from the focusing mirror. The time of flight to the target from the last reflection was also recorded in the simulation procedure. Each traced neutron contributed its t^2 to the total sensitivity figure $N_n \cdot t^2$ that was finally normalized to the initial neutron flux from the moderator. Sensitivity as function of distance between neutron source and target (L) is shown in Fig. VI-3(b). The simulation has several parameters that affect the sensitivity: emission area of the moderator, distance between moderator and annihilation target, diameter of the annihilation target, starting and ending distance for truncated focusing mirror reflector, minor semi-axis of the ellipsoid, and the reflecting value “ m ” of the mirror. Sensitivity is a complicated functional in the space of these parameters. An important element of our ongoing design work is to understand the projected cost for the experiment as a function of these parameters.

A sensitivity in NNbarX in units of the ILL experiment larger than 100 per year of (i.e. a 300-fold gain over the anticipated three-year run) seems feasible from these simulations. Configurations of parameters that would correspond to even larger sensitivities are achievable, but for the baseline simulation shown in the Fig. VI-3 we have chosen a set of parameters that we believe will

Table VI-1: Comparison of parameters in NNbarX simulations with existing practice.

Parameter	Units	NNbarX Simulations	Existing MW Facility Value	Ref.
Source brightness ($E < 400$ meV)	$n/(s\text{ cm}^2\text{ sterad MW})$	3.5×10^{12}	4.5×10^{12}	[55]
Moderator viewed area	cm^2	707	190	[55]
Accepted solid angle ¹	sterad	0.2	0.034	[68]
Vacuum tube length	m	200	100	[4]
¹² C target diameter	m	2.0	1.1	[4]

¹ The solid angle quoted from JSNS is the total for a coupled parahydrogen moderator feeding five neighboring beamlines (each of which would see a fifth of this value), whereas at NNbarX the one beam accepts the full solid angle.

be reasonably achievable and economical after inclusion of more engineering details than can be accommodated in our simulations to date.

As emphasized above, the optimal optical configuration for an $n-\bar{n}$ search is significantly different from anything that has previously been built, so the full impact on the sensitivity of cost and other engineering considerations is not straight-forward to predict at this early stage of the project. To demonstrate that the key parameters contributing to the sensitivity predicted by these simulations do not dramatically depart from existing engineering practice, we include below a table identifying the value of these same parameters at existing MW-scale spallation neutron sources for the source and optical parameters, and the 1991 ILL experiment for the overall length L .

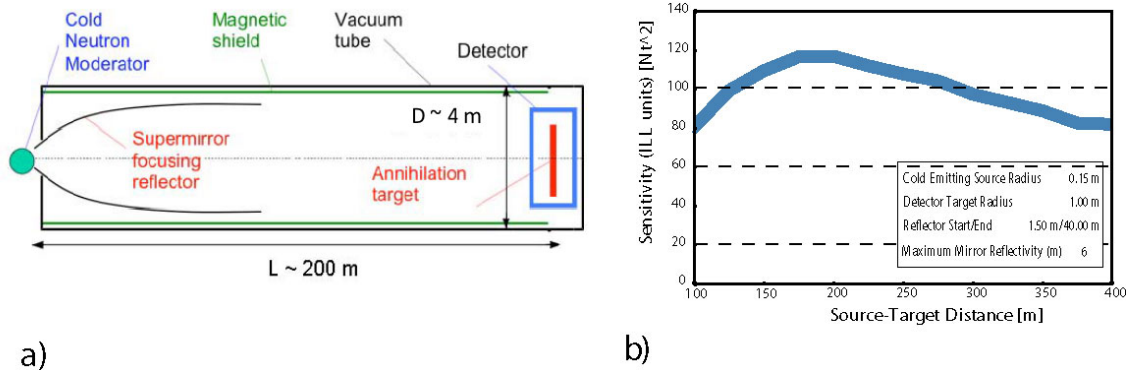


Figure VI-3: The NNbarX layout and a sensitivity calculation. Panel (a) is a schematic diagram of a candidate NNbarX geometry, depicting the relative location of the cold neutron source, reflector, target, annihilation detector and beam dump. Panel (b) depicts a calculation of the $n-\bar{n}$ oscillation sensitivity for a geometry similar to that in panel (a), where all parameters are fixed except for the source-target distance L . The semi-major axis of the elliptical reflector is equal to $L/2$, so one focus is at the source and the other is at the target.

VI.3.3 Requirements for an Annihilation Detector

As mentioned in Sec. VI.1, a free $n-\bar{n}$ transformation search NNbarX experiment could require a vacuum of 10^{-5} Pa and magnetic fields of $|\mathbf{B}| < 1$ nT along the flight path of the neutrons. The target vacuum is achievable with standard vacuum technology, and the magnetic fields could be achieved with an incremental improvement on the ILL experiment through passive shielding and straight-forward active field compensation [4,69,70].

In the design of the annihilation detector, our strategy is to develop a state-of-the-art realization of the detector design used in the ILL experiment [4]; see Fig. VI-4. Major subsystems of the NNbarX annihilation detector (radially in the outward direction) will include: (i) the annihilation target; (ii) the detector vacuum region; (iii) the tracker; (iv) the time of flight systems (before and after the tracker); (v) the calorimeter; and (vi) the cosmic veto system. Requirements for these subsystems are formulated below. In general, the $n-\bar{n}$ detector doesn't require premium performance, but due to relatively large size needs rather careful optimization of the cost. The detector should be built along the detector vacuum region with several layered detection subsystems (sections (iii) - (vi)) and should cover a significant solid angle (in θ -projection from $\sim 20^\circ$ to 160° corresponding to the solid angle coverage of $\sim 94\%$). In the ϕ -projection, the detector configuration can be cylindrical, octagonal, hexagonal, or square (similar to the ILL experiment [4]).

The spallation target geometry of NNbarX introduces a new consideration in the annihilation detector design, because of the possible presence of fast neutron and proton backgrounds. These

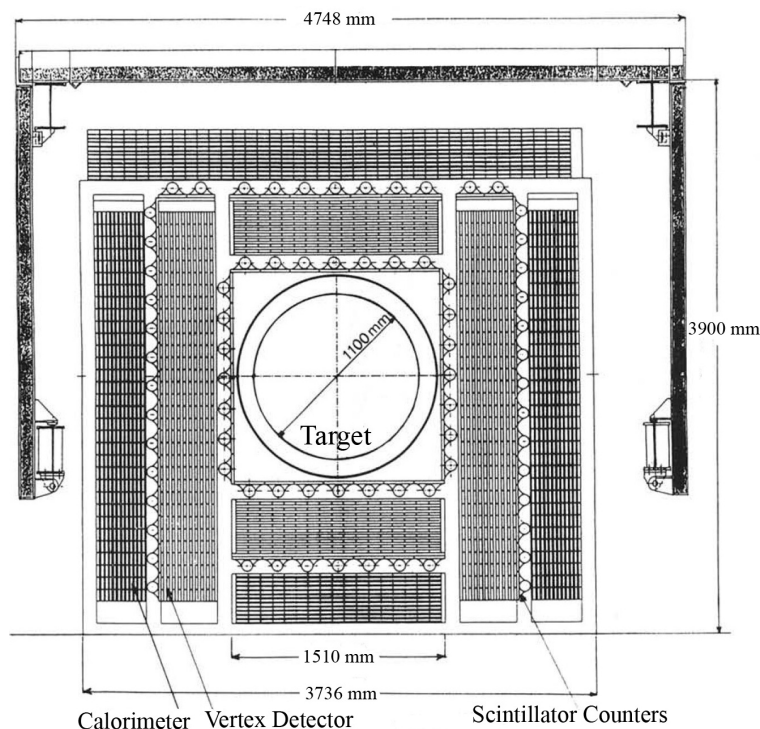


Figure VI-4: Cross-sectional drawing of the ILL/Grenoble $n-\bar{n}$ annihilation detector apparatus [4].

backgrounds were effectively completely eliminated from the ILL experiment, which produced fewer high energy particles in the reactor source and eliminated the residual fast backgrounds using a curved guide system to couple the cold source to the $n-\bar{n}$ guide. For NNbarX, we utilize a strategy of integrating our shielding scheme for fast particles into the design of the source and beamline, and optimizing the choice of tracker detectors to differentiate between charged and neutral tracks. We note that the residual fast backgrounds at the detector are a strong function of the guide tube length, detector threshold, and pulse structure for the proton beam. In particular, if needed, we can perform a slow chopping of the proton beam (1 ms on, 1 ms off) to effectively eliminate fast backgrounds completely.

VI.3.3.1 Annihilation Target

A uniform carbon disc with a thickness of $\sim 100 \mu\text{m}$ and diameter $\sim 2 \text{ m}$ would serve as an annihilation target. It would be stretched on a low- Z material ring and installed in the center of the detector vacuum region. The choice of carbon is dictated by low capture cross section for thermal neutrons $\sim 4 \text{ mb}$ and high annihilation cross-section $\sim 4 \text{ kb}$. The fraction of hydrogen in the carbon film should be controlled below $\sim 0.1\%$ to reduce generation of capture γ s.

VI.3.3.2 Detector Vacuum Region

The detector vacuum region should be a tube with inner diameter $\sim 4 \text{ m}$ and wall thickness $\sim 1.5 \text{ cm}$. The wall should be made of low- Z material (Al) to reduce multiple scattering for tracking and provide a low (n, γ) cross-section. Additional lining of the inner surface of the vacuum region with ${}^6\text{LiF}$ pads will reduce the generation of γ s by captured neutrons. The detector vacuum region is expected to be the source of $\sim 10^8 \gamma$ s per second originating from neutron capture. Unlike in the neutron beam flight vacuum region, no magnetic shielding is required inside the detector vacuum region. As mentioned before, the vacuum level should be better than 10^{-4} Pa via connection with the neutron beam vacuum region. We plan to have a section of the vacuum tube in the detector recessed. This area will have no support or detector elements in the neutron beam, which will reduce the rate of neutron captures.

VI.3.3.3 Tracker

The tracker should be radially extended from the outer surface of the detector vacuum tube by $\sim 50 \text{ cm}$ and should have solid angle coverage of $\sim 20^\circ$ to 160° . It should provide rms $\leq 1 \text{ cm}$ accuracy of annihilation vertex reconstruction to the position of the target in the θ -projection (compared to 4 cm in ILL experiment). This is a very important resource for the control of background suppression in the detector. Reconstruction accuracy in the ϕ -projection can be a factor of 3 - 4 lower. Vertex information will be also used for the total momentum balance of annihilation events both in the θ - and ϕ -projections. Relevant tracker technologies can include straw tubes, proportional and drift detectors. Limited Streamer Tubes (LST), as used in the ILL experiment, are presumed to be worse than proportional mode detectors due to better discrimination of the latter to low-energy capture γ s.

A system similar to the ATLAS transition radiation tracker (TRT) is currently under consideration for the tracking system. The ATLAS TRT covers a pseudorapidity range less than 2 and has a measured barrel resolution of $118 \mu\text{m}$ and an end-cap resolution of $132 \mu\text{m}$. The ATLAS TRT is capable of providing tracking for charged particles down to a transverse momentum of $p_T = 0.25 \text{ GeV}$ with an efficiency above 90%, but typically places a cut of $p_T > 1.00 \text{ GeV}$ due to combinatorics on the large number of tracks in collision events. For tracks that have at least 15 TRT hits, a transverse momentum $p_T > 1.00 \text{ GeV}$, and are within 1.3 mm of the anode, the efficiency was found to be 94.4% for the 7 TeV ATLAS data with similar results for the 0.9 TeV ATLAS data set [71–74]. For a cut of $p_T > 0.25 \text{ GeV}$, the efficiency drops down to 93.6%. For higher momentum tracks (e.g. $p_T > 15.00 \text{ GeV}$), the efficiency increases to 97% and is more indicative of the single-straw efficiency [75]. The efficiency drops at the edges of the straw due to geometric and reconstruction effects. The straw tubes in the TRT have a diameter of 4 mm and are made from wound kapton reinforced with thin carbon fibers. The anode at the center of each straw is gold plated tungsten wire with a diameter of $31 \mu\text{m}$. The cathodes were kept at -1.5 kV, while the anodes were kept at ground. The tubes are filled with a gas mixture of 70% Xe, 27% CO₂, and 3% O₂, however we will have to optimize our gas mixture for a different set of backgrounds in this experiment, particularly fast n -backgrounds and proton backgrounds. If it will be determined that the tracker should be moved inside the detector vacuum region for better accuracy (also giving rise to the problem of gas and electrical vacuum feedthroughs), then the requirements on the detector tube material and thickness should be revisited.

VI.3.3.4 Time of Flight System

The time of flight (TOF) systems should consist of two layers of fast detectors (e.g. plastic scintillation slabs or tiles) before and after the tracker with solid angle coverage of $\sim 20^\circ$ to 160° . With appropriate segmentation, TOF should provide directional information for all tracks found in the tracker. The TOF systems could also be a part of the trigger. With two layers separated by $\sim 50 \text{ cm}$ - 60 cm , the TOF systems should have timing accuracy sufficient to discriminate the annihilation-like tracks from the cosmic ray background originating outside the detector volume.

VI.3.3.5 Calorimeter

The calorimeter will range out the annihilation products and should provide trigger signal and energy measurements in the solid angle $\sim 20^\circ$ to 160° . The average multiplicity of pions in annihilation at rest equals 5, so an average pion can be stopped in $\sim 20 \text{ cm}$ of dense material (like lead or iron). For low multiplicity (but small probability) annihilation modes, the amount of material can be larger. Calorimeter configuration used in the ILL experiment with 12 layers of Al/Pb interspersed with gas detector layers (LST in ILL experiment) might be a good approach for the calorimeter design. Detailed performance for the measurement of total energy of annihilation events and momentum balance in θ - and ϕ -projections should be determined from simulations. The proportional mode of calorimeter detector operation possibly can be less affected by copious low-energy γ -background than the LST mode. An approach using MINERVA-like wavelength shifting fibers coupled to scintillating bars is also being considered [76].

VI.3.3.6 Cosmic Veto System

The cosmic veto system (CVS) should identify all cosmic ray background. All annihilation products should be totally stopped in the calorimeter. Large area detectors similar to MINOS scintillator supermodules [77] might be a good approach to the configuration of the CVS. Possible use of timing information should be studied in connection with the TOF system. CVS information might not be included in the trigger due to high cosmogenic rates, particularly in the stage-one horizontal $n-\bar{n}$ configuration on the surface, but should be recorded for all triggers in the off-line analysis.

VI.4 NNbarX SIMULATION

Developing a detector model through simulation that allows us to reach our goal of zero background and optimum signal event detection efficiency is the primary goal of our simulation campaign, which is currently underway. We are using Geant 4.9.6 [78] to simulate the passage of annihilation event products through the annihilation detector geometry with concurrent remote development coordinated through GitHub [79]. A detailed treatment of $n-\bar{n}$ annihilation modes in ^{12}C is under development, however for this report, we present a list of $n-\bar{n}$ annihilation modes in ^{16}O [3] (see Table 6.2), which we expect to be similar to the physics of NNbarX. The event generator for $n-\bar{n}$ annihilation modes in ^{12}C uses programs developed for the IMB experiment and Kamiokande II collaborations [80,81] validated in part by data from the LEAR experiment [82]. The branching ratios for the $n-\bar{n}$ annihilation modes and fragmentation modes of the residual nucleus were taken

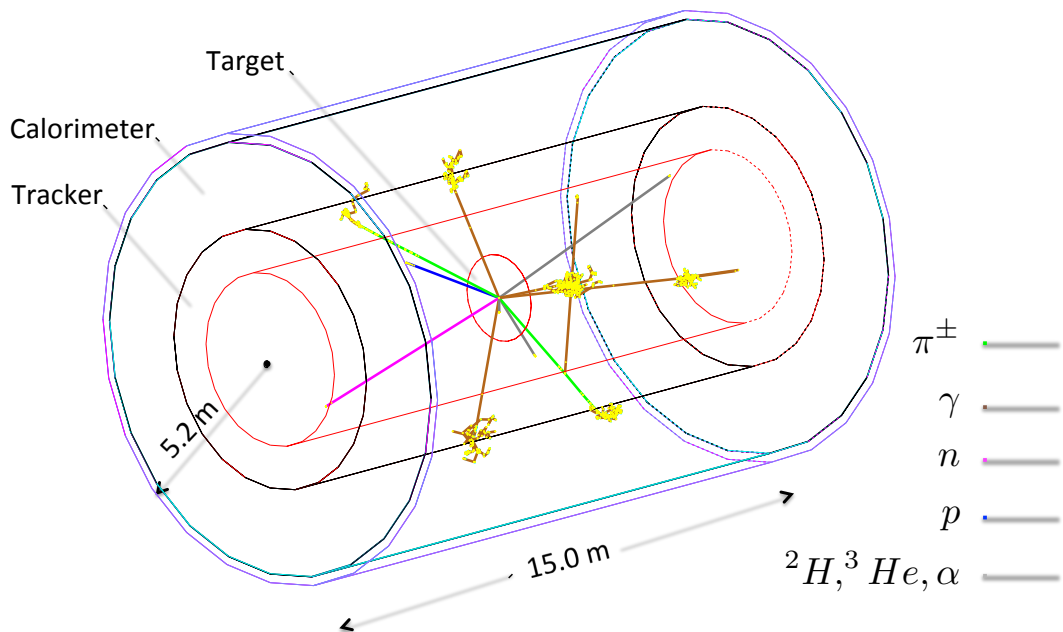


Figure VI-5: Event display generated in our preliminary Geant4 [78] simulation for a $\pi^+\pi^-2\pi^0$ annihilation event in a generalized NNbarX detector geometry. Given the short lifetime of the π^0 , they decay immediately to 2γ , as shown above.

Table VI-2: List of $n\bar{n}$ annihilation modes and branching ratios from the Super-Kamiokande simulation study [3].

$n\bar{n}$ Annihilation Mode	Branching Ratio
$\pi^+\pi^-3\pi^0$	28%
$2\pi^+2\pi^-\pi^0$	24%
$\pi^+\pi^-2\pi^0$	11%
$2\pi^+2\pi^-2\pi^0$	10%
$\pi^+\pi^-\omega$	10%
$2\pi^+2\pi^-$	7%
$\pi^+\pi^-\pi^0$	6.5%
$\pi^+\pi^-$	2%
$2\pi^0$	1.5%

from Ref. [3,83–85]. The cross sections for the π -residual nucleus interactions were based on extrapolation from measured π - ^{12}C and π -Al cross sections. Excitation of the $\Delta(1232)$ resonance was the most important parameter in the nuclear propagation phase. Nuclear interactions in the event generator include π and ω elastic scattering, π charge exchange, π -production, π -absorption, inelastic ω -nucleon scattering to a π , and ω decays inside the nucleus. Fig. VI-5 shows an event display from our preliminary Geant4 simulation of a $\pi^+\pi^-2\pi^0$ annihilation event in a detector geometry with a generalized tracker and calorimeter.

VI.5 THE NNbarX RESEARCH AND DEVELOPMENT PROGRAM

In October of 2012, the Fermilab Physics Advisory Committee strongly supported the physics of NNbarX and recommended that “R&D be supported, when possible, for the design of the spallation target, and for the overall optimization of the experiment, to bring it to the level required for a proposal to be prepared.” At the core of this activity is integrating models for the source, neutron optics and detectors into a useful tool for evaluating overall sensitivity to annihilation events and fast backgrounds, and developing a cost scaling model. In addition to this activity, the NNbarX collaboration has identified several areas where research and development may substantially improve the physics reach of the experiment: target and moderator design, neutron optics optimization and the annihilation detector design.

As touched on Sec. VI.3.2, for the target and moderator, there exist a number of improvements which have already been established as effective that might be applied to our baseline conventional source geometry. For example, one can shift from a *cannelloni* target to a lead-bismuth eutectic (LBE) target [56], utilize a reentrant moderator design [59], and possibly use reflector/filters [60], supermirror reflectors [61], and high-albedo materials such as diamond nanoparticle composites [62–64]. At present, the collaboration envisions a program to perform neutronic simulations and possibly benchmark measurements on several of these possibilities, with high-albedo reflectors as a priority.

At present, we envision at least a factor of two improvement arising from some combination of these improvements.

For neutron optics, members of the collaboration are currently involved in the production of high m supermirror guides. Although the basic performance is established, optimizing the selection of supermirror technology for durability (*vs* radiation damage) and cost could have a very large impact on the ultimate reach of the experiment.

Finally, for the detector, the collaboration is using the WNR facility at LANSCE to determine the detection efficiency and timing properties of a variety of detectors from 10 MeV to 800 MeV neutrons. Detectors under evaluation include proportional gas counters with various gas mixtures, straw tubes and plastic scintillators. Evaluating different available detector options and modernizing the annihilation detector should improve the background rejection capability and permit reliable scaling to more stringent limits for $n-\bar{n}$ oscillations. The main technical challenges in for NNBarX is to minimize the cost of critical hardware elements, such as the large-area super-mirrors, large-volume magnetic shielding, vacuum tube, shielding of the high-acceptance front-end of the neutron transport tube, and annihilation detector components. These challenges will be addressed in the R&D phase for the NNBarX experiment.

VI.6 SUMMARY

Assuming beam powers up to 1 MW on the spallation target and that 1 GeV protons are delivered from the *Project X* linac, the goal of NNbarX will be to improve the sensitivity of an $n-\bar{n}$ search ($N_n \cdot t^2$) by at least a factor 30 (compared to the previous limit set in ILL-based experiment [4]) with a horizontal beam experiment; and by an additional factor of ~ 100 at the second stage with the vertical layout. The R&D phase of the experiment, including development of the conceptual design of the cold neutron spallation target, and conceptual design and optimization of the performance of the first-stage of NNbarX is expected to take 2-3 years. Preliminary results from this effort suggest that an improvement over the ILL experiment by a factor of more than 100 may be realized even in this horizontal mode, but more work is needed to estimate the cost of improvements at this level. The running time of the first stage of NNbarX experiment is anticipated to be three years. The second stage of NNbarX will be developed depending upon the demonstration of technological principles and techniques of the first stage.

References

- [1] C. Dover, A. Gal, and J. M. Richard, *Phys. Rev. D* **27**, 1090 (1983)
- [2] E. Friedman and A. Gal, *Phys. Rev. D* **78**, 016002 (2008)
- [3] K. Abe *et al.* (Super-Kamiokande Collaboration), “The search for $n-\bar{n}$ oscillation in Super-Kamiokande I,” (2011), arXiv:1109.4227 [hep-ex]
- [4] M. Baldo-Ceolin *et al.*, *Z. Phys. C* **63**, 409 (1994)

- [5] J. Chung *et al.*, Phys. Rev. D **66**, 032004 (2002)
- [6] M. Bergevin, *Search for Neutron-Antineutron Oscillations at the Sudbury Neutrino Observatory*, Ph.D. thesis, University of Guelph (2010)
- [7] V. A. Kuzmin, Pisma Zh. Eksp. Teor. Fiz. **12**, 335 (1970), JETP Lett. **12**, 228 (1970), http://www.jetpletters.ac.ru/ps/1730/article_26297.pdf
- [8] S. L. Glashow, in *Proceedings of Neutrino 79*, edited by A. Haatuft and C. Jarlskog (University of Bergen and European Physical Society, 1979) <http://ccdb5fs.kek.jp/cgi-bin/img/allpdf?197910312>
- [9] R. N. Mohapatra and R. E. Marshak, Phys. Rev. Lett. **44**, 1316 (1980)
- [10] A. Sakharov, JETP Lett. **5**, 24 (1967)
- [11] A. Dolgov, Phys. Rept. **222**, 309 (1992)
- [12] A. Dolgov, Surv. High Energy Phys. **13**, 83 (1998)
- [13] H. Georgi and S. Glashow, Phys. Rev. Lett. **32**, 438 (1974)
- [14] S. Raby *et al.*, “DUSEL theory white paper,” FERMILAB-PUB-08-680-T (2008), arXiv:0810.4551 [hep-ph]
- [15] G. 't Hooft, Phys. Rev. Lett. **37**, 8 (1976)
- [16] G. 't Hooft, Phys. Rev. D **14**, 3432 (1978)
- [17] V. Kuzmin, V. Rubakov, and M. Shaposhnikov, Phys. Lett. B **155**, 36 (1985)
- [18] J. Pati and A. Salam, Phys. Rev. D **10**, 275 (1974)
- [19] R. N. Mohapatra and J. Pati, Phys. Rev. D **11**, 566 (1975)
- [20] R. N. Mohapatra and J. Pati, Phys. Rev. D **11**, 2558 (1975)
- [21] T. K. Kuo and S. T. Love, Phys. Rev. Lett. **45**, 93 (1980)
- [22] L.-N. Chang and N.-P. Chang, Phys. Lett. B **92**, 103 (1980)
- [23] R. N. Mohapatra and R. E. Marshak, Phys. Lett. B **94**, 183 (1980)
- [24] R. Cowsik and S. Nussinov, Phys. Lett. B **101**, 237 (1981)
- [25] S. Rao and R. Shrock, Phys. Lett. B **116**, 238 (1982)
- [26] S. P. Misra and U. Sarkar, Phys. Rev. D **28**, 249 (1983)
- [27] S. Rao and R. Shrock, Nucl. Phys. B **232**, 143 (1984)
- [28] S. J. Huber and Q. Shafi, Phys. Lett. B **512**, 365 (2001)
- [29] K. S. Babu and R. N. Mohapatra, Phys. Lett. B **518**, 269 (2001)

- [30] S. Nussinov and R. Shrock, Phys. Rev. Lett. **88**, 171601 (2002)
- [31] R. N. Mohapatra, S. Nasri, and S. Nussinov, Phys. Lett. B **627**, 124 (2005)
- [32] K. S. Babu, R. N. Mohapatra, and S. Nasri, Phys. Rev. Lett. **97**, 131301 (2006)
- [33] B. Dutta, Y. Mimura, and R. Mohapatra, Phys. Rev. Lett. **96**, 061801 (2006)
- [34] Z. Berezhiani and L. Bento, Phys. Rev. Lett. **96**, 081801 (2006)
- [35] K. S. Babu, P. Bhupal Dev, and R. N. Mohapatra, Phys. Rev. Lett. **79**, 015017 (2009)
- [36] R. N. Mohapatra, J. Phys. G **36**, 104006 (2009)
- [37] P. Gu and U. Sarkar, Phys. Lett. B **705**, 170 (2011)
- [38] K. S. Babu, P. S. Bhupal Dev, E. C. F. S. Fortes, and R. N. Mohapatra, “Post-sphaleron baryogenesis and an upper limit on the neutron-antineutron oscillation time,” (2013), arXiv:1303.6918 [hep-ph]
- [39] J. M. Arnold, B. Fornal, and M. B. Wise, Phys. Rev. D **87**, 075004 (2013)
- [40] C. Bambi, A. D. Dolgov, and K. Freese, Nucl. Phys. **B763**, 91 (2007), [arXiv:hep-ph/0606321 [hep-ph]]
- [41] Y. G. Abov, F. S. Dzheparov, and L. B. Okun, JETP Lett. **39**, 599 (1984), http://www.jetpletters.ac.ru/ps/1302/article_19685.pdf
- [42] J. Beringer *et al.* (Particle Data Group), Phys. Rev. D **86**, 010001 (2012)
- [43] V. Kopeliovich and I. Potashnikova, JETP Lett. **95**, 1 (2012), [arXiv:1112.3549 [hep-ph]]
- [44] A. Vainshtein, “Neutron-antineutron oscillations vs. nuclei stability,” Project X Physics Study (2012), <http://j.mp/11eRBuj>
- [45] M. Buchoff, “Lattice calculations of neutron-antineutron matrix elements,” Project X Physics Study (June 2012), <https://indico.fnal.gov/getFile.py/access?contribId=140&sessionId=8&resId=0&materialId=slides&confId=5276>
- [46] T. H. R. Skyrme, Proc. Roy. Soc. Lond. **A260**, 127 (1961)
- [47] T. H. R. Skyrme, Nucl. Phys. **31**, 556 (1962)
- [48] A. Martin and G. C. Stavenga, Phys. Rev. **D85**, 095010 (2012), [arXiv:1110.2188 [hep-ph]]
- [49] A. Martin and G. C. Stavenga, “Skyrme suppression or enhancement of neutron-antineutron oscillations,” Project X Physics Study (June 2012), <http://j.mp/11NDUCq>
- [50] B. Blau *et al.*, Neutron News **20**, 5 (2009)
- [51] W. Fischer *et al.*, Physica B **234**, 1202 (1997)
- [52] T. E. Mason *et al.*, Physica B **385**, 955 (2006)

- [53] E. B. Iverson, P. D. Ferguson, F. X. Gallmeier, and I. I. Popova, *Trans. Am. Nucl. Soc.* **89**, 673 (2003)
- [54] E. B. Iverson (Oak Ridge National Laboratory)(May 2013), private communication
- [55] F. Maekawa *et al.*, *Nucl. Inst. Meth. A* **620**, 159 (2010)
- [56] M. Wohlmuther *et al.*, “The improved SINQ target,” 10th International Topical Meeting on Nuclear Application of Accelerators (April 2011)
- [57] W. Wagner *et al.*, *J. Neutron Research* **6**, 249 (1997)
- [58] W. M. Snow, *Nucl. Inst. Meth. A* **611**, 144 (2009)
- [59] P. Ageron *et al.*, *Nucl. Inst. Meth. A* **284**, 197 (1989)
- [60] M. Mocko and G. Muhrer, *Nucl. Inst. Meth. A* **704**, 27 (2013)
- [61] Industrial Manufacturer of supermirrors, <http://www.swissneutronics.ch>
- [62] V. Nesvizhevsky *et al.*, *Nucl. Inst. Meth. A* **595**, 631 (2008)
- [63] E. Lychagin *et al.*, *Nucl. Inst. Meth. A* **611**, 302 (2009)
- [64] E. Lychagin *et al.*, *Phys. Lett. B* **679**, 186 (2009)
- [65] Y. Kamyshev *et al.*, Proceedings of the ICANS-XIII meeting of the International Collaboration on Advanced Neutron Sources (1995)
- [66] P. Boni, F. Grunauer, and C. Schanzer, *Nucl. Inst. Meth. A* **624**, 162 (2010)
- [67] MCNPX, <http://mcnpx.lanl.gov/documents.html>
- [68] T. Kai *et al.*, *Nucl. Inst. Meth. A* **550**, 329 (2005)
- [69] “Project X Physics Study,” (June 2012), <https://indico.fnal.gov/event/projectxps12>
- [70] W. Altmannshofer *et al.*, “Physics opportunities with Stage 1 of *Project X*,” (2012), http://www.fnal.gov/directorate/lbne_reconfiguration/
- [71] S. Schaepe, in *Advancements in Nuclear Instrumentation Measurement Methods and their Applications*, edited by M. Schyus and A. Lyoussi (2011)
- [72] J. M. Stahlman (ATLAS TRT Collaboration), *Phys. Proc.* **37**, 506 (2012)
- [73] A. S. Boldyrev *et al.*, *Instrum. Exp. Tech.* **55**, 323 (2012)
- [74] A. Vogel, “13th Vienna Conference on Instrumentation,” <http://cds.cern.ch/record/1537991?ln=en>
- [75] R. Van Kooten (Indiana University)(May 2013), private communication
- [76] K. McFarland, *Nucl. Phys. B (Proc. Suppl.)* **159**, 107 (2006)

- [77] D. G. Michael *et al.*, Nucl. Inst. Meth. A **596**, 190 (2008)
- [78] “GEANT4: A toolkit for the simulation of the passage of particles through matter,” <http://geant4.cern.ch/>
- [79] Github, <https://github.com/>
- [80] T. W. Jones *et al.*, Phys. Rev. Lett. **52**, 720 (1984)
- [81] M. Takita *et al.*, Phys. Rev. D **34(3)**, 902 (1986)
- [82] E. S. Golubeva, A. S. Ilinov, and L. A. Kondratyuk, in *International Workshop on Future Prospects of Baryon Instability Search in p decay and $n-\bar{n}$ Oscillation Experiments*, Vol. C96-03-28 (1996) p. 295
- [83] C. Berger *et al.*, Phys. Lett. B **240**, 237 (1990)
- [84] Y. Fukuda *et al.*, Nucl. Inst. Meth. A **501**, 418 (2003)
- [85] A. S. Botvina, A. S. Iljinov, and I. S. Mishustin, Nucl. Phys. A **507**, 649 (1990)

VII New, Light, Weakly-coupled Particles with *Project X*

*Brian Batell, William Wester,
Patrick deNiverville, Ranjan Dharmapalan, David McKeen,
Maxim Pospelov, Adam Ritz, and Richard Van de Water*

VII.1 INTRODUCTION

The empirical evidence for new physics, such as dark matter and neutrino mass, does not necessarily point to a specific mass scale, but instead to a hidden sector, weakly-coupled to the Standard Model (SM). This point has recently been amplified by the LHC's exploration of the weak scale which, despite the impressive discovery of a SM-like Higgs boson, has yet to uncover new physics. Hidden sectors containing light degrees of freedom, with mass in the MeV–GeV range, are motivated by various questions about dark matter, neutrinos, and early universe cosmology as we discuss below. An intense proton source such as *Project X*, with a fixed target and rare meson decay program, would provide an ideal setting in which to explore this new physics landscape.

If we focus on the compelling evidence for dark matter, a number of anomalies in direct and indirect detection have led recently to a broader theoretical perspective, beyond the characteristic weakly interacting massive particle (WIMP) with a weak-scale mass. The simple thermal relic scenario, with abundance fixed by freeze-out in the early universe, allows a much wider mass range if there are light (dark force) mediators which control the annihilation rate. Current direct detection experiments lose sensitivity rapidly once the mass drops below a few GeV, and experiments at the intensity frontier provide a natural alternative route to explore this dark matter regime. Moreover, dark matter may not be a thermal relic at all, and could be composed of sub-MeV very weakly interacting slim particles (WISPs), e.g., axions, sterile neutrinos, gravitinos, dark photons, etc. Possible inconsistencies of the Λ CDM picture of structure formation on galactic scales, and the advent of precision CMB tests of light degrees of freedom at the era of recombination have also focussed attention of the possibility of new light degrees of freedom.

These empirical (or bottom-up) motivations for exploring new light weakly-coupled particles (NLWCPs) can also be placed within a more systematic framework. As we discuss in the next subsection, a general effective field theory perspective of the interaction between new gauge singlet fields with the SM points to a specific set of operators, known as *portals*. These extend the usual right-handed neutrino coupling, which provides a natural explanation for neutrino mass, to include interactions of dark singlet scalars with the Higgs, kinetic mixing of a new U(1) dark photon (or Z') with the hypercharge gauge boson, and the coupling of axion-like pseudoscalars to the axial vector current. These couplings are also quite generic in top-down models of new physics. Light pseudo-Nambu-Goldstone bosons, such as axions, are generic in scenarios where new symmetries are broken at a high scale, and scalars and pseudoscalars can also arise from compactification of

extra dimensions. Extensions of the SM gauge group to include new U(1) sectors are also quite generic in string theory.

Portal interactions naturally describe the generic coupling of light degrees of freedom in a hidden sector with the SM. The combination of relatively light sub-GeV mass, along with a weak (but not super-weak) coupling, lends itself to production at high luminosity accelerator-based facilities. In many cases the suppressed interaction rate also requires large volume detectors to search for rare scattering events. These features point to the intensity frontier, and the high luminosity proton source at *Project X* as ideally suited to host an experimental program exploring this sector.

VII.1.1 Hidden Sectors

A conventional parametrization of the interactions between the SM and a hidden sector assumes that any light hidden sector states are SM gauge singlets. This automatically ensures weak interactions, while the impact of heavier charged states is incorporated in an effective field theory expansion of the interactions of these light fields at or below the weak scale,

$$\mathcal{L} \sim \sum_{n=k+l-4} \frac{c_n}{\Lambda^n} O_{\text{SM}}^{(k)} O_{\text{hidden}}^{(l)}, \quad (\text{VII.1.1})$$

where the two classes of operators are made from SM and hidden fields, respectively. The generic production cross section for hidden sector particles via these interactions scales as $\sigma \sim E^{2n-2}/\Lambda^{2n}$. It follows that the lower dimension interactions, namely those that are unsuppressed by the heavy scale Λ , are preferentially probed at lower energy. Such hidden sectors are natural targets for the intensity frontier. Given the LHC's discovery of a SM-like Higgs boson, it is appropriate to delineate these interactions in a form which builds in the SM electroweak gauge group structure. In this case, the set of low-dimension interactions, usually termed *portals*, is quite compact. Up to dimension five ($n \leq 1$), assuming SM electroweak symmetry breaking, the list of portals includes:

$$\begin{aligned} \text{Dark photons} & -\frac{\kappa}{2} B_{\mu\nu} V^{\mu\nu} \\ \text{Dark scalars} & (AS + \lambda S^2) H^\dagger H \\ \text{Sterile neutrinos} & y_N L H N \\ \text{Pseudoscalars} & \frac{\partial_\mu a}{f_a} \bar{\Psi} \gamma^\mu \gamma^5 \Psi \end{aligned}$$

On general grounds, the coupling constants for these interactions are either unsuppressed, or, for pseudoscalars, minimally suppressed by any heavy scale of new physics, and thus it would be natural for new weakly-coupled physics to first manifest itself via these portals. Indeed, we observe that the right-handed neutrino coupling is amongst this list, which provides the simplest renormalizable interpretation for neutrino mass and oscillations. It is natural to ask if the other portals are also exploited in various ways, and many have been discussed recently in the dark matter context.

VII.1.1.1 Light Dark Matter

Dark matter provides one of the strongest empirical motivations for new particle physics, with a vast array of evidence coming from various disparate sources in astrophysics and cosmology.

While the vast majority of the particle physics community has focused on the possibility of WIMPs with a mass at the weak scale and interaction strength similar to the SM weak interactions, this is certainly not the only possibility. With the lack of evidence for new states at the weak scale from the LHC, a broader approach to the physics of DM and new experimental strategies to detect its non-gravitational interactions are called for. In particular, the particle(s) that comprise dark matter may be much lighter than the weak scale. Crucially, in the regime of sub-GeV dark matter, direct searches looking for the nuclear recoil of DM particles in the halo lose sensitivity. High intensity proton beams offer a new opportunity to search for light DM particles.

An important requirement of light thermal relic dark matter is the presence of new mediators which connect the SM to the dark sector, which open up new annihilation channels. The same mediators can then be utilized as a bridge to the SM and give signatures in proton beam fixed target experiments. Simple models involving dark matter coupling through a dark photon that kinetically mixes with the SM have been constructed in Refs. [1,2], and these models pass all terrestrial, astrophysical and cosmological constraints.

VII.1.1.2 Dark Photons

A new U(1) vector gauge boson V_μ can couple via kinetic mixing [3] with the hypercharge gauge boson of the SM: $\mathcal{L} \supset -(\kappa/2)V^{\mu\nu}F_{\mu\nu}$, providing one of the few renormalizable interactions between the SM and a hidden sector. In terms of the physical mass eigenstates, the interaction above generates a coupling between the dark photon and ordinary matter, $\mathcal{L} \supset e\kappa V_\mu \bar{\Psi}_{SM}\gamma^\mu\Psi_{SM}$. The strength of the kinetic mixing can range over many orders of magnitude depending on how it is generated at the high scale. For example, in supersymmetric models, it is quite naturally a loop factor below the scale of the electromagnetic coupling. Interest in dark photons in recent years has been motivated by a variety of experimental and observational data. The observation of a rise in the cosmic ray positron spectrum [4,5] is suggestive of TeV-scale dark matter interacting through a new dark force mediated by the dark photon [6,7]. Furthermore, a dark photon with a mass in the range of several MeV to a few GeV gives a positive contribution to the anomalous magnetic moment of the muon [8,9], potentially resolving the 3σ discrepancy between theory and experiment [10]. Indeed new experimental programs to search for such dark photons decaying to SM final states has commenced at Thomas Jefferson National Laboratory and at the Institute for Nuclear Physics of the Johannes Gutenberg University of Mainz using electron-beam fixed-target experiments [11–14].

VII.1.1.3 Dark Scalars

Given the discovery of the Higgs boson by the LHC experiments, the possibility of a Higgs portal to a hidden sector has become a reality. The Higgs portal couples new scalars to the SM via the operator $\mathcal{L} \supset (AS + \lambda S^2)H^\dagger H$. Higgs mediated interactions between light fermions are the amongst the weakest in the SM, and characterize the sensitivity of the current generation of direct detection experiments looking for WIMP dark matter; indeed S provides a simple WIMP candidate if $A = 0$. The small SM width of the Higgs, combined with the existence of the low dimension portal, makes probes of Higgs couplings a primary test of new physics. The LHC limits on the Higgs invisible width impose constraints on light scalars coupled through the Higgs portal, but precision tests through rare decays of B and K mesons at the intensity frontier can provide greater sensitivity

in the relevant kinematically accessible mass range. Producing these states via proton beams is more difficult at low energy due to the Yukawa suppression of the Higgs coupling to light quarks, and the small parton densities for sea quarks. It should be noted though that a dark $U(1)$ rendered massive via the Higgs mechanism in the hidden sector naturally allows a Higgs portal coupling to the *dark Higgs*, and this can be probed more efficiently via dark Higgs-strahlung.

VII.1.1.4 Singlet Neutrinos

A conventional weakly coupled particle that falls within this classification is the sterile neutrino. While the right-handed neutrinos of a type I see-saw may be too heavy to mediate interactions of interesting strength, light sterile neutrinos could help to resolve neutrino oscillation anomalies, and are another light dark matter candidate. These scenarios can be tested at long-baseline facilities, either by precise tests of the neutrino oscillation pattern, or for heavier mass via precise measurements of neutrino scattering in the near detector. It is important to note that larger-than-weak couplings of new singlet neutrinos to the baryon current are not well constrained by other experiments. Such baryonic neutrinos [15,16] could play a role in various low mass anomalies in direct detection, and could be searched for at high luminosity proton fixed target experiments.

VII.1.1.5 Axion-like Particles

The QCD axion is a highly motivated dark matter candidate, as it derives naturally in the context of quantum chromodynamics via spontaneous breaking of a new symmetry that forces CP -conservation by the strong interaction. While the parameter space for which axions may contribute significantly to dark matter is best probed with resonant cavities such as the ADMX experiment, other pseudoscalars produced in high scale symmetry breaking can also naturally be light and mediate interactions with a hidden sector via the pseudoscalar portal. Axion-like particles (ALPs), for which the mass is not tied to the symmetry breaking scale which solves the strong CP problem, may therefore be probed at the intensity frontier [17].

VII.1.1.6 Other Possibilities

We have summarized some of the scenarios analyzed in the recent literature, which involve couplings to the lowest dimension singlet portals. There are of course many other possibilities, for which an intense proton source could provide sensitivity. We should mention the possibility of allowing for parity-violation in the mediator couplings, as initially studied in some generality for dark $U(1)$ vectors [18,19], and couplings to flavor-dependent lepton and baryon currents. While such scenarios are generally more complex, and may require additional states for anomaly cancelation, we note that the existing sensitivity can be comparatively weak.

VII.1.2 Current Experimental Sensitivity

The past five years has seen a renewed interest in experimental probes of light weakly-interacting particles, with a focus on testing the portal couplings. In this subsection, we briefly summarize the current landscape.

Neutrino beams and proton fixed targets: There is already a significant infrastructure of short and long-baseline neutrino beam experiments. Most utilize intense proton sources impacting a target, with a decay volume in which charged pions, kaons and muons decay to produce neutrinos. Facilities such as MINOS, NOvA, T2K, and MiniBooNE already provide significant sensitivity to sterile neutrinos and non-standard interactions (NSI's). These facilities can also exploit the large volume (near-)detectors to study light states coupled through the other portals. However, the need to suppress the large neutrino background actually favors running in beam-dump mode, without the large decay volume. A number of constraints have been deduced from existing data, but as yet the only dedicated analysis for light dark matter coupled via the vector portal is being explored at MiniBooNE [20].

Rare meson decays: The search for rare decays has for many years imposed stringent constraints on models of new physics. The kaon physics program at *Project X* could play an important role in searches for hidden sectors. The ORKA experiment, aiming to measure the $K^+ \rightarrow \pi^+ \nu \bar{\nu}$ rate, will have sensitivity to suppressed decays to light dark matter coupled via a dark photon. Similarly decays of kaons and B mesons are sensitive tests of suppressed couplings via the scalar and pseudoscalar portals.

Electron fixed targets: A number of experiments at JLab and MAMI/Mainz, e.g., APEX, HPS, DarkLight, and others [11–14,21] have recently been developed to search primarily for light dark photons through their decays to electrons and muons. Electron beams are generally lower in energy than the existing proton beams, but have the advantage of a cleaner electromagnetic production process.

Meson factories: Significant sensitivity to various portals is available via heavy meson factories such as BaBar, Belle, Kloe, BES-III, and in the future Belle-II. The ultimate luminosity is lower than for proton fixed targets, but the precision detectors allow significant sensitivity up to higher mass for e.g. light scalars, pseudoscalars and dark photons decaying primarily to SM states. While some analyses are still underway, future progress in this area may come from Belle-II.

Direct detection: Current direct detection experiments, searching for nuclear recoils, are now probing the threshold of Higgs-mediated scattering for weak-scale WIMPs. However, sensitivity drops rapidly to zero for masses below a few GeV. There are proposals to extend this reach with alternate technologies, e.g., CCD's at DAMIC [22], and also the analysis of very low energy electron recoils [23]. However, currently experiments at the intensity frontier have significantly greater reach.

LHC: The energy frontier of course also provides sensitivity to light hidden sector states, primarily through unusual jet structures, eg. lepton jets in the case where SM decays are unsuppressed [24,25], or through missing energy events [26–28]. However, as noted above, for light mediators coupled through the renormalizable portals the production rates go down and radiation of hidden sector states is suppressed. Therefore, the energy frontier does not currently provide the strongest sensitivity to hidden sectors with light mediators.

In the next section, we focus on the specific sensitivity and advantages of proton fixed target experiments.

VII.2 OPPORTUNITIES AT NEUTRINO FACILITIES

Neutrino experiments provide an excellent opportunity to search for light weakly-coupled particles due to the large number of protons on target (currently reaching $\sim 10^{21}$ POT), the position of a near or single detector within a kilometer of the target, which in turn has a large mass with low energy thresholds and sensitive event characterization and background rejection. This potential was pointed out in Ref. [29], which explored the sensitivity of the LSND experiment to probe a variety of hidden sector particles such as dark photons, dark Higgs bosons, and dark matter. Refs. [2,30] explore the potential of the LSND, MiniBooNE, NuMi/MINOS, and T2K experiments to search for light dark matter. Ref. [31] further explores the sensitivity of LSND, MiniBooNE, MINOS, and CHARM to axions and dark photons.

Neutrino experiments are designed to produce neutrinos at a sizable hadronic rate via meson decays, and then detect their weak-scale scattering at the sub percent level. Thus, new weakly coupled states, produced with a rate at or below that of neutrinos, and with interaction strengths on the order of G_F or possibly below can be probed with these experiments. Such states can be produced in the primary proton-target collisions through a variety of physics processes, travel to a detector due to their weak coupling to SM matter, and then leave a signature in the detector through their decay to SM particles or by scattering with nucleons or electrons.

There are many hidden sector particle candidates that can be probed using neutrino experiments. There is still a great deal of work to be done to understand the sensitivity of these experiments over the full model and parameter ranges in these scenarios, beyond the investigations in the references presented above. Rather than discuss all of the possibilities here, we will highlight in detail a specific proposal to search for light dark matter with the MiniBooNE experiment [20]. This proposal represents the most detailed and precise investigation on the physics potential of neutrino experiments to search for hidden sector physics to date.

Indeed, as emphasized above, a unique advantage of these large neutrino detectors is the ability to search for new weakly-coupled particles via scattering. This opens up dark sector searches to ‘invisible modes’, where the dark photon decays to light NLWCPs that then travel the distance to the detector and scatter. The MiniBooNE experiment is sensitive to a model of light dark matter, which achieves the required relic abundance via thermal freeze-out through a dark photon mediator coupled to the SM via kinetic mixing. Such portal couplings render these models the least restricted by other terrestrial and astrophysical constraints. At MiniBooNE energies, the dark photon can be produced in the decays of the neutral pseudoscalar bosons $\phi^0, \eta \rightarrow \gamma V$ of which MiniBooNE has produced a huge sample. These dark photons subsequently decay to a pair of dark matter particles, which then travel to the detector and scatter. These searches therefore nicely compliment those being done at JLAB and MAMI/Mainz that look for dark photon decay to Standard Model particles.

Generically, beyond MiniBooNE the mass range that can be covered is dictated by the proton beam energy and the production mechanism involved. In the case of dark sector models with portal couplings to the visible sector, the accessible DM mass range is from a few MeV up to a few GeV for typical proton machines used for neutrino production (e.g. the FNAL Booster and Main Injector). It is important to emphasize that this covers a region at low DM masses that cannot currently be explored in underground direct detection experiments.

The proposal [20] describes the the potential to search for light sub-GeV WIMP dark matter at MiniBooNE. An important aspect of the proposal is to take advantage of the ability to steer the proton beam past the target and into an absorber, leading to a significant reduction in the neutrino background and allowing for a sensitive search for elastic scattering of WIMPs off nucleons or electrons in the detector. Additional background reduction strategies involve utilizing precision timing to account for the small delay of massive dark matter propagating to the detector, as compared to neutrinos, and also the distinct kinematics of the scattering [20]. Dark matter models involving a dark photon mediator can be probed in a parameter region consistent with the required thermal relic density, and which overlaps the region in which these models can resolve the muon $g - 2$ discrepancy. The expected number of signal events is shown in Fig. VII-1 for a range of parameter points. The signal significance for various operational modes is described in more detail in [20].

The experimental approach outlined for MiniBooNE to search for light NLWCPs is applicable to other neutrino facilities. For instance the MicroBooNE LAr detector can also make a search comparable to that outlined for MiniBooNE with a long enough beam-off-target run. Other neutrino experiments such as MINOS, NOvA, and T2K have potential to search for low mass NLWCPs. Refs. [2,30] have demonstrated the potential of such experiments to probe light dark matter, but more detailed studies by the experimental collaborations would be required to precisely determine the reach in the parameter space of these models.

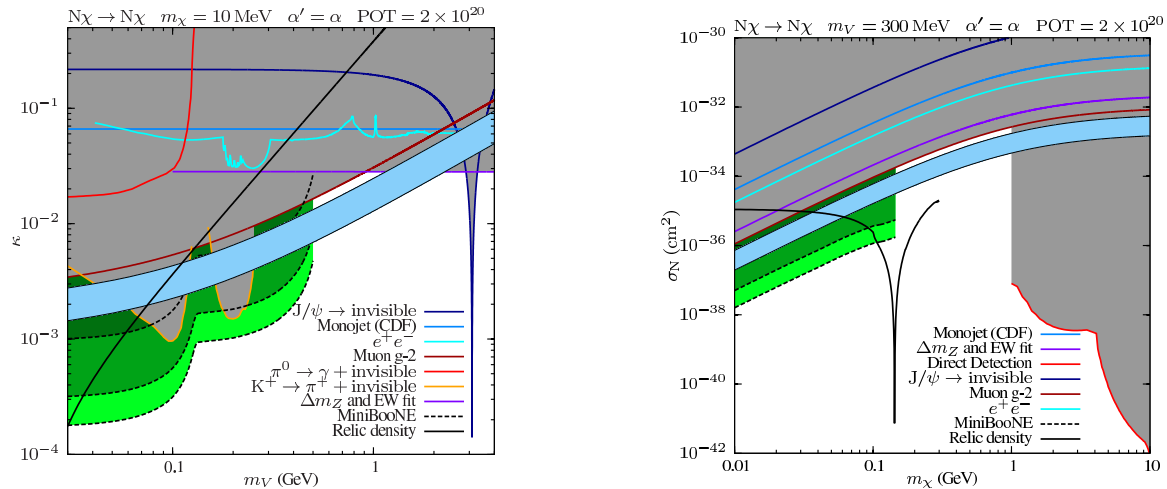


Figure VII-1: The MiniBooNE sensitivity to light dark matter scattering. This is shown in the plane of kinetic mixing versus vector mass (left), assuming a WIMP mass of 10 MeV, and in the plane of non-relativistic per-nucleon scattering cross section versus dark matter mass (right), using a vector mediator mass of 300 MeV. The light green band indicates greater than 10 events at MiniBooNE given a 2×10^{20} POT beam-off-target run. The various constraints and sensitivities are shown in the legend, the light blue band is the muon $g - 2$ signal region, and the required thermal relic density is shown as the black line. See Ref. [20] for more details.

VII.3 Project X BEAM PARAMETERS

In the following we briefly summarize the *Project X* beam parameters relevant to new particle searches. Such searches will benefit from increased intensity at each step of the staged approach, as this translates into greater search sensitivity given detectors able to provide sufficient background rejection. *Project X* is also ideally suited to a broad search for a range of possible NLWCPs, via flexibility in beam energies, targets, timing structures, and other configurations. It is expected that optimization over many different possible beam parameters will target searches for specific models or for specific areas of unexplored parameter space.

a) Stage 1 of *Project X* can provide 1000 kW at 1 GeV from a spallation target, which is essentially a high- Z , high-mass beam-dump. The beam timing is a continuous train of 50-ps wide proton pulses separated by 25,000 ps (25 ns). Pion production per Watt of beam power is essentially flat between 1 GeV and 8 GeV, so the Stage-1 beam dump would have a neutral pion flux of ~ 20 times that of the 8-GeV Booster beamline (this includes the lack of focusing relative to the BNB). The sharp pulse train timing will be useful in rejecting prompt neutrino backgrounds and searching for particles with mass below the pion threshold. Stage 1 would provide significantly more protons to both the BNB and MI, and hence any beam dump experiments on these beamlines.

b) Stage 2 of *Project X* will provide Stage-1 resources and another 1000 kW at 3 GeV from low-medium (carbon-gallium) targets, with the same Stage-1 time structure. The higher energy would allow higher particle mass searches due to the production of η mesons.

c) Stage 3 of *Project X* will continue the resources of Stages 1 and 2, and in addition replace the 8-GeV Fermilab Booster beam with an 8-GeV, 200-kW source pulsed at 10 Hz.

A future search with a dedicated beam dump experiment on the Main Injector would benefit from the higher energy 120-GeV protons. For an experiment such as the MiniBooNE proposal, this would allow searches for dark photons and dark matter up to masses of a few GeV, covering the gap in the muon $g - 2$ region up to the mass range at which current direct detection limits apply.

VII.4 NEW DETECTOR TECHNOLOGIES

The opportunity of searching for motivated new physics from a possible dark sector lends itself not only to exploiting existing and planned accelerator facilities but also to exploiting newly developed and improving detector technologies. In the following discussion, we assume a proton beam dump configuration where an intense proton beam is incident upon a target that may allow for the production of new light weakly coupled particles. Such particles will travel through shielding material until they either scatter or decay in a downstream detector. Presumably, beam related backgrounds will be dominated by neutrinos as other particles will be absorbed by shielding. Unlike a conventional neutrino beam facility that would try to concentrate the parent π and K mesons that decay into muons and neutrinos, an incident proton beam can specifically be directed onto a target without such focusing such that the neutrinos are spread out and have a lower density compared with possible directly-produced NLWCPs. In addition, having the ability to adjust the incident beam energy will change the composition of any neutrino background with lower energy neutrinos having a smaller interaction cross section in a downstream detector. Other possible handles for reducing

the neutrino background include precise timing information, as discussed in [20], to distinguish the travel time to scatter off GeV-mass NLWCPs from neutrinos traveling at essentially the speed of light.

The different strategies for reducing backgrounds to near negligible levels make the overall approach similar to a direct detection dark matter experiment, that has the greatest sensitivity when backgrounds are negligible. With negligible backgrounds, experiments gain in sensitivity faster with increased intensity. Beyond the simple counting type experiment, new detector technologies that are sensitive either to low energy scatters off the nucleus or surrounding electrons, or are sensitive to possible final state Standard Model decay products, can be exploited for a particular search. For example, detectors based upon liquid noble elements like liquid argon can be used to look for new weakly interacting particle scatters with or without a TPC that might allow for particle identification in case the new particle also decays into Standard Model particles. Detectors with low energy thresholds (such as DAMIC) could also be employed in such an experiment.

In short, there are a number of directions for using new detector technologies in the search for new light weakly coupled particles. Like the worked out example of the MiniBooNE proposal, we see that existing detectors can cover interesting regions of parameter space. The parameter space depends on the initial beam parameters and *Project X* would naturally allow for a broad range of possibilities. In addition, the ways in which hidden sector particles may either scatter off detector materials or perhaps decay into detectable Standard Model particles also gives a large range of possibilities and optimizations.

VII.5 SUMMARY

The possibility of new physics in the form of light weakly coupled particles from a hidden sector is motivated in various ways, from both bottom-up and top-down arguments. A general effective field theory perspective points to the minimal set of renormalizable portal interactions with the Standard Model as the primary couplings to probe for the existence of a neutral hidden sector. It turns out that existing neutrino experiments are particularly well suited to make the first measurements that cover interesting regions of parameter space, such as those motivated by the muon $g - 2$ anomaly or by astrophysical observations. A wider, more systematic, exploration would be possible at a high intensity facility such as *Project X* having many different configurations for initial beam energy, timing, and other parameters. Detectors can be optimized for generic searches or for more specific well-motivated searches. Who knows, but it may be a novel beam dump experiment at *Project X* that just might be the first to reveal a new level of understanding of New Physics!

References

- [1] M. Pospelov, A. Ritz, and M. B. Voloshin, Phys. Lett. **B662**, 53 (2008), [arXiv:0711.4866 [hep-ph]]
- [2] P. deNiverville, M. Pospelov, and A. Ritz, Phys. Rev. **D84**, 075020 (2011), [arXiv:1107.4580 [hep-ph]]

- [3] B. Holdom, Phys. Lett. **B166**, 196 (1986)
- [4] O. Adriani *et al.* (PAMELA Collaboration), Nature **458**, 607 (2009), [arXiv:0810.4995 [astro-ph]]
- [5] M. Aguilar *et al.* (AMS Collaboration), Phys. Rev. Lett. **110**, 141102 (2013)
- [6] N. Arkani-Hamed, D. P. Finkbeiner, T. R. Slatyer, and N. Weiner, Phys. Rev. **D79**, 015014 (2009), [arXiv:0810.0713 [hep-ph]]
- [7] M. Pospelov and A. Ritz, Phys. Lett. **B671**, 391 (2009), [arXiv:0810.1502 [hep-ph]]
- [8] P. Fayet, Phys. Rev. **D75**, 115017 (2007), [arXiv:hep-ph/0702176 [HEP-PH]]
- [9] M. Pospelov, Phys. Rev. **D80**, 095002 (2009), [arXiv:0811.1030 [hep-ph]]
- [10] G. W. Bennett *et al.* (Muon $g-2$ Collaboration), Phys. Rev. **D73**, 072003 (2006), [arXiv:hep-ex/0602035 [hep-ex]]
- [11] J. D. Bjorken, R. Essig, P. Schuster, and N. Toro, Phys. Rev. **D80**, 075018 (2009), [arXiv:0906.0580 [hep-ph]]
- [12] R. Essig, P. Schuster, N. Toro, and B. Wojtsekhowski, JHEP **1102**, 009 (2011), [arXiv:1001.2557 [hep-ph]]
- [13] H. Merkel *et al.* (A1 Collaboration), Phys. Rev. Lett. **106**, 251802 (2011), [arXiv:1101.4091 [nucl-ex]]
- [14] S. Abrahamyan *et al.* (APEX Collaboration), Phys. Rev. Lett. **107**, 191804 (2011), [arXiv:1108.2750 [hep-ex]]
- [15] M. Pospelov, Phys. Rev. **D84**, 085008 (2011), [arXiv:1103.3261 [hep-ph]]
- [16] R. Harnik, J. Kopp, and P. A. N. Machado, JCAP **1207**, 026 (2012), [arXiv:1202.6073 [hep-ph]]
- [17] A. Ringwald, Phys. Dark Univ. **1**, 116 (2012), [arXiv:1210.5081 [hep-ph]]
- [18] P. Fayet, Phys. Lett. **B96**, 83 (1980)
- [19] P. Fayet and M. Mezard, Phys. Lett. **B104**, 226 (1981)
- [20] R. Dharmapalan *et al.* (MiniBooNE Collaboration), “Low mass WIMP searches with a neutrino experiment: A proposal for further MiniBooNE running,” (2012), arXiv:1211.2258 [hep-ex]
- [21] J. R. Boyce (LIPSS Collaboration, DarkLight Collaboration, HPS Collaboration, APEX Collaboration), J. Phys. Conf. Ser. **384**, 012008 (2012)
- [22] J. Barreto *et al.* (DAMIC Collaboration), Phys. Lett. **B711**, 264 (2012), [arXiv:1105.5191 [astro-ph.IM]]

- [23] R. Essig, A. Manalaysay, J. Mardon, P. Sorensen, and T. Volansky, Phys. Rev. Lett. **109**, 021301 (2012), [arXiv:1206.2644 [astro-ph.CO]]
- [24] M. J. Strassler and K. M. Zurek, Phys. Lett. **B651**, 374 (2007), [arXiv:hep-ph/0604261 [hep-ph]]
- [25] N. Arkani-Hamed and N. Weiner, JHEP **0812**, 104 (2008), [arXiv:0810.0714 [hep-ph]]
- [26] J. Goodman, M. Ibe, A. Rajaraman, W. Shepherd, T. M. Tait, *et al.*, Phys. Rev. **D82**, 116010 (2010), [arXiv:1008.1783 [hep-ph]]
- [27] P. J. Fox, R. Harnik, J. Kopp, and Y. Tsai, Phys. Rev. **D85**, 056011 (2012), [arXiv:1109.4398 [hep-ph]]
- [28] I. M. Shoemaker and L. Vecchi, Phys. Rev. **D86**, 015023 (2012), [arXiv:1112.5457 [hep-ph]]
- [29] B. Batell, M. Pospelov, and A. Ritz, Phys. Rev. **D80**, 095024 (2009), [arXiv:0906.5614 [hep-ph]]
- [30] P. deNiverville, D. McKeen, and A. Ritz, Phys. Rev. **D86**, 035022 (2012), [arXiv:1205.3499 [hep-ph]]
- [31] R. Essig, R. Harnik, J. Kaplan, and N. Toro, Phys. Rev. **D82**, 113008 (2010), [arXiv:1008.0636 [hep-ph]]

VIII Hadronic Structure with *Project X*

*Markus Dieffenthaler, Xiaodong Jiang, Andreas Klein, Wolfgang Lorenzon,
Naomi C. R. Makins, and Paul E. Reimer*

VIII.1 INTRODUCTION

The proton is a unique bound state, unlike any other yet confronted by physics. We know its constituents, quarks and gluons, and we have a theory, QCD, to describe the strong force that binds these constituents together, but two key features make it a baffling system that defies intuition: the confining property of the strong force, and the relativistic nature of the system. Real understanding of the proton can only be claimed when two goals are accomplished: precise calculations of its properties from first principles, and the development of a meaningful picture that well approximates the system's dominant behavior, likely via effective degrees of freedom.

The excitement and challenge of the quest for this intuitive picture is well illustrated by the ongoing research into the spin structure of the proton, and in particular, into the contribution from quark orbital angular momentum (OAM). As experiment provides new clues about the motion of the up, down, and sea quarks, theory continues to make progress in the interpretation of the data, and to confront fundamental questions concerning the very definition of L in this context. Yet crucial pieces are still missing on the experimental side. One substantial missing piece is the the lack of any spin-dependent data from one of the most powerful probes of hadronic substructure available, the Drell-Yan process.

VIII.2 PROTON SPIN PUZZLE AND ORBITAL ANGULAR MOMENTUM

In its simplest form, the proton spin puzzle is the effort to decompose the proton's total spin into its component parts

$$\frac{1}{2} = \frac{1}{2}\Delta\Sigma + \Delta G + L_q + L_g. \quad (\text{VIII.2.1})$$

$\Delta\Sigma$ is the net polarization of the quarks, summed over flavor, and is known to be around 25% [1,2]. The gluon polarization, ΔG , is currently under study at the RHIC collider; the data collected to date favor a positive but modest contribution. What remains is the most mysterious contributions of all: the orbital angular momentum of the partons.

With the spin sum above as its capstone goal, the global effort in hadronic spin structure seeks to map out the proton's substructure at the same level of scrutiny to which the atom and the nucleus have been subjected. To this end, experiments with high-energy beams map out the proton's parton distribution functions (PDFs): the number densities of quarks and gluons as a function of momentum, flavor, spin, and, most recently, space. Deep-inelastic scattering (DIS) has yielded the most precise information on the unpolarized and helicity-dependent PDFs $f_1^q(x)$ and $g_1^q(x)$ for quarks.

Here q represents quark flavor and includes the gluon, g , while x is the familiar Bjorken scaling variable denoting the fraction of the target nucleon’s momentum carried by the struck quark. (The logarithmic dependence of the PDFs on the hard scattering scale has been suppressed for brevity.) For antiquarks, these distributions are accessed most cleanly by the Drell-Yan and W -production processes in proton-nucleon scattering. As with semi-inclusive DIS (SIDIS) or deep-inelastic jet production, both of these processes are purely leptonic in one half of their hard-scattering diagrams (see Fig. VIII-1), which facilitates clean interpretation and enables the event-level determination of the parton kinematics. The unique sensitivity of Drell-Yan and W -production to sea quarks is clearly shown: an antiquark is needed at the annihilation vertex in both cases. The Fermilab E866 experiment used Drell-Yan scattering to make its dramatic determination of the pronounced $\bar{d}(x)/\bar{u}(x)$ excess in the sea; the PHENIX and STAR experiments at RHIC are currently measuring W -production with polarized proton beams to determine the antiquark helicity PDFs $\Delta\bar{u}(x)$ and $\Delta\bar{d}(x)$ with new precision.

Over the past decade, attention has shifted to two new classes of parton distribution functions that offer a richer description of the proton’s interior than $q(x)$ and $\Delta q(x)$. These are the TMDs (transverse momentum dependent PDFs) and the GPDs (generalized parton distributions). The two descriptions are complementary: they correlate the partons’ spin, flavor, and longitudinal momentum x with transverse momentum \mathbf{k}_T in the TMD case and with transverse position \mathbf{b}_T in the GPD case. Both offer access to L , via different experimental approaches. The GPD approach relies on the measurement of exclusive photon and meson production with lepton beams at large Q^2 . This proposal focuses on the TMDs, which are accessed most cleanly via the azimuthal distributions of the final-state products of the SIDIS and Drell-Yan processes with polarized beams and/or targets. The details of these “single-spin azimuthal asymmetries” are presented in Sec VIII.2.1.

When parton transverse momentum \mathbf{k}_T is included—i.e., momentum transverse to that of the s - or t -channel virtual boson—one obtains the *transverse momentum distributions*. Theoretical analysis of the SIDIS process has led to the identification of eight such TMDs at leading twist [3,4]. Their operator structure is shown schematically in Fig. VIII-2. Three of these survive on integration over \mathbf{k}_T : the transverse extensions $f_1^q(x, \mathbf{k}_T^2)$ and $g_1^q(x, \mathbf{k}_T^2)$ of the familiar PDFs and a third distribution, $h_1^q(x, \mathbf{k}_T^2)$ termed transversity. The remaining five TMDs bring \mathbf{k}_T into the picture at an intrinsic level, and vigorous theoretical work has been devoted to deciphering their significance. The most intensely studied are the Sivers [5,6] distribution $f_{1T}^{\perp,q}(x, \mathbf{k}_T^2)$ and the Boer-Mulders [7] distribution $h_{1T}^{\perp,q}(x, \mathbf{k}_T^2)$. As shown in Fig. VIII-2, they describe the correlation of the quark’s momentum with the transverse spin of either the proton (Sivers) or the quark itself (Boer-Mulders). At first sight, the

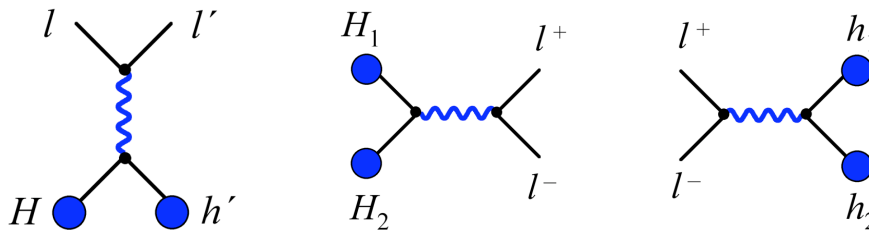


Figure VIII-1: Tree-level hard-scattering processes of the three reactions where TMD universality has been established (a) semi-inclusive DIS (b) Drell-Yan / W -production (c) e^+e^- annihilation.

operator differences depicted in the figure seem absurd: in the Sivers case, for example, how can the quark’s momentum distribution change if one simply rotates the proton’s spin direction by 180 degrees? A solution is presented when one considers the *orbital angular momentum* of the quarks, L_q . If the up quarks’ OAM is aligned with the proton spin, then the quarks will be oncoming—blue-shifted—on *different sides* of the proton depending on its spin orientation. The search for a rigorous, model-independent connection between the Sivers distribution and quark OAM is ongoing (see Refs. [8–10] for examples of recent approaches). The connection is as yet model-dependent, but what is clear is that the existence of the Sivers function *requires* nonzero quark OAM.

VIII.2.1 Spin, Orbital Angular Momentum, and QCD

Orbital angular momentum provides one of the most dramatic illustrations of the challenge of understanding the most fundamental bound state of QCD, the proton. In atomic and nuclear physics, L is a conserved quantity: a good quantum number that leads to the shell structure of these familiar systems. Not so with the proton. As the masses of the light quarks are so much smaller than the energy-scale of the system (e.g., the mass of the proton itself: 938 MeV compared with the 3–5 MeV of the up and down quarks), the system is innately relativistic. In relativistic quantum mechanics, L is *not* a conserved quantity: neither it nor spin commute with even the free Dirac Hamiltonian, and

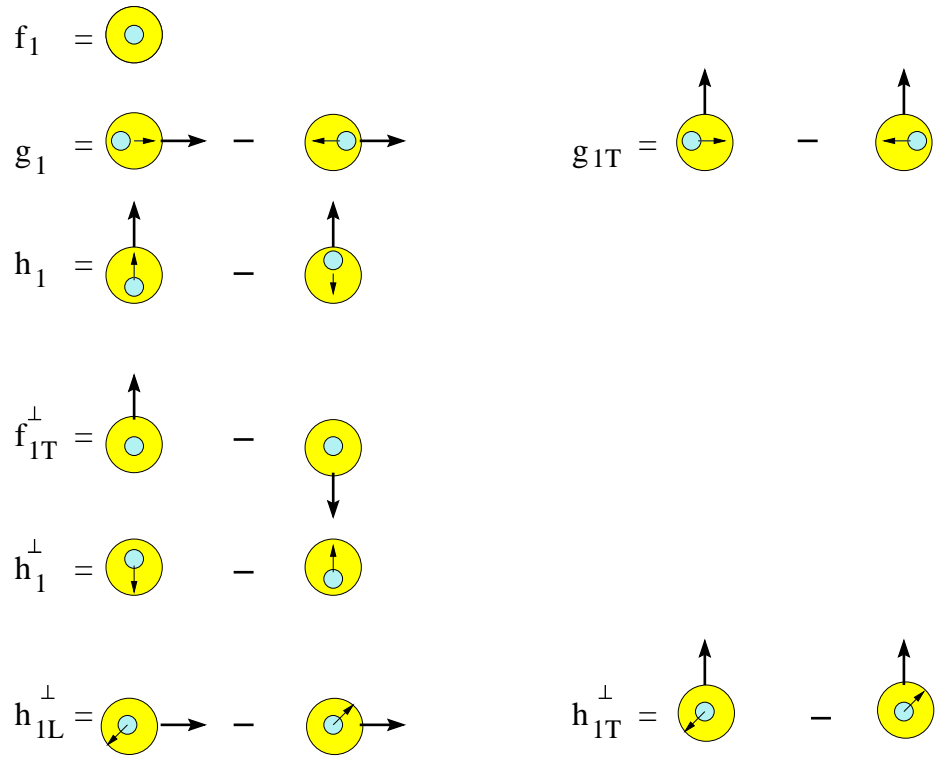


Figure VIII-2: Operator structures of the the eight leading-twist TMDs. The horizontal direction is that of the virtual boson probing the distribution. The large and small circles represent the proton and quark respectively, while the attached arrows indicate their spin directions.

so a shell structure within the proton is excluded. A simple calculation of the ground state of a light Dirac fermion bound in a central potential, for example, shows that the ground-state spinor is in a mixed state of L : $L = 0$ for the upper components and $L = 1$ for the lower components [11].

Furthermore, the definition of quark OAM is under active dispute. The simple spin sum of Eq. (VIII.2.1) conceals a wealth of complexity in the definition of its components. Two versions of this decomposition have dominated the discussion to date. They are colloquially referred to as the Jaffe [12] and Ji [13] decompositions, though they have been addressed by numerous authors; see Refs. [14–17] for elegant summaries of the issues.

The Ji decomposition can be expressed as

$$\mathbf{J}_{\text{proton}} = \int \psi^\dagger \frac{1}{2} \boldsymbol{\Sigma} \psi d^3x + \int \psi^\dagger \mathbf{x} \times \frac{1}{i} \mathbf{D} \psi d^3x + \int \mathbf{x} \times (\mathbf{E}^a \times \mathbf{B}^a) d^3x, \quad (\text{VIII.2.2})$$

where a is a color index. It has three gauge-invariant terms which, in order, represent the quark spin $\Delta\Sigma$, quark OAM L_q , and total angular momentum J_g of the gluons. The advantage of this decomposition is its rigorous connection to experiment via the Ji sum rule [13], which relates J_q for each quark flavor q to the second moment of two GPDs

$$\mathbf{J}_q = \lim_{t \rightarrow 0} \int \mathbf{x} [H_q(x, \xi, t) + E_q(x, \xi, t)] d^3x. \quad (\text{VIII.2.3})$$

The actual measurement of these GPDs is an enormous experimental task; it was initiated at HERMES and will be continued with greater precision at Jefferson Laboratory and COMPASS. The Ji decomposition can also be addressed by lattice QCD, which has already been used to compute moments of the GPDs under certain approximations (e.g., Ref. [18]). One disadvantage of this decomposition is the lack of a gauge-invariant separation of the gluon J_g into spin and orbital pieces. A second disadvantage is the problem of interpreting its definition of L_q as $\mathbf{x} \times \mathbf{D}$. The appearance of the covariant derivative $\mathbf{D} = \boldsymbol{\nabla} + i\mathbf{g}$ brings gluons into the definition. This is not the familiar, field-free OAM, $\mathbf{x} \times \mathbf{p}$, that is addressed by quark models of the proton.

The Jaffe decomposition is

$$\mathbf{J}_{\text{proton}} = \int \psi^\dagger \frac{1}{2} \boldsymbol{\Sigma} \psi d^3x + \int \psi^\dagger \mathbf{x} \times \frac{1}{i} \boldsymbol{\nabla} \psi d^3x + \int \mathbf{E}^a \times \mathbf{A}^a d^3x + \int E^{ai} \mathbf{x} \times \boldsymbol{\nabla} A^{ai} d^3x. \quad (\text{VIII.2.4})$$

It has four gauge-invariant terms, which in order represent the quark spin, quark OAM, gluon spin, and gluon OAM. Here, L_q is the field-free, canonical operator $\mathbf{x} \times \boldsymbol{\nabla}$. The gluon spin and OAM are separated in a gauge-invariant way, and in the infinite-momentum frame, parton distribution functions for the four pieces can be defined. The disadvantage of the Jaffe decomposition is that it is unclear how to measure its L_q and L_g terms, either in the lab or on the lattice, as they are nonlocal operators unless one selects a specific gauge (the lightcone gauge, $A^+ = 0$).

At present, we are thus confronted with one definition of L_q that can be measured but not interpreted, and another that can be interpreted but not measured. The “dynamical” OAM, $\mathbf{x} \times \mathbf{D}$, of the Ji decomposition brings us face-to-face with the confining nature of QCD: we cannot avoid interactions in a theory where quarks cannot be freed. Can we learn to interpret this quantity? This remains an open question, as only the “canonical” OAM definition, $\mathbf{x} \times \boldsymbol{\nabla}$, obeys the commutation relations of angular momentum algebra.

VIII.3 POLARIZED DRELL-YAN: THE MISSING SPIN PROGRAM

If we are to resolve the puzzle of quark spin in general and quark OAM in particular, it is vital to make a direct measurement of the Sivers distribution for antiquarks. The only process with which this task can be cleanly accomplished is Drell-Yan, with its innate sensitivity to antiquarks. A potential alternative, W -production, cannot be used in this endeavor as the unobserved neutrino blurs the final-state azimuthal distributions.

The need for a spin-dependent Drell-Yan program has become an urgent priority for the hadron-structure community world-wide. The three processes depicted in Fig. VIII-1 are the only ones where the TMD formalism has been theoretically shown to yield universal functions: PDFs and fragmentation functions that are process-independent. Of the three, only Drell-Yan has not yet been explored with polarized beams and/or targets. It is the missing component in the ultimate goal of a global analysis of TMD-related data. The crucial nature of this missing spin program arises from three facts: the innate sensitivity of Drell-Yan to antiquarks, its freedom from fragmentation functions, and the unique possibility it affords to test the TMD formalism.

VIII.3.1 Measurement of the Sivers Sign Change with a Polarized Proton Beam

The previous sections have framed the context in which polarized Drell-Yan experiments would be placed, and described its crucial place in the spin puzzle. We now turn to the specific motivation for using a polarized proton beam.

For Drell-Yan kinematics, $x_f \approx x_b - x_t$, where x_b and x_t are the longitudinal momentum fractions of the annihilated quarks from the beam and target, respectively. As with E906/SeaQuest, E866, and their predecessor experiments, the high x_b values selected by the forward $x_f > 0$ spectrometer mean that the partons from the beam will almost certainly be quarks, with the antiquark coming from the target. Taking u -quark dominance into consideration (due to the charge-squared weighting of the cross section and the preponderance of up quarks in the proton at high x), the measurement will be heavily dominated by valence up quarks from the polarized proton beam. The proposed measurement will thus be sensitive to Sivers function for up quarks, $f_{1T}^{\perp,u}(x, \mathbf{k}_T^2)$, times the familiar unpolarized PDF for anti-up quarks, $\bar{u}(x)$.

Given the unique access to sea quarks afforded by the Drell-Yan process, the reader may wonder why this proposal aims to measure the Sivers function for valence quarks, and valence up quarks at that—the flavor most precisely constrained by SIDIS data from HERMES and COMPASS.

The goal of this first spin-dependent Drell-Yan measurement is exactly to compare Drell-Yan and SIDIS, in order to test the 10-year-old prediction of a sign change in the Sivers function from SIDIS to Drell-Yan. Given the theoretical definition of the Sivers function [7], this sign change follows directly from field theory and CPT invariance [19]. Observing the sign change is essential to our interpretation of present and future TMD data in terms of angular momentum and spin. The sign change also offers a rigorous test of QCD in the nonperturbative regime—a rare thing indeed. Observation of the Sivers sign change is one of the DOE milestones for nuclear physics and is the first step for any spin-dependent Drell-Yan program [20].

Beyond the verification of the TMD framework and the tantalizing access it affords to OAM in the proton, there is rich physics behind the Sivers sign change itself. This physics lies in the

definition of the Sivers function. The function was first proposed as a possible explanation of the “E704 effect”: the large left-right analyzing power observed in inclusive pion production from a transversely polarized proton beam of 200 GeV incident on a beryllium target. The polarized beam at Fermilab E704 was a tertiary beam obtained from the production and subsequent decay of hyperons. (Its intensity was thus far below that required for Drell-Yan measurements.) As has happened repeatedly when spin degrees of freedom are introduced for the first time in experimental channels, new effects were observed at E704 that provoked rich new areas of study. The measured analyzing power was $A_N \propto \mathbf{S}_{\text{beam}} \cdot (\mathbf{p}_{\text{beam}} \times \mathbf{p}_{\text{pion}})$. This single-spin asymmetry is odd under so-called “naive time-reversal”, the operation that reverses all vectors and pseudo-vectors but does not exchange initial and final states. The only way to produce such an observable with a T -even interaction is via the interference of T -even amplitudes. The interfering amplitudes must have different helicity structures—one spin-flip and one non-spin-flip amplitude are required—and they must differ by a nontrivial phase. Both of these requirements are greatly suppressed in the perturbative hard-scattering subprocess, so the source of the E704 effect must be soft physics [21]: an interference in either the initial or final state. The original Sivers idea was of an initial-state interference [5,6]. A complementary proposal from Collins suggested a spin-orbit effect within the fragmentation process [22].

The breakthrough that led to our modern understanding of the E704 analyzing power occurred many years later when the HERMES collaboration measured pion single-spin asymmetries for the first time in deep-inelastic scattering, i.e., using a lepton rather than proton beam [23,24]. Unlike inclusive $pp \rightarrow \pi$, the SIDIS process $ep \rightarrow e'\pi$ allows complete kinematic determination of one side of the hard scattering diagram and involves two distinct scattering planes (as do all three processes in Fig. VIII-1). With this additional control, HERMES was able to separate single-spin effects arising from initial- and final-state interactions [25]. An electron beam interacts much more weakly than a hadron beam. It was widely assumed that initial-state interactions would be excluded in SIDIS, thereby isolating the final-state “Collins mechanism”, but the data showed otherwise: both initial- and final-state effects were found to be sizable. The explanation was provided in 2002 by Brodsky, Hwang, and Schmidt [8]. They revisited the QCD factorization theorems and discovered that previously-neglected gauge links between the struck quark and target remnant—soft gluon reinteractions necessary for gauge invariance—had to be included in the very definition of the parton distribution functions. Their paper presented a proof-of-principle calculation showing how a naive- T -odd distribution function could be generated at leading twist, and therefore observable in lepton SIDIS at high Q^2 : by interfering two diagrams within the PDF’s definition, one with no gauge-link rescattering and an $L = 0$ quark, and one with a single gluon exchanged and an $L = 1$ quark.

This PDF is what is now called the Sivers function, $f_{1T}^{\perp,q}$. Its definition and its very existence at leading twist are intimately related to gauge invariance and our understanding of QCD as a gauge theory. Its universality has been demonstrated—to within a sign—only for SIDIS and Drell-Yan (Fig. VIII-1). The sign change arises from the different topology of the gauge links in these two hard-scattering processes (Fig. VIII-3). In the SIDIS case, the reinteraction is attractive as it occurs between the struck quark and the target remnant. For the Drell-Yan case, the reinteraction is repulsive as it connects the parton from the beam to the remnant from the target (and vice versa). As Dennis Sivers has put it, the Sivers function and its sign change teach us about the gauge structure of QCD itself.

Testing the Siverson sign change is vital to the ongoing study of TMDs. It is the inevitable first step for any Drell-Yan spin program and is the key goals of this proposal. By polarizing the Main Injector beam, Fermilab will be able to continue its long and distinguished history of landmark Drell-Yan measurements and take the first step toward becoming the site of the missing piece of the global spin program.

VIII.3.2 Polarized Beam Drell-Yan Measurements at Fermilab

The physics goals described in Sec. VIII.3.1 can only be achieved with a combination of a large acceptance spectrometer for the correct kinematics, beam energy and, most importantly, high luminosity. With the addition of a polarized source and polarization maintaining Siberian snakes [26], Fermilab will offer a rare convergence of these three conditions at one facility for a Drell-Yan determination of the valence-quark Siverson distribution.

The SeaQuest spectrometer, illustrated in Fig. VIII-4, was specifically designed to achieve the desired large, forward acceptance. This acceptance is critical to obtaining the proper range in parton momentum fraction x , i.e., $x_b = 0.35 - 0.85$ covering the valence quark region, and $x_t = 0.1 - 0.45$ covering the sea quark region. This coverage dictates an event sample primarily from events in which a target antiquark and beam quark interact.

In order to be certain that the di-lepton pair that is detected is from a Drell-Yan interaction, the invariant mass of the virtual photon must, in general, be above $M_{J/\psi}$. The available phase space for a di-lepton pair falls as the center-of-mass energy, \sqrt{s} , falls. At the same time, backgrounds from uncorrelated pion decay in-flight will increase with decreasing \sqrt{s} . These two considerations make it difficult to envision a fixed target Drell-Yan measurement with a beam energy less than approximately 50 GeV. On the other hand, the Drell-Yan cross section for fixed x_t and x_b scales as $1/s$ implying that a smaller beam energy is desirable. The combination of these two factors places an extracted beam from the Fermilab Main Injector near the “sweet spot” for this type of measurement.

The measurement of the Siverson distribution sign change and the connection of the Siverson distribution with OAM has generated great interest around the globe. There are now plans for a wide

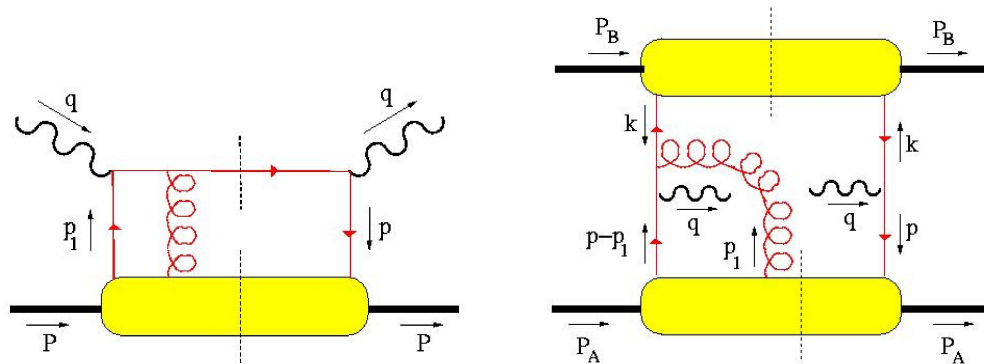


Figure VIII-3: Gauge-link topology of the one-gluon exchange forward scattering amplitudes involved in the Siverson function in the (a) semi-inclusive DIS and (b) Drell-Yan scattering processes.

variety of experiments to measure polarized Drell-Yan either with a polarized beam or a polarized target (see Table VIII-1). While each of these experiments can contribute to the overall picture, none offer the sensitivity over a wide kinematic range that can be achieved at Fermilab. COMPASS at CERN and Panda at GSI plan to perform fixed target experiments with either pion, proton or anti-proton beams, whereas PAX at GSI, and NICA at JINR plan collider experiments with polarized proton beams. NICA and the polarized Drell-Yan programs at RHIC will be sensitive to the interaction between valence quarks and sea antiquarks. PAX and COMPASS plan to measure the interaction between valence quarks and valence antiquarks, and are not sensitive to sea antiquarks. And Panda is designed to study J/ψ formation rather than Drell-Yan physics due to the low antiproton beam energy. The only experiment scheduled to run in the near future is COMPASS, which will measure A_N in one x_f -bin centered at $x_f = 0.2$ in the invariant mass region $4 < M < 9$ GeV. COMPASS is scheduled to take data in 2014 for one year and expects to measure the sign of the Sivers function in the same kinematics as semi-inclusive DIS with a statistical precision on $\delta A_N/A_N$ of 1–2%.

With the SeaQuest spectrometer and the Fermilab Main Injector beam energy, the sensitivity of a measurement is limited by statistical precision. A quick examination of the proposed experiments in Table VIII-1 shows that Fermilab can achieve three orders of magnitude more integrated luminosity than other facilities. The sensitivity that could be achieved at Fermilab is illustrated in Fig. VIII-5, compared with a fit of existing SIDIS Sivers distribution data by Anselmino, *et al.* [32,33].

The combination of high luminosity and large x -coverage makes Fermilab arguably the best place to measure single-spin asymmetries in polarized Drell-Yan scattering with high precision. At Fermilab, the only ingredient that is missing is It would allow for the first time to perform a me icient
preci

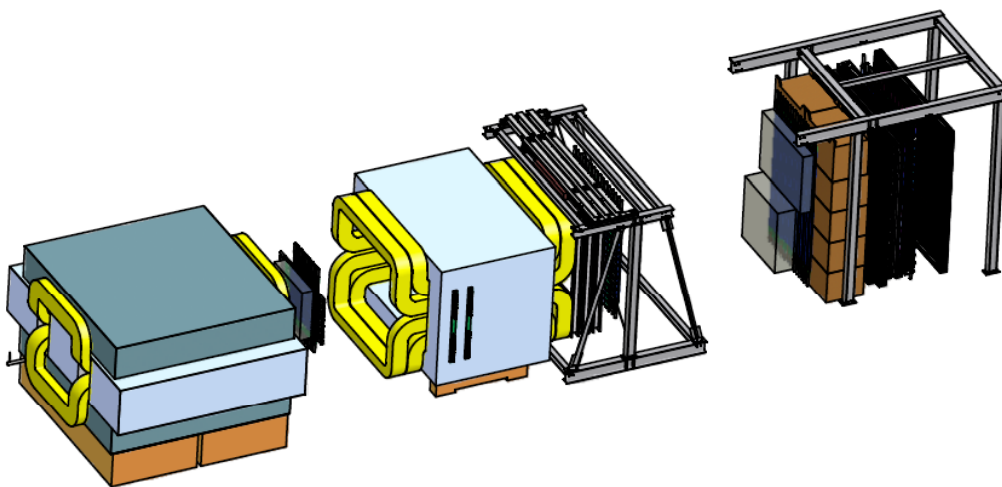
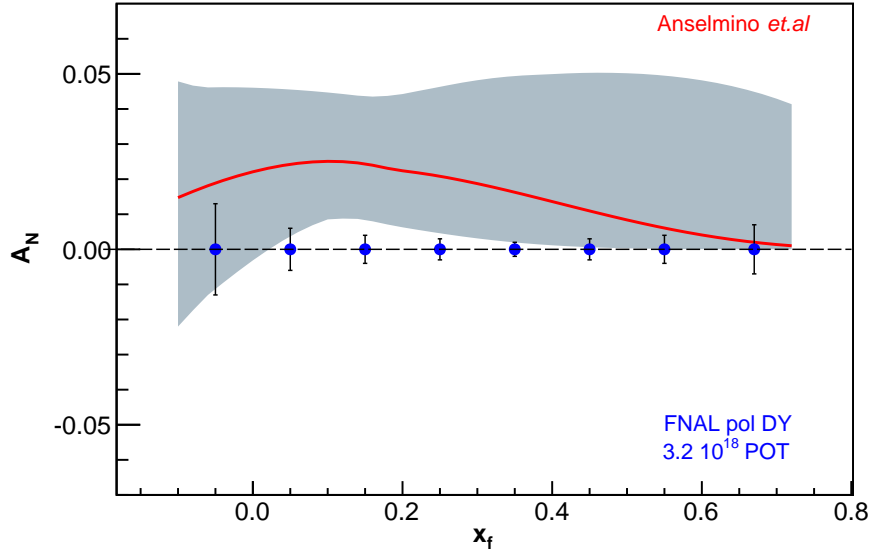


Figure VIII-4: Schematic view of the SeaQuest Spectrometer as it was during the 2012 commissioning run.

Table VIII-1: Planned polarized Drell-Yan experiments. x_b and x_t are the parton momentum fractions in the beam and target, respectively.

Experiment	Particles	Energy (GeV)	x_b or x_t	Luminosity ($\text{cm}^{-2}\text{s}^{-1}$)	Expected start
COMPASS [27] (CERN)	$\pi^\pm + p^\uparrow$	160 $\sqrt{s} = 17.4$	$x_t = 0.2\text{--}0.3$	1×10^{32}	2014
PAX [28] (GSI)	$p^\uparrow + \bar{p}$	collider $\sqrt{s} = 14$	$x_b = 0.1\text{--}0.9$	2×10^{30}	>2017
PANDA [29] (GSI)	$\bar{p} + p^\uparrow$	15 $\sqrt{s} = 5.5$	$x_t = 0.2\text{--}0.4$	2×10^{32}	>2016
NICA [30] (JINR)	$p^\uparrow + p$	collider $\sqrt{s} = 20$	$x_b = 0.1\text{--}0.8$	1×10^{30}	>2014
PHENIX [31] (BNL)	$p^\uparrow + p$	collider $\sqrt{s} = 200$	$x_b = 0.05\text{--}0.1$	2×10^{32}	>2018
Pol. Fermilab [‡] (Fermilab)	$p^\uparrow + p$	120 $\sqrt{s} = 15$	$x_b = 0.35\text{--}0.85$	2×10^{35}	>2015

[‡] $L = 1 \times 10^{36} \text{ cm}^{-2}\text{s}^{-1}$ (SeaQuest LH₂ target limited),
 $L = 2 \times 10^{35} \text{ cm}^{-2}\text{s}^{-1}$ (10% of Main Injector beam limited).

**Figure VIII-5:** Single-spin asymmetry A_N as a function of x_f . A_N (red line) is related to the Sivvers SSA amplitude by $A_N = (2/\pi)A_{\text{UT}}^{\sin\phi_b}$. The gray shaded area represents the $\sqrt{20}\sigma$ error band [32,33]. The expected statistical uncertainties (blue solid circles) for a 70% polarized beam on an unpolarized target and 3.2×10^{18} protons on target are (arbitrarily) plotted on the zero line.

VIII.3.3 OAM in the Sea

As theory continues to wrestle with fundamental questions of the origins of the proton's spin and OAM, experiment continues to measure. An enticingly coherent picture of quark OAM has emerged from the measurements of the Sivers function made via polarized SIDIS by the HERMES and COMPASS collaborations [25,34]. When subjected to a global fit [10,32,35,36] and combined with the chromodynamic lensing model of Ref. [9], they indicate $L_u > 0$ and $L_d < 0$ [37].

This agrees with the most basic prediction of the meson-cloud model of the proton. In this model, the proton is described as a superposition of a zeroth-order bare proton state of three constituent uud quarks and a first-order cloud of nucleon-pion states. The seminal idea behind this model is that hadrons, not quarks and gluons, are the best degrees of freedom with which to approximate the essential features of the proton. The pion cloud has two components: $n\pi^+$ and $p\pi^0$, weighted by the Clebsch-Gordan coefficients of these two isospin combinations. Immediately, we have an explanation for the dramatic excess of \bar{d} over \bar{u} observed by Fermilab E866/NuSea [38,39]: with the sea quarks wrapped up in the lightest hadronic states, the π^0 cloud contributes \bar{d} and \bar{u} in equal measure but the π^+ contributes only \bar{d} . Further, as the pions have zero spin, the antiquarks should be unpolarized. This agrees with the HERMES SIDIS data on $\Delta\bar{u}(x)$ and $\Delta\bar{d}(x)$ [40,41], both of which were found to be consistent with zero.

The meson cloud's picture of orbital angular momentum is dramatic. As the constituents are heavy in this picture, nonrelativistic quantum mechanics applies and L is once again a good quantum number. In what state of L is the pion cloud? The pions have negative parity while the nucleons have positive parity. To form a positive-parity proton from $n\pi^+$ or $p\pi^0$, the pions must carry $L = 1$. The lowest-order prediction of the meson cloud model is thus of an orbiting cloud; application of Clebsch-Gordan coefficients yields $L_u > 0$ and $L_d < 0$ [37,42].

Unfortunately, this apparently coherent picture is at odds with lattice-QCD calculations, which give $L_u < 0$ and $L_d > 0$ at the Q^2 scales of the Sivers measurements [43,44]. Recent work from a number of directions suggests that the resolution of this puzzle lies in the proton sea. As the sea quarks' spin polarization is near zero, and as the sea quarks' disconnected diagrams are difficult to treat on the lattice (they were omitted in Refs. [43,44]), a tendency to neglect them has emerged in the spin community. As a result, the simple fact has eluded us that the L_u and L_d determined from quark models and from SIDIS data refer to quarks only, while the lattice-QCD calculations include both quarks and antiquarks of the given flavor. Several recent developments have highlighted the perils of this bias. First, data from HERMES and BRAHMS on single-spin azimuthal asymmetries for kaon production have shown mild-to-dramatic differences between them [25,45,46]. A fast, final-state π^+ meson "tags" u and \bar{d} quarks (i.e., enhances their contribution to the cross section), while a K^+ tags u and \bar{s} . The only difference between the two is the antiquark; if it is causing pronounced changes in Sivers or Boer-Mulders asymmetries, it may be indicative of antiquark OAM. (Alternative explanations, such as higher-twist effects, also exist.) Second, Wakamatsu [47] has confronted the baffling negative sign of $L_u - L_d$ from lattice QCD by calculating L_u and L_d in the chiral quark soliton model, using both the Jaffe and Ji definitions. The paper shows not only the stark difference between the two definitions, but also separates the sea and valence quark contributions. In both definitions, the \bar{u} and \bar{d} antiquarks are the dominant players, and in the Jaffe definition, are entirely responsible for the negative sign of this quantity. Third, the χ QCD Collaboration [48] has, for the first time, succeeded in including disconnected diagrams in a lattice calculation of L .

They find the same: the sea quarks carry as much or more OAM as the valence quarks. Finally, we return to the meson cloud picture. Its orbiting cloud of $L = 1$ pions gives as much OAM to the antiquarks as to the quarks.

VIII.3.4 Polarized Target Drell-Yan Measurements at Fermilab

The same combination of spectrometer acceptance, proton beam energy and available luminosity that enabled the polarized beam measurement is at play for polarized target measurements. In this case, the missing piece in the implementation is a polarized hydrogen target. This is currently being developed by modifying and refurbishing an existing, superconducting magnet and polarized target system. With this target and an integrated 2.7×10^{18} protons delivered, the experiment expects to record and reconstruct 1.1×10^6 Drell-Yan events. The statistical precision on the asymmetry as a function of x_T from these events is shown in Fig. VIII-6.

VIII.3.5 Improvements with *Project X* Luminosity

The measurements outlined in Secs. VIII.3.2 and VIII.3.4 are statistically limited. An examination of Figs. VIII-5 and VIII-6 quickly reveals that these are both initial measurements. A true exploration of the Siverts distribution for both valence and sea quarks will benefit greatly from increased integrated luminosity.

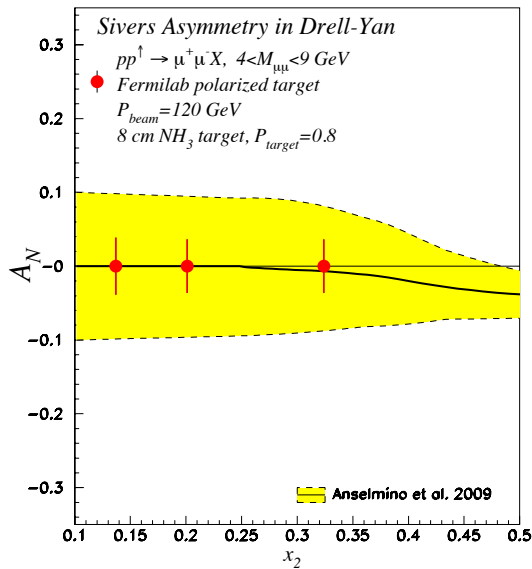


Figure VIII-6: Estimated statistical precision for the Drell-Yan sea-quark Siverts asymmetry vs. x_2 . Also shown is the prediction from Anselmino [33,36] for the magnitude of the asymmetry based on a fit of existing data. Note that we have extended the estimate below its valid minimum of x_2 of 0.2, in order to guide the eye. There is currently no good prediction available for the asymmetry below that value. The statistical uncertainties are based on 2.8×10^{18} protons on target.

The present luminosity is limited by the duration of the “slow spill” during the Main Injector cycle; by the number of protons in the “slow spill”; and by the spectrometer’s rate capabilities. *Project X* Stage 1 and 2 will allow for a factor of 7 more unpolarized protons per Main Injector spill. The proposed polarized target and associated utilities are likely capable of handling a factor of 2 increase in proton intensity. Additional investment would be required to take full advantage of the *Project X* luminosity.

The ability of the SeaQuest spectrometer and analysis to record and reconstruct events in this situation depends critically on the duty factor of the the proton beam. Improvements to the spectrometer’s rate capabilities in the *Project X* era can easily be foreseen, including: finer segmentation in the tracking chamber; the use of GEMs to replace the tracking chambers with the highest rate; finer segmentation in the triggering system; and an open aperture magnet that would allow for better triggering and track reconstruction. Later stages of *Project X* will allow for even greater increases in unpolarized proton beam intensity. Utilizing this additional luminosity would require additional investments in the spectrometer.

For the polarized beam experiment, the increase in proton beam intensity must start with an improved polarized proton source. The present plan [26] is to use a 1 mA polarized proton source to eventually deliver 1×10^{13} protons/spill to the experiment. Although the polarized source is not in the baseline for *Project X*, there are already foreseen improvements to the source proposed for Fermilab E1027 that could lead to up to a 5 mA polarized source and a corresponding increase in proton delivery to the experiment with the additional *Project X* Stage I improvements.

References

- [1] D. de Florian, R. Sassot, M. Stratmann, and W. Vogelsang, Phys. Rev. Lett. **101**, 072001 (2008), [arXiv:0804.0422 [hep-ph]]
- [2] D. de Florian, R. Sassot, M. Stratmann, and W. Vogelsang, Phys. Rev. **D80**, 034030 (2009), [arXiv:0904.3821 [hep-ph]]
- [3] P. J. Mulders and R. D. Tangerman, Nucl. Phys. **B461**, 197 (1996), [arXiv:hep-ph/9510301 [hep-ph]]
- [4] A. Bacchetta, M. Diehl, K. Goeke, A. Metz, P. J. Mulders, *et al.*, JHEP **0702**, 093 (2007), [arXiv:hep-ph/0611265 [hep-ph]]
- [5] D. W. Sivers, Phys. Rev. **D41**, 83 (1990)
- [6] D. W. Sivers, Phys. Rev. **D43**, 261 (1991)
- [7] D. Boer and P. J. Mulders, Phys. Rev. **D57**, 5780 (1998), [arXiv:hep-ph/9711485 [hep-ph]]
- [8] S. J. Brodsky, D. S. Hwang, and I. Schmidt, Phys. Lett. **B530**, 99 (2002), [arXiv:hep-ph/0201296 [hep-ph]]
- [9] M. Burkardt, Nucl. Phys. **A735**, 185 (2004), [arXiv:hep-ph/0302144 [hep-ph]]

- [10] A. Bacchetta and M. Radici, Phys. Rev. Lett. **107**, 212001 (2011), [arXiv:1107.5755 [hep-ph]]
- [11] Z.-T. Liang and T.-C. Meng, Z. Phys. **A344**, 171 (1992)
- [12] S. Bashinsky and R. L. Jaffe, Nucl. Phys. **B536**, 303 (1998), [arXiv:hep-ph/9804397 [hep-ph]]
- [13] X.-D. Ji, Phys. Rev. Lett. **78**, 610 (1997), [arXiv:hep-ph/9603249 [hep-ph]]
- [14] M. Wakamatsu, J. Phys. Conf. Ser. **295**, 012038 (2011), [arXiv:1012.0612 [hep-ph]]
- [15] M. Wakamatsu, Phys. Rev. **D81**, 114010 (2010), [arXiv:1004.0268 [hep-ph]]
- [16] M. Wakamatsu, Phys. Rev. **D83**, 014012 (2011), [arXiv:1007.5355 [hep-ph]]
- [17] M. Burkardt and G. Schnell, Phys. Rev. **D74**, 013002 (2006), [arXiv:hep-ph/0510249 [hep-ph]]
- [18] M. Göckeler *et al.* (QCDSF and UKQCD Collaborations), Phys. Rev. Lett. **98**, 222001 (2007), [arXiv:hep-lat/0612032 [hep-lat]]
- [19] J. C. Collins, Phys. Lett. **B536**, 43 (2002), [arXiv:hep-ph/0204004 [hep-ph]]
- [20] “Report to NSAC of the subcommittee on performance measures,” (2008), <http://science.energy.gov/~media/np/nsac/pdf/docs/perfmeasevalfinal.pdf>
- [21] G. L. Kane, J. Pumplin, and W. Repko, Phys. Rev. Lett. **41**, 1689 (1978)
- [22] J. C. Collins, Nucl. Phys. **B396**, 161 (1993), [arXiv:hep-ph/9208213 [hep-ph]]
- [23] A. Airapetian *et al.* (HERMES Collaboration), Phys. Rev. **D64**, 097101 (2001), [arXiv:hep-ex/0104005 [hep-ex]]
- [24] A. Airapetian *et al.* (HERMES Collaboration), Phys. Rev. Lett. **84**, 4047 (2000), [arXiv:hep-ex/9910062 [hep-ex]]
- [25] A. Airapetian *et al.* (HERMES Collaboration), Phys. Rev. Lett. **94**, 012002 (2005), [arXiv:hep-ex/0408013 [hep-ex]]
- [26] E. D. Courant *et al.* (SPIN@Fermi Collaboration), “Updated report acceleration of polarized protons to 120–150 GeV/c at Fermilab,” (2011), arXiv:1110.3042 [physics.acc-ph]
- [27] F. Gautheron *et al.* (COMPASS Collaboration), “COMPASS-II proposal,” (May 2010), http://wwwcompass.cern.ch/compass/proposal/compass-II_proposal/compass-II_proposal.pdf
- [28] V. Barone *et al.* (PAX Collaboration), “Antiproton-proton scattering experiments with polarization,” (2005), technical proposal, arXiv:hep-ex/0505054 [hep-ex]
- [29] U. Wiedner *et al.* (PANDA Collaboraton), “PANDA (AntiProton Annihilations at Darmstadt): Strong interaction studies with antiprotons,” (January 2004), Letter of Intent, http://www-panda.gsi.de/archive/public/panda_loi.pdf

- [30] “The Spin Physics Detector SPD,” (June 2010), http://nica.jinr.ru/files/Spin_program/spd-v21.pdf
- [31] L. Bland *et al.*, “Transverse-spin Drell-Yan physics at RHIC,” (May 2007), http://spin.riken.bnl.gov/rsc/write-up/dy_final.pdf
- [32] M. Anselmino *et al.*, Phys. Rev. **D79**, 054010 (2009), [arXiv:0901.3078 [hep-ph]]
- [33] M. Anselmino, private communication
- [34] V. Y. Alexakhin *et al.* (COMPASS Collaboration), Phys. Rev. Lett. **94**, 202002 (2005), [arXiv:hep-ex/0503002 [hep-ex]]
- [35] M. Anselmino *et al.*, “The Sivers function from SIDIS data,” (2008), arXiv:0807.0166 [hep-ph]
- [36] M. Anselmino *et al.*, Eur. Phys. J. **A39**, 89 (2009), [arXiv:0805.2677 [hep-ph]]
- [37] N. C. R. Makins, in *INT Workshop INT-12-49W Orbital Angular Momentum in QCD* (2012) http://www.int.washington.edu/talks/WorkShops/int_12_49W/People/Makins_N/Makins.pdf
- [38] E. A. Hawker *et al.* (FNAL E866/NuSea Collaboration), Phys. Rev. Lett. **80**, 3715 (1998), [arXiv:hep-ex/9803011 [hep-ex]]
- [39] R. S. Towell *et al.* (FNAL E866/NuSea Collaboration), Phys. Rev. **D64**, 052002 (2001), [arXiv:hep-ex/0103030 [hep-ex]]
- [40] A. Airapetian *et al.* (HERMES Collaboration), Phys. Rev. **D71**, 012003 (2005), [arXiv:hep-ex/0407032 [hep-ex]]
- [41] A. Airapetian *et al.* (HERMES Collaboration), Phys. Rev. Lett. **92**, 012005 (2004), [arXiv:hep-ex/0307064 [hep-ex]]
- [42] A. W. Thomas, Phys. Rev. Lett. **101**, 102003 (2008), [arXiv:0803.2775 [hep-ph]]
- [43] P. Hägler *et al.* (LHP Collaboration), Phys. Rev. **D77**, 094502 (2008), [arXiv:0705.4295 [hep-lat]]
- [44] D. Richards, in *The Physics of Excited Nucleons*, edited by H. W. Hammer, V. Kleber, H. Schmieden, and U. Thoma (Springer, Berlin, 2007) arXiv:0711.2048 [nucl-th]
- [45] A. Airapetian *et al.* (HERMES Collaboration), Phys. Rev. **D87**, 012010 (2013), [arXiv:1204.4161 [hep-ex]]
- [46] I. Arsene *et al.* (BRAHMS Collaboration), Phys. Rev. Lett. **101**, 042001 (2008), [arXiv:0801.1078 [nucl-ex]]
- [47] M. Wakamatsu, Eur. Phys. J. **A44**, 297 (2010), [arXiv:0908.0972 [hep-ph]]
- [48] K. F. Liu *et al.* (χ QCD Collaboration), PoS **LATTICE2011**, 164 (2011), [arXiv:1203.6388 [hep-ph]]

IX Hadronic Spectroscopy with *Project X*

Jürgen Engelfried and Stephen Godfrey

IX.1 HADRON SPECTROSCOPY

IX.1.1 Introduction

Hadron spectroscopy is the manifestation of QCD in the soft, low Q^2 , regime. There have been significant developments in theory in recent years, particularly as the result of improved and more complete results from lattice QCD; see Chapter X and Refs. [1–7]. Lattice QCD has established the existence of non quark model states in the physics QCD spectrum [2–7]. These non-quark-model states would represent a new form of hadronic matter with explicit gluonic degrees of freedom, the so called hybrids and glueballs, and multi-quark states beyond the quark-model $q\bar{q}$ mesons and qqq baryons. However, despite searching for these states for over twenty years, these states have yet to be unambiguously established experimentally. Reviews on the subject are given in Refs. [8–11]. See also the Particle Data Group [12]. There remains considerable interest in unambiguously identifying such states, as demonstrated by the high interest in the reports by the CLEO, BaBar and Belle collaborations for evidence of possible exotic states, the so called $X Y Z$ states [13], which are among the most cited publications from these experiments. The discovery of hybrids is the motivation for the GlueX experiment at Jefferson Lab and a primary motivation for the CEBAF 12 GeV upgrade [14]. GlueX uses high energy photons to excite mesons which many models predict will excite the gluonic degree of freedom to produce hybrids [15,16]. The GlueX program can only explore a limited mass range due to the photon beam energy so while it may be able to discover hybrid mesons and unambiguously establish their existence, it would not be able to fully map out the hybrid spectrum.

Here, we outline an idea for an experiment at *Project X*, which we call the Fermilab Exotic Hadrons Spectrometer (FEHS). Its purpose is to map out the hybrid meson spectrum, complete the light meson spectrum and resolve some long standing puzzles in hadron spectroscopy using high energy kaon beams that *Project X* has the unique capability of producing. The prototype for this experiment is the Large Aperture Superconducting Solenoid (LASS) experiment at SLAC [17], which advanced our understanding of strange and strangeonium spectroscopy to a degree that has yet to be surpassed.

IX.1.2 Physics Motivation

There have been great strides in quantitatively mapping out the hadron spectrum using lattice QCD [1–7]. Recent results indicate the existence of states with explicit gluonic degrees of freedom [2–7]. These gluonic degrees of freedom manifest themselves as “glueballs,” which are hadrons without valence quark content [6,7], and “hybrids,” which are states with both valence quarks and explicit

gluonic degrees of freedom [2–5]. Because the excited gluonic field could carry J^{PC} quantum numbers other than 0^{++} , the gluonic quantum numbers can couple to $q\bar{q}$ quantum numbers resulting in J^{PC} quantum numbers that are not accessible to a $q\bar{q}$ pair alone. Observation of a state with such exotic quantum numbers, 0^{--} , 0^{+-} , 1^{-+} , 2^{+-} , 3^{-+} ..., is considered the smoking-gun signature for states beyond the simple $q\bar{q}$ quark-model states. Lattice QCD predicts a rich spectrum of both isovector and isoscalar exotic hybrids, and the hadron spectrum from one set of recent calculations [3–5] is shown in Fig. IX-1, along with the glueball spectrum [6]. It is crucial that these calculations be verified by experiment.

Over the years a number of candidate glueball states have been reported but due to the dense spectrum of conventional hadrons it has been difficult to unambiguously identify a glueball candidate and rule out conventional explanations [8]. It is expected that the lowest lying glueballs are scalar mesons ($J^{PC} = 0^{++}$) which are difficult to disentangle from $q\bar{q}$ states with the same quantum numbers [10]. Furthermore, the physical hadronic states are expected to be some linear combination of $q\bar{q}$, glueballs and higher Fock space components rather than pure $q\bar{q}$ or glueballs. Other glueballs with conventional quantum numbers are expected in the 2 GeV mass region but they are also expected to be difficult to distinguish from conventional states [6]. The lowest lying glueballs with exotic quantum numbers are expected to lie $\simeq 2.5$ GeV and will be more difficult to produce. As a consequence of the expected glueball properties they are likely to be difficult to unambiguously identify as unconventional non- $q\bar{q}$ states.

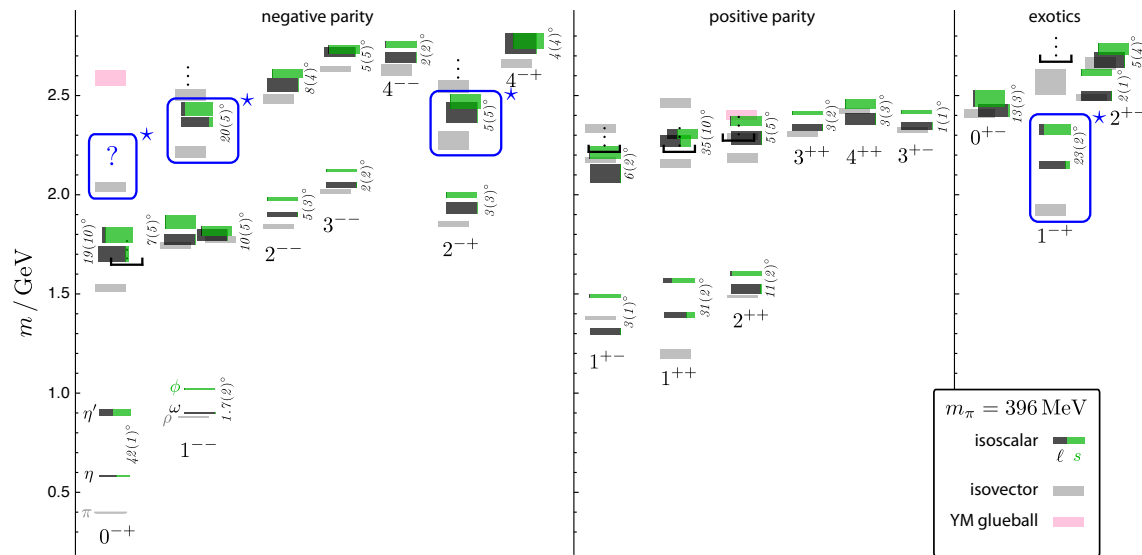


Figure IX-1: The light isoscalar meson spectrum as calculated using lattice QCD labelled by J^{PC} . The box height indicates the one sigma statistical uncertainty above and below the central value. The light (u , d) strange (s) quark content of each state ($\cos^2 \alpha$, $\sin^2 \alpha$) is given by the fraction of (black, green) and the mixing angle is also shown. Grey boxes indicate the positions of isovector meson states extracted on the same lattice [5]. Pink boxes indicate the position of glueballs in the quarkless Yang-Mills theory [6]. The candidate states for the lightest hybrid mesons are indicated by the blue boxes and stars [4]. From Refs. [3,4].

Predictions of hybrid meson properties suggest that they are likely to be easier to discover than glueballs for a number of reasons. Primarily, it is expected that hybrid states with exotic quantum numbers exist low enough in mass that they should be abundantly produced. The phenomenological properties of hybrids have been studied using several different models [18–20] and hybrid properties such as quantum numbers, masses and decays can be used to help in their discovery. There are two approaches to distinguish hybrids from conventional states. In the first, one looks for an excess of observed states compared to quark model predictions. The drawback to this approach is that it depends on a good understanding of hadron spectroscopy in a mass region that remains rather murky. The other approach is to search for exotic quantum numbers that are not consistent with quark model predictions. The discovery of such exotic quantum numbers would be irrefutable evidence of something new. Predicted properties of the lowest lying isovector and isoscalar hybrids are given in Table IX-1. Lattice QCD predicts that the lowest hybrid excitations are expected at approximately 1.9 GeV for the isovector 1^{-+} state and ~ 2.1 GeV and ~ 2.3 GeV for the mainly light and $s\bar{s}$ isoscalar 1^{-+} states respectively [3–5]. Note that the isoscalars have mixed light and $s\bar{s}$ content. We also expect strange hybrids. However, strange mesons have a denser spectrum described by the more limited set of J^P quantum numbers due to the flavored states not being eigenstates of charge-conjugation. The immediate consequence is that there are no exotic strange mesons and therefore no smoking gun signature for hybrid strange mesons.

Observation of the 0^{+-} and 2^{+-} multiplets as well as measuring the mass splittings with the 1^{+-} states would validate the lattice QCD calculations. The decay properties probe the internal structure of the parent state so the predictions of a specific model are very sensitive to the details of the model. The decay predictions presented in Table IX-1 [18–20] are obtained using flux tube description of the gluonic degrees of freedom. There appears to be a general property of hybrids that gluonic excitations cannot transfer angular momentum to the final states as relative angular momentum but rather, it must appear as internal angular momentum of the $q\bar{q}$ pairs. This results in an important selection rule of these models is that low-lying hybrids do not decay to identical mesons and that the preferred decay channels are to $S + P$ -wave mesons. A consequence is that hybrids tend to not couple strongly to simple final states making them in many cases difficult to reconstruct. However, these results should not be taken as gospel, which is why we need experimental measurements to test these ideas.

Using the hybrid decay properties given in Table IX-1, we give examples of final states that a successful experiment should be able to study: $b_2 \rightarrow a_1^+ \pi^- \rightarrow (\rho^0 \pi^+) \pi^- \rightarrow \pi^+ \pi^- \pi^+ \pi^-$ where the final state particles are charged, $h_2 \rightarrow b_1^0 \pi^0 \rightarrow (\omega \pi^0) \gamma \gamma \rightarrow \pi^+ \pi^- \gamma \gamma \gamma \gamma$, where there are multiple final state photons, and $h'_2 \rightarrow K_1^+ K^- \rightarrow \rho^0 K^+ K^- \rightarrow \pi^+ \pi^- K^+ K^-$, requiring the identification of strange particles. The $s\bar{s}$ hybrids, η'_1 and h'_2 , are predicted by some models to be relatively narrow and are expected to decay to well-established strange resonances. The decay of $s\bar{s}$ states to strange final states are enhanced relative to non-strange decays. To map out the $s\bar{s}$ hybrids will require measuring charged, neutral, and strange mesons in the final state. More generally, clearly identifying a large number of low lying hybrids would provide indisputable evidence for the the existence of exotic hybrid mesons. To do so requires systematically studying the strange and non-strange decay modes.

In addition to exotic hybrids one also expects hybrids with conventional J^{PC} quantum numbers. They will appear among conventional states with the same quantum numbers, so identifying the hybrids requires having a good understanding of the meson spectrum. To do so requires the ability to systematically study many final states, which will require considerable statistics to be able to advance our knowledge of these states.

Table IX-1: Properties of exotic hybrid mesons. Masses are taken from lattice QCD calculations [3–5]. The estimates for widths and decay modes are taken from Ref. [19] for the PSS (Page, Swanson and Szczepaniak) [19] and IKP (Isgur, Kokoski and Paton) [18] models.

	Mass (MeV)	J^{PC}	Total Width (MeV)		Decays
			PSS	IKP	
π_1	1900	1^{-+}	80-170	120	$b_1\pi, \rho\pi, f_1\pi, a_1\eta, \eta(1295)\pi$
η_1	2100	1^{-+}	60-160	110	$a_1\pi, f_1\eta, \pi(1300)\pi$
η'_1	2300	1^{-+}	100-220	170	$K_1(1400)K, K_1(1270)K, K^*K$
b_0	2400	0^{+-}	250-430	670	$\pi(1300)\pi, h_1\pi$
h_0	2400	0^{+-}	60-260	90	$b_1\pi, h_1\eta, K(1460)K$
h'_0	2500	0^{+-}	260-490	430	$K(1460)K, K_1(1270)K, h_1\eta$
b_2	2500	2^{+-}	10	250	$a_2\pi, a_1\pi, h_1\pi$
h_2	2500	2^{+-}	10	170	$b_1\pi, \rho\pi$
h'_2	2600	2^{+-}	10-20	80	$K_1(1400)K, K_1(1270)K, K_2^*K$

In addition to verifying the existence of these new forms of hadronic matter, there remain many issues in conventional hadron spectroscopy. The first issue is that the quark model predicts numerous states in the 1–2 GeV mass region that have not been observed. To fully understand conventional hadron spectroscopy, it is important that more of these missing states are discovered and their properties measured. A problem in improving our knowledge of mesons are that they are more difficult to produce via t -channel exchange, and there is little control of the flavor quantum number. In addition, these states are often broad and overlapping, the isospin zero states can and do mix, and there is the possibility of glueballs, hybrids and multiquark states in the spectrum. The LASS experiment at SLAC had considerable success in filling in some of the gaps in the strange and $s\bar{s}$ meson sectors. The leading $s\bar{s}$ states have been seen up to $J = 5$, along with a few radial excitations. However, some of the states have never been confirmed, with contradictory observations from other experiments, and numerous states remain missing. Furthermore, the LASS experiment was completed decades ago.

To understand the physics, the LASS results should only be viewed as the start for unravelling the meson spectrum. It is time to find more of the radially excited states, fill in the orbitally excited multiplets, and proceed to the more complicated $u\bar{u}$ and $d\bar{d}$ isoscalar and isovector mesons to test lattice-QCD calculations. Because of the complications of mixing between isoscalar states due to gluon annihilation and the possibilities of glueballs, the strange mesons are a good starting point as they do not have these complications. In addition, because they are a heavy-light system, they probe glue dynamics in a different environment than do mesons made out of equal mass quarks. However, as mentioned previously, because they are not eigenstates of charge-conjugation there are no exotic quantum numbers in the kaon sector and hence no smoking gun signal of hybrid states. A detailed survey of the $s\bar{s}$ states would be a useful next step as they form a bridge between the heavy quarkonia ($c\bar{c}$ and $b\bar{b}$) and the light quark mesons.

The second issue concerns puzzles and contradictory results in conventional hadron spectroscopy

[8,12]. An example of such a puzzle is the $1^{++} s\bar{s}$ state. The $f_1(1420)$ is a candidate for the axial vector partner $s\bar{s}$ of the a_1 meson. However, LASS also observed a $1^{++} s\bar{s}$ state which fits in nicely as the $^3P_1 s\bar{s}$ state but saw no evidence for the $f_1(1420)$. The $\eta(1440)$ is another longstanding puzzle. It is alleged by some to be a glueball although several conventional $q\bar{q}$ are expected in this mass region. Until the experimental situation clears up the glueball interpretation will remain suspect. The FEHS experiment would be able to clear up these and many other puzzles that have festered for many years.

A final issue in conventional hadron spectroscopy is really how the first two issues affect the search for gluonic hadrons and multi-quark states. The main impediment to finding exotic states with conventional quantum numbers is our incomplete understanding of the conventional mesons. To unambiguously recognize hybrids or glueballs will require a much better understanding of conventional mesons.

We have focused primarily on the meson sector, because the baryon sector is denser and without exotic quantum numbers. Consequently, it will be difficult to distinguish non-quark model states from conventional baryons. Also, in recent years the CLAS experiment at Jefferson Lab has improved our understanding of baryons. Nevertheless, the *Project X* spectroscopy program can make important contributions to our knowledge of baryons. The quark model predicts a very rich spectroscopy that has not been comprehensively tested. Baryons have mainly been produced in s -channel πN and $\bar{K}N$ formation experiments. Quark model calculations predict that some states couple strongly to these channels and others will almost completely decouple. These features have been supported by experiment. Thus, one way to find missing baryons is to study channels which couple more strongly to these missing states. Another way is to produce baryons as decay states from higher states in the πp and Kp channels. Both approaches should be possible with the high intensity beams available at *Project X*. In addition, because the number of baryons increases rapidly above 2 GeV, high statistics experiments will be needed to disentangle the large number of states expected. One sector that is relatively unexplored is the sss Ω baryons. A suitable experiment at *Project X* should be able to observe and study these states. It is important that the theoretical predictions for baryons be more completely tested by experiment by the observation of many of the missing baryons and measurement of their properties.

Unravelling the spectroscopy will need high statistics experiments to perform partial wave analysis to filter by J^{PC} quantum numbers. To assist us in this process a guide to expected properties will be useful. There exist fairly complete calculations for expected masses and decays of conventional states using the quark model and lattice QCD. While quantitative predictions might have large uncertainties, qualitative predictions have proven to be reasonably reliable. The bottom line is that for many years progress in light hadron spectroscopy has been limited and there is a compelling need for good quality data to advance the subject.

IX.1.3 Experimental Setup

As pointed out above, the LASS spectrometer at SLAC [17] was the principal experiment contributing to the physics of excited hadrons. That said, the secondary beam-line at SLAC had a very poor duty factor, and LASS ran with only 4–5 kaons per pulse to avoid pileup, and 100–180 pulses per second, resulting in fewer than 1000 kaons per second [21].

A new experiment should aim to increase LASS's statistics by about a factor 50. FEHS could run with a beam rate of about 50000 kaons per second, with a flat-top extraction this corresponds to about 20 μs between beam particles and presents no problem whatsoever for the beam instrumentation or the experimental setup. For these reasons, a slightly updated copy of the LASS spectrometer would be the first approximation for the experimental setup for FEHS.

IX.1.3.1 Beam Line and Target

The LASS spectrometer featured a RF separated beam line of up to 16 GeV/ c momentum, and was usually run at around 11 GeV/ c . At higher beam momentum, higher mass states can be produced, but the length of the beam line needed for the RF separation increases with the square of the momentum, while the decay losses decrease only linearly with the momentum. At higher momentum, say ~ 20 GeV/ c , it will be necessary to use superconducting RF cavities to achieve a sufficient p_t kick for the separation.

One could also consider using an unseparated beam. Depending on the momentum of the primary (proton-)beam and the secondary beam momentum, typically the kaon:pion ratio is about 1:10, leading to a higher, but still tolerable, flux in the spectrometer. The final choice of the beam momentum will need a detailed study of the all the above mentioned effects.

In LASS, the beam particles were tagged with the help of two threshold Cherenkov counters, the first 6m long filled with H₂ at 40 psia (to count only pions) and the second 1.28m long filled with CO₂ at 75 psia (to count pions and kaons). The signals from the two counters (anti-)coincidences were used to tag pions, kaon, and protons. In FEHS, beam particle tagging can be performed in the same way.

LASS featured a 33.5" long liquid-hydrogen target. FEHS could use the same without difficulty.

IX.1.3.2 The Spectrometer

The experimental target at LASS was inside a solenoid magnetic field, surrounded by wire chambers, followed downstream by a dipole magnet, again surrounded by multiwire proportional chambers. This setup provided a nearly 4π coverage and proved to be very successful. It was also adopted by the GlueX experiment [22] at Jefferson Lab.

For FEHS this setup can also be used. Conventional wire chambers equipped with modern readout electronics are sufficient for the flux conditions described above.

Particle identification in LASS was performed via a pair of threshold Cherenkov detectors and a scintillator hodoscope forming a TOF system. Depending on the beam momentum, a similar PID system can be used for FEHS.

IX.1.3.3 Detector Summary

In summary, the LASS spectrometer remains a suitable model for the FEHS experiment as well. The detectors to be used (wire chambers, scintillator hodoscopes) are proven technology and optimizing

the designs for FEHS should not present serious problems. Simulation studies have to be carried out to choose the beam momentum and to define the sizes and resolutions of the different detector systems.

IX.1.4 Summary

We have a long way to go before we can say that we understand hadron spectroscopy. While there has been considerable progress made in lattice QCD, these results need to be reproduced by experimental observation and measurements of the states' properties. The unambiguous discovery of states with explicit glue degrees of freedom would be a major event as seen by the excitement generated by recent candidate particles. The details will provide important insights into quark and gluon dynamics. They will help answer the question of how the glue degree of freedom manifests itself as collective excitations or by some other description.

In addition, it is sobering to realize that we still do not understand conventional meson spectroscopy very well. Our knowledge and understanding of higher orbital and radial excitations is sparse at best. It is worth remembering that there are many long-standing puzzles. This poor understanding is hindering our ability to search for non $q\bar{q}$ states. With a better understanding of conventional states it should be possible to distinguish hybrid states with non-exotic quantum numbers from conventional states. This would be especially important for strange mesons for which charge conjugation is not a good quantum number.

The preferred approach is to search for hybrid states with exotic properties. The least controversial characteristic is to look for states with exotic J^{PC} quantum numbers with most calculations predicting a 1^{-+} state to be accessible with mass less than 2 GeV. The observation of a resonance signal in this channel would be strong evidence for the discovery of a hybrid and is considered to be the starting point of any experimental search. This is the approach taken by the GlueX collaboration.

To answer these questions and make progress in hadron spectroscopy a hadron spectrometer facility should be a part of the *Project X* physics program. The principal goal of the facility should be to search for gluonic excitations in hadrons and map out the spectroscopy of these states. It is also important that the next generation of hadron spectroscopy experiments fill in as many of the missing conventional meson and baryon states as possible.

To make progress in this field it is important that we study many properties of hadrons in many different channels to unravel the physics. The data will come from measurements at many different machines using different production mechanisms such as J/ψ radiative decays into light hadron final states studied by BESIII at IHEP in Beijing, photoproduction of states by GlueX at Jefferson Lab, $p\bar{p}$ annihilation by PANDA at GSI in Germany and high energy π , K and \bar{p} beams by the COMPASS experiment at CERN. However, the old LASS experiment has demonstrated that a dedicated high statistics hadroproduction experiment can make unique, important contributions.

To address these questions the detector should have 4π acceptance for charged and neutral particles with high detection efficiency, excellent tracking resolution and particle identification and be capable of acquiring very high statistics. The program will need π and K beams of 20 GeV maximum energy with an appropriate sized experimental area to accommodate the detector.

The production mechanism in hadroproduction will complement other ongoing experiments such as GlueX and BESIII as it will produce many different states in a wide variety of channels.

References

- [1] Z. Fodor and C. Hoelbling, *Rev. Mod. Phys.* **84**, 449 (2012), [arXiv:1203.4789 [hep-lat]]
- [2] J. J. Dudek, R. G. Edwards, M. J. Peardon, D. G. Richards, and C. E. Thomas, *Phys. Rev. Lett.* **103**, 262001 (2009), [arXiv:0909.0200 [hep-ph]]
- [3] J. J. Dudek, R. G. Edwards, B. Joo, M. J. Peardon, D. G. Richards, *et al.*, *Phys. Rev.* **D83**, 111502 (2011), [arXiv:1102.4299 [hep-lat]]
- [4] J. J. Dudek, *Phys. Rev.* **D84**, 074023 (2011), [arXiv:1106.5515 [hep-ph]]
- [5] J. J. Dudek, R. G. Edwards, M. J. Peardon, D. G. Richards, and C. E. Thomas, *Phys. Rev.* **D82**, 034508 (2010), [arXiv:1004.4930 [hep-ph]]
- [6] C. J. Morningstar and M. J. Peardon, *Phys. Rev.* **D60**, 034509 (1999), [arXiv:hep-lat/9901004 [hep-lat]]
- [7] Y. Chen, A. Alexandru, S. J. Dong, T. Draper, I. Horvath, *et al.*, *Phys. Rev.* **D73**, 014516 (2006), [arXiv:hep-lat/0510074 [hep-lat]]
- [8] S. Godfrey and J. Napolitano, *Rev. Mod. Phys.* **71**, 1411 (1999), [arXiv:hep-ph/9811410 [hep-ph]]
- [9] C. A. Meyer and Y. Van Haarlem, *Phys. Rev.* **C82**, 025208 (2010), [arXiv:1004.5516 [nucl-ex]]
- [10] V. Crede and C. A. Meyer, *Prog. Part. Nucl. Phys.* **63**, 74 (2009), [arXiv:0812.0600 [hep-ex]]
- [11] E. Klempt and A. Zaitsev, *Phys. Rept.* **454**, 1 (2007), [arXiv:0708.4016 [hep-ph]]
- [12] J. Beringer *et al.* (Particle Data Group), *Phys. Rev.* **D86**, 010001 (2012)
- [13] S. Godfrey and S. L. Olsen, *Ann. Rev. Nucl. Part. Sci.* **58**, 51 (2008), [arXiv:0801.3867 [hep-ph]]
- [14] J. Dudek *et al.*, *Eur. Phys. J.* **A48**, 187 (2012), [arXiv:1208.1244 [hep-ex]]
- [15] F. E. Close and J. J. Dudek, *Phys. Rev. Lett.* **91**, 142001 (2003), [arXiv:hep-ph/0304243 [hep-ph]]
- [16] F. E. Close and J. J. Dudek, *Phys. Rev.* **D69**, 034010 (2004), [arXiv:hep-ph/0308098 [hep-ph]]
- [17] D. Aston *et al.* (LASS Collaboration), “The LASS spectrometer,” SLAC-R-0298 (1987)
- [18] N. Isgur, R. Kokoski, and J. E. Paton, *Phys. Rev. Lett.* **54**, 869 (1985)
- [19] P. R. Page, E. S. Swanson, and A. P. Szczepaniak, *Phys. Rev.* **D59**, 034016 (1999), [arXiv:hep-ph/9808346 [hep-ph]]
- [20] F. E. Close and P. R. Page, *Nucl. Phys.* **B443**, 233 (1995), [arXiv:hep-ph/9411301 [hep-ph]]

-
- [21] B. Ratcliff(2013), private communication
- [22] M. Dugger *et al.* (GlueX Collaboration), “A study of meson and baryon decays to strange final states with GlueX in Hall D,” Proposal to the 39th Jefferson Lab Program Advisory Committee (2012), arXiv:1210.4508 [hep-ex]

X Lattice-QCD Calculations for *Project X*

*Thomas Blum, Ruth S. Van de Water,
Michael Buchhoff, Norman H. Christ, Andreas S. Kronfeld, David G. Richards*

X.1 PHYSICS MOTIVATION

As discussed in the previous chapters, the *Project X* accelerator complex will host a broad range of high-precision measurements that probe quantum-mechanical loop effects and are sensitive to physics at higher energy scales than are directly explored at the LHC. Through the use of intense beams and sensitive detectors, the various *Project X* experiments will search for processes that are extremely rare in the Standard Model (SM) and look for tiny deviations from Standard-Model expectations.

In many cases, the comparison between the measurements and Standard-Model predictions are currently limited by theoretical uncertainties from nonperturbative hadronic amplitudes such as decay constants, form factors, and meson-mixing matrix elements. Lattice gauge theory provides the only known first-principles method for calculating these hadronic matrix elements with reliable and systematically-improvable uncertainties, by casting the basic equations of QCD into a form amenable to high-performance computing. Thus, facilities for numerical lattice QCD are an essential theoretical complement to the experimental high-energy physics program.

The lattice-QCD community in the US and worldwide is expanding its program to meet the needs of the *Project X* physics program, as well as other upcoming intensity-frontier experiments. In some cases, such as for the determination of CKM matrix elements that are parametric inputs to Standard-Model predictions, improving the precision of existing calculations is sufficient, and the expected increase in computing power due to Moore's law will enable a continued reduction in errors. In other cases, like the muon $g - 2$ and the nucleonic probes of non-SM physics, new hadronic matrix elements are required; these calculations are typically computationally more demanding, and methods are under active development.

The future success of the *Project X* physics program hinges on reliable Standard-Model predictions on the same timescale as the experiments and with commensurate uncertainties. In this chapter we discuss several key opportunities for lattice-QCD calculations to aid in the interpretation of experimental measurements at *Project X*. We focus on four general categories of calculations for which the technical issues are different: kaons, the muon anomalous magnetic moment, nucleons, and hadron spectroscopy and structure. We summarize the current status of lattice-QCD calculations in these areas; more detailed information can be found in the talks on the *Project X* Physics Study website [1] and in the references. We also discuss future prospects for lattice-QCD calculations in these areas, focusing on the computational and methodological improvements needed to obtain the precision required by experiments at *Project X*.

This chapter is organized as follows. In Sec. X.2, we provide a brief introduction to numerical lattice QCD. We summarize the dramatic progress in lattice-QCD calculations in the past decade,

highlighting calculations that validate the whole paradigm of numerical lattice-QCD. This review sets the stage for Sec. X.3, which describes a broad program of lattice-QCD calculations that will be relevant for experiments at *Project X*, and that will be possible on the timescale of *Project X*. Broadly, the lattice-QCD intensity-frontier effort has two main thrusts: (i) improving the precision of present calculations and (ii) extending lattice gauge theory to new quantities relevant for upcoming experiments. Both require greater computational resources, and, where possible, we make forecasts for the expected uncertainties in five years based on the assumption that computing resources continue to increase according to Moore’s law and that funding to support postdocs and junior faculty in lattice gauge theory does not decrease. In Sec. X.4, we describe in some detail the computational resources needed to undertake the calculations discussed earlier. Finally, in Sec. X.5, we recap the key lattice-QCD matrix elements needed to maximize the scientific output of the *Project X* experimental physics program, and we summarize the case for continued support of the US and worldwide lattice-QCD effort.

X.2 INTRODUCTION TO LATTICE QCD

Lattice gauge theory formulates QCD on a discrete Euclidean spacetime lattice, thereby transforming the infinite-dimensional quantum field theory path integral into a finite-dimensional integral that can be solved numerically with Monte Carlo methods and importance sampling. In practice, lattice-QCD simulations are computationally intensive and require the use of the world’s most powerful computers. The QCD Lagrangian has $1 + N_f + 1$ parameters: the gauge coupling g^2 , the N_f quark masses m_f , and the CP -violating parameter $\bar{\theta}$. Because measurements of the neutron electric dipole moment (EDM) bound $\bar{\theta} < 10^{-10}$, most lattice-QCD simulations set $\bar{\theta} = 0$. The gauge-coupling and quark masses in lattice-QCD simulations are tuned by calibrating to $1 + N_f$ experimentally-measured quantities, typically hadron masses or mass-splittings. Once the parameters of the QCD action are fixed, everything else is a prediction of QCD.

There are many ways to discretize QCD, particularly the fermions, but all of them recover QCD in the continuum limit, i.e., when the lattice spacing $a \rightarrow 0$. The various fermion formulations in use have different advantages (such as computational speed or exact chiral symmetry) and different sources of systematic uncertainty; hence it is important to compute quantities with more than one method for independent validation of results. The time required for numerical simulations increases as the quark mass decreases (the condition number of the Dirac operator, which must be inverted, increases with decreasing mass), so quark masses in lattice simulations have usually been higher than those in the real world. Typical lattice calculations now use quark masses such that the pion mass $m_\pi \lesssim 300$ MeV, while state-of-the-art calculations for some quantities attain pions at or slightly below the physical mass of $m_\pi \sim 140$ MeV. Over the coming decade, improvements in algorithms and increases in computing power will render chiral extrapolations unnecessary.

Most lattice-QCD simulations proceed in two steps. First one generates an ensemble of gauge fields with a distribution $\exp[-S_{\text{QCD}}]$; next one computes operator expectation values on these gauge fields. A major breakthrough in lattice-QCD occurred with the advent of gauge-field ensembles that include the effects of the dynamical u , d , and s quarks in the vacuum. Lattice-QCD simulations now regularly employ “ $N_f = 2 + 1$ ” sea quarks in which the light u and d sea-quark masses are degenerate and somewhat heavier than the physical values, and the strange-sea quark mass takes its physical

value. Further, “ $N_f = 2 + 1 + 1$ ” simulations that include a charm sea quark are now underway; dynamical charm effects are expected to become important as precision for some quantities reaches the percent level. During the coming decade, even $N_f = 1 + 1 + 1 + 1$ simulations which include isospin-breaking in the sea are planned.

The easiest quantities to compute with controlled systematic errors and high precision in lattice-QCD simulations have only a hadron in the initial state and at most one hadron in the final state, where the hadrons are stable under QCD (or narrow and far from threshold). These quantities, often referred to as “gold-plated,” include meson masses and decay constants, semileptonic and rare decay form factors, and neutral meson mixing parameters, and enable determinations of all CKM matrix elements except $|V_{tb}|$. Many interesting QCD observables are not gold-plated, however, such as resonances like the ρ and K^* mesons, fully hadronic decay matrix elements such as for $K \rightarrow \pi\pi$ and $B \rightarrow DK$, and long-distance dominated quantities such as D^0 - \bar{D}^0 mixing. That said, lattice QCD with current resources is beginning to tackle such quantities, particularly in $K \rightarrow \pi\pi$ decay.

Many errors in lattice-QCD calculations can be assessed within the framework of effective field theory. Lattice-QCD calculations typically quote the following sources of uncertainty:

- *Monte Carlo statistics and fitting*;
- *tuning lattice spacing and quark masses* by calibrating to a few experimentally-measured quantities such as m_π , m_K , m_{D_s} , m_{B_s} , m_Ω , and f_π ;
- *matching lattice gauge theory to continuum QCD* using fixed-order lattice perturbation theory, step-scaling, or other partly or fully nonperturbative methods;
- *chiral and continuum extrapolation* by simulating at a sequence of light (up and down) quark masses and lattice spacings and extrapolating to $m_{\text{lat}} \rightarrow m_{\text{phys}}$ and $a \rightarrow 0$ using functional forms derived in chiral and weak-coupling QCD perturbation theory;
- *finite volume corrections*, which may be estimated using effective theory and/or studied directly by simulating lattices with different spatial volumes.

The methods for estimating uncertainties can be verified by comparing results for known quantities with experiment. Lattice-QCD calculations successfully reproduce the experimentally-measured low-lying hadron spectrum [2–12], as shown in Fig. X-1. Lattice-QCD results agree with nonlattice determinations of the charm- and bottom-quark masses [13–15] and strong coupling α_s [13, 16–21], but now surpass the precision obtained by other methods. Further, lattice-QCD calculations correctly predicted the mass of the B_c meson [22, 23], the leptonic decay constants f_D and f_{D_s} [24, 25], and the $D \rightarrow K\ell\nu$ semileptonic form factor [26, 27] (see Fig. X-2) before the availability of precise experimental measurements. These successful predictions and postdictions validate the methods of numerical lattice QCD, and demonstrate that reliable results can be obtained with controlled uncertainties.

We note that the huge strides made in lattice-QCD have been largely fueled by increased support for lattice-QCD infrastructure and scientific staff in the United States, as well as similar efforts across the globe. Despite these considerable advances, however, for most quantities lattice errors remain significantly larger than those in the corresponding experimental measurements. Thus lattice

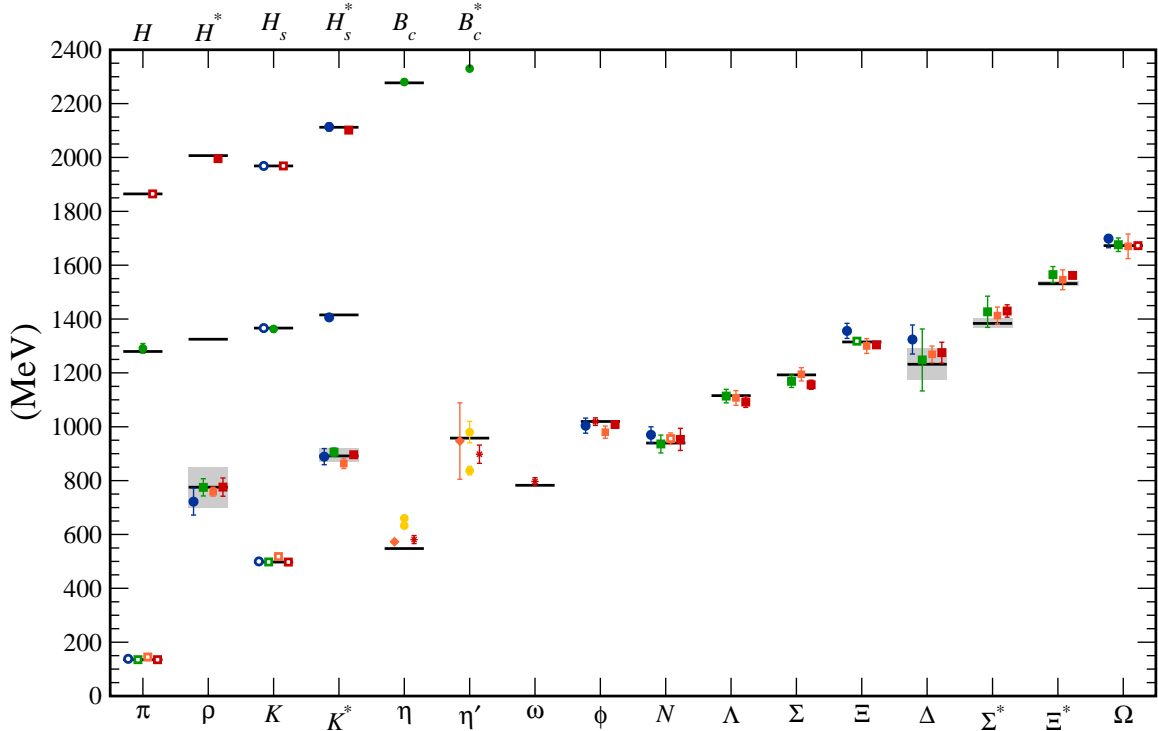


Figure X-1: Hadron spectrum from many different lattice-QCD calculations [2–12]. Open symbols denote masses used to fix bare parameters; closed symbols represent *ab initio* calculations. Horizontal black bars (gray boxes) show the experimentally measured masses (widths). b -flavored meson masses ($B_c^{(*)}$ and $H_{(s)}^{(*)}$) near 1300 MeV are offset by -4000 MeV. Circles, squares and diamonds denote staggered, Wilson and domain-wall fermions, respectively. Asterisks represent anisotropic lattices ($a_t/a_s < 1$). Red, orange, yellow and green and blue signify increasing ensemble sizes (i.e., increasing range of lattice spacings and quark masses). From Ref. [28].

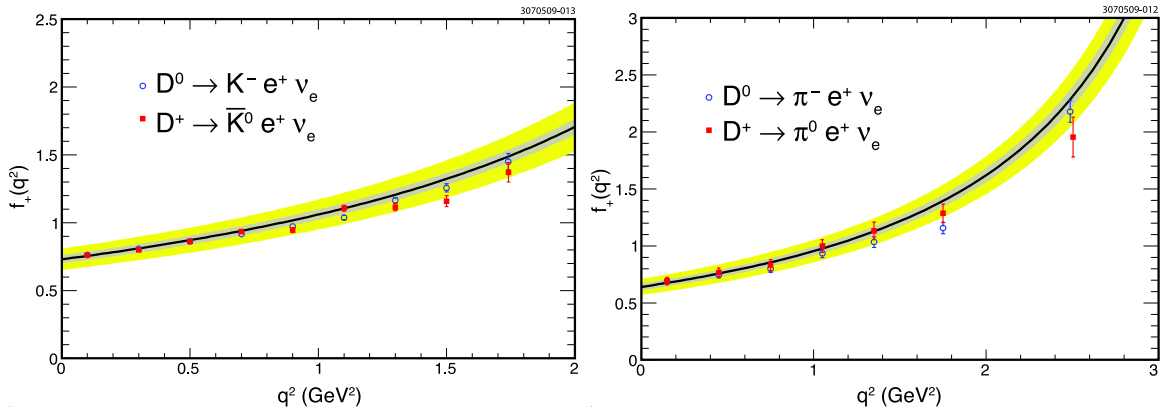


Figure X-2: Comparison of $N_f = 2 + 1$ lattice-QCD calculations of D -meson form factors [26, 29] (curves with error bands) with measurements from CLEO [30] (points with error bars). From Ref. [30].

QCD remains the bottleneck in these cases. If we are to further squeeze the vise on the Standard Model with precise measurements at *Project X* and elsewhere, we must continue to push forward with lattice QCD.

X.3 LATTICE QCD AND *Project X* EXPERIMENTS

In this section we describe a broad program of lattice-QCD calculations that will be possible over the time scale of *Project X* operations assuming that computer resources increase following Moore's law. We organize this discussion according to physics topic or class of experiments for which the calculations are needed. In each subsection, we summarize the physics goals and their relationship to the experimental program, describe the status of present lattice-QCD calculations, and explain what can be achieved over the next five to ten years.

While the challenges to further reductions in errors depend on the quantity, there are many common features. A key advance over the next five years will be the widespread simulation of physical u and d quark masses, obviating the need for chiral extrapolations. Such simulations have already been used for studies of the spectrum and several matrix elements including the leptonic decay constant ratio f_K/f_π and the neutral kaon mixing parameter \hat{B}_K [31–35].

A second advance will be the systematic inclusion of isospin-breaking and electromagnetic (EM) effects. Once calculations attain percent-level accuracy, as is the case at present for quark masses, f_K/f_π , the $K \rightarrow \pi \ell \nu$ and $B \rightarrow D^* \ell \nu$ form factors, and \hat{B}_K , one must study both of these effects. A partial and approximate inclusion of such effects is already made for light quark masses, f_π , f_K and \hat{B}_K . Full inclusion would require nondegenerate u and d quarks and the incorporation of QED into the simulations.

A final across-the-board improvement that will likely become standard in the next five years is the use of charmed sea quarks. These are already included in two of the major streams of gauge-field ensembles being generated [36,37].

X.3.1 Neutrino Experiments

Here we describe opportunities for lattice QCD to assist the *Project X* neutrino experimental program described in Chapter II. *Project X* will provide intense neutrino sources and beams that can be used to illuminate nearby detectors at Fermilab or far detectors at other facilities.

As discussed in Chapter II, one of the largest sources of uncertainty in accelerator-based neutrino experiments is from the determination of the neutrino flux. This is because the beam energies are in the few-GeV range, for which the interaction with hadronic targets is most complicated by the nuclear environment. At the LBNE experiment, in particular, the oscillation signal occurs at energies where quasielastic scattering dominates. Therefore a measurement or theoretical calculation of the ν_μ quasielastic scattering cross section as a function of energy E_ν provides, to first approximation, a determination of the neutrino flux. The cross section for quasielastic $\nu_\mu n \rightarrow \mu^- p$ and $\bar{\nu}_\mu p \rightarrow \mu^+ n$ scattering is parameterized by hadronic form factors that can be computed from first principles with lattice QCD.

Once the LBNE far detector is large enough, and is shielded from cosmic rays either by an underground location or an above-ground veto system, it will enable a proton-decay search that can improve upon the projected reach of current facilities. The interpretation of experimental limits on the proton lifetime as constraints on new-physics models depend upon the expectation values $\langle \pi, K, \eta, \dots | O_{\text{BSM}} | p \rangle$ of non-SM operators; these can be computed with lattice QCD.

X.3.1.1 Nucleon Axial-vector Form Factor

The cross section for quasielastic scattering processes— $\nu_\ell n \rightarrow \ell^- p$ or $\bar{\nu}_\ell p \rightarrow \ell^+ n$, where ℓ^\pm is a charged lepton—is a key element of many aspects of neutrino physics [38]. The hadronic process is expressed via form factors, which must be known well to gain a full understanding of neutrino scattering when the neutrino energy, E_ν , on a fixed target is in the range $E_\nu < 3$ GeV. This knowledge is important both for using neutrinos to understand nuclear structure (which has ramifications for many *Project X* experiments) and for understanding measurements of neutrino-oscillation parameters, in the precision era starting now with NOVA and T2K, and continuing on into *Project X* operations with LBNE.

The two most important form factors are the vector and axial-vector form factors, corresponding to the V and A components of W^\pm exchange. The vector form factor can be measured in elastic ep scattering. In practice, the axial-vector form factor has most often been modeled by a one-parameter dipole form [39]

$$F_A(Q^2) = \frac{g_A}{(1 + Q^2/M_A^2)^2}, \quad (\text{X.3.1})$$

although other parametrizations have been proposed [40–43]. The normalization $g_A = F_A(0) = -1.27$ is taken from neutron β decay [14]. The form in Eq. (X.3.1) matches the asymptotic behavior at large Q^2 (see, e.g., Ref. [44]), but in the low Q^2 range relevant neutrino experiments, it does not rest on a sound foundation. It is worth noting that measurements of the vector form factor over a wide energy range do *not* satisfy the dipole form [45].

Fits to Eq. (X.3.1) over different Q^2 ranges yield different results for the fit parameter M_A , e.g., $M_A \approx 1.03$ GeV from NOMAD and other higher-energy experiments ($3 \text{ GeV} < E_\nu < 80 \text{ GeV}$) [46], but $M_A \approx 1.35$ GeV from MiniBooNE at lower energy ($0.4 \text{ GeV} < E_\nu < 2 \text{ GeV}$) [47]. The difference may stem from nuclear effects, but without an *ab initio* determination of the axial-vector form factor, one cannot know. Indeed, fits employing a model-independent parametrization based on analyticity and unitarity [43] find a consistent picture, obtaining $M_A = 0.89^{+0.22}_{-0.07}$ GeV for a model-independent definition of M_A . The theoretical basis of Ref. [43] is the same as that used successfully for meson decay form factors, say for the determination of $|V_{ub}|$ [48–50].

The lattice-QCD community has a significant, ongoing effort devoted to calculating $F_A(Q^2)$ [51–55]. Unfortunately, however, the results for the axial charge $g_A = F_A(0)$ have not agreed well with neutron β decay experiments; see, e.g., Ref. [56] for a review. Recently, however, two papers with careful attention to excited-state contamination in the lattice correlation functions and the chiral extrapolation [57] and lattice data at physical pion mass [58] find results in agreement with experiment, $g_A \approx 1.25$. In addition to sensitivity to the chiral extrapolation, it is important to treat finite-volume effects more carefully than is often the case. A caveat here is that Refs. [57,58] simulate with only $N_f = 2$ sea quarks. If these findings hold up with $2 + 1$ and $2 + 1 + 1$ flavors of sea

quark, the clear next step is to compute the shape of the form factors with lattice QCD. If the calculations of the vector form factor reproduce experimental measurements, then one could proceed to use the lattice-QCD calculation of the axial-vector form factor in analyzing neutrino data.

X.3.1.2 Proton decay Matrix Elements

Proton decay is forbidden in the Standard Model but is a natural prediction of grand unification. Extensive experimental searches have, to date, found no evidence for proton decay, but future experiments will continue to improve the limits. To obtain constraints on model parameters requires knowledge of hadronic matrix elements $\langle \pi, K, \eta, \dots | O_{\Delta B=1} | p \rangle$ of the baryon-number violating operators $O_{\Delta B=1}$ in the effective Hamiltonian. Estimates of these matrix elements based on the bag model, sum rules, and the quark model vary by as much as a factor of three, and lead to an $O(10)$ uncertainty in the model predictions for the proton lifetime. Therefore, *ab initio* QCD calculations of proton-decay matrix elements with controlled systematic uncertainties of even $\sim 20\%$ would represent a significant improvement, and be sufficiently precise for constraining GUT theories.

Recently the RBC and UKQCD Collaborations obtained the first direct calculation of proton-decay matrix elements with $N_f = 2 + 1$ dynamical quarks [59]. The result is obtained from a single lattice spacing, and the total statistical plus systematic uncertainties range from 20–40%. Use of gauge-field ensembles with finer lattice spacings and lighter pions, combined with a new technique to reduce the statistical error [60], however, should enable a straightforward reduction of the errors to the $\sim 10\%$ level in the next five years.

X.3.2 Kaon Physics

Here we describe opportunities for lattice QCD to assist the *Project X* kaon physics program described in Chapter III. In many cases, hadronic matrix elements from lattice QCD are crucial for interpreting the experimental measurements as tests of the Standard Model and constraints on new physics. The ORKA experiment, which could well begin running before *Project X*, will measure the *CP*-conserving rare decay $K^+ \rightarrow \pi^+ \nu \bar{\nu}$ and collect ~ 200 events/year, assuming the Standard-Model rate. With Stage 1 of *Project X* this rate will increase to ~ 340 events/year, enabling a measurement of the branching fraction to $\sim 3\%$ precision. Stage 2 of *Project X* will enable a measurement of the branching fraction for the *CP*-violating rare decay $K_L \rightarrow \pi^0 \nu \bar{\nu}$ to $\sim 5\%$, again assuming the Standard-Model rate. The *Project X* kaon-physics experiments will also measure numerous other kaon observables such as $\Gamma(K_{e2})/\Gamma(K_{\mu 2})$, $K^+ \rightarrow \pi^+ \ell^+ \ell^-$, and $K_L \rightarrow \pi^0 \ell^+ \ell^-$. Correlations between these channels will allow discrimination between different new-physics scenarios, provided sufficiently precise theoretical predictions from lattice QCD and elsewhere.

The worldwide lattice-QCD community has a well-established and successful kaon physics program. The matrix elements needed to obtain pion and kaon leptonic decay constants, light-quark masses, the $K \rightarrow \pi \ell \nu$ semileptonic form factor, and neutral kaon mixing are all gold-plated, and can therefore be computed with lattice QCD to a few percent or better precision. Many lattice-QCD collaborations are attacking these quantities with $N_f = 2 + 1$ [13,32,61–71] and now $N_f = 2 + 1 + 1$ [34,35,72,73] gauge-field ensembles, thereby providing independent cross checks and enabling global lattice-QCD averages [74,75]. A highlight of the lattice-QCD kaon physics

Table X-1: History, status and future of selected lattice-QCD calculations needed for the determination of CKM matrix elements relevant to the kaon sector. Forecasts from the 2007 white paper (where available) assumed computational resources of 10–50 TF years. Present lattice errors are taken from Refs. [34,71,77,83]. Forecasts for 2018 assume that computer resources increase following Moore’s law.

Quantity	CKM element	Present expt. error	Forecast (2007) for 2012 lattice error	Present (2013) lattice error	2018 lattice error
f_K/f_π	$ V_{us} $	0.2%	0.5%	0.4%	0.15%
$f_+^{K\pi}(0)$	$ V_{us} $	0.2%	–	0.4%	0.2%
B_K	$\text{Im}(V_{td}^2)$	0.5%	3.5–6%	1.6%	< 1%
$B \rightarrow D^* \ell \nu$	$ V_{cb} $	1.3%	–	1.8%	< 1%

effort is the calculation of the neutral-kaon mixing parameter B_K , which enables a constraint on the apex of the CKM unitarity triangle when combined with experimental measurements of indirect CP -violation in the kaon system. Until recently, the unitarity-triangle constraint from ϵ_K was limited by the $\sim 20\%$ uncertainty in the hadronic matrix element B_K [76]. Several years ago, the lattice-QCD community identified B_K as a key goal for lattice flavor physics, and devoted significant theoretical and computational effort to its improvement. Now several independent lattice-QCD results for B_K are in good agreement [63,70,77,78], and the error on the average is $\lesssim 1.5\%$ [79]. In fact, B_K is now a sub-dominant source of uncertainty in the ϵ_K band, below the parametric error from $A^4 \propto |V_{cb}|^4$ and the perturbative truncation errors in the Inami-Lim functions η_{cc} and η_{ct} [80,81].

Table X-1 shows the status of lattice-QCD calculations, comparing lattice errors in various matrix elements to those in the corresponding experimental measurements. Where available, we also include forecasts made in 2007 for the expected errors in ~ 2012 [82], which have proven to be quite accurate. Given the maturity of these calculations, we expect the forecasts for 2018 to be reasonably accurate as well. It is important to note that, of the quantities in Table X-1, only for f_K/f_π was a result available in 2007 with all errors controlled. All other calculations have matured from having several errors uncontrolled to all errors controlled over the last five years.

The amplitudes listed so far all have one hadron in the initial state and zero or one in the final state and are especially straightforward to determine for several reasons. For example, the finite-volume errors are suppressed exponentially. Recent advances in the methods of computational quantum field theory, numerical algorithms and computer technology, however, are expanding the types of calculations that can be pursued and the experiments that can be addressed. For example, although the conceptual framework for computing $K \rightarrow \pi\pi$ amplitudes has been available for twenty years, it was only in 2012 that the amplitude for $I = 2$ was brought under control [84,85]. Progress is also being made in the calculation of long-distance amplitudes; methods are being tested for K_L - K_S mass difference ΔM_K [86] and will eventually be extended to rare semileptonic kaon decays.

X.3.2.1 $K \rightarrow \pi\pi$ Decays

The advances in lattice-QCD calculations of weak interactions involving the strange quark open the exciting possibility to search for physics beyond the standard model via experimental measure-

ments of direct CP -violation in the kaon system. The NA48 and KTeV experiments have measured $\text{Re}(\epsilon'/\epsilon)$ to around 10% precision [87,88], but the ability to constrain new physics with ϵ' has been handicapped by the uncertainty in the $K \rightarrow \pi\pi$ hadronic matrix elements. Initial results suggest that calculation of the two complex decay amplitudes A_0 and A_2 describing the decays $K \rightarrow (\pi\pi)_I$ for $I = 0$ and 2 respectively are now realistic targets for large-scale lattice QCD calculations. This would allow a verification of the $\Delta I = 1/2$ rule and a first-principles calculation of ϵ'/ϵ within the Standard Model. Further, new physics in ϵ' is tightly correlated with that in rare kaon decays; see, e.g., Sec. III.2.2 and Refs. [89,90]. Thus the payoff of improved lattice-QCD calculations of $K \rightarrow \pi\pi$ decays with a precision comparable to experiment will be significant.

The complex $I = 2$, $K \rightarrow \pi\pi$ decay amplitude A_2 has now been computed in lattice QCD with 15% errors [84,85]. Because the kaon mass is relatively small, the decay final states are dominated by two pions. In such cases, QCD rescattering effects can be controlled using the method of Lellouch and Lüscher [91,92]. In the next two years, the addition of two smaller lattice spacings should reduce the dominant discretization error, leading to a total error of $\sim 5\%$. At this level, isospin violation must be included, which may be within reach on a five-year timescale.

The $I = 0$ amplitude is considerably more challenging, and only trial calculations with unphysical kinematics and ~ 400 MeV pions have been attempted to date [93]. The overlap between the $I = 0$, $\pi\pi$ state and the vacuum results in quark-disconnected diagrams and a noise to signal ratio that grows exponentially with time. In addition, the simple quark-field boundary conditions used in the $I = 2$ channel cannot give the correct relative momentum to final-state pions with $I = 0$. A promising solution is to impose G -parity boundary conditions on both the valence and sea quarks to produce two-pion final states with $I = 0$ and physical kinematics. The first results for A_0 from a single relatively coarse ensemble for an energy conserving decay with physical pion and kaon masses are expected in 2014, and should reveal the method's ultimate effectiveness. The systematic error associated with the nonzero lattice spacing, which was the dominant uncertainty for the $I = 2$ calculation ($\sim 15\%$), will require simulations at a second lattice spacing and thus take longer to control, but a 10% error for A_0 appears possible by 2018.

In summary, a full calculation of ϵ' with a total error at the 20% level may be possible in two years. Given this precision, combining the pattern of experimental results for $K \rightarrow \pi\nu\bar{\nu}$ with ϵ'/ϵ can already help to distinguish between new-physics models, as discussed in Sec. III.2.2 and illustrated in Fig. III-4; see also Refs. [89,90].

X.3.2.2 $K \rightarrow \pi\nu\bar{\nu}$ Decays

The Standard-Model branching fractions for the rare kaon decays $K^+ \rightarrow \pi^+\nu\bar{\nu}$ and $K_L \rightarrow \pi^0\nu\bar{\nu}$ are known to a precision unmatched by any other quark flavor-changing-neutral-current process, so $K \rightarrow \pi\nu\bar{\nu}$ decays are promising channels for new-physics discovery. The hadronic uncertainties are under good theoretical control because the form factors can be obtained using experimental $K \rightarrow \pi\ell\nu$ data combined with chiral perturbation theory. Further, long-distance contributions involving multiple operator insertions from the effective weak Hamiltonian are subdominant due to quadratic GIM suppression. The limiting source of uncertainty in the Standard-Model predictions for $\text{BR}(K^+ \rightarrow \pi^+\nu\bar{\nu})$ and $\text{BR}(K_L \rightarrow \pi^0\nu\bar{\nu})$ is the parametric error from $|V_{cb}|^4$ and is approximately $\sim 10\%$ [81, 94]. Therefore a reduction in the uncertainty on $|V_{cb}|$ is essential for interpreting the results of the

forthcoming measurements by NA62, KOTO, ORKA, and subsequent experiments at *Project X* as tests of the Standard Model.

The CKM matrix element $|V_{cb}|$ can be obtained from exclusive $B \rightarrow D^{(*)}\ell\nu$ decays provided lattice-QCD calculations of the hadronic form factors. For the $B \rightarrow D^*\ell\nu$ form factor at zero recoil, the gap between experimental errors (1.3%) and lattice errors (presently $\sim 1.8\%$) has narrowed considerably over the last five years [83]. In the next five years, the lattice error is expected to drop below the experimental error, as shown in Table X-1. Particularly important for this will be the use of lattices with small lattice spacings and physical light-quark masses, and the extension of the calculation to nonzero recoil [95]. This projected improvement in the $B \rightarrow D^*\ell\nu$ form factor will reduce the error in $|V_{cb}|$ to $\lesssim 1.5\%$, and thereby reduce the error on the Standard-Model $K \rightarrow \pi\nu\bar{\nu}$ branching fractions to $\lesssim 6\%$. With this precision, the theoretical uncertainties in the Standard-Model predictions will be commensurate with the projected experimental errors in time for the first stage of *Project X*.

X.3.2.3 Long-distance Amplitudes for Rare Kaon Decays

Errors from long-distance contributions are subdominant in the Standard Model predictions for $K \rightarrow \pi\nu\bar{\nu}$ due to quadratic GIM suppression, but are significant in other rare kaon decays such as $K \rightarrow \pi\ell^+\ell^-$. Currently the Standard-Model estimates for the $K \rightarrow \pi\ell^+\ell^-$ branching fractions rely on chiral perturbation theory and have large uncertainties that are not competitive with those on $K \rightarrow \pi\nu\bar{\nu}$. If they can be brought under theoretical control, however, $K \rightarrow \pi\ell^+\ell^-$ may afford additional search channels that, through correlations with other observables, provide additional handles to distinguish between new-physics scenarios. See Sec. III.2.1.2 and Ref. [89] for further details. Thus the extension of lattice-QCD methods to compute long-distance weak amplitudes would have considerable impact on the search for new physics.

The gold-plated kaon decays $K \rightarrow \ell\nu$ and $K \rightarrow \pi\ell\nu$, as well as the nonleptonic decay $K \rightarrow \pi\pi$, are dominated by first-order weak processes in which a single W^\pm is exchanged. In the past, the only second-order quantities that were accessible to lattice QCD were those which are dominated by short distances, e.g., the CP -violating parameter ϵ_K in K^0 - \bar{K}^0 mixing. These can be represented by matrix elements of local operators. However, roughly 5% of ϵ_K [96] and 30% of the K_L - K_S mass difference, ΔM_K , [97,98] come from long-distance contributions with two flavor-changing interactions separated by distances of order $\Lambda_{\text{QCD}}^{-1}$. Then both interactions, each represented by a four-fermion operator, must be explicitly included in a lattice calculation, a challenge which may now be possible to meet with near-future computing resources. Again, the effects of real intermediate states (rescattering effects) introduce finite-volume distortions. It has recently been demonstrated, however, that, in the case of kaons, these distortions can be corrected in a nonperturbative manner [99,100].

A pilot numerical study of ΔM_K using these methods is now underway [86,101,102]. The calculation is more challenging than those for the $K \rightarrow \pi\pi$ amplitudes, with a key issue being the need to include charm quarks so as to enforce GIM cancellations. First results from a single lattice spacing with unphysically heavy pions are due soon [86], and a calculation at the physical light-quark masses may be finished in another year. Because this calculation is still at an early stage in development, it is difficult to forecast the level of resources that will be required to obtain an accurate, controlled result. Pursuing this calculation will, however, be a major priority of the US lattice-QCD kaon physics program.

The lattice-QCD calculation of ΔM_K will pave the way for computations of the long-distance contributions to neutral kaon mixing and rare kaon decays. The difficulties here are similar to those for ΔM_K , including the need for dynamical charm. A method for calculating long-distance contributions to rare kaon decays such as $K^+ \rightarrow \pi^+ \nu \bar{\nu}$, $K_L \rightarrow \pi^0 \nu \bar{\nu}$ and $K \rightarrow \pi \ell^+ \ell^-$ in lattice QCD has been proposed in Ref. [103]. These calculations are a higher priority for lattice QCD than the long-distance contribution to ϵ_K , in light of the ongoing NA62 experiment, the planned KOTO experiment, and the proposed high-sensitivity kaon measurements at Fermilab. Because lattice-QCD calculations of long-distance contributions to rare decays have not yet begun, it is premature to forecast time scales for completion or uncertainties obtained.

X.3.3 Muon Experiments

Here we describe opportunities for lattice QCD to assist the *Project X* muon experimental program described in Chapter IV. The intense *Project X* beam with flexible time structure makes possible a range of muon experiments from searches for charged-lepton flavor violation to a measurement of the muon electric dipole moment.

Stage 1 of *Project X* will enable the Mu2e experiment to improve the reach for $\mu \rightarrow e$ conversion on nuclei by 10–100 orders-of-magnitude. The higher wattage of *Project X* Stage 2 will further improve the sensitivity of Mu2e, with an expected reach four orders-of-magnitude better than current limits. Stage 2 will also make possible other searches for charged-lepton flavor violation such as $\mu \rightarrow 3e$. If $\mu \rightarrow e$ conversion is indeed discovered at *Project X* lattice-QCD calculations of the light- and strange-quark contents of nucleon will be needed to make model predictions for the $\mu \rightarrow e$ conversion rate and distinguish between possible new-physics theories.

The new Muon $g - 2$ Experiment (E989) to improve the determination of the muon anomalous magnetic moment will run at Fermilab before the *Project X* accelerator upgrade. Although E989 is not part of *Project X*, a second-generation $g - 2$ experiment would be possible with *Project X* if it seemed warranted based on improvements in the theoretical calculation and the evolution of the discrepancy with respect to the Standard Model; see Sec. IV.3.5. Lattice QCD provides the only means to calculate the Standard-Model hadronic light-by-light contribution to $g - 2$ from first principles with controlled uncertainties that are systematically improvable.

X.3.3.1 μ -to- e Conversion

Charged-lepton flavor violation (CFLV) is so highly suppressed in the Standard Model that any observation of CLFV would be unambiguous evidence of new physics. Many new-physics models, however, allow for CLFV and predict rates close to current limits; see Sec. IV.2 for examples.

Many experiments searching for charged-lepton flavor violation are running or are on the horizon. The MEG experiment at PSI is currently searching for $\mu \rightarrow e \gamma$, and an improved search for $\mu \rightarrow e e e$ at PSI (the Mu3e Experiment) has also been proposed. The Mu2e Experiment with *Project X* aims to search for $\mu N \rightarrow e N$ with a sensitivity four orders of magnitude below the current best limit. If CLFV is observed in these experiments, combining the measured rates of $\mu \rightarrow e \gamma$ and $\mu \rightarrow e$ conversion on different target nuclei can distinguish between models and reveal information on underlying theory [104]. Model predictions for the $\mu \rightarrow e$ conversion rate off a target nucleus

depend upon the light- and strange-quark contents of the nucleon; see Sec. IV.2. These same quark scalar density matrix elements also needed to interpret dark-matter detection experiments in which the dark-matter particle scatters off a nucleus [105–107]. Lattice-QCD can provide nonperturbative calculations of the scalar quark content of the nucleon with controlled uncertainties.

Most lattice efforts on this front have focused on the determination of the strange-quark content of the nucleon. This is because the strange quark is least amenable to other perturbative approaches: it is too light for the use of perturbative QCD, but too heavy for the reliable use of $SU(3)$ baryon chiral perturbation theory. Calculations of $m_s \langle N | \bar{s}s | N \rangle$ have been performed with $N_f = 2 + 1$ and even $N_f = 2 + 1 + 1$ flavors using a variety of lattice-fermion actions [108–117]. Most groups compute the desired matrix element from direct simulation, but some exploit the Feynman-Hellmann relation

$$m_s \langle N | \bar{s}s | N \rangle = m_s \frac{\partial m_N}{\partial m_s}. \quad (\text{X.3.2})$$

The results obtained with different methods and lattice formulations agree at the $1\text{--}2\sigma$ level, and a recent compilation quotes an error on the average $m_s \langle N | \bar{s}s | N \rangle$ of about 25% [117]. With this precision, the current lattice results already rule out the much larger values of $m_s \langle N | \bar{s}s | N \rangle$ favored by early nonlattice estimates [118–120]. Lattice-QCD can also provide first-principles calculations of the pion-nucleon sigma term [108,110–112,116] and the charm-quark content of the nucleon [115, 121]. A realistic goal for the next five years is to pin down the values of all of the quark scalar density matrix elements for $q = u, d, s, c$ with $\sim 10\text{--}20\%$ uncertainties; even greater precision can be expected on the timescale of a continuation of Mu2e at Stage 2 of *Project X*.

X.3.3.2 Muon Anomalous Magnetic Moment

The muon anomalous magnetic moment provides one of the most precise tests of the SM and places important constraints on extensions of it [122]. The current discrepancy between experiment and the Standard Model has been reported in the range of 2.9–3.6 standard deviations [123–125]. With new experiments planned at Fermilab (E989) and J-PARC (E34) that aim to improve on the current 0.54 ppm measurement at BNL [126] by at least a factor of four, it will continue to play a central role in particle physics for the foreseeable future.

In order to leverage the improved precision on $g - 2$ from the experiments, the theoretical uncertainty on the Standard Model prediction must be shored-up, as well as be brought to a comparable level of precision [122]. The largest sources of uncertainty in the SM calculation are from the nonperturbative hadronic contributions. The hadronic corrections enter at order α^2 through the hadronic vacuum polarization (0.36 ppm), shown in Fig. X-3, and α^3 through hadronic light-by-light scattering (0.22 ppm), shown in Fig. X-4, as well as higher order hadronic vacuum polarization contributions. Lattice QCD can provide calculations of the hadronic vacuum polarization (HVP) and hadronic light-by-light (HLbL) contributions to the muon ($g - 2$) from QCD first principles with reliable uncertainties and, ultimately, greater precision than currently available from nonlattice methods.

Hadronic vacuum polarization The HVP contribution to the muon anomaly, $a_\mu(\text{HVP})$, has been obtained to a precision of 0.6% using experimental measurements of $e^+e^- \rightarrow \text{hadrons}$ and $\tau \rightarrow$

hadrons [124,125]. The result including τ data is about two standard deviations larger than the pure e^+e^- determination, and reduces the discrepancy with the Standard Model to below three standard deviations [124]. The former requires isospin corrections which may not be under control. Alternatively, ρ - γ mixing may explain the difference and bring the τ -based result in line with that from e^+e^- [127]. A direct lattice-QCD calculation of the hadronic vacuum polarization with $\sim 1\%$ precision may help shed light on the apparent discrepancy between e^+e^- and τ data. Ultimately, a lattice-QCD calculation of $a_\mu(\text{HVP})$ with sub-percent precision can circumvent these concerns by supplanting the determination from experiment with one from first-principles QCD.

The hadronic vacuum polarization contribution is obtained by computing the two-point correlation function of the electromagnetic quark current, Fourier-transformed to momentum space, and then inserting the result into the one-loop QED integral for the interaction of the muon with an external photon field. Lattice-QCD simulations enable a direct, nonperturbative computation of the renormalized vacuum polarization function $\Pi(Q^2)$ as a function of the Euclidean momentum-squared Q^2 [128].

The HVP contribution to the muon anomalous magnetic moment has been computed in lattice QCD by several groups [128–133], and statistical errors on lattice calculations of $a_\mu(\text{HVP})$ are currently at about the 3–5% level. Important systematic errors remain, and these are being addressed through a combination of theoretical advances and brute-force computing. Because simulating QCD on a computer requires a finite-sized lattice, lattice-QCD simulations can only access discrete momentum values in units of $2\pi/L$, where L is the length of a side of the box. As a consequence, lattice-QCD data are sparse and noisy in the low- Q^2 region. The integral over Q^2 is dominated by momenta of order m_μ , which is below the range directly accessible in current lattice simulations; thus the value of $a_\mu(\text{HVP})$ is sensitive to the functional form used to extrapolate $Q^2 \rightarrow 0$. A new fitting approach based on Padé approximants [134] will eliminate this model dependence. Further, smaller values of Q^2 can also be simulated directly using “twisted” boundary conditions for the lattice fermions [135] and increasing the lattice box size, both of which are being pursued [133]. Another significant source of uncertainty in $a_\mu(\text{HVP})$ is from the chiral extrapolation of the numerical simulation data to the physical light-quark masses. Anticipated increases in computing resources will enable simulations directly at the physical quark masses, thereby eliminating this systematic. The charm-quark contribution to HVP may be at the few-percent level (comparable to the hadronic light-by-light contribution), so calculations are underway using $N_f = 2 + 1 + 1$ gauge-field ensembles with dynamical charm quarks [136]. A new method to extend the low momentum

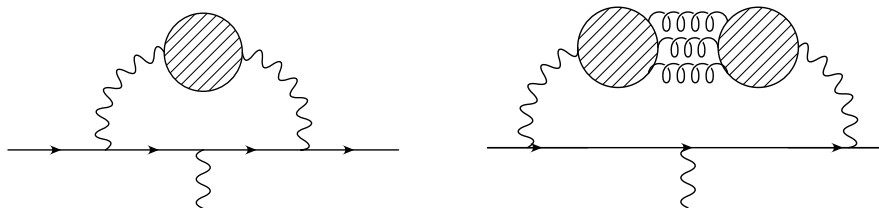


Figure X-3: Hadronic vacuum polarization diagrams contributing to the Standard-Model muon anomaly. The horizontal lines represent the muon. The blob formed by the quark-antiquark loop represents all possible hadronic intermediate states. Right panel: disconnected quark line contribution in which the quark loops are connected by gluons.

region to smaller values of momentum transfer, much like twisted boundary conditions, uses analytic continuation to access small time-like momenta [137]. It has the advantage that the energy, and therefore momentum transfer, can be varied continuously but at the expense of either introducing model-dependence into the calculation (to extend time to $\pm\infty$), or by truncating the time integral (sum), introducing an additional finite-size effect. While the authors do not expect the new method to increase the precision of HVP and similar calculations, it does avoid the difficulty of fitting the lattice data versus momentum transfer and its attendant problems (for low momenta), and provides an independent cross-check of the standard method to compute $a_\mu(\text{HVP})$ with different systematic uncertainties.

Given the above combination of theoretical improvements, plus increased computing resources, large error reductions in lattice-QCD calculations of $a_\mu(\text{HVP})$ over the next one to two years are not only possible, but likely. The dominant quark-connected contribution $a_\mu(\text{HVP})$, shown on the left side of Fig. X-3, will be calculated with few-percent errors on the timescale of the Muon $g - 2$ experiment (E989). This will provide a valuable cross-check of the semi-experimental determination from $e^+e^- \rightarrow \text{hadrons}$. The quark-disconnected contribution, shown on the right side of Fig. X-3, is computationally more demanding, but will be computed within the next five years. Because the disconnected contribution is expected to contribute at the $\sim 1\%$ level, a rather large uncertainty in this term can be tolerated.

Hadronic light-by-light The HLbL contribution to the muon anomaly cannot be extracted from experiment, as for the HVP contributions. Thus present estimates of this contribution rely on models [138,139], and report errors estimated to be 25–40% range. This uncertainty is neither fully controlled nor systematically improvable. If not reduced, these errors will dominate over the HVP error as the latter is reduced via more experimental data and lattice-QCD calculations. Thus, there is a crucial need for an *ab initio* calculation, and the HLbL contribution is the highest theoretical priority for $(g - 2)_\mu$.

Lattice-QCD can provide a calculation of $a_\mu(\text{HLbL})$ from QCD first principles with controlled uncertainties that are systematically improvable. The importance of this calculation to the experimental program is well-known to the lattice-QCD community, and significant progress has been made on this topic. The lattice-QCD calculation of the HLbL contribution is challenging, however, and still in early stages.

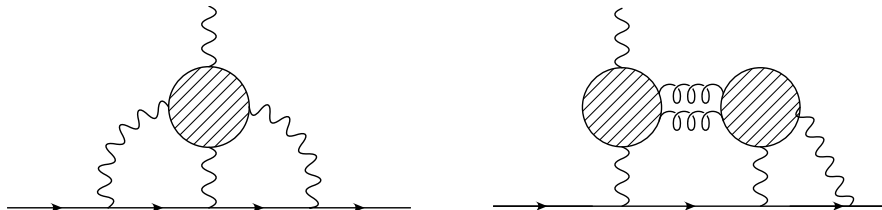


Figure X-4: Hadronic light-by-light scattering diagrams contributing to the Standard-Model muon anomaly. The horizontal lines represent the muon. The blob formed by the quark loop represents all possible hadronic intermediate states. Right panel: one of the disconnected quark line contributions in which the quark loops are connected by gluons.

The most promising strategy to calculate $a_\mu(\text{HLbL})$ is via lattice QCD plus lattice QED. Then the muon and photons are treated nonperturbatively along with the quarks and gluons [140]. First results using this approach for the single quark-loop part of the HLbL contribution (Fig. X-4, left panel) have been reported recently [141]. The method can be checked in pure QED, where the LbL term has been calculated directly in perturbation theory, allowing a benchmark for the procedure. This test has been performed successfully [142], showing the significant promise of the method. Much effort is still needed to reduce statistical errors, extrapolate to zero momentum transfer, and many systematic errors (e.g., due to the finite lattice volume, unphysical heavy pions, and nonzero lattice spacing) remain uncontrolled. However, first signs of the HLbL contribution rising above the Monte-Carlo noise are encouraging. The calculation is quenched with respect to QED, i.e., the sea quarks' electric charge is neglected, so contributions from quark-disconnected diagrams with two separate quark loops connected only by a pair of gluons are missing. The disconnected contributions may be similar in size to the connected ones, so inclusion of these contributions will be essential for a complete calculation with controlled errors. This obstacle can be overcome simply by including of photons in the gauge field ensemble generation, by reweighting the quenched ensembles to include the virtual sea quark contributions, or by brute-force calculation of the disconnected diagrams. All these approaches are under investigation.

Calculations are also being carried out that will check both model and lattice-QCD calculations: for example, the $\pi^0 \rightarrow \gamma^{(*)}\gamma^{(*)}$ vertex function [143], the axial-vector–vector–vector three-point function [144], and the chiral magnetic susceptibility [145]. The first of these is also directly related to experimental measurements of the Primakoff effect, $\gamma A \rightarrow \gamma\gamma$, which is dominated (like HLbL) by the pion pole. The four-point vector correlation function in QCD needed for the HLbL amplitude, computed at select fiducial values of the momenta at each vertex, is also under study.

In order to bring the error on the HLbL contribution to, at, or below, the projected experimental uncertainty on the time scale of the Muon $g - 2$ experiment, one must reduce the error on $a_\mu(\text{HLbL})$ to approximately 10% or better by 2016–17. Assuming this accuracy, a reduction of the HVP error by a factor of 2, and the expected reduction in experimental errors, then the present central value would lie $7\text{--}8\sigma$ from the SM prediction. Reaching this milestone is certainly possible with sustained theoretical and computational effort from the lattice-QCD community and continued advances in computer power, but is not guaranteed. In particular, new theoretical developments, which are impossible to predict, may be needed to match the target experimental precision.

X.3.4 Nucleon Matrix Elements and Fundamental Physics

Here we describe opportunities for lattice-QCD to assist the *Project X* physics program to study fundamental physics with nucleons, as described in Chapters V and VI. The 1 GeV beam of *Project X* Stage 1 can power a spallation target facility optimized for particle physics, enabling experiments for ultracold neutrons and electric dipole moments (EDMs). The interpretation of many of these experimental measurements as constraints on TeV-scale or GUT-scale new physics requires knowledge of nucleon matrix elements that can be computed in lattice QCD. The LBNE detector can be used to search for proton decay and will improve upon current limits, once the far detector is sufficiently large and shielded from cosmic rays. The proton-decay matrix elements needed to interpret experimental limits on the proton lifetime as constraints on new-physics models are similar to those

needed to interpret neutron β -decay experiments, so we briefly mention them in this section; more details can be found in Sec. X.3.1.2.

Although many nucleon matrix elements are gold plated, lattice-QCD calculations involving baryons are generally more challenging than for mesons. They are more computationally demanding because statistical noise in baryon correlation functions grows rapidly with Euclidean time. Further, the extrapolation to physical light-quark masses is more difficult because baryon chiral perturbation theory converges less rapidly.

The most studied nucleon matrix element is that of the axial charge g_A . Because it can be measured precisely in neutron β -decay experiments, g_A provides a benchmark for the accuracy of lattice-QCD nucleon matrix element calculations. Past lattice calculations of g_A have quoted ~ 6 – 10% uncertainties [53,146–148], but the central values have all been systematically lower than the experimental measurement by about 10% , indicating the presence of underestimated uncertainties. Two recent $N_f = 2$ lattice-QCD calculations of g_A have improved upon these calculations with a more careful treatment of excited-state contamination in the three-point correlation functions [57] and simulations at the physical pion mass [58], and obtain results consistent with experiment. These results, however, have yet to be confirmed with $N_f = 2 + 1$ flavors. The expected increase in computing power over the next five years should allow simulations with larger volumes and more widespread use of physical light-quark masses, while new algorithms should greatly reduce the statistical errors. Percent-level lattice-QCD calculations of g_A are therefore expected on this timescale.

Lattice-QCD calculations of proton and neutron electric dipole moments, proton and neutron decay matrix elements, and n - \bar{n} oscillation matrix elements are in earlier stages. Percent-level precision is not needed, however, for these quantities to be of use to *Project X*. Typically ~ 10 or 20% accuracy is sufficient, which is an achievable target in the next five years.

X.3.4.1 Proton and Neutron Electric Dipole Moments

Flavor physics experiments—aided, in part, by lattice-QCD calculations—have demonstrated that Standard-Model CP violation is not large enough to explain the baryon asymmetry of the universe. Consequently, there must be as yet undiscovered CP violating interactions beyond the Standard Model. These could still show up in quark flavor-changing processes, but also elsewhere, such as in nonzero electric dipole moments (EDMs) of leptons and nucleons [149].

There are two possible sources of an electric dipole moment in the Standard Model. Cabibbo-Kobayashi-Maskawa CP violation makes a contribution to the nucleon EDM at the three-loop level and lies well beyond experimental sensitivity. The strong CP -violating interaction, $\bar{\theta}G\tilde{G}$, directly makes a contribution. Experimental limits on the size of the neutron EDM (d_N) constrain the size of $|\bar{\theta}| \lesssim 10^{-10}$, but this constraint is not known precisely because of uncertainties in model estimates for $d_N/\bar{\theta}$. Further, non-SM sources of CP violation generate higher-dimension, EDM-inducing operators at low scales. In some cases the BSM model predictions require nonperturbative hadronic matrix elements. Interestingly, the strong- CP contribution appears to flip sign between neutron and proton, while the BSM contributions need not flip sign.

Lattice-QCD can provide first-principles QCD calculations of the strong- CP contribution to $d_N/\bar{\theta}$ with improved precision and controlled uncertainties, as well of matrix elements of non-SM EDM-inducing operators. Pilot lattice-QCD calculations have already been carried out for

this strong- CP contribution to the neutron and proton EDMs using two methods: (i) calculating the energy difference between two spin states of the nucleon in an external electric field [150], and (ii) computing the form factor of the electromagnetic current [151,152]. Currently the statistical errors are still $\sim 30\%$, both because of the general property that nucleon correlation functions have large statistical errors and because the calculation involves correlations with the topological charge density, which introduces substantial statistical fluctuations. A lattice-QCD calculation of the matrix elements of dimension-6 operators needed for BSM theories is also underway [153]. This research is still in an early phase, and a reasonable and useful goal for the coming five years is a suite of matrix elements with solid errors at the 10–20% level.

X.3.4.2 Proton and Neutron Decays

Experimental measurements of neutron β -decay can place constraints on TeV-scale new-physics models, in particular those with scalar or tensor interactions, provided values for the nucleon scalar and tensor charges g_S and g_T . The next generation of neutron β -decay experiments is expected to increase their sensitivity to scalar and tensor interactions by an order of magnitude. Model estimates of g_S and g_T disagree and provide only loose bounds, but lattice-QCD can provide precise results for these quantities.

The calculation of neutron decay matrix elements is part of the lattice-QCD program to study nucleon structure: see, e.g., Ref. [154]. A realistic goal for lattice-QCD in the next five years is to pin the values of g_S and g_T down to 10–20%. Given this level of accuracy, experimental neutron β -decay measurements are more sensitive to scalar and tensor contact terms than a 25 fb^{-1} run at the 8 TeV LHC [155]. Further, studies have shown this precision will be sufficient to exploit the anticipated experimental sensitivity of the proposed UCN experiment at LANL [156].

The proton-decay matrix elements $\langle \pi, K, \eta, \dots | O_{\Delta B=1} | p \rangle$ needed to interpret experimental limits on proton decay as constraints on GUT model parameters are similar to the neutron-decay matrix elements discussed above. Only a single small-scale lattice-QCD effort by the RBC and UKQCD Collaborations has been devoted to calculating proton-decay matrix elements so far. Recently they obtained the first direct calculation of these matrix elements with $N_f = 2 + 1$ dynamical quarks with uncertainties of $\sim 20\text{--}40\%$. They will include finer lattice spacings and lighter pion masses in a future work. With these improvements, it should be straightforward to reduce the errors in proton-decay matrix elements to the $\sim 10\%$ level in the next five years.

X.3.4.3 Neutron-antineutron Oscillations

A low-energy process that could provide distinct evidence for baryon number violation from BSM physics is the transition of neutrons to antineutrons, which violates baryon number by two units [157]. This process can be observed through the annihilation of the resulting antineutron. Experimentally, this can be searched for with large scale proton decay detectors such as Super-K [158], and also with experiments with nearly-free neutrons where flux and time of flight is optimized [159]. In particular, a neutron-antineutron oscillation experiment at *Project X* could improve the limit on the $n\text{-}\bar{n}$ transition rate by a factor of ~ 1000 .

For many grand unified theories (GUTs) with Majorana neutrinos and early universe sphaleron processes, the prediction for the oscillation period is between 10^9 and 10^{11} seconds [160–164]. However, this estimate is based on naive dimensional analysis, and could prove to be quite inaccurate when the nonperturbative QCD effects are properly accounted for. Calculations of these matrix elements with reliable errors anywhere below 50% would provide valuable guidance for new-physics model predictions.

Lattice-QCD calculations can provide both the matrix elements of the six-fermion operators governing this process and calculate the QCD running of these operators to the scale of nuclear physics. There are four independent operators, differing in their color and spin structure [165,166]. Despite the fact that the operators involve more quark fields, the calculations are in many ways simpler than those for the matrix elements discussed above, e.g., $\langle N|\bar{s}s|N\rangle$. In particular, there are no quark-disconnected diagrams or spectator quarks. Thus, we can ultimately expect very accurate results.

Initial work on these matrix elements is currently underway [167]. The main challenge at this stage is to make sufficient lattice measurements to obtain a statistically significant signal. A first result is expected in the next 1–2 years, with anticipated errors of $\sim 25\%$; results with errors of $\sim 10\%$ or smaller should be achievable over the next five years.

X.3.5 Hadronic Physics

Here we describe opportunities for lattice QCD to assist the *Project X* hadronic physics program described in Chapters VIII and IX. *Project X* will provide intense proton, pion, and kaon beams that enable measurements of the hadron spectrum and of the proton structure; these will help address outstanding questions in QCD. The spectroscopy experiment outlined in Chapter IX will use a high-statistics kaon beam incident on a liquid hydrogen target to map out the hybrid meson spectrum and fill in the light-meson spectrum. A comparison of the measured hadron spectrum with first-principles lattice-QCD calculations provides a crucial test of our understanding of nonperturbative QCD dynamics. The *Project X* hadron structure program will perform Drell-Yan measurements with a polarized proton beam to study the role of quark orbital angular momentum (OAM) in the fundamental structure of the proton. The initial goal is to make the first spin-dependent Drell-Yan measurement and compare the measured Sivers function for valence up quarks to that obtained from semi-inclusive deep inelastic scattering. The subsequent goal is make a direct measurement of the Sivers distribution for antiquarks, which cannot be accessed via semi-inclusive DIS. Lattice QCD can provide first-principles calculations of nucleon structure quantities such as generalized parton distribution functions and transverse momentum distribution functions. Comparison of these theoretical predictions with experiment is needed to establish a complete and consistent understanding of the proton (and neutron) spin, and ultimately resolve the proton-spin puzzle.

X.3.5.1 Hadron Spectroscopy

The confrontation of experimental data on the spectrum with high-precision calculations in lattice QCD is a vital test of our understanding of QCD in the strong-coupling regime. Whilst the precise calculation of the lowest-lying states represents an important milestone in our ability to solve QCD,

the calculation of the excited-state spectrum at sufficient precision to delineate the states provides an unrivaled opportunity to explore in detail the dynamics of the theory, and to identify the collective degrees of freedom that describe it.

The lattice calculations shown in Figure 9.1 [8,168] provide a powerful indication of the presence of mesons with exotic quantum numbers in the energy regime accessible to the emerging generation of experiments, and indeed the existence of “hybrids,” states in which the gluons assume a structural role, with both exotic and non-exotic quantum numbers. The calculation of the spectrum of isoscalar mesons reveals exotic states in the neighborhood of their isovector cousins, and enables the flavor content to be determined [7,8].

These calculations are incomplete. Most notably, the spectrum is characterized by states that are resonances unstable under the strong interactions, and are thereby encapsulated within momentum-dependent phase shifts which may then be parametrized in terms of a mass and decay width. In lattice calculations, shifts in the energy spectrum at finite volume can be related to infinite-volume phase shifts [91,169]. Recently, the energy dependence of the ρ resonance in $\pi\pi$ elastic scattering has been mapped in unprecedented detail using this method [170–173], and the mass and width extracted to high precision albeit at unphysically large quark masses, as illustrated in Figure X-5.

The calculations cited above lay much of the theoretical and computational groundwork for the future program of lattice spectroscopy, and the next few years present an exciting opportunity for lattice QCD even to *predict* the underlying features of the spectrum in advance of experiment. With the first experiments at the 12 GeV upgrade of Jefferson Laboratory anticipated in 2015, an on-going program at COMPASS at CERN, and the potential *Project X* experiment outlined in Chapter IX, a vibrant program of computational spectroscopy is a key component of the worldwide lattice effort.

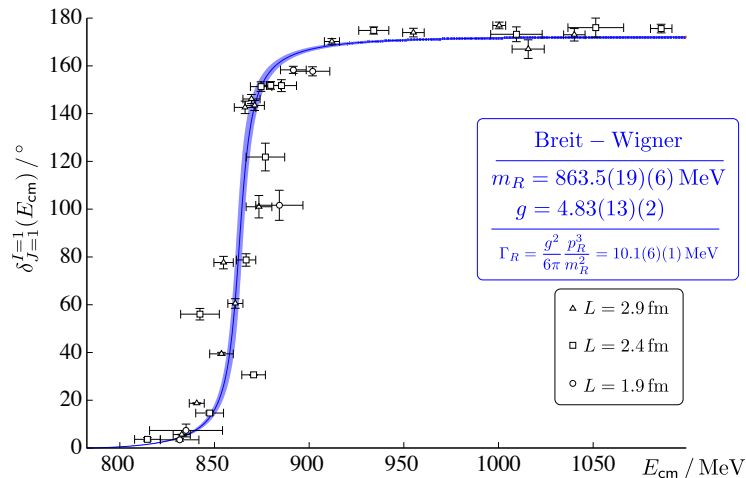


Figure X-5: The elastic scattering phase-shift from lattice QCD for $\pi\pi$, $I = 1$, P -wave scattering as a function of center-of-mass frame scattering energy and a description by a single Breit-Wigner resonance. In the legend, the first error shown on the ρ mass and width is statistical, while the second error is due to the uncertainties in the lattice pion mass and anisotropy parameter. The small width of the ρ stems from the lack of phase-space for decay into two 392 MeV pions. From Ref. [173]

Recent advances in calculating the excited-state spectrum of QCD in the U.S. have exploited anisotropic lattices with the Wilson-clover fermion action, which have a fine temporal lattice spacing enabling the resolution of many levels in the spectrum, but a coarser spatial lattice spacing to alleviate the cost on currently available computers. This has enabled the delineation of many energy eigenstates at the sub-percent level needed to resolve the spectrum, and to identify their continuum quantum numbers; these calculations have been at pion masses of around 400 MeV and above. The availability over the next five years of the emerging generation of leadership-class capability computing, and dedicated capacity computing, will enable calculations to be performed at the physical light- and strange-quark masses, at sufficiently fine lattice spacings to render the use of an anisotropic lattice redundant, and with sufficient precision to delineate the energy spectrum. Paramount to the success of such calculations will be a theoretical effort at developing methods of treating coupled-channel effects and multi-hadron states that appear above the inelastic threshold [174–179].

An integral program of first-principles lattice calculations of the spectrum, a meson spectroscopy effort with different beams, and a worldwide amplitude-analysis effort will provide an unrivaled opportunity to understand the low-energy degrees of freedom that govern the spectrum, and to inform the expected decay channels so as to guide experiment.

X.3.5.2 Nucleon Structure

As discussed in Chapter VIII, the quark orbital angular momentum is accessed in the Ji decomposition of the proton spin Eq. (VIII.2.2) as moments of generalized parton distribution functions, which are being aggressively studied by various groups [53,55,180,181]. In particular, the quark OAM contribution has been computed by the LHP collaboration in 2+1 flavor QCD [53]. In this calculation, the lightest pion mass was about 300 MeV and the largest box was about 3.5 fm on a side. It was found that the OAM of the up and down quarks is opposite in sign to model expectations, and it is thought that this may be due to the omission of quark-disconnected contributions, which are computationally expensive. The connected contributions from up and down quarks cancel each other out, while a recent study in quenched QCD by the χ QCD collaboration showed that the disconnected contributions do not cancel each other out [181]. Whether this continues to hold for the 2+1 flavor theory and at physical quark masses is an important question.

Important structure quantities like quark momentum fractions and helicities, form factors, axial and tensor charges, and transverse momentum distributions (TMDs) are also being actively pursued (see the recent review by Lin [182]). The QCDSF collaboration has recently reported agreement with experiment for the axial charge g_A computed in two-flavor QCD at the physical point with a quoted total error of a bit more than 3% [58]. They observe large finite volume effects in their data, however, which are removed by fitting to SSE chiral perturbation theory. Further, they obtain values of g_A below the experimental value for most of their simulated pion masses, and there is no hint of increasing behavior with decreasing quark mass in their results until one is directly at the physical point. Other groups also find low values of g_A [52,55,57,148,183], even down to $m_\pi = 170$ MeV [184] and 150 MeV [185], so the QCDSF result, while interesting, needs further study. The LHP collaboration has done a detailed study using several source-sink separations for three-point correlation functions down to $m_\pi = 150$ MeV which indicates large excited state effects for the momentum fraction, form factors, and charge radii [185]. Likewise, the ETM collaboration recently

reported results for nucleon structure using 2+1+1 flavor twisted-mass QCD with m_π down to 210 MeV. These results suggest that precise nucleon structure calculations are feasible but will require concerted effort and significant resources.

The RBC/UKQCD and LHP collaborations are starting computations of hadron structure observables using the domain-wall fermion action directly at the physical pion mass on a large lattice (5.5 fm) with spacing $a = 0.114$ fm. Measurements on a finer $a = 0.086$ fm lattice are expected to start in about a year's time, and will provide a continuum limit. A Japanese group using the K computer at Kobe has generated an ensemble using improved Wilson fermions on a 10 fm box, also with the physical pion mass. Planned studies using this very large box will be important in addressing finite size effects.

Nucleon structure calculations are not at the level of precision of their lighter meson cousins, owing to larger attendant statistical fluctuations and even more rapid exponential decay of correlators. Even so, experience, new techniques, and growing computer resources are allowing improved calculations. Recent results provide clear indications that longstanding discrepancies in g_A , nucleon charge radii, and structure functions are due to chiral, excited state, and finite-size systematic errors. The new generation of calculations at the physical pion mass on large lattices should largely eliminate these, beginning an era of precision nucleon matrix element calculations. These calculations will be difficult since current ones already struggle to achieve sub-five percent statistical errors in the best cases when m_π takes nearly physical values. It is hoped that new error-reduction methods like all-mode averaging [60] and sustained effort on the new ensembles will allow for smaller errors than have been possible in the past (preliminary results for g_A using domain-wall fermions with $m_\pi = 170$ are encouraging). The computation of quark-disconnected diagrams needed for isoscalar quantities, while even more difficult, is also being actively addressed [181,186,187], and will become more computationally feasible over the next five to ten years with the anticipated increase in computing capabilities and resources.

X.4 COMPUTATIONAL RESOURCES

In this section we discuss the computational and software infrastructure resources needed to reach the scientific goals set out above. We focus on the efforts and plans in the US, but comparable efforts are ongoing in Europe and Japan.

The lattice gauge theory research community in the United States coordinates much of its effort to obtain computational hardware and develop software infrastructure through the USQCD Collaboration. Support for USQCD has been obtained from the high-energy physics and nuclear physics offices of DOE in the form of (i) funds for hardware and support staff, (ii) computational resources on leadership-class machines through INCITE awards, and (iii) SciDAC awards for software and algorithm development. The first has consisted of two 4–5 year grants, the second of which extends until 2014. Since its inception, the INCITE program has awarded computing resources to USQCD every year. SciDAC has funded three software projects for lattice QCD, the most recent beginning in 2012. All three components have been critical for progress in lattice QCD in the past decade. The primary purpose of USQCD is to support the high-energy and nuclear physics experimental programs in the US and worldwide. To this end, USQCD establishes scientific priorities, which are

documented in white papers. USQCD's internal and INCITE computing resources are then allocated, in a proposal driven process, to self-directed smaller groups within USQCD to accomplish these goals.

At present, members of USQCD are making use of dedicated hardware funded by the DOE through the LQCD-ext Infrastructure Project, as well as a Cray XE/XK computer, and IBM Blue Gene/Q and Blue Gene/P computers, made available by the DOE's INCITE Program. During 2013, USQCD, as a whole, expects to sustain approximately 300 teraflop/s on these machines. USQCD has a PRAC grant for the development of code for the NSF's petascale computing facility, Blue Waters, and expects to obtain a significant allocation on this computer during 2013. Subgroups within USQCD also make use of computing facilities at the DOE's National Energy Research Scientific Computing Center (NERSC), the Lawrence Livermore National Laboratory (LLNL), and centers supported by the NSF's XSEDE Program. In addition, the RBC Collaboration has access to dedicated Blue Gene/Q computers at the RIKEN BNL Research Center at Brookhaven National Laboratory and the University of Edinburgh. For some time, the resources USQCD has obtained have grown with a doubling time of approximately 1.5 years, consistent with Moore's law, and this growth rate will need to continue to meet the scientific objectives described previously.

Gauge-field configurations must be generated in series, generally requiring high-capability machines such as the Blue Gene/Q and the Cray XE/XK. The advent of petascale supercomputers is for the first time enabling widespread simulations with physical up and down quark masses at small lattice spacings and large volumes. This development will enable major advances on a range of important calculations. For the next five years, the US lattice-QCD effort in high-energy physics will generate large sets of gauge-field ensembles with the domain-wall fermion (DWF) [188–190] and highly improved staggered quark (HISQ) [191] lattice actions. Each of these formulations has its own advantages. Further, for the most important calculations, it is helpful to employ more than one lattice formulation in order to ensure that systematic errors are truly under control. Computations of operator expectation values on these gauge-field ensembles can be run in parallel and are well-suited for high-capacity PC and GPU clusters such as the dedicated lattice-QCD facilities at Fermilab and Jefferson Lab. Therefore continued support of both the national supercomputing centers and of dedicated USQCD hardware will be needed to meet the US lattice-QCD community's scientific goals.

The software developed by USQCD under a SciDAC grant enables US lattice gauge theorists to use a wide variety of architectures with very high efficiency, and it is critical that USQCD software efforts continue at their current pace. Historically, the advance preparation of USQCD for new hardware has enabled members to take full advantage of early science time that is often available while new machines are coming online and being tested. Over time, the development of new algorithms has had at least as important an impact on the field of lattice QCD as advances in hardware, and this trend is expected to continue, although the rate of algorithmic advances is not as smooth or easy to predict as that of hardware.

X.5 SUMMARY

Lattice-QCD calculations now play an essential role in the search for new physics at the intensity frontier. They provide accurate results for many of the hadronic matrix elements needed to real-

ize the potential of present experiments probing the physics of flavor. The methodology has been validated by comparison with a broad array of measured quantities, several of which had not been well measured in experiment when the first good lattice calculation became available. In the US, this effort has been supported in an essential way by hardware and software support provided to the USQCD Collaboration.

In the next decade, lattice-QCD has the welcome opportunity to play an expanded role in the search for new physics at the intensity frontier. This chapter has laid out an ambitious vision for future lattice calculations matched to the experimental priorities of the planned *Project X* physics program:

- We will steadily improve the calculations of the hadronic parameters (decay constants, semileptonic form factors, and mixing matrix elements) needed to obtain the CKM matrix elements and constrain the CKM unitarity triangle. We will also continue to improve the determinations of the quark masses and α_s . We forecast improvements by factors of 2–4 over the next five years, with most quantities having errors at or below the percent level. The quark masses and CKM matrix elements enter Standard-Model rates for many rare processes. Most notably, the anticipated improvement in the $B \rightarrow D^* \ell \nu$ form factor (needed for $|V_{cb}|$) will reduce the uncertainty in the Standard-Model predictions for $K \rightarrow \pi \nu \bar{\nu}$ to the target experimental precision.
- We will calculate proton and neutron matrix elements relevant for determining neutrino-nucleon scattering cross sections, interpreting muon-to-electron conversion measurements as constraints on new-physics models, constraining TeV- and GUT-scale physics via measurements of EDMs and neutron β -decay, and searches for proton decay and neutron-antineutron oscillations. These calculations are in earlier stages than the precision quark-flavor computations described above. Further, baryon correlation functions suffer from larger statistical uncertainties than for mesons. For discovery modes, ~ 10 – 20% precision should be useful and straightforward. Even for precision matrix elements, such as the axial-vector form factor arising in neutrino scattering, reducing the errors to $\sim 5\%$ will be feasible, certainly over the course of *Project X*.
- We will calculate more computationally demanding matrix elements that are needed for the interpretation of planned (and in some cases old) kaon and charged lepton experiments. These include the hadronic contributions to the muon $g - 2$, long-distance contributions to kaon mixing and to $K \rightarrow \pi \nu \bar{\nu}$ decays, and the SM prediction for CP violation in $K \rightarrow \pi \pi$ decays (ϵ'). Here we require new methods, but the methodology is at a fairly advanced stage of development. Many of these calculations are in early stages, so future errors are difficult to anticipate. However, we will devote substantial theoretical and computational effort to these calculations commensurate with their high experimental priority, so prospects are good for obtaining the errors needed by the experiments.
- Key to achieving these goals will be the use of physical light-quark masses. At the accuracy we propose to obtain for many quantities, we will need to include the effects of isospin breaking, electromagnetism, and dynamical charm quarks.
- Implementation of the program outlined here will require dedicated lattice-QCD computing hardware, leadership-class computing, and efficient lattice-QCD software. Therefore contin-

ued support of USQCD computing infrastructure and personnel is essential to fully capitalize on the enormous investments in the high-energy physics and nuclear-physics experimental programs.

The future success of the *Project X* physics program hinges on reliable Standard-Model predictions on the same time scale as the experiments and with commensurate uncertainties. Many of these predictions require nonperturbative hadronic matrix elements that can only be computed numerically with lattice-QCD. The lattice-QCD community is well-versed in the plans and needs of the experimental intensity-physics program over the next decade, and will continue to pursue the necessary supporting theoretical calculations. Indeed, lattice-QCD calculations for the intensity frontier may play a key role in definitively establishing the presence of physics beyond the Standard Model and in determining its underlying structure.

References

- [1] “Project X Physics Study,” <https://indico.fnal.gov/event/projectxps12>
- [2] C. Aubin *et al.* (MILC Collaboration), Phys. Rev. **D70**, 094505 (2004), [arXiv:hep-lat/0402030 [hep-lat]]
- [3] A. Bazavov *et al.*, Rev. Mod. Phys. **82**, 1349 (2010), [arXiv:0903.3598 [hep-lat]]
- [4] S. Aoki *et al.* (PACS-CS Collaboration), Phys. Rev. **D79**, 034503 (2009), [arXiv:0807.1661 [hep-lat]]
- [5] S. Dürr *et al.* (BMW Collaboration), Science **322**, 1224 (2008), [arXiv:0906.3599 [hep-lat]]
- [6] W. Bietenholz *et al.* (QCDSF and UKQCD Collaborations), Phys. Rev. **D84**, 054509 (2011), [arXiv:1102.5300 [hep-lat]]
- [7] N. H. Christ *et al.* (RBC and UKQCD Collaborations), Phys. Rev. Lett. **105**, 241601 (2010), [arXiv:1002.2999 [hep-lat]]
- [8] J. J. Dudek *et al.* (Hadron Spectrum Collaboration), Phys. Rev. **D83**, 111502 (2011), [arXiv:1102.4299 [hep-lat]]
- [9] E. B. Gregory, A. C. Irving, C. M. Richards, and C. McNeile, Phys. Rev. **D86**, 014504 (2012), [arXiv:1112.4384 [hep-lat]]
- [10] C. Bernard *et al.* (Fermilab Lattice and MILC Collaborations), Phys. Rev. **D83**, 034503 (2011), [arXiv:1003.1937 [hep-lat]]
- [11] E. B. Gregory *et al.* (HPQCD Collaboration), Phys. Rev. **D83**, 014506 (2011), [arXiv:1010.3848 [hep-lat]]
- [12] D. Mohler and R. M. Woloshyn, Phys. Rev. **D84**, 054505 (2011), [arXiv:1103.5506 [hep-lat]]

- [13] C. McNeile, C. T. H. Davies, E. Follana, K. Hornbostel, and G. Lepage (HPQCD Collaboration), Phys. Rev. **D82**, 034512 (2010), [arXiv:1004.4285 [hep-lat]]
- [14] J. Beringer *et al.* (Particle Data Group), Phys. Rev. **D86**, 010001 (2012)
- [15] K. G. Chetyrkin *et al.*, Phys. Rev. **D80**, 074010 (2009), [arXiv:0907.2110 [hep-ph]]
- [16] I. Allison *et al.* (HPQCD Collaboration), Phys. Rev. **D78**, 054513 (2008), [arXiv:0805.2999 [hep-lat]]
- [17] C. T. H. Davies *et al.* (HPQCD Collaboration), Phys. Rev. **D78**, 114507 (2008), [arXiv:0807.1687 [hep-lat]]
- [18] S. Aoki *et al.* (PACS-CS Collaboration), JHEP **0910**, 053 (2009), [arXiv:0906.3906 [hep-lat]]
- [19] E. Shintani *et al.* (JLQCD Collaboration), Phys. Rev. **D82**, 074505 (2010), [arXiv:1002.0371 [hep-lat]]
- [20] B. Blossier *et al.* (ETM Collaboration), Phys. Rev. Lett. **108**, 262002 (2012), [arXiv:1201.5770 [hep-ph]]
- [21] S. Bethke *et al.*, “Workshop on Precision Measurements of α_s ,” (2011), arXiv:1110.0016 [hep-ph]
- [22] I. F. Allison *et al.* (HPQCD and Fermilab Lattice Collaboration), Phys. Rev. Lett. **94**, 172001 (2005), [arXiv:hep-lat/0411027 [hep-lat]]
- [23] A. Abulencia *et al.* (CDF Collaboration), Phys. Rev. Lett. **96**, 082002 (2006), [arXiv:hep-ex/0505076 [hep-ex]]
- [24] C. Aubin *et al.* (Fermilab Lattice, MILC, and HPQCD Collaboration), Phys. Rev. Lett. **95**, 122002 (2005), [arXiv:hep-lat/0506030 [hep-lat]]
- [25] M. Artuso *et al.* (CLEO Collaboration), Phys. Rev. Lett. **95**, 251801 (2005), [arXiv:hep-ex/0508057 [hep-ex]]
- [26] C. Aubin *et al.* (Fermilab Lattice, MILC, and HPQCD Collaborations), Phys. Rev. Lett. **94**, 011601 (2005), [arXiv:hep-ph/0408306 [hep-ph]]
- [27] L. Widhalm *et al.* (Belle Collaboration), Phys. Rev. Lett. **97**, 061804 (2006), [arXiv:hep-ex/0604049 [hep-ex]]
- [28] A. S. Kronfeld, Ann. Rev. Nucl. Part. Sci. **62**, 265 (2012), [arXiv:1203.1204 [hep-lat]]
- [29] C. Bernard *et al.*, Phys. Rev. **D80**, 034026 (2009), [arXiv:0906.2498 [hep-lat]]
- [30] D. Besson *et al.* (CLEO Collaboration), Phys. Rev. **D80**, 032005 (2009), [arXiv:0906.2983 [hep-ex]]
- [31] S. Aoki *et al.* (PACS-CS Collaboration), Phys. Rev. **D81**, 074503 (2010), [arXiv:0911.2561 [hep-lat]]

- [32] S. Dürr *et al.* (BMW Collaboration), Phys. Lett. **B701**, 265 (2011), [arXiv:1011.2403 [hep-lat]]
- [33] S. Dürr *et al.* (BMW Collaboration), JHEP **1108**, 148 (2011), [arXiv:1011.2711 [hep-lat]]
- [34] A. Bazavov *et al.* (MILC Collaboration), Phys. Rev. Lett. **110**, 172003 (2013), [arXiv:1301.5855 [hep-ph]]
- [35] R. J. Dowdall, C. T. H. Davies, G. P. Lepage, and C. McNeile (HPQCD Collaboration), “ V_{us} from π and K decay constants in full lattice QCD with physical u , d , s and c quarks,” (2013), arXiv:1303.1670 [hep-lat]
- [36] R. Baron *et al.* (ETM Collaboration), JHEP **1008**, 097 (2010), [arXiv:0911.5061 [hep-lat]]
- [37] A. Bazavov *et al.* (MILC Collaboration), Phys. Rev. **D87**, 054505 (2013), [arXiv:1212.4768 [hep-lat]]
- [38] J. A. Formaggio and G. P. Zeller, Rev. Mod. Phys. **84**, 1307 (2012)
- [39] C. H. Llewellyn Smith, Phys. Rept. **3**, 261 (1972)
- [40] J. J. Kelly, Phys. Rev. **C70**, 068202 (2004)
- [41] R. Bradford, A. Bodek, H. S. Budd, and J. Arrington, Nucl. Phys. Proc. Suppl. **159**, 127 (2006), [arXiv:hep-ex/0602017 [hep-ex]]
- [42] A. Bodek, S. Avvakumov, R. Bradford, and H. S. Budd, Eur. Phys. J. **C53**, 349 (2008), [arXiv:0708.1946 [hep-ex]]
- [43] B. Bhattacharya, R. J. Hill, and G. Paz, Phys. Rev. **D84**, 073006 (2011), [arXiv:1108.0423 [hep-ph]]
- [44] G. P. Lepage and S. J. Brodsky, Phys. Rev. **D22**, 2157 (1980)
- [45] J. Arrington, C. D. Roberts, and J. M. Zanotti, J. Phys. **G34**, S23 (2007), [arXiv:nucl-th/0611050 [nucl-th]]
- [46] V. Lyubushkin *et al.* (NOMAD Collaboration), Eur. Phys. J. **C63**, 355 (2009), [arXiv:0812.4543 [hep-ex]]
- [47] A. A. Aguilar-Arevalo *et al.* (MiniBooNE Collaboration), Phys. Rev. **D81**, 092005 (2010), [arXiv:1002.2680 [hep-ex]]
- [48] J. A. Bailey *et al.* (Fermilab Lattice and MILC Collaborations), Phys. Rev. **D79**, 054507 (2009), [arXiv:0811.3640 [hep-lat]]
- [49] H. Ha *et al.* (Belle Collaboration), Phys. Rev. **D83**, 071101 (2011), [arXiv:1012.0090 [hep-ex]]
- [50] J. P. Lees *et al.* (BaBar Collaboration), Phys. Rev. **D86**, 092004 (2012), [arXiv:1208.1253 [hep-ex]]

- [51] A. Ali Khan *et al.* (QCDSF Collaboration), Phys. Rev. **D74**, 094508 (2006), [arXiv:hep-lat/0603028]
- [52] T. Yamazaki *et al.* (RBC and UKQCD Collaborations), Phys. Rev. **D79**, 114505 (2009), [arXiv:0904.2039 [hep-lat]]
- [53] J. D. Bratt *et al.* (LHP Collaboration), Phys. Rev. **D82**, 094502 (2010), [arXiv:1001.3620 [hep-lat]]
- [54] C. Alexandrou *et al.* (ETM Collaboration), Phys. Rev. **D83**, 045010 (2011), [arXiv:1012.0857 [hep-lat]]
- [55] C. Alexandrou *et al.* (ETM Collaboration), “Nucleon form factors and moments of generalized parton distributions using $N_f = 2 + 1 + 1$ twisted mass fermions,” (2013), arXiv:1303.5979 [hep-lat]
- [56] P. Hägler, Phys. Rept. **490**, 49 (2010), [arXiv:0912.5483 [hep-lat]]
- [57] S. Capitani *et al.*, Phys. Rev. **D86**, 074502 (2012), [arXiv:1205.0180 [hep-lat]]
- [58] R. Horsley *et al.* (QCDSF Collaboration), “Nucleon axial charge and pion decay constant from two-flavor lattice QCD,” (2013), arXiv:1302.2233 [hep-lat]
- [59] Y. Aoki, E. Shintani, and A. Soni (RBC Collaboration), “Proton decay matrix elements on the lattice,” (2013), arXiv:1304.7424 [hep-lat]
- [60] T. Blum, T. Izubuchi, and E. Shintani, “A new class of variance reduction techniques using lattice symmetries,” (2012), arXiv:1208.4349 [hep-lat]
- [61] S. Dürr *et al.* (BMW Collaboration), Phys. Rev. **D81**, 054507 (2010), [arXiv:1001.4692 [hep-lat]]
- [62] E. Follana, C. T. H. Davies, G. P. Lepage, and J. Shigemitsu (HPQCD Collaboration), Phys. Rev. Lett. **100**, 062002 (2008), [arXiv:0706.1726 [hep-lat]]
- [63] J. Laiho and R. S. Van de Water, PoS **Lattice 2011**, 293 (2011), [arXiv:1112.4861 [hep-lat]]
- [64] A. Bazavov *et al.* (MILC Collaboration), PoS **LATTICE2010**, 074 (2010), [arXiv:1012.0868 [hep-lat]]
- [65] Y. Aoki *et al.* (RBC and UKQCD Collaborations), Phys. Rev. **D83**, 074508 (2011), [arXiv:1011.0892 [hep-lat]]
- [66] V. Lubicz, F. Mescia, S. Simula, and C. Tarantino (ETM Collaboration), Phys. Rev. **D80**, 111502 (2009), [arXiv:0906.4728 [hep-lat]]
- [67] P. A. Boyle *et al.* (RBC and UKQCD Collaboration), Eur. Phys. J. **C69**, 159 (2010), [arXiv:1004.0886 [hep-lat]]
- [68] A. Bazavov *et al.* (MILC Collaboration), PoS **LAT2009**, 079 (2009), [arXiv:0910.3618 [hep-lat]]

- [69] T. Blum *et al.*, Phys. Rev. **D82**, 094508 (2010), [arXiv:1006.1311 [hep-lat]]
- [70] C. Kelly (RBC and UKQCD Collaborations), PoS **Lattice 2011**, 285 (2012), [arXiv:1201.0706 [hep-lat]]
- [71] A. Bazavov *et al.* (Fermilab Lattice and MILC Collaborations), Phys. Rev. **D87**, 073012 (2012), [arXiv:1212.4993 [hep-lat]]
- [72] F. Farchioni *et al.* (ETM Collaboration), PoS **LATTICE2010**, 128 (2010), [arXiv:1012.0200 [hep-lat]]
- [73] A. Bazavov *et al.* (MILC Collaboration), PoS **LATTICE2011**, 107 (2011), [arXiv:1111.4314 [hep-lat]]
- [74] J. Laiho, E. Lunghi, and R. S. Van de Water, Phys. Rev. **D81**, 034503 (2010), updates at <http://www.latticeaverages.org>, [arXiv:0910.2928 [hep-ph]]
- [75] G. Colangelo *et al.* (FlaviaNet Lattice Averaging Group), Eur. Phys. J. **C71**, 1695 (2011), [arXiv:1011.4408 [hep-lat]]
- [76] E. Gámiz *et al.* (HPQCD Collaboration), Phys. Rev. **D73**, 114502 (2006), [arXiv:hep-lat/0603023 [hep-lat]]
- [77] S. Dürr *et al.* (BMW Collaboration), Phys. Lett. **B705**, 477 (2011), [arXiv:1106.3230 [hep-lat]]
- [78] T. Bae *et al.* (SWME Collaboration), Phys. Rev. Lett. **109**, 041601 (2012), [arXiv:1111.5698 [hep-lat]]
- [79] J. Laiho, E. Lunghi, and R. Van de Water, PoS **Lattice 2011**, 018 (2012), updates at <http://www.latticeaverages.org>, [arXiv:1204.0791 [hep-ph]]
- [80] J. Brod and M. Gorbahn, Phys. Rev. Lett. **108**, 121801 (2012), [arXiv:1108.2036 [hep-ph]]
- [81] J. Brod, “Rare K Decays in the Standard Model,” Project X Physics Study (2012), <https://indico.fnal.gov/getFile.py/access?contribId=23&sessionId=5&resId=0&materialId=slides&confId=5276>
- [82] R. Brower *et al.* (USQCD Collaboration), “Fundamental parameters from future lattice calculations,” (2007), <http://www.usqcd.org/documents/fundamental.pdf>
- [83] J. A. Bailey *et al.* (Fermilab Lattice and MILC Collaborations), PoS **LATTICE2010**, 311 (2010), [arXiv:1011.2166 [hep-lat]]
- [84] T. Blum *et al.* (RBC and UKQCD Collaborations), Phys. Rev. Lett. **108**, 141601 (2012), [arXiv:1111.1699 [hep-lat]]
- [85] T. Blum *et al.* (RBC and UKQCD Collaborations), Phys. Rev. **D86**, 074513 (2012), [arXiv:1206.5142 [hep-lat]]
- [86] J. Yu (RBC and UKQCD Collaborations), PoS **LAT2012**, 129 (2012)

- [87] J. R. Batley *et al.* (NA48 Collaboration), Phys. Lett. **B544**, 97 (2002), [arXiv:hep-ex/0208009 [hep-ex]]
- [88] E. Abouzaid *et al.* (KTeV Collaboration), Phys. Rev. **D83**, 092001 (2011), [arXiv:1011.0127 [hep-ex]]
- [89] A. J. Buras, G. Colangelo, G. Isidori, A. Romanino, and L. Silvestrini, Nucl. Phys. **B566**, 3 (2000), [arXiv:hep-ph/9908371]
- [90] U. Haisch, “Some thoughts about rare kaon decays,” Project X Physics Study (2012), <https://indico.fnal.gov/getFile.py/access?contribId=22&sessionId=5&resId=0&materialId=slides&confId=5276>
- [91] M. Lüscher, Commun. Math. Phys. **105**, 153 (1986)
- [92] L. Lellouch and M. Lüscher, Commun. Math. Phys. **219**, 31 (2001), [arXiv:hep-lat/0003023 [hep-lat]]
- [93] T. Blum *et al.* (RBC and UKQCD Collaborations), Phys. Rev. **D84**, 114503 (2011), [arXiv:1106.2714 [hep-lat]]
- [94] J. Brod, M. Gorbahn, and E. Stamou, Phys. Rev. **D83**, 034030 (2011), [arXiv:1009.0947 [hep-ph]]
- [95] S.-W. Qiu *et al.* (Fermilab Lattice and MILC Collaborations), PoS **Lattice 2011**, 289 (2011), [arXiv:1111.0677 [hep-lat]]
- [96] A. J. Buras, D. Guadagnoli, and G. Isidori, Phys. Lett. **B688**, 309 (2010), [arXiv:1002.3612 [hep-ph]]
- [97] S. Herrlich and U. Nierste, Nucl. Phys. **B419**, 292 (1994), [arXiv:hep-ph/9310311]
- [98] J. Brod and M. Gorbahn, Phys. Rev. **D82**, 094026 (2010), [arXiv:1007.0684 [hep-ph]]
- [99] N. H. Christ (RBC and UKQCD Collaborations), PoS **LATTICE2010**, 300 (2010), [arXiv:1012.6034 [hep-lat]]
- [100] N. H. Christ (RBC and UKQCD Collaborations), PoS **LATTICE2011**, 277 (2011), [arXiv:1201.2065 [hep-lat]]
- [101] J. Yu, PoS **LATTICE2011**, 297 (2011), [arXiv:1111.6953 [hep-lat]]
- [102] N. H. Christ, T. Izubuchi, C. T. Sachrajda, A. Soni, and J. Yu (RBC and UKQCD Collaborations), “Long distance contribution to the K_L - K_S mass difference,” (2012), arXiv:1212.5931 [hep-lat]
- [103] G. Isidori, G. Martinelli, and P. Turchetti, Phys. Lett. **B633**, 75 (2006), [arXiv:hep-lat/0506026 [hep-lat]]
- [104] V. Cirigliano, R. Kitano, Y. Okada, and P. Tuzon, Phys. Rev. **D80**, 013002 (2009), [arXiv:0904.0957 [hep-ph]]

- [105] A. Bottino, F. Donato, N. Fornengo, and S. Scopel, *Astropart. Phys.* **13**, 215 (2000), [arXiv:hep-ph/9909228 [hep-ph]]
- [106] J. R. Ellis, K. A. Olive, and C. Savage, *Phys. Rev.* **D77**, 065026 (2008), [arXiv:0801.3656 [hep-ph]]
- [107] R. J. Hill and M. P. Solon, *Phys. Lett.* **B707**, 539 (2012), [arXiv:1111.0016 [hep-ph]]
- [108] R. D. Young and A. W. Thomas, *Phys. Rev.* **D81**, 014503 (2010), [arXiv:0901.3310 [hep-lat]]
- [109] D. Toussaint and W. Freeman (MILC Collaboration), *Phys. Rev. Lett.* **103**, 122002 (2009), [arXiv:0905.2432 [hep-lat]]
- [110] S. Dürr *et al.* (BMW Collaboration), *Phys. Rev.* **D85**, 014509 (2012), [arXiv:1109.4265 [hep-lat]]
- [111] R. Horsley *et al.* (QCDSF and UKQCD Collaborations), *Phys. Rev.* **D85**, 034506 (2012), [arXiv:1110.4971 [hep-lat]]
- [112] S. Dinter *et al.* (ETM Collaboration), *JHEP* **1208**, 037 (2012), [arXiv:1202.1480 [hep-lat]]
- [113] H. Ohki *et al.* (JLQCD Collaboration), *Phys. Rev.* **D87**, 034509 (2013), [arXiv:1208.4185 [hep-lat]]
- [114] M. Engelhardt, *Phys. Rev.* **D86**, 114510 (2012), [arXiv:1210.0025 [hep-lat]]
- [115] W. Freeman and D. Toussaint (MILC Collaboration), “The intrinsic strangeness and charm of the nucleon using improved staggered fermions,” (2012), arXiv:1204.3866 [hep-lat]
- [116] P. E. Shanahan, A. W. Thomas, and R. D. Young, *Phys. Rev.* **D87**, 074503 (2013), [arXiv:1205.5365 [nucl-th]]
- [117] P. Junnarkar and A. Walker-Loud, “The scalar strange content of the nucleon from lattice QCD,” (2013), arXiv:1301.1114 [hep-lat]
- [118] A. E. Nelson and D. B. Kaplan, *Phys. Lett.* **B192**, 193 (1987)
- [119] D. B. Kaplan and A. Manohar, *Nucl. Phys.* **B310**, 527 (1988)
- [120] R. L. Jaffe, *Phys. Lett.* **B229**, 275 (1989)
- [121] M. Gong *et al.* (χ QCD Collaboration), “Strangeness and charm content of nucleon from overlap fermions on 2+1-flavor domain-wall fermion configurations,” (2013), arXiv:1304.1194 [hep-ph]
- [122] J. L. Hewett, H. Weerts, *et al.*, *Fundamental Physics at the Intensity Frontier* (U.S. Department of Energy, Germantown, MD, 2012) arXiv:1205.2671 [hep-ex]
- [123] T. Aoyama, M. Hayakawa, T. Kinoshita, and M. Nio, *Phys. Rev. Lett.* **109**, 111808 (2012), [arXiv:1205.5370 [hep-ph]]

- [124] M. Davier, A. Höcker, B. Malaescu, and Z. Zhang, *Eur. Phys. J.* **C71**, 1515 (2011), [arXiv:1010.4180 [hep-ph]]
- [125] K. Hagiwara, R. Liao, A. D. Martin, D. Nomura, and T. Teubner, *J. Phys.* **G38**, 085003 (2011), [arXiv:1105.3149 [hep-ph]]
- [126] G. W. Bennett *et al.* (Muon $g - 2$ Collaboration), *Phys. Rev.* **D73**, 072003 (2006), [arXiv:hep-ex/0602035 [hep-ex]]
- [127] F. Jegerlehner and R. Szafron, *Eur. Phys. J.* **C71**, 1632 (2011), [arXiv:1101.2872 [hep-ph]]
- [128] T. Blum, *Phys. Rev. Lett.* **91**, 052001 (2003), [arXiv:hep-lat/0212018]
- [129] M. Göckeler *et al.* (QCDSF Collaboration), *Nucl. Phys.* **B688**, 135 (2004), [arXiv:hep-lat/0312032]
- [130] C. Aubin and T. Blum, *Phys. Rev.* **D75**, 114502 (2007), [arXiv:hep-lat/0608011 [hep-lat]]
- [131] X. Feng, K. Jansen, M. Petschlies, and D. B. Renner (ETM Collaboration), *Phys. Rev. Lett.* **107**, 081802 (2011), [arXiv:1103.4818 [hep-lat]]
- [132] P. Boyle, L. Del Debbio, E. Kerrane, and J. Zanotti, *Phys. Rev.* **D85**, 074504 (2012), [arXiv:1107.1497 [hep-lat]]
- [133] M. Della Morte, B. Jäger, A. Jüttner, and H. Wittig, *JHEP* **1203**, 055 (2012), [arXiv:1112.2894 [hep-lat]]
- [134] C. Aubin, T. Blum, M. Golterman, and S. Peris, *Phys. Rev.* **D86**, 054509 (2012), [arXiv:1205.3695 [hep-lat]]
- [135] C. T. Sachrajda and G. Villadoro, *Phys. Lett.* **B609**, 73 (2005), [arXiv:hep-lat/0411033 [hep-lat]]
- [136] X. Feng, G. Hotzel, K. Jansen, M. Petschlies, and D. B. Renner, “Leading-order hadronic contributions to a_μ and α_{QED} from $N_f = 2 + 1 + 1$ twisted mass fermions,” (2012), arXiv:1211.0828 [hep-lat]
- [137] X. Feng *et al.*, “Computing the hadronic vacuum polarization function by analytic continuation,” (2013), arXiv:1305.5878 [hep-lat]
- [138] J. Prades, E. de Rafael, and A. Vainshtein, in *Lepton Dipole Moments*, edited by B. L. Roberts and W. J. Marciano (2009) arXiv:0901.0306 [hep-ph]
- [139] A. Nyffeler, *Phys. Rev.* **D79**, 073012 (2009), [arXiv:0901.1172 [hep-ph]]
- [140] M. Hayakawa, T. Blum, T. Izubuchi, and N. Yamada, *PoS LAT2005*, 353 (2006), [arXiv:hep-lat/0509016 [hep-lat]]
- [141] T. Blum, M. Hayakawa, and T. Izubuchi, *PoS LATTICE2012*, 022 (2012), [arXiv:1301.2607 [hep-lat]]

- [142] S. Chowdhury, *Lattice Calculation of the Hadronic Light-by-light Contribution to the Anomalous Magnetic Dipole Moment of Muon*, Ph.D. thesis, University of Connecticut (2009)
- [143] X. Feng *et al.* (JLQCD Collaboration), *Phys. Rev. Lett.* **109**, 182001 (2012), [arXiv:1206.1375 [hep-lat]]
- [144] K. Melnikov and A. Vainshtein, *Phys. Rev.* **D70**, 113006 (2004), [arXiv:hep-ph/0312226 [hep-ph]]
- [145] B. L. Ioffe, V. S. Fadin, and L. N. Lipatov, *Quantum Chromodynamics: Perturbative and Nonperturbative Aspects* (Cambridge University, Cambridge, UK, 2010)
- [146] H.-W. Lin and K. Orginos, *Phys. Rev.* **D79**, 034507 (2009), [arXiv:0712.1214 [hep-lat]]
- [147] H.-W. Lin, T. Blum, S. Ohta, S. Sasaki, and T. Yamazaki, *Phys. Rev.* **D78**, 014505 (2008), [arXiv:0802.0863 [hep-lat]]
- [148] T. Yamazaki *et al.* (RBC and UKQCD Collaborations), *Phys. Rev. Lett.* **100**, 171602 (2008), [arXiv:0801.4016 [hep-lat]]
- [149] M. Pospelov and A. Ritz, *Ann. Phys.* **318**, 119 (2005), [arXiv:hep-ph/0504231 [hep-ph]]
- [150] E. Shintani, S. Aoki, and Y. Kuramashi, *Phys. Rev.* **D78**, 014503 (2008), [arXiv:0803.0797 [hep-lat]]
- [151] E. Shintani *et al.*, *Phys. Rev.* **D72**, 014504 (2005), [arXiv:hep-lat/0505022]
- [152] R. Horsley *et al.*, “The electric dipole moment of the nucleon from simulations at imaginary vacuum angle theta,” (2008), arXiv:0808.1428 [hep-lat]
- [153] T. Bhattacharya, V. Cirigliano, and R. Gupta, *PoS LATTICE2012*, 179 (2012), [arXiv:1212.4918 [hep-lat]]
- [154] J. R. Green *et al.*, *Phys. Rev.* **D86**, 114509 (2012), [arXiv:1206.4527 [hep-lat]]
- [155] H.-W. Lin, “Lattice QCD for precision nucleon matrix elements,” (2011), arXiv:1112.2435 [hep-lat]
- [156] T. Bhattacharya *et al.*, *Phys. Rev.* **D85**, 054512 (2012), [arXiv:1110.6448 [hep-ph]]
- [157] R. N. Mohapatra and R. E. Marshak, *Phys. Rev. Lett.* **44**, 1316 (1980)
- [158] K. Ganezer, “The search for $n-\bar{n}$ oscillations at Super-Kamiokande I,” *Search for Baryon and Lepton Number Violations* (2007), <http://inpa.lbl.gov/BLNV/blnv.htm>
- [159] M. Baldo-Ceolin *et al.*, *Z. Phys.* **C63**, 409 (1994)
- [160] S. Nussinov and R. Shrock, *Phys. Rev. Lett.* **88**, 171601 (2002), [arXiv:hep-ph/0112337 [hep-ph]]

- [161] K. S. Babu, P. S. Bhupal Dev, and R. N. Mohapatra, Phys. Rev. **D79**, 015017 (2009), [arXiv:0811.3411 [hep-ph]]
- [162] R. N. Mohapatra, J. Phys. **G36**, 104006 (2009), [arXiv:0902.0834 [hep-ph]]
- [163] P. T. Winslow and J. N. Ng, Phys. Rev. **D81**, 106010 (2010), [arXiv:1003.1424 [hep-th]]
- [164] K. S. Babu and R. N. Mohapatra, Phys. Lett. **B715**, 328 (2012), [arXiv:1206.5701 [hep-ph]]
- [165] S. Rao and R. Shrock, Phys. Lett. **B116**, 238 (1982)
- [166] W. E. Caswell, J. Milutinovic, and G. Senjanovic, Phys. Lett. **B122**, 373 (1983)
- [167] M. I. Buchoff, C. Schroeder, and J. Wasem, PoS **LATTICE2012**, 128 (2012), [arXiv:1207.3832 [hep-lat]]
- [168] J. J. Dudek, R. G. Edwards, M. J. Peardon, D. G. Richards, and C. E. Thomas, Phys. Rev. **D82**, 034508 (2010), [arXiv:1004.4930 [hep-ph]]
- [169] M. Lüscher, Nucl. Phys. **B354**, 531 (1991)
- [170] X. Feng, K. Jansen, and D. B. Renner, Phys. Rev. **D83**, 094505 (2011), [arXiv:1011.5288 [hep-lat]]
- [171] C. B. Lang, D. Mohler, S. Prelovsek, and M. Vidmar, Phys. Rev. **D84**, 054503 (2011), [arXiv:1105.5636 [hep-lat]]
- [172] S. Aoki *et al.* (PACS-CS Collaboration), Phys. Rev. **D84**, 094505 (2011), [arXiv:1106.5365 [hep-lat]]
- [173] J. J. Dudek, R. G. Edwards, and C. E. Thomas, Phys. Rev. **D87**, 034505 (2013), [arXiv:1212.0830 [hep-ph]]
- [174] C. Liu, X. Feng, and S. He, Int. J. Mod. Phys. **A21**, 847 (2006), [arXiv:hep-lat/0508022 [hep-lat]]
- [175] M. Doring, U.-G. Meissner, E. Oset, and A. Rusetsky, Eur. Phys. J. **A47**, 139 (2011), [arXiv:1107.3988 [hep-lat]]
- [176] S. Aoki *et al.* (HAL QCD Collaboration), Proc. Japan Acad. **B87**, 509 (2011), [arXiv:1106.2281 [hep-lat]]
- [177] R. A. Briceño and Z. Davoudi, “Moving multi-channel systems in a finite volume,” (2012), arXiv:1204.1110 [hep-lat]
- [178] M. T. Hansen and S. R. Sharpe, Phys. Rev. **D86**, 016007 (2012), [arXiv:1204.0826 [hep-lat]]
- [179] P. Guo, J. Dudek, R. Edwards, and A. P. Szczepaniak, “The coupled-channel scattering on a torus,” (2012), arXiv:1211.0929 [hep-lat]
- [180] A. Sternbeck *et al.*, PoS **LATTICE2011**, 177 (2011), [arXiv:1203.6579 [hep-lat]]

- [181] K. F. Liu *et al.* (χ QCD Collaboration), PoS **LATTICE2011**, 164 (2011), [arXiv:1203.6388 [hep-ph]]
- [182] H.-W. Lin, PoS **LATTICE2012**, 013 (2012), [arXiv:1212.6849 [hep-lat]]
- [183] B. J. Owen *et al.*, Phys. Lett. **B723**, 217 (2013), [arXiv:1212.4668 [hep-lat]]
- [184] M. Lin and S. Ohta (RBC and UKQCD Collaborations), PoS **LATTICE2012**, 171 (2012), [arXiv:1212.3235 [hep-lat]]
- [185] J. R. Green *et al.*, “Nucleon structure from lattice QCD using a nearly physical pion mass,” (2012), arXiv:1209.1687 [hep-lat]
- [186] G. Bali *et al.*, PoS **LATTICE2011**, 174 (2011)
- [187] C. Alexandrou *et al.*, PoS **LATTICE2012**, 184 (2012), [arXiv:1211.0126 [hep-lat]]
- [188] D. B. Kaplan, Phys. Lett. **B288**, 342 (1992), [arXiv:hep-lat/9206013 [hep-lat]]
- [189] V. Furman and Y. Shamir, Nucl. Phys. **B439**, 54 (1995), [arXiv:hep-lat/9405004 [hep-lat]]
- [190] P. M. Vranas, Phys. Rev. **D74**, 034512 (2006), [arXiv:hep-lat/0606014 [hep-lat]]
- [191] E. Follana *et al.* (HPQCD Collaboration), Phys. Rev. **D75**, 054502 (2007), [arXiv:hep-lat/0610092 [hep-lat]]

INSERT

BLUE PAGE

HERE

Project X Broader Impacts

June 2013

Edited by:

David Asner/Pacific Northwest National Laboratory
Pushpa Bhat/Fermi National Accelerator Laboratory
Stuart Henderson/Fermi National Accelerator Laboratory
Robert Plunkett/ Fermi National Accelerator Laboratory

I	INTRODUCTION	5
II	PROJECT X SPALLATION AND IRRADIATION FACILITY	11
II.1	Summary	15
II.1.1	Mission Support	15
II.1.2	Target Station Options	19
II.2	Introduction	20
II.3	Mission Needs	21
II.3.1	Conclusions from Project X Energy Station Workshop.....	21
II.3.2	Nuclear Energy Requirements	25
II.3.3	Fusion Energy Science Requirements.....	28
II.3.4	Nuclear Physics Requirements	31
II.3.5	Nuclear Physics Isotopes Requirements.....	35
II.3.6	Common Issues in Materials Irradiation Testing.....	36
II.4	Target Station	37
II.4.1	Target Station Concept	37
II.4.2	Existing and Planned Spallation Neutron Source Facilities	44
II.4.3	Assumptions of Project X Operations.....	46
II.4.4	Target Station Capabilities & Challenges	47
II.4.5	Technical Feasibility	50
II.4.6	Meeting the Mission Needs.....	51
II.5	Conclusions and Recommendations.....	60
II.6	References	61
III	MUON SPIN ROTATION AT PROJECT X	63
III.1	Summary.....	65
III.2	The science case for μSR.....	66
III.2.1	Materials science	66
III.2.2	Chemistry	91
III.3	Techniques of Muon Spin Rotation.....	94
III.3.1	Brief Historical Summary.....	94
III.3.2	Beams and timing structures	94
III.4	World Facilities, Capabilities, and Needs	96
III.4.1	Overview of current and expected needs	99
III.4.2	Considerations specific to North America.....	99
III.5	Technical Capabilities of Project X for μSR	100
III.5.1	Stage 1 Project X and μ SR	100
III.5.2	Beam Structure	100
III.5.3	Beam Intensity	102

III.5.4	Discussion	103
III.6	Research and Development	104
III.6.1	Targeting	104
III.6.2	Multi-muon CW Capability with Advanced Detectors	105
III.6.3	Storage Rings	105
III.7	Developing a μSR community for Fermilab	105
III.7.1	General Considerations.....	105
III.7.2	The Path Forward.....	106
III.8	Conclusions.....	106
III.9	References.....	107
APPENDIX 1 – Accelerator Driven Systems		115
APPENDIX 2 – Project X Muon Spin Rotation Forum		119
APPENDIX 3 – DOE/BES Priorities in materials science.....		121

I INTRODUCTION

The proposed Project X proton accelerator at Fermilab, with multi-MW beam power and highly versatile beam formatting, will be a unique world-class facility to explore particle physics at the intensity frontier. Concurrently, however, it can also facilitate important scientific research beyond traditional particle physics and provide unprecedented opportunities in applications to problems of great national importance in the nuclear energy and security sector.

The high intensity proton beam from Project X with an optimally designed target station can serve as an experimental facility for studies of electric dipole moments of neutrons and nuclei, fusion and fission energy R&D, irradiation testing of materials, and production of certain radioactive isotopes. High power proton accelerators are also envisioned as drivers for subcritical nuclear reactor systems for the transmutation of nuclear waste and generation of electrical power; these are significant and vital applications. Project X can be used as a platform to demonstrate some of the key concepts and technologies of Accelerator Driven Systems (ADS). The high power proton beams can also be used to produce intense neutron beams or low energy muons for materials science research.

The rich and diverse research program with Project X, in particle physics and beyond, has been described in detail in Part II of this book. In this Part, we describe the broader impacts – applications in the nuclear energy sector including R&D for accelerator driven systems, nuclear physics, and materials science. We briefly outline them here.

Applications in Fusion Energy Science & Nuclear Energy

While the primary driver for the development of Project X is particle physics research, the high beam power and intensity in conjunction with a flexible target station offers the potential to address important questions in nuclear energy (irradiation testing of fast reactor structural materials, integral testing of fast reactor fuel rodlets, separate-effects testing of fission reactor fuel materials), fusion energy science (irradiation testing of fusion structural materials), and nuclear physics (cold neutrons, isotope production, nuclear electric dipole moment research).

Advanced nuclear energy systems have the potential to deliver significant improvements in sustainability, safety, reliability and proliferation-resistance relative to the conventional, Generation II nuclear power systems. National needs in Advanced Nuclear Energy Systems have been articulated in a number of recent reports. The Department of Energy's Nuclear Energy Roadmap [1] outlines the four main objectives of the Nuclear Energy R&D Program, as follows:

1. Develop technologies and other solutions that can improve the reliability, sustain the safety, and extend the life of current reactors;
2. Develop improvements in the affordability of new reactors to enable nuclear energy to help meet the Administration's energy security and climate change goals;
3. Develop sustainable nuclear fuel cycles;
4. Understand and minimize the risks of nuclear proliferation and terrorism.

An important cross-cutting technical capability which is needed to advance the goals of the program is that of materials irradiation at relevant neutron fluxes, energy spectra, and volumes.

The Fusion Energy community has emphasized as a central thrust the goal of developing the materials science and technology needed to harness fusion power. A report on research needs [2] highlights the need to “establish a fusion-relevant neutron source to enable accelerated evaluations of the effects of radiation-induced damage to materials.”

The materials science community articulated in *Basic Research Needs for Advanced Nuclear Energy Systems* [3] the fundamental challenge of understanding and controlling chemical and physical phenomena “...from femtoseconds to millennia, at temperatures to 1000°C and for radiation doses to hundreds of displacements per atom. This is a scientific challenge of enormous proportions, with broad implications in the materials science and chemistry of complex systems.”

These research needs highlight the tremendous challenges in developing materials that can withstand high temperatures and extreme radiation environments. Figure I-1 shows the operating regions in material temperature and displacement damage (measured in lattice displacements per atom) for current fission reactors and future fission and fusion reactors. Meeting the challenges of developing novel materials for these environments will require new, very intense, neutron sources as essential tools.

There is substantial interest in the U.S. and around the world in the development of accelerator-based irradiation sources. Modern high-power superconducting continuous wave linear accelerators are capable of producing prototypical conditions that simulate the steady-state operation of fission and fusion reactors at relevant neutron fluxes. The high beam power available from Project X provides neutron fluxes that rival or exceed those obtained at reactor-based irradiation sources. An optimized Target Station at Project X, driven by a MW-class beam can support Nuclear Energy initiatives in Fuel Cycle Technologies, Nuclear Reactor Technologies, and Advanced Modeling and Simulation. The materials irradiation testing capabilities of such a Target Station could enable, for example, efforts to ensure the sustainability and safety of the current fleet of reactors for lifetime extensions, development of new higher performance and safer reactor fuels and materials, development of innovative economical small reactors, development of new advanced reactor concepts such as those

using liquid metal or molten salt coolants, development of transmutation fuels for reducing legacy wastes requiring deep geologic storage.

The continuous wave (CW) proton beam from Project X will be a unique facility in the world that can provide an unprecedented experimental and demonstration facility for fission and fusion energy and nuclear physics R&D, filling an important gap in the irradiation testing needs of the U.S. and the world. Such a facility would provide a unique opportunity for cooperation between the DOE Office of Nuclear Energy and the DOE Office of Science through sharing of capital infrastructure and resources.

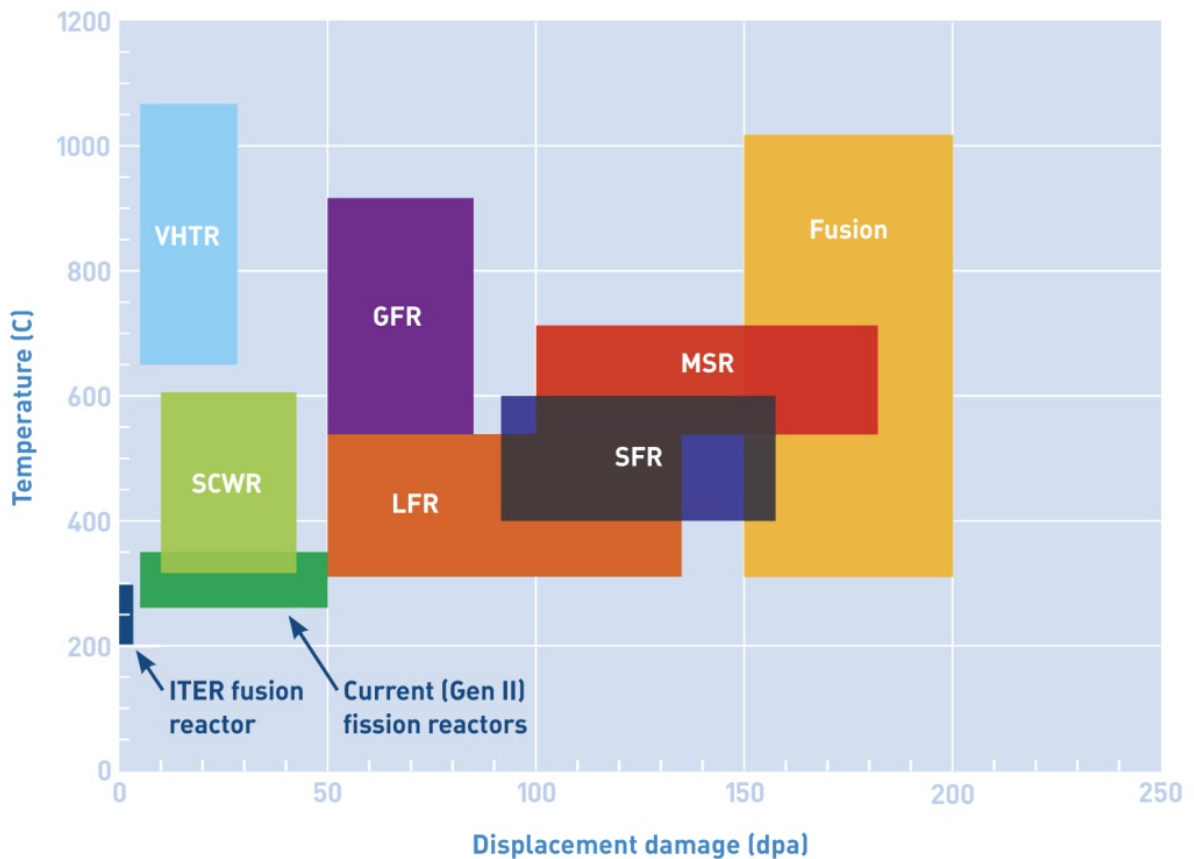


Figure I-1: Operating regions in material temperature and displacement damage, measured in lattice displacements per atom (dpa), for current fission reactors and future fission and fusion reactors. Fission reactors include very-high-temperature reactors (VHTR), supercritical water-cooled reactors (SCWR), gas-cooled fast reactors (GFR), lead-cooled fast reactors (LFR), sodium-cooled fast reactors (SFR), and molten-salt reactors (MSR). From: S.J. Zinkle, OECD/NEA Workshop on Structural Materials for Innovative Nuclear Energy Systems, Karlsruhe, Germany, June 2007.

A related technology thrust is in the development of advanced externally driven reactor systems as a means for transmutation of waste from power reactors. Such accelerator-driven system (ADS) concepts have been considered in the U.S. in the past and are under study worldwide, principally in China, Europe and India. An important topic in the Nuclear Energy Roadmap [1] is R&D in sustainable fuel cycle options, for which externally driven transmutation systems are one element. Should the priorities in the U.S. change in the future in favor of developing externally driven reactor technologies, Project X would be an ideal R&D platform for ADS.

An accelerator-driven subcritical reactor system requires a high power, highly-reliable, proton accelerator coupled to a subcritical core through a spallation target system. A technical assessment of accelerator and spallation target technology [4] was recently carried out in order to assess the readiness of the technology for ADS applications. The study concluded that the technical developments carried out over the last ~15 years place this technology at a point where it is ready to support an ADS demonstration mission. In fact, the European ADS program has reached similar conclusions and is embarking on the construction of a MW-class accelerator-driven subcritical system to principally serve an irradiation mission [5].

Project X provides an ideal test-bed for the development of ADS concepts and technologies. The MW-class continuous wave beam in the GeV-range is precisely the beam which is needed for ADS development. An optimized target station at Project X will be capable of supporting the development and demonstration of ADS and its associated technologies and concepts. ADS is discussed in more detail in Appendix -1.

Applications in Nuclear Physics

The continuous wave proton beam from Project X along with a versatile target station can provide unique opportunities for highly sensitive experiments with neutrons to test fundamental symmetries and models of physics beyond the standard model (SM) – especially valuable if new physics is discovered at the LHC. Copious quantities of cold and ultra cold neutrons and rare radioactive isotopes such as ^{225}Ra , ^{223}Rn , ^{211}Fr can be produced and used in searches for electric dipole moments (EDM) of neutrons and nuclei. EDMs, particularly the neutron and heavy atom EDMs are highly sensitive probes for sources of CP violation beyond those present in the SM.

Project X spallation facility also presents an opportunity to probe neutron-antineutron (NNbar) oscillations with free neutrons, with unprecedented sensitivities. Improvements

would be achieved by creating a unique facility, combining a dedicated high intensity cold neutron source with advanced neutron optics technology and special detectors with demonstrated capability to detect antineutron annihilation events with minimal or no background. Existing neutron sources at research reactors and spallation sources cannot provide the required space and the necessary access to the cold source that would enable set-up of a highly sensitive $\bar{n}X$ oscillation search experiment. A dedicated source devoted exclusively to fundamental neutron physics at Project X represents an exciting tool to explore fundamental nuclear and particle physics questions accessible through cold neutrons.

Applications in Materials Science

Materials Science needs have been articulated in the extensive Basic Research Needs reports which are based on a series of DOE Basic Energy Sciences (BES) workshops [3].

Project X will offer the possibility of addressing problems in materials science through the creation of a facility to exploit polarized, low-energy muons created via the decay of pions, which can be copiously produced by Project X beams. Such a facility would be unique in the U.S., and significantly increase extremely limited global capacity for the technique, known as Muon Spin Rotation (μ SR).

μ SR is a powerful probe of materials which has made important contributions to a wide range of topics of interest to a broad cross-section of the scientific community. Strongly represented in the user community are researchers studying superconductivity, quantum magnetism and chemistry, and μ SR has been successfully used to make considerable advances in these fields. Important advances have also been made in the study of semiconductors, biological and soft-matter systems, and quantum diffusion. In recent years, the advent of "ultralow energy" μ SR beams has allowed for stunning contributions in the study of thin films, multi-layers and surface science.

μ SR research facilities exist in Canada, Switzerland, the UK (ISIS/RAL) and Japan (first at KEK and now at J-PARC). There is a plan to construct a facility in South Korea (RISP). All existing facilities are over-subscribed and must reject many good proposals. There has been no capability for experiments utilizing μ SR in the United States since the closure of the LAMPF muon facility in the 1990's. Such a program utilizing the high power beams provided by Project X would be a cost-effective approach to establishing world-leading μ SR capability in the U.S., in support of the research needs of the materials science community.

References

- [1] Nuclear Energy Research and Development Roadmap Report To Congress, April 2010, US DOE: http://energy.gov/sites/prod/files/NuclearEnergy_Roadmap_Final.pdf
- [2] Research Needs for Magnetic Fusion Energy Sciences: <http://burningplasma.org/web/ReNeW/ReNeW.report.web2.pdf>
- [3] Basic Research Needs Workshop Reports: <http://science.energy.gov/bes/news-and-resources/reports/basic-research-needs/>
- [4] Accelerator and Target Technology for Accelerator Driven Transmutation and Energy Production: http://science.energy.gov/~media/hep/pdf/files/pdfs/ADS_White_Paper_final.pdf
- [5] H. Ait Abderrahim et. al., Nuclear Physics News, vol. 20, no. 1, 2010, p. 24.

II PROJECT X SPALLATION AND IRRADIATION FACILITY

D.W. Wootan, D.M. Asner, M.A. Peterson, D. Senior
Pacific Northwest National Laboratory

Prepared for the U.S. Department of Energy
under Contract DE-AC05-76RL01830

Pacific Northwest National Laboratory
Richland, Washington 99352

June 2013

Acronyms and Abbreviations

ADS	accelerator-driven subcritical systems
ANL	Argonne National Laboratory
ATR	Advanced Test Reactor
CW	continuous wave
DOE	U.S. Department of Energy
DOE-NE	U.S. Department of Energy Office of Nuclear Energy
EIS	Environmental Impact Statement
ESS	European Spallation Source
FES	Office of Fusion Energy Sciences
FFMF	Fission Fusion Materials Facility
FNAL	Fermi National Accelerator Laboratory
INL	Idaho National Laboratory
ISIS TS1	ISIS Target Station 1
JAEA	Japan Atomic Energy Agency
J-PARC	Japan Proton Accelerator Research Complex
LANL	Los Alamos National Laboratory
LANSCE	Los Alamos Neutron Science Center
LBE	liquid lead bismuth eutectic
LBNE	Long Baseline Neutrino Experiment
linac	Project X Linear Accelerator
MEGAPIE	Megawatt Pilot Experiment
MTS	Materials Test Station
ORNL	Oak Ridge National Laboratory
PIE	post-irradiation examination
PNNL	Pacific Northwest National Laboratory
PSI	Paul Scherrer Institute
PXES	Project X Energy Station
R&D	research and development

SINQ	Swiss Spallation Neutron Source
SNS	Spallation Neutron Source
TEF-T	Transmutation Experimental Facility-ADS Target Test Facility
UK	United Kingdom

II.1 Summary

Project X is a high intensity continuous wave (CW) proton beam accelerator [1] proposed to be built at Fermi National Accelerator Laboratory (FNAL) in the next decade as described in the RDR (Part I) of this book. The recent papers “Accelerator and Target Technology for Accelerator Driven Transmutation and Energy Production” [2], “Accelerators for America’s Future” [3], “Proceedings of the Workshop on Applications of High Intensity Proton Accelerators” [4], and “Fermilab Project-X Nuclear Energy Application: Accelerator, Spallation Target and Transmutation Technology Demonstration“ [5] have endorsed the idea that the next generation particle accelerators could enable technological breakthroughs for nuclear physics and fission and fusion energy applications. The MW scale CW proton beam from Project X as described in the RDR can serve a variety of functions beyond those of traditional particle physics research.

While the primary driver for development of Project X is particle physics research, the high beam power and intensity offers the potential for a flexible target station to address important questions in other fields such as nuclear energy (irradiation testing of fast reactor structural materials, integral testing of fast reactor fuel rodlets, separate-effects testing of fission reactor fuel materials), fusion energy science (irradiation testing of fusion structural materials), and nuclear physics (cold neutrons, and isotopes for nuclear electric dipole moment research). Accordingly, the Project X target station concept has been developed to evaluate the ability of this unique accelerator facility to pursue world-leading materials science and nuclear physics research.

The continuous wave (CW) proton beam from this accelerator will be a unique facility in the world and due to the CW nature of the beam it would provide a reactor-like irradiation environment that can provide an unprecedented experimental and demonstration facility for nuclear physics, fusion, and fission energy R&D that can fill an important gap in the irradiation testing needs of the U.S. and the world. Such a facility would provide a unique opportunity for cooperation by sharing resources and capital infrastructure between the DOE Office of Nuclear Energy and the DOE Office of Science.

II.1.1 Mission Support

A versatile Project X target station could support the DOE Office of Nuclear Energy missions to develop used nuclear fuel management strategies and technologies, develop sustainable fuel cycle technologies and options, and develop new and advanced reactor designs and technologies that advance the state of reactor technology to improve competitiveness and advance nuclear power as an energy resource. The materials irradiation testing capabilities of such a Target Station could enable, for example, efforts to ensure the sustainability and safety of the current fleet of reactors for lifetime extensions, development

of new higher performance and safer reactor fuels and materials, development of innovative economical small reactors, development of new advanced reactor concepts such as those using liquid metal or molten salt coolants, development of transmutation fuels for reducing legacy wastes requiring deep geologic storage, and potential investigation of neutron source driven systems as a means for transmutation of waste from power reactors. [6]

A versatile Project X target station could support DOE Office of Science Fusion Energy Science mission goal [22] of developing the scientific understanding required to design and deploy the materials needed to support a burning plasma environment, a key step in the research and development of practical fusion energy applications. “The pursuit of fusion energy embraces the challenge of bringing the energy-producing power of a star to earth for the benefit of mankind. This pursuit is one of the most challenging programs of scientific research and development that has ever been undertaken.” The promise is an energy system whose fuel is nearly inexhaustible and results in modest radioactivity and zero carbon emissions to the atmosphere. There is currently no facility available anywhere in the world that can provide fusion-relevant neutron flux and material radiation damage rates in a reasonable volume [7].

A flexible, integrated Project X target station could also support the Office of Nuclear Physics in the DOE Office of Science mission to develop a roadmap of matter that will help unlock the secrets of how the universe is put together. The Project X Target Station will enable a new generation of symmetry-testing experiments with the goal of advancing the understanding of basic nuclear physics phenomena that support fundamental searches for physics beyond the Standard Model. The MW scale CW proton beam from Project X can produce copious quantities of cold neutrons (CN), very cold neutrons (VCN) and ultra-cold neutrons (UCN), as well as special short-lived Ra, Fr, and Rn isotopes that can be utilized in sensitive searches for physics beyond the Standard Model [8]. Examples of potential experimental facilities that could be integrated into the Target Station include searches for neutron-antineutron oscillations ($\bar{N}N$) and nuclear electric dipole moments (EDMs). A permanent EDM violates both time reversal symmetry and parity. The existence of an EDM can provide the “missing link” for explaining why the universe contains more matter than antimatter [9].

A possible additional application of the Project X target station could support one of the missions of the Office of Nuclear Physics in the DOE Office of Science – to develop and produce radioactive isotopes. The Project X program could produce isotopes only where there is no U.S. private sector capability or production capacity is insufficient to meet U.S. needs. It is not envisioned that the Target Station would be used in a production mode, with the associated schedule, separations, and yield issues, but rather in a mode to facilitate production of research quantities of unique isotopes that cannot be obtained without the very

high neutron energy spectrum or high power proton beam, on a schedule consistent with normal Project X accelerator operations [9].

The Project X Target Station can provide a test bed for accelerator physics and accelerator technology by addressing accelerator target issues such as:

- Beam-Target Interface
- Radiation damage/transmutation reaction impurities
- Remote Handling
- Liquid metal target components
- Solid/rotating metal target components

Materials selected for accelerator targets, diagnostics, structures, and mechanical systems are typically based on limited data from fission reactors and the fusion community. There is potential for a much different response in a high power accelerator due to high flux of high energy particles. The Target Station could allow irradiation testing in environments more prototypical of accelerator targets.

Table II-1 summarizes the capabilities of the Project X Target Station to support the various DOE programs in the Office of Nuclear Energy, and the Office of Science.

	Fission Reactor Materials (SFR, LFR, HTGR, LWR, MSR)	Fusion Materials	Nuclear Physics Isotopes	Cold Neutrons VCN, UCN
Office of Nuclear Energy <ul style="list-style-type: none"> • Fuel Cycle Technologies <ul style="list-style-type: none"> ○ Used Fuel Disposition R&D ○ Fuel Cycle R&D • Advanced Modeling & Simulation • Nuclear Reactor Technologies <ul style="list-style-type: none"> ○ LWR Sustainability Program ○ Advanced Reactor Technologies ○ Small Modular Reactors ○ Space Power Systems 	x			
Office of Science <ul style="list-style-type: none"> • Nuclear Physics <ul style="list-style-type: none"> ○ Low Energy Nuclear Physics Research ○ Theoretical Nuclear Physics Research ○ Isotope Development and Production for Research and Applications 	x		x	x
Office of Science <ul style="list-style-type: none"> • Fusion Energy Science <ul style="list-style-type: none"> ○ Fusion Materials and Technology 	x	X		

Table II-1: Summary of Programs Benefiting from Project X Target Station

II.1.2 Target Station Options

The basic concept that is proposed for the Project X target station is one beam line of about 1 MW power directed either horizontally or vertically to a liquid lead, liquid lead-bismuth, or solid tungsten spallation target. The proposed Project X Target Station accelerator beam parameters are 0.91 MW beam power, 1 mA beam current, and 1 GeV beam energy. The Project X Stage 1 beam timing for the 1 GeV beam incorporates a 60 msec beam-off period every 1.2 seconds, resulting in a 95% duty factor for the otherwise continuous wave (CW) beam, as described in Appendix-I of the RDR. Two options for the Target Station are being considered, one is an Energy Station focused on DOE Nuclear Energy missions and Fusion Energy Science materials irradiation testing, and the second is an Integrated Target Station that combines the materials testing mission with Nuclear Physics experiments such as ultra-cold neutrons for NNbar and neutron-EDM experiments and production of unique isotopes for atomic-EDM experiments. Various configurations of liquid and solid spallation targets and surrounding irradiation testing configurations are being evaluated. The spallation target produces copious neutrons with an energy spectrum similar to a liquid metal cooled fast reactor. Neutrons produced in the spallation region escape into the surrounding solid lead matrix region cooled by helium gas, liquid water, liquid sodium, liquid lead, or lead-bismuth. This matrix region contains several modules for various types of experiments such as fusion materials irradiation testing, fission reactor materials irradiation, production of nuclear physics isotopes for atomic-EDM searches, or production of cold neutrons for NNbar and n-EDM nuclear physics experiments. Each module contains independent cooling loops and materials that produce appropriate nuclear environments.

The neutron spectrum in these different modules could be tailored to the requirements by using moderating or filtering materials. Preliminary investigations indicate that fairly large volumes (~600 liters) of high neutron flux ($>10^{14}$ n/cm²/sec) can be created that rival or surpass the limited test volumes available in existing high power test reactors. Multiple test modules are envisioned in the target region, surrounding the spallation target, each with an independent test region and coolant loop. Each test module could be designed to be removed and reinstalled independently of the others. Vacuum insulation layers can be used to isolate modules with extreme temperature variations from the matrix region. These reconstitutable modules provide tremendous flexibility in designing tests to meet evolving needs. Extensive instrumentation and temperature control are also key attributes that can be used to provide a testing environment tailored to particular program needs.

Since the moderator and cooling regions of UCN sources utilize only a fraction of the spallation neutrons produced in the target, this capability could be included as one of the Project X Target Station irradiation modules and still allow several other fast spectrum test modules. Relative priorities of research needs could determine the makeup and configuration of test modules.

One advantage of an accelerator based system, for an experiment, over a reactor is the proximity of the instrumentation to the experiment. This makes gas handling and other aspects of instrumented tests a lot easier to design and operate. This also allows real-time measurement capabilities (e.g. direct pressure measurement) that can't be done when the experiment is 33 meters or more away from the instrumentation.

The CW beam produces a high neutron flux and the high duty factor provides a neutron irradiation capability to accumulate fluence comparable to large research reactors, but with the volume and flexibility to tailor the neutron spectrum, temperature, coolant, and structural materials to match a wide variety of both thermal and fast spectrum reactor types. Except for the Swiss Spallation Neutron Source (SINQ) cyclotron accelerator at PSI, the other existing neutron spallation facilities are pulsed systems. They are all designed for producing neutron beams, such as for scattering studies, and not necessarily for materials irradiation. The Los Alamos Neutron Science Center (LANSCE at LANL) and Spallation Neutron Source (SNS at ORNL) facilities are comparable in power to the proposed Target Station, but have pulse frequencies of 20 or 60 Hz, lower duty factors, and are not designed with the flexibility for tailored irradiation testing that is envisioned for the Project X-driven Target Station [11].

All of the other planned neutron spallation facilities are pulsed systems, except for perhaps the Indian ADS system, compared to the continuous wave Target Station beam. The Japan Proton Accelerator Research Complex (J-PARC) and Indian systems are planned to be oriented to ADS R&D and would have subcritical fuel regions surrounding the spallation target. The SNS second target station and the European Spallation Source (ESS) are planned to be mainly neutron beam facilities, but could be used for limited materials irradiation [11]. The spallation target station in Project X offers an opportunity to leverage and benefit from the design efforts over the years on the proposed Materials Test Station (MTS) at LANL [8].

Because existing cold neutron beamlines, such as SNS and LANSCE were designed for generic neutron scattering, there was no opportunity to optimize the target moderator for nuclear/particle physics research, or to establish a dedicated ultra-cold neutron source. The Spallation target in Project X provides a unique possibility to optimize the performance of the target for the sensitivity needed by each experiment.

II.2 Introduction

Fermilab is developing a design of a High Intensity Proton Accelerator complex, known as Project X, to support future Particle Physics Programs at the Intensity Frontier. Fermilab's accelerator research and development (R&D) program is focused on the superconducting radio-frequency technologies for the proposed Project X. Pacific Northwest National Laboratory (PNNL) and Argonne National Laboratory (ANL), two U.S. Department of

Energy (DOE) National Laboratories with experience in Nuclear Energy, are supporting Fermilab by focusing on developing and evaluating the concept of a high-intensity continuous wave proton beam target station for nuclear physics, fusion energy, and fission energy applications. PNNL developed a report on the Project X Energy Station [15] that explored the potential opportunities related to supporting DOE Nuclear Energy R&D.

That report was the impetus for the Project X Energy Station Workshop in January 2013 [12]. The objective of the workshop was to identify and explore the nuclear relevant R&D that would be possible in a Nuclear Energy Station associated with the Project X Accelerator and identify the design requirements for conducting the research. Previous workshops have focused on the nuclear and particle physics research associated with Project X [8]. Participants in this workshop were U.S. researchers working on accelerator-based applications, nuclear and material science, applications of high-intensity proton beams and targets, advanced nuclear reactor concepts, advanced nuclear fuel cycles, light-water reactor sustainability, enhanced and accident tolerant fuels, and isotope production. The workshop identified the synergy and benefits that the Project X could bring to the nuclear research community.

The U.S. Nuclear Energy mission will always require the use of test reactors, but one should investigate whether an Integrated Target Station associated with Project X could accelerate and enhance the ability to test and evaluate early research concepts for nuclear physics, fusion energy science, and nuclear energy. In the following section (section II.3), we describe the nuclear environment and testing needs for the nuclear energy, fusion energy science, and nuclear physics R&D missions. Section II.4 describes the options for configuring the Project X Target Station, and how it might meet the mission needs. Section II.5 provides the conclusions.

II.3 Mission Needs

II.3.1 Conclusions from Project X Energy Station Workshop

The Project X Energy Station Workshop provided a good forum for bringing together ideas, issues, and expertise from the accelerator, particle physics, and nuclear energy communities. The participants developed a better understanding of the nuclear materials testing needs and how those needs can be satisfied in a Project X target facility [12].

In particular, the Workshop identified unique mission priorities that a Project X Target Station could provide:

- Fusion structural materials irradiation
- Fast reactor structural materials irradiation
- Fast reactor fuels integral effects testing

- Fuels in-situ separate effects testing

High-value mission needs were identified that could take advantage of the unique characteristics of the Project X beam to conduct research of interest to DOE-NE. The guiding principles behind identification of the mission needs included the following:

- Does the Project X beam provide unique conditions of interest to the materials and fuels community?
- What niche materials and fuels applications are enabled by the Project X beam conditions?
- What materials and fuels applications are complementary to (not duplicative of) existing reactor- and accelerator-based irradiation facilities (with an emphasis on domestic capabilities)?

The Energy Station Workshop identified the highest priority mission needs relevant to the target station, in rough order of priority [12]:

- Fusion reactor structural materials – there is no facility available anywhere in the world that can provide fusion-relevant neutron flux and achieve a minimum of 20 displacements per atom (dpa) per calendar year in a reasonable irradiation volume.
- Fast reactor structural materials – there are limited numbers of fast reactors internationally, and none in the United States. Therefore, the Project X Target Station would be very valuable for study of these materials as is for fusion reactor materials. The fast spectrum and high dpa rates provided by the Target Station would be a significant improvement over thermal reactor irradiations, with tailored flux which can achieve close to the right spectrum, but at relatively low dpa rates. In addition to materials relevant to conventional fast reactors, there are newer fast reactor concepts (e.g., the TerraPower traveling wave reactor) to be tested that require ultra-high doses to simulate very long service lifetimes (e.g., 400+ dpa in cladding alloys).
- In-situ, real-time measurements of various separate-effects phenomena in fuels or materials (e.g., microstructural evolution, pellet-clad chemical interactions, fission gas release) – Such in-situ measurements are, in principle, more feasible in an accelerator-based system than in a reactor, and they are very valuable for modelers, but sensor technology will require concurrent development. In-situ measurements are relevant for fusion materials and fast reactor fuels and materials, and could be useful for thermal reactor fuels and materials as well, because of the difficulty of obtaining such information in test reactors. Separate-effects investigations of this type would likely require encapsulated fuel pellet samples.
- Integral effects testing of fast reactor fuels, including driver fuel, minor actinide burning fuel, and transmutation of spent fuel: These tests would provide valuable information regarding fuels for many of the same reasons described above for fast

reactor materials. Integral effects would likely require rodlet-scale testing.

A possible additional application of the Project X Target Station is production of unique research isotopes that cannot be obtained without the very high neutron energy spectrum. Examples include ^{32}Si and ^{225}Ac . It is not envisioned that the Target Station would be used in a production mode, with the associated schedule, separations, and yield issues, but rather in a mode to facilitate production of research quantities of isotopes on a schedule consistent with normal Project X accelerator operations.

A variety of other potential materials- and fuels-related areas of study were discussed that did not seem to offer such compelling cases for use of the Project X Target Station when considered in the context of existing reactor- and accelerator-based facilities. Some of the areas discussed in this category included irradiation of thermal reactor materials and fuels (with the one exception mentioned above), neutron- or synchrotron-based materials science, high-energy neutron cross-section measurement, and transient testing. In addition, the question of direct irradiation in the proton beam was considered. In general, the difficulties of relating proton to neutron irradiation, particularly at high neutron energies that cannot be benchmarked by comparison with reactor data, seem to outweigh the potential advantages of reaching high dpa rates by directly using the proton beam for irradiation. Additional difficulties include very high and non-prototypic He generation rates and H implantation.

There is a range of sample sizes for structural materials of interest, from very small (millimeter-scale) to relatively large (maybe 10 cm) that should be accommodated in the irradiation facility. The smaller end of the size range is appropriate for fundamental studies of irradiation damage mechanisms, while the larger end of the range is appropriate for bulk samples needed for engineering property measurements. Thus, the irradiation volume must be designed to accommodate the full range, i.e., there must be areas with relatively uniform (and high) flux over centimeter-scale dimensions. Also, the irradiation facility should include some replaceable large modules, as well as fixed, perhaps smaller, irradiation positions to accommodate specimens for long-term irradiations to achieve high dose (200+ dpa).

For both materials and fuels irradiation testing, active temperature control of test specimens during irradiation is an absolute requirement. While relatively straightforward during steady-state operation, the issue of beam trips and downtime (both planned and unplanned) must be addressed. These transients exist on both short time scales (beam trips and downtime during normal operation) and longer time scales (planned and unplanned extended outages). Some of these events could have consequences for irradiation damage mechanisms (e.g., cascade annealing, atomic diffusion, phase transformations), particularly for samples located in the highest-flux regions in the vicinity of the proton beam and spallation target. Farther away from the target, the short time scale events are likely to be smeared out and less

consequential. Extended temperature transients can introduce significant uncertainty in irradiation data interpretation. Therefore, there needs to be specifications related to temperature control during off-normal events. It was suggested that perhaps SNS or the International Fusion Materials Irradiation Facility offer a potential model for some of the specifications associated with beam trips and down time.

The issue of beam availability is a significant one for materials or fuels irradiation testing. For materials, maximizing the dose rate per calendar year is desirable, while for fuels maximizing the irradiation time per calendar year is desirable. For both, higher availability is desirable. Project X Target Station availability of 70% is probably needed to provide the desired dose and fission rates.

Implications of the high-energy tail resulting from spallation will require further consideration, but there are potentially positive as well as negative implications. For fusion materials, the high energy tail offers the potential to achieve a variety of dose and He generation rates, which could significantly enhance the understanding of irradiation damage mechanisms and effects in a regime that has received very little attention (due to lack of fusion-relevant neutron sources with high dose rates). For fission reactor materials, on the other hand, the high-energy tail could be problematic due to non-prototypical high He generation and, possibly, transmutation rates. Ultimately, the impact of the high energy tail for both fusion and fast reactor materials will need to be assessed on an alloy-by-alloy basis.

In general, it appears that the Project X Target Station will need to accommodate at least rodlet- sized fuel pins to be useful to the fuels community for evaluating fast reactor fuels. There also was consensus that it does not make sense to consider equipping Project X Target Station to perform post- irradiation examination (PIE) on fuels or materials because existing infrastructure and capabilities are maintained already in the DOE complex at great cost. However, at a minimum, the Project X Target Station facility will have to have the capability to handle irradiated materials (and potentially fuels) and properly package those samples for shipment to other DOE sites for PIE. This is a non-trivial capability that needs to be considered carefully. In addition, it is highly desirable for the facility to have the capability to receive, as well as ship, irradiated materials and fuels. For example, it would be beneficial to irradiate previously irradiated materials to reduce the time necessary to reach high dose. Similarly, for research on spent fuel transmutation, the facility must be able to receive previously irradiated and properly packaged spent fuel.

Another capability that must exist, either in-house at FNAL or cooperatively arranged with other DOE labs (e.g., INL, PNNL, ORNL), is experiment and module design expertise. Even if existing capabilities are utilized at the DOE laboratories, FNAL will require safety analysis and design review expertise to evaluate experiment and module designs submitted by users. In addition, FNAL will need to evaluate bounding safety cases for experiment and module

design. As an example, FFTF and Experimental Breeder Reactor II both had user's guides that outlined all the requirements that experiments had to meet to be accepted by the reactor facility. FNAL may want to consider development of such a user's guide for the target station. Finally, it is strongly recommended that FNAL involve safety, security, environment, and quality assurance organizations early in development of the target station design to identify and resolve issues while they are still manageable.

The neutron flux and spectrum will need to be benchmarked (e.g., with flux wires or equivalent) soon after the facility becomes operational to facilitate accurate neutronics modeling for subsequent experiments.

II.3.2 Nuclear Energy Requirements

A versatile Project X target station could support the DOE Office of Nuclear Energy missions. The DOE Office of Nuclear Energy Research and Development Roadmap, April 2010 [6] listed four main research and development objectives:

- Develop technologies and other solutions that can improve the reliability, sustain the safety, and extend the life of current reactors;
- Develop improvements in the affordability of new reactors to enable nuclear energy to help meet the Administration's energy security and climate change goals;
- Develop sustainable nuclear fuel cycles;
- Understanding and minimization of risks of nuclear proliferation and terrorism.

In order to meet each of these four objectives, the DOE NE roadmap focuses on:

- Aging phenomenon and degradation of system structures and components such as reactor core internals and reactor pressure vessels, as well as fuel reliability and safety performance issues, develop and test advanced monitoring and NDE technologies, improve materials data such as composite cladding;
- Fundamental nuclear phenomena and development of advanced fuels and materials to improve the economics and safety of advanced reactors such as corrosion resistant materials, radiation resistant alloys for fast spectrum concepts;
- Development of a suite of sustainable fuel cycle options that improve uranium resource utilization, maximize energy generation, minimize waste generation, improve safety, and limit proliferation risk, down-selecting fuels for once-through fuel cycles, modified open fuel cycles, and closed fuel cycles;
- Development of the tools and approaches for understanding, limiting, and managing proliferation risks, such as options that enable decreasing the attractiveness and accessibility of used fuel and intermediate materials, and transmuting materials of potential concern.

The main Nuclear Energy initiatives that have R&D needs that could benefit from the Project X Target Station are Fuel Cycle Technologies, Nuclear Reactor Technologies, and Advanced Modeling and Simulation. Table II-2 lists the major focus areas under these initiatives that could benefit from the Project X Target Station [6]. Table II-3 lists the various neutronic environments needed for irradiation testing to support the different fission reactor concepts.

Initiative	Focus Areas	Testing Needs
Fuel Cycle Technologies	Used Fuel Disposition R&D Fuel Cycle R&D	Structural material properties as a function of dpa and temperature Small scale tests to provide proof or validation of system elements
Advanced Modeling & Simulation	Nuclear Fuels Advanced Nuclear Reactors	Experimental data to validate state-of-the-art computer modeling and simulation of reactor systems and components
Nuclear Reactor Technologies	LWR Sustainability Program Advanced Reactor Technologies Small Modular Reactors Space Power Systems	Basic physics Material research and testing Integral tests of fuel, structural materials Feature tests of components Fuel performance with minor actinides

Table II-2: Summary of DOE Nuclear Energy Initiatives that Could Benefit from the Project X Target Station

Parameter	LWR	SFR	LFR	MSR	HTGR
Temperature range (°C)	~300	~550	500-800	700-800	600-850
Max damage rate (dpa)	50-100	100-200	100-200	100-200	5-30
Max helium conc (appm)	~0.1	~40	~40	~3	~3
Max Neutron Energy (MeV)	<1-2	<1-3	<1-3	<1-2	<1-2
Coolant	water	sodium	lead or lead-bismuth eutectic	Molten salt	Helium

Table II-3: Summary of Nuclear Energy Fission Reactor Testing Environments

The Fuel Cycle Research and Development (FCRD) program conducts long term science based R&D for fuel cycle technologies. This includes 1) developing technologies to improve the sustainability of current reactors, 2) developing improvements in affordability of new small modular reactors and high temperature reactors through improved structural materials and fuels, 3) Developing sustainable nuclear fuel cycles, and 4) minimizing proliferation risks.

Fuel Cycle Research and Development Areas include structural materials, nuclear fuels, reactor systems, instrumentation and controls, power conversion systems, process heat transport systems, dry heat rejection, separations processes, waste forms, risk assessment methods, computational modeling and simulation, and small scale tests to provide proof or validation of system elements. Three variations of fuel cycles are being investigated, Once-through, Modified open, and Full recycling (transmutation).

The FCRD program is developing transmutation fuel technologies to reduce the quantity of high level nuclear waste for deep geologic disposal. Plutonium and minor actinides such as neptunium and americium are included in the fuel matrix where they are burned along with the other fuel isotopes in fast spectrum reactors.

These transmutation fuels cannot be qualified for use until candidate fuels have been irradiated and tested in a prototypic environment. Gaining access to fast spectrum irradiation testing facilities is very difficult, since there are only a few facilities in Asia that can do this type of testing.

A key challenge facing the nuclear fuel cycle is reducing the radiotoxicity and lifetime of spent nuclear fuel. Partitioning or sorting of nuclear waste isotopes and accelerator-based transmutation combined with geological disposal can lead to an acceptable societal solution to the problem of managing spent nuclear fuel. Accelerators can also drive next-generation reactors that burn non-fissile fuel, such as thorium, that can be burned with the use of particle beams. Both or either of these approaches could lead to an increase in power generation through greenhouse gas emission-free nuclear energy and could provide a long-term strategy for the growth of nuclear power in the U.S. (See Appendix—1 for more details on this topic.)

The following considerations apply to irradiation testing capability to support DOE NE reactor and fuel cycle R&D programs:

- Stable, well characterized test spaces
- Capable of testing fuels and materials from coupon size up to assembly sizes (~100 liters)
- Neutron environment characteristic of both thermal and fast spectrum nuclear reactors
- Fuel pin coolant environments of water, sodium, lead, gas, molten salt
- Flexibility of fuels to be tested – homogeneous/heterogeneous, LEU, Pu/Th bearing

- Instrumentation capable of characterizing fuel, clad coolant temperatures from ambient up to 300 to 1000°C
- Neutron flux range of up to 5×10^{15} n/cm²/s
- Damage rates that range from a few dpa up to 50 dpa per year
- Associated post irradiation examination or shipping capabilities

Next-generation reactors, whether based on any of these technologies, require materials that are much more radiation resistant than those used in today's reactors. Next generation reactor materials will also have to survive in the high temperature, potentially reactive environments. Accelerators can spur the development of these next-generation materials by producing radiation environments similar to those found in future reactors, providing a platform for materials development that does not currently exist.

II.3.3 Fusion Energy Science Requirements

A versatile Project X target station could support DOE Office of Science Fusion Energy Science mission goal [22] of developing the scientific understanding required to design and deploy the materials needed to support a burning plasma environment, a key step in the research and development of practical fusion energy applications. “The pursuit of fusion energy embraces the challenge of bringing the energy-producing power of a star to earth for the benefit of mankind. This pursuit is one of the most challenging programs of scientific research and development that has ever been undertaken.” The promise is an energy system whose fuel is nearly inexhaustible and results in modest radioactivity and zero carbon emissions to the atmosphere. There is currently no facility available anywhere in the world that can provide fusion- relevant neutron flux and material radiation damage rates in a reasonable volume [7].

The Office of Fusion Energy Science has four strategic goals [22]:

- Advance the fundamental science of magnetically confined plasmas to develop the predictive capability needed for a sustainable fusion energy source;
- Pursue scientific opportunities and grand challenges in high energy density plasma science to explore the feasibility of the inertial confinement approach as a fusion energy source, to better understand our universe, and to enhance national security and economic competitiveness;
- Support the development of the scientific understanding required to design and deploy the materials needed to support a burning plasma environment; and
- Increase the fundamental understanding of basic plasma science, including both burning plasma and low temperature plasma science and engineering, to enhance economic competitiveness and to create opportunities for a broader range of science

based applications.

To support goal number 3 above, a fusion materials irradiation capability is needed to address critical gaps in irradiation capability needed to qualify materials for future science missions. Materials development and performance is a long-standing feasibility issue and is a critical factor in realizing the environmental and safety potential of fusion. Many materials related details in burning fusion plasma facilities are needed to provide high confidence in their design. The conditions of radiation damage, thermal heat flux, and high energy particle bombardment are the most extreme that exist on earth. Nuclear fission reactors and ion beam irradiation facilities can be used to make incremental, at best, scientific progress, since those facilities lack the volume, flux, and spectral characteristics to perform experiments on materials and subcomponents in a simulated fusion environment. A test platform capable of isothermal irradiation effects testing with neutron flux equivalent to the first wall of a DT fusion power reactor. “Mature technologies for a fusion-relevant neutron source include proton beam/high-Z target spallation sources like SNS, MTS, Project X, and D+-Li stripping sources like IFMIF. Viable facility options that meet the mission needs described above include US participation in IFMIF, MTS, and Project X.” [7]

Specific requirements include [7]:

- >0.4 liter high-flux volume for irradiation testing with equivalent 14 MeV neutron flux $>10^{14}$ n/cm²/s
- 20 dpa/year so that degradation from volumetric swelling, irradiation creep, phase instabilities, helium embrittlement, and solid transmutation can be observed in a reasonable time
- Medium and low flux irradiation volumes to test subcomponent assemblies and partially integrated experiments exposed to temperature, mechanical loads, and corrosive media
- >70% availability to provide exposures >100 MW-year/m² in a few years
- Relevant temperature ranges controlled to within 5%
- Flux gradients <20% per cm to provide consistent exposures over the volume

Success in these efforts will spread beyond fusion needs into a broad range of capabilities in material nanostructure, predictive behavior, and custom engineered material properties. Tailoring materials at the microstructural level might allow mitigation of neutron degradation properties while maintaining high performance macroscopic properties and margins of safety. This materials irradiation capability combined with an associated modeling program could improve the confidence in predicting how a particular material will perform under the conditions it is exposed to as well as designing new materials to optimize performance for specific locations. The materials knowledge base developed could be applicable for many harsh-environment applications.

The DOE fusion program is part of an international effort to develop magnetically confined nuclear fusion reactors such as the International Thermonuclear Experimental Reactor (ITER) under development in France by an international consortium, and subsequent demonstration and commercial power plants. Materials must be developed that can survive the fusion environment. Low activation materials are required to allow maintenance. There is a parallel program developing inertial fusion concepts. Materials surrounding the fusion ignition region must also survive in a demanding environment.

Technology gaps for fusion reactor research and development requiring materials qualification include:

- Plasma facing components
- Low activation materials
- Solid breeder materials
- Safety

Both low activation structural materials and tritium-producing blanket materials are being developed for fusion applications. Structural material properties are needed as a function of dpa and temperature with a cumulative ~ 150 - 200 dpa and a temperature range of 550 - 1000 °C. Prototypic neutron energies are predominantly at 14 MeV. Maximum helium and hydrogen concentrations are ~ 1500 appm and ~ 6750 appm.

First wall and structural materials in a future fusion power plant will be exposed to a 14 MeV neutron flux which cannot be created in a test reactor. The design, licensing, and safe operation of a fusion reactor will require materials to be qualified in a neutron source that simulates fusion-relevant neutron spectra and temperatures. An accelerator is the only way to generate a neutron flux environment that approaches fusion reactor first-wall conditions.

A neutron source for the qualification of fusion reactor materials should meet the following criteria:

- Neutron spectrum with neutrons up to the energies corresponding to the first wall/blanket conditions in a future fusion reactor
- Continuous mode operation with high availability
- 20 - 50 dpa/fpy in high flux region allowing accelerated testing
- Irradiation volume on the order of 0.5 - 1 liter in the high flux region

The fusion program at the ITER facility plans to test at least seven blanket types in test blanket modules

- Helium-cooled Lithium-Lead blanket
- Dual-Coolant (He and LiPb) type Lithium-Lead (DFLL and DCLL) blankets

- Dual-Coolant (He and LiPb) Lithium-Lead Ceramic Breeder (LLCB) blanket
- Helium-cooled Ceramic/Beryllium blanket
- Water-cooled Ceramic/Beryllium blanket

A fusion materials irradiation testing capability for the Project X Test Station could be used for testing each of these materials under prototypic conditions.

II.3.4 Nuclear Physics Requirements

A *Forum on Spallation Sources for Particle Physics* was held at FNAL in March, 2012 [8]. Much of the discussion of Nuclear Physics requirements and projections of how the Project X Target Station could support Nuclear Physics was extracted from the materials presented at that forum. A versatile Project X Target Station could support the Office of Nuclear Physics in the DOE Office of Science mission to develop a roadmap of matter that will help unlock the secrets of how the universe is put together. The Project X Target Station could enable a new generation of symmetry-testing experiments with the goal of advancing the understanding of basic nuclear physics phenomena that support fundamental searches for physics beyond the Standard Model. Examples of potential experimental facilities that could be integrated into the Target Station include searches for neutron- antineutron oscillations (NNbar) and nuclear electric dipole moments (EDMs). The MW scale CW proton beam from Project X can produce copious quantities of cold neutrons (CN), very cold neutrons (VCN) and ultra-cold neutrons (UCN), as well as special short-lived Ra, Fr, and Rn isotopes (^{219}Rn , ^{223}Rn , ^{211}Fr , ^{221}Fr , ^{223}Fr , ^{223}Ra , ^{225}Ra , $^{225-229}\text{Ac}$) to support fundamental searches for physics beyond the Standard Model. These particular radon, francium, and radium isotopes have favorable nuclear and atomic properties for enhanced EDM searches, and the Project X target station could potentially supply these isotopes in abundance. For example, the projected EDM of ^{225}Ra is 1000 times larger than the EDM of mercury. The potential electron EDM of Francium is greatly enhanced due to relativistic effects. A permanent EDM violates both time reversal symmetry and parity. “The existence of an EDM can provide the “missing link” for explaining why the universe contains more matter than antimatter.”

Ultra-Cold Neutrons

Ultra-cold neutrons have the following properties:

- Can be stored in material bottles for hundreds of seconds and piped around corners
- Typical velocities 0-8 m/s (0-350 neV) ($kT < 4$ mK)
- Wavelengths > 50 nm
- 100% polarizable with magnetic fields
- Lifetime < 1000 seconds

Primary spallation neutrons are too fast to be useful for most nuclear physics applications, such as a NNbar search or nEDM search. Creation of ultra-cold neutrons (UCN) would involve moderation to thermal energies with a moderator such as heavy water, cooling to very cold neutrons (VCN) using cryogenic material such as solid methane, and then to UCN temperatures using liquid helium. Radiative heating of moderator and heat removal are design challenges. Optimization of moderator configuration is needed to provide maximum yield of cold neutrons, which can then be enhanced for VCN and UCN production. Channeling of the VCN-UCN to the NNbarX detector system might utilize high-m super reflectors and graphite. Table II-4 lists UCN projects operating or under construction around the world.

Source	Type	Ec(neV)	UCN/cm ³	Status	Purpose
LANL	Spallation/D2	180	35	operating	UCNA/Users
ILL	Reactor/turbine	250	40	operating	n-EDM/users
Pulstar	Reactor/D2	335	120	construction	Users
PSI	Spallation/D2	250	1,000	construction	n-EDM
TRIUMF	Spallation/HE-II	210	10,000	planning	n-EDM/users
Munich	Reactor/D2	250	10,000	R&D	gravity
SNS	N beam/HE-II	130	400	R&D	n-EDM

Table II-4: World's UCN Projects [8]

The Project X Target Station accelerator will have relatively low heating compared to reactors, and should have a favorable duty cycle (>70%). UCN production will likely be limited by energy deposition in the moderator. The ratio of UCN flux to volumetric heating improves at larger distances from the spallation target, but at the expense of cold neutron flux to source power.

UCN can be produced using a D₂O moderator tank, thermal radiation shields to maintain temperatures of ~4K, and a cold source such as liquid H₂, liquid ⁴He, solid D₂, or solid CH₄ to get temperatures ~0.8K. CH₄ is the brightest known cold neutron moderator but is not usable at high power sources due to radiation damage. Other reflectors, such as high albedo materials like diamond nanoparticles might be used as radiation-hard reflectors near the moderator to improve cold/VCN brightness [13]. Multilayer mirrors might also improve UCN populations provided to experiments.

An example of an existing ultra-cold neutron source is at the SINQ facility, shown in Figure II-1. In the SINQ UCN source, spallation neutrons are produced inside a cannelloni-style target (lead inside Zircaloy tubes, 21 cm diameter and 55 cm long) and then thermalized in an

ambient-temperature heavy-water moderator. The thermalized neutrons are further down-scattered in a 10-liter volume of solid D_2 (50 cm diameter, 15 cm thick) cooled to 5K. UCN escape from the D_2 volume into a storage tank, from which they pass through guides to experimental areas. [8]

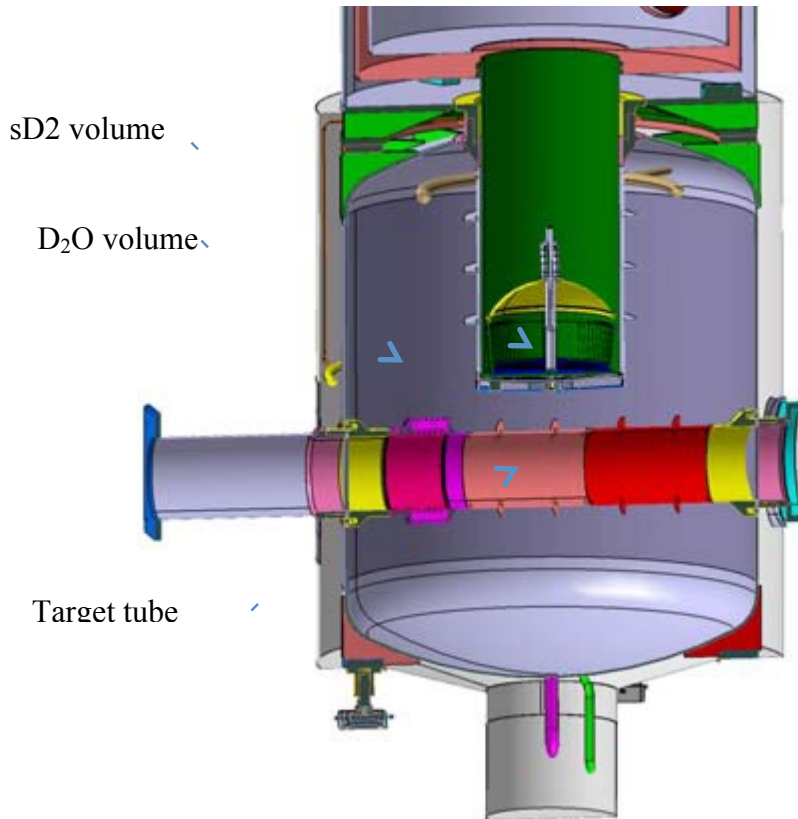


Figure II-1: SINQ Spallation UCN Source

LANL has developed concepts for producing UCN in LANSCE involving two tungsten spallation targets with 40L He /H₂ in between or a cylindrical proton target with the beam rastered around the circumference with UCN moderator material (potential pre-moderators of heavy water or beryllium to reduce heating) in the center, all imbedded in a bismuth (300K) matrix [8].

Neutron-Antineutron Oscillation (NNbar) Search

The idea for a NNbar oscillation search (described in Part 2) is to 1) observe a sample of neutrons in a vacuum in the absence of a magnetic field for as long as possible, 2) observe as many neutrons as possible, 3) detect the neutron-antineutron transition by the annihilation reaction, and 4) measure the probability of appearance or set a limit. A capability for searching for neutron-antineutron transitions could be new physics for Project X with little competition. There is a strong experimental motivation for developing this capability since

there is a possibility of increasing the detection probability by a factor of >100 with minimal background. There is a strong theoretical motivation in that new theories of neutrino mass, low-scale quantum gravity, low scale baryogenesis models, etc., accommodate neutron-antineutron transition probabilities that could be testable by a new experiment. The spallation target in Project X is a unique possibility to optimize the performance of the target for the sensitivity needed by a single experiment. Optimization was not possible before due to constraints (construction and regulational) at reactors or to having multi-user facilities at SNS, PSI, etc. A previous \bar{n} search was conducted at ILL in 1989-1991 [14]. Improvements that might be possible with the Project X spallation source include [8]:

- Larger number of neutrons
- Lower neutron velocities, larger time (VCN, UCN)
- Larger source to target flight distance
- Use more of the 4π geometry
- Use diffusive reflection for fast neutrons
- Use super-mirror reflectors
- Use neutron focusing ellipsoidal mirrors
- Use gravity for neutron manipulation

The primary issue for a \bar{n} search using the Project X target station is optimizing the source/transport geometry to provide a robust source of UCN and to transport those UCN to a detector. The SINQ design for a UCN source is an example of a spallation system oriented towards UCN production.

Neutron Electric Dipole Moment (n-EDM)

Recent NSAC Review Priorities stated that n-EDM research is the highest priority for neutron science [8]:

“The successful completion of a n-EDM experiment, the initiative with the highest scientific priority in US neutron science, would represent an impressive scientific and technical achievement for all of nuclear physics, with ramifications well beyond the field”.

Table II-5 describes some of the n-EDM experiments around the world. A next generation n-EDM experiment (described in Part 2) that focuses on an integrated design of source and detector could make large gains in UCN density (e.g. 10^4 - $10^5/\text{cm}^3$). The lower end of this range overlaps with the TRIUMF goal of $10^4/\text{cm}^3$. While the goal of n-EDM at SNS is to be statistics limited, follow-on studies at Project X could exploit the statistically limited techniques developed at SNS [8].

Experiment	UCN Density	Description
Sussex-RAL-ILL (past experiment)	0.7 UCN/cm ³	Room temperature, in vacuo, $d_n < 3 \times 10^{-26}$ e-cm
Sussex-RAL-ILL CryoEDM	1000 UCN/cm ³	Superfluid 4He
SNS	430 UCN/cm ³	Superfluid 4He
PSI	1000 UCN/cm ³	In vacuo
TRIUMF	10,000-50,000 UCN/cm ³	

Table II-5: Past and Future n-EDM Efforts [8]

Atomic Electric Dipole Moment (EDM)

The search for static electric dipole moments in atoms and electrons (EDM) (described in Part 2) could be flagship experiments to search for physics beyond the Standard Model. The search for EDMs requires high yields of radioactive isotopes of Rn, Fr, and Ra. Project X could extend yields of such isotopes by factors of 100-10000 over existing facilities. Project X will enable a new generation of symmetry-testing experiments and bring exciting opportunities for discovering physics beyond the Standard Model. An EDM search probes energy scales beyond the LHC. The existence of an EDM can possibly help explain the mystery of matter dominance in the universe [8].

Parameters of existing ISOL spallation targets (CERN/ISOLDE, TRIUMF/ISAC, Oak Ridge HRIBF, Legnaro INFN/SPES) can be extrapolated to much higher beam power at the 1 GeV Project X Target Station. Issues to address include [8]:

- Effusion delays from large target chamber.
- Thermal conductivities and temperature limits of refractory thorium compounds, ThC₂, ThO₂, ThN.
- Thermal simulations coupling beam power deposition with thermal conduction, radiation, and stress effects.
- Operating temperatures ~2000°C to release isotopes

II.3.5 Nuclear Physics Isotopes Requirements

A possible additional application of the Project X Target Station could be support to the Office of Nuclear Physics in the DOE Office of Science mission to develop and produce radioactive isotope products. The program produces isotopes only where there is no U.S. private sector capability or other production capacity is insufficient to meet U.S. needs. It is not proposed that the Target Station would be used in a production mode, with the associated

schedule, separations, and yield issues, but rather in a mode to facilitate production of research quantities of unique isotopes that cannot be obtained without the very high neutron energy spectrum or high power proton beam on a schedule consistent with normal Project X accelerator operations.

There are limited isotope production capabilities in the US. Two examples of isotopes are ^{238}Pu and medical/industrial isotopes. For ^{238}Pu production, there is no current domestic source for NASA to use as a power supply for deep space missions. DOE has identified some potential for production in HIFR and ATR, and completed some preliminary tests, but has not initiated that option. In the past, this isotope was purchased from Russia, but this source is no longer available. Medical/industrial isotopes are produced in limited amounts from ATR, HFIR, University reactors, and cyclotrons to meet current needs. Examples of potential research radioisotopes identified in the Project X Energy Station Workshop include ^{32}Si and ^{225}Ac [12]. Whether or not production of research quantities of particular isotopes using the Project X Target Station direct 1 GeV proton beam or spectrally tailored neutron flux regions should be pursued will depend on case-by-case evaluations of product quantity, purity, detrimental reactions, expense, etc.

II.3.6 Common Issues in Materials Irradiation Testing

Materials are an immediate priority for both the fission and fusion communities. Extending the lifetime of the current fleet of light water reactors depends on understanding how the materials fail as they age. New generations of power reactors may operate at higher temperatures. New fuel types may be able to burn more efficiently, thereby extending the time between outages and extracting more energy from the fuel, thereby extending our energy resources. Fuel burnup in reactors is limited to about 20% primarily because the cladding mechanical integrity is reduced by radiation damage and elevated temperature. For fast reactor and fusion applications, helium accumulation from (n, α) reactions causes embrittlement. Table II-6 lists some common materials issues for fission, fusion, and accelerator spallation facilities.

Materials Compatibility Issues	Materials properties issues	Integrated performance issues
<ul style="list-style-type: none"> • Coolant • Cladding • Target • Moderator • Transmutation products • Decomposition products • Thermal and Irradiation Stability Issues • Target material swelling • Cladding swelling • Moderator swelling • Target spalling • Irradiation damage effects • Chemical stability • Phase stability 	<ul style="list-style-type: none"> • Thermal conductivity • Heat capacity • Melting point • Emissivity • High temperature strength • Creep behavior • Thermal expansion • Vapor pressure 	<ul style="list-style-type: none"> • Effects of fission or transmutation product buildup • Stoichiometry changes during irradiation • Gas release • Thermal performance • Target material restructuring • Power-to-Melt behavior • Changes in properties with burnup • Fabricability • Target burn efficiency

Table II-6: Common Materials Issues for Fission, Fusion, and Spallation R&D

II.4 Target Station

II.4.1 Target Station Concept

The concept for the Project X Target Station is a beam line of 1 MW power directed to a 10-cm diameter liquid lead or lead-bismuth spallation target. The spallation target produces copious neutrons at fusion- and fission-relevant energies. Neutrons produced in the spallation region escape into the surrounding target region, which contains several test modules with independent coolant loops. These test modules could be interchangeable, allowing the facility to accommodate multiple users. The neutron spectra in the test modules could be tailored by using moderating or filtering assemblies, as necessary. Preliminary calculations indicate that large volumes are available (~600 liters with neutron flux $>1 \times 10^{14}$ n/cm²/sec) that rival or surpass the limited test volumes in existing high power test reactors. Further, unlike fission reactors, the Project X Target Station provides significant high-energy neutron flux at positions within and near the spallation target to achieve high dose rates (20-40 dpa per 365 operating days at 1 MW beam power) with fusion-relevant He generation rates. The highest dose rates would be associated with sample volumes on the order of a few liters.

Figure II-2 shows a cross-sectional schematic depiction of the initial notional concept of how the Project X Target Station could be configured. Figure II-3 shows potential configurations and representative neutron spectra of the independent test modules. More details can be found in the workshop presentation materials [12] (select the presenter for each day to access the presentation) and in the PNNL whitepaper [15]. The proton beam from the Project X accelerator is extracted at a proton beam energy of 1 GeV and a beam current of 1 mA, for a total beam power of 1 MW. This beam is directed on a spallation target to produce neutrons. For these initial studies, the proton beam is assumed to be spread uniformly over the target diameter, because the exact mechanism of spreading the beam (such as rastering or defocusing) has not been determined.

The proton beam directed on the heavy metal liquid spallation target creates fairly large volumes of neutron flux that rival or surpass the limited test volumes available in existing test reactors. The initial concept for the spallation target is a 10-cm diameter flowing liquid lead bismuth eutectic (LBE) target that produces approximately 30 neutrons per proton. The 1 GeV protons penetrate approximately 50 cm into the LBE target. The melting point of LBE is $\sim 126^{\circ}\text{C}$, so a 200°C inlet temperature, 300°C outlet temperature, and maximum of 2 m/s flow velocity (based on erosion and corrosion concerns) appear reasonable. The optimum target diameter is one that provides adequate heat removal while maximizing the neutron flux. Smaller diameters produce higher neutron flux levels close to the target, but the beam power is deposited over a smaller volume. For example, reducing the target diameter from 10 cm to 5 cm increases the peak neutron flux from 0.6×10^{15} to 1×10^{15} n/cm²/sec. A similar LBE spallation target technology was demonstrated in the Megawatt Pilot Experiment (MEGAPIE) in 2006 [16]. The neutrons produced in the spallation reaction have an energy spectrum similar to a fission spectrum, but with a high energy tail extending to the beam energy. Use of a solid spallation target, such as tungsten, has also been considered, and this results in a higher peak flux but shorter axial extent. This accelerator beam and spallation target arrangement could be developed in either a vertical or a horizontal layout. A horizontal layout is shown in Figure II-2, which offers benefits for the accelerator design, because it would eliminate the need for a 90-degree bend in the beam.

Two options for the Target Station are being considered, one is an Energy Station focused on DOE Nuclear Energy missions and Fusion Energy Science materials irradiation testing, and the second is an Integrated Target Station that combines the materials testing mission with Nuclear Physics experiments such as ultra-cold neutrons for NNbarX and EDM isotopes. Various configurations of liquid and solid spallation targets are being evaluated. The spallation target produces copious neutrons with an energy spectrum similar to a liquid metal cooled fast reactor. Neutrons produced in the spallation region escape into the surrounding solid lead matrix region, which is can be cooled by helium gas, liquid water, liquid sodium, liquid lead, or lead-bismuth. This matrix region contains several modules for various types of experiments such as fusion materials irradiation testing, fission reactor materials

irradiation, production of nuclear physics isotopes for EDM searches, or production of cold neutrons for NNbar nuclear physics experiments. Each module contains independent cooling loops and materials that produce appropriate nuclear environments.

The neutron spectrum in these different modules could be tailored to produce different spectra by using moderating or filtering materials. Preliminary investigations indicate that fairly large volumes (~600 liters of high neutron flux ($>10^{14}$ n/cm²/sec) can be created that rival or surpass the limited test volumes available in existing high power test reactors. Multiple test modules are envisioned in the target region, surrounding the spallation target, each with an independent test region and coolant loop. Each test module could be designed to be removed and reinstalled independently of the others. Vacuum insulation layers can be used to isolate modules with extreme temperature variations from the matrix region. These reconstitutable modules provide tremendous flexibility in designing tests to meet evolving needs. Extensive instrumentation and temperature control are also key attributes that can be used to provide a testing environment tailored to particular program needs.

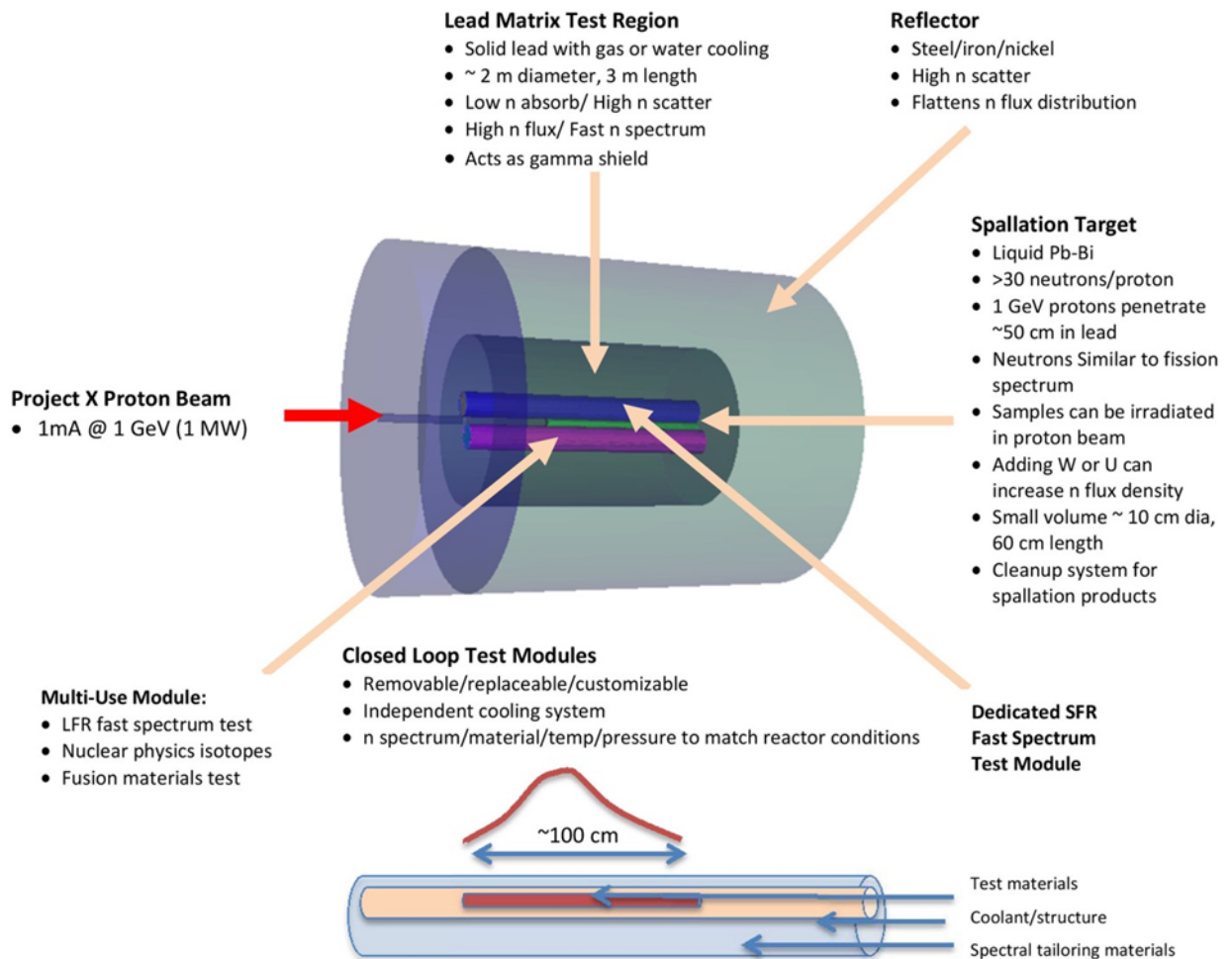
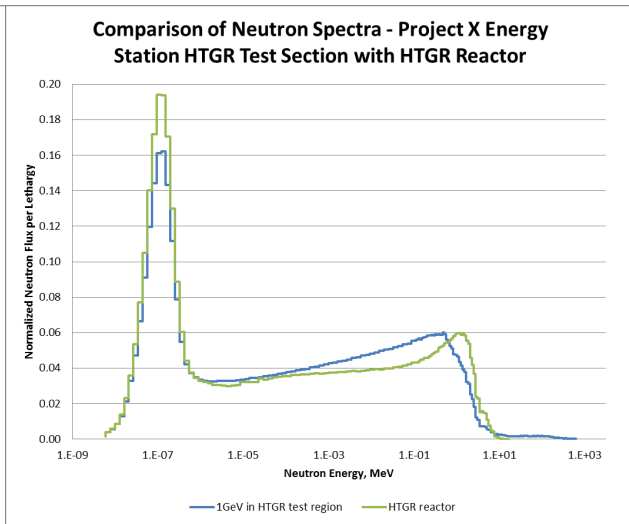
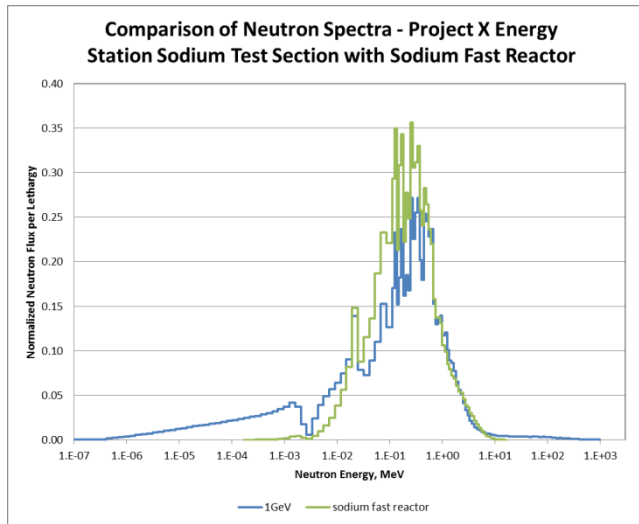
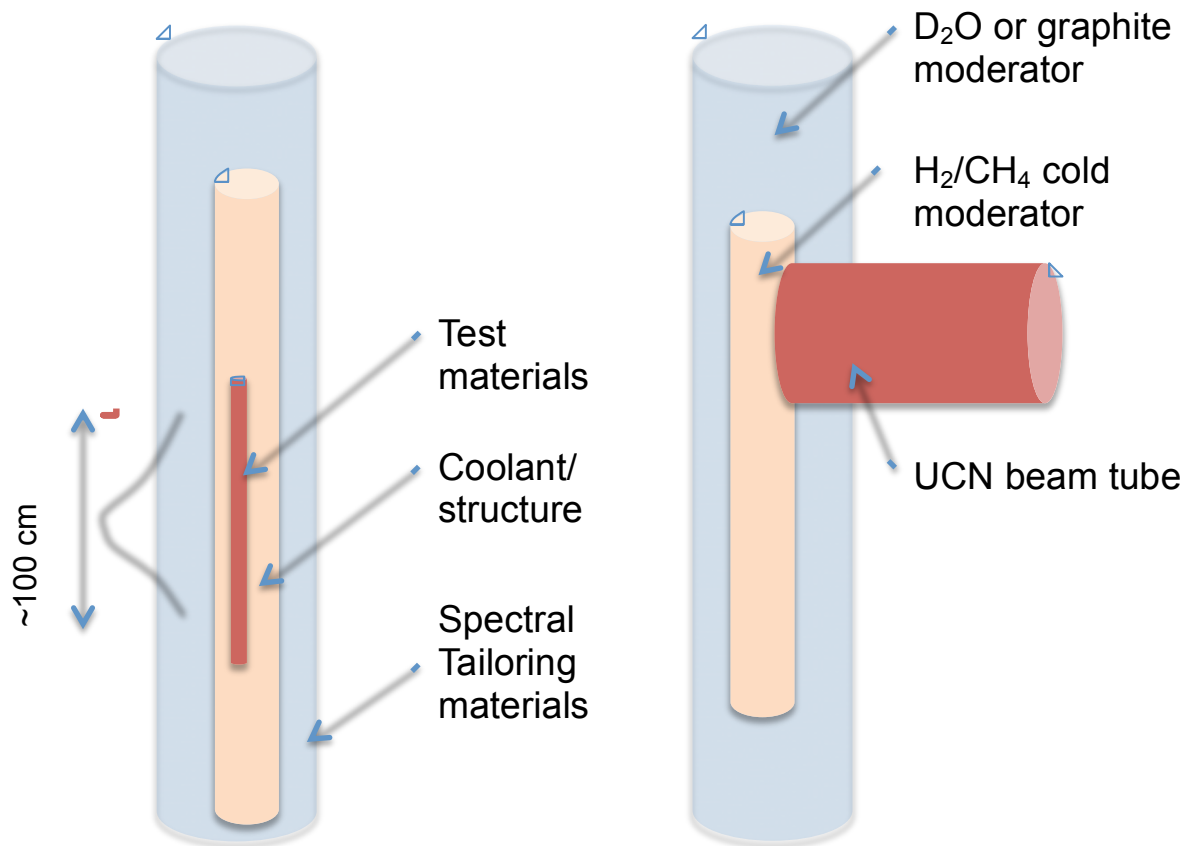


Figure II-2: Target Station Concept



Simplified Materials Testing Module

Simplified UCN Module

Figure II-3: Simplified Target Station Test Modules and representative neutron spectra for proposed Project X test modules (blue traces) and SFR and HTGR reactors (green traces).

The spallation target is surrounded by a high-scatter, low-absorption test matrix that reduces the radial leakage of neutrons from the system. A solid lead matrix 200 cm in diameter and 300 cm long, with the surface of the spallation target recessed 100 cm from the front matrix surface was used in the reference case. The heat deposited in the matrix can be removed by air or gas coolant channels, or water around the periphery. This matrix has holes to provide space for test loops and other fixed irradiation spaces. The distribution of neutron flux in the test matrix is shown in Figure II-4. Simulations of the neutron and proton tracks in the spallation target and lead matrix are shown in Figure II-5. The lead can be seen to be an effective neutron scatter material and the protons are nearly all confined to the flowing lead spallation target region. Volumes at various neutron flux levels are shown in Table II-7. The region with a neutron flux greater than 1×10^{14} n/cm²/s extends axially over 100 cm, allowing long samples to be irradiated. Peak dpa rates in iron range up to 20 dpa/year. Other materials considered for the test matrix included Zircalloy, which has better strength at high temperatures compared to lead, but is not as effective at scattering, resulting in lower neutron flux levels.

The various closed-loop test modules are arranged in the test matrix around the spallation target. The number of test modules can be varied depending on demand. The target station could start with one module, and then additional modules could be added as needed. Figure II-6 shows some potential configurations for the Project X Target Station. Options considered include liquid or solid spallation targets and inclusion of D₂O or graphite moderator regions to generate UCN. The option of including target capsules directly in the proton beam have also been considered, which might be useful for thorium carbide targets for generating EDM isotopes. The native neutron spectrum in the target matrix is similar to that in a lead fast reactor, so little modification of the spectrum would be needed to test that environment. Modules for testing other fast reactor environments, such as sodium fast reactors or gas fast reactors, would require minimal tailoring of the neutron spectrum. Thermal reactor environments, such as pressurized water reactors, boiling water reactors, graphite reactors, or molten salt reactors could also be reproduced, if needed, in a module of less than 30-cm diameter. Modules can be tailored for a variety of environments, such as fusion reactor materials testing, isotope production, or cold neutrons for physics tests. The size of these modules will depend on the amount of room required to reproduce specific reactor operating conditions of temperatures, pressures, materials, and neutron spectrum. The optimum distance of the module from the spallation source depends on the combination of neutron spectrum, dpa rates, and He and H generation rates desired. These modules could be arranged in a vertical or horizontal arrangement around a horizontal beam spallation target. Multiple test modules are envisioned, each with an independent test region and coolant loop. Each test module can be removed and reinstalled independently of the others. These reconstitutable assemblies can provide tremendous flexibility in designing tests that

meet client needs, which will evolve over time. Extensive instrumentation and temperature control are also key attributes that can be used to provide a testing environment tailored to particular program needs. Effects of any differences in neutron spectra between those simulated by flux tailoring in the Target Station modules and the individual reactor concepts can be evaluated through comparable materials irradiations and interpretation of the results. Closed-loop modules have been utilized in test reactors such as the Fast Flux Test Facility (sodium), BOR-60 (sodium, lead), and ATR (pressurized water).

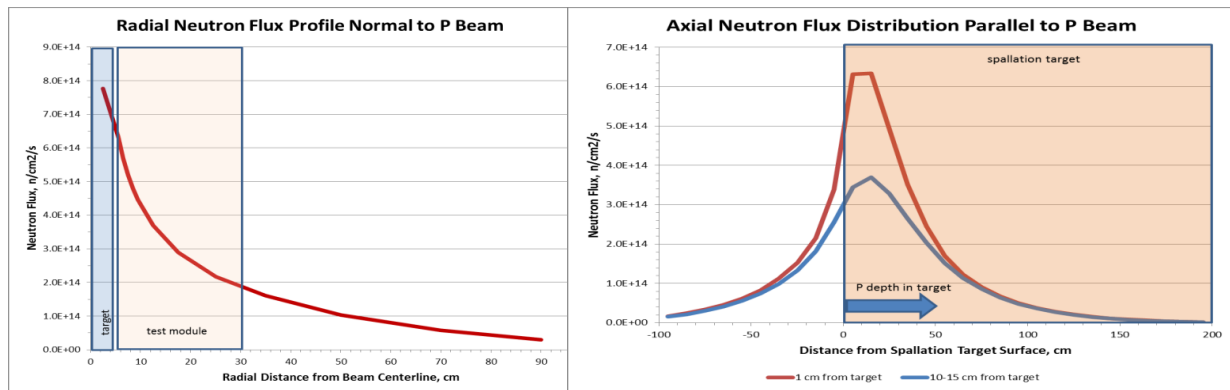
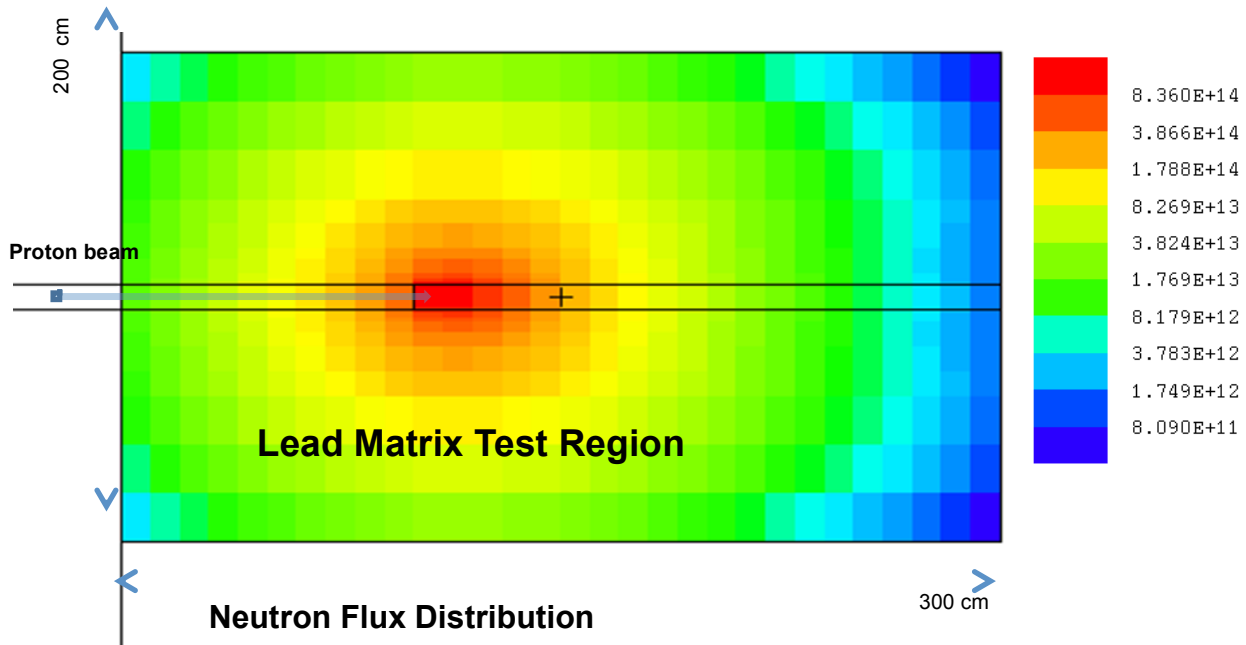


Figure II-4: Neutron Flux Distribution in Lead Matrix Test Regions

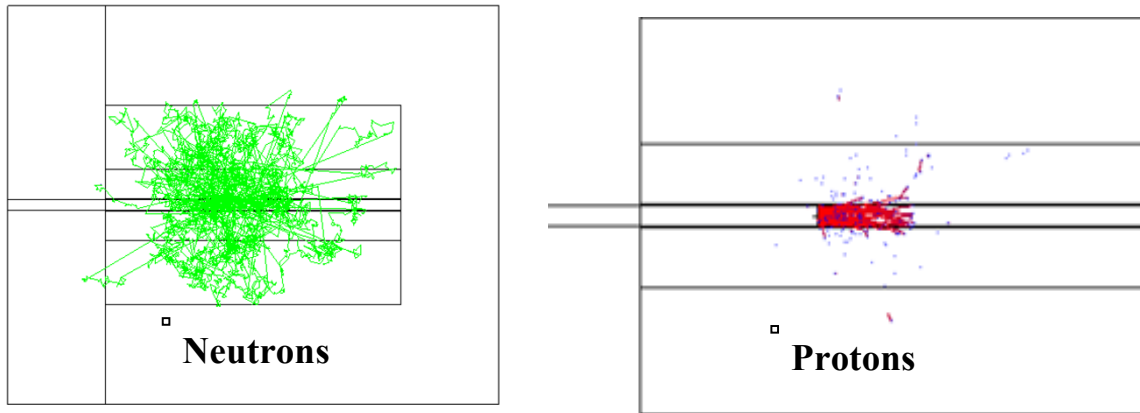


Figure II-5: Neutron and Proton Tracks from 1 GeV protons in Spallation Target

Neutron Flux Range (n/cm ² /s)	Axial Extent (cm)	Outer Extent (cm)	Volume (liters)
>5e14	30	8	~2.8
>3e14	50	15	~23
>1e14	110	60	~600
>5e13	160	80	~2000
>1e13	250	100	~9000

Table II-7: Neutron Flux Volumes in Lead Matrix Test Region

Figure II-6 shows some of the potential options for configurations that provide different environments, including combining the irradiation testing and nuclear physics missions.

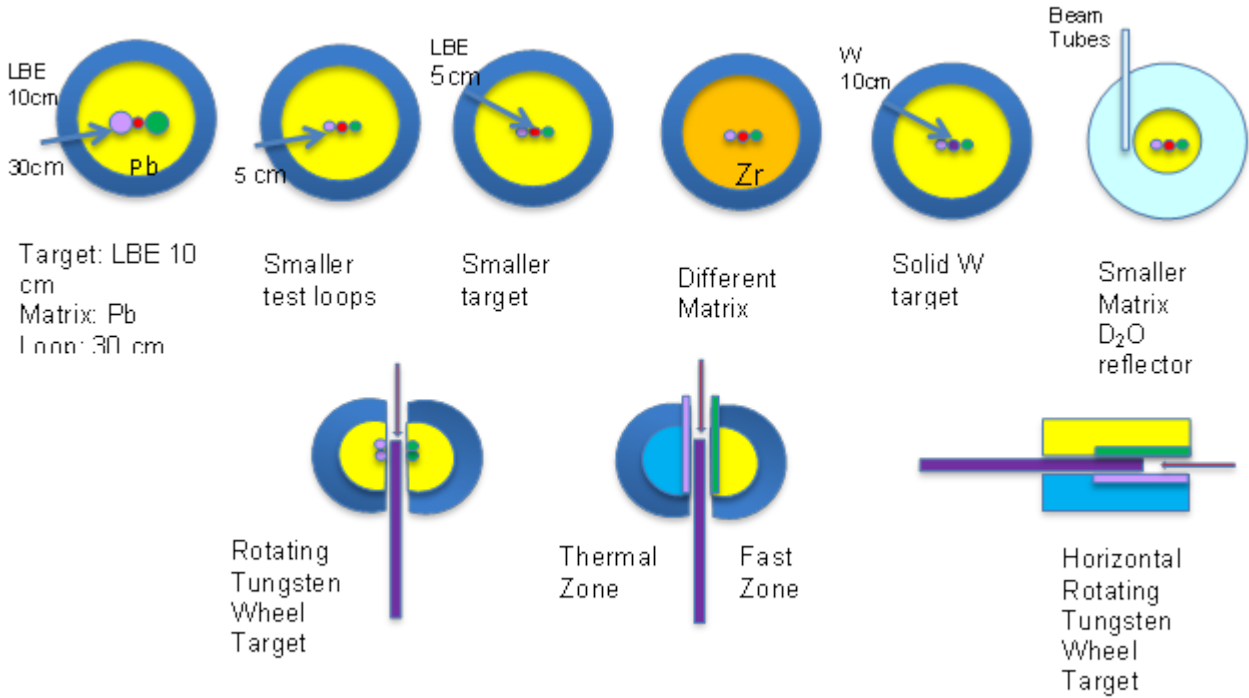


Figure II-6: Options for Configuring Project X Target Station

II.4.2 Existing and Planned Spallation Neutron Source Facilities

Table II-8 compares the Project X Target Station concept with existing proton-induced spallation neutron source facilities. The proposed Target Station accelerator beam parameters used in the current studies are a continuous wave proton beam of 1 MW beam power, 1 mA beam current, and 1 GeV beam energy. The RDR parameters for the 1 GeV Project X beam are 0.91 MW beam power, 1 mA beam current, and 1 GeV beam energy. The Project X Stage 1 beam timing for the 1 GeV beam incorporates a 60 msec beam-off period every 1.2 seconds, resulting in a 95% duty factor for the otherwise continuous wave (CW) beam. This CW beam produces a high neutron flux and the high duty factor provides a neutron irradiation capability to accumulate fluence comparable to large research reactors, but with the volume and flexibility to tailor the neutron spectrum, temperature, coolant, and structural materials to match a wide variety of both thermal and fast spectrum reactor types. Except for the Swiss Spallation Neutron Source (SNS) cyclotron accelerator, the existing neutron spallation facilities are pulsed systems. They are all designed for producing neutron beams, primarily for scattering studies, and not optimized for materials irradiation. The Los Alamos Neutron Science Center (LANSCE) and Spallation Neutron Source (SNS) facilities are comparable in power to the proposed Target Station, but have pulse frequencies of 20 or 60 Hz, lower duty factors, and are not designed with the flexibility for tailored irradiation testing that is envisioned for the Project X-driven Target Station.

	Project X Target Station	LANSC E Lujan – LANL ^(a)	SNS – ORNL ^(b)	SINQ MEGAPI E – PSI ^(c)	SINQ Solid Target – PSI ^(d)	ISIS TS1 – UK ^(e)
Initial Operation	~2021	1972	2006	2006	1996	1984
Target	LBE	W	Hg	LBE	Pb/Zr	W
Beam Current, mA	1 (0.91)	1.25	1.4	1.25	2.3	0.2
Beam Energy, GeV	1	0.8	1	0.59	0.59	0.8
Beam Power, MW	1 (0.91)	1	1.4	0.8	1.2	0.16
Beam Frequency, Hz	CW, 40 MHz	20	60	CW	CW	50
Pulse Length, μ s		0.25	0.7			0.1
Duty Factor, %	>50		6			2.5
Neutron Flux, $n/cm^2/s$ (vol, liters)	6e14 peak >3e14 (23L) >1e14 (600L)	beam	beam	beam	beam	beam
(a) Los Alamos Neutron Science Center–Lujan – Los Alamos National Laboratory (b) Spallation Neutron Source – Oak Ridge National Laboratory (c) Swiss Spallation Neutron Source, Megawatt Pilot Experiment – Paul Scherrer Institute (d) Swiss Spallation Neutron Source, Solid Target – Paul Scherrer Institute (e) ISIS Target Station 1 – United Kingdom						

Table II-8: Comparison of the Target Station with Existing Spallation Sources (Source: http://pasi.org.uk/Target_WP1)

Table II-9 compares the Project X Target Station concept with proposed or planned proton spallation accelerator neutron source facilities. All of the other planned neutron spallation facilities are pulsed systems, except for perhaps the Indian ADS system, compared to the continuous wave Target Station beam. The Japan Proton Accelerator Research Complex (J-PARC) and Indian systems are planned to be oriented to ADS R&D and would have subcritical fuel regions surrounding the spallation target. The SNS second target station and the European Spallation Source (ESS) are planned to be mainly neutron beam facilities, but could be used for limited materials irradiation. The spallation target station in Project X offers an opportunity to leverage and benefit from the design efforts over the years on the proposed Materials Test Station (MTS) at LANL [8].

	Project X Target Station	MTS/FFMF ^(a) – LANL	SNS Long Pulse – ORNL	J-PARC TEF-T ^(b) – JAEA ^(c)	ESS - Sweden	ADS – India
Initial Operation	~2021	Not Scheduled	?	?	~2018	?
Target	LBE	W (dual) LBE cooled	W/Ta or Hg	LBE	W He cooled	Pb, LBE, W
Beam Current, mA	1 (0.91)	1.25	1.15	0.4	50	10-30
Beam Energy, GeV	1	0.8	1.3	0.6	2.5	1
Beam Power, MW	1 (0.91)	1	1.5	0.2	5	10-30
Beam Frequency, Hz	CW, 40 MHz	120	20	25-50	14	CW
Pulse Length, μ s		1000	1000	500	2860	
Duty Factor, %	>50	7.5		1.25	5	
Neutron Flux, n/cm ² /s (vol, liters)	6e14 peak >3e14 (23L) >1e14 (600L)	1.6e15 (0.2 L) 40 fuel rodlets; 0.45 L materials	beam	ADS	2.2e15(0.4 L) target 1.2e15 (5L) reflector	ADS
(a) Fission Fusion Materials Facility						
(b) Transmutation Experimental Facility-ADS Target Test Facility						
(c) Japan Atomic Energy Agency						

Table II-9: Comparison of Target Station with Proposed/Planned Spallation Sources
(Source: http://pasi.org.uk/Target_WP1)

Because existing cold neutron beamlines, such as SNS and LANSCE were designed for generic neutron scattering, there was no opportunity to optimize the target moderator for nuclear/particle physics research, or to establish a dedicated ultra-cold neutron source. The Spallation target in Project X is a unique possibility to optimize the performance of the target for the sensitivity needed by each experiment.

II.4.3 Assumptions of Project X Operations

The Target Station could be structured as a National User Facility (NUSF) similar to what has been done at ATR. This would maximize collaboration between DOE, Universities, industry, and even allow foreign participation. Potential users would propose tests that would be evaluated by a committee. Utilization would also be open to international testing.

The use of reconstitutable assemblies lessens testing costs, providing for a potentially broader utilization, especially by universities. The facility could grow to become a unique and valuable University educational resource for teaching as well as research.

MW scale CW proton beams can serve a variety of functions beyond those of traditional particle physics research. It is assumed that the Project X Target Station can be operated as a joint facility to simultaneously support experimental research and development in the following areas:

- Office of Science - nuclear physics ultra-cold neutrons (NNbar and n-EDM) for standard model tests
- Office of Science – ISOL nuclei (isotopes for atomic EDM studies standard model tests),
- Office of Science - research isotopes
- Office of Science – fusion energy science materials irradiation testing
- Office of Nuclear Energy – fission energy applications

Copious production of special short-lived isotopes could be generated to support fundamental searches for physics beyond the Standard Model.

11.4.4 Target Station Capabilities & Challenges

There was consensus at the Project X Energy Station Workshop at Fermilab that combining the particle/nuclear physics mission with the nuclear energy mission into a single target station would be preferable to having two separate target stations competing for proton beam current (assuming each mission receives approximately half of the available current).

Both liquid and solid targets in various configurations were discussed at the workshop and are continuing to be explored. The concept of the Target Station, some potential configurations and the surrounding lead matrix region that would contain multiple modules for experiments have been discussed earlier in Section 11.4.1. The modules will host various types of experiments such as materials irradiation testing, neutron or nuclear EDM searches; and each module will have independent cooling loops and materials to produce appropriate environment needed by specific experiments.

The envisioned Target Station capabilities include:

- Flexible design allowing support to multiple missions for NE, NP, FES
- Benefits of test reactor volumes and neutron fluxes without reactor issues – licensing, fuel supply, safety, waste
- Robust technology and design that allows evolution to tomorrow's technology
- Continuous wave, high availability, high beam current provides potential for

irradiation tests to high fluence

- Energy distribution of spallation neutrons similar to fast reactor fission spectrum but with high energy tail up to proton energy
- Ability to tailor neutron spectrum from fast to thermal as well as the gamma to neutron flux ratio
- H and He generation in materials higher than in reactor allowing accelerated aging testing
- Potential for research isotope production and/or neutron beams simultaneous with irradiation test

Engineering Challenges

One of the primary engineering challenges with the Target Station design is providing for continuous operations with remote change out of test modules. For multiple test modules or closed loops, it would be preferable to be able to change out one module with minimal effects on other modules. Continuation of cooling/heating for separate modules while one module is replaced is a design goal. The approach is to provide separate cooling of the lead matrix surrounding the test modules and vacuum insulation to enable independent temperature environments in each module. The shielding design will need to be robust enough to account for radiation streaming when one module is removed, necessitating a remote change-out capability. A lead shield plug may be required to be inserted at the same time as a module is removed.

Another important engineering challenge is to accommodate concurrent multi-mission capabilities with much different environments, ranging from cryogenic moderators for ultra-cold neutrons, fission and fusion neutron energies, heavy water, liquid metals, and temperatures up to 1000°C conditions. Interaction of these various environments will need to be carefully considered in the configuration of the integrated Test Station.

Use of Proton Beam for Material Damage Studies

Researchers have long studied the use of charged particle irradiation as a supplement or surrogate for neutron irradiation. As far back as the 1960s, heavy ion irradiation experiments were conducted to achieve high damage levels (dpa) in a short amount of time in support of fast reactor structural materials development [17]. More recent work has included investigating irradiation damage mechanisms for fusion reactor first wall and structural materials [18], irradiation assisted stress corrosion cracking in light water reactor cladding materials, and embrittlement of reactor pressure vessel steels [20]. Other researchers have used neutron irradiation to simulate charged particle damage as a way of assessing the performance of materials intended for use in space, including semiconductor materials used for solar cells. [19]

The principal challenge of translating charged particle irradiation to neutron irradiation is addressed by identifying the appropriate temperature offset such that the microstructural feature of interest produced by irradiation is comparable. In general, this means ensuring a comparable irradiation-induced interstitial-to-vacancy annihilation rate between neutron and charged particle irradiation. With a proton beam of 1-3 MeV, such microstructural equivalency has been demonstrated in stainless steels, pressure vessel steels, and Zr-base alloys with a 50 to 100°C shift in temperature (higher temperature for proton irradiation versus neutron irradiation) [20].

There is potential to use the 1 GeV proton beam from the Project X accelerator directly for fission or fusion reactor materials irradiation testing in the Target Station spallation target or the beam dump. Such an approach would more efficiently use the proton beam than conversion to neutrons via spallation. It would also provide more volume for test specimens and experiment hardware, and reduce shielding requirements.

While structural materials are typically irradiated in a test reactor, the use of charged particle irradiation does offer some advantages beyond those listed above. Very high damage rates (dpa/s) are possible with a proton beam, typically a factor of 100 to 1000 higher than fission neutrons. This allows relatively short irradiation times to achieve high damage levels. Short irradiation times also translate to relatively inexpensive irradiation experiments compared to test reactors. Protons do not penetrate materials as deeply as neutrons, due to electronic energy loss during scattering, so irradiation of bulk samples for mechanical or thermal property testing is probably not feasible. However, protons penetrate deeply enough such that sufficient interaction volume is available to assess fundamental scientific questions associated with irradiation damage mechanisms and microstructural evolution. For example, a 30 MeV proton beam will penetrate on the order of a millimeter into stainless steel with a relatively uniform damage profile over that depth [21]. Activation tends to be slightly less with proton irradiation than with neutron irradiation at comparable energies. However, at 1 GeV, there will be some activation of target materials.

It is unlikely there will be sufficient proton flux or irradiation volume in the Project X beam dump to accommodate irradiation of large test specimens that are typically used to measure engineering properties. However, it is possible that an irradiation facility could be designed into the beam path to accommodate direct proton irradiation of millimeter-scale samples suitable for microstructural evaluation and perhaps measurements such as microhardness. The proton beam energy is sufficient to irradiate a volume of material entirely suitable for fundamental scientific investigations of irradiation damage mechanisms and microstructural evolution during irradiation. Such a capability would provide a valuable complement to neutron irradiation testing facilities currently available by allowing relatively short and inexpensive irradiation experiments to elucidate fundamental mechanisms while allowing large test matrices and providing the ability to down-select the most promising materials for

subsequent test reactor irradiations for evaluating irradiation effects on bulk material properties. There are some limitations to the use of proton irradiation, including lack of constituent element transmutation and implantation of potentially high concentrations of hydrogen. Therefore, it is important to carefully consider, on a case-by-case basis, the test matrix and experiment objectives to ensure they are consistent with the use of proton irradiation. For some applications, these factors might not be detrimental, and in some cases they might be advantageous (e.g. hydrogen implantation in fusion reactor first wall materials).

A number of computational studies are needed to fully explore the capability of materials irradiation testing using the Project X proton beam. These include calculations of the expected penetration depth and damage rate from the 1 GeV proton beam at 1 mA current in typical fission or fusion structural materials. This would lead to an estimate of the temperature offset required for the proton beam to achieve the same microstructural effects as fission neutrons. An activation calculation would be needed to evaluate the adequacy the beam dump shielding. Together, these calculations would provide an assessment of the feasibility of performing meaningful radiation materials science research in the Project X beam.

II.4.5 Technical Feasibility

The technical feasibility of the Project X Target Station can be addressed in two parts, 1) the accelerator, and 2) the spallation target station.

Project X Accelerator

The Project X R&D Program is being undertaken by a collaboration of twelve national laboratories and universities, and four Indian laboratories (Project X Collaboration). A comprehensive R&D program is underway, aimed at mitigating the primary technical and cost risk associated with the Project X accelerator. The existing Reference Design is supported by detailed electromagnetic and beam dynamics modeling and simulations, and provides the context for the R&D program. The primary supporting technologies required to construct the Project X accelerator exist today. Fermilab, with national and international collaborators, has an extensive development program in superconducting radio frequency acceleration. This program has produced both spoke resonator and elliptical accelerating structures that meet the requirements of Project X. The Project X Integrated Experiment (PXIE) will be demonstrating the accelerator front end components and is the focus of an intensive development and systems testing program. Proof-of-concept components exist. While Project X is currently pre-CD-0, a preliminary, bottoms-up, cost estimate exist and the state of development is sufficient to support an expeditious move to construction (CD-3), in

parallel with ongoing development, over the next three-four years. The Project X accelerator is ready to construct.

Project X Integrated Target Station

The Project X Target Station is currently in the pre-conceptual design phase, but no significant technological challenges have been identified and specifying of mission and technical requirements is ongoing. The design of the target station can leverage significant experience in liquid metal reactor technologies, such as the fast Flux Test Facility (FFTF); design and conduct of reactor irradiation testing at DOE NE reactors such as FFTF at Hanford (with reconstitutable irradiation rigs and fabricated closed loops), ATR in Idaho, and HFIR at ORNL; design and operation of the 1MW liquid metal target at the SNS at ORNL, design concepts for the MTS at LANL, the demonstrated 1 MW liquid lead bismuth spallation target MEGAPIE, the fusion materials irradiation testing design of the IFMIF and predecessors, and the demonstrated UCN source at the SINQ accelerator facility. Closed-loop modules have been utilized in test reactors such as the Fast Flux Test Facility (sodium), BOR-60 (sodium, lead), and ATR (pressurized water).

The Target Station would operate as a national user facility, presumably with the cost shared between organizations that utilize it.

II.4.6 Meeting the Mission Needs

Fusion Energy Science

At the Energy Station workshop held at Fermilab, attended by accelerator physicists and engineers as well as nuclear materials experts from the fission and fusion communities, the most compelling application identified for the Project X target station is irradiation of fusion reactor structural materials. It was noted that there is currently no facility available anywhere in the world that can provide fusion-relevant neutron flux and achieve a minimum of 20 dpa per calendar year in a reasonable irradiation volume.

Unlike fission reactors, the Project X Target Station provides significant high-energy neutron flux at positions within and near the spallation target to achieve high dose rates (20-40 dpa per 365 operating days at 1 MW beam power) with fusion-relevant He generation rates. The highest dose rates would be associated with sample volumes on the order of a few liters. Figure II-7 below shows a representative neutron spectrum with a significant population of fusion-relevant 14 MeV neutrons that cannot be achieved in a fission reactor.

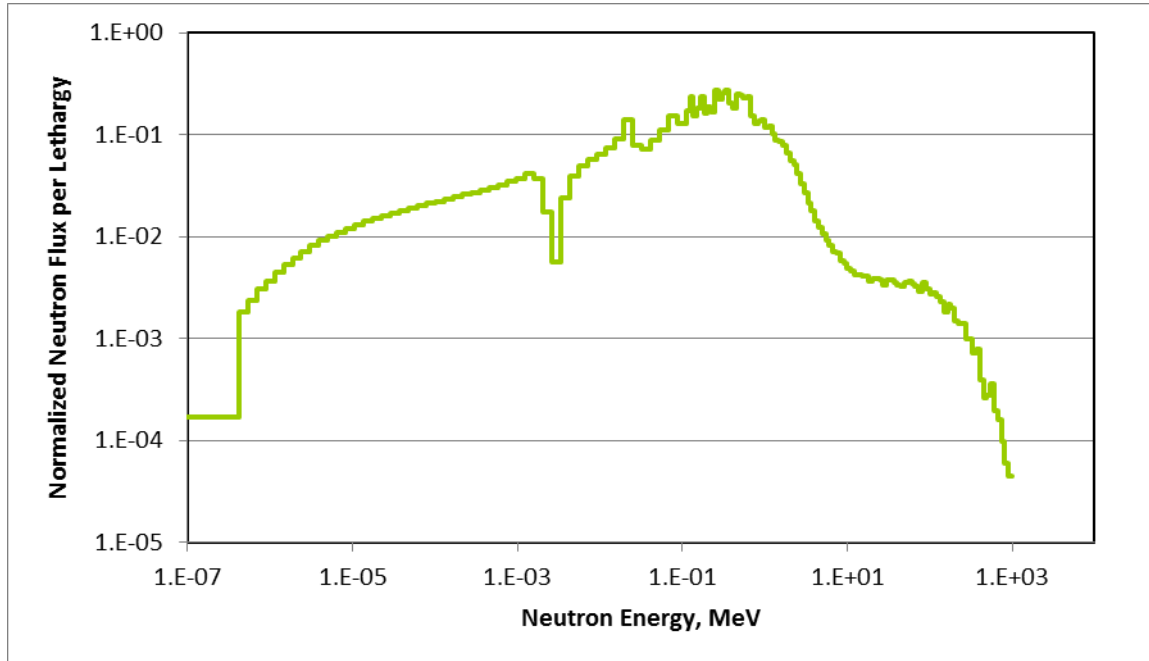


Figure II-7: Project X Target Station Spallation Neutron Spectrum with 1 GeV Incident Proton Beam [15].

To ensure maximum relevance to the fusion materials community, the proposed Project X Target Station can accommodate a range of sample sizes for structural materials of interest, from very small (mm-scale) to relatively large (maybe 10 cm). The smaller end of the size range is appropriate for fundamental studies of irradiation damage mechanisms, while the larger end of the range is appropriate for bulk samples needed for engineering property measurements. Because of its ample irradiation volume (due to the intensity of the incident proton beam) the Project X Target Station can accommodate the full range of sample sizes. Further, the target and incident beam can be designed to ensure there are areas of relatively uniform (and high) flux over cm-scale dimensions. At the same time, the irradiation facility can include not only replaceable large modules as described above, but also fixed, irradiation positions to accommodate specimens for long-term irradiations to achieve high dose (150+ dpa).

One question that must be addressed to further evaluate the feasibility of performing fusion materials irradiation tests are the effects of beam transients. For any irradiation experiment, active temperature control of test specimens during irradiation is an absolute requirement. While relatively straightforward during steady-state operation, the issue of incident proton beam trips and downtime (both planned and unplanned) must be addressed. These transients exist on both short time scales (beam trips and downtime during normal operation) and longer time scales (planned and unplanned extended outages). It is possible that some of the events could have consequences for irradiation damage mechanisms (e.g. cascade annealing,

atomic diffusion, phase transformations), particularly for samples located in the highest-flux regions adjacent to the proton beam and spallation target. Recent experiences at SNS provide examples of real-world accelerator operation that offer an indication of the degree of reliability to be expected in such a system.

As shown in the figure above, there is a high-energy tail resulting from spallation that is not prototypic of a fusion neutron spectrum. This is an issue that will require further consideration, but there are potentially good as well as bad implications. For fusion materials, the high-energy tail offers the potential to achieve a variety of dose and He generation rates in irradiation experiments, which could significantly enhance the understanding of irradiation damage mechanisms and effects in a regime that has received very little attention (due to lack of fusion-relevant neutron sources with high dose rates).

Specific capabilities of the Project X Target Station relative to Fusion Energy Science include:

- Dedicated fusion loop for materials testing with high energy neutron spectrum test environment at relevant temperatures
- Room for separate lead, helium, water loops that can be used to simultaneously test materials interactions
- The dpa accumulation and high energy neutron spectrum component can simulate fusion environments better than reactors
- Potential testing in the proton beam can provide high dpa and high equivalent neutron energy effects
- H and He generation rates for corresponding damage accumulation could allow testing of fusion materials
- Candidate fusion blanket materials can be irradiated in prototypical conditions of coolant, temperature, and high neutron flux
- Temperature is a critical parameter in materials irradiation and precise temperature control will be a key aspect of the Target Station Test Module design

Nuclear Energy

The materials irradiation testing capabilities of the Target Station could enable, for example, efforts to ensure the sustainability and safety of the current fleet of reactors for lifetime extensions, development of new higher performance and safer reactor fuels and materials, development of innovative economical small reactors, development of new advanced reactor concepts such as those using liquid metal or molten salt coolants, development of transmutation fuels for reducing legacy wastes requiring deep geologic storage, and investigation of accelerator driven systems as a means for transmutation of waste from power reactors.

The Project X Target Station could provide both thermal spectrum and fast spectrum test environments at the relevant temperatures. While thermal spectrum irradiation test volumes can be accessed at ATR and HFIR, there are currently no available U.S. fast reactor spectrum irradiation volumes. A key advantage of the versatile Target Station concept is that there is room for separate sodium, lead, helium, molten salt, and water loops with independent cooling systems that could provide the environments needed to simultaneously test materials for each concept. As future irradiation testing needs develop, the Target Station could be adapted to a variety of configurations, unlike dedicated reactor facilities. Metal hydrides such as zirconium hydride or calcium hydride have been demonstrated effective in providing spectral tailoring in a sodium fast reactor environment, so they could also be used for spectral tailoring as needed for each concept. The higher proportion of high energy neutrons would provide higher H and He generation rates for the same corresponding dpa accumulation, which could allow accelerated aging testing of materials.

Candidate fuel and cladding materials can be irradiated in a prototypic environment of coolant, neutron spectrum, and temperature. The temperature is a critical parameter in materials irradiation, and precise temperature control will be a key aspect of the Target Station design. The peak neutron flux in the test regions approach those achieved in existing fast test reactors. The independent closed loop modules provide the flexibility to support multiple simultaneous irradiation test regions and maximize irradiation volumes.

For general materials irradiation testing, the Project X Target Station can be used to investigate:

- Correlating charged particle damage with existing reactor neutron damage data
- Proton, neutron and gamma induced reactions
- Gas generation
 - Hydrogen implantation, migration, blistering
 - Helium generation from alpha production reactions
- Reactor materials testing
 - Cladding and structural materials
 - Control rod absorber materials
 - Reactor vessel and internal component materials
 - Pre-screening tests for reactor irradiation testing
- Accelerator materials testing
 - Chopper, scraper, absorber, dump materials
 - Beam window materials
 - Low activation materials
 - Radiation resistant materials (effects of impurities, heat treatment, temperatures)
 - Can reach 20-40 dpa/yr

Nuclear Physics

The Project X Target Station UCN source could be configured similar to the SING UCN source, with spallation neutrons produced in the target (liquid lead or solid tungsten) and then thermalized in an ambient-temperature heavy-water moderator, and then further down-scattered in a volume of solid D₂ cooled to 5K. UCN can be directed from the D₂ volume into a storage tank, from which they can pass through guides to experimental areas.

Project X (1mA @1GeV protons on thorium target) predicted yields of important EDM isotopes: ²¹⁹Rn>10¹⁴, ²²³Rn~10¹¹, ²¹¹Fr~10¹³, ²²¹Fr>10¹⁴, ²²³Fr>10¹², ²²³Ra>10¹⁴, ²²⁵Ra>10¹³, ²²⁵⁻²²⁹Ac>10¹⁴. This compares to a 1 mCi ²²⁹Th source yield of 4x10⁷ ²²⁵Ra/s. Project X might yield 1x10¹³ ²²⁵Ra/s, which is a 1-2 order of magnitude increase in projected EDM sensitivity. Project X might yield 10¹¹ ²²³Rn/s, which is 3-4 orders of magnitude greater than TRIUMF ISAC. High efficiency extraction of important isotopes could be accomplished by chemical separation of irradiated targets for isotopes with half-lives of days. Extraction of isotopes with half-lives of minutes might require online extraction from hot carbide spallation targets. [8] The goal of nEDM@SNS is to be statistics limited. Project X is a following opportunity that would exploit the statistically limited techniques developed at SNS .[8]

Isotope Production

The Project X Target Station could support isotope production by providing irradiation environments spectrally tailored for isotope production at the relevant temperatures and coolant for the targets. Spectrum tailoring can be used to enhance production of specific isotopes using a variety of moderators such as D₂O, graphite, beryllium, and metal hydrides. A rabbit system can be used for rapid insertion and removal of short half- life radioisotopes. Rather than just allow neutrons to leak out of the various test regions to be captured in shield materials, the option of use of these leakage neutrons for isotope production, such as ²³⁸Pu or ⁶⁰Co could be considered.

Specific characteristics of the Project X Target Station relevant to isotope production include:

- Low activation target and structural materials specific to isotope production can be developed.
- Target/capsule material compatibilities can be tested for isotope production in other facilities.
- Dedicated isotope production loop with capability to vary neutron spectrum test environment and temperatures to optimize for isotopes of interest
- Room for separate loops that can be used to simultaneously produce and test a variety of isotopes

- Testing in the proton beam can provide accelerator produced isotopes
- Higher neutron energies than reactors can enhance production of isotopes only produced by fast neutrons
- Temperature is a critical parameter in some isotope target irradiations and precise temperature control will be a key aspect
- A rabbit system can be integrated into the test module for rapid insertion and retrieval of short lived radioisotopes
- Reflector region can utilize “waste” neutrons for isotope production such as ^{60}Co or ^{238}Pu
- Spallation reactions produce broad range of reaction products and the target cleanup system could be designed to separate particular isotopes of interest

How Target Station Matches the Mission Needs

The following tables (Table II-10) provide a summary of the Project X Target Station capability to support the various mission needs.

	Mission Needs	Testing Environments	Target Station Considerations
<p>Office of Nuclear Energy</p> <ul style="list-style-type: none"> • Fuel Cycle Technologies <ul style="list-style-type: none"> ○ Used Fuel Disposition R&D ○ Fuel Cycle R&D • Advanced Modeling & Simulation • Nuclear Reactor Technologies <ul style="list-style-type: none"> ○ LWR Sustainability Program ○ Advanced Reactor Technologies ○ Small Modular Reactors ○ Space Power Systems 	<ul style="list-style-type: none"> • Fuels and materials up to ~100 liters • Instrumentation capable of characterizing fuel clad, coolant temperatures up to 1000 °C • Associated PIE or shipping capabilities 	<ul style="list-style-type: none"> • Stable, well characterized test environments • Fast reactors SFR, LFR, GFR • Fuel pin coolant environments of sodium, lead, gas, molten salt, water • Neutron flux up to 5×10^{15} n/cm²/s • Damage rates up to 50 dpa/year 	<ul style="list-style-type: none"> • Multiple independent closed loops for irradiation testing with sodium, lead, etc., • Fast reactor neutron spectrum • Tailoring of neutron spectrum, materials, temperatures to match other reactor environments • Ability to irradiate fuel pin rodlets under prototypic conditions • Remote handling and shipping

	Mission Needs	Testing Environments	Target Station Considerations
Office of Science <ul style="list-style-type: none"> • Fusion Energy Science <ul style="list-style-type: none"> ○ Fusion Materials and Technology 	<ul style="list-style-type: none"> • Fusion materials testing environment • 14 MeV neutrons • Structural materials properties as a function of dpa and temperature • Plasma facing components • Low activation structural materials • Solid breeder materials • Safety 	<ul style="list-style-type: none"> • Stable, well characterized test environments • Materials surrounding fusion ignition region • >0.4 liter volume • >10¹⁴ equivalent 14 MeV neutron flux • >20 dpa/year • Medium and low flux volumes exposed to temperature, mechanical loads, corrosive media • Exposures >100MW-y/m² • flux gradients <20%per cm 	<ul style="list-style-type: none"> • Dedicated fusion material irradiation testing loop • 20 dpa/yr • Temperatures up to 1000 °C

	Mission Needs	Testing Environments	Target Station Considerations
Office of Science <ul style="list-style-type: none"> • Nuclear Physics <ul style="list-style-type: none"> ○ Low Energy Nuclear Physics Research ○ Theoretical Nuclear Physics Research ○ Isotope Development and Production for Research and Applications 	<ul style="list-style-type: none"> • Source of Ultra cold neutrons for n-EDM, NNbarX • Source of isotopes for ISOL atomic EDM • Capability for R&D for research isotopes 	<ul style="list-style-type: none"> • Stable, well characterized test environments • UCN n velocities <4mK • UCN density >3x10⁴ UCN/cm³ 	<ul style="list-style-type: none"> • Separate closed loop with heavy water, Be, metal hydride, moderator region, • Cryogenic cooled He, H₂, HE-2, CH₄ volume for producing Ultra cold neutrons, reflected CN beam transport to n-EDM, NNbarX experiments • Capability for irradiating Thorium spallation target capsules in proton beam region to produce ISOL isotopes • Capability of inserting and removing short- lived isotope production targets (rabbit system)

Table II-10: Comparison of Project X Target Station Capabilities with Mission Needs

II.5 Conclusions and Recommendations

The broader impacts of the Project X Target Station include providing enabling technologies for the advancement of R&D for:

- Office of Science Fusion Energy Science - fusion materials irradiation testing
- Office of Science Nuclear Physics - providing an ultra-cold neutron source for \overline{n} -EDM searches
- Office of Science Nuclear Physics – specialty isotopes for atomic EDM and similar studies
- Office of Science Nuclear Physics – research isotopes
- Office of Nuclear Energy – fission reactor fuels and materials irradiation testing

Broader impacts of the Project X Target Station beyond the Particle Physics missions include:

- The Target Station, based on using Project X high energy protons impinging on a heavy metal target to produce spallation neutrons, could provide a new continuous neutron source to complement materials testing at aging US research reactors
- No major technical challenges to designing and building such a facility (continuous spallation source operating in Switzerland for years)
- The Target Station is well suited for fission/fusion materials studies, isotope production, transmutation studies, and a cold neutron source
- The CW beam from the Project-X linac will be a unique facility in the United States to address key physics and technology demonstration

The key advantage of the Project X Target Station is that it would be a single powerful facility with the flexibility to meet a variety of needs as currently envisioned. It will also have the flexibility to adapt to changing needs in the future.

The configuration and design of the Project X Target Station is still at a pre-conceptual level and additional work is recommended to evaluate the following fundamental parameters that can significantly affect the layout of the target station:

- Vertical versus horizontal proton beam alignment on spallation target
- Beam window or windowless spallation target design
- Solid rotating spallation target versus liquid heavy metal target
- Multiple spallation targets with beam split between them
- Limiting beam power density by expanding beam diameter or beam rastering over larger surface
- Radiation heating/temperature limitations for coupling cold neutron capability in spallation target

It is recommended that the integrated approach to the Target Station be pursued vigorously through further studies of configurations, combining the materials irradiation testing for fusion and fission environments/needs with the nuclear physics experimental needs.

II.6 References

1. Fermilab Project X website (<http://projectx.fnal.gov/>)
2. Accelerator and Target Technology for Accelerator Driven Transmutation and Energy Production, <http://www.science.doe.gov/hep/files/pdfs/ADSWhitePaperFinal.pdf>
3. Accelerator for America's Future, W. Henning and C. Shank, editors, <http://www.acceleratorsamerica.org/files/Report.pdf>
4. R. Raja, S. Mishra, Applications of High Intensity Proton Accelerators – Proceedings of the Workshop, World Scientific, July 30, 2010.
5. Y. Gohar, D. Johnson, T. Johnson, S. Mishra, Fermilab Project X Nuclear Energy Application: Accelerator, Spallation Target and Transmutation Technology Demonstration, <https://indico.fnal.gov/getFile.py/access?resId=1&materialId=8&confId=3579>
6. Nuclear Energy Research and Development Roadmap Report To Congress, April 2010, US DOE Office of Nuclear Energy (http://energy.gov/sites/prod/files/NuclearEnergy_Roadmap_Final.pdf)
7. Report of the FESAC Subcommittee on the Prioritization of Proposed Scientific User Facilities for the Office of Science, March 21, 2013 http://science.energy.gov/~media/fes/fesac/pdf/2013/FESAC_Facilities_Report_Final.pdf
8. Project X Forum on Spallation Sources for Particle Physics, March 2012, Fermilab <https://indico.fnal.gov/getFile.py/access?contribId=2&sessionId=1&resId=0&materialId=slides&confId=5372>
9. "U.S. Particle Physics: Scientific Opportunities, A Strategic Plan for the Next Ten Years", http://science.energy.gov/~media/hep/pdf/files/pdfs/p5_report_06022008.pdf
10. Isotopes for the Nation's Future, A Long Range Plan, NSAC Isotopes Subcommittee, August 27, 2009 (http://science.energy.gov/~media/np/nsac/pdf/docs/nsaci_ii_report.pdf)
11. http://pasi.org.uk/Target_WP1
12. DM Asner, et al., 2013, *Project X Energy Station Workshop Report*, PNNL-22390, Pacific Northwest National Laboratory, Richland, Washington.; Also see <https://indico.fnal.gov/conferenceTimeTable.py?confId=5836#20130129.detailed>
13. R Cubitt, et al., NIMA 622, 182-185 (2010)
14. M. Baldo-Ceolin, et al., Z. Phys. C63 (1994) 409
15. Wootan DW and DM Asner. 2012. *Project X Nuclear Energy Station*. PNNL-21134, Pacific Northwest National Laboratory, Richland, Washington. Available at <https://indico.fnal.gov/materialDisplay.py?materialId=6&confId=5836>

16. Wagner W, F Gröschel, K Thomsen and H Heyck. 2008. "MEGAPIE at SINQ – The First Liquid Metal Target Driven by a Megawatt Class Proton Beam." *Journal of Nuclear Materials* 377(1):12-16.
17. Garner, FA. 1983. "Impact of the Injected Interstitial on the Correlation of Charged Particle and Neutron-Induced Radiation Damage," *Journal of Nuclear Materials*, 117:177-197.
18. Mazey, DJ. 1990. "Fundamental Aspects of High-Energy Ion-Beam Simulation Techniques and their Relevance to Fusion Materials Studies," *Journal of Nuclear Materials*, 174:196-209.
19. Ruzin, A, G Casse, M Glasner, A Zanet, F Lemeilleur and S Watts. 1999. "Comparison of Radiation Damage in Silicon Induced by Proton and Neutron Irradiation," *IEEE Transactions on Nuclear Science*, 46(5):1310-1313.
20. Was, GS. 2007. *Fundamentals of Radiation Materials Science*. Berlin: Springer.
21. Was, GS and TR Allen. 2007. "Radiation Damage from Different Particle Types," in *Radiation Effects in Solids*, KE Sickafus, EA Kotomin, and BP Uberuaga, Eds. Berlin: Springer.
22. <http://science.energy.gov/fes/>

III MUON SPIN ROTATION AT PROJECT X

**A powerful addition to the Science Portfolio of the
Department of Energy and Fermilab**

**R. Plunkett, R. Tschirhart, A. Grasselino, A. Romanenko
Fermi National Accelerator Laboratory**

**G. MacDougall
University of Illinois at Champaign-Urbana**

**R. H. Heffner
Los Alamos National Laboratory**

June 2013

Acknowledgments

The authors would like to acknowledge the following contributors to the Project X Muon Spin Rotation Forum: P. Oddone, S. Henderson, S. Holmes, A. Suter, E. Morenzoni, G. Luke, R. Kiefl, P. Percival, S. Kilcoyne, R. Cywinski, Y. Miyake, C. Polly, S. Striganov.

Thanks to V. Lebedev , N. Mokhov, E. Won, and B. Kiburg for useful conversations, and to P. Bhat for many useful suggestions.

III.1 Summary

This section discusses the wider application of Project X to problems in material science, specifically through the creation of a facility to exploit polarized, low-energy muons created via the decay of pions, which can be copiously produced by Project X beams. Such a facility would be unique in the United States and can significantly increase extremely limited global capacity for the technique, known as Muon Spin Rotation (μ SR in the following).

Most commonly, the μ SR technique uses a spin-polarized beam of muons with kinetic energies of 4 MeV or less. Such muons are produced by decay of pions at rest, and utilize conservation of angular momentum in the two-body decay with a left-handed neutrino partner to produce a polarized beam (Figure III-1). Muons are implanted into samples of materials, and decay after precessing in the local magnetic field. Detection of the angular distribution of decay positrons (for μ^+) as a function of time gives information on the local static field distribution and the field fluctuation rate. Experiments can be carried out in either zero or finite applied fields. Simple in concept, μ SR has found wide application in characterization of materials, particularly in studies of magnetism and superconductivity.

Methods exist for lowering the energy of the polarized muons further, creating a beam of quasi-thermal muons with kinetic energies of typically 1-30 keV. These “LEM” beams (for Low Energy Muons) present an exceptional scientific opportunity for probing phenomena within the first 200 nm of the surface of materials, and are a subject of intense research interest.

We propose utilizing the unique time structure of Project X to create a facility to exploit the μ SR technique via a number of different avenues. Several experimental halls will receive dedicated pulses from Project X. Other beamlines will utilize muons created by a thin target inserted into the proton stream sent to the spallation target area, giving adequate intensities to produce one or more LEM beams. In this way, the great flexibility of Project X can be used to create a facility with unique capabilities for programs utilizing the whole range of muon spin rotation techniques.

There is no μ SR facility currently in operation in the United States. The materials science research community relies heavily on off-shore facilities which are in very high demand. Therefore, the proposed facility at Fermilab will be highly beneficial to the US research community and a powerful addition to the science portfolio of DOE.

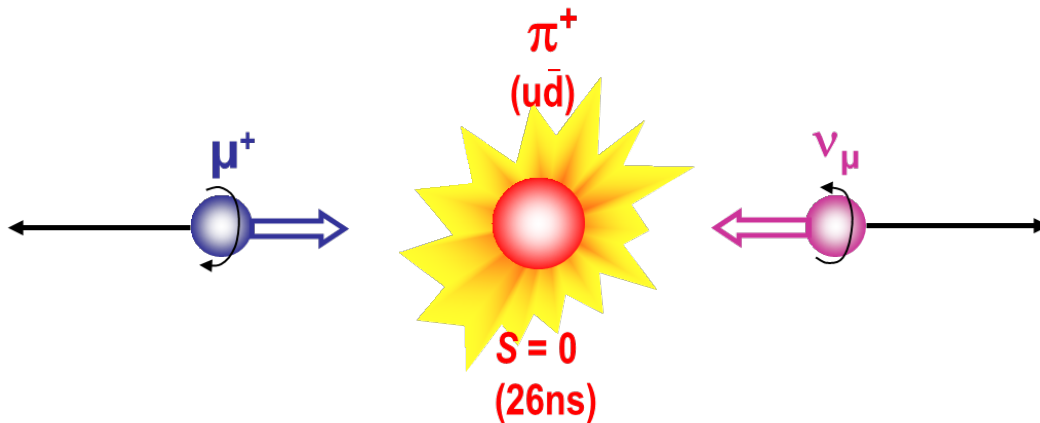


Figure III-1: Decay of a charged pion, in its rest frame, showing the polarization of the decay products. The neutrino is always left-handed, constraining the polarization of the muon.

III.2 The science case for μ SR

μ SR has made important contributions to a wide range of topics of interest to the condensed-matter science community, including such topics as superconductivity, quantum magnetism and chemistry. Important advances have also been made, by employing μ SR, in the study of semiconductors, biological and soft-matter systems, and quantum diffusion. In recent years, the advent of "ultra-low energy" μ SR beams has produced unique contributions in the study of thin films, multi-layers and surface science.

In this section, we discuss some of the past and continuing successes of μ SR as a probe of matter, with an eye to demonstrating some of its unique characteristics. Because μ SR is highly complementary to other widely-used probes - including NMR, x-ray scattering and neutron scattering- there is a very large potential user base in North America and abroad.

III.2.1 Materials science

In materials science, μ SR is primarily a probe of static and dynamic magnetic correlations inside materials of interest. Like other resonance probes, such as NMR and ESR, μ SR gains this information in real-space by monitoring the time-evolution of the muon magnetic moment. Unlike other probes which polarize host atoms with strong magnetic fields, μ SR injects naturally spin-polarized muons to probe local magnetism.

Also, instead of using rf-fields to gather information, a μ SR experimenter collects daughter electrons or positrons resulting from the symmetry-violating decay of the muon itself.

Like all probes of matter, μ SR has advantages and disadvantages. In particular, its unique characteristics make a powerful *complement* to several other probes of matter, in some cases providing information unobtainable in any other way. Some of these characteristics are outlined below:

- μ SR is a real-space probe, which gives information similar to NMR but distinct from reciprocal-space probes such as neutron scattering and resonant x-ray scattering. It sacrifices detailed information about long-wavelength correlations, but has the ability to directly detect phase separation and measure volume fractions of competing phases.
- As a foreign probe of magnetism, μ SR can measure the properties of any system in which a muon can be stopped. There are no particular requirements or restrictions regarding constituent atoms or material properties. This also affords the flexibility to use a wide range of sample environments.
- μ SR does not require the presence of external magnetic fields, allowing for the measurement of glassiness or magnetism in materials in which the applied fields used in NMR have a non-negligible effect.
- μ SR is sensitive to the presence of dynamic fluctuations in the 10's of picosecond to microsecond timescale. This is slower than fluctuations probed by traditional neutron spectrometers, but much quicker than those probed by NMR or AC susceptibility.
- The supreme sensitivity of the muon spin is regularly used to detect local fields as small as 0.1G in crystals as small as 2mm^3 . This has been leveraged to detect the existence of local moments as small as $0.001\mu_B$.
- Through the detection of vortex lattices, μ SR is one of the few techniques (along with small angle neutron scattering) capable of measuring superconducting penetration depths and coherence lengths in the vortex phase of type-II superconductors. Low energy μ SR is now providing some of the first measures of penetration depths in the Meissner state of superconducting materials.
- The relatively high signal-to-noise in modern μ SR instruments allows for spectra to be collected in less than one hour. This allows experimenters to detail material

response to fields or to determine detailed phase diagrams of a new material in a matter of days, consistent with the time allotted for a single μ SR experiment.

- The advent of novel low-energy (keV range) muon beams now allows for the depth-range implanting of probe magnetic moments, opening up new avenues for research of surface and interface effects in new magnetic materials.

Magnetism

The study of magnetism is the most common area of application of μ SR, due to the sensitivity of the muon and its capability to probe both static and dynamic local fields. Magnetic volume fractions are determined by measuring the amplitude of the precessing signal in a zero-field μ SR experiment, or alternatively, by measuring the non-decaying amplitude of the signal in a weak transverse field experiment. In the first method, the frequency of the oscillation will be proportional to the ordered moment size, and the amplitude proportional to ordered volume fraction. In the second, that portion of the signal due to the ordered volume will decay in a fraction of a microsecond, allowing one to unambiguously associate the remaining precessing signal with the paramagnetic volume fraction.

Historically, the ability of μ SR to study materials in low or zero applied magnetic field, and the unique fluctuation range to which it is sensitive, have allowed the technique to make a large impact in the study of spin glasses [Uemura1980; Uemura1985; Pinkvos1990; MacLaughlin1983; Heffner1983] and geometrically frustrated magnets [Carretta2008]. The high signal-to-noise ratio has been utilized to map out phase diagrams and study quantum phase transitions [Dalmas de Reotier 1997; Niedermeyer1998; Uemura2007; Carlo2009; Luetkens2009; Pratt2011], and to make careful measurements of order parameters to extract critical exponents [Dalmas de Reotier 1997; Pratt2011]. The high sensitivity has been useful in the study of spin singlets or highly renormalized moments in reduced dimensional [Kojima1995; Kadono1996, Kojima1997; Matsuda1997], frustrated [Carretta2008] or heavy fermion magnetic materials [Amato1997]. Parallel to ongoing developments in each of these fields, recent work with low-energy muons has also produced insights into the effect of surfaces or interfaces in thin-film magnets and magnetic heterostructures [Shay2009; Suter2011; Boris2012; Hofman2012].

Frustrated Magnetism, Phase Diagrams and Critical Exponents

Several of these benefits were displayed in a recent high-profile study of the quasi-2D organic antiferromagnet κ -(BEDT-TTF)₂Cu₂(CN)₃ by Pratt *et al.* [Pratt2011] – see Figure III-2. This material is a largely isotropic Mott insulator which contains spin-1/2 Cu²⁺

moments in weakly interacting two-dimensional planes. The moments are in a plane with a frustrated triangular configuration, and κ -(BEDT-TTF)₂Cu₂(CN)₃ is one of the leading candidates to be the long-sought *quantum spin liquid*, wherein magnetic order is suppressed to zero temperature and the ground state is a singlet comprising a macroscopically large number of entangled spins. Thermodynamic probes have established that this material contains no well-defined magnetic order down to 20mK, despite a sizeable nearest-neighbor exchange of $J \sim 250\text{K}$, but at the time of this study, at least one NMR study had demonstrated the emergence of inhomogeneous moments below 4K and with applied fields above 2T [Shimizu2006].

This zero-field μSR study has confirmed and expanded upon these initial NMR results. Pratt *et al* showed that the magnetic field distribution is consistent with what is expected from randomly oriented nuclear dipole moments- thus ruling out the existence of electronic moments larger than $\sim 0.001\mu_B$. Through careful weak transverse field (WTF) μSR measurements, they were able to observe a sudden increase in the root-mean-squared field as applied fields were increased above $H_0 = 14\text{mT}$. They associated this as a transition to a weak (small moment) antiferromagnetic state with field $B_{\text{rms}} < 0.5\text{mT}$. A series of WTF measurements further allowed them to track the phase boundary in parameter space and determine that it scaled according to expectations for a Bose-Einstein condensate in two-dimensions. The measured critical field was consistent with a spin gap $\Delta_s \sim 3.5\text{mK}$ - five orders of magnitude smaller than J and indicative of an emergent low-energy scale for the relevant physics.

The authors measured the temperature dependence of the magnetic fluctuation rate, identifying four distinct temperature regimes at zero field. By extending this analysis to finite fields, a second quantum critical point was identified at $H_1=4\text{T}$ and a gap involving vortex-like excitations called visons, with $\Delta_v \gg \Delta_s$ was inferred, consistent with previous NMR results and thermal conductivity data [Yamshita2008]. Combining their μSR results with NMR data, the authors constructed a detailed H-T phase diagram extending to fields as high as 10 T and temperatures as high as 10 K, complete with critical exponents for comparison with theory. The data allowed Pratt *et al.* to conclude that this system is best described by a spin-liquid model where the H_0 is associated with the Bose condensation of magnons, and H_1 transition is associated with a deconfinement transition, where $S=1$ spin wave excitations fragment into freely propagating $S=1/2$ spinons.

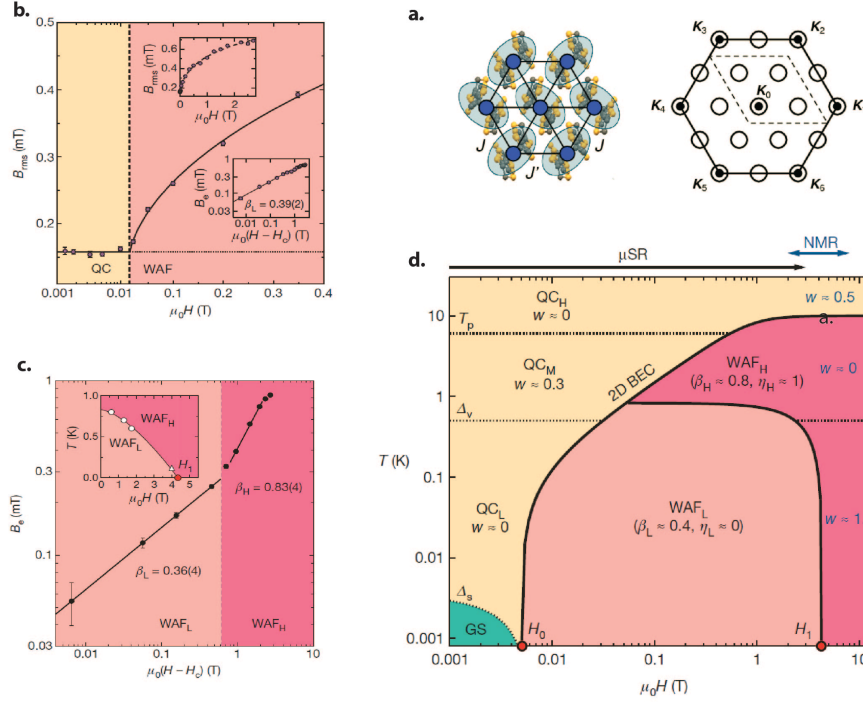


Figure III-2: Phase diagram and critical behavior of κ -(BEDT-TTF)₂Cu₂(CN)₃ - (a.) Sketches of real and reciprocal space lattice structures, demonstrating the symmetry of the $S=1/2$ BEDT-TTF dimers in the two-dimensional plane. (b.) Field dependence of the μ SR linewidth, measured to 120mK. The increase above $H_0(120\text{mK})= 14\text{mT}$ represents a transition from a quantum critical phase to a small moment antiferromagnetic phase at this temperature. Upper inset shows higher field behaviour, and lower inset shows critical scaling analysis which led to the determination of H_0 . (c.) Similar analysis investigating a second quantum critical transition at $H_1=4\text{T}$, between two qualitatively different antiferromagnetic phases. (d.) A phase diagram extracted from analysis similar to (b.) and (c.) at several different fields and temperatures. Included are critical scaling exponents, extracted from analysis of fluctuation rates in zero field, and information from a separate NMR study. Adapted from [Pratt2011].

Through similar measurements μ SR has been used to explore the properties of other frustrated triangular [Olariu2006] and Kagome [Ofer2009] lattice systems. In three dimensions μ SR has long been used to explore the statics and dynamics of so-called pyrochlore antiferromagnets, wherein magnetic moments lie on a network of corner sharing tetrahedra. The observed behavior in these systems varies but is frequently unconventional. Examples include spin-glass-like behavior in the absence of disorder in YMo_2O_7 [Dunsiger1996] and ground states with partially or entirely dynamic spin fluctuations persisting to the lowest measurable temperatures [Gardner1999; Dunsiger2006; Dalmas de Reotier2006; Dalmas de Reotier2012]. In recent years, μ SR

has played a major complementary role to neutron scattering in exploring order in frustrated systems with neutron absorbing $5d$ transition metal ions. Examples include the identification of magnetically ordered and disordered states below the metal insulator transitions in $\text{Eu}_2\text{Ir}_2\text{O}_7$ [Zhao2011] and $\text{Nd}_2\text{Ir}_2\text{O}_7$ [Disseler2012], respectively, or the confirmation of the order state in a multi-probe review of magnetism in Na_2IrO_3 [Choi2012].

Quantum Phase Transitions and Phase Separation

The above study of Pratt shows the usefulness of measuring critical exponents to discriminate between various theoretical models of magnetic systems. However, μSR has also played a key role in the study of *first-order* phase transitions, where the critical behavior is avoided. One recent example is a study by Uemura *et al.* of the first-order quantum phase transitions in MnSi and $(\text{Sr}_{1-x}\text{Ca}_x)\text{RuO}_3$ [Uemura2007]. MnSi has long been of interest as a prototype for weak moment itinerant antiferromagnetism and, more recently, for the partially ordered state seen at high pressures and fields. SrRuO_3 is a correlated metal, which is an end member of the famous Ruddleson-Popper series $\text{Sr}_{n+1}\text{Ru}_n\text{O}_{3n+1}$ ($n \rightarrow \infty$). It has a ferromagnetic transition at $T_c=150\text{K}$, which can be destroyed by replacing Sr^{2+} cations with isovalent Ca^{2+} . Uemura *et al.* studied the order-disorder transition in MnSi by selecting muons of the correct velocity to penetrate the front wall of a hydrostatic pressure cell and implant in a single-crystal sample. Through an examination of frequency and amplitude of muon spin precession in a series of zero field and weak transverse field μSR measurements, they were able to demonstrate that the relative sample volume occupied by the magnetically ordered phase was shrinking with increasing pressure, going to zero identically at the previously identified critical pressure, but without appreciably changing the ordered moment size. Further, by examining signal relaxation in a series longitudinal field experiments, they were able to show that the spin fluctuations expected at a continuous quantum phase transition were suppressed. Overall, this painted a picture wherein the quantum phase transition in MnSi is of first order and magnetism is destroyed via a "trading-off" between ordered and disordered volumes over an extended range in pressure. Uemura *et al.* also demonstrated similar behavior at ambient pressure with doping in ceramic samples of $(\text{Sr}_{1-x}\text{Ca}_x)\text{RuO}_3$. In these materials, the authors were able to reproduce *bulk* magnetization data taken on the same samples using *microscopic* parameters obtained from μSR measurements.

These results have spurred intense debate about the character of quantum phase transitions in metallic systems. Real space phase separation has also been observed in the phase diagrams of many other magnetic systems and, as seen in Figure III-3, has become a major theme in the study of unconventional superconducting compounds.

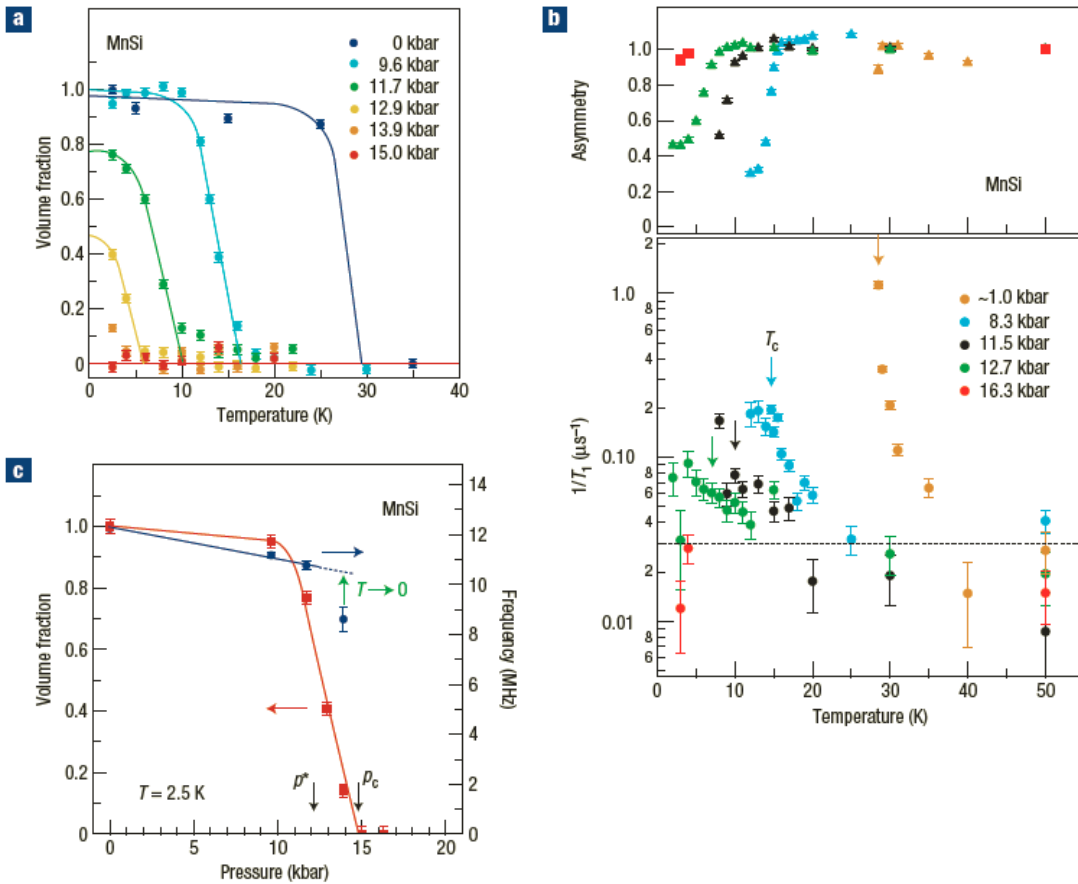


Figure III-3: μ SR results on the volume fraction, relaxation rate and spin precession frequency in MnSi. (a.) Temperature and pressure dependence of the magnetic volume fraction in single-crystalline MnSi, with static magnetic order determined in weak transverse fields of 100G. V_f remains finite at $T \rightarrow 0$ at the pressure p between 11.7 and 13.9 kbar, indicating phase separation between magnetically ordered and paramagnetic volumes. (b.) The muon spin relaxation rate $1/T_1$ and the relative magnitude of the corresponding muon asymmetry in MnSi in an LF of 200 G. Divergent critical behavior of $1/T_1$, seen at $p \rightarrow 1$ kbar, is gradually suppressed with increasing pressure. No anomaly of $1/T_1$ is seen at T_c (indicated by arrows) at $p=12.7$ kbar ($p^* < p < p_c$). At $p=16.3$ kbar, $1/T_1$ becomes smaller than the technical limit of detection, indicated by the dashed line. (c.) Pressure dependence of V_f and the zero-field muon spin precession frequency at $T=2.5$ K. The finite frequency near p_c indicates a first-order phase transition. The frequency at $p=13.9$ kbar at $T=2.5$ K $\sim 0.5T_c$ is expected to increase for $T \rightarrow 0$ as illustrated by the green arrow.

Magnetic Multipoles

As a purely dipole probe of magnetism, μ SR has also been able to meaningfully contribute to the discussion surrounding more unconventional forms of magnetism, such as those involving higher-order magnetic multipoles [Kuramoto2009]. One recent example is NpO_2 , an actinide compound characterized by a large heat capacity anomaly at $T_0 = 25.5\text{K}$ [Osborne1953], but without any sign of spin order or structural distortions apparent in neutron scattering [Cariuffo1987], Mossbauer resonance [Friedt1985] or x-ray diffraction data [Mannix1999]. Somewhat surprisingly, μ SR demonstrated a well-defined precession signal below T_0 , indicative of time-reversal symmetry breaking at low temperatures [Kopmann1998, Figure III-4]. It was in attempting to reconcile the seemingly contradictory μ SR measurements with previous results that theorists first suggested that the transition at T_0 is characterized by the ordering of magnetic octupoles [Santini2000; Santini2006]. This hypothesis has since been confirmed by resonant x-ray scattering. In a similar vein, measurements of the local field by μ SR have helped identify octupolar order parameters in the substitutional alloy $\text{Ce}_x\text{La}_{1-x}\text{B}_6$ [Takagiwa2002; Kubo2003; Kubo2004] and the filled skutterudite $\text{SmRu}_4\text{P}_{12}$ [Hachitani2006; Ito2007].

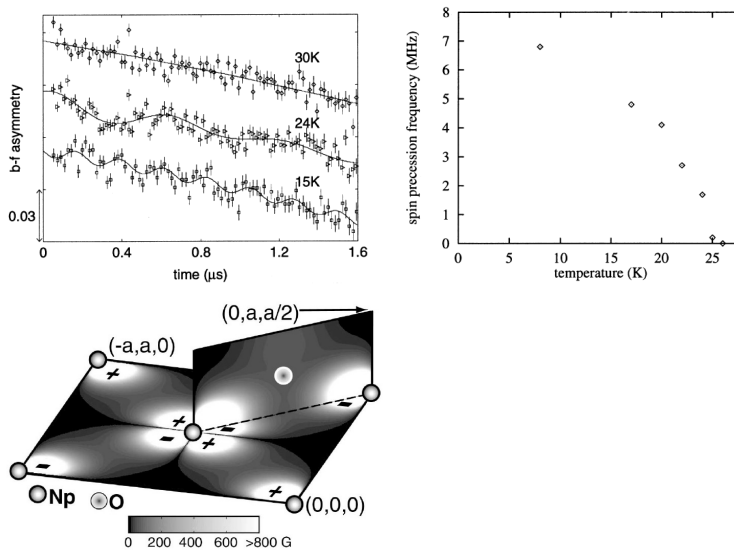


Figure III-4: Time-reversal symmetry breaking in NpO_2 - (left) Some ZF- μ SR spectra recorded for NpO_2 . Whereas the μ SR asymmetry decays monotonically at $T=30\text{K}$, the appearance of oscillations at lower temperatures indicates the onset of magnetic order in this sample. The temperature dependence of the oscillation frequency (center), implies a magnetic transition with $T_c \sim 25\text{K}$. From [Kopmann1998]. This observation was at odds with existing neutron and Mossbauer measurements, and led to the prediction of an octupolar order parameter in this system (right).

Reduced Dimensionality and Nano-structures

Traditional forms of μ SR have long been used to study singlet formation, order, fluctuations, and defects in quasi-1D spin chains and ladders, or quasi-2D planar materials. However, with the advent of low-energy μ SR, several new fruitful avenues of research have emerged.

Low energy μ SR (LEM) is being used extensively to investigate the role of reduced dimensionality in determining magnetic or superconducting properties. In one study, atomic layer-by-layer molecular beam epitaxy was used to construct several superlattices comprising n layers of antiferromagnetic La_2CuO_4 separated by non-magnetic spacer layers of $\text{La}_{2-x}\text{Sr}_x\text{CuO}_4$. It was found that, upon approaching the two-dimensional limit, antiferromagnetic long-range order gives way to a novel spin-liquid state characterized by strong quantum fluctuations and reduced spin-stiffness [Suter2011]. In another study, a quasi-1 dimensional "wire" of superconducting $\text{La}_{1.94}\text{Sr}_{0.06}\text{CuO}_4$ was investigated to elucidate the coupling between the superconducting and magnetic order parameters in this system. It was found that the Néel temperature associated with the antiferromagnetic order increased as superconductivity was suppressed by high current density, implying a repulsive interaction between the two order parameters [Shay2009]. There are now several examples of materials, such as TbPc_2 nanomagnets [Hofman2012] or spin glasses [Pratt2005; Morenzoni2008], where reduced sample thickness is seen to enhance spin fluctuations over that seen in the bulk.

Heterostructures investigated include Fe/Ag/Fe trilayers [Luetkens2003], and nickel-oxide superstructures [Boris2011]. In the Fe-Ag-Fe study, LEM was able to track the oscillating spin polarization density in the spacer layer, integral to the exchange coupling between the ferromagnetic end layers and leading to long-range order. In a clever study by Boris *et al* [Boris2011], it was demonstrated, through the investigation with LEM of carefully grown superlattices, that correlation effects could induce an insulating and antiferromagnetic ground state in layers of LaNiO_3 , which is a paramagnetic metal in the bulk (Figure III-5). This study stands as a prototypical example of how a man-made heterostructure can be used to control and manipulate intrinsic material properties such as electron-electron correlations. Through studies such as these, LEM is emerging as one of the most powerful methods in materials science for exploring depth dependent magnetic behavior in artificial systems.

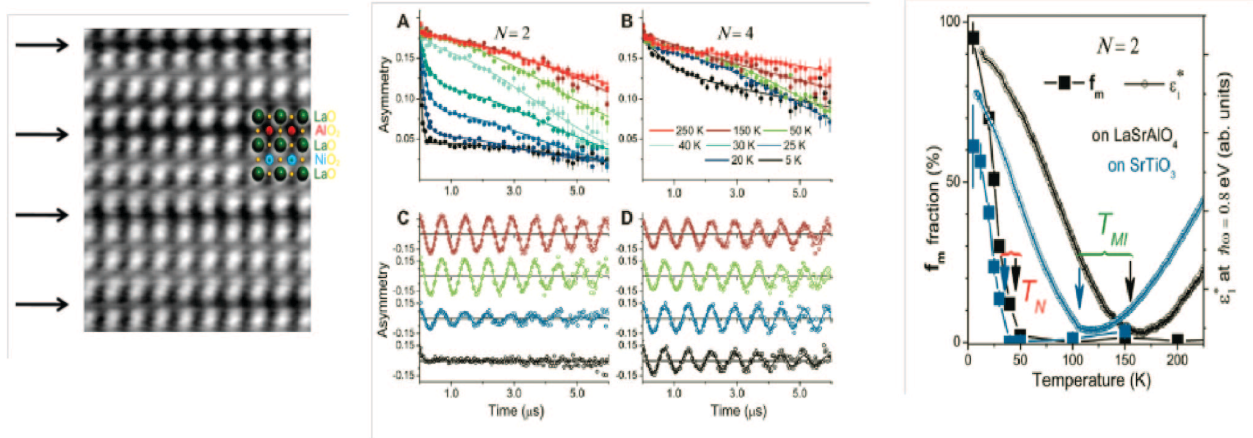


Figure III-5: μ SR study of nickel oxide superstructures- (left) A high-angle dark field TEM image of one of the samples studied by Boris *et al.* with low-energy μ SR [Boris2011]. This sample contains two unit cells of LaNiO_3 atop one unit cell of LaAlO_3 . (middle) A series of zero-field (A,B) and weak transverse field (C,D) μ SR spectra on samples with $N=2$ (A,C) and $N=4$ (B,D) layered superlattices of LaNiO_3 , grown on LaSrAlO_4 . In contrast to $N=4$, the $N=2$ samples distinctly show the onset of magnetic order in the entire volume fraction at low temperature. (right) Plots of the magnetic volume fraction from μ SR and the real part of the dielectric function for two $N=2$ samples, each as a function of temperature. The results show a sequence of static charge and spin order in these samples, rather than the paramagnetic metallic behavior seen in the bulk.

Superconductivity

Beyond magnetism, one of the most active areas of μ SR research is the investigation of unconventional superconductivity. Details about the vortex lattice in a type-II superconductor can be inferred from the distribution of local magnetic fields, measured directly in a transverse field μ SR experiment.

There is a large body of work, not only on the high-transition temperature (T_c) copper-oxide superconductors, but also iron arsenide/chalcogenide, heavy fermion, boron carbide and organic superconducting materials, among others. In each of these families, the superconducting ground state is known or thought to exist near a state containing magnetic order, and the interaction between magnetic and superconducting order parameters is a frequent research theme. With its exquisite sensitivity to both magnetic and superconducting order parameters with spatial resolution of tens of Angstroms, μ SR has been able to contribute significantly to this body of scientific knowledge.

Phase separation versus co-existence and the superconducting phase diagram

Particularly prominent in the literature are instances where μ SR has identified static or dynamic magnetic order in a material of interest and investigated phase separation or co-existence with superconductivity at the microscopic scale. The issue of phase coexistence has been addressed in a number of materials, with results that depend on the superconducting family being investigated. For example, in the hybrid ruthenate-cuprate $\text{RuSr}_2\text{GdCu}_2\text{O}_8$, the co-existence of ferromagnetism and superconductivity has been firmly established [Bernhard1999]. In contrast, in the heavy-fermion material $\text{CeCu}_{2.2}\text{Si}_2$, magnetic order and superconductivity are seen to occupy different volumes of the sample and compete [Luke1998]. Such issues are of fundamental importance and key to unraveling the complex physics underlying unconventional superconductivity. As such, μ SR studies of magnetism and the construction of phase diagrams based on this data have played an influential role in conversation surrounding many compounds.

Within the community of superconductivity researchers, μ SR is perhaps best known for its many early contributions to the exploration of the copper-oxide high-temperature superconductors, and the significant work that has followed. These contributions were made possible due to the strong signal-to-noise ratio of μ SR and the ability of the probe to gain useful information from powder samples. For example, the μ SR technique was used to identify a magnetic freezing transition at low temperatures in underdoped high- T_c superconductors shortly after their discovery [Budnick1988; Wiedinger1989; Kiefl1989] and was also the first technique to detect static magnetic order in the parent compounds $\text{Ln}_2\text{CuO}_{4-y}$ ($\text{Ln} \equiv \text{Nd, Pr, Sm}$) of the electron-superconductors [Luke1989]. μ SR was the first technique to observe incommensurate magnetic order in the so-called '1/8 compounds' [Luke1991], where superconducting transition temperature is suppressed at dopings where magnetism is stabilized. In related compounds, phase separated incommensurate order and superconductivity were observed simultaneously [A.T. Savici Physical Review B **66** (2002) 014524], and magnetic volume fraction was shown to be controllable with applied magnetic field [Savici2005]. A spin-glass phase identified in underdoped $\text{La}_{2-x}\text{Sr}_x\text{CuO}_4$ and $\text{YBa}_{1-x}\text{Ca}_x\text{CuO}_6$ [Harshman1988; Niedermayer1998] is thought to co-exist with superconductivity on the nanoscale for some range of hole doping. Coexistence of glassy magnetism and superconductivity has also been demonstrated in powder and crystals of $\text{YBaCuO}_{7.5}$ [Sanna2004; Miller2006], which is of particular significance since these materials are thought to be cleaner than their cation-doped counterparts. In the electron-doped cuprate $\text{Pr}_{2-x}\text{Ce}_x\text{CuO}_4$, random magnetic moments are found to grow into long range antiferromagnetism with application of fields as small as 90 Oe [Sonier2003].

More recently, there has been intense interest in the iron arsenide/chalcogenide family of high-temperature superconductors. These materials were discovered in 2008 and found to share much of the phenomenology seen in the widely studied cuprate superconductors, despite some qualitative differences. Almost immediately after their discovery, μ SR was quick to identify signals associated with commensurate order in the parent compounds of a number of distinct iron-pnictide families and indications of incommensuration with slight doping in some materials [Klauss2008; Kaneko2008; Aczel2008; Carlo2009; Park2009]. Many early studies suggested the macroscopic phase separation, especially in electron-doped materials [Park2009; Goko2009; Sanna2011; Laplace2012]. However, as with the cuprates, microscopic phase co-existence was eventually confirmed in a number of different iron-arsenide families [Drew2009; Marsik2010; Bernhard2012], and μ SR is playing a fundamental role in developing standard phase diagrams [e.g., Drew2009; Leutkens2009; Shermandini2011, Figure III-6]. Work continues to identify and explore the magnetic properties of new families of iron-based superconductors- for example $\text{Li}_x(\text{NH}_2)_y(\text{NH}_3)_{1-y}\text{Fe}_2\text{Se}_2$, where the superconducting T_c was seen to be enhanced through the addition of a molecular space layer between planes of superconducting FeSe [Burrard-Lucas2013]. Similar phenomenology and important connections to magnetism are being found in other exotic superconductors, such as $\text{Sr}_{2-x}\text{Ca}_x\text{RuO}_4$ [Carlo2012] or the so-called '115' heavy fermion compounds (e.g. CeCoIn_5) [Higemoto2002; Schenck2002; Spehling2009].

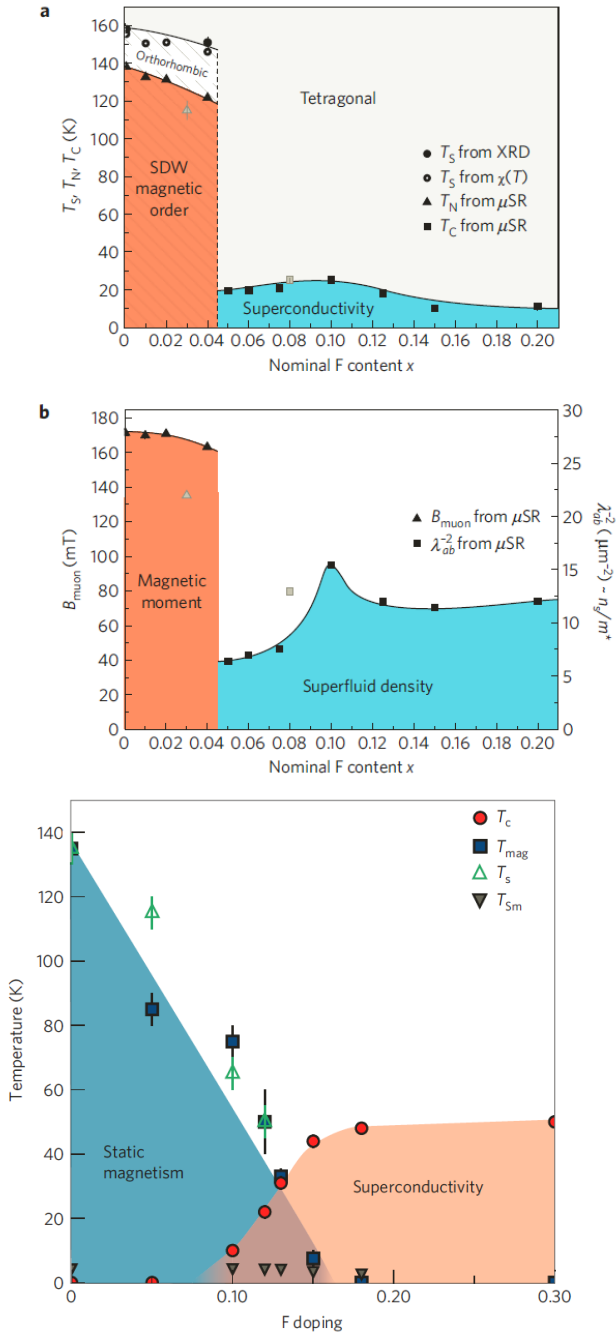


Figure III-6: Dueling phase diagrams for the iron based superconducting compounds, published in the same issue of Nature Materials in 2009. The upper is the result of a μ SR, x-ray and Mossbauer investigation of $\text{LaO}_{1-x}\text{FxFeAs}$ and seems to indicate that the transition temperature and moment size associated with a spin-density-wave order drop off precipitously with doping, before superconductivity develops [Luetkins2009]. The lower is a phase diagram resulting from μ SR, resistivity and magnetization study of $\text{SmFeAsO}_{1-x}\text{Fx}$, which seems to indicate a more gradual demise of magnetism with doping and a distinct co-existence region [Drew2009].

Penetration depth and gap symmetries

In a μ SR experiment, superconductivity is most frequently observed as large internal field inhomogeneities resulting from quantized flux lines (*vortices*) in the mixed state of a type-II superconductor when a transverse field is applied. The details of the μ SR lineshape (Fourier transform of field distribution) in this circumstance depends on the spatial arrangement of these vortices in the sample, which itself carries fundamental information about the superconducting state [Sonier2000]. In this sense, μ SR is a powerful complement to small-angle neutron scattering (SANS), which can find similar information in reciprocal space when large, clean single crystals are available.

Very common are μ SR and SANS measurements of the magnetic penetration depth, λ , in the vortex state of a superconductor. λ is an important characteristic length scale whose behavior is linked to the underlying physical mechanism of superconductivity, and can be extracted from the second moment of the field distribution when a well-ordered vortex lattice exists. A distinct advantage for μ SR over SANS in this regard is that useful information can be extracted from either powders or small single crystals, with increased sample purity and homogeneity. A series of now famous μ SR experiments [Uemura1991; Uemura1993; Niedermayer1993] performed in the early 1990's on samples of cuprate superconductors with different charge carrier concentrations established universal behavior for the variation of the superconducting transition temperature T_c with λ^{-2} in these compounds. In the London limit of type-II superconductors, λ^{-2} is proportional to superfluid density. As such, the experimental “Uemura plot”, as it is known today, is recognized by the superconductivity community as a major accomplishment and one of the key properties of high- T_c superconductors requiring an explanation by any ultimate theory (Figure III-7).

As interesting as the absolute value, are studies of the *temperature dependence* of λ , which has proven useful in determining the isotropy of the superconducting gap. For example, the observation of a linear temperature dependence by μ SR is in the early 1990's confirmed the *d*-wave pairing symmetry of the Cooper pairs in the vortex state of the high- T_c materials [Sonier1994]. In striking contrast, experiments on the iron-based high- T_c superconductors have revealed the existence of a two *s*-wave pairing gaps [Williams2009], often touted as one of the biggest difference between the two classes of compounds.

A similar study of the ruthenate superconductor Sr_2RuO_4 found no nodes in the gap, but rather evidence for a square flux line lattice [Luke2000], in contrast to the usual hexagonal lattice. With its heightened sensitivity to local fields, μ SR was additionally able to discern the onset of a weak (~ 0.5 G) time-reversal symmetry-breaking field at the

superconducting T_c [Luke1998_2]. For these reasons, Sr_2RuO_4 is now thought to contain a triplet p_x+ip_y pairing symmetry, and is considered one of the strongest candidate materials to exhibit *topological superconductivity* [Qi2011]. Time-reversal symmetry breaking fields seen with muons have similarly been used to identify exotic gap functions in heavy fermion materials $(\text{U,Th})\text{Be}_{13}$ [Heffner1990] and UPt_3 [Luke 1993], praseodymium-based superconductors $\text{PrOs}_4\text{Sb}_{12}$ [Aoki2003] and $\text{PrPt}_4\text{Ge}_{12}$ [Maisuradze2010] and noncentrosymmetric superconductors LaNiGa_2 [Hillier2012] and LaNiC_2 [Hillier2009].

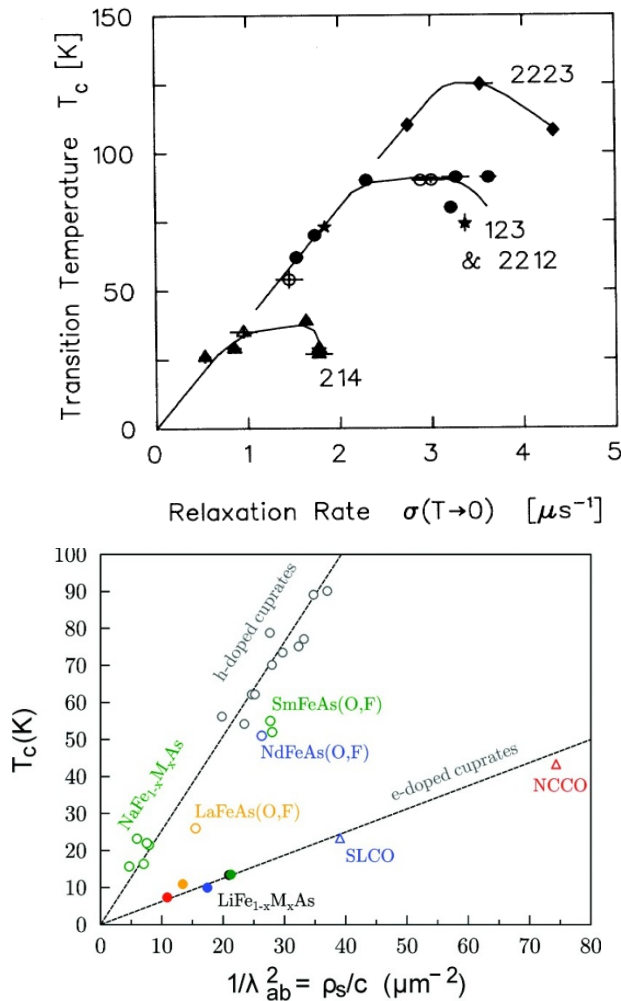


Figure III-7: (upper) The original Uemura plot, first published in 1989 [Uemura1989]. Shown is the superconducting transition temperature of several hole-doped cuprate superconducting materials versus the Gaussian relaxation rate of the μSR asymmetry. For the mixed phase of a type-II superconductor, this latter quantity is proportional to the inverse penetration depth squared. (lower) A recent version of the same plot, which also includes electron-doped cuprates and data from the new class of iron-based superconductors [Pitcher2010].

Vortex matter

In the past decade, there has been increasing interest in the flux line lattice itself as a mesoscale structure, where the vortex is seen as the fundamental building block. Muon spin rotation (μ SR) and small-angle neutron scattering (SANS) have been two very important techniques used in the investigation of the structure of vortices within the bulk of superconductors. Low-energy μ SR is also able to explore the character of vortices at surfaces. In addition to studies of the position and symmetry of vortex arrays, these techniques can be used to investigate vortex fluctuations, pinning, melting, and decomposition of the flux lines into 2-dimensional “pancake” vortices in anisotropic materials.

Vortex-lattice *melting* in a high- T_c superconductor was first observed by a group using both μ SR and SANS to study the anisotropic material $\text{Bi}_{2.15}\text{Sr}_{1.85}\text{CaCu}_2\text{O}_{8+\delta}$ [Lee1993; Cubitt1993]. The μ SR study also provided the first indication of melting into a liquid of 2-dimensional “pancake” vortices in independent layers above a crossover field. A later μ SR study has provided *solid* proof for the existence of pancake vortices in this material [Kossler1998], and a μ SR study of under- and overdoped $\text{Bi}_2\text{Sr}_2\text{CaCu}_2\text{O}_{8+\delta}$ [Balsius1999] has provided the first evidence for a *two-stage* melting transition — in which the intralayer coupling of vortices is first overcome by thermal fluctuations, followed by interlayer decoupling of the pancake vortices. Melting of the vortex lattice was clearly observed by μ SR deep in the superconducting state of underdoped $\text{YBa}_2\text{Cu}_3\text{O}_{7-\delta}$ [Sonier2000_2], whereas other techniques had only observed melting at low field near the superconducting transition temperature T_c .

A vortex line lattice in the organic superconductor $\kappa\text{-(BEDT-TTF)}_2\text{Cu(SCN)}_2$ was the first clearly identified via an investigation with μ SR [Lee1997]. Upon increasing the field a dimensional crossover in the vortex structure was observed. An additional crossover observed at low fields and high temperature was consistent with the theoretical prediction for the thermally induced breakup of vortex lines comprised of weakly coupled pancake vortices.

In recent years, μ SR has furnished a great deal of information on the shape and size of the *vortex core size* as a function of temperature and magnetic field [for a timely review, see J.E. Sonier2007, also Figure III-8]. It is now appreciated that vortex cores contain bound quasi-particle states, whose character depends on the properties of the underlying superconducting state. It has been seen in several μ SR studies of *s*-wave and *d*-wave

superconductors that the size of the vortex cores shrink with increasing applied field [Sonier1999; Kadono2001; Ohishi2002; Price2002; Sonier2004; Callaghan2005; Kadono2006], understood to result from the delocalization of highest energy bound core quasiparticle states [Ichioka1999]. It has been shown that the delocalized quasiparticle states inferred from μ SR can quantitatively explain measured transport coefficients in some *s*-wave superconductors [Callaghan2005]. In many systems, these quasiparticle interactions are even seen to drive a change in the symmetry of the vortex lattice, for example in the form of a hexagonal to square transition observed with applied field [Ohishi2002; Sonier2004; Kadono2006]. In fact, the opening angle of the vortex lattice structure is useful information and has been used to comment on the form taken by the superconducting gap in some materials [Yaouanc1998]. In case of the cuprates [Miller2002; Sonier2007_2], there is growing evidence in μ SR spectra of local antiferromagnetic correlations in vortex cores, further fueling debate about the interplay between magnetism and superconductivity in these materials.

Depth-dependent studies

As with magnetism, the advent of low-energy μ SR is providing basic and material-specific information about superconductivity in reduced dimensions. Demonstrating the relatively unique role that low-energy μ SR plays as a depth sensitive measure of fields, while studying a thin-film of $\text{YBa}_2\text{Cu}_3\text{O}_{7-x}$, researchers measured *for the first time, in 2000*, the exponential screening of an applied field at the surface of a superconductor—one of the defining characteristics of the classical theory of superconductivity and first predicted 65 years earlier [Jackson2000]. Building off this historic success, researchers later used deviations from exponential decay in a thin film of superconducting Pb to verify non-local (i.e. Pippard) effects in superconductors, also predicted over 50 years before [Suter2004, Figure III-8]. Separate studies confirmed interesting predictions for the mixed phase of superconductivity, such as the broadening of vortex core sizes at the sample surfaces [Niedermayer1999].

The power of this new probe is also being leveraged to further the ongoing debate surrounding high-temperature cuprate superconductivity- for example by identifying an isotope effect in optimally-doped $\text{YBa}_2\text{Cu}_3\text{O}_{7-x}$ [Khasanov 2004] or observing the Giant Proximity Effect in strongly underdoped $\text{La}_{2-x}\text{Sr}_x\text{CuO}_4$ films when placed near optimally-doped samples [Morenzoni2011].

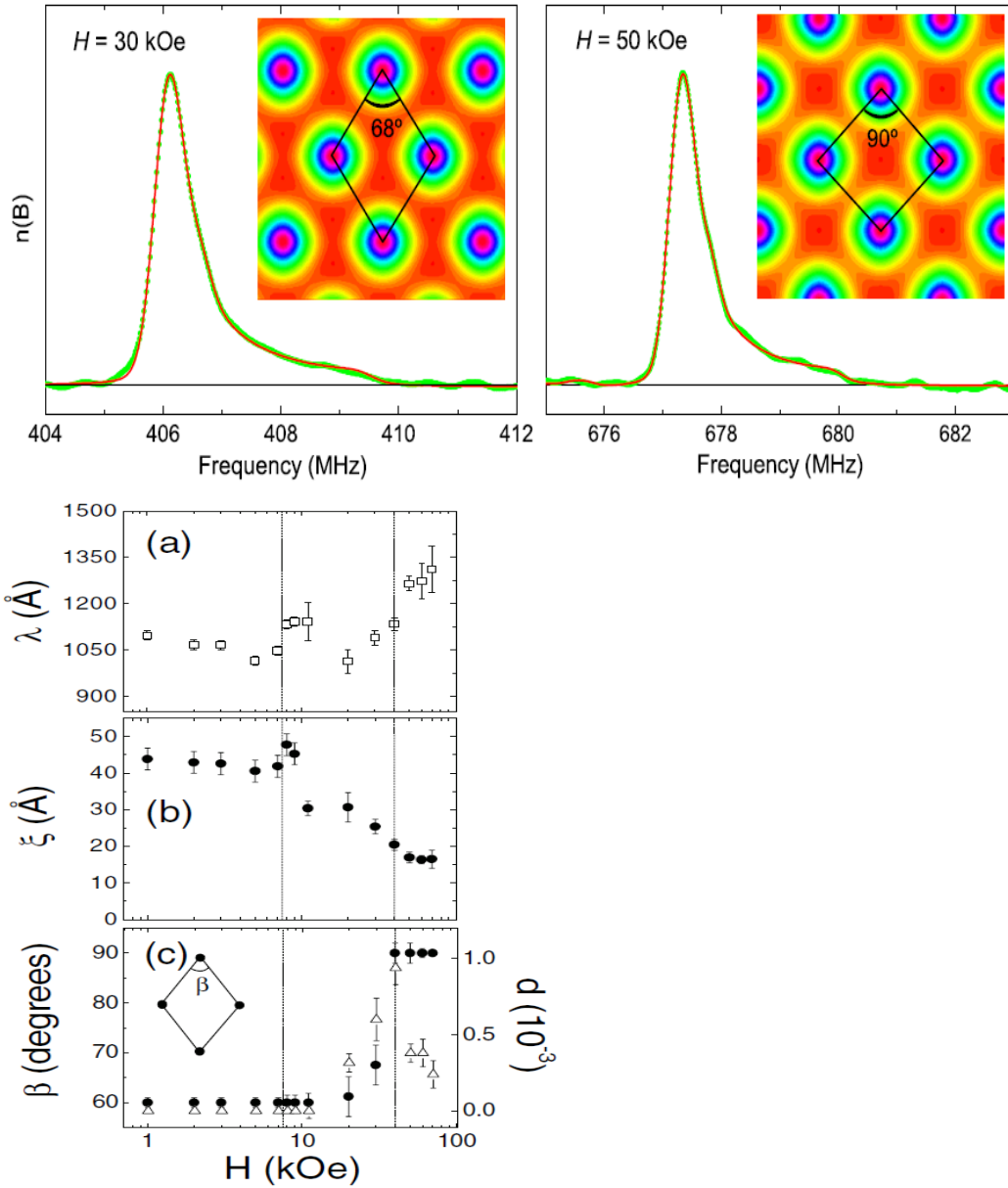


Figure III-8: (Upper) Fourier transforms of two μ SR spectra taken with $TF=30$ kOe and 50 kOe on conventional superconductor V_3Si . Green curves represent data and red fit lines Ginzburg-Landau vortex lattice models. Also shown are contour maps of the field distribution, inferred from fits. (Lower) Material parameters as a function of applied field, extracted from fits within the model. Apparent is a change in vortex lattice symmetry with applied field, accompanied by a field-induced vortex core shrinking. From [Sonier2007; Sonier2004].

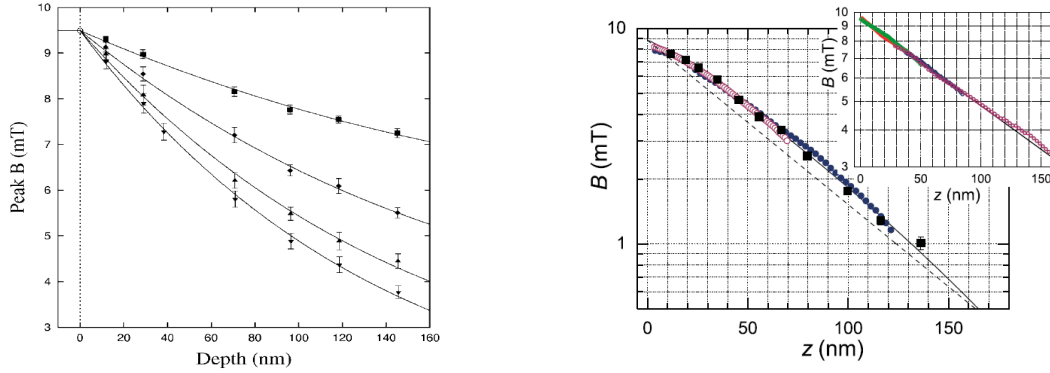


Figure III-9: (left) Low-energy μ SR measurements of the local magnetic field at the surface of the superconductor $\text{YBa}_2\text{Cu}_3\text{O}_{7.6}$ in the Meissner state. Data was taken at $T=20\text{K}$, 50K , 70K and 80K , from top to bottom. Solid lines are fits to expectations from classical theories of superconductivity [Jackson2000]. (right) Main panel shows a plot of field as a function of depth in Pb, known to be a strongly coupled superconductor, at $T=3\text{K}$ (main panel). The dotted line represents pure exponential expulsion, and deviation from this line is a signature of non-local (i.e., Pippard) effects. The same measurement for YBCO (inset) shows the field expelled exponentially at the surface [Suter2004].

Quantum Diffusion and Battery Materials

Qualitatively different from the studies above are experiments which use the muon as an *active* probe of material properties. One notable example is the groundbreaking work done using μ SR to develop theories of quantum diffusion theory, especially as it relates to light interstitials in solid state materials. The study of hydrogen diffusion in metals has been of interest for well over a century to both pure and applied science communities [Fukai1985]. Starting in the 1970's, μ SR was used to test classical theories, in which it was assumed that light interstitials diffused by hopping over barrier potentials between trapping sites. By the early 1980's, it was clear from muon studies at low temperatures that the classical theories were incomplete. The development of modern theories of *quantum tunneling* (i.e. coherent transport) of interstitial atoms in materials stems directly from efforts to understand these early μ SR experiments. With the advent of hydrogen storage technologies and battery materials which depend on the diffusion of Li^+ cations, quantum tunneling theories are of intense current interest. The muon has a mass of approximately $1/9^{\text{th}}$ the proton's mass, is available in both the positive (muon) and neutral (muonium) forms, and affords the capability to extract detailed microscopic correlation/residency times. As a result of these qualities, μ SR has and continues to provide the best and often the sole tests of these theories.

Examples can be found in the recent experimental and theoretical efforts to understand the role of dissipation (i.e., coupling the muon's quantum motion with the electronic and

lattice degrees of freedom) or disorder in assisting or limiting diffusive transport. It was understood early on that the temperature dependence of the diffusion rate of muons in materials should vary as $T^{-\alpha}$, with $\alpha \sim 9$. However, experiments on simple metals revealed much smaller values of $\alpha \sim 0.6-0.7$. This was understood as an electron drag effect, where the positive muon moves as a screened charge interacting with both host phonons and electrons, and quantum tunneling processes are hindered by the inability of the electronic screening cloud to follow the muon adiabatically. The integral role of host electrons in the diffusion process was ingeniously demonstrated by a μ SR investigation of aluminum at low temperatures. Originally identified as a material with modest diffusion rates, papers by Karlsson et al. and Kadano *et al* demonstrated that diffusion significantly increased when the material was cooled below its superconducting transition, where electron interactions are "gapped out" and rendered ineffective. They further showed that diffusion can again be hindered in the presence of a modest field, when the delicate superconducting state is destroyed [Karlsson1995; Kadono1997, Figure III-10].

Experiments that probe the interactions of the tunneling particle (*viz.* neutral muonium in an insulator) with either dynamic phonon or static structural/impurity types of disorder constitute another class of μ SR experiments. A study of solid N_2 [Storchak1994] is the first confirmed case of the two-phonon mechanism for quantum diffusion of muonium (Mu), showing the previously predicted T^7 temperature dependence in the low- T regime and a T^{-7} law at intermediate T . Subsequent work on other materials has successfully used neutron scattering measurements of low-energy phonons to predict tunneling rates measured in μ SR experiments. The localization of a tunneling particle by static disorder is also revealed by the above work, a theme further explored in alkali halides such as KCl:Na [Kadono1996]. There it was found that for modest impurity concentrations the crystal volume is characteristically (for long range inhomogeneity) divided up into two parts, reflection portions of the sample near and far from "pinning" sites.

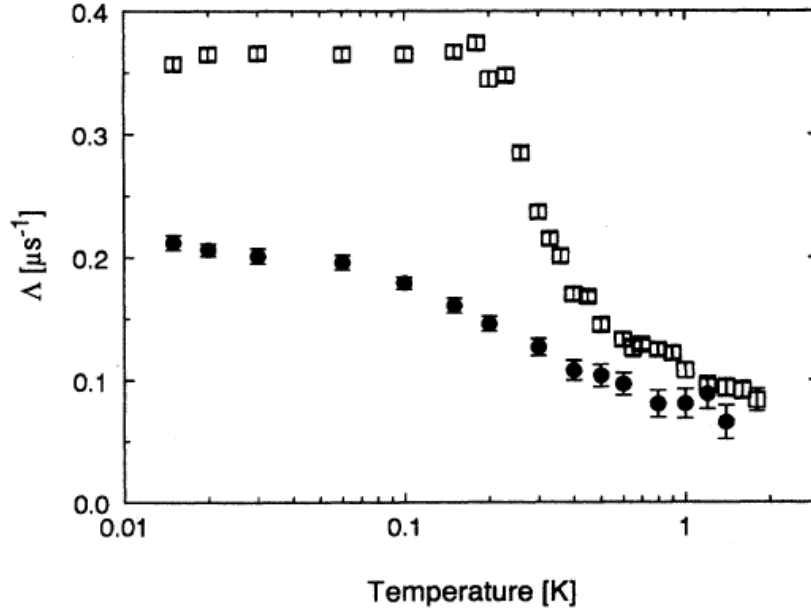


Figure III-10: The linewidth (depolarization rate) as a function of temperature for a sample of Li-doped aluminum, which superconducts at 0.5K. Data for the superconducting state (open symbols) are contrasted with data taken in the presence of a weak transverse field (filled symbols), which acts to drive the system back to a normal metallic state. Depolarization rate is related to muon hopping rate, and this data provides strong evidence that drag effects associated with conduction electrons (gapped out in the superconducting state) play a dominant role in diffusion processes in metals at low temperature. From [Karlson1995].

μ SR-inspired theories of diffusion have found immediate application in the search for reliable hydrogen storage materials, of importance to the development of commercial fuel cell technologies. Furthermore, μ SR has been able to comment in a constructive way on the viability of several *next-generation* storage materials, beyond simple hydrogen absorbing metals. One example is Ti-doped sodium alanate, identified recently as a compound with favorable storage and kinetics characteristic for vehicular applications [Bogdanovic1997]. The observation of muon spin oscillations in this non-magnetic materials recently led Kadono *et al.* to suggest that muonium (and by extension hydrogen) forms a radical H-Mu-H \cdot bond when at interstitial sites, and it is the forming and breaking of this bond which is the rate-limiting step in hydrogen kinetics in this material [Kadono2008]. Another study identified similar bonds in borohydrides $M(\text{BH}_4)_2$ ($M \in \{\text{Li}^+, \text{Na}^+, \text{K}^+\}$) and found a distinct correlation between the frequency of H-Mu-H formation and the electronegativity of M^+ . This observation indicated that μ SR can be used as a microscopic indicator of the stability of super-hydrogenated $M(\text{BH}_4)_2$ states [Sugiyama2010]. Perhaps most surprisingly, one very recent μ SR study has suggested the formation of interstitial hydrogen (CH_2) groups in sheets of graphene (single-layer

graphite) and stable up to 1250 K, identifying this miraculous material as a potentially cheap and effective future hydrogen storage material [Ricco2011, Figure III-11].

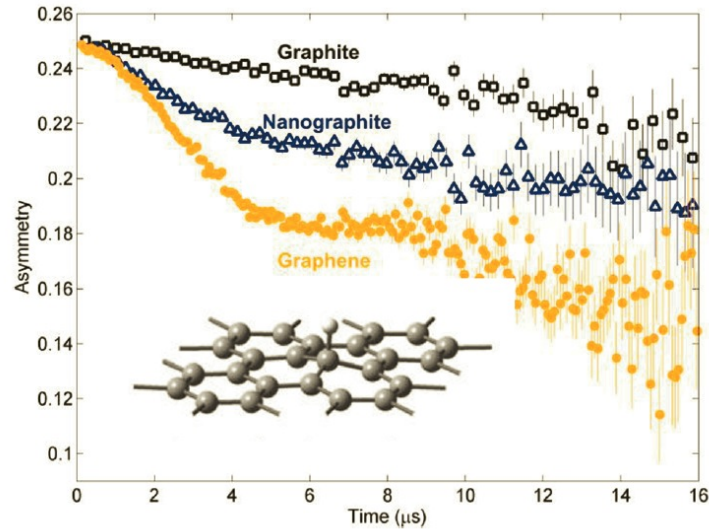


Figure III-11: Plots of muon decay asymmetry for three different carbon systems. Of particular note is the clear precession which emerges when the graphite is reduced to a single layer (i.e. graphene). Like a hydrogen atom, on an ideal graphene layer muonium gets chemisorbed, as shown in the inset. From [Ricco2011].

Tangentially related are μ SR investigations of lithium-based compounds, which have found a role in the last 15 years as cathodes in the newest generation of reliable rechargeable batteries. In these systems, the operation of the battery depends on the flow of Li^+ cations between two insertion electrodes, and the diffusion constant of this cation is of primary importance. Despite the long research history on Li-ion batteries, a proper characterization of lithium diffusion in these materials was only measured in 2000 using μ SR. Through a combination of zero-field and longitudinal-field μ SR measurements on the spinel material $\text{Li}_x[\text{Mn}_{1.96}\text{Li}_{0.04}]\text{O}_4$, Kaiser *et al* were able to measure characteristic hopping rates and ideal "charging temperatures" for two different values of x [Kaiser2000]. This was possible since the muons in these systems hydrogen bond to atomic O^{2-} and are rendered immobile for temperatures of interest. In recent work on the quasi-2D system Li_xCoO_2 [Sugiyama2009] and the phospho-olivines [Sugiyama2012], Sugiyama *et al* have developed μ SR as a powerful tool for measuring Li^+ self-diffusion constants, complementing conventional NMR measurements which are complicated by the presence of transition-metal moments [Tomeno1998; Nakamura1999].

Semiconductor Physics

Introduction of hydrogen in the process of semiconductor fabrication is a very common method of passivating active electrical impurities. The microscopic details of how this occurs are difficult to access with standard magnetic resonance techniques due to the low concentrations of hydrogen typically used. Conversely, the use of muon as a proxy for a light isotope of hydrogen allows researchers to explore the effects of a single dopant in semiconductor samples. In many cases, μ SR studies has been the primary source of detailed information on the various charge states and dynamics of isolated hydrogen in semiconductors, often confirmed *a posteriori* with alternate methods. Early μ SR investigations of semiconductors identified the static properties of the muon and its paramagnetic state muonium (*i.e.* with its bound electron) charge states. More recent work has focused on ascertaining the dynamics of the charge states and/or site migrations of this hydrogen-like impurity. Current studies focus on a broad range of technologically important semiconductors, such as amorphous silicon where hydrogen mobilization is the major cause of solar cell degradation.

The results of μ SR studies in semiconductors are widely recognized by researchers who investigate defects to be the main source of experimental information on *isolated* hydrogen in bulk semiconductors. Hydrogen easily incorporates into semiconductors, such as during crystal growth, film deposition, or device processing steps, and forms stable bound states with intentional dopants, defects and other types of impurities. These interactions result in a dramatic, and often unexpected, modification of the electrical and optical properties of the host. Hydrogen has a high diffusivity and reactivity with other defects, and is usually studied minutes or even days after it is introduced into the sample. Hence, although it is almost always detected as part of a complex with other defects, direct information on the structure of isolated hydrogen is virtually non-existent. In particular, only a single isolated hydrogen center has been characterized, the AA9 center in silicon, first detected using EPR. Indeed, most of the experimental information on isolated hydrogen comes instead from μ SR studies of muonium ($\text{Mu} \equiv \mu^+e^-$), which is, in essence, a light hydrogen-like atom [Cox2009; Patterson1988; Kiefl1990; Chow1998; Lichti1999].

The majority of experiments on the rich physics of muonium in semiconductors falls into one of two categories: (1) investigations of the electronic structure of muonium in its three charged states, Mu^0 , Mu^+ and Mu^- or (2) studies of the "dynamics" of these centers.

Electronic structure studies of muonium are concerned with determining the crystalline site of the muon, the arrangements of neighboring atoms, and the strength of the interactions between the muon and its surroundings. Thus far, there have been over 20 distinct muonium centers identified in tetrahedrally coordinated Group IV, Group III-V

and Group II-VI semiconductors [see, e.g., Gil1999]. These states are denoted as Mu_{BC}^0 , Mu_{BC}^+ , Mu_{T}^0 and Mu_{T}^- . The now standard notation labels the charge state of muonium and its general location in the lattice, with the subscript T symbolizing the tetrahedral interstitial site and BC the bond-center location. These experiments and their comparison with theory were crucial in emphasizing the need to include lattice relaxations in calculations of hydrogen (and also other defects) in solid state materials, and continue to be a stringent test of the many theoretical calculations regarding the electronic structures of hydrogenic centers. Furthermore, since the hydrogen analogs of many of the muonium centers are expected to exist in semiconductors, they form the fundamental building blocks upon which any model of hydrogen dynamics must be built.

The second important research area, that of muonium dynamics, include studies of muonium diffusion, cyclic charge state changes, spin exchange scattering with free carriers, interconversion between the various muonium states, and more recently, reactions with impurities in the material. These investigations are clearly crucial to a detailed understanding of hydrogen motion in the crystal, its reactions with free carriers, and ultimately, with defects in the material. Two examples illustrate this point: The first is the observation of the dramatic difference [Chow1996] in the diffusion rates of Mu_{T}^0 and Mu_{T}^- , such as in GaAs, where Mu_{T}^- is moving about ten orders of magnitude slower than its neutral counterpart. These results argue that although the positive and negative charge states of hydrogen are the dominant ones in p-type and n-type materials respectively, the actual diffusion of hydrogen may well be controlled by the transient H^0 species present in the material at high temperatures.

The second example concerns the dynamics of transitions between muonium states: the most detailed model of these transitions exist for muonium in silicon [Hitti1999; Hitti1997; Kreitzman1995]. The transition rates obtained from these measurements compare well with the few available analogous measurements on isolated hydrogen, hence indicating (i) that the conclusions from muonium investigations should be transferable to hydrogen and (ii) that any model that relies on only a single hydrogen species at high temperatures is very likely to be inadequate.

Finally, it should be noted that μSR is poised to take a defining role in the characterization of films and heterostructures constructed using *magnetic* semiconductors, of intense interest to researchers of spintronics. Spintronics (or spin-electronics) involves the control and manipulation of spin instead of charge degrees-of-freedom in solid state systems, thought to be a means of increasing processing times, non-volatility, and reduced power consumption in electronic circuitry [Zutic2004]. In this context, μSR is making valuable contributions to the characterization of dilute magnetic semiconductors, such as $(\text{Ga}_{1-x}\text{Mn}_x)\text{As}$. In these materials, magnetic cations are doped

into III-V semiconductors. In one recent study [Dunsiger2010], the unique characteristics of low-energy μ SR allowed for probe muons to be implanted in a thin film of $(\text{Ga}_{1-x}\text{Mn}_x)\text{As}$ and determine that the known ferromagnetic ground state was present in 100% of the sample volume, settling a lingering question of whether such a homogeneous state was even possible in these systems [e.g. Storchak2008]. The character of the magnetic ground state also seemed unaffected by the metal-insulator transition on the doping axis, prompting a re-evaluation of the theoretical models being used to discuss these compounds. In a separate study [Deng2011], similar conclusions were reached about the volume fraction of ferromagnetic order in bulk magnetic semiconducting compound, $\text{Li}(\text{Zn},\text{Mn})\text{As}$ confirming theoretical prediction [Masek2007] and opening up new avenues of research.

On a different tack, Drew *et al.* have also shown the usefulness of low-energy μ SR as a near unique, depth-resolved measure of the spin polarization of charge carriers within *buried* layers of real devices [Drew2008, Figure III-12]. In this study, researchers implanted probe muons at different depths in a fully functional spin valve device, made up of a spacer layer of organic semiconductor tris-(8-hydroxyquinoline) aluminum (Alq_3) between two ferromagnetic electrode layers. By measuring the shape of the local magnetic field distribution in the presence and absence of a spin-polarized current and as a function of depth, they were able to get a quantitative measure of the spin diffusion length, cleanly separated from interface effects. By correlating their data with bulk magnetoresistance measurements at different temperatures, they conclusively showed that spin diffusion is a key parameter of spin transport in organic materials. Similar studies are now being used to explore new device concepts for future spintronics applications [Schulz2010].

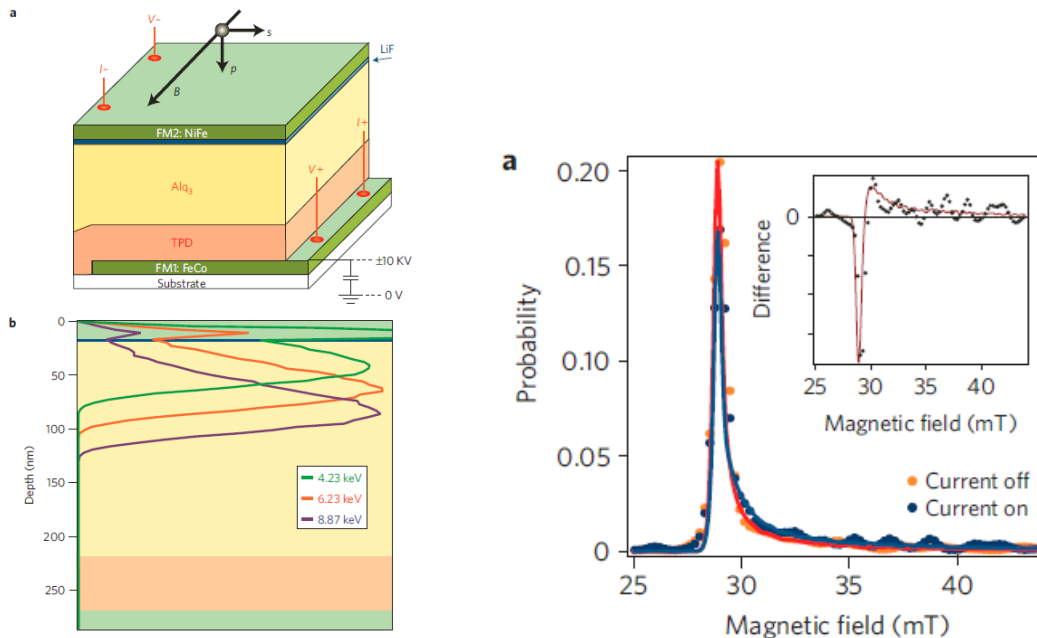


Figure III-12: (left) Schematic diagram of the spin valve system investigated by Drew *et al.* (top), and the depth profile of implanted muons with different initial energies (right) An example spectrum taken with 6.23 keV muons in the presence of a 29mT applied field. Data with a current density of 0 and 3mA are shown in red and blue, respectively. Circles show small, but statistically significant difference between the two datasets. Lines are the result of model calculations for a dipolar field distribution due to rough interfaces and due to current-induced injection of polarized spin carriers. The small oscillation apparent in the data is understood as a finite size effect. From [Drew2009_2].

III.2.2 Chemistry

Applications of muons in chemistry are mostly related to hydrogen atom and free radical chemistry. When a positive muon stops in a non-metallic material it binds an electron to form the atom muonium (Mu). Since the reduced mass of Mu is close to H, their atomic properties are very similar and Mu can be considered a light isotope of hydrogen. Reaction of Mu with an unsaturated molecule results in a free radical incorporating a muon in place of a proton. Thus free radical properties and reactions can be studied by utilizing Mu as an isotopic tracer. Applications of muonium range from the study of kinetic isotope effects in fundamental gas-phase reactions to the use of Mu as a probe of chemistry under extreme conditions, such as those in the primary cooling-water cycle of a nuclear reactor or the high pressure/temperature reaction vessel of a facility designed to destroy hazardous waste. A key aspect of such studies is that Mu can be (and has been) studied under conditions not accessible by more conventional H atom and free radical studies.

An example of free radical chemistry involving muonium is the study of the chemistry of guest molecules inside gas hydrates similar to the infamous “ice crystals” that were involved in the Deepwater Horizon oil rig disaster in the Gulf of Mexico. Flames and explosions propagate through free radical reactions, yet almost nothing is known about the diffusion and interactions of atoms and radicals through the cavities of gas hydrate crystal structures. An experiment at TRIUMF has recently detected and characterized for the first time organic free radicals in clathrate hydrate structures at close to ambient temperatures.

The most fundamental muonium chemistry program is the work of Fleming et al. on gas-phase kinetics [Fleming1976; Reid1987; Gonzalez1989]. The data produced in these experiments are invaluable to theorists working in the area of chemical reaction dynamics, either because they are more precise than equivalent data on H atom reactions, or because prediction of Mu/H kinetic isotope effects is easier than calculation of absolute rate constants. In more recent work the Fleming group have extended the bounds of H + H₂ studies by employing muonic helium ⁴He μ as a heavy hydrogen isotope [Fleming2011]. A general interest article in Science [Fleming2011_2, Figure III-13] generated much media interest and editorial commentary in science magazines such as Nature News, New Scientist and Chemistry World.

A more technological application of muonium chemistry involves measuring Mu reaction rates in supercritical water. This is needed because accurate modeling of aqueous chemistry in the heat transport systems of pressurized water-cooled nuclear reactors (PWRs) requires data on the rate constants of reactions involved in the radiolysis of water. Unfortunately, available experimental data do not extend to the high temperatures used in current PWRs, typically around 320°C; and the next generation design employs higher, supercritical temperatures (~650°C). It has been common practice to extrapolate experimental data on diffusion coefficients and rate constants from their measured ranges (mostly less than 200°C), but it would be dangerous to rely on this for the supercritical regime [Ghandi2003]. Furthermore, experiments at TRIUMF have shown that bimolecular rate constants exhibit extreme non-Arrhenius behaviour, with a maximum followed by a minimum as the temperature rises past the critical point [Percival2007].

Muonium-substituted free radicals were first detected by μ SR in 1978 [Roduner1978], but full characterization of muoniated free radicals requires the complementary technique of muon avoided-level crossing resonance (LCR) [Kiefl1986, Percival1987]. LCR makes possible the determination of nuclear hyperfine constants other than that of the muon, providing key data for radical identification and thence, for example, analysis of intramolecular dynamics [Percival1988, Yu1990]. A recent example is the study of the free radical reactivity of novel low-valent organosilicon, organogermanium, and organophosphorus compounds [McCollum2009; West2010; Percival2011; Percival2012].

Such materials are at the forefront of modern inorganic chemistry, mostly because of their applications in the design of catalysts (e.g. the work of Chauvin, Grubbs and Schrock, Nobel Prize in Chemistry 2005).

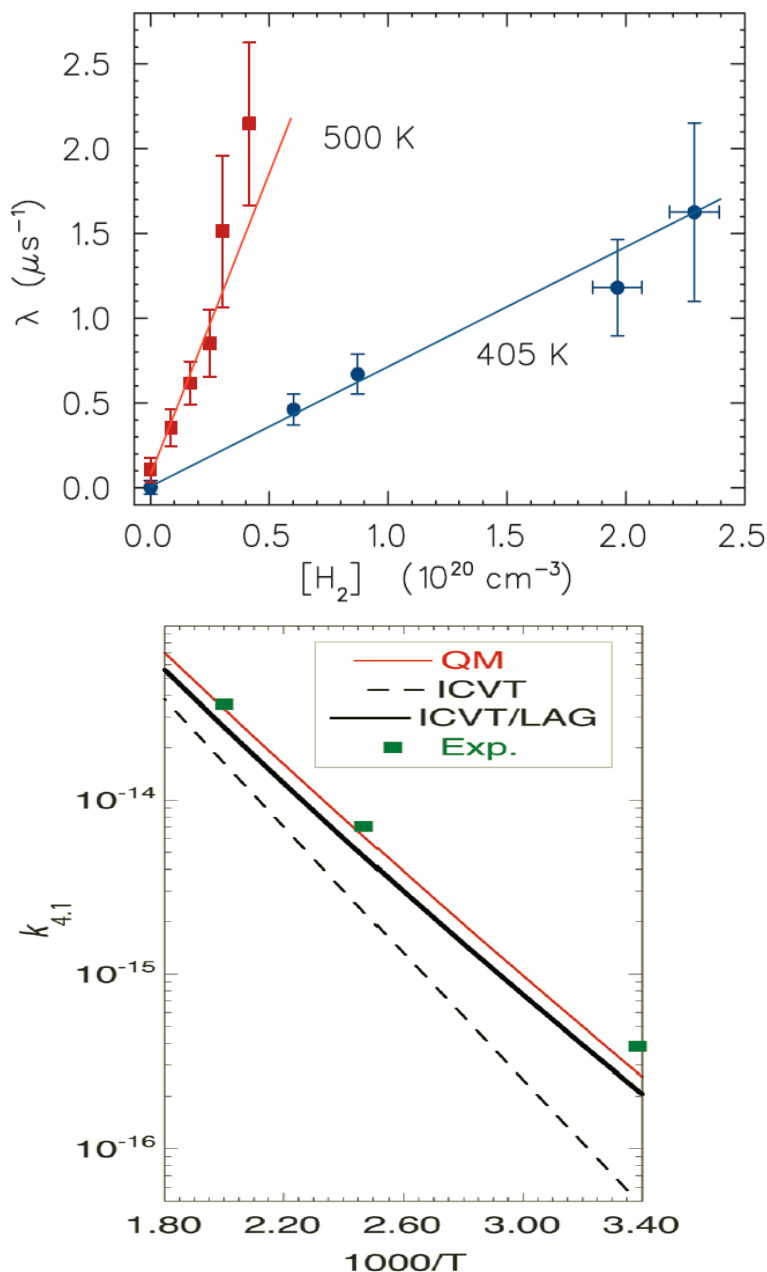


Figure III-13: Data from the study of Fleming et al., wherein researchers provided an unprecedented test of chemical kinetic theories through the use of muonic helium $4\text{He}\mu$ as a heavy hydrogen isotope (denoted 4.1H). The upper panel shows measured relaxation rates versus concentration of H_2 at two different temperatures. The lower shows rate constants of the $4.1\text{H}+\text{H}_2$ reaction, extracted from slopes in the previous plot, as compared to expectations from theory. From [Fleming2011_2].

III.3 Techniques of Muon Spin Rotation

III.3.1 Brief Historical Summary

The technique of muon spin relaxation, rotation or resonance, known collectively as μ SR, was first suggested in an historic 1957 paper in *Physical Review* by Garwin, Lederman and Weinrich, in which parity non-conservation in the weak decay of the muon was demonstrated. These authors wrote that "it seems possible that polarized positive and negative muons will become a powerful tool for exploring magnetic fields in nuclei ..., atoms and interatomic regions." Pioneering efforts at the old cyclotron facilities (LBL, SREL and NEVIS) spawned developments in the technique and its scientific reach. Attempts to realize the original vision of Garwin et al. on a practical scale - where high data rates with relatively clean backgrounds would be available - would have to await construction of the high-intensity meson factories at LAMPF (Los Alamos, USA, 1972), SIN (now PSI, Villigen, Switzerland, 1974) and TRIUMF (Vancouver, Canada, 1974), which could deliver high luminosity muon beams. A major breakthrough occurred in 1985 when Bowen *et al.* built the first 100% polarized surface muon beam (originally called an Arizona beam) at LBL.

The vision of Garwin et al. has been carried out in Canada, Switzerland, the UK (ISIS/RAL) and Japan (first at KEK and now at J-PARC). There is a plan to construct a facility in South Korea (RISP). All existing facilities are heavily subscribed, and must reject many good proposals. There has been no capability for experiments utilizing μ SR in the United States since the closure of the LAMPF muon facility in the 1990's.

III.3.2 Beams and timing structures

Types of μ SR beams

The production of muons appropriate for μ SR begins with pion production in a proton beam. Pion decay to polarized muons is common to all forms of μ SR beams. The polarization of the muons is a rather significant application of the fundamentally parity-violating nature of the weak interaction.

Surface muons are produced by the decay of these pions after they have come to rest in the target material. The low energy beams of polarized muons produced are collected by magnetic optics and transported to the sample stations, with appropriate care being taken to maintain the polarization which is the essence of the technique.

Low Energy Muons, (LEM)

In this technique, a beam of surface muons of kinetic energy 4 MeV are cooled to quasi-thermal energies of 1-30 keV. There are two methodologies currently in use or under investigation. In the first, the surface muons are directed onto a moderator, typically a thin metal plate covered with a layer of a solid noble gas. The emerging muons have been shown [Morenzoni1994; Morenzoni2000] to retain a high degree of polarization, and the technique is in regular use at the PSI μ E4 line.

A second methodology relies on resonant laser ionization of muonium created by surface muons in a moderator. This technique is used at pulsed sources such as ISIS and J-PARC, and creates a beam of muons with selectable energies in the approximate range 0.1-1.0 keV, with very good energy precision. The overall polarization of the beam is less because of depolarizing interactions in the muonium atoms, which dilutes the available asymmetries.

Decay-in-Flight Muons

Lastly, muon beams created by the decay-in-flight of pions produce muons which can penetrate containers, and are thus optimized for studies of chemical or high pressure phenomena. An example of such a beams is μ E1 at PSI, with available muon momenta up to 125 GeV/c. Such a beam is likely to be an attractive option for Project X and will be the subject of further studies. It is not part of the design concept outlined in this document.

Time structures for experimental μ SR

In *conventional continuous (CW) μ SR*, the arrival of a muon at the sample serves as a start signal to a fast timing circuit, with the stop signal being provided by detection of the decay positron from the embedded muon – see Figure III-14. Because of the need to associate each detected positron with one and only one specific stopped muon (pile-up rejection) , this technique is traditionally limited to muon input rates of approximately 50 kHz. Another way of thinking of this is that only one muon at a time is accepted and allowed to decay.

To increase the rates of detected events, and to optimize experiments with existing accelerators, *pulsed μ SR* may be used. In this technique, the time resolution is the convolution of the pulsed beam structure with the spread caused by the 26 ns lifetime of the parent pion. No attempt is made to determine the individual start times of arriving muons at the sample. This method gives increased statistics and shorter data-taking times,

but has certain limitations when large internal or external magnetic fields cause rapid precession of the embedded muon spins.

As already noted, conventional μ SR is limited to a single detected muon at a time. In addition, there are backgrounds associated with muons stopping near the experimental sample being studied. This background limits the sensitivity of the technique. An elegant solution to this problem has been developed [Abela1999], referred to as *MORE* (Muons on Request). In this system, fast electrostatic kickers send muons to each experiment only when it signals its readiness to accept a pulse, hence limiting the exposure of the equipment to spurious muons. This technique can be very advantageous, and is expected to be implemented in the relevant parts of the proposed Project X system.

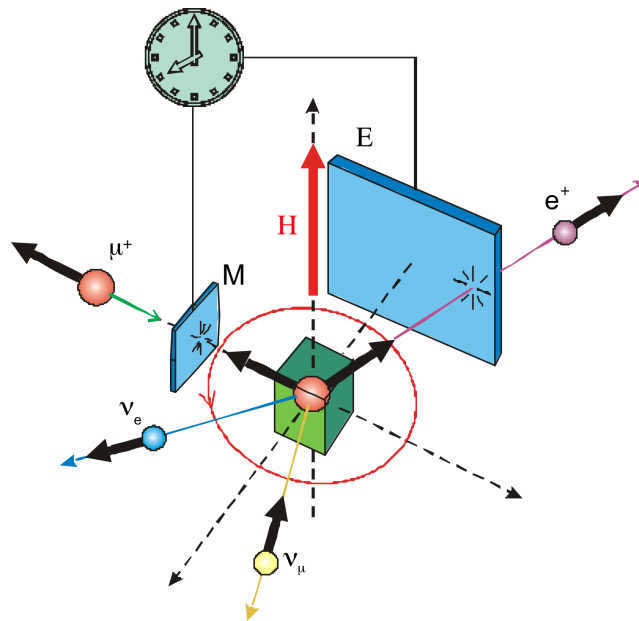


Figure III-14: Illustration of the timing setup for conventional μ SR

III.4 World Facilities, Capabilities, and Needs

At the time of this writing (2013) there are four μ SR facilities in operation worldwide: two in Europe (PSI and ISIS), one in North America (TRIUMF), and one in Asia (J-PARC). Two facilities (PSI, TRIUMF) are based on the pseudo-continuous muon sources, while ISIS and J-PARC are pulsed sources. Both continuous and pulsed beams have their pros and cons as discussed in the previous section. Key parameters of the existing facilities are summarized in the table below. A discussion of the individual facilities follows. All of the facilities are heavily used by physicists from all-over the world with a significant ($\sim 20\text{-}30\%$) US-based researcher fraction.

Facility	Muon beams	Time structure	Beam parameters	Upgrade plans
PSI	High energy (4-50 MeV), surface (4 MeV), low energy (0-30 keV)	Pseudo-continuous (CW), MORE available	600 MeV, 2.2mA \cong 1.4×10^{16} protons/sec $\sim 6.5 \times 10^8$ surface μ^+ /sec at the most intense beamline LEM: 1.5×10^8 μ^+ /sec, 4500 μ^+ /sec to sample	N/A
ISIS	High energy (20-120 MeV/c) surface (27 MeV/c)	Double pulse width ~ 80 ns separated by 300ns, repeats every 20 ms (50 Hz)	800 MeV protons, 200 μ A, 2.5×10^{13} protons/pulse surface (27 MeV/c): 1.5×10^6 μ^+ /sec decay (60 MeV/c): 4×10^5 μ^+ /sec, 7×10^4 μ^- /sec	N/A
TRIUMF	High energy, surface	Pseudo-continuous (CW)	Cyclotron, $1.5-2 \times 10^6$ μ^+ /sec	N/A
J-PARC	High energy, surface	Pulsed, ~ 50 ns pulse every 20 ms	Cyclotron, 1.8×10^6 μ^+ /sec (2009) at 120 kW, planned 1.5×10^7 μ^+ /sec at 1 MW	3 more beamlines under construction (one is low energy muons)

Table III-1: Worldwide μ SR facilities operational today.

Paul Scherrer Institute (PSI), Switzerland

Paul Scherrer Institute is a leading Swiss research institution with multiple facilities including neutron source, synchrotron light source, and muon source. There are 6 μ SR instruments in 5 beam lines and diverse sample environments (17 cryostats, 2 furnaces, special setups for pressure, photon irradiation, E-Fields). The personnel at the μ SR facility comprises 9 staff (tenure and tenure track), 4 postdocs, 5 PhD students, and ~ 3 technicians and computer support staff.

For the Laboratory for Muon Spectroscopy (LMU), typically there are 360 visits/year, ~200 new proposals, >700 beam days for users. The oversubscription factor is 2 to 3.5.

ISIS, UK

The ISIS pulsed neutron and muon source at the Rutherford Appleton Laboratory in Oxfordshire, UK, is a world-leading center for research in the physical and life sciences. Recent proposal rounds for the facility gave the following structure:

- 19 different countries (UK + 11 European + 7 outside Europe)
- 67 separate research groups
- 738 days applied for: 417 available (1.8 oversubscription)
- ~35% of applicants are regular neutron source users

TRIUMF, Vancouver, Canada

For muon spectroscopy TRIUMF has multiple beamlines, 7 spectrometers, 7 cryostats, 2 furnaces. Recently the facility has added two new beamlines (M9A, M20). The facility has beta-NMR with beam time extremely limited (~ 1-2 weeks/year). Staffing includes 2 FTE from TRIUMF and 6 FTE on research grants.

J-PARC, Tokai, Japan

The MUSE facility D-line is operational, with 3 more beamlines under construction. One is low-energy (U-line) and is commissioning. At J-PARC, low energy muons are intended to be produced by a laser-based technique. Figure III-15 compare beam requests to beam availability over the last five years.

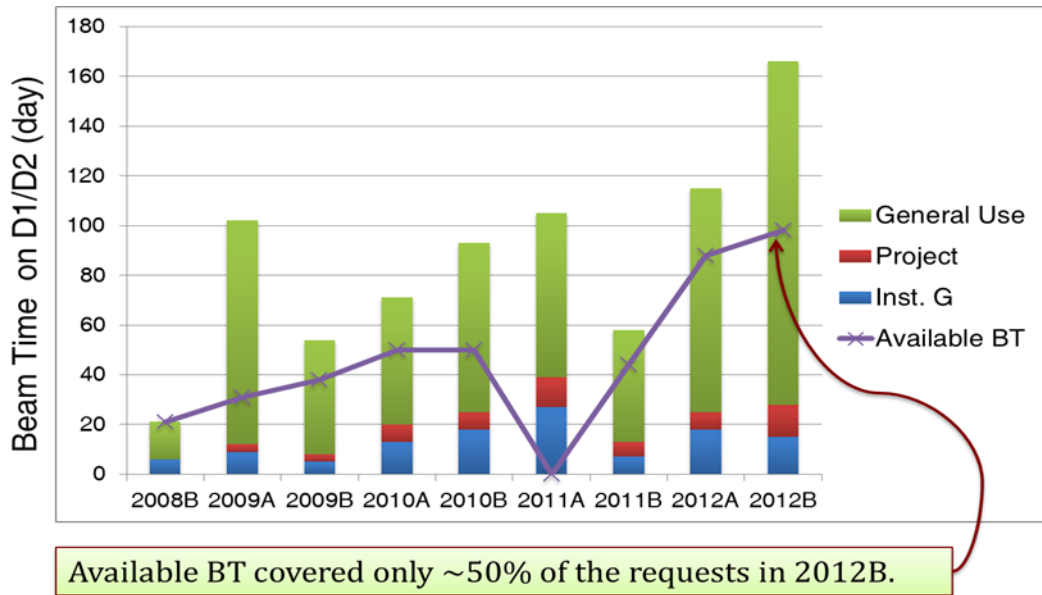


Figure III-15: Experimental requests at J-PARC D-line μ SR facility [Kadono2013]

III.4.1 Overview of current and expected needs

Both pulsed and CW μ SR facilities are in high demand as evidenced by an average factor of 2 overbooking at all of the facilities with as high as 3.5 factors reported at PSI for low energy muons. Therefore, another state-of-the-art facility is likely to be of high international demand even without extending the existing user base. If the new facility is beyond state-of-the-art it is expected to be of extremely high demand.

Even though mesoscale phenomena at surfaces and interfaces is one of the fastest developing branches of the condensed matter physics and material science, there is only one low energy muon facility in operation world-wide (PSI), and one more commissioning. An obvious need exists to extend this application of μ SR.

III.4.2 Considerations specific to North America

The USA represents the world's largest condensed matter physics community with a current share of about 20% of all μ SR experiments worldwide. However, no state-of-the-art μ SR facility is present on the US soil. World demand for this technique is expected to be high, strengthening the need for national expertise. There is a high degree of complementarity with neutron scattering techniques as discussed in section (A). The implementation of a LEM facility will provide capability never before seen in the United States.

III.5 Technical Capabilities of Project X for μ SR

III.5.1 Stage 1 Project X and μ SR

The technical capabilities of Stage 1 Project X have been discussed in Part One of this book. For the purposes of this document we are primarily interested in 1) the extreme *flexibility* in timing structure offered by Project X, and 2) the *high power* available at 1 GeV in a quasi-CW configuration of bunches. As we will see in the following, it is possible to exploit these features of the accelerator complex to create a user facility for μ SR which provides all the available technologies for experimenters, often in a way which can be reprogrammed to adjust to technological developments or scientific needs. This will expand the scientific capacity of the complex in a way which benefits the U.S. scientific program with special emphasis on the needs of the DOE/Basic Energy Sciences user community. In this section we will review the unique timing structures available at Project X, and give estimates for the intensity of the muon source(s) that can result from exploitation of the accelerator.

III.5.2 Beam Structure

We propose a two-pronged beam structure for μ SR. For the purposes of LEM μ SR the achieved efficiencies of the thermalization process are small, – hence the total beam power is a relevant figure of merit. For this purpose we propose to add a surface muon target and associated beamlines for LEM in the high-power beamline discussed in Volume One of this book. Such beamlines typically consume 10% of the available proton power, a parameter that can be tuned by detailed target design. Current or future LEM technologies can be used with the surface muons to create the desired thermalization. The needs of the user community must determine the exact configuration of beamlines.

Independently of the spallation beamline, we propose a set of μ SR beamlines which use low-power targeting. By programming the high-frequency chopper at the low-energy end of the Project X Linac, we can produce the beam structure shown in Figure III-16. This structure can simultaneously serve the needs of the spallation program, the muon experimental program, and μ SR. The μ SR pulses are groups of pulses separated by 24 ns. Repeating the structure every 5 μ s gives the possibility of using a series of programmable kickers [Abela1999] to separate the resulting surface muon beams to service 4 end stations with a repetition rate per station of 50 kHz (20 μ s between pulses). The number of pulses given to each endstation per 20 μ s interval is programmable, and the endstation receiving each of the 4 independent pulse trains can also be selected by

programming the sequence of kicker pulses. The combination of programmable pulse structure and selectable endstations gives a high, perhaps unprecedented, level of flexibility to the facility. A possible overall layout is shown in Figure III-17.

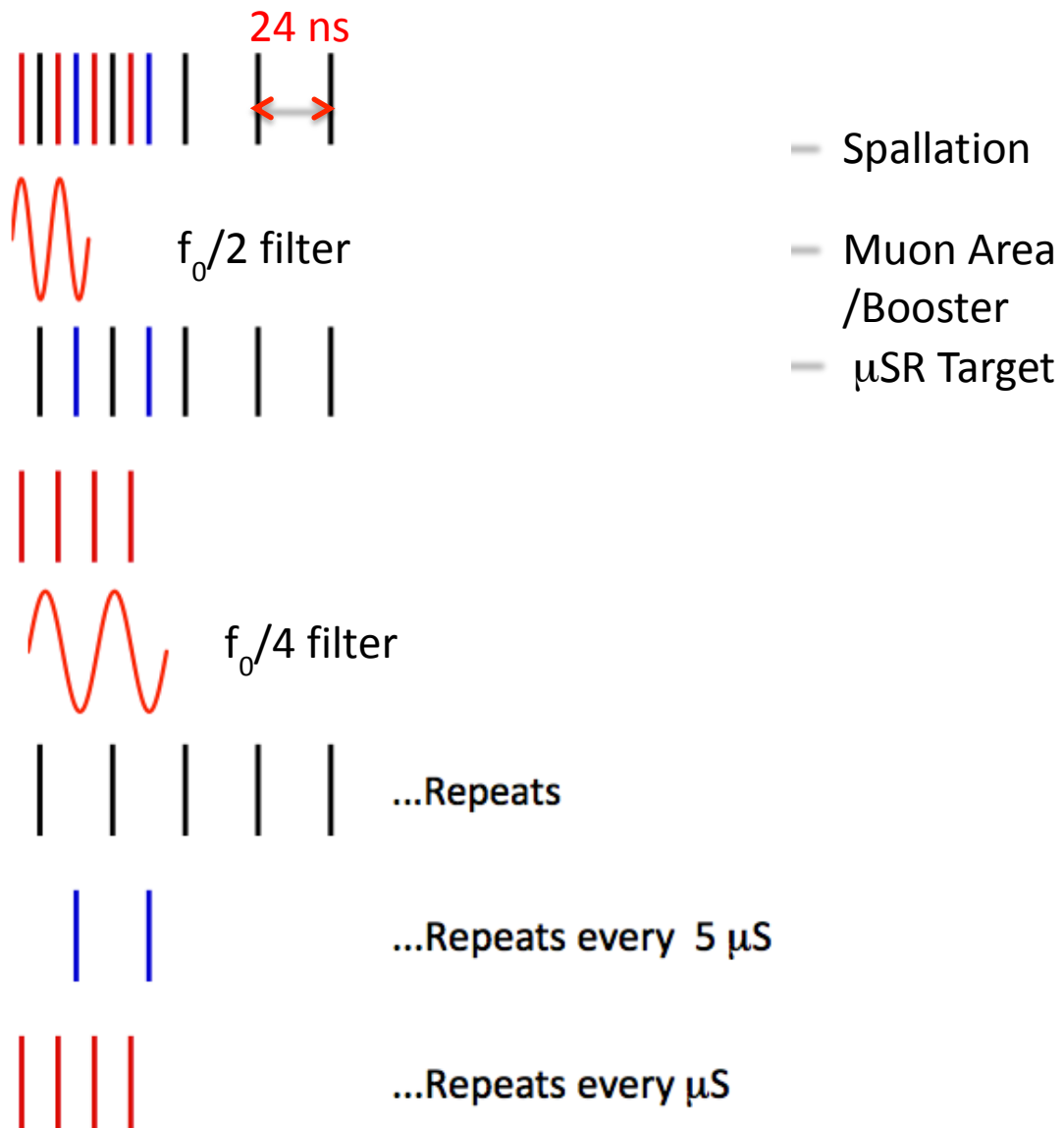


Figure III-16: Conceptual beam structure including dedicated μ SR beamline. See text for details.

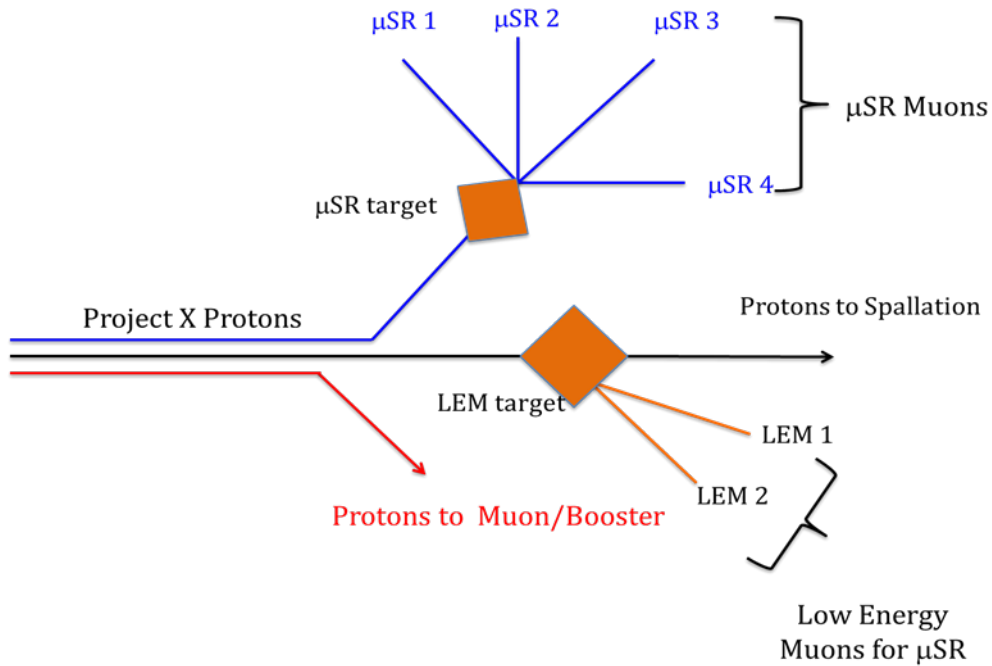


Figure III-17: Design concept for Stage-1 beam layout servicing μ SR endstations.

III.5.3 Beam Intensity

For the purposes of this document, we assume a dedicated beam structure with two sets of pulses as shown in Figure III-16, and two single pulses. The single pulses are appropriate for single-muon μ SR, while the double pulses can service a pulsed μ SR experiment. Importantly, this beam is independent of the high power pulse train which goes to the spallation area and services LEM experiments. We assume 2 LEM beamlines will be made available.

For the purposes of estimating intensity, we use the following parameters, based on experience at the PSI μ E4 beamline:

- i) A conversion factor between protons on target and muons at the experiment of 2×10^{-7} . This factor consists of 5×10^{-8} achieved performance and a factor of 4 from anticipated possible optimizations of a new, dedicated system [Morenzoni2012].
- ii) A number of protons per Project X bunch of 1.3×10^8 . This is consistent with a of 0.9 mA and 40 bunches/ μ s.
- iii) A conversion efficiency for creation of LEM muons of 1.0×10^{-5} .

With these assumptions we obtain:

- i) 2.6×10^6 muons/sec for each of 2 pulsed μ SR beamlines.

ii) A saturated rate of 5×10^4 muons/sec for each of 2 conventional single-muon mSR beamlines.

iii) 1.1×10^4 LEM muons for each of 2 stations.

It should be noted that all of these can run simultaneously. The total power demands of the dedicated μ SR proton lines in this reference concept are 6.8 kW, with each pulsed target receiving 2.25 kW and each conventional station 1.1 kW.

III.5.4 Discussion

The need for μ SR facilities is well-established, and can be expected to grow in the next decade, for example in the use of LEM to explore finite size and interface effects in thin magnetic films. Figure III-18 shows the wide variety of user applications that have been seen at the ISIS facility in recent years. There is every reason to expect that a μ SR facility as outlined above would attract a similar spectrum of interest from the Materials Science and Applied Physics Communities, both inside the United States and worldwide.

LEM muons are of very high current interest, and require MW scale hadron facilities to produce the requisite fluxes of keV muons, because of the inherent inefficiencies in the known conversion processes. The LEM beamlines discussed in the previous section would add invaluable capacity to a very limited set of world facilities in this area. Including such a capability from an early point in the Project X design will allow us to take advantage of optimizations in acceptance and targetry, an exciting possibility not always available to older facilities. In this way the intensity of the LEM beams we discuss can be made very high, on a scale that is competitive with or exceeds beamlines in Europe or Asia. Project X μ SR provides an opportunity for the United States to become a leader in this research methodology.

The design concept is extremely flexible. The beamlines μ SR1- μ SR4 can be programmed by a combination of the driving proton time structure from the Project X linac, the system of muon kickers downstream of the muon production target, and the demand for muons from the experiments (MORE). The intensity of the pulsed muon beamlines will be as high or higher than similar lines in ISIS and J-PARC.

It should be pointed out that the μ SR beam area will also be available for fundamental physics experiments with surface muons. It will be possible to leave space for additional beamlines if desired, which can be fed from more frequent pulses in the Project X linac as the stages of that machine evolve.

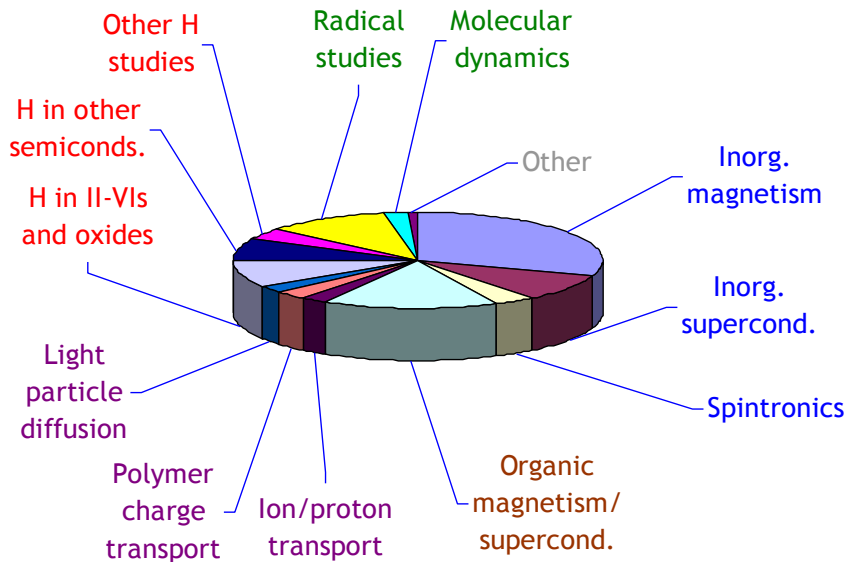


Figure III-18: Variety of user applications at the ISIS facility [Kilcoyne2012]

III.6 Research and Development

No research field is static. In this section we point out some areas in which the science of μ SR may be enhanced by participation of Fermilab in the ongoing development of the technique, and which may prove of eventual use in the program.

III.6.1 Targeting

Fermilab has extensive experience in design and implementation of targets for high intensity proton beams. Projects have been executed for diverse environments, ranging from the APO antiproton creation facility to the underground NuMI long-baseline neutrino beam. The target group at Fermilab is involved in state-of-the-art projects such as the LBNE long-baseline neutrino project, whose final goals are in the multi-MW range for power on target. Moreover, the group has extensive professional connections with other targetry groups around the world, including the UK and RAL. Advancements in targetry design, beginning with simulation studies (typically using MARS) and proceeding through detailed engineering, can be expected to produce optimized target designs for Project X applications, including for μ SR, with concomitant improvements in the efficiency and intensity of the beamlines.

III.6.2 Multi-muon CW Capability with Advanced Detectors

The inability of bulk CW μ SR to benefit from high intensities has been discussed above. One widely discussed approach to reducing the pile-up problems, which limit the usable rate is higher segmentation of both the incoming muon and outgoing positron detectors. Pattern recognition using such detectors may prove able to increase the usable bulk CW μ SR rate by as much as one or two orders of magnitude.

Fermilab's technical expertise in the area of precision position-sensitive particle detectors is immense. Projects as diverse as silicon strip and pixel detectors for collider experiments (CDF, CMS and D0), to scintillating fiber trackers (D0), to precision CCD instruments for astronomy (DES) have been designed, prototyped, assembled, installed, and operated by lab staff, both on the site and remotely. There is an active research group engaged in advancing knowledge about such detectors, as well as advanced test and fabrication equipment and on-site access to a test beam. It is certain that an interest in creating a μ SR facility at Fermilab would benefit from cross-fertilization with this ongoing effort.

III.6.3 Storage Rings

Fermilab has a long history of interest in the possible development of muon storage rings. These efforts include studies of muon colliders, long-baseline neutrino factories, and more recently the NuSTORM proposal for a short-baseline neutrino source located on the Fermilab site. The collection of low-energy muons in a small storage ring would allow the manipulation of the time structure of extracted pulses in such a way as to compress hundreds of Project X pulses into a 10-20 ns pulse. The intensity of such a pulse would be very large (possibly $> 10^8$ muons/sec). This would allow experiments to be carried out very rapidly and accurately. While conceivably a transformational technology, much further work will need to be done to establish the workability of this concept.

III.7 Developing a μ SR community for Fermilab

III.7.1 General Considerations

As accelerator technology has developed, its uses in both the general scientific community and the overall economy have multiplied. Perhaps the best example of reuse of knowledge from particle physics accelerator science is the proliferation and abundant utility of synchrotron light sources, technology derived from electron-positron colliders. Applications of spallation neutron scattering from proton machines has also found wide application and a dedicated community of users within Material Science.

The μ SR community in the United States is reliant on off-shore facilities. It is to be expected that this community will naturally take advantage of a modern, flexible facility, as proposed here, and will grow to include new users and ideas. New local capacity at Fermilab will be part of a change facilitated by Project X and should prove highly attractive to users. However, there are actions that should be carried out in order to maximize the impact of this technology.

III.7.2 The Path Forward

In order to make μ SR in the United States as effective as possible, three paths should be pursued: Adequate user facilities, appropriate laboratory culture and support, and outreach.

User facilities should include technical capacity to handle samples, easily accessible end station setup, staging areas, and technical capacity to make necessary modifications quickly. It is worth noting that the Fermilab test beam effort has already pioneered many of these concepts for users worldwide. Importantly, the facility proposed in this document gives a dedicated user environment which co-exists with other uses of the extremely flexible Project X architecture.

Laboratory culture includes an open and welcoming environment with well-defined hardware and administrative interfaces which do not require years of experience to accomplish a program of experiments, or a single experiment. This has been pioneered by synchrotron light sources, and their example clearly can be adapted. Steps to move towards this model should be taken early, during design and construction of Project X.

Outreach is necessary to bridge the divide between the research areas of fundamental particle physics and user-driven applications. Workshops, colloquia, personal visits and visitor support will all play an important role in both designing the μ SR facility and in understanding its exploitation. The early input of the user community is vital to the success of the undertaking.

III.8 Conclusions

In this document we have pointed out the strong science available via the μ SR technique. Project X Stage 1 at Fermilab provides an opportunity to create a world-class facility using the already planned beam timing structure. This facility fits naturally into the expected uses of the high-intensity Project X beams, and can produce a suite of beamlines and techniques which is compelling. There is adequate time to solicit the input

of the Materials Science community to ensure that the facility will meet the needs of the users.

The proposed μ SR facility provides a window on the materials world which will contribute significantly to the scientific arsenal of the United States. Project X provides a unique opportunity to establish such a facility in well-designed way which complements the broad range of fundamental and applied science available at a high power proton linear accelerator.

III.9 References

- [Abela1999] R. Abela *et al.*, *Hyperfine Interactions* **120/121** (1999) 575.
- [Aczel2008] A.A. Aczel *et al.*, *Physical Review B* **78** (2008) 214503.
- [Aoki2003] Y. Aoki *et al.*, *Physical Review Letters* **91** (2003) 067003.
- [Balsius1999] T. Balsius *et al.*, *Physical Review Letters* **82** (1999) 4926.
- [Bernhard1999] C. Bernhard *et al.*, *Physical Review B* **59** (1999) 14099.
- [Bernhard2012] C. Bernhard, *Physical Review B* **86** (2012) 184509.
- [Bogdanovic1997] B. Bogdanovic and M. Schwickardi, *J. Alloys Cmpd.* **253**, 1 (1997).
- [Boris2011] A.V. Boris *et al.*, *Science* **332** (2011) 937.
- [Budnick1988] J.I. Budnick *et al.*, *Europhysics Lett.* **5** (1988) 651.
- [Burrard-Lucas2013] M. Burrard-Lucas *et al.*, *Nature Materials* **12** (2013) 15]..
- [Callaghan] Callaghan F D, Laulajainen M, Kaiser C V and Sonier J E, *Physical Review Letters* **95** (2005) 197001.
- [Cariuffo1987] R. Cariuffo *et al.*, *Solid State Communications* **64** (1987) 149.
- [Carlo2009] J.P. Carlo *et al.*, *Physical Review Letters* **102** (2009) 087001.
- [Carlo2012] J.P. Carlo *et al.*, *Nature Materials* **11** (2012) 323.
- [Carretta2011] P. Carretta and A. Keren in *Introduction to Frustrated Magnetism: Materials, Experiment, Theory*. Springer Series in Solid-State Sciences **164** (2011) 79

- [Choi2012] S.K. Choi *et al.*, Physical Review Letters **108** (2012) 127204.
- [Chow1996] K.H. Chow *et al.*, Physical Review Letters **76** (1996) 3790.
- [Chow1998] K.H. Chow, B.Hitti and R.F. Kiefl in *Identification of Defects in Semiconductors*, ed. M. Stavola (Academic Press, New York 1998), p.137.
- [Cox2009] S.F.J. Cox, Reports on Progress in Physics **72** (2009) 116501.
- [Cubitt1993] R. Cubitt *et al.*, Nature **365** (1993) 407.
- [Dalmas de Reotier 1997] P. Dalmas de Réotier and A Yaouanc, Journal of Physics: Condensed Matter **9** (1997) 9113–9166.
- [Dalmas de Reotier2006] P. Dalmas de Réotier *et al.*, Physical Review Letters **96** (2006) 127202.
- [Dalmas de Reotier2012] P. Dalmas de Réotier *et al.*, Physical Review B **86** (2012) 104424.
- [Deng2011] Z. Deng *et al.*, Nature Communications **2** (2011) 1.
- [Disseler2012] S.M. Disseler *et al.*, Physical Review B **85** (2012) 174441.
- [Drew2009] A.J. Drew *et al.*, Nature Materials **8** (2009) 310.
- [Drew2009] A.J. Drew *et al.*, Nature Materials **8** (2009) 109.
- [Dunsiger1996] S. R. Dunsiger *et al.*, Physical Review B **54** (1996) 9019.
- [Dunsiger2006] S. R. Dunsiger *et al.*, Physical Review B **73** (2006) 172418.
- [Dunsiger2010] S.R. Dunsiger, Nature Materials **9** (2010) 299.
- [Fleming1976] D.G. Fleming, *et al.*, J. Chem. Phys. **64** (1976) 1281.
- [Fleming2011] D.G. Fleming, *et al.*, J. Chem. Phys. **135** (2011) 184310.
- [Fleming2011_2] D.G. Fleming *et al.*, Science **331** (2011) 448.
- [Friedt1985] J. M. Friedt, F. J. Litterst and J. Rebizant, Physical Review B **32** (1985) 257.
- [Fukai1985] Y. Fukai and H. Sugimoto, Advances in Physics **34** (1985) 263.
- [Gardner1999] J. S. Gardner *et al.*, Physical Review Letters **82** (1999) 1012.

- [Gil1999] J.M. Gil *et al.*, Physical Review Letters **83** (1999) 5294.
- [Ghandi2003] K. Ghandi and P.W. Percival.. *J. Phys. Chem.* **A107** (2003) 3005.
- [Goko2009] T. Goko *et al.*, Physical Review B **80** (2009) 024508.
- [Gonzalez1989] A.C. Gonzalez, *et al.*, J. Chem. Phys. **91** (1989) 6164.
- [Hachitani2006] K. Hachitani, H. Fukazawa and Y. Kohori, Physical Review B **73** (2006) 052408.
- [Harshman1988] D.R. Harshman *et al.*, Physical Review B **38** (1988) 852.
- [Heffner1990] R.H. Heffner *et al.*, Physical Review Letters **65** (1990) 2816.
- [Hillier2009] A. D. Hillier, Physical Review Letters **102** (2009) 117007.
- [Hillier2012] A.D. Hillier *et al.*, Physical Review Letters **109** (2012) 097007.
- [Hitti1997] B. Hitti *et al.*, Hyperfine Interactions **105** (1997) 321.
- [Hitti1999] B. Hitti *et al.*, Physical Review B **59** (1999) 4918.
- [Hofman2012] A. Hofmann *et al.*, ACS Nano **6** (2012) 8390.
- [Ichioka1999] M. Ichioka, A. Hasegawa and K. Machida, Physical Review B **59** (1999) 184; M. Ichioka, A. Hasegawa and K. Machida, Physical Review B **59** (1999) 8902.
- [Ito2007] T.U. Ito *et al.*, Journal of the Physical Society of Japan **76** (2007) 053707.
- [Jackson2000] T.J. Jackson *et al.*, Physical Review Letters **84** (2000) 4958.
- [Kadono1996] R. Kadono *et al.*, Physical Review B **53** (1996) 3177.
- [Kadono1996] R. Kadono *et al.*, Physical Review B **54** (1996) R9628.
- [Kadono1997] R. Kadono *et al.*, Physical Review Letters **79** (1997) 107.
- [Kadono2001] R. Kadono *et al.*, Physical Review B **63** (2001) 224520.
- [Kadono2006] R. Kadono *et al.*, Physical Review B **74** (2006) 024513.
- [Kadono2013] R. Kadono, presentation to J-PARC International Advisory Committee, February 25-26, 2013, Tokai, Japan.

- [Karlsson1995] E. Karlsson *et al.*, Physical Review B **52** (1995) 6417.
- [Kaiser2000] C.T. Kaiser *et al.*, Physical Review B **62** (2000) R9236.
- [Kaneko2008] K. Kaneko *et al.*, Physical Review B **78** (2008) 212502.
- [Khasanov2004] R. Khasanov *et al.*, Physical Review Letters **92** (2004) 057602.
- [Kiefl1986] R.F. Kiefl, *et al.*, Phys. Rev. A. **34** (1986) 681.
- [Kiefl1989] R.F. Kiefl *et al.*, Physical Review Letters **63** (1989) 2136.
- [Kiefl1990] R.F. Kiefl and T.L. Estle in *Hydrogen in Semiconductors*, ed. by J. Pankove and N.M. Johnson (Academic, New York 1990), p.547.
- [Kilcoyne2012] S. Kilcoyne, presentation at Fermilab Muon Spin Rotation Workshop, October 2012.
- [Klauss2008] H.H. Klauss *et al.* Physical Review Letters **101** (2008) 077005.
- [Kojima1995] K. M. Kojima *et al.*, Physical Review Letters **74** (1995) 281.
- [Kojima1997] K. M. Kojima *et al.*, Physical Review Letters **78** (1997) 1787.
- [Kopmann1998] W. Kopmann *et al.*, Journal of Alloys and Compounds **271-273** (1998) 463.
- [Kossler1998] W.J. Kossler *et al.*, Physical Review Letters **80** (1998) 592.
- [Kreitzman1995] S.R. Kreitzman *et al.*, Physical Review B **51** (1995) 13117.
- [Kubo2003] K. Kubo and Y. Kuramoto, Journal of the Physical Society of Japan **72** (2003) 1859.
- [Kubo2004] K. Kubo and Y. Kuramoto, Journal of the Physical Society of Japan **73** (2004) 216.
- [Kuramoto2009] J. Kuramoto, H. Kusunose and A. Kiss, Journal of the Physical Society of Japan **78** (2009) 072001.
- [Laplace2012] Y. Laplace *et al.*, Physical Review B **86**, 020510(R) (2012).
- [Lee1993] S. L. Lee *et al.*, Physical Review Letters **71** (1993) 3862.
- [Lee1997] S. L. Lee *et al.*, Physical Review Letters **79** (1997) 1563.

- [Lichti1999] R.L. Lichti, in *Hydrogen in Semiconductors, II*, ed. by N. Nickel (Academic Press, New York 1999), p.311.
- [Leutkens2003] H. Luetkens *et al.*, Physical Review Letters **91** (2003) 017204.
- [Leutkens2009] H. Leutkens *et al.*, Nature Materials **8** (2009) 305.
- [Luke1989] G.M. Luke *et al.*, Nature **338** (1989) 49.
- [Luke1991] G.M. Luke *et al.*, Physica C **185-189** (1991) 1175.
- [Luke1993] G.M. Luke *et al.*, Physical Review Letters **71** (1993) 1466.
- [Luke1998] G.M. Luke *et al.*, Physical Review Letters **80** (1998) 3843.
- [Luke1998_2] G.M. Luke *et al.*, Nature **394** (1998) 558.
- [Luke2000] G.M. Luke *et al.*, Physica B **289** (2000) 373.
- [Maisuradze2010] A. Maisuradze *et al.*, Physical Review B **82** (2010) 024524.
- [Mannix1999] D. Mannix, G. H. Lander and J. Rebizant, Physical Review B **60** (1999) 15187.
- [Marsik2010] P. Marsik *et al.*, Physical Review Letters **105** (2010) 057001.
- [Masek2007] J. Masek *et al.*, Physical Review Letters **98** (2007) 067202.
- [Matsuda1997] M. Matsuda *et al.*, Physical Review B **55** (1997) 11953.
- [McCollum2009] B.M. McCollum, *et al.*, . Chem. Eur. J. 15 (2009) 8409.
- [Miller2002] R. I. Miller *et al.*, Physical Review Letters **88** (2002) 137002.
- [Miller2006] R.I. Miller *et al.*, Physical Review B **73** (2006) 144509.
- [Morenzoni1994] E. Morenzoni, *et al.*, Physical Review Letters **72** (1994) 2794.
- [Morenzoni2000] E. Morenzoni, *et al.*, Physica **B289-290** (2000) 653.
- [Morenzoni2008] E. Morenzoni *et al.*, Physical Review Letters **100** (2008) 147205.
- [Morenzoni2011] E. Morenzoni *et al.*, Nature Communications **2** (2011) 272.
- [Morenzoni2012] E. Morenzoni, private communication.

- [Nakamura1993] K. Nakamura *et al.*, Solid State Ionics **121** (1999) 301.
- [Niedermayer1993] Ch. Niedermayer *et al.*, Physical Review Letters **71** (1993) 1764.
- [Niedermayer1998] Ch. Niedermayer *et al.* Physical Review Letters **80** (1998) 3843.
- [Niedermayer1999] Ch. Niedermayer *et al.*, Physical Review Letters **83** (1999) 3932.
- [Ofer2009] O. Ofer and A. Keren, Physical Review B **79** (2009) 134424.
- [Ohishi2002] Ohishi K *et al.* Physical Review B **65** (2002) 140505.
- [Olariu2006] A. Olariu *et al.*, Physical Review Letters **97** (2006) 167203.
- [Osborne1953] D.W. Osborne and E.F. Westrum, J. Chem. Phys. **21** (1953) 1884.
- [Park2009] J.T. Park *et al.*, Physical Review Letters **102** (2009) 117006.
- [Patterson1988] B.D. Patterson, Reviews of Modern Physics **60** (1988) 69.
- [Percival1987] P.W. Percival *et al.*, Chem. Phys. Lett. **133** (1987) 465.
- [Percival1988] P.W. Percival, *et al.*, Chem. Phys. **127** (1988) 137.
- [Percival2007] P.W. Percival, *et al.*, Rad. Phys. Chem., **76** (2007) 1231.
- [Percival2011] P.W. Percival, *et al.*, Chem. Eur. J. **17** (2011) 11970.
- [Percival2012] P.W. Percival *et al.*, Organometallics, **31** (2012) 2709.
- [Pitcher2010] M.J. Pitcher *et al.*, Journal of the American Chemical Society **132** (2010) 10467.
- [Pratt2005] Pratt *et al.*, Physical Review B **72** (2005) 121401R.
- [Pratt2011] F.L. Pratt *et al.*, Nature **471** (2011) 612.
- [Price2002] A. N. Price *et al.*, Physical Review B **65** (2002) 214520.
- [Qi2011] X.-L Qi and S.-C Zhang, Reviews of Modern Physics **83** (2011) 1057.
- [Reid1987] I.D. Reid *et al.*, J. Chem. Phys. **86** (1987) 5578.
- [Ricco2011] M. Ricco *et al.*, Nano Letters **11** (2011) 4919.
- [Roduner1978] E. Roduner *et al.*, Chem. Phys. Lett., **57** (1978) 37.

- [Sanna2004] S. Sanna *et al.* Physical Review Letters **93** (2004) 207001.
- [Sanna2011] S. Sanna *et al.* Physical Review Letters **107**, (2011) 227003.
- [Santini2000] P. Santini and G. Amoretti, Physical Review Letters **85** (2000) 2188.
- [Santini2006] P. Santini *et al.*, Physical Review Letters **97** (2006) 207203.
- [Savici2002] A.T. Savici Physical Review B **66** (2002) 014524.
- [Savici2005] A.T. Savici *et al.*, Physical Review Letters **95** (2005) 157001.
- [Schulz2010] L. Schulz *et al.*, Nature Materials **10** (2010) 39.
- [Shay2009] M. Shay, Physical Review B **80** (2009) 144511.
- [Shermandini2011] Z. Shermandini *et al.*, Physical Review Letters **106** (2011) 117602.
- [Shimizu2006] Y. Shimizu *et al.*, Physical Review B **73** (2006) 140407R.
- [Sonier2003] J.E. Sonier *et al.*, Physical Review Letters **91** (2003) 147002.
- [Sonier1994] J.E. Sonier *et al.*, Physical Review Letters **72** (1994) 744.
- [Sonier1999] J.E. Sonier *et al* Physical Review Letters **83** (1999) 4156.
- [Sonier2000] J.E. Sonier, J.H. Brewer and R.F. Kiefl, Reviews of Modern Physics **72** (2000) 769.
- [Sonier2000_2] J.E. Sonier *et al.*, Physical Review B **61** (2000) R890.
- [Sonier2004] J.E. Sonier *et al.*, Physical Review Letters **93** (2004) 017002.
- [Sonier2007] J.E. Sonier *et al.*, Reports on Progress in Physics **70** (2007) 1717–1755.
- [Sonier2007_2] J.E. Sonier *et al*, Physical Review B **76** (2007) 064522.
- [Storchak1994] V. Storchak *et al.*, Physical Review Letters **74** (1994) 3056.
- [Storchak2008] V.G. Storchak, Physical Review Letters **101** (2008) 027202.
- [Sugiyama2009] J. Sugiyama. Physical Review Letters **103** (2009) 147601.
- [Sugiyama2010] J. Sugiyama *et al.*, Physical Review B **81** (2010) 092103.
- [Sugiyama2012] J. Sugiyama, Physical Review B **85** (2012) 054111.

- [Suter2004] A. Suter *et al.*, Physical Review Letters **92** (2004) 087001.
- [Suter2011] A. Suter *et al.*, Physical Review Letters **106** (2011) 237003.
- [Takagiwa2002] H. Takagiwa *et al.*, Journal of the Physical Society of Japan **71** (2009) 31.
- [Tomeno1998] I. Tomeno and M Oguchi, Journal of the Physical Society of Japan **67** (1998) 318.
- [Uemura1991] Y.J. Uemura *et al.*, Physical Review Letters **66** (1991) 2665.
- [Uemura1993] Y.J. Uemura *et al.*, Nature **364** (1993) 605.
- [West2010] R. West and P.W. Percival. Dalton Transactions, **39** (2010) 9209.
- [Wiedinger1989] A. Wiedinger *et al.*, Physical Review Letters **62** (1989) 102.
- [Williams2009] T.J. Williams, Physical Review B **80** (2009) 094501.
- [Yamashita2008] S. Yamashita *et al.*, Nature Physics **4** (2008) 459–462.
- [Yaouanc1998] A. Yaouanc *et al.*, Journal of Physics: Condensed Matter **10** (1998) 9791.
- [Yu1990] D. Yu, *et al.*, Chem. Phys. **142**, 229.
- [Zhao2011] S.R. Zhao *et al.*, Physical Review B **83** (2011) 180402.
- [Zutic2004] I. Zutic *et al.*, Reviews of Modern Physics **76** (2004) 323.

APPENDIX 1 – Accelerator Driven Systems

Since the early 1990's, accelerator driven systems (ADS) – subcritical assemblies driven by high power proton accelerators through a spallation target which is neutronically coupled to the core – have been proposed for addressing certain missions in advanced nuclear fuel cycles. There are several programs at laboratories around the world evaluating the role of ADS in nuclear waste transmutation and energy production. A summary of Accelerator Driven Systems history, technology and technical readiness can be found in [1].

Outside of the US, research into ADS for both transmutation and power generation has been accelerating. In 2001 the European Technical Working Group evaluated the state of ADS technologies and recommended the construction of an experimental ADS. In 2002 an expert group, convened by the Organization for Economic Cooperation and Development's Nuclear Energy Agency (OECD/NEA), authored a comprehensive report entitled *Accelerator Driven Systems (ADS) and Fast Reactors in Advanced Nuclear Fuel Cycles* [2]. In it, they conclude

“On the whole, the development status of accelerators is well advanced, and beam powers of up to 10 MW for cyclotrons and 100 MW for linacs now appear to be feasible. However, further development is required with respect to the beam losses and especially the beam trips to avoid fast temperature and mechanical stress transients in the reactor.”

Technology demonstration has gained momentum with the Belgian government's announcement of its intention to construct MYRRHA [3], an 85-MW prototype ADS at the Belgian Nuclear Research Centre, SCK•CEN. The government has committed to finance 40% of the construction cost, and is preparing for a construction start in 2015. In addition, ADS Program plans have recently been formulated in China. These plans [4] call for a development program leading to a very high power accelerator driving a GW-scale subcritical core by the early 2030s. To reach this ambitious goal a dedicated ADS laboratory is being established. Likewise, the Indian government is considering construction of a prototype ADS facility at a similar scale of MYRRHA. ADS technology development programs exist in Europe, Japan, South Korea, India, China and Russia which are focused on both waste transmutation and power generation.

Accelerator Driven Systems may be employed to address several missions, including:

- Transmuting selected isotopes present in nuclear waste (e.g., actinides, fission products) to reduce the burden these isotopes place on geologic repositories.
- Generating electricity and/or process heat.
- Producing fissile materials for subsequent use in critical or sub-critical systems by irradiating fertile elements.

The principal advantages that accelerator-driven sub-critical systems have relative to critical reactors are twofold: greater flexibility with respect to fuel composition, and potentially enhanced safety. Accelerator driven systems are ideally suited to burning fuels which are problematic from the standpoint of critical reactor operation, namely, fuels that would degrade neutronic characteristics of the critical core to unacceptable levels due to small delayed neutron fractions and short neutron lifetimes, such as ^{233}U and minor actinide fuel. Additionally, ADS allows the use of non-fissile fuels (e.g., Th) without the incorporation of U or Pu into fresh fuel. The enhanced safety of ADS is due to the fact that once the accelerator is turned off, the system shuts down. If the margin to critical is sufficiently large, reactivity-induced transients can never result in a super-critical accident with potentially severe consequences. Power control in accelerator-driven systems is achieved through the control of the beam current, a feature that can be utilized for fuel burnup compensation.

To date no country employs a fuel cycle that destroys the minor actinides (MA) present in used LWR fuel. Minor actinide destruction through transmutation is one mission that ADS are well suited to address. Unlike critical fast reactors which generally incorporate uranium or thorium in the fuel for safe operation, ADS can potentially operate on a pure MA feed stream, meaning a smaller number of ADS can be deployed to burn a fixed amount of minor actinides. ADS can recycle the MA multiple times until it is completely fissioned, such that the only actinide waste stream from these systems would derive from the recycling residuals, which could yield a significant reduction (by a factor of hundreds) in the amount of actinide waste per kW-hr of electricity generated, as compared to a once-through fuel cycle. Because accelerator driven systems do not require fuels containing uranium or thorium, they are more efficient at destroying MA waste – up to seven times more efficient according to one study [1] – than critical reactors, based on grams of minor actinides fissioned per MW-hr of energy generated.

A facility for transmutation of waste would also generate substantial power. An ADS generates high-quality process heat, can be operated at high temperature which could be utilized to produce another form of energy (e.g. biofuels or diesel fuel) or could be used to generate electrical power.

Several proposed ADS concepts with the goal of power production utilize thorium-based fuel to take advantage of some of its benefits, including greater natural abundance (3-4 times greater than uranium), proliferation resistance, and significantly reduced production of transuranics which are a major source of radiotoxicity and decay heat relative to uranium-based fuel. An ADS system based on Th fuel would not require incorporation of fissile material into fresh fuel, and could operate almost indefinitely in a closed fuel cycle.

An accelerator driven system consists of a high-power proton accelerator, a heavy-metal spallation target that produces neutrons when bombarded by the high-power beam, and a sub-critical core that is neutronicly coupled to the spallation target. To achieve good neutronic coupling the target is usually placed at the center of a cylindrical core. The core consists of nuclear fuel, which may be liquid (e.g., molten salt) or solid as in conventional nuclear reactors.

ADS technology has evolved considerably since the last National Research Council study and report nearly two decades ago [5]. There have been several key advances in the last two decades, which make ADS a viable technology that is ready to proceed to the demonstration phase:

- The construction, commissioning and operation of a high-power continuous wave front-end system that meets the beam current performance required for up to 100 mA ADS accelerator system (the Low-Energy Demonstration Accelerator (LEDA) at Los Alamos)
- The construction, commissioning and MW-level operation with acceptable beam loss rates of a modern linear accelerator based on independently-phased superconducting accelerating structures (the Spallation Neutron Source at ORNL)
- The construction and deployment of a wide variety of pulsed and continuous-wave superconducting accelerating structures for proton/ion acceleration over a wide range in particle velocities, which is a key ingredient to achieving high reliability operation
- The high-power beam test of a liquid Pb-Bi eutectic spallation target loop at the Paul Scherrer Institute in Switzerland (the MEGAPIE project), and the operation of a MW-class liquid metal spallation target system at SNS.

Perhaps more important, recent analyses of subcritical reactor response to beam interruptions reveal greater tolerance to and therefore more relaxed requirements for beam trips, which had been a key criticism of previous ADS concepts.

The principal mission of Project X is particle physics. However, the continuous wave MW-class beam in the GeV energy range that is produced is precisely the beam which is needed to demonstrate and further develop key ADS technologies. Should the priorities for externally driven reactor technologies change in the US, Project X would be an ideal research and development platform.

An optimized Target Station would provide the flexibility for supporting key R&D with an emphasis on spallation neutron target and transmutation studies [6]. The R&D focus is on developing, demonstrating and verifying several critical aspects of neutron spallation target systems for ADS:

- Lead-bismuth target R&D including oxygen control, cleanup chemistry, safety in in-beam conditions
- Development and testing of windowless concepts
- Materials irradiation studies relevant to the ADS environment
- Characterization of neutron yield, spectra, spatial distributions, etc.

Fuel studies as described elsewhere in this report are also relevant to the ADS mission. The flagship experiment, which can be carried out with Project X, involves the transmutation of nuclear fuel coupled with reliable accelerator operation.

Finally, Project X provides a platform for the exploration and demonstration of key accelerator technology and accelerator physics solutions that are required for ADS. These include the development and demonstration of very high reliability accelerator operation through automated fault recovery, deployment of specialized diagnostic and control systems, accelerator-target coupling studies, and beam-loss control and mitigation.

References

- [1] Accelerator and Target Technology for Accelerator Driven Transmutation and Energy Production:
http://science.energy.gov/~media/hep/pdf/files/pdfs/ADS_White_Paper_final.pdf
- [2] “Accelerator Driven Systems (ADS) and Fast Reactors in Advanced Nuclear Fuel Cycles,” 2002: <http://www.nea.fr/ndd/reports/2002/nea3109.html>
- [3] H. Ait Abderrahim et. al., Nuclear Physics News, vol. 20, no. 1, 2010, p. 24.
- [4] W.-L. Zhan , “ADS Programme and Key Technology R&D in China,” Proc. 2013 International Particle Accelerator Conference, Shanghai, May 2013.
- [5] “Nuclear Wastes: Technologies for Separations and Transmutation,” National Research Council, National Academies Press, 1996.
- [6] Y. Gohar, D. Johnson, T. Johnson, S. Mishra, Fermilab Project X Nuclear Energy Application: Accelerator, Spallation Target and Transmutation Technology Demonstration:
<http://indico.fnal.gov/getFile.py/access?resId=1&materialId=8&confId=3>

APPENDIX 2 – Project X Muon Spin Rotation Forum

- A) The Project X Muon Spin Rotation Forum occurred at Fermilab October 17–19, 2012
- B) Charge: The muon spin rotation (μ SR) forum will engage μ SR leaders in a discussion of current facilities, the current worldwide μ SR science program, opportunities and requirements of a next generation facility and a discussion on how Project X could serve this community. In particular, opportunities for future bulk μ SR studies with high energy (>4 MeV) and surface muon beams (4 MeV), and low energy (0-30 keV) beams will be discussed.
- C) List of presentations and presenters:
- October 17th, regular Fermilab colloquium:
'Muon Spin Rotation Spectroscopy-Utilizing Muons in Solid State Physics'
A. Suter (PSI)
- October 18th, first day of forum:
- Welcoming remarks,
P. Oddone (FNAL director)
- 'Current Plans and Future Vision of the Fermilab Accelerator Complex',
S. Henderson (FNAL Associate director for accelerators).
- Discussion of PX Stage 1 and R&D Plan',
S. Holmes (FNAL, PX Project Manager)\
- 'Goals and Charge to the μ SR Forum',
R. Tschirhart (FNAL)
- 'Overview of TRIUMF Facilities',
P. Percival (SFU/TRIUMF)
- 'Overview of PSI Facilities'
E. Morenzoni (PSI)
- 'Overview of ISIS Facilities',
S. Kilcoyne (University of Huddersfield)
- 'Possibilities with the Fermilab Muon Campus',
Chris Polly (FNAL)
- 'Towards a next generation muon facility',

R. Cywinski (University of Huddersfield)

‘Making the Case for a Muon Materials Science Facility at FNAL, A
personal view.’,
R. Heffner (LANL)

‘ μ SR Studies of Superconductivity and Magnetism at a Next Generation
Muon Source’,
G. Luke (McMaster University)

October 19th, second day of forum:

‘J-PARC muon beam facilities and slow muon production with laser resonant
ionization’
Yasuhiro Miyake (KEK)

‘Science/Condensed Matter’
Robert Kiefl (TRIUMF)

‘Surface Muon Production at PSI’,
Andreas Suter (PSI), Daniela Kiselev (PSI)

‘Low Energy Muon Production by Moderation’,
Elvezio Morenzoni (PSI)

‘Low energy muon production estimates at Project X’,
Sergei Striganov (FNAL)

APPENDIX 3 – DOE/BES Priorities in materials science

We present in this appendix, lists of known national priorities in DOE funded materials science. Areas of relevancy for muon science are in bold italic type.

2008 DOE/BES Grand Challenges - from observational to control science

- *Control of materials' processes at electronic (quantum) level.*
- Design new forms of matter with tailored properties.
- *Understand and control emergent, collective phenomena.*
- Master energy/information technology on *nanoscale* to rival living systems.
- *Characterize and control matter very far from equilibrium.*

2012 BESAC Subcommittee on Mesoscale Science

- *Master defect mesostructure and its evolution.*
- Optimize transport and response properties by design/control of mesoscale structure.
- *Elucidate non-equilibrium and many-body physics of electrons.*
- Harness fluctuations and degradation for control of metastable *mesoscale* systems.
- Directing assembly of hierarchical functional materials.

This document was prepared as an account of work sponsored by the United States Government. While this document is believed to contain correct information, neither the United States Government nor any agency thereof, nor The Regents of the University of California, nor any of their employees, makes any warranty, express or implied, or assumes any legal responsibility for the accuracy, completeness, or usefulness of any information, apparatus, product, or process disclosed, or represents that its use would not infringe privately owned rights. Reference herein to any specific commercial product, process, or service by its trade name, trademark, manufacturer, or otherwise, does not necessarily constitute or imply its endorsement, recommendation, or favoring by the United States Government or any agency thereof, or The Regents of the University of California. The views and opinions of authors expressed herein do not necessarily state or reflect those of the United States Government or any agency thereof or The Regents of the University of California.